12-1-1997

Real-Time Testing and Analysis of a Full-Scale Viscoelastically Damped Steel Frame

Christopher C. Higgins

Kazuhiko Kasai

LEHIGH
University

REAL-TIME TESTING AND ANALYSIS OF A FULL-SCALE VISCOELASTICALLY DAMPED STEEL FRAME

by

Christopher C. Higgins
Assistant Professor, Clarkson University
Former ATLSS Graduate Research Assistant

Kazuhiko Kasai
Professor, Tokyo Institute of Technology
Former Associate Professor and ATLSS Research Faculty

ATLSS Report No. 97-14

December 1997

ATLSS is a National Center for Engineering Research on Advanced Technology for Large Structural Systems

117 ATLSS Drive
Bethlehem, PA 18015-4729

Phone: (610)758-3535
Fax: (610)758-5553

www.lehigh.edu/~inatl/inatl.html
Email: inatl@lehigh.edu

Acknowledgments

The authors would like to express their appreciation to Professors John W. Fisher, Le-Wu Lu, and Richard Sause, and to Mr. Leslie E. Robertson for their guidance throughout this research project.

The authors would also like to thank 3M Company, Bethlehem Steel, Lukens Steel, and Nippon Steel for their contributions to the project. The National Science Foundation supported the project through its cooperative agreement with the ATLSS Engineering Research Center and the second author's Presidential Young Investigator Award. The Federal Emergency Management Agency (FEMA), through the Earthquake Engineering Research Institute's (EERI's) Graduate Fellowship in Earthquake Hazard Reduction, provided further support for this research.

Many thanks go to the laboratory staff, John Hoffner, Todd Anthony, Steve Leonard, Roger Moyer, and Ed Tomlinson, and the technical and administrative staff of the ATLSS Center for their assistance. Sincere thanks are also extended to graduate students William Bruin, Robert Connor, Perry Green, and Ian Hodgson who were always there with an idea or an extra set of hands.

TABLE OF CONTENTS

LIST OF TABLES

CHAPTER 3

CHAPTER 4

CHAPTER 5

CHAPTER 6

CHAPTER 7

LIST OF FIGURES

CHAPTER 2

CHAPTER 3

CHAPTER 4

CHAPTER 5

CHAPTER 6

CHAPTER 7

ABSTRACT

An experimental and analytical investigation of a full-scale frame with viscoelastic (VE-) dampers was conducted. All tests were conducted in real-time due to the velocity sensitive properties of the VE-material. Harmonic, seismic, and wind forces were considered.

A methodology was developed to test the full-scale lower three story portion of a 10-story prototype frame. The methodology employs time history analysis of the 10-story VE-frame, with a fractional derivative model for the VE-damper behavior, to determine the imposed displacement history at the third story level of the test specimen.

A seismic prototype frame was developed to permit investigation of the earthquake response for a VE-damped frame. The VE-frame exhibited frequency, temperature, and amplitude sensitivities typical of the VE-material. Damping ratio for the frame was relatively stable, while the frame stiffness was highly dependent on damper temperature. Experiments provided comprehensive data including overall frame and local member and connection responses and indicated elastic member response for the different earthquakes considered. Correlative analyses were performed which reasonably predicted the seismic response for typical short duration earthquakes using several models for the VE-damper including: fractional derivative, global Rayleigh damping, and local Rayleigh damping models.

A wind prototype frame was developed to permit investigation of the along-wind and across-wind response for a VE-damped frame. Long duration wind experiments indicated heat convection between the damper and environment should considered. Analyses indicated the VE-dampers significantly reduced the natural frequency vibration which would otherwise be induced by wind gusts.

CHAPTER 1.0 INTRODUCTION

1.1 Introduction

Almost every structure is subjected to forces resulting from natural hazards. Of these natural hazards, earthquake and wind induced forces are of primary concern to the structural engineer. Geographic location of the building generally determines which of these hazards controls design of a structure. Some locations are more prone to earthquakes, while others are subject to high winds, and still others possess equal earthquake and wind hazards.

Wind and seismic forces are random in nature and induce dynamic response of building structures. The two types of dynamic forces have very different frequency contents, intensities, and durations. Wind forces are concentrated in the low frequency regime, occur often, and are generally longer in duration. Earthquakes contain moderate frequencies, occur less frequently and can be significantly intense but are of short duration. These very different characteristics can result in different controlling design criteria depending upon the dynamic properties of a particular building. The size and height of a building have a strong influence on which hazard controls the final design. In general, tall and long period structures are controlled by wind criteria, and shorter period structures are controlled by seismic criteria.

Design criteria for wind and earthquake hazards are often quite different. Current seismic design provisions for steel framed buildings, such as the National Earthquake Hazard Reduction Program (NEHRP) Recommended Provisions for Seismic Regulations for New Buildings [NEHRP, 1994] and Uniform Building Code (UBC) [UBC, 1994], accept the possibility of damage during an earthquake by permitting inelastic behavior to provide energy dissipation. While these design provisions have been successful in maintaining the life safety of building occupants, they may not adequately protect the socio-economic value of the structure. Reliance on inelastic behavior for energy dissipation can result in damage to structural members. This damage may be severe and require demolition or repair of the structure after the earthquake, resulting in significant economic costs. At the same time, design of buildings to remain elastic using only the small inherent damping within the structure is economically prohibitive. Application of supplemental energy dissipation devices, such as viscoelastic dampers (VE-), shows significant potential for providing economic structures which can remain elastic even when subjected to large earthquakes [Kasai and Fu, 1995]. VE-dampers are already being implemented for seismic applications including both new design and retrofit of existing structures. A 13 story steel frame building in San Jose, California and a non-ductile reinforced concrete building in San Diego, California have been retrofitted with VE-dampers. A new mass transit train station roof in Taipei has been designed with VE-dampers to mitigate both seismic and wind vibrations.

Design criteria for wind forces provide for elastic behavior of a building structure when subjected to code prescribed wind loads [ASCE, 1996]. Additional design criteria may include minimizing undesirable building motion in strong and gusty winds, ensuring serviceability of the

structure and mechanical systems at design wind loads, and precluding localized interior damage [Simiu and Scanlan, 1996][Robertson, 1975]. Strength and stiffness requirements for a tall building subjected to code specified forces can be readily achieved, however satisfying other serviceability criteria can be difficult and costly using only the small amount of damping inherent within the structure. As a result, supplemental damping devices to control wind vibrations are becoming more common in tall building design [Hirsch, 1994]. One type of supplemental damping device is the viscoelastic damper. VE-dampers were first used to reduce wind induced vibrations in 1969 for the World Trade Center Towers (110 stories, New York City), and have more recently been used to mitigate wind vibrations in the Columbia SeaFirst building (73 stories, Seattle) and the Two Union Square building (60 stories, Seattle).

Research on the application of VE-dampers for earthquake resistant design has resulted in design provisions and analysis methods for dampers and structural members which are at present not complete. These provisions are based on individual damper tests and reduced-scale shaking table tests and the current models and design methodologies have not been verified by actual VE-frame performance during earthquakes or full-scale tests of VE-damped structures. In general past research has focused on global frame response and neglected local member forces, thus overlooking the interaction between dampers and frame members and subsequent out-of-phase response of the peak member forces. While VE-dampers have been used to mitigate wind vibrations for several decades, there is a lack of design guidance and limited information regarding analysis theory and methods. Past work has focused on examples of applications without providing supporting substantive analysis or design theory.

1.2 Objectives

This report addresses the application of viscoelastic dampers to steel framed buildings to reduce both seismic and wind induced response and has the following main objectives:

- Provide previously unavailable full-scale experimental data for VE-damped structural systems subjected to large magnitude earthquake and wind forces.
- Develop methodologies to test the dynamic response of full-scale VE-damped structures including both wind and seismic forces.
- Provide data which include local frame member force response, overall structure equilibrium, VE-damper response and temperature rise, as well as overall frame response.
- Conduct tests on an individual VE-damper to determine damper material properties subjected to different initial damper temperatures, loading frequencies, and strain amplitudes. Compute analytical properties for an available VE-damper finite element model. Perform correlative analyses of individual damper test results.
- Conduct tests on the frame without dampers to evaluate frame stiffness, damping, local connection response, and develop an analytical model of the unbraced frame.
- Conduct tests on the VE-damped frame to evaluate initial damper temperature, loading frequency, and VE-material strain amplitude sensitivities of the VE-frame.
- Perform correlative analyses of test results to evaluate the effectiveness of existing analysis methods for predicting structural response. Provide refinement for methods where necessary.
- Provide or refine existing practical design methodologies for VE-damped frames.

1.3 Organization of Report

This report is organized into eight chapters as follows:

Chapter 2 presents linear and nonlinear theories of VE-materials and their harmonic properties, constitutive rules for modeling, and typical VE-damper configurations. Previous research related to wind and seismic applications of VE-dampers is also reviewed.

Chapter 3 describes tests of an individual VE-damper used to characterize material properties, identify important damper parameters, and determine damper behavior under short duration and long duration dynamic loads. Correlative analyses of the experimental damper response are also described.

Chapter 4 presents results of tests on the steel frame before installation of VE-dampers. Test results including overall frame stiffness, connection response, and damping ratio are presented. An analytical model of the unbraced frame is developed for use in subsequent analyses of the VE-frame.

Chapter 5 presents experimental and analytical findings for the VE-frame subjected to sinusoidal loading at different VE-damper initial temperatures, loading frequencies, and VE-damper strain amplitudes. In addition to sinusoidal tests, relaxation test results are presented which address VE-frame behavior for slowly applied loads. Measured local member and damper forces as well as connection responses are presented in addition to overall force

equilibrium and global frame response. Sinusoidal responses at different VE-damper initial temperatures, loading frequencies, and VE-material strain amplitudes are analyzed using sophisticated nonlinear time-history analysis and simplified elastic analysis methods. Advantages and disadvantages for each method are summarized.

Chapter 6 presents experimental and analytical findings for seismic behavior of the VE-frame. The unique testing methodology is described, a prototype building subjected to earthquake forces is developed, and the damper and frame design methodology is presented. Measured local member and damper forces are presented in addition to overall force equilibrium and global frame response. Analyses are performed to determine seismic response of the VE-frame and design recommendations are made based on the test results.

Chapter 7 provides experimental and analytical findings for the VE-frame subjected to simulated wind forces. A prototype building subjected to wind forces is developed and the design methodology is presented. Measured local member and damper forces are presented in addition to overall force equilibrium and global frame response. Analyses are performed to determine the role of VE-dampers on wind induced vibrations and a random vibration analysis procedure is presented for wind applications.

Chapter 8 presents a research summary, significant findings, and recommendations for future research.

CHAPTER 2.0 BACKGROUND

2.1 Introduction

Viscoelastic materials are typically made of polymers or glassy substances. The structure of polymer VE-materials is characterized by long molecular chains which may be strongly or weakly linked [Nashif *et al.*, 1985]. Damping arises from the stretching and time-dependent relaxation of these molecular chains when subjected to deformations. When deformed, the material exhibits the combined properties of an elastic solid and viscous liquid. Actual response of the material is highly dependent on loading frequency, temperature, and to a lesser extent on strain amplitude.

2.2 Linear Viscoelastic Theory

A linear viscoelastic law can used to describe the material behavior when subjected to direct shear [Bergman and Hanson, 1993]. Typical steady state response of a VE-material subjected to sinusoidal shear deformation is shown in Fig. 2.1. The shear stress $\tau(t)$ and shear strain $\gamma(t)$ can be expressed:

$$\gamma(t) = \gamma_o \sin(\omega t) \qquad [2.1]$$

$$\tau(t) = \tau_o \sin(\omega t + \delta) \qquad [2.2]$$

where γ_o is the peak shear strain, τ_o is the peak stress, ω is the circular frequency of loading (rad/sec), and δ is the phase lag angle (rad) between stress and strain. The shear stress leads the shear strain by a lag time δ/ω as shown in Fig. 2.1. Shear stress can also be expressed as:

$$\tau(t) = \gamma_o\left[G' \sin(\omega t) + G'' \cos(\omega t)\right] \qquad [2.3]$$

where G' is the storage modulus or the component which is in-phase with strain (representing the energy stored and recovered per cycle) and G'' is the loss modulus or the component which is out-of-phase with strain (representing the energy dissipated per cycle) defined as:

$$G' = \frac{\tau_o}{\gamma_o}\cos(\delta) \qquad [2.4]$$

$$G'' = \frac{\tau_o}{\gamma_o}\sin(\delta) \qquad [2.5]$$

Combining Eq. 2.1 with Eq. 2.3 and making use of the relationship $\cos^2(\omega t) + \sin^2(\omega t) = 1$, results in the equation of an ellipse representing the steady state $\tau(t)$-$\gamma(t)$ hysteresis for the material (Fig. 2.2):

$$\tau(t) = G'\gamma(t) \pm G''\sqrt{\gamma_o^2 - \gamma(t)^2} \qquad [2.6]$$

The hysteresis is a combination of a straight line $\tau(t) = G'\gamma(t)$ which represents the elastic component and $\tau(t) = \pm G''\sqrt{\gamma_o^2 - \gamma(t)^2}$, which represents the viscous or energy dissipation component as shown in Fig. 2.3. Considering the phase relationships of these properties, the storage modulus indicates stiffness and the loss modulus indicates the energy dissipation capability of the material. The loss factor η is defined as:

$$\eta = \frac{G''}{G'} = \tan(\delta) \qquad [2.7]$$

Larger values of η result in fat hysteresis loops of large area while small η values result in thin hysteresis around a straight line as illustrated in Fig 2.4. As described by Eq. 2.7, η is directly related to the magnitude of the lag angle between shear stress and strain. Therefore, larger hysteresis and energy dissipation results as the shear stress becomes more out-of-phase with strain.

An alternative formulation for the stress and strain response can be described using complex variables. Eqs. 2.1 and 2.2 can be expressed as:

$$\gamma(t) = \gamma_o e^{i\omega t} \qquad [2.8]$$

$$\tau(t) = \tau_o e^{i\omega t} \qquad [2.9]$$

At steady state, the complex modulus G^* is defined as:

$$G^* = \frac{\tau(t)}{\gamma(t)} \qquad [2.10]$$

Substituting Eqs. 2.8 and 2.9 into Eq. 2.10, it can be shown G^* becomes independent of time t and can be expressed as a combination of a real component G' and an imaginary component G'':

$$G^* = \frac{\tau(t)}{\gamma(t)} = \frac{\tau_o}{\gamma_o} e^{i\omega} = \frac{\tau_o}{\gamma_o}(\cos\delta + i\sin\delta) = G' + iG'' = G'(1 + i\eta) \qquad [2.11]$$

This relationship is useful for determining G' and G'' from experimental tests of VE-dampers as will be discussed in Chapter 3. This is implemented by noting from Fig. 2.2:

$$\left|G^*\right| = \frac{\tau_o}{\gamma_o} = \sqrt{G'^2 + G''^2} \qquad [2.12]$$

Constitutive modeling of VE-materials must account for the frequency sensitivity of the material. This can be accomplished by adjusting the $\tau(t)$-$\gamma(t)$ constitutive relationship and the time derivatives of these. There are two well known constitutive models for VE-materials: the integer derivative rule and the fractional derivative rule. The integer derivative rule uses integer derivatives of the $\tau(t)$-$\gamma(t)$ relationship. A typical integer derivative model consists of different arrangements of springs and dashpots to represent the VE-damper material behavior. To model the frequency ranges of interest, this model requires a large number of constitutive terms.

The fractional derivative model (FDM) uses fractional derivatives of the $\tau(t)$-$\gamma(t)$ relationship and can provide good results over a wider frequency range using only a few constitutive terms. The first use of FDM for modeling of VE-materials was first proposed by Gemant [1936] and the method has been used in the mechanical and aerospace engineering fields, as well as for seismic analysis of base isolated structures [Koh and Kelly, 1990]. The fractional derivative constitutive rule [Kasai *et al.*, 1993] is defined as:

$$\tau(t) + aD^{\alpha}\tau(t) = G\left[\gamma(t) + bD^{\alpha}\gamma(t)\right] \qquad [2.13]$$

where a and b are constants, G = an elastic parameter, and α is the fractional derivative order ($0 < \alpha < 1.0$), D^{α} is the fractional derivative operator, $D^{\alpha}\tau(t)$ and $D^{\alpha}\gamma(t)$ are defined according to the Riemann-Liouville integral. Using the fractional derivative rule, it has been

shown [Kasai *et al.*, 1993] that the storage modulus G' and loss modulus G'' can be expressed as:

$$G' = G\frac{\left[1+b\omega^{\alpha}\cos(\alpha\pi/2)\right]\left[1+a\omega^{\alpha}\cos(\alpha\pi/2)\right]+\left[ab\omega^{2\alpha}\sin^{2}(\alpha\pi/2)\right]}{\left[1+a\omega^{\alpha}\cos(\alpha\pi/2)\right]^{2}+\left[a\omega^{\alpha}\sin(\alpha\pi/2)\right]^{2}} \quad [2.14]$$

$$G'' = G\frac{\left[b\omega^{\alpha}\sin(\alpha\pi/2)\right]\left[1+a\omega^{\alpha}\cos(\alpha\pi/2)\right]-\left[a\omega^{\alpha}\sin(\alpha\pi/2)\right]\left[1+b\omega^{\alpha}\cos(\alpha\pi/2)\right]}{\left[1+a\omega^{\alpha}\cos(\alpha\pi/2)\right]^{2}+\left[a\omega^{\alpha}\sin(\alpha\pi/2)\right]^{2}} \quad [2.15]$$

and the loss factor η as:

$$\eta = \frac{G''}{G'} = \frac{[b-a]\omega^{\alpha}\sin(\alpha\pi/2)}{1+[a+b]\omega^{\alpha}\cos(\alpha\pi/2)+ab\omega^{2\alpha}} \quad [2.16]$$

These relationships provide a material constitutive rule which permits accurate modeling of the material behavior over a sufficiently wide frequency range.

2.3 Nonlinear Viscoelastic Behavior Due to Temperature Rise

VE-material properties are strongly dependent on temperature in addition to loading frequency and amplitude. Temperature dependence for G' is shown schematically in Fig. 2.5 where θ_{ref} is the reference temperature, θ_1 and θ_2 are temperatures below and above the reference temperature ($\theta_1 < \theta_{ref} < \theta_2$). For a given frequency ω, G' is shown as points A, B, and C for temperatures θ_1, θ_{ref} , and θ_2 respectively. For colder temperatures, G' is larger than at warmer temperatures, however, the shape of the G'-temperature relationship is similar for the three temperatures. This permits application of the temperature-frequency equivalence property

which relates $G'(\omega)$ at any temperature θ to the reference temperature θ_{ref} [Kasai *et al.*, 1993] (Fig. 2.5b):

$$G'(\omega)\big|_{\theta ref} = G'(c\omega)\big|_{\theta} \qquad [2.17]$$

where $c(\theta)$ is a shifting factor and is a function of temperature. The shifting factor can be computed according to Ferry [1980]:

$$c = e^{-p_1(\theta-\theta_{ref})/(p_2+\theta-\theta_{ref})} \qquad [2.18]$$

where p_1 and p_2 are constants depending on the specific VE-material.

During dynamic loading of a VE-damper, the VE-material dissipates energy in the form of heat. As the temperature rises within the VE-material, the stiffness and damping of the damper can change. This results in nonlinear behavior for the material as it softens during loading. This effect is shown in Fig. 2.6a where the stiffness at later cycles is reduced compared to earlier cycles as the temperature rises as shown in Fig. 2.6b. Temperature effects can be accommodated by updating the parameters in the constitutive model using the temperature shifting factor described previously. The constants a and b [Kasai *et al.*, 1993] for the fractional derivative model can be related to the values at the reference temperature:

$$a = a_{ref} c^{\alpha} \qquad [2.19]$$

$$b = b_{ref} c^{\alpha} \qquad [2.20]$$

Using this modification, parameters used in the fractional derivative model are made independent of temperature. This temperature independence occurs as seen from Eq. 2.14, because $G'(\omega)$ and $G'(c\omega)$ remain the same regardless of the value of c (Fig. 2.5b). As a result, only modification of a and b are necessary to shift G' as the VE-damper temperature

changes. Actual implementation of the constitutive rule and temperature shifting factors for the dampers used in this study are illustrated in Appendix A.

2.4 Typical VE-Dampers

Typical VE-dampers consist of a layer or layers of VE-material bonded to steel plates as illustrated in Fig. 2.7. The material is placed between two plates which undergo relative deformation resulting in shearing of the material as shown in Fig. 2.8. The in-phase damper stiffness K_d' is related to VE-material storage modulus G', the total VE-material shear area A, and VE-material thickness h as:

$$K_d' = \frac{G'A}{h} \qquad [2.21]$$

The out-of-phase damper stiffness K_d'' is related to VE-material loss modulus G'', the total VE-material shear area A, and VE-material thickness h as:

$$K_d'' = \frac{G''A}{h} = \eta_d K_d' \qquad [2.22]$$

where η_d is the material loss factor. The complex damper stiffness K^*_d is related to the in-phase damper stiffness and loss factor as:

$$K^*_d = K_d' + iK_d'' = K_d'(1 + i\eta_d) \qquad [2.23]$$

Average damper shear strain $\gamma(t)$ is determined by dividing the damper deformation u(t) (Fig. 2.8) by the material thickness h as:

$$\gamma(t) = \frac{u(t)}{h} \qquad [2.24]$$

Average shear stress $\tau(t)$ in the VE-material is computed as:

$$\tau(t) = \frac{P(t)}{A} \qquad [2.25]$$

where P(t) is the damper force. The peak damper force P_o can be determined from the material loss factor η_d, in-phase damper stiffness K'_d, and peak damper deformation u_o as:

$$P_o = K'_d u_o \sqrt{1+\eta_d} \qquad [2.26]$$

Large structural dampers typically contain alignment bolts which allow shearing deformation but limit out-of-plane deformations and separation of the plates thus preventing tensile stresses perpendicular to the VE-layer as discussed further in Chapter 4. The VE-damper is made part of a diagonal brace, or located on K-bracing so that lateral deformation of the structure results in shearing deformation of the VE-damper. Some previous configurations used for VE-dampers are illustrated in Fig. 2.9.

2.5 Previous Work (Wind Applications)

While VE-dampers for wind applications have been used for many years, relatively little work has been published regarding detailed design methodologies, response analysis, or theory regarding interaction of wind forces and building response resulting from introduction of VE-dampers. VE-damper performance and material properties under harmonic excitation were

presented for VE-dampers by Mahmoodi [1969]. Application of VE-dampers for wind response mitigation and performance of the selected dampers has been described for the Columbia SeaFirst building [Mahmoodi and Keel, 1986][Keel and Mahmoodi, 1986]. Wind tunnel studies predicting structural response from a global increase in damping (from VE-dampers) have been performed [Skilling *et al.*, 1986]. Cermak *et al.* [1993] conducted wind tunnel studies of a suspension roof with VE-dampers connected to the aerodynamic model. The damping provided by the VE-dampers and used in the aerodynamic model was estimated using methods developed for seismic applications. Long term performance of VE-dampers, indicating no significant aging or environmental effects, has been reported [Aiken *et al.*, 1990]. Response of the World Trade Center Towers from ambient wind conditions has been used to determine the actual amount of damping in the structure and reported measurements indicated the design damping level was achieved with the VE-dampers [Mahmoodi *et al.*, 1987].

2.6 Previous Work (Seismic Applications)

The interest in VE-dampers for seismic design applications is a relatively recent development, however, significant research has been conducted in this area. Research conducted to date includes experimental and analytical studies, as well as the development of design methodologies.

Experimental work is comprised of tests on individual VE-dampers or reduced scale studies building frames and subassemblages. One of the first experimental studies of an individual VE-damper for seismic applications was conducted by Bergman and Hanson [1986]. Individual tests of reduced scale VE-dampers have also been conducted to characterize damper properties as part of shaking table studies [Chang *et al.*, 1991], [Lin *et al.*, 1991], [Chou, 1994]. Individual dampers have been studied to investigate potential applications, to characterize the material properties, provide data for analytical prediction of damper response. Other tests of individual VE-dampers were conducted to verify design assumptions before acceptance and installation [Blondet, 1993]. In general, individual damper tests demonstrated frequency and temperature sensitivities of the material, and indicated significant damping provided by the material and potential for reducing seismic response.

Testing of steel structural systems with VE-dampers has been restricted to reduced-scale structural models, including shaking table studies and sinusoidal eccentric mass shaker excitations. Several shaking table studies have been conducted. Soong *et al.* [1990][Lin *et al.*, 1991], conducted tests of an approximately ¼ scale three-story steel frame. A ¼ scale nine story steel moment resisting frame with VE-dampers was investigated by Aiken and Kelly [1991][Aiken *et al.*, 1993]. A 2/5 scale five story VE-damped steel moment resisting frame was studied by Chang *et al.* [1991]. Chang *et al.* [1994] also tested a 2/5 scale three story VE-damped steel moment resisting frame into the inelastic range. A five story steel frame, at moderate scale, was subjected to sinusoidal excitations using an eccentric mass shaker [Lai *et al.* 1995][Chang *et al.* 1995]. Although this study increased the scale of the specimen, the applied forces and displacements were not increased. In general, for these studies, temperature

effects were reported as being significant to the performance of the structure and the VE-dampers reduced frame response compared to equivalent undamped structures. No significant interaction among structural members and VE-dampers was reported and the global frame response was the focus of these studies.

Many analytical studies have been performed to model individual VE-damper behavior and structural response of VE-damped systems. Different models have been developed to predict individual damper performance including models using assemblies of springs and dashpots [Kirekawa *et al.*, 1992], and fractional derivative models [Kasai *et al.*, 1993][Tsai and Lee, 1993].

Several approaches have been used to predict structural response of VE-damped buildings. These include a global Rayleigh damping method, which computes an equivalent viscous damping using a modal strain energy approach to model the VE-damping [Chang *et al.*, 1992][Soong and Lai, 1991][Inaudi *et al.*, 1993], local Rayleigh damping approach which models the VE-dampers as a dashpot and spring in parallel [Abbas and Kelly, 1993], and fractional derivative models for the damper which includes frequency sensitivities [Tsai and Lee, 1993] and both frequency and temperature effects [Kasai *et al.*, 1993][Kasai *et al.*, 1994]. Modal analysis procedures for VE-damped structures were presented by Munshi and Kasai [1994] and simplified methods for estimating the damping and seismic response of VE-damped frames were developed by Sause *et al.* [1994]. Simplified static methods with modifications to predict member and damper forces [Kasai and Fu, 1993]. Zhang and Soong [1992]

investigated the optimum placement of VE-dampers within the structure. Kasai and Munshi [1994] investigated the response of VE-damped structures with yielding elements.

Several deign methodologies have been proposed for earthquake resistant design using VE-dampers. Abbas and Kelly [1993] presented a design method using simplified analytical procedures which model the damper as a combination of a spring and dashpot. Chang *et al.* [1993a][1993b] proposed a trial and error design procedure using a modal strain energy method to predict equivalent viscous damping ratio for the VE-structure. Zhang and Soong [1992] proposed a similar method. Kasai and Fu [1995] proposed a NEHRP code based approach, simplified preliminary design method, and modifications for design of frame members including out-of-phase effects from the dampers. None of these proposed design methodologies have been verified through full-scale tests or past performance of VE-frame response during actual earthquake induced motions.

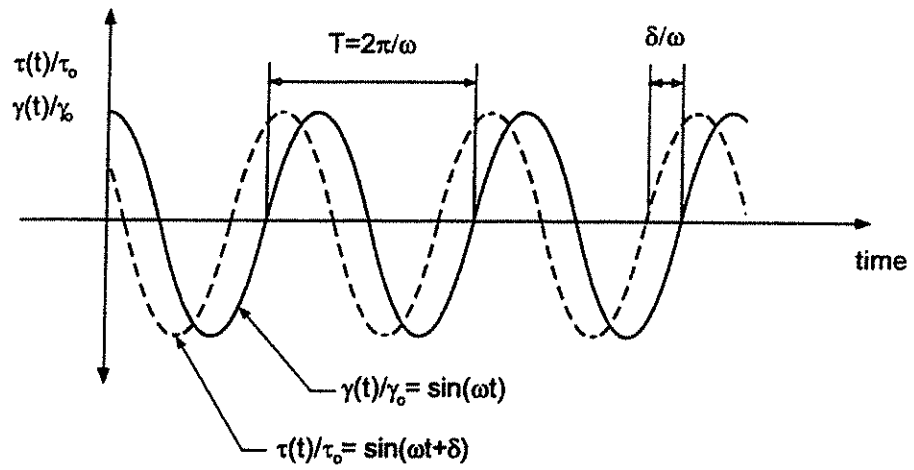

Fig. 2.1 - Normalized harmonic time lag response between shear stress and strain.

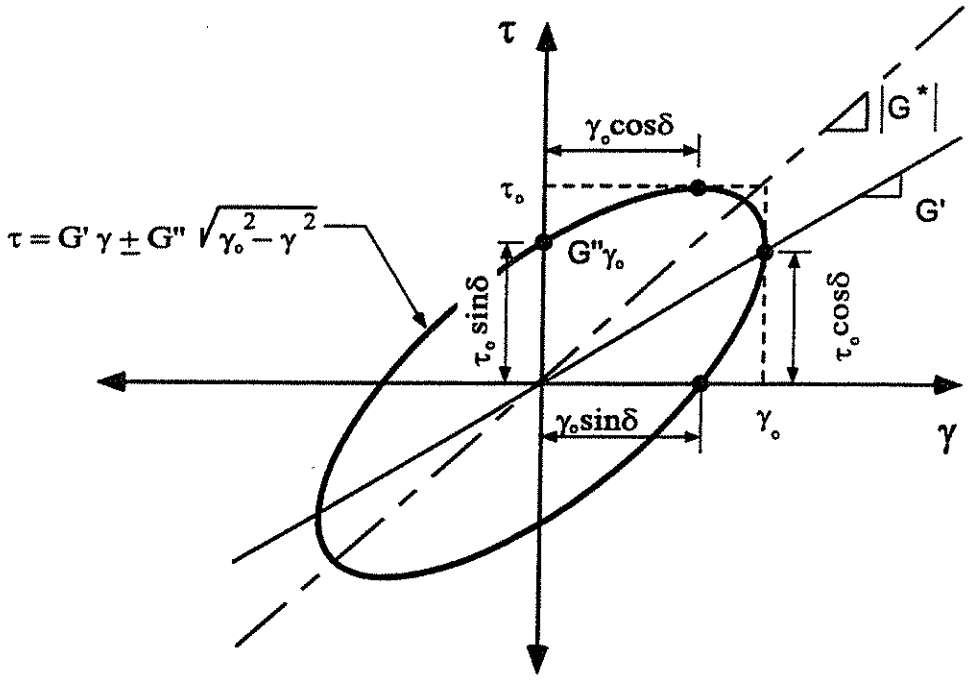

Fig. 2.2 - Harmonic shear stress-strain response of VE-material.

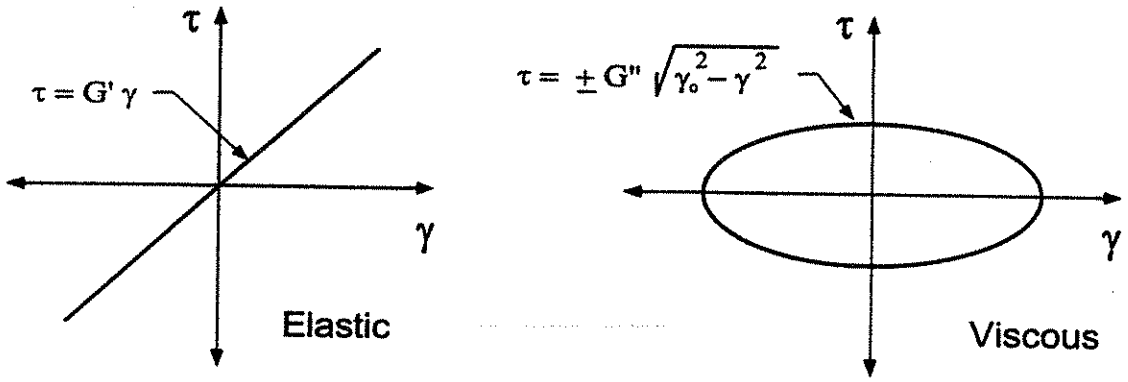

Fig. 2.3 - Elastic and viscous components of harmonic viscoelastic material behavior.

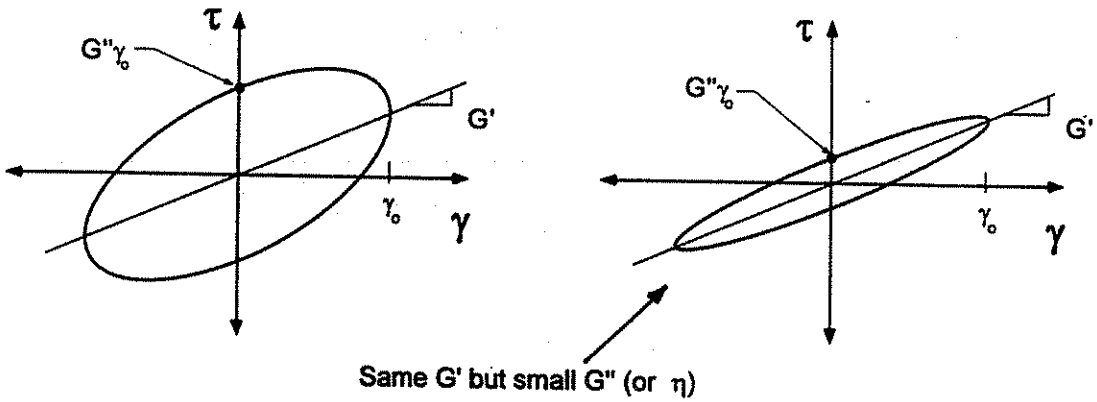

Fig. 2.4 - Relationship between area of elliptical stress-strain response and loss factor η.

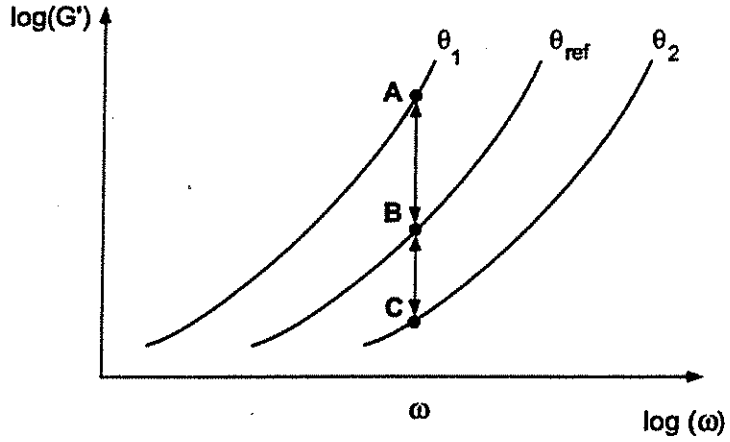

Fig. 2.5a - Temperature dependence for G' indicating larger G' for colder temperatures and smaller G' for warmer temperatures, yet shape of curves are similar for all temperatures.

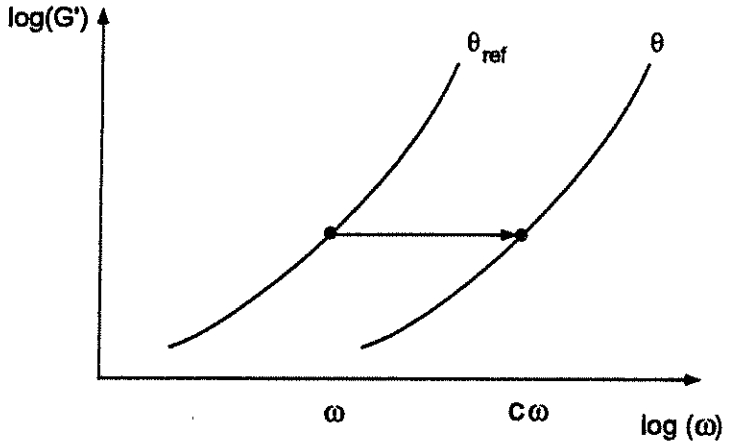

Fig. 2.5b - Role of temperature shifting factor c.

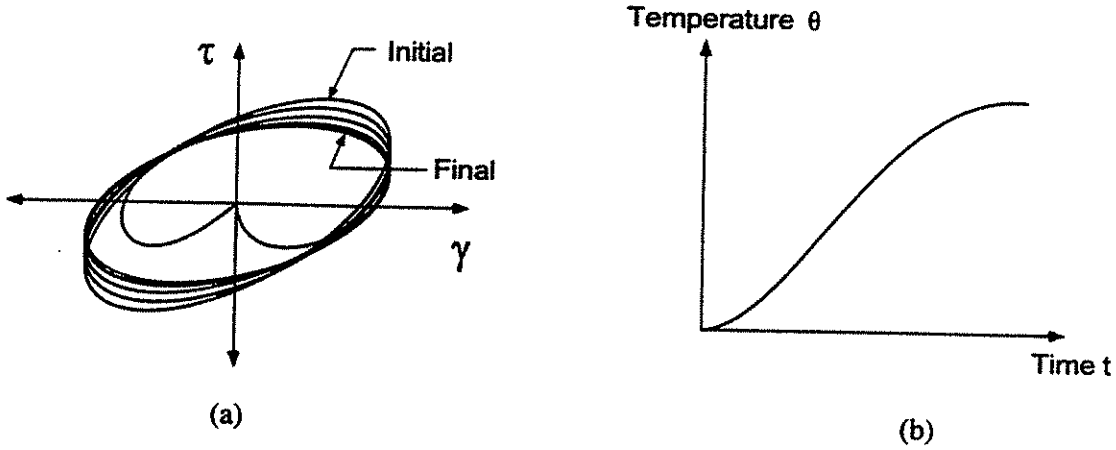

Fig. 2.6 - Damper stiffness decreases (a) as temperature rises (b).

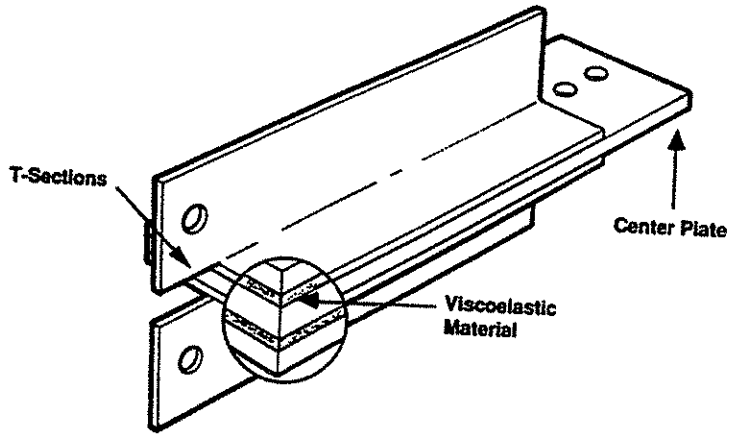

Fig. 2.7 - Typical VE-damper.

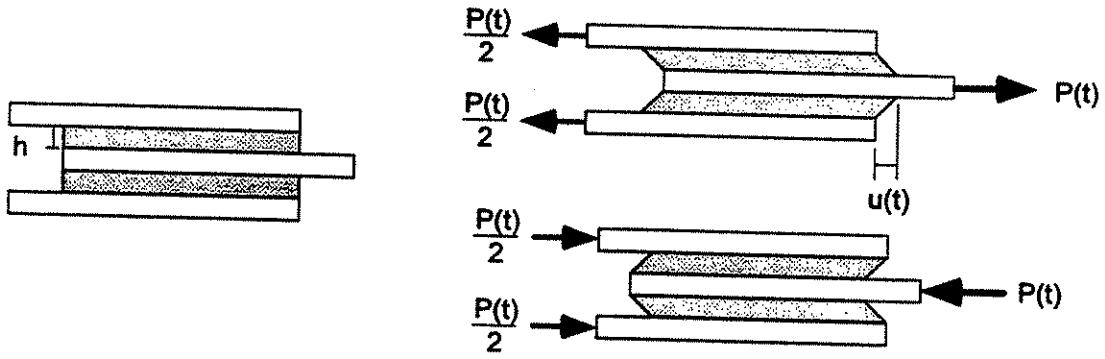

Fig. 2.8 - Shear deformation of VE-material.

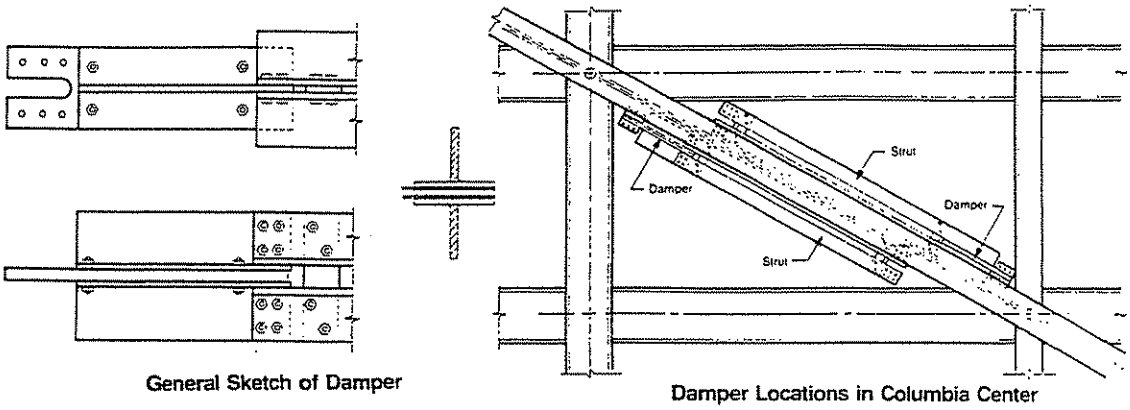

Fig. 2.9a - VE-dampers used in Columbia Seafirst Center [Keel and Mahmoodi, 1986].

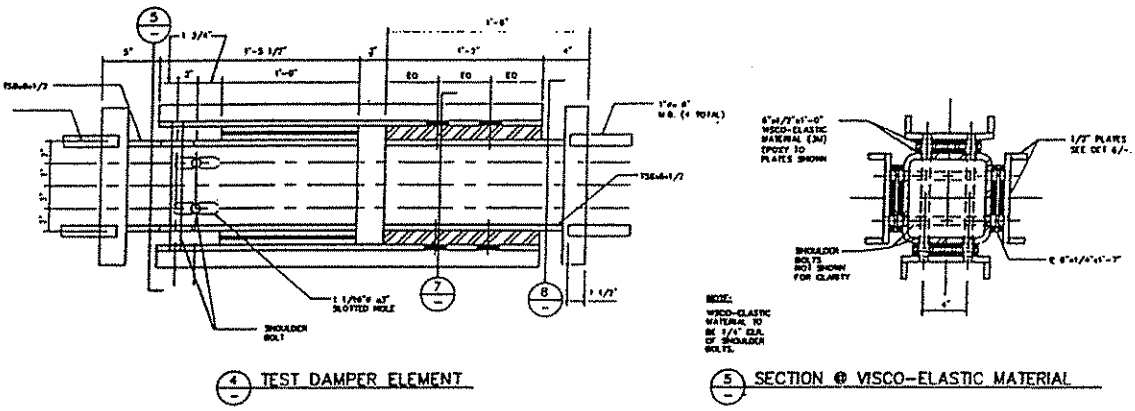

Fig. 2.9b - VE-dampers used for Santa Clara Courthouse retrofit [Blondet, 1993].

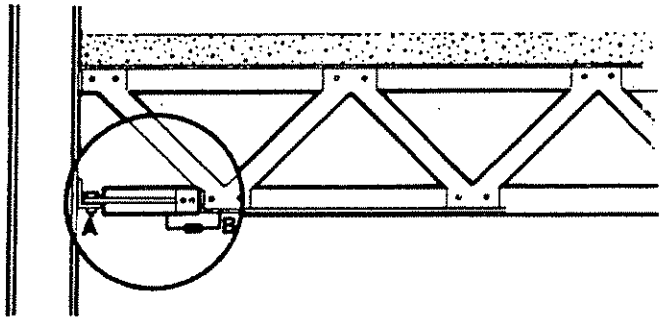

Fig. 2.9c - VE-dampers used in World Trade Center Towers [3M, 1995].

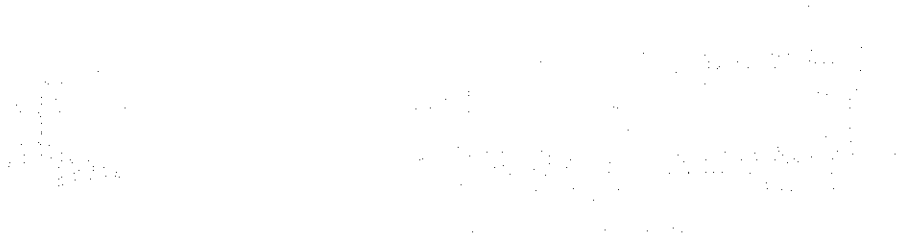

CHAPTER 3.0 INDIVIDUAL DAMPER EXPERIMENT and ANALYSIS

3.1 Introduction

VE-dampers typically consist of VE-material bonded between steel plates and relative deformation of the plates results in shearing deformation of the VE-material. Behavior of a VE-damper is dependent on three parameters: temperature, loading frequency, and strain amplitude. At lower temperatures, higher frequencies, and smaller amplitudes, VE-dampers are typically stiffer than at higher temperatures, lower frequencies, and larger amplitudes. When subjected to dynamic forces, VE-dampers dissipate energy through the build-up of heat. As the temperature rises within the VE-damper due to energy dissipation, the damper softens resulting in non-linear response of the material.

To assess the behavior and determine the material properties of the VE-dampers to be used in subsequent frame tests, a series of experiments were conducted on a full-scale individual damper. The individual damper was identical to those installed in the VE-damped frame as will be discussed in Chapter 5. Experimental parameters investigated included several loading frequencies, damper strain amplitudes, initial temperatures, and loading durations. Following experimental tests, material properties were calculated and analyses performed to correlate the measured damper response.

3.2 Experimental Specimen and Test Set-up

The individual VE-damper was designed specifically for a prototype building subjected to seismic forces and damper design is discussed in Chapter 6. The damper consisted of eight pads of 5/8 in. thick VE-material bonded between an 8x8x1/2 steel tube and four MC 8x13.75 channel sections as shown in Figs. 3.1 and 3.2. Cross sections of the damper through the channel to tube connection and VE-material are shown in Figs. 3.1b and 3.1c respectively. The VE-material used in the damper was 3M Brand ISD 110, an acrylic based polymer. Eight pads of VE-material were located on the faces of the steel tube to provide a total shear area of 1248 in^2. The four faces of the steel tubing permitted placement of a large area of VE-material in a relatively small volume of space. Channel sections were selected to provide sufficient axial buckling strength ensuring force transfer from the channels to the VE-material. A 1.5 in. gap was located near the top of the tube (Fig. 3.1) to allow relative deformation to take place between the tube ends and permit shear deformation of the VE-material as shown in Fig. 3.3. Channel sections were slot welded to the tube section above the gap. Shoulder bolts were provided to ensure alignment of the channels with the tube and limit out-of-plane deformation of the damper. Overall length was 78 in. and the damper represents one of the largest dampers tested in North America as illustrated in Fig. 3.4.

The VE-damper was placed in a loading frame as shown in Fig. 3.5. A single 220 kip capacity, dynamic double-acting hydraulic actuator was used to apply displacements to the

damper. All tests were performed under displacement control. Feedback for actuator control was provided by a 1.5 in. displacement transducer which monitored actual VE-material deformation. Hydraulic oil was supplied to the actuator by a 120 gpm, 3000 psi hydraulic supply, 40 gpm hydraulic service manifold, and 40 gpm servo-valve. The servo-valve was controlled using PC-based Vickers control software.

Data were acquired using a PC-based Keithley Metrabyte DAS1802-ST-DA data acquisition board and two EXP-1800 multiplexing boards. Sampling rates were varied for different tests and are shown in Table 3.1. Instrumentation for the individual damper experiments consisted of 32 channels of data. Channels consisted of strain gages, displacement transducers, thermocouples, and a load cell. Strain gages were used to determine the axial forces and out-of-plane bending in the steel members. Signal conditioning for the strain gages was performed using ATLSS Strain Gage Conditioners [Higgins, 1996]. Displacement transducers were used to monitor the VE-material deformation, elastic deformation of the steel tube, and loading structure. Very fine, 0.003 in. diameter, T-type thermocouples, manufactured by Omega Engineering Inc., were used to measure the VE-material temperature. These very fine diameter thermocouples possess a very small time constant which permit almost instantaneous temperature measurement within the VE-material. Thermocouples were placed at specified locations within the VE-pads to monitor internal temperatures as illustrated in Fig. 3.6. Thermocouples were located in the mid-thickness of the VE-material pads. Installation of thermocouples was performed by inserting a 18 gage hypodermic needle into the VE-material, allowing sufficient time for the material to relax, withdrawing the needle, and inserting the thermocouple in the hole left by the needle. Thermocouples are

made of two dissimilar metals which are in contact at a point. As the temperature changes, a voltage is produced at the point of contact between the metals. The magnitude of voltage change is very small (40 μV/°C for T-type thermocouples). As a result, the signal generated by the thermocouples required significant amplification and filtering to provide reliable measurements of damper temperature with the data acquisition system. Instrumentation layout and description for all sensors is illustrated in Fig. 3.7.

To investigate the influence of temperature on damper performance, the initial VE-damper temperature was varied from 16 to 32 °C. An insulated enclosure was built around the damper to permit accurate temperature control of the damper as shown in Fig. 3.8. The dampers were heated or cooled with forced air to achieve the desired initial temperature. A thermocouple, inserted within the VE-material, was used for control of the forced air heating or cooling. All initial temperatures were controlled within a selected tolerance of ± 0.1 °C. A handheld digital meter, Omega HH23 handheld microprocessor digital thermometer, was used to manually measure initial temperatures from the control thermocouple.

3.3 Sinusoidal Loading

To determine the VE-damper properties for use in later analyses, a series of sinusoidal tests were performed. Investigated test parameters included different loading frequencies, damper strain amplitudes, and initial temperatures as shown in Table 3.2. The maximum frequency was limited to 2 hz due to limitations of the hydraulic actuator control system. The system

limitations resulted from flow capacity and frequency response of servo-valves as well as the control algorithms employed by the software. Amplitudes investigated ranged from 5% to 100% shear strain in the VE-material and five cycles of constant amplitude were performed for each test. Initial temperatures investigated (16 to 32 °C) correspond to a practical range of ambient temperatures VE-dampers would experience during service conditions within an enclosed building structure.

Small strain amplitudes of 5% were used to determine the VE-material properties for use in the VE-finite element described later. Small strain amplitudes are used because little or no temperature rise occurs within the VE-dampers at 5% shear strain. This permits characterization of VE-properties independent of the temperature rise resulting from loading. Example 5% strain stress-strain behavior for a single cycle is shown in Fig. 3.9 and the VE-material temperature is shown in Fig. 3.10. As shown in Fig. 3.10, there was no measurable temperature rise within the VE-material for the 5% strain amplitude.

Experimentally determined stress-strain response for the VE-damper indicate the well-known frequency, temperature and amplitude sensitivities of the material. Example stress-strain response for different strain amplitudes of 5, 25, and 50% with constant initial temperature of 24 °C and 0.5 hz loading frequency are shown in Fig. 3.11. Example stress-strain response for different initial temperatures of 20, 24, 28, and 32 °C with constant 25% strain amplitude and 0.5 hz loading frequency are shown in Fig. 3.12. Example stress-strain response for different frequencies of 0.1, 0.5, 1.0 and 2.0 hz with constant 25% strain amplitude and 24 °C initial temperature are shown in Fig. 3.13. Measured temperature rise within the VE-material is

shown in Fig. 3.14 for 28 °C initial damper temperature, 0.5 hz loading frequency, and nominal strain amplitudes of 5, 25, 50, and 100%.

VE-material properties for harmonic loading were obtained by determining the loss modulus G″ from the stress-strain response (Fig. 2.2) as:

$$G'' = \frac{\tau|_{\gamma=0}}{\gamma_o} \qquad [3.1]$$

where $\tau|_{\gamma=0}$ is the value of shear stress when the strain is zero, and γ_o is the maximum strain. The complex modulus $|G^*|$ is computed from the stress-strain response (Fig. 2.2) as:

$$|G^*| = \frac{\tau_o}{\gamma_o} \qquad [3.2]$$

where τ_o is the maximum shear stress. The storage modulus G′ is then calculated as:

$$G' = \sqrt{|G^*|^2 - G''^2} \qquad [3.3]$$

The relationships between the parameters G′, G″, $|G^*|$ are derived from perfectly elliptical stress-strain response. Therefore, from a geometrical sense, G′ represents the single point on the ellipse when the abscissa is maximum. Eq. 3.3 was used to calculate G′ because accurate determination of the storage modulus directly from the stress-strain response can produce varying results depending on selection of the stress at maximum strain due to imperfect experimental elliptical stress-strain response as shown in Fig. 3.15. The second half cycle was used for computing the properties because the first cycle did not achieve the target strain and significant temperature rise had not occurred in the material. Experimental values for the harmonic VE-material properties and measured temperature rise are shown in Table 3.3.

Results of the individual damper sinusoidal tests indicated the VE-material properties (G' and η_d) are similar to those provided by the manufacturer as shown in Figs. 3.16, 3.17, and 3.18.

In later figures and tables, force and deformation are used to describe the response of the VE-dampers. Damper force P(t) is related to the shear stress $\tau(t)$ as:

$$P(t) = \tau(t)A \qquad [3.4]$$

where A is the total shear area of the VE-material. Damper deformation u(t) is related to the shear strain $\gamma(t)$ as:

$$u(t) = \gamma(t)h \qquad [3.5]$$

where h is the thickness of the VE-material.

An additional result of the sinusoidal tests was validation of the use of strain gages to measure the axial force within the VE-damper. Axial strain in the damper was determined by averaging the measured strain from the four strain gages on the tube cross section. The axial load was computed using the nominal cross sectional properties of the structural tube, modulus of elasticity, and measured axial strain. The axial force in the damper, determined from the strain gages and measured by the load cell attached to the hydraulic actuator were similar as shown in Fig. 3.19.

3.4 Random Short Duration Loading

Random short duration tests were also performed on the individual damper. Test durations ranged from approximately 30 to 60 seconds and contained variable strain amplitudes and frequency components. These tests represent typical VE-damper response resulting from earthquake induced motions. Displacement histories for the random short duration tests were determined from time-history analysis of a building structure containing VE-dampers, subjected to earthquake ground accelerations. The methodology used to determine the deformation response of the VE-damper will be described in Chapter 6. Three different earthquakes were chosen for random short duration tests of the individual damper, important response properties for these tests are shown in Table 3.4. Displacement response of the VE-damper to these earthquake induced deformations is shown in Figs. 3.20a, 3.21a, and 3.22a. Corresponding frequency contents of these records, computed from FFT of the displacement response, are shown in Figs. 3.20b, 3.21b, and 3.22b. All the FFTs show the majority of the response is below 1 hz, with peaks near 0.5 hz. These peaks near 0.5 hz are associated with the natural frequency of the seismic analytical model used to determine the damper deformation response as will be discussed in Chapter 6.

Displacement time-histories from analysis were discretized and used as command signals to the hydraulic actuator for the test. Measured force-displacement response for the VE-damper subjected to the different earthquake displacement histories are shown in Figs. 3.23a, 3.24a, and 3.25a. Temperature rise within the VE-material during the different earthquake tests are shown in Figs. 3.23b, 3.24b, and 3.25b. The area of the hysteretic response exhibited by the

dampers demonstrated significant energy dissipation capability for all earthquakes. Peak dampers strains approach 100% and peak damper forces are near 190 kips for all three earthquakes, but for the short duration earthquakes (30 seconds) temperature rise was about 5 °C compared with 7 °C for the Mexico City response (60 seconds). The higher temperature rise exhibited by the Mexico City response results from the increased number of cycles and duration of loading.

Analytical correlation of these earthquake induced damper responses is presented in section 3.8.

3.5 Long Duration Loading

In addition to seismic applications, VE-dampers are also used for the control of structures subjected to wind inducted vibrations. Wind effects are much different than seismic effects. Wind forces are in the low frequency range and can act over a much longer period of time. Temperature rise within the VE-damper during long duration wind events may influence the damper performance. To assess the long duration loading response of the individual damper, two cases were considered: constant amplitude sinusoidal and random long duration loading.

Two different return period wind velocities were chosen for long duration tests of the individual damper: 50, and 500 years which are explained in Chapter 7. Artificially simulated wind forces were determined for wind velocities of these return periods, and displacement

histories for the VE-damper were determined from time-history analysis of a wind prototype building subjected to the computed wind forces. The methodology used to determine the displacement response of the VE-damper subjected to wind induced forces is described in Chapter 7. VE-damper displacement time history from analysis of the 500 year return period wind forces is shown in Figs. 3.26a-3.26d. Corresponding frequency contents of this record, computed from FFT of the displacement response, is shown in Fig. 3.27. All the FFTs show the majority of the response is below 0.2 hz, with peaks near 0.02 hz. The low frequency response is associated with the wind spectrum which is in this low frequency regime as will be discussed in Chapter 7. There is also a small response peak near 0.4 hz which is associated with the natural frequency of the wind analytical model used to determine the damper deformation response as will be discussed in Chapter 7.

Random long duration tests were conducted by using the discretized damper displacement time-history from the wind analysis as the command signal to the hydraulic actuator. Measured force-displacement response for the VE-damper subjected to the 500 year event displacement history are shown in Figs. 3.28a and 3.28b for the first and last half of the test respectively. As shown in these figures, there is no apparent change in stiffness from the start of the test and the end of the test. Measured temperature rise within the VE-material for the 500 year wind event is shown in Fig. 3.29. As seen in this figure, the temperature rises during the first 10 minutes and then only rises slightly during the later part of the test. This indicates heat is transferred from the damper to the environment at approximately the same rate it is generated and that heat convection should be considered for long duration events.

Long duration constant amplitude sinusoidal tests were also performed. The frequency of loading was selected to correspond with the natural frequency of the wind prototype building (0.37 hz as will be discussed in Chapter 7). The variable amplitude displacement history was converted to an equivalent constant amplitude sinusoidal displacement history. Amplitude of the equivalent sinusoidal displacement was determined by multiplying the RMS of the random response by a scale factor of 1.4, based on research [Mander *et al.*, 1993] which represents a narrow band random loading as an equivalent constant amplitude sinewave. The displacement amplitude was 0.12 in. for the 500 year return period wind event and 0.07 in. for the 50 year return period wind event. These correspond to 19.2% and 10% damper strains respectively. One hour duration tests were performed for these strain amplitudes at the specified frequency. Measured force-deformation response for the VE-damper subjected to the 500 year constant amplitude sinusoidal displacement history are shown in Figs. 3.30a and 3.30b. Fig. 3.30a shows the initial response while Fig. 3.30b shows the later response demonstrating a significant decrease in stiffness due to temperature rise. This is further illustrated in Fig. 3.31 which shows a continuous decrease in damper force during the experiment. Temperature rise within the VE-material for the 500 year amplitude is shown in Figs. 3.32. The temperature rises quickly during initial loading and then rises only slightly due to heat transfer from the damper to the environment and less input energy due to the reduced stiffness caused by temperature rise.

3.6 Prediction of VE-Damper Temperature Rise

The temperature rise within the VE-dampers θ (°C) was predicted according to Kasai *et al.* [1993] as:

$$\theta = \frac{1}{s\rho}\int \tau d\gamma \qquad [3.6]$$

where s is specific heat (= 7.55922 $\left(\frac{\text{kbf}}{\text{lb}}\right)\frac{\text{in}}{^{\circ}\text{C}}$) and ρ is density (= 0.03757 $\frac{\text{lb}}{\text{in}^3}$) which results in $s\rho$ = 0.284 $\left(\frac{\text{kbf}}{\text{in}^2}\right)\frac{1}{^{\circ}\text{C}}$ for the VE-material, τ is the shear stress (ksi), and γ is the shear strain. The method does not consider heat transfer between the damper and environment. Temperature rise predicted by Eq. 3.6 is compared to selected tests in Fig. 3.33. This simple method reasonably predicted VE-material temperature rise for short duration loading cases.

3.7 Measurement of Elastic Damper Stiffness

VE-dampers, like those used in this study, are typically attached to a steel brace and the interaction between the brace and damper affects the behavior of the VE system. The combined damper and brace assembly is termed *'added component'*. The brace and damper are connected in series and the complex stiffness of the added component K^*_a contains in-phase stiffness K'_a and out-of-phase stiffness $\eta_a K'_a$:

$$K^*_a = K'_a(1+i\eta_a) = \frac{K_b K^*_d}{K_b + K^*_d} \qquad [3.7]$$

where η_a is the loss factor of the added component, K^*_d is the complex damper stiffness, and K_b is the brace in-phase elastic stiffness. From Chapter 2, $K^*_d = K'_d(1+i\eta_d)$ and $K'_d = G'A/h$. Damping provided by the brace is assumed negligible and the complex brace stiffness then contains only in-phase parts. K'_a and η_a are determined according to Eqs. 3.8 and 3.9 respectively [Kasai and Fu, 1995] as:

$$K'_a = \frac{K_b K'_d}{(K_b/\Gamma) + K'_d} \qquad [3.8]$$

$$\eta_a = \frac{\eta_d}{\left[1 + (1+\eta_d^2)K'_d/K_b\right]} \qquad [3.9]$$

$$\Gamma = 1 + \frac{\eta_d^2}{(1 + K_b/K'_d)} \qquad [3.10]$$

where η_d is the loss factor for the damper, K'_d is the in-phase stiffness of the VE-damper, $\eta_d K'_d$ is the out-of-phase stiffness of the VE-damper.

The in-phase elastic stiffness of the brace K_b plays a significant role in determining the performance of the VE-damper and VE-structure as described by Eqs. 3.8 and 3.9. If the steel brace is not sufficiently stiff, excessive deformation will occur in the steel and not the VE-material resulting in reduced damper effectiveness. A very stiff brace will permit almost all the deformation to take place within the VE-material resulting in increased damper efficiency. Therefore, it is important to determine the elastic stiffness of the steel members which make-

up the brace. The elastic stiffness of the brace was determined by measuring the total deformation of the damper and removing the VE-material deformation component. The remaining deformation is the elastic deformation of the steel members which make-up the brace. An example overall load-deformation of the damper, elastic deformation of the steel brace, and local VE-material deformation are shown in Fig. 3.34. The elastic brace stiffness was determined from a best fit line through the data as 4800 kips/in.

A simplified method was developed to predict the brace stiffness. This method, illustrated in Fig. 3.35, considers the elastic axial deformation of different sections of the added component to a unit force and computes the stiffness as:

$$K_b = \frac{1}{\sum_{i=1}^{N} \frac{F_i L_i}{A_i E}} \qquad [3.11]$$

where A_i is the cross sectional area of the ith steel section, E is the modulus of elasticity (=29,000 ksi), L_i is the length of the ith section, N is the number of different cross sections which make-up the damper (seven for the current damper), F_i is the average force in the section being considered. The method assumes a linear transfer of force between the VE-material and steel members. Thus, forces in added component segments containing VE-material use an average force as illustrated in Fig. 3.35. The proposed method predicts an elastic brace stiffness of 4725 kips/in for the damper which corresponds well with the experimental stiffness as shown in Fig. 3.34. It is important to note this elastic brace stiffness does not include any possible reduction in stiffness due to connections between the damper and steel frame members. This issue is addressed further in Chapter 5.

3.8 Correlative Analysis of Individual Dampers

Analytical correlation of the experimental damper response was performed using a previously developed viscoelastic finite element [Kasai *et al.*, 1993]. The element uses the fractional derivative model for the stress-strain relationship described in section 2.2 and has been implemented in an available computer program, PC-ANSR [Maison, 1992]. Parameters used in the constitutive rule were obtained from the experimentally determined values for storage modulus and loss factor as illustrated in Appendix A. Obtained values were: G=14.0 psi, a= 0.003698, b=7.537, α=0.622, T_{ref}=24.0 °C, p_1=17.8755, and p_2=88.5054. The element material constitutive rule is integrated in a step-by-step analysis procedure to determine the dynamic response of the VE-damper. At each time step, the amount of energy dissipated and the temperature rise are calculated using thermo-mechanics principles and heat transfer theory [Kasai *et al.*, 1993]. Based on the temperature rise and satisfying the VE temperature-frequency equivalence property using a shifting factor, parameters for the constitutive rule are updated at each time step. Continuous updating of the parameters results in a nonlinear constitutive rule.

Analysis of the individual VE-damper was performed using the experimental displacement response as the imposed displacement history on the analytical model as illustrated in Fig. 3.36. Several initial temperatures, loading frequencies and strain amplitudes of sinusoidal excitation were investigated. The sinusoidal test cases which were analyzed are indicated by an # in Tables 3.3a to 3.3e. In addition to the sinusoidal loading, analyses of random short and long duration loading cases were also performed.

Examples of the analytically predicted stress-strain response are compared with the experimental response in Figs. 3.37a to 3.43b. Experimental responses in Figs. 3.37a to 3.43b are designated as b) while the analytically predicted responses are designated as a). Analytically predicted temperature rise is compared to the measured experimental temperature rise in Table 3.5. Analytical results of sinusoidal loading cases indicate the finite element model reasonably predicted the damper force-deformation response, temperature rise, and resulting stiffness and damping changes over the range of parameters investigated. However, as shown in Figs. 3.37a and 3.37b, the model overestimated the stiffness and damping at the 16 °C temperature. This overestimation is due to the sensitivity of the temperature shifting parameters. Temperature shifting parameters p_1 and p_2 are computed by fitting a curve through the full range of temperature data. The curve is particularly sensitive in the low temperature range and flat in the higher temperature range as shown in Fig. 3.44. Increased accuracy of the finite element in the low temperature range can be achieved by fitting the temperature shifting parameters with greater precision at the specific temperature of interest. Additional experimental data would be required at lower temperatures to produce better shifting parameters in this temperature range.

Correlative analyses of the earthquake response were also performed. Analytically predicted force-deformation responses are compared with the experimentally obtained responses in Figs. 3.45, 3.46, and 3.47 for the three earthquakes considered. An example of the predicted and measured temperature rise for the Mexico City earthquake is shown in Fig. 3.48. Results

indicate the analytical model reasonably predicts damper force-deformation response, temperature rise, and resulting stiffness and damping changes for the short duration events.

Finally, correlative analyses were also conducted for long duration loading cases. An example of the analytically predicted force-deformation response for the damper is shown in Figs. 3.49a for the first half and 3.49b for the last half of the 500 year wind event. The model accurately predicts damper response at early stages of the event as shown in Fig. 3.50a, however, it does not accurately predict response at later parts of the response as shown in Fig. 3.50b. This inaccuracy in the later part of the record results from significant heat transfer between the damper and environment not currently considered in the VE-finite element. The importance of heat transfer is illustrated in Fig. 3.51 which shows the measured temperature rise and predicted temperature rise for the VE-element if heat transfer is neglected. A new element which includes heat convection between the damper and environment is being developed [Kasai *et al.*, 1997a]. Initial analyses with this new element indicate damper behavior during long duration loading events can be predicted by considering heat transfer effects.

3.9 Conclusions

Results of the individual damper experimental and analytical program are summarized below:

- Tests of the VE-damper demonstrated the well known frequency, temperature and amplitude sensitivities for VE-materials.
- Experimental VE-material properties (G' and η_d) correspond well with values provided by the manufacturer.
- Strain gages located on the damper can be used to accurately measure damper axial forces.
- Temperature rise within the damper can be reasonably predicted using Eq. 3.6 for short duration loading where heat transfer between the damper and environment are not significant.
- Brace elastic stiffness K_b, which plays an important role in determining damper performance, can be estimated using a simplified analytical procedure as illustrated in Fig. 3.35.
- Damper performance, over a sufficiently wide frequency, temperature, and strain amplitude range, can be predicted using the fractional derivative based VE-finite element for short duration loading cases when no significant heat transfer occurs between the damper and environment.
- Limitations of the element were observed at low temperatures due to the sensitivity in the temperature shifting parameters in this range. The model can be improved in the low

temperature range by more precisely fitting the temperature shifting parameters at the low temperatures.

- Heat transfer between the VE-damper and environment should be considered to accurately predict damper behavior for long duration loading when significant heat transfer occurs between the damper and environment.

Loading Frequency (hz)	Data Acquisition Sampling Frequency (hz)	Time Between Samples (sec)
0.1	33	0.0303
0.5	165	0.0061
1.0	331	0.0030
2.0	399	0.0025

Table 3.1 - Individual VE-damper data acquisition sampling rates.

16 °C		20 °C		24 °C		28 °C		32 °C	
Loading Frequency (hz)	Strain Amplitude (%)	Loading Frequency (hz)	Strain Amplitude (%)	Loading Frequency (hz)	Strain Amplitude (%)	Loading Frequency (hz)	Strain Amplitude (%)	Loading Frequency (hz)	Strain Amplitude (%)
0.1	5	0.1	5	0.1	5	0.1	5	0.1	5
0.1	25	0.1	25	0.1	25	0.1	25	0.1	25
0.1	50	0.1	50	0.1	50	0.1	50	0.1	50
-	-	0.1	100	0.1	100	0.1	100	0.1	100
0.5	5	0.5	5	0.5	5	0.5	5	0.5	5
0.5	25	0.5	25	0.5	25	0.5	25	0.5	25
-	-	0.5	50	0.5	50	0.5	50	0.5	50
-	-	-	-	-	-	0.5	100	0.5	100
1.0	5	1.0	5	1.0	5	1.0	5	1.0	5
-	-	1.0	25	1.0	25	1.0	25	1.0	25
-	-	-	-	1.0	50	1.0	50	1.0	50
-	-	-	-	-	-	1.0	100	1.0	100
2.0	5	2.0	5	2.0	5	2.0	5	2.0	5
-	-	-	-	2.0	25	2.0	25	2.0	25
-	-	-	-	-	-	-	-	2.0	50
Total No.:	7	Total No.:	10	Total No.:	12	Total No.:	14	Total No.:	15

Table 3.2 - Individual VE-damper test matrix.

Sinusoidal Loading 16 °C Initial Temperature						
Loading Rate (hz)	Nominal VE Strain (%)	Achieved VE-Strain (%)	Storage Modulus (psi)	Loss Factor	Initial Temp. (°C)	Final Temp. (°C)
0.1	5%	5.3%	158.8	1.35	16.0	16.0
#	25%	25.7%	134.6	1.38	16.0	16.5
	50%	51.4%	122.6	1.41	16.0	18.2
0.5	5%	5.1%	412.0	1.29	16.0	16.0
	25%	***	***	***	16.0	17.8
1.0	5%	5.6%	624.5	1.11	16.0	16.0
2.0	5%	3.8%	816.0	1.01	16.0	16.1

*** Poor actuator control.

Correlative analysis performed.

Table 3.3a - Individual VE-damper material properties for 16 °C initial damper temperature.

Sinusoidal Loading 20 °C Initial Temperature						
Loading Rate (hz)	Nominal VE Strain (%)	Achieved VE-Strain (%)	Storage Modulus (psi)	Loss Factor	Initial Temp. (°C)	Final Temp. (°C)
0.1	5%	5.4%	93.2	1.25	20.0	20.0
	25%	25.6%	91.5	1.26	20.0	20.2
	50%	51.0%	77.9	1.28	20.0	21.5
	100%	101.0%	65.5	1.33	20.1	24.6
0.5	5%	6.0%	235.2	1.33	20.0	20.0
	25%	28.2%	206.7	1.38	20.0	20.9
	50%	***	***	***	20.0	23.2
1.0	5%	5.2%	358.0	1.31	20.0	20.0
	25%	28.5%	271.4	1.37	20.0	21.7
2.0	5%	3.5%	539.0	1.25	20.0	20.0

*** Poor actuator control.

Table 3.3b - Individual VE-damper material properties for 20 °C initial damper temperature.

Sinusoidal Loading 24 °C Initial Temperature						
Loading Rate (hz)	Nominal VE Strain (%)	Achieved VE-Strain (%)	Storage Modulus (psi)	Loss Factor	Initial Temp. (°C)	Final Temp. (°C)
0.1	5%	5.4%	58.4	1.12	24.0	24.0
#	25%	25.8%	57.1	1.14	24.0	24.1
	50%	51.2%	51.3	1.15	24.1	24.8
	100%	101.4%	47.6	1.19	23.9	26.8
0.5	5%	5.6%	135.3	1.31	24.0	24.0
#	25%	27.3%	125.9	1.34	24.0	24.5
	50%	51.1%	120.7	1.31	24.0	25.7
1 #	5%	5.6%	213.6	1.35	24.0	24.0
	25%	26.6%	188.0	1.36	24.0	24.7
	50%	44.2%	164.3	1.40	23.9	26.1
2.0	5%	5.1%	314.6	1.33	24.0	24.0
#	25%	17.6%	305.0	1.36	24.0	24.7

Correlative analysis performed.

Table 3.3c - Individual VE-damper material properties for 24 °C initial damper temperature.

Sinusoidal Loading 28 °C Initial Temperature						
Loading Rate (hz)	Nominal VE Strain (%)	Achieved VE-Strain (%)	Storage Modulus (psi)	Loss Factor	Initial Temp. (°C)	Final Temp. (°C)
0.1	5%	5.3%	41.8	1.00	28.0	28.0
	25%	25.7%	41.3	1.01	28.0	28.1
	50%	50.4%	36.1	1.03	28.0	28.4
	100%	99.2%	34.9	1.03	28.1	30.0
0.5	5%	5.4%	94.5	1.23	28.0	28.0
	25%	24.6%	83.1	1.24	28.0	28.3
	50%	47.2%	80.7	1.22	27.9	29.0
	100%	98.4%	75.1	1.23	28.0	32.1
1.0	5%	5.2%	131.8	1.32	28.0	28.0
	25%	25.8%	120.1	1.32	28.0	28.3
	50%	50.7%	103.8	1.33	28.0	28.3
	100%	****	***	***	28.1	29.8
2.0	5%	5.7%	192.0	1.34	28.0	28.0
	25%	22.1%	191.0	1.39	28.0	28.7

*** Poor actuator control.

Table 3.3d - Individual VE-damper material properties for 28 °C initial damper temperature.

Sinusoidal Loading 32 °C Initial Temperature						
Loading Rate (hz)	Nominal VE Strain (%)	Achieved VE-Strain (%)	Storage Modulus (psi)	Loss Factor	Initial Temp. (°C)	Final Temp. (°C)
0.1	5%	5.3%	29.7	0.86	32.0	32.0
	25%	26.0%	28.3	0.84	32.0	32.1
	50%	51.2%	27.1	0.89	32.0	32.3
#	100%	100.8%	24.5	0.92	32.0	33.1
0.5	5%	4.8%	57.4	1.13	32.0	32.0
	25%	26.0%	57.2	1.09	32.0	32.2
	50%	54.7%	54.7	1.12	32.1	32.7
	100%	102.4%	51.7	1.14	32.0	35.0
1.0	5%	5.7%	89.0	1.26	32.0	32.0
#	25%	26.1%	80.6	1.25	32.0	32.3
	50%	53.0%	74.0	1.27	31.9	33.3
	100%	75.8%	67.2	1.27	32.0	34.1
2.0	5%	6.6%	125.3	1.31	32.0	32.0
	25%	26.9%	109.9	1.33	32.0	32.5
	50%	35.6%	105.0	1.33	32.0	32.8

Correlative analysis performed.

Table 3.3e - Individual VE-damper material properties for 32 °C initial damper temperature.

Earthquake Respone	Duration (sec)	Peak Force (kips)	Peak Stress (psi)	Peak Disp. (in)	Peak Strain (%)	Temp. Rise (°C)
El Centro * 1.5	27	193.0	154.6	0.558	89.3%	4.4
Hachinohe * 1.5	28	192.8	154.5	0.512	81.9%	5.2
Mexico City (Frigorifico)	58	189.1	151.5	0.648	103.7%	6.9

Table 3.4 - Summary of individual damper response to simulated earthquake displacements.

Loading Rate (hz)	Nominal VE Strain (%)	Initial Temp. (°C)	Measured Final Temp. (°C)	Analysis Final Temp. (°C)
0.1	5%	16.0	16.5	16.8
0.1	25%	24.0	24.1	24.2
0.5	25%	24.0	24.5	24.7
1.0	5%	24.0	24.0	24.1
2.0	25%	24.0	24.7	24.8
0.1	100%	32.0	33.1	33.3
1.0	25%	32.0	32.3	32.4

Table 3.5 - Experimental and analytically predicted temperature rise under harmonic loading.

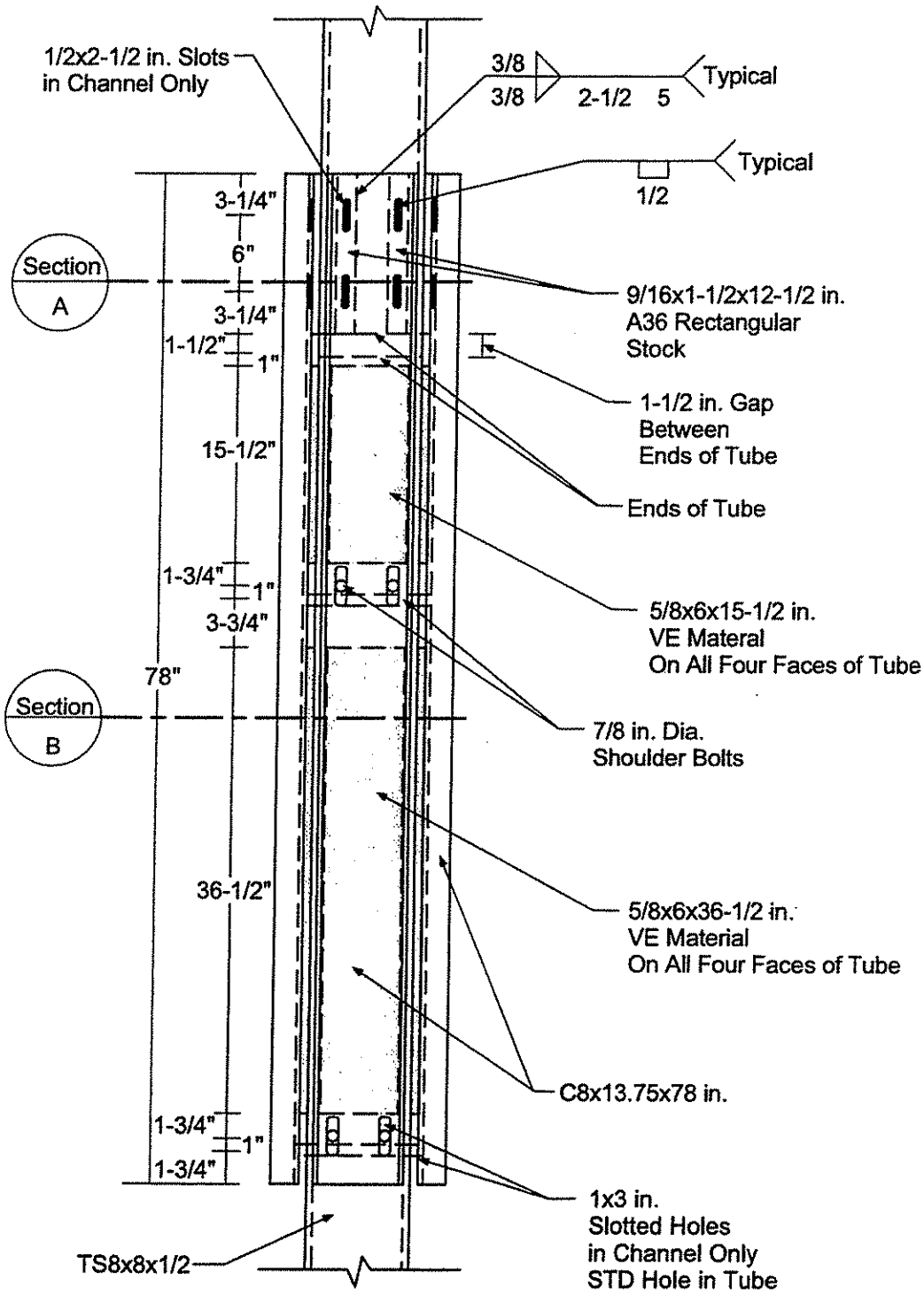

Fig. 3.1a - Individual VE-damper configuration.

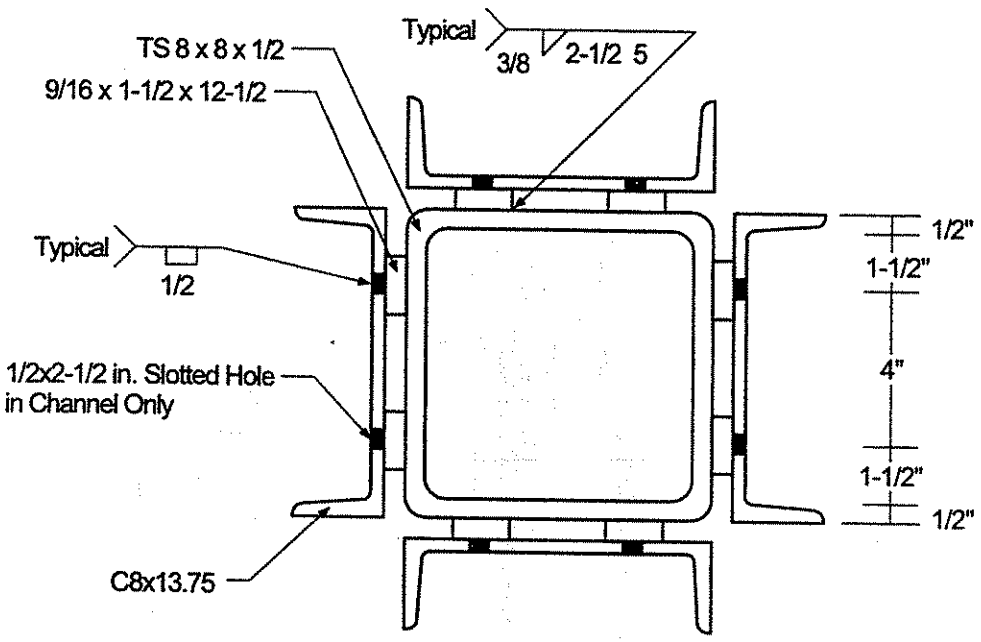

b) Cross Section A

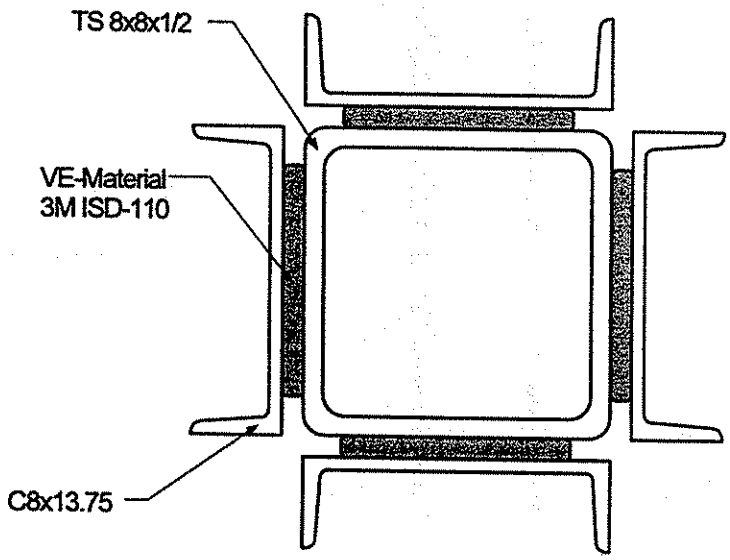

c) Cross Section B

Fig. 3.1b and c - Cross sections of VE-damper.

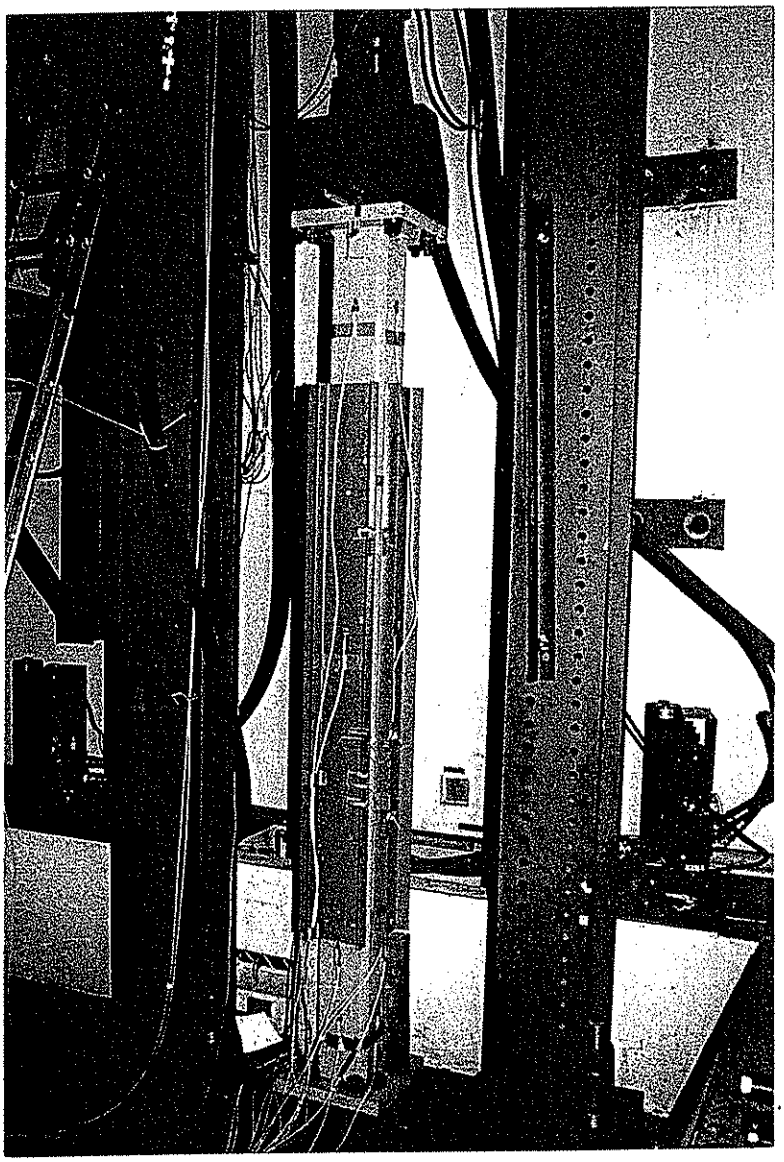

Fig. 3.2 - Individual VE-damper test specimen.

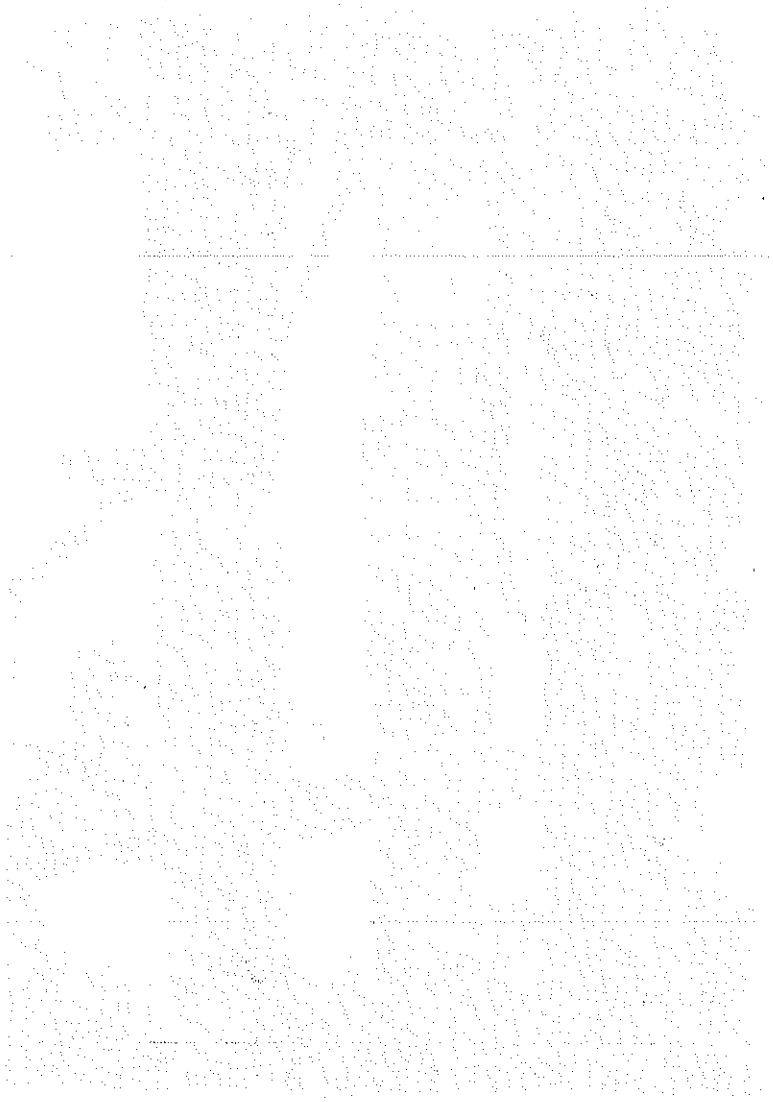

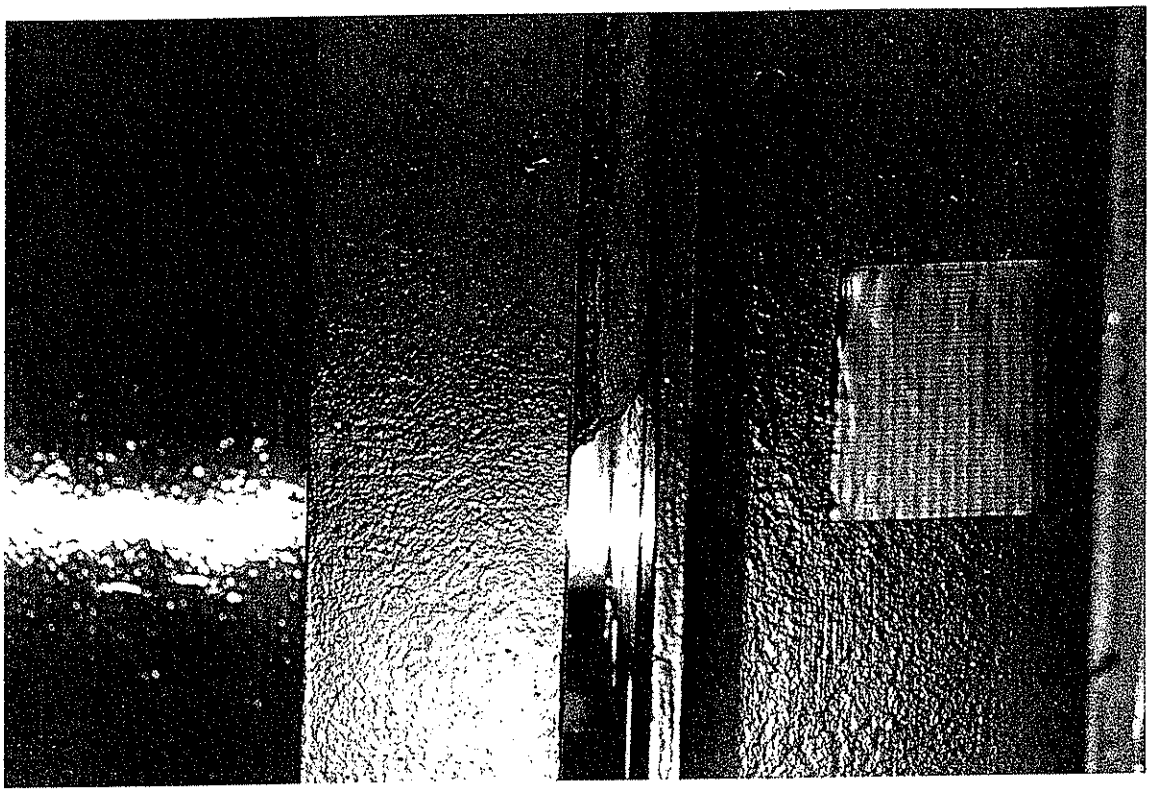

Fig. 3.3 - Shear strain in VE-material resulting from relative deformation of the damper ends.

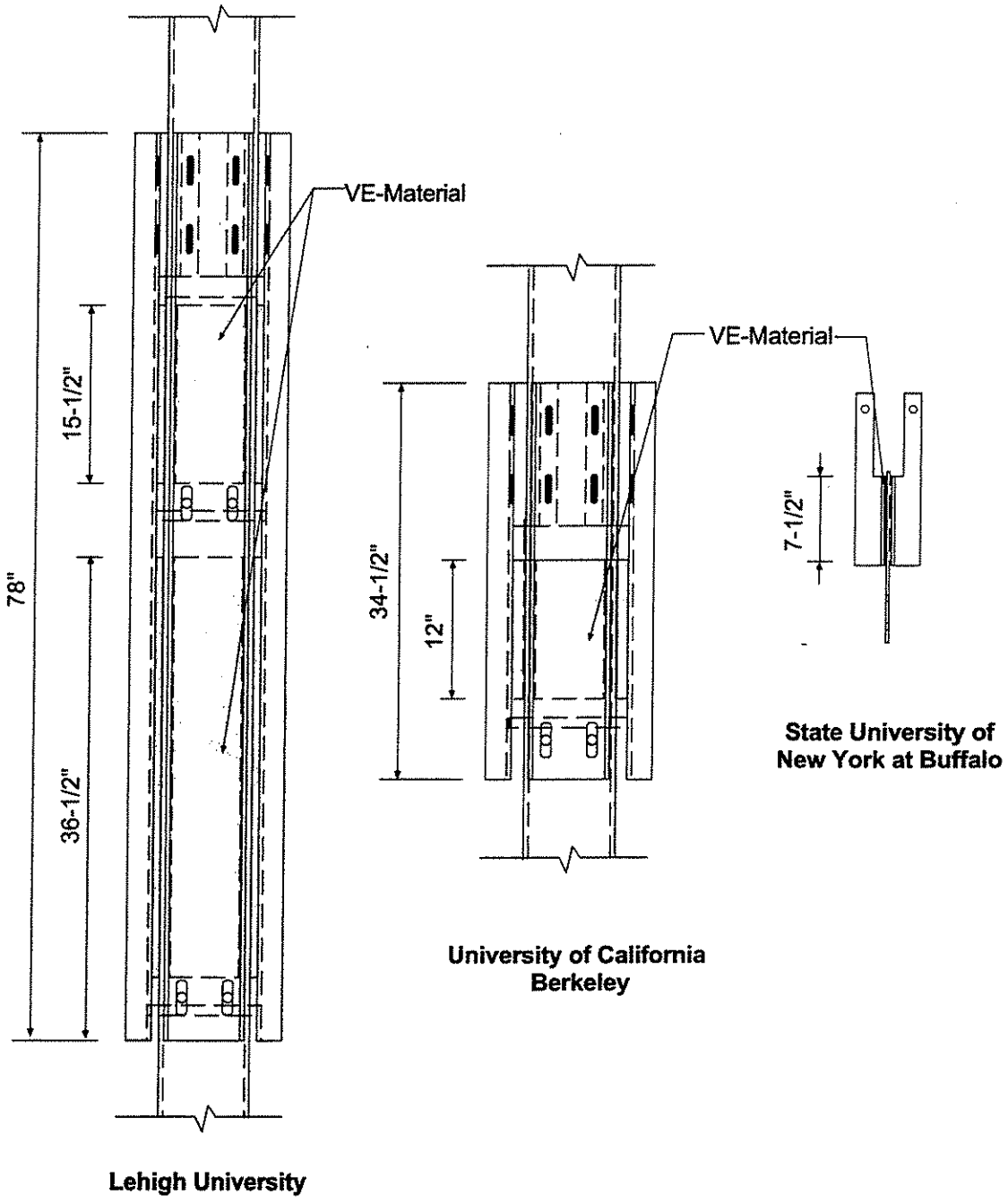

Fig. 3.4 - Comparison of VE-dampers tested in North America.

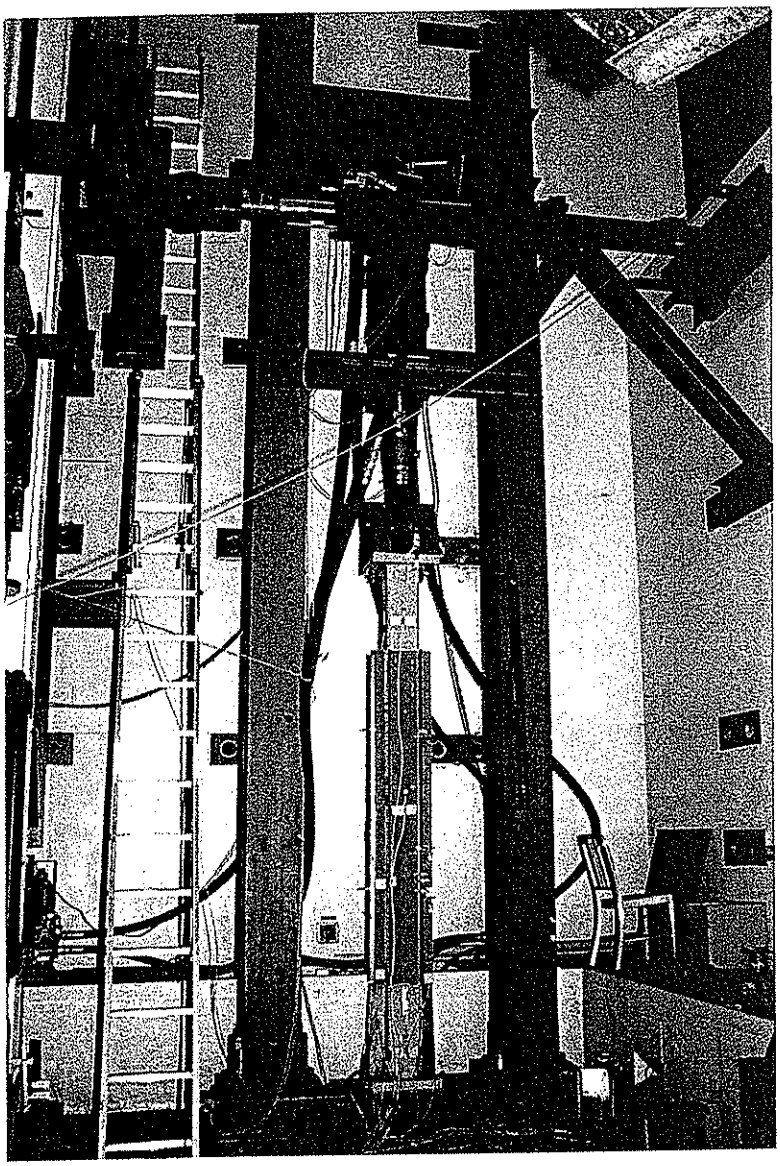

Fig. 3.5 - Loading frame used to test individual damper.

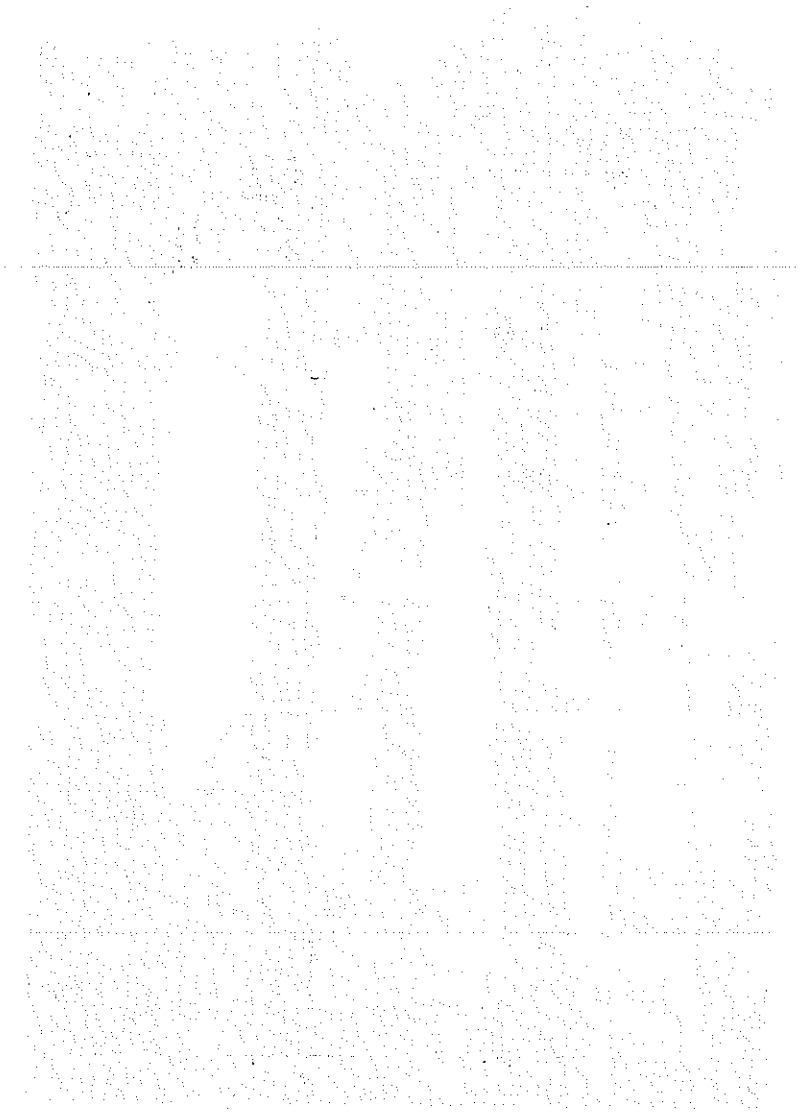

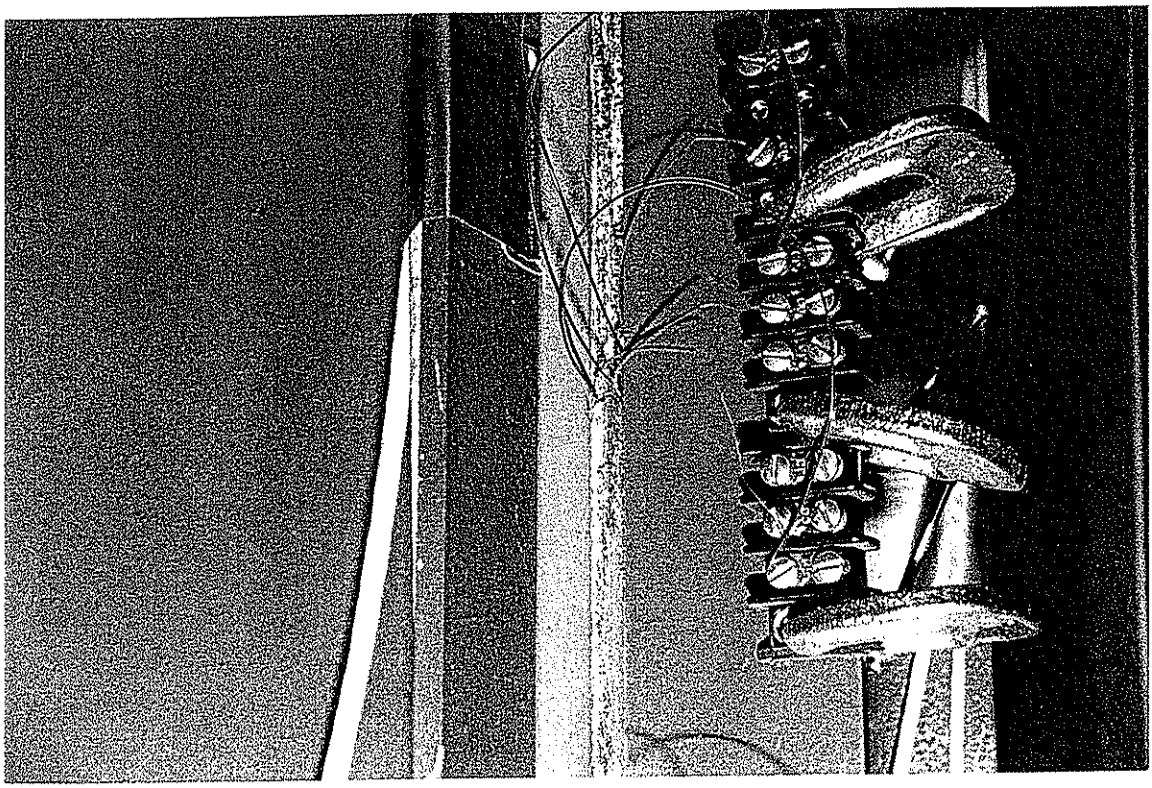

Fig. 3.6 - Thermocouples inserted in the VE-material used to measure temperature.

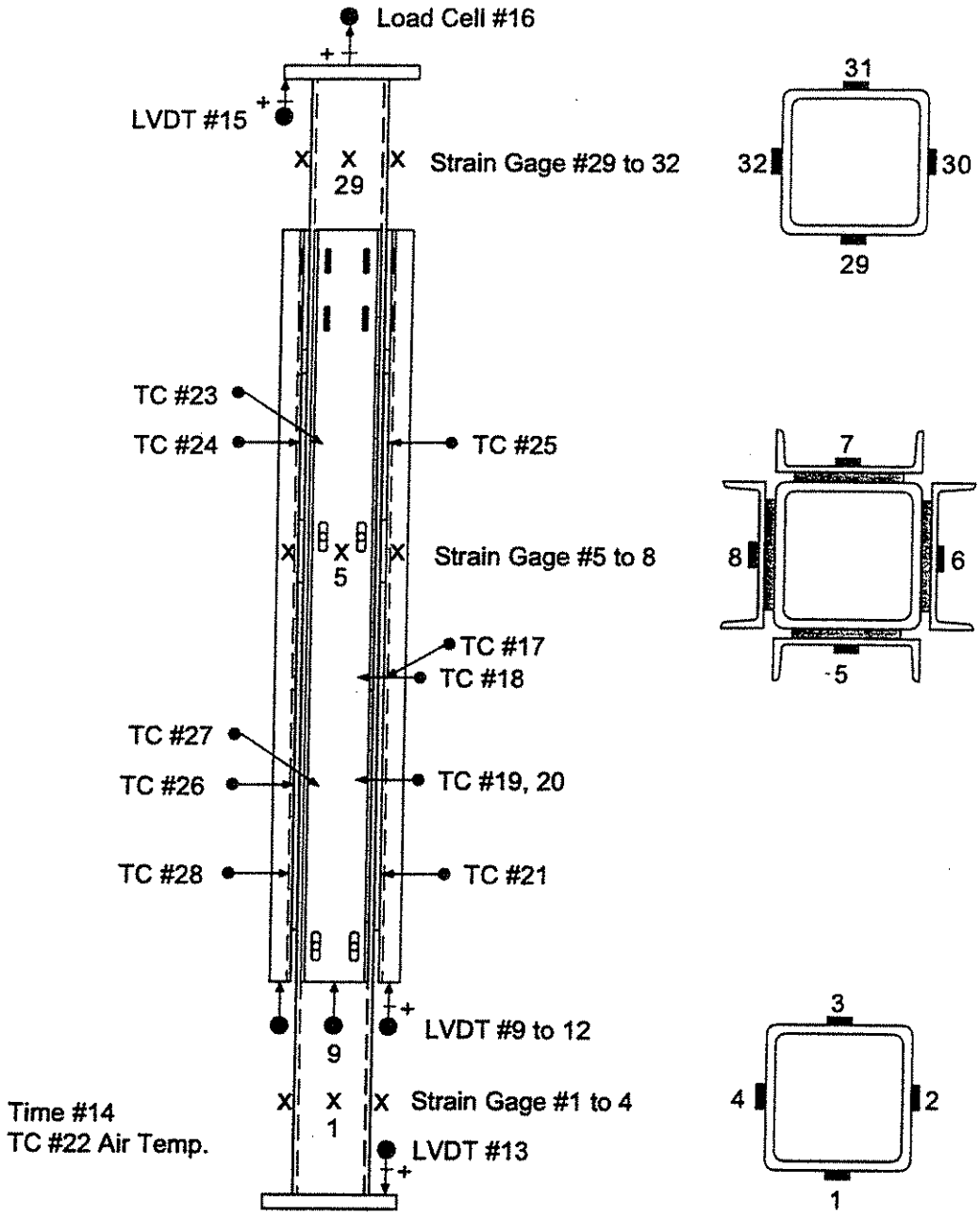

Fig. 3.7 - Instrumentation layout and channel identification.

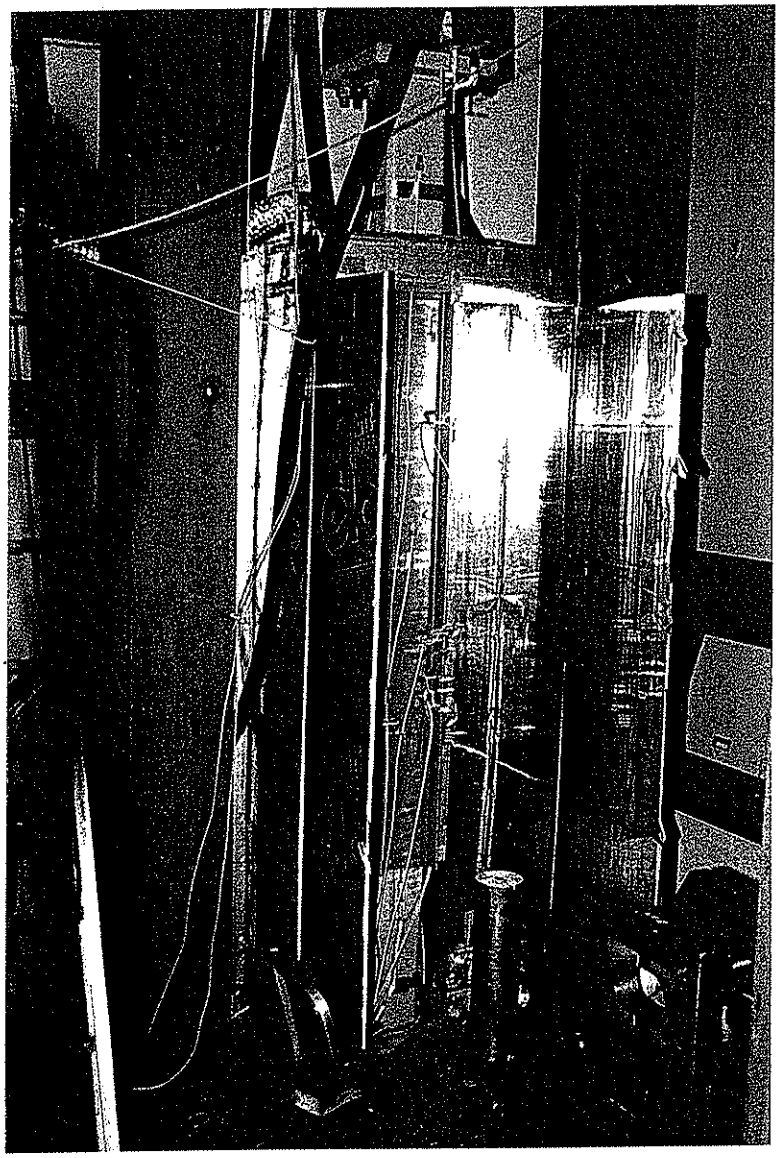

Fig. 3.8 - Insulated enclosure used to heat and cool damper to specified initial temperatures.

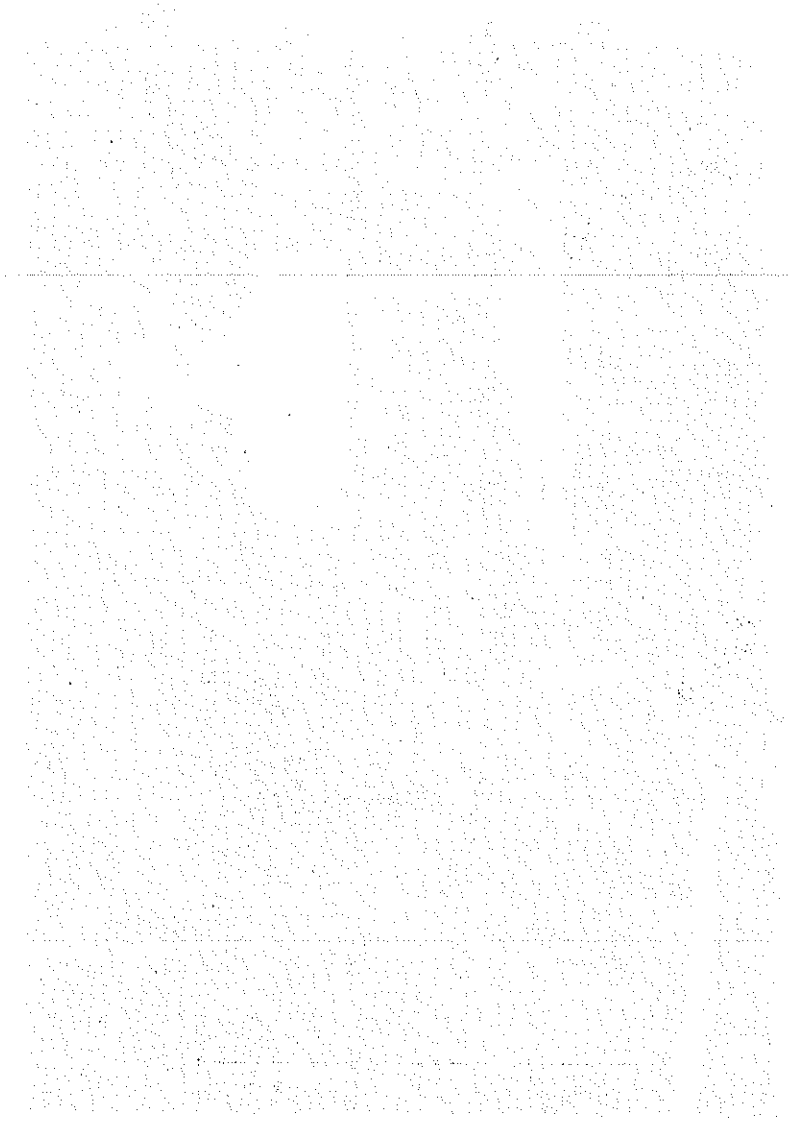

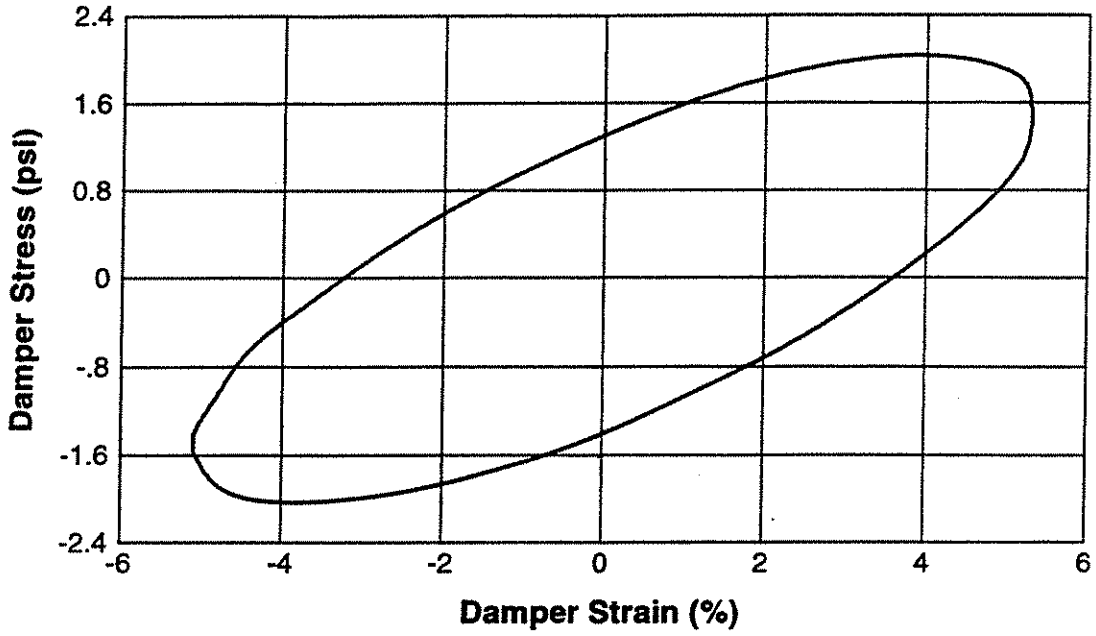

Fig. 3.9 - Example measured stress-strain response for the VE-damper at 5% strain. Loading frequency shown is 0.5 hz and initial temperature is 32 °C.

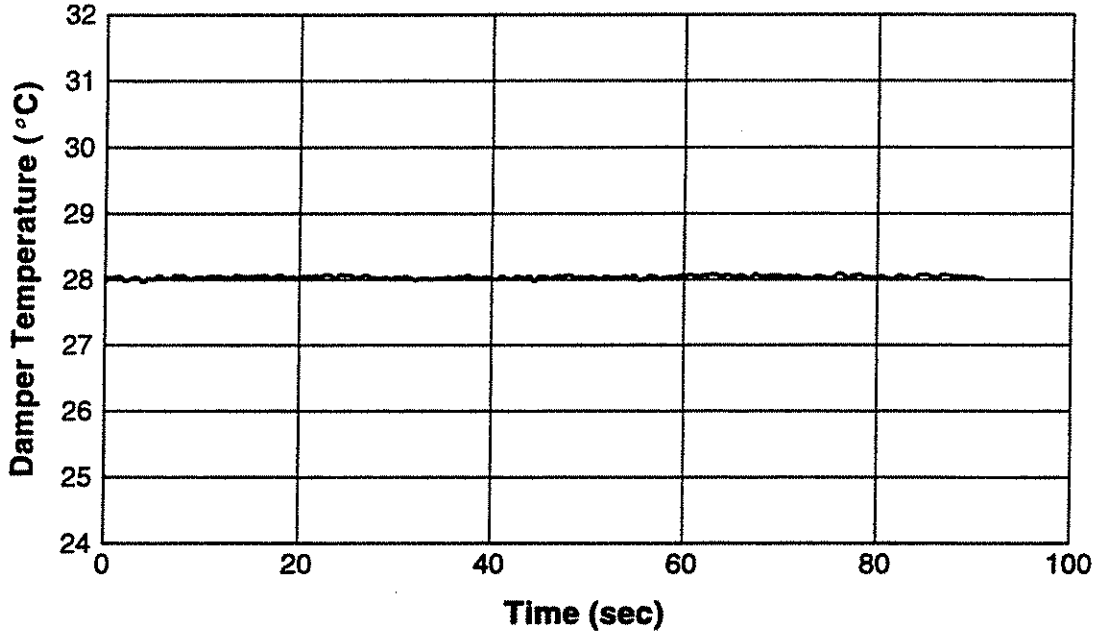

Fig. 3.10 - Example measured VE-damper temperature for 5% strain amplitude tests.

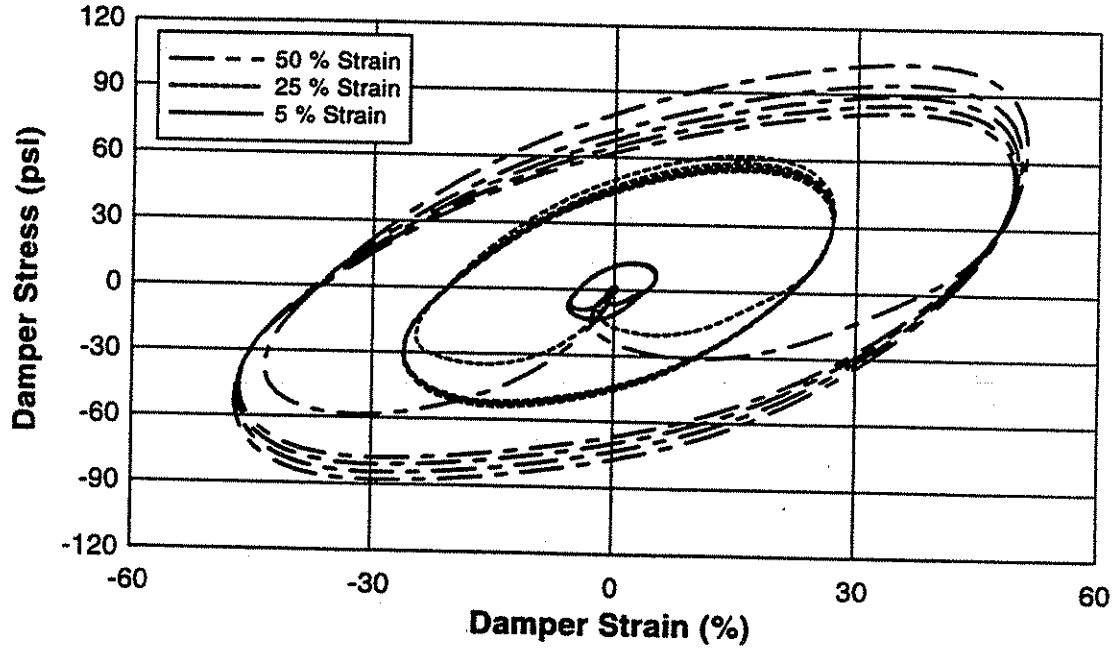

Fig. 3.11 - Example measured VE-damper stress-strain response for 5, 25, and 50% strain with constant loading frequency of 0.5 hz and initial temperature is 24 °C.

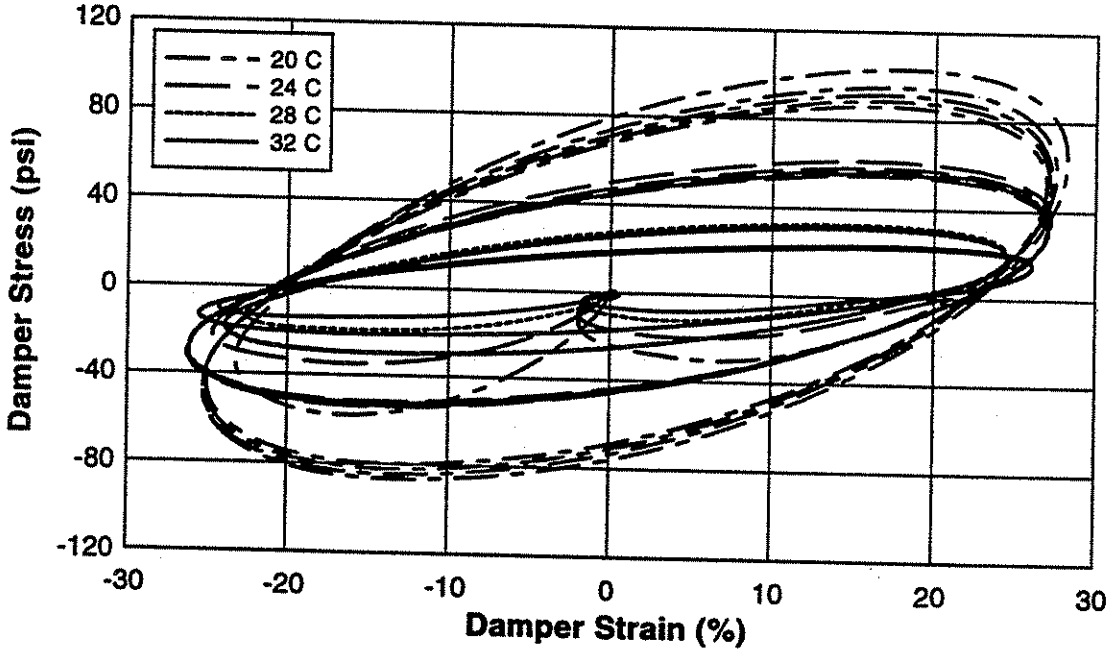

Fig. 3.12 - Example measured VE-damper stress-strain response for initial temperatures of 20, 24, 28, and 32 °C with constant loading frequency of 0.5 hz and strain of 25 %.

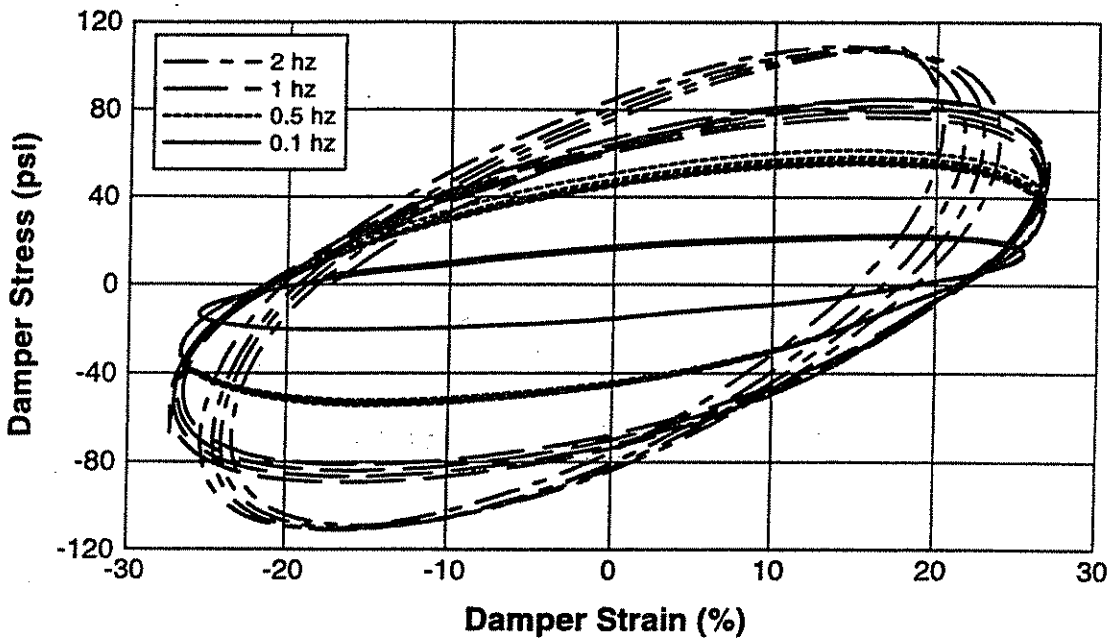

Fig. 3.13 - Example measured VE-damper stress-strain response for loading frequencies of 0.1, 0.5, 1.0, and 2.0 hz with strain of 25 % and initial temperature of 24 °C.

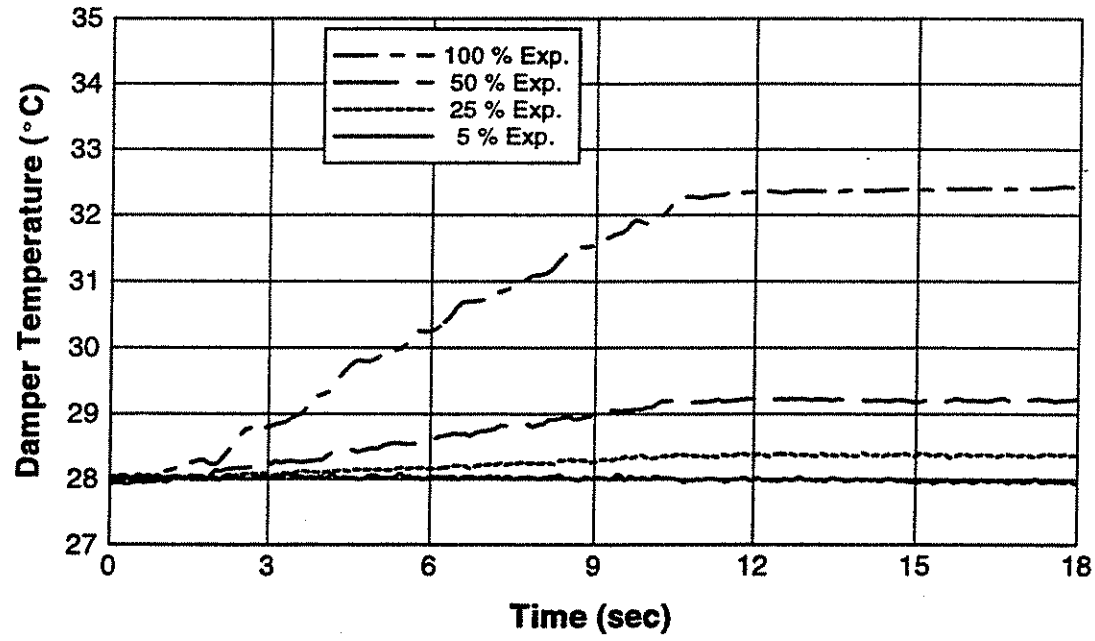

Fig. 3.14 - Measured VE-damper temperature rise for strains of 5, 25, 50, and 100% with a loading frequencies of 0.5 hz and initial temperature of 28 °C.

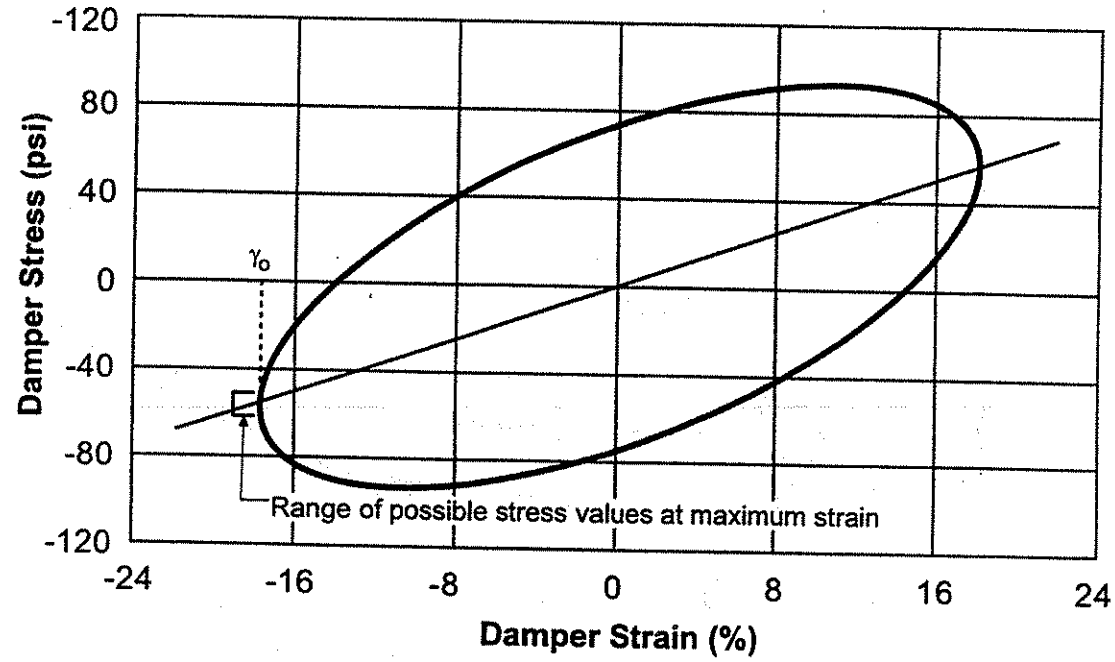

Fig. 3.15 - Possible error associated with determination of the shear stress at peak strain due to imperfect measured stress-strain response.

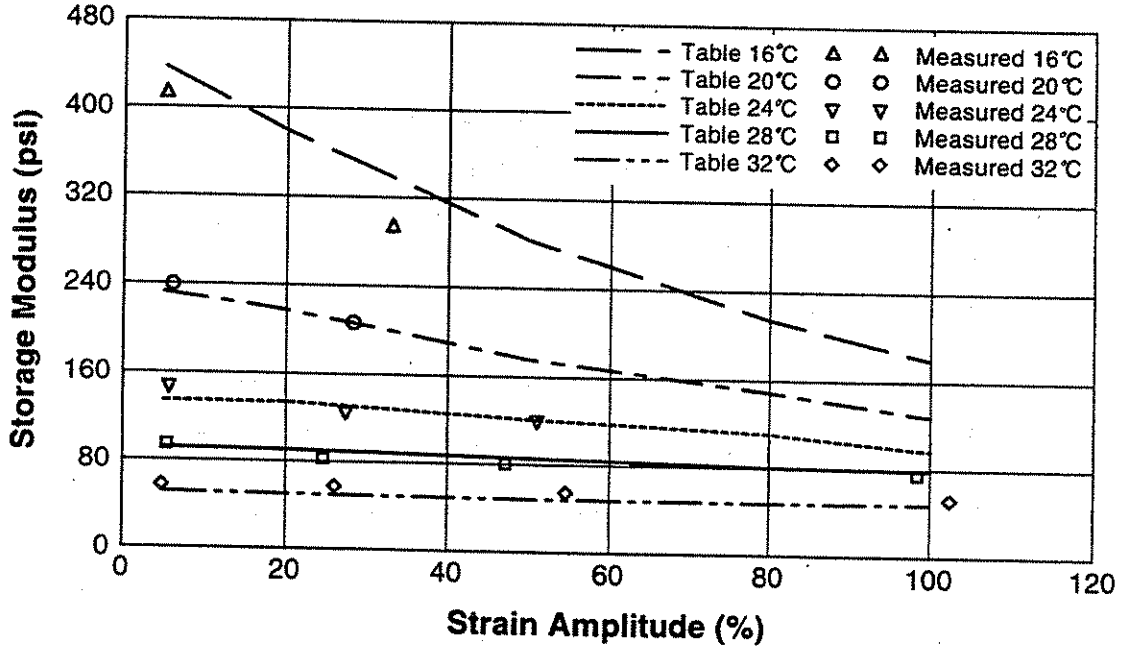

Fig. 3.16 - Comparison of measured storage modulus values with those provided by the manufacturer for 0.5 hz loading frequency with initial temperatures of 16 to 32 °C and strains of 5 to 100%.

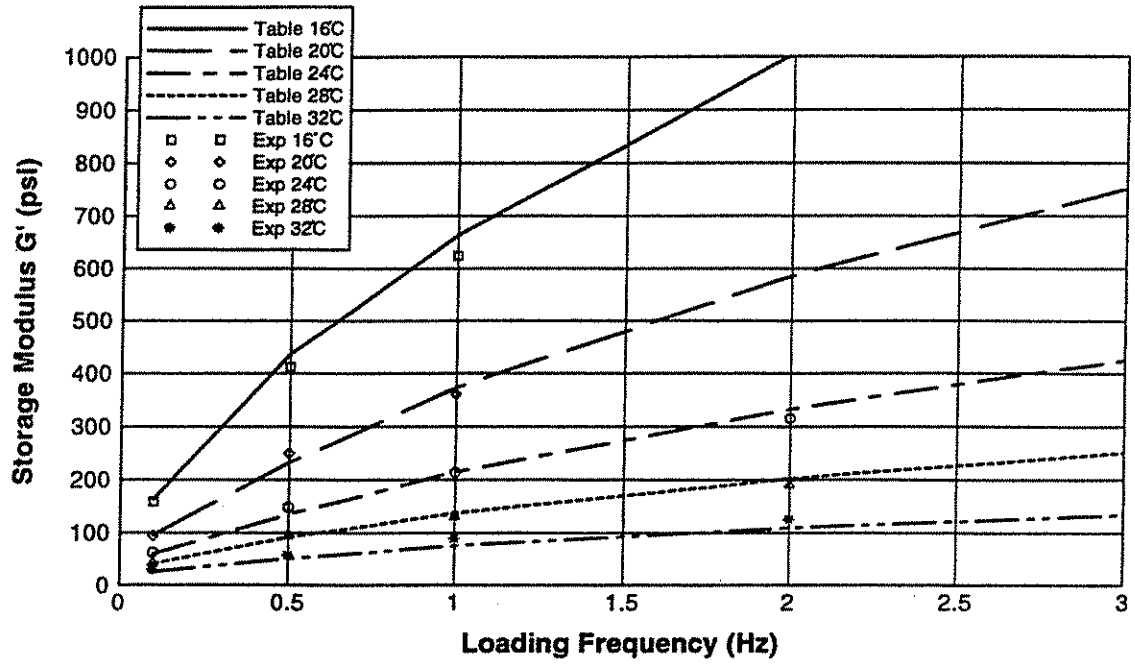

Fig. 3.17 - Comparison of measured storage modulus values with those provided by the manufacturer for 5% strain with loading frequencies of 0.1 to 2.0 hz and initial temperatures of 16 to 32 °C.

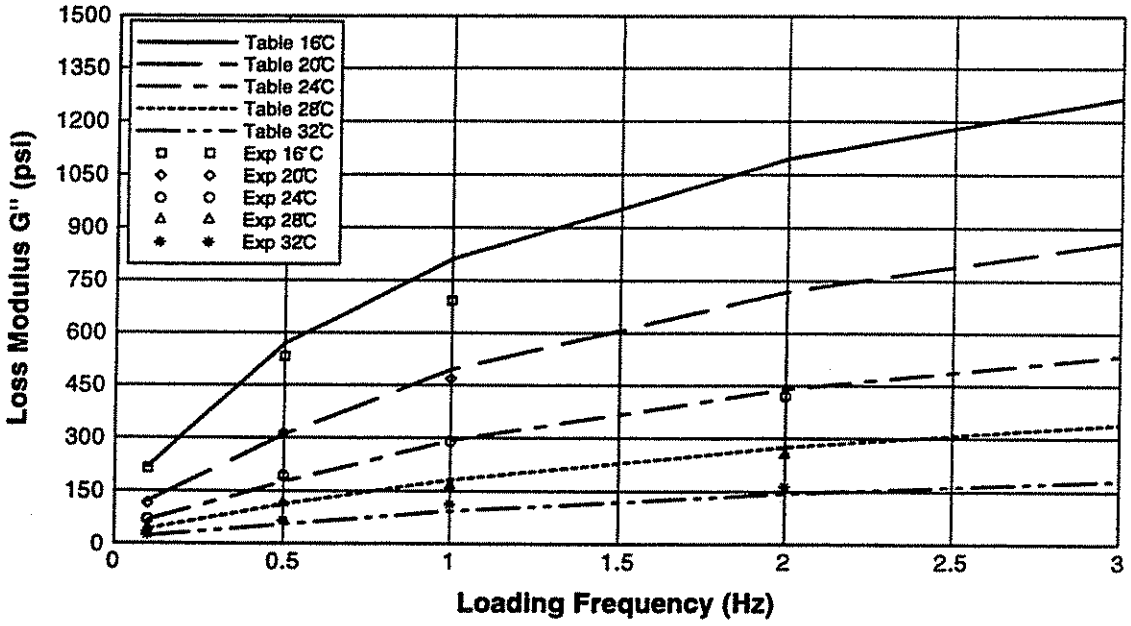

Fig. 3.18 - Comparison of measured loss modulus values with those provided by the manufacturer for 5% strain with loading frequencies of 0.1 to 2.0 hz and initial temperatures of 16 to 32 °C.

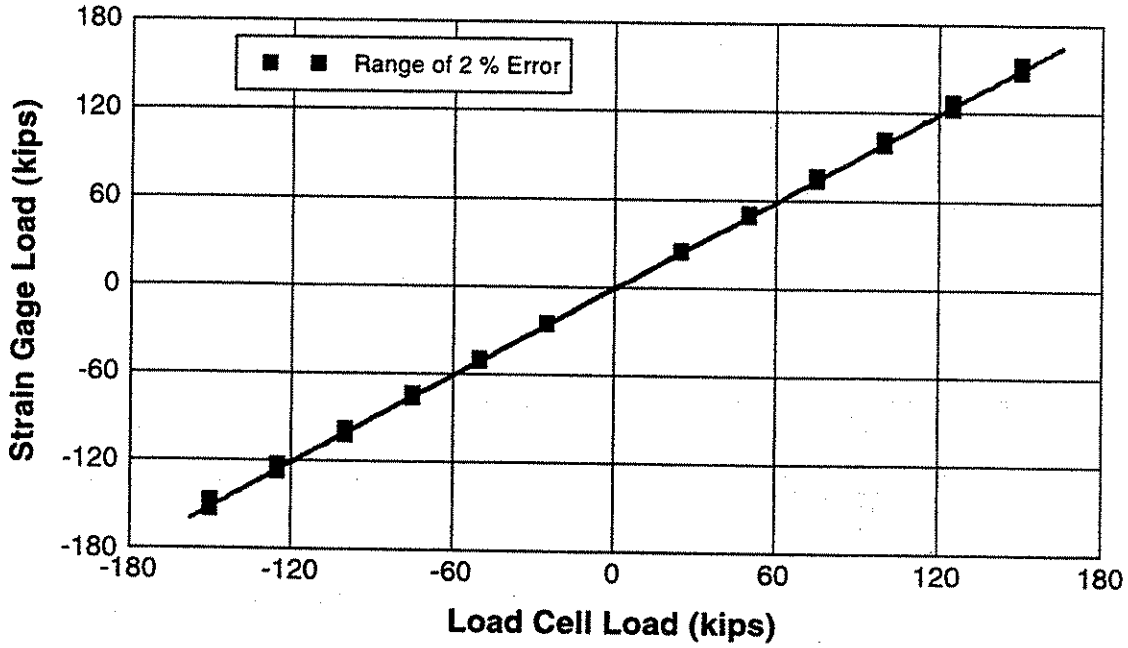

Fig. 3.19 - Comparison of damper axial force determined directly from actuator load cell and that computed from strain gages bonded to the damper.

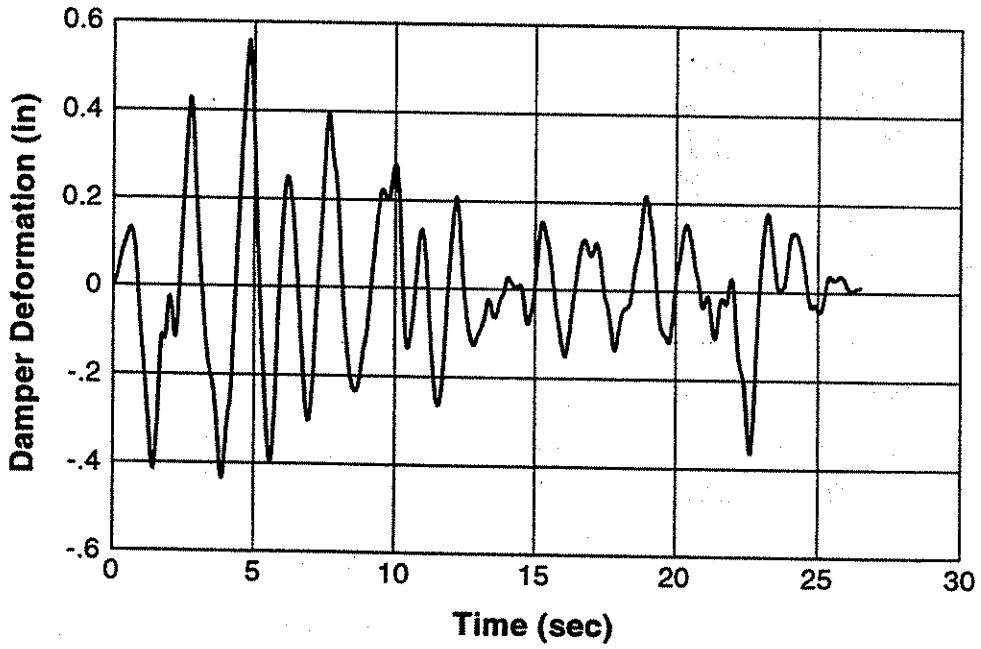

Fig. 3.20a - Individual damper earthquake deformation time history for 1.5 x El Centro 1940.

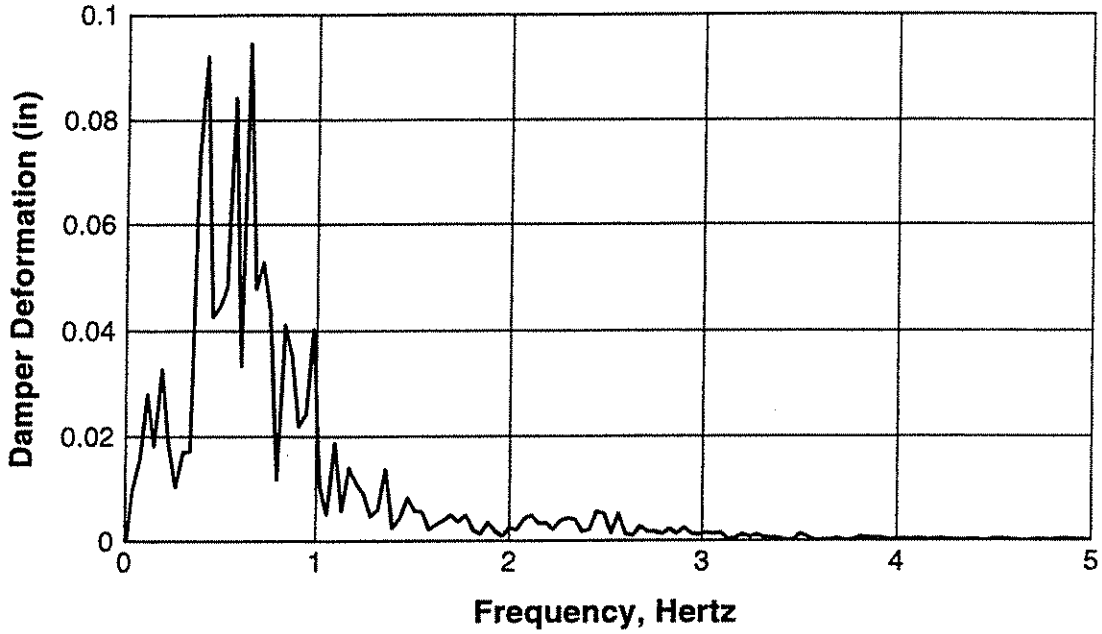

Fig. 3.21b - FFT of individual damper deformation time history for 1.5 x El Centro 1940.

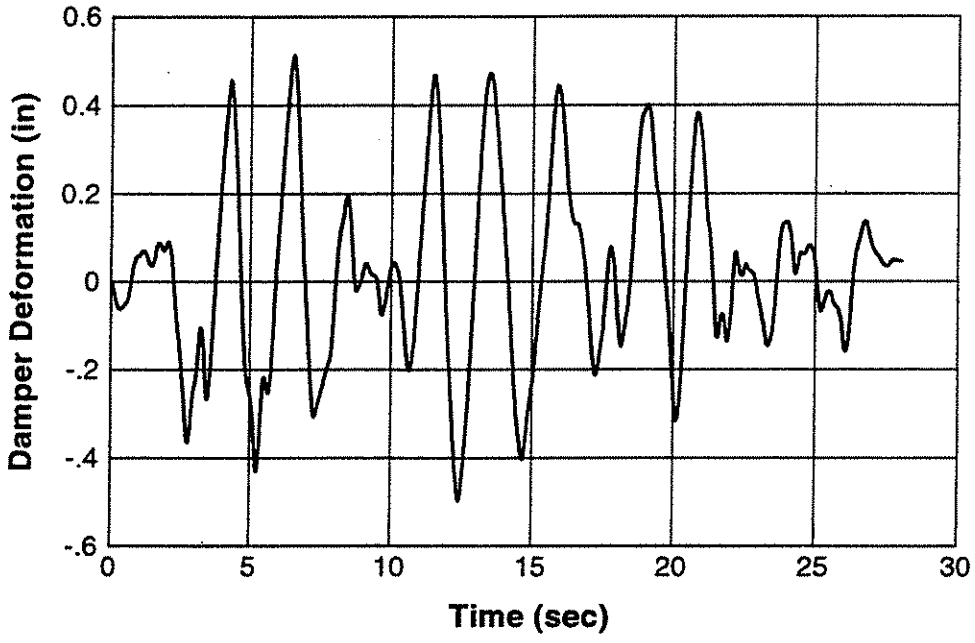

Fig. 3.21a - Individual damper earthquake deformation time history for 1.5 x Hachinohe.

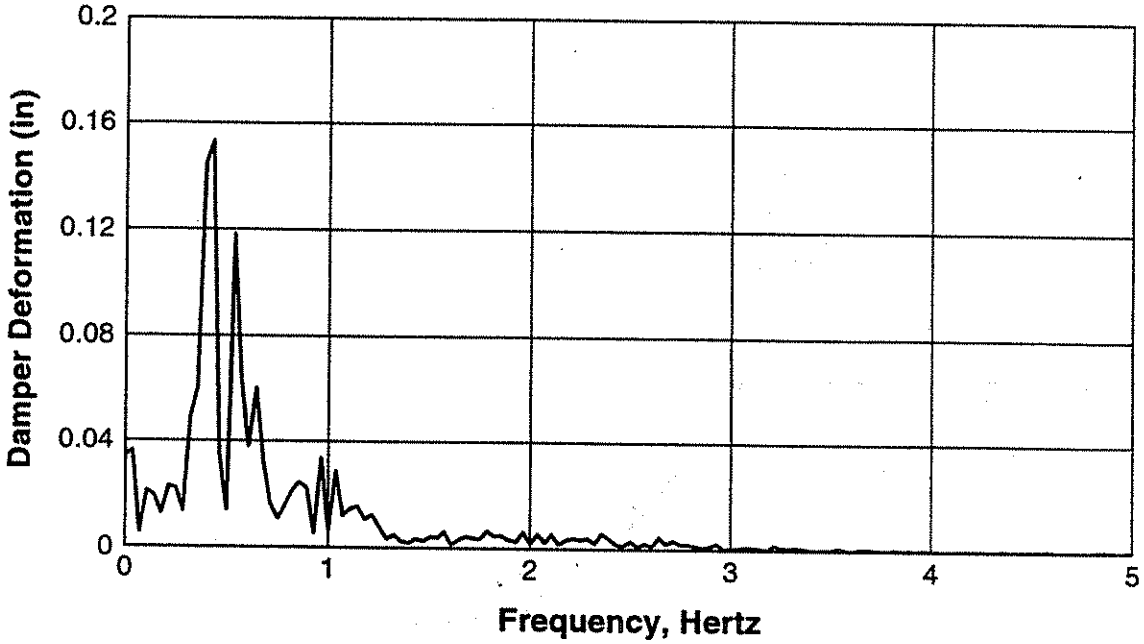

Fig. 3.21b - FFT of individual damper deformation time history for 1.5 x Hachinohe.

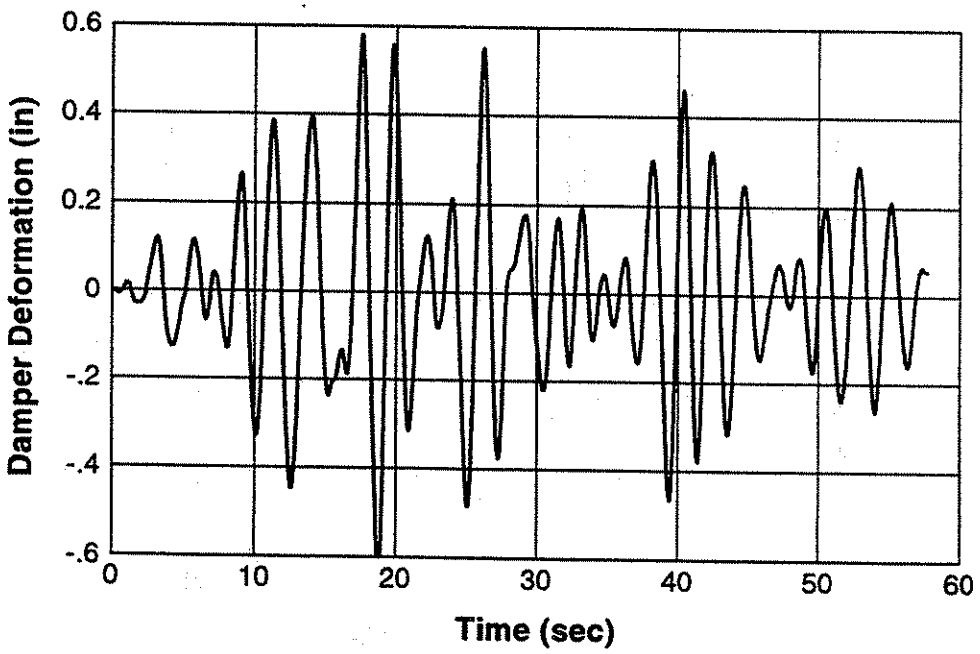

Fig. 3.22a - Individual damper earthquake deformation time history for Mexico City 1985 Central de Abastos - Frigorifico.

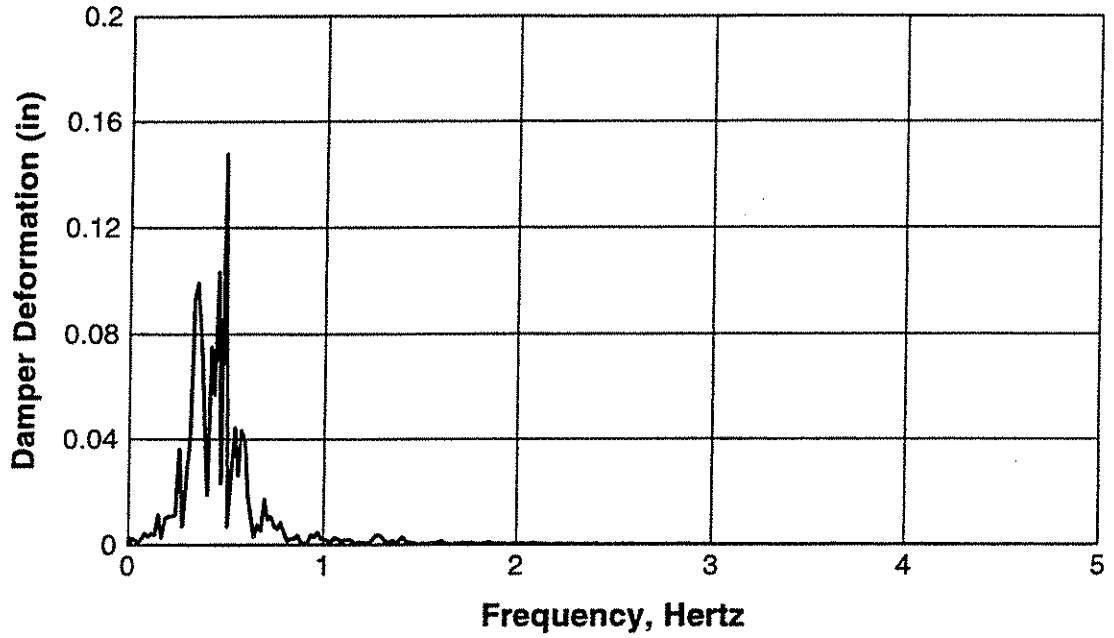

Fig. 3.22b - FFT of individual damper deformation time history for Mexico City 1985 Central de Abastos - Frigorifico.

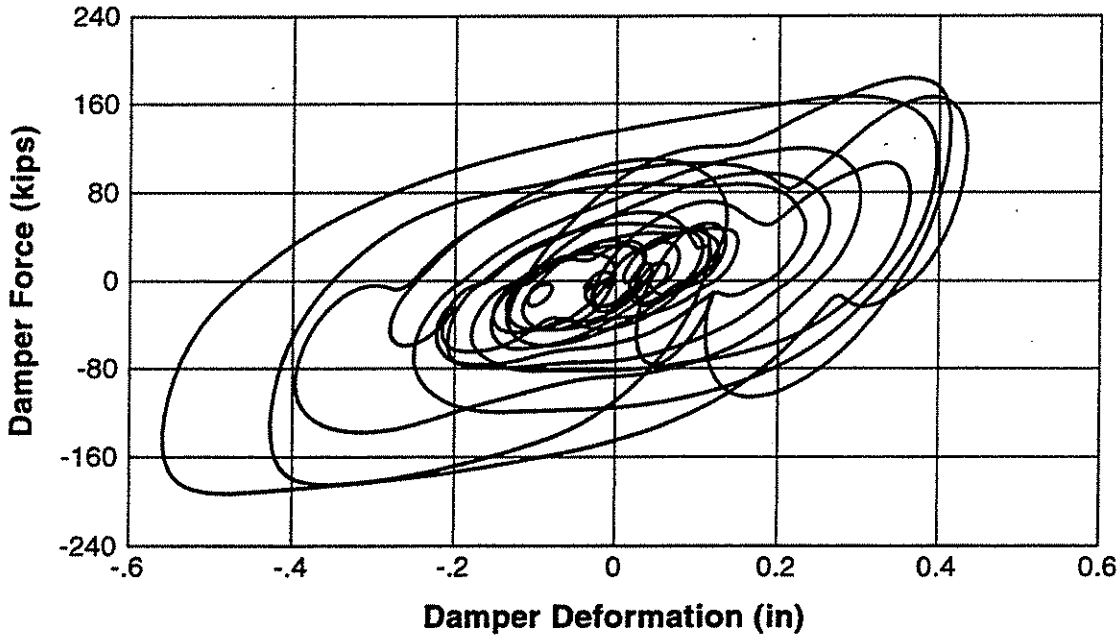

Fig. 3.23a - Individual damper force-deformation response for 1.5 x El Centro 1940.

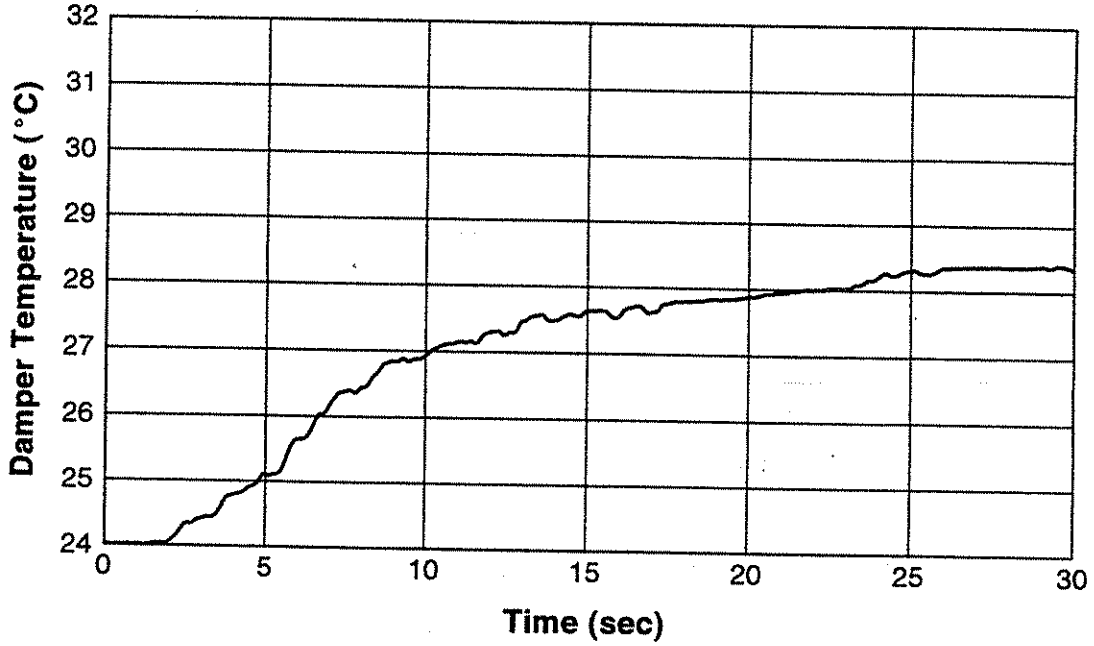

Fig. 3.23b - Individual damper temperature rise for 1.5 x El Centro 1940.

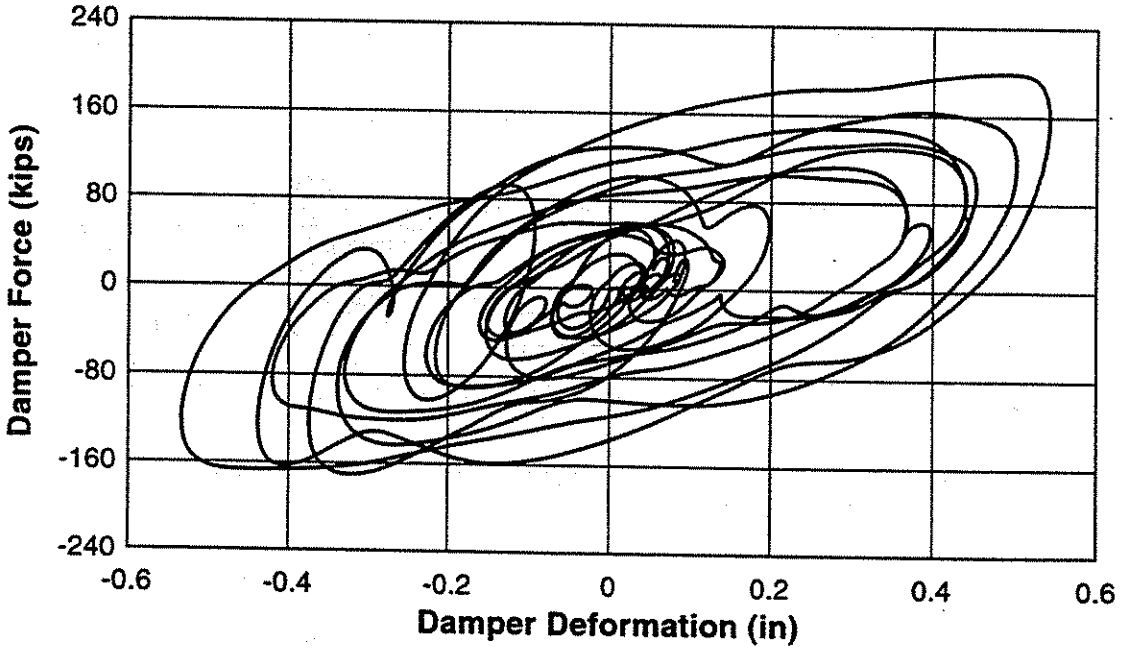

Fig. 3.24a - Individual damper force-deformation response for 1.5 x Hachinohe.

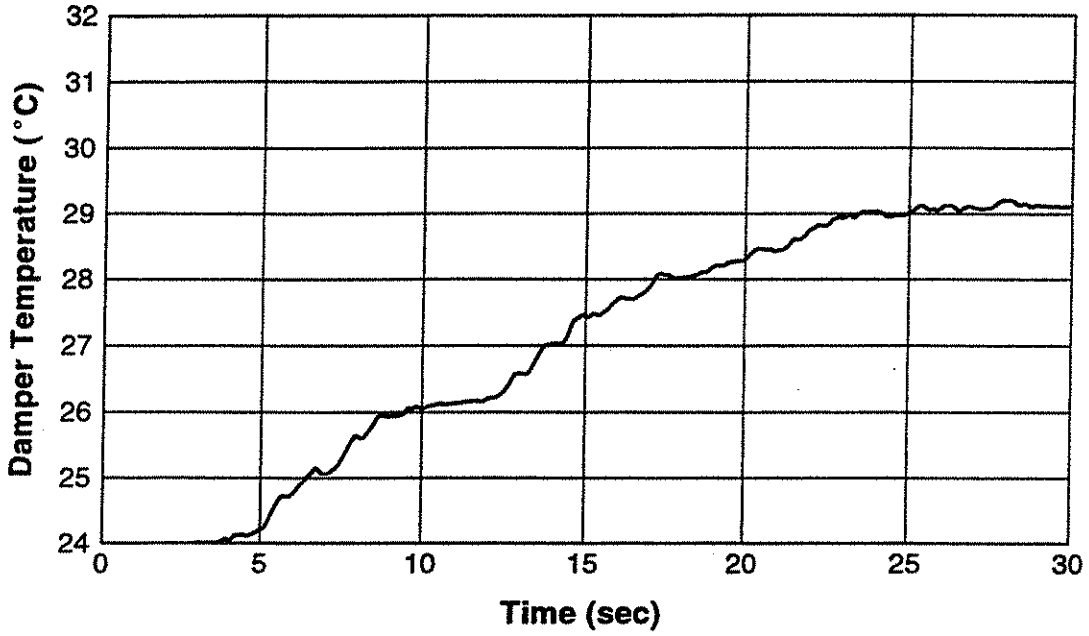

Fig. 3.24b - Individual damper temperature rise for 1.5 x Hachinohe.

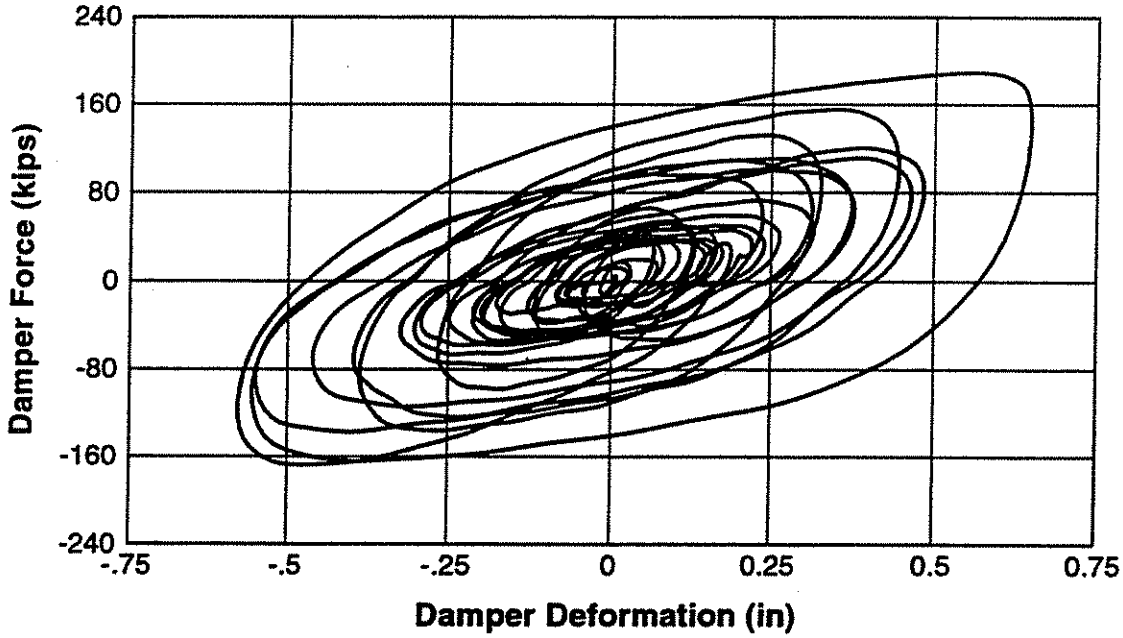

Fig. 3.25a - Individual damper force-deformation response for Mexico City 1985 Central de Abastos - Frigorifico.

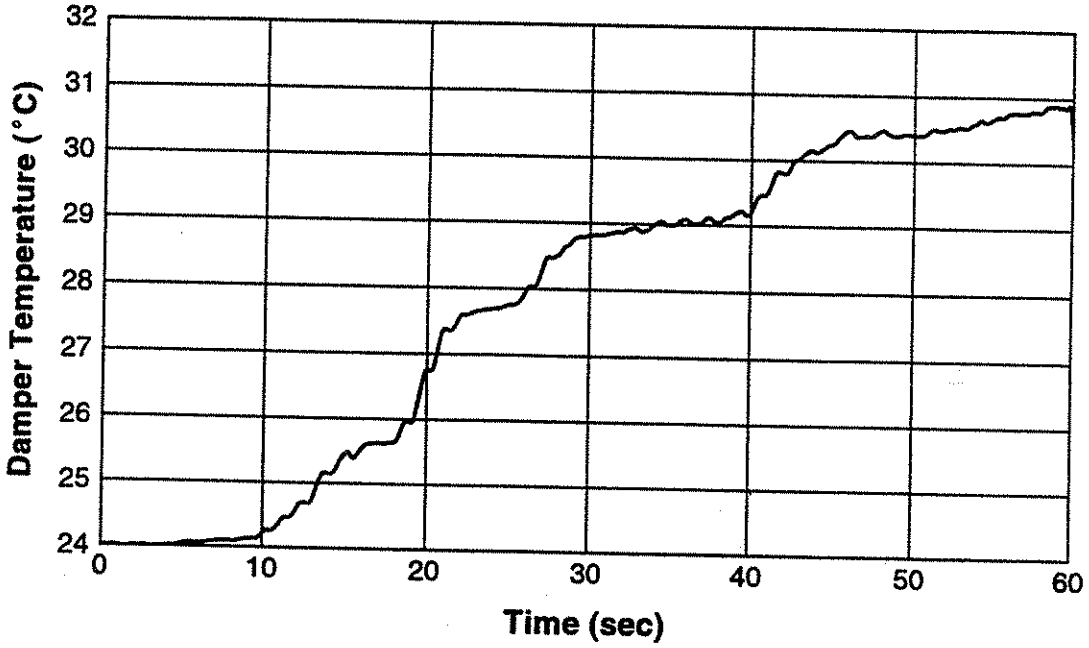

Fig. 3.25b - Individual damper temperature rise for Mexico City 1985 Central de Abastos - Frigorifico.

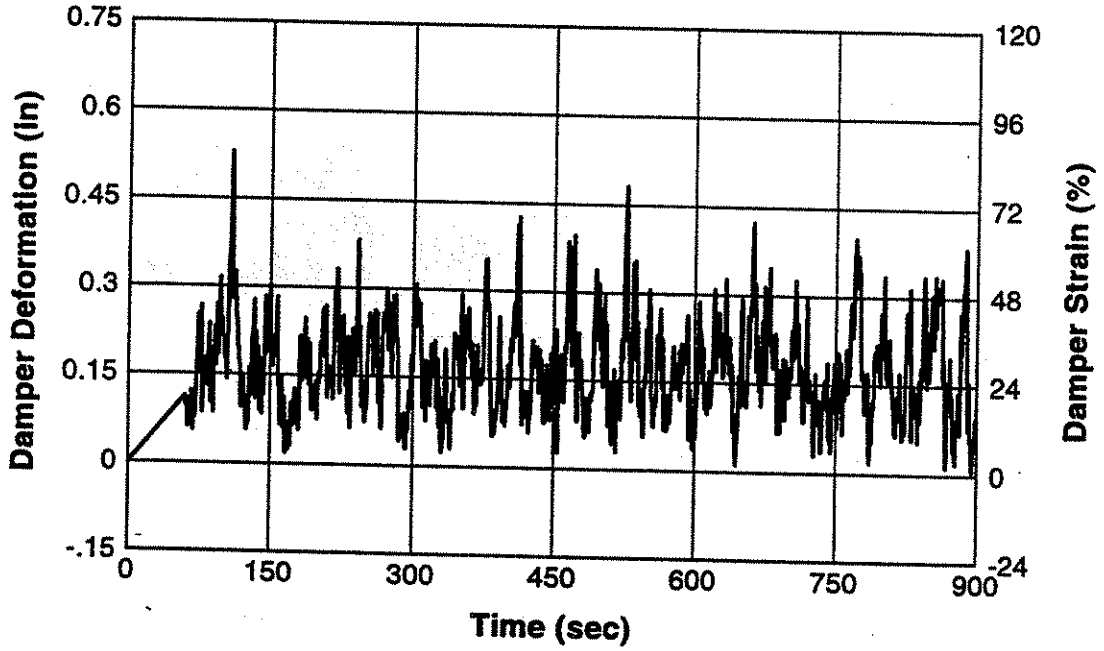

Fig. 3.26a - First quarter of hour-long simulated along-wind damper displacement response for 500 year return period event.

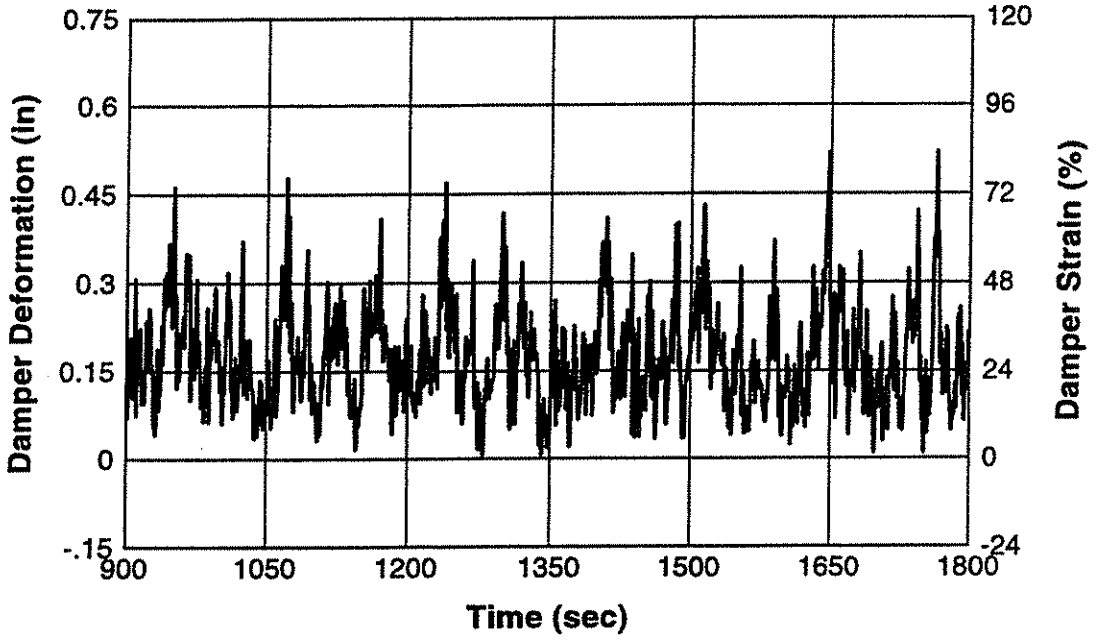

Fig. 3.26b - Second quarter of hour-long simulated along-wind damper displacement response for 500 year return period event.

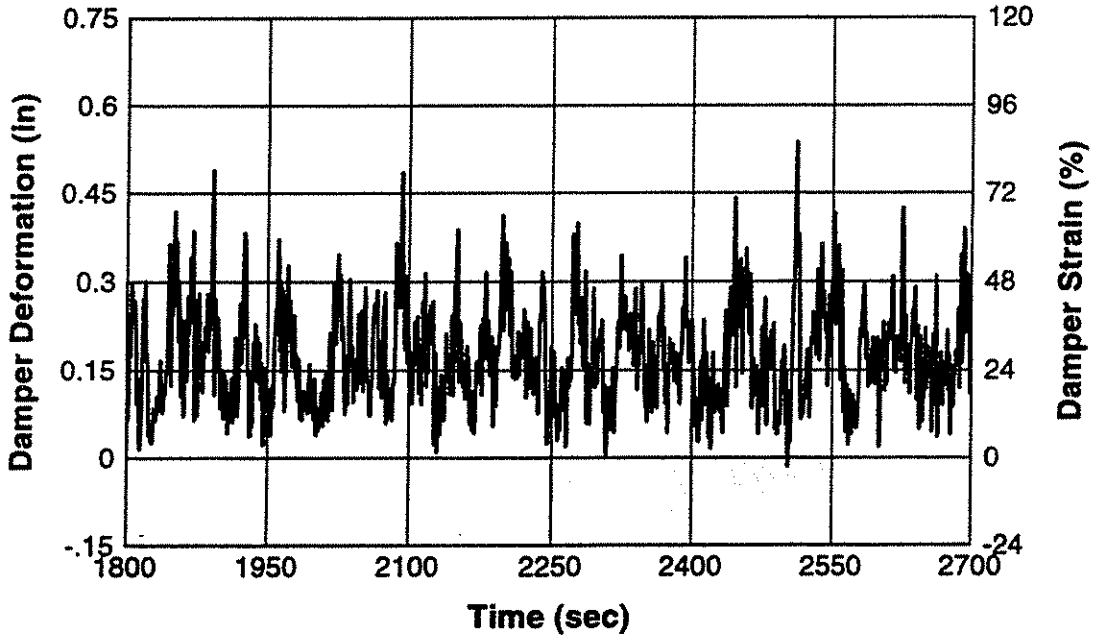

Fig. 3.26c - Third quarter of hour-long simulated along-wind damper displacement response for 500 year return period event.

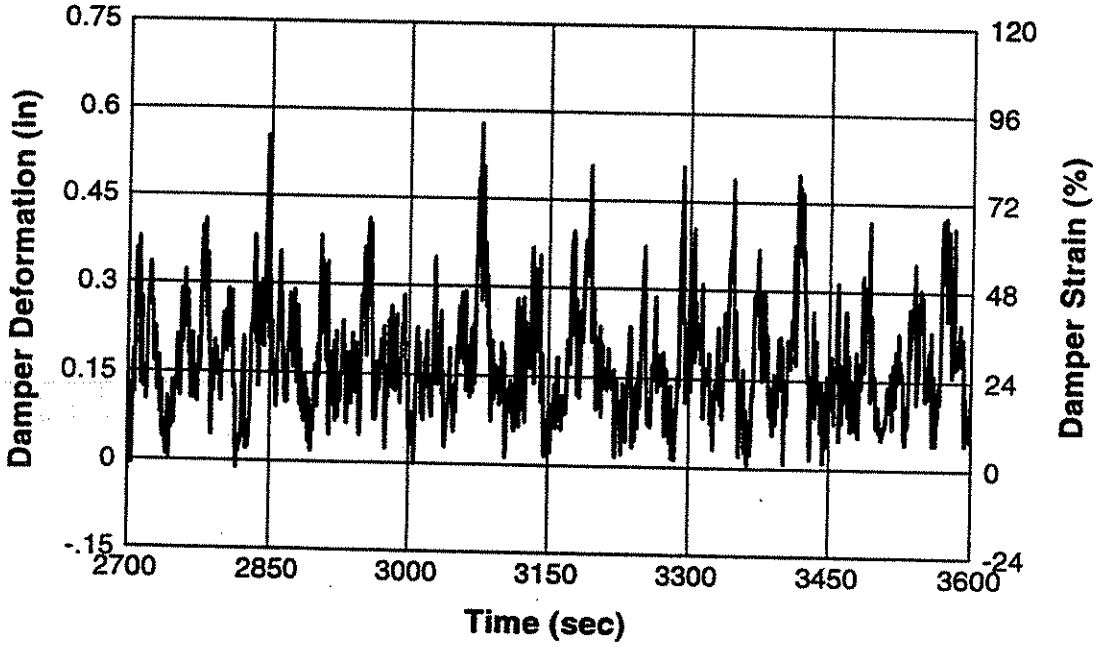

Fig. 3.26d - Fourth quarter of hour-long simulated along-wind damper displacement response for 500 year return period event.

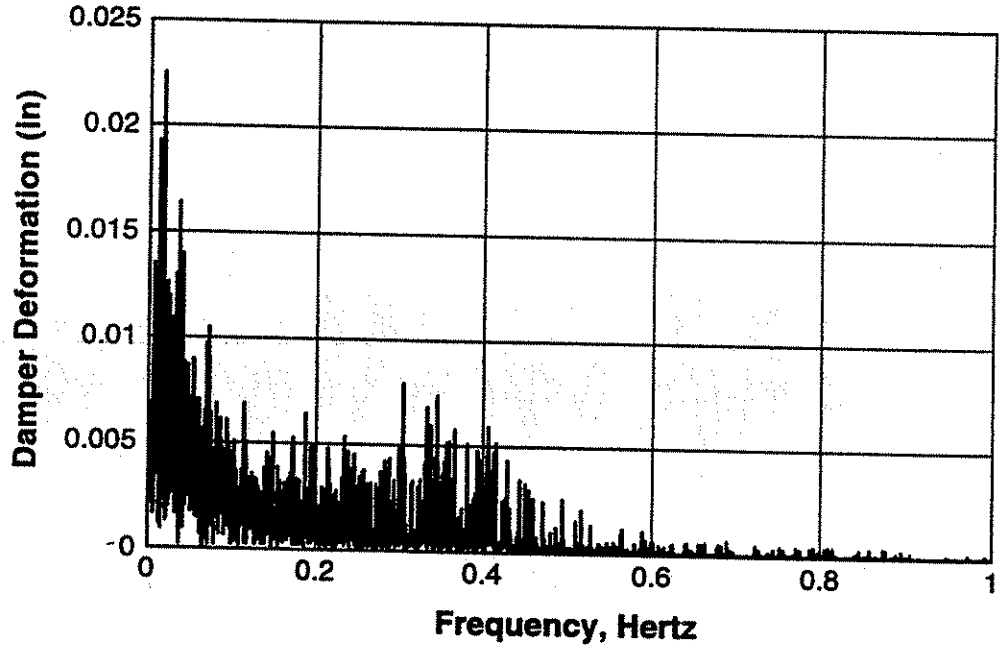

Fig. 3.27 - FFT of individual damper displacement time history for along-wind 500 year return period event

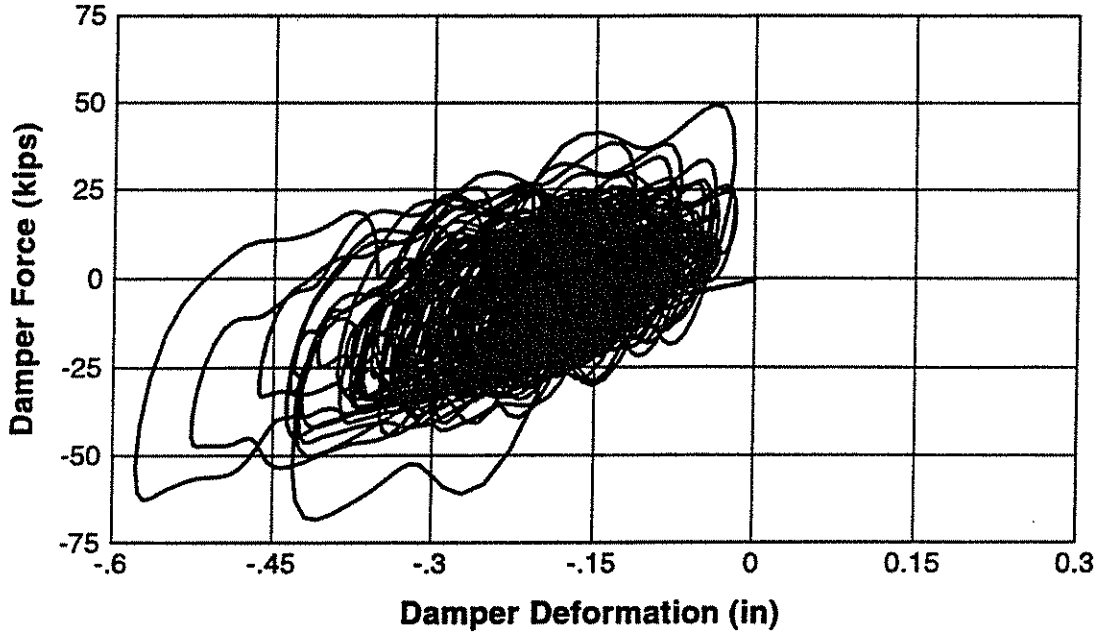

Fig. 3.28a - Measured force-deformation response at beginning of hour-long simulated along-wind 500 year return period event.

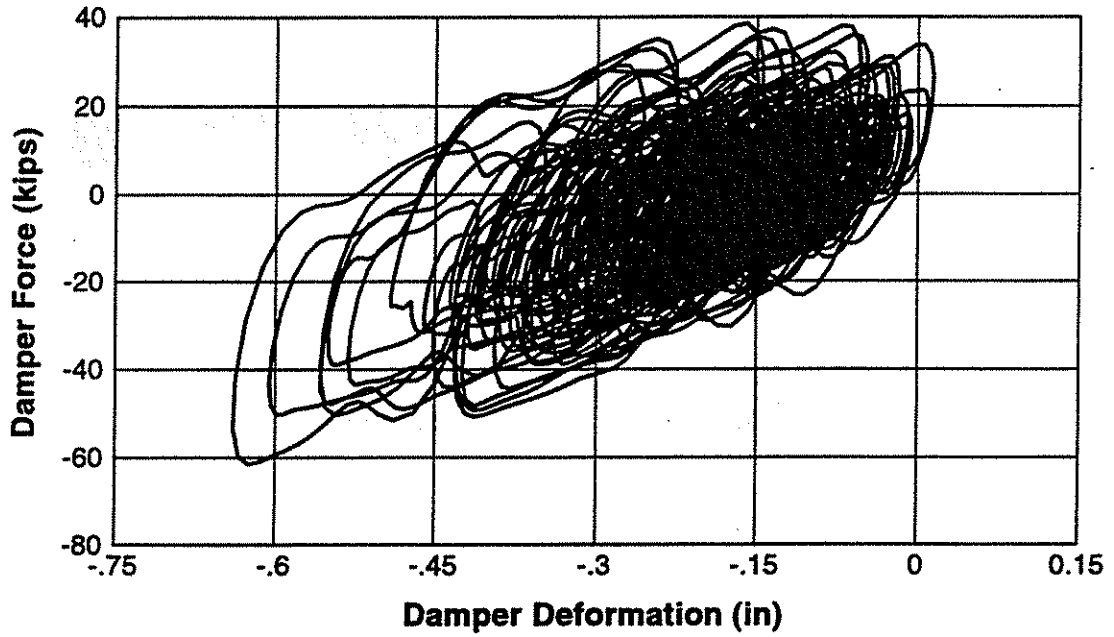

Fig. 3.28b - Measured force-deformation response at end of hour-long simulated along-wind 500 year return period event.

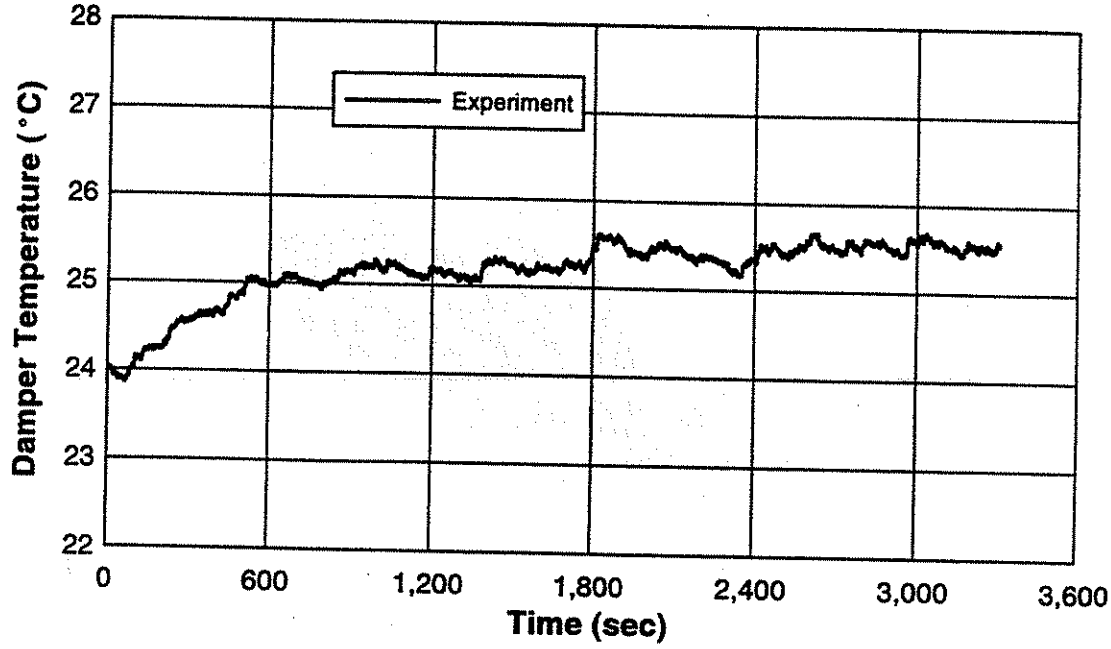

Fig. 3.29 - Measured temperature rise during hour-long simulated along-wind 500 year return period event.

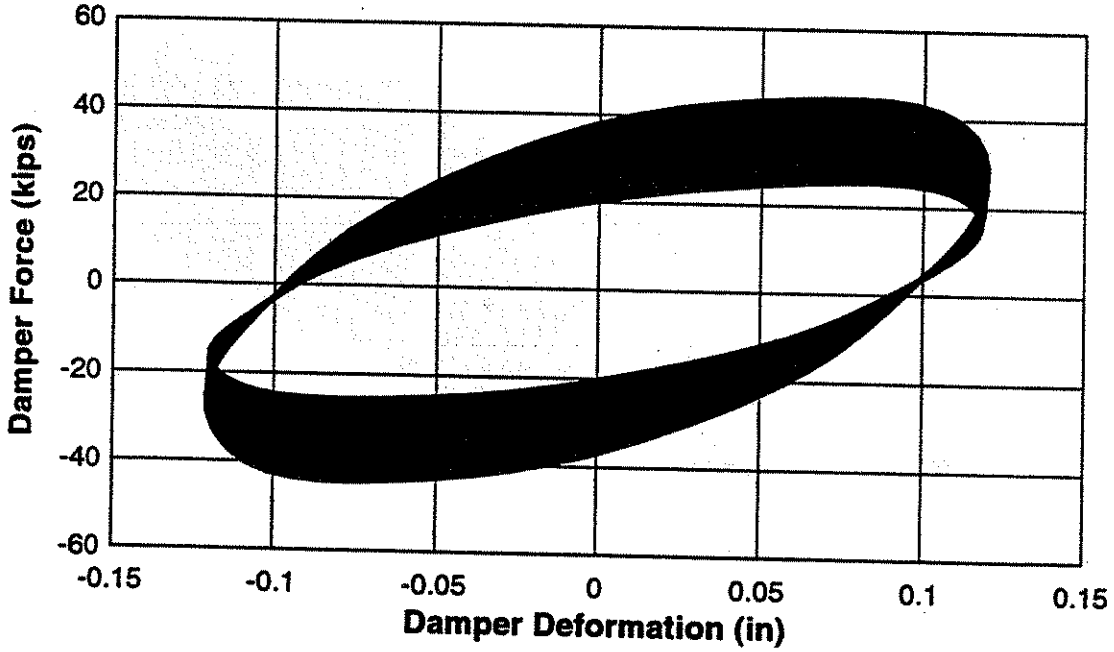

Fig. 3.30a - Measured force-deformation response at beginning of hour-long constant amplitude sinusoidal loading at 0.37 hz and 19% strain.

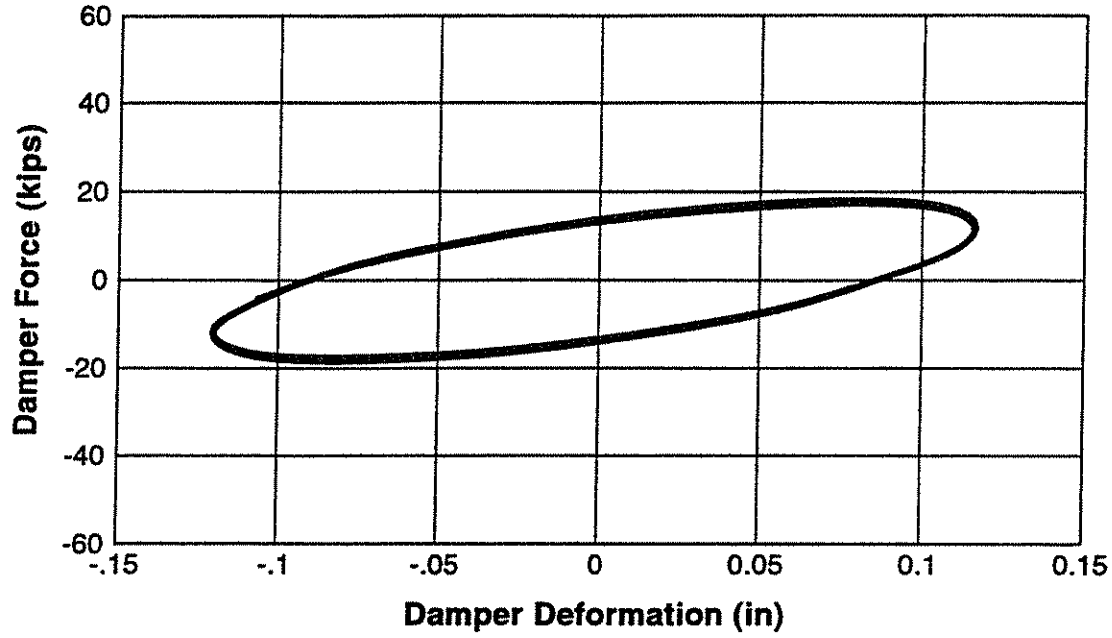

Fig. 3.30b - Measured force-deformation response at end of hour-long constant amplitude sinusoidal loading at 0.37 hz and 19% strain.

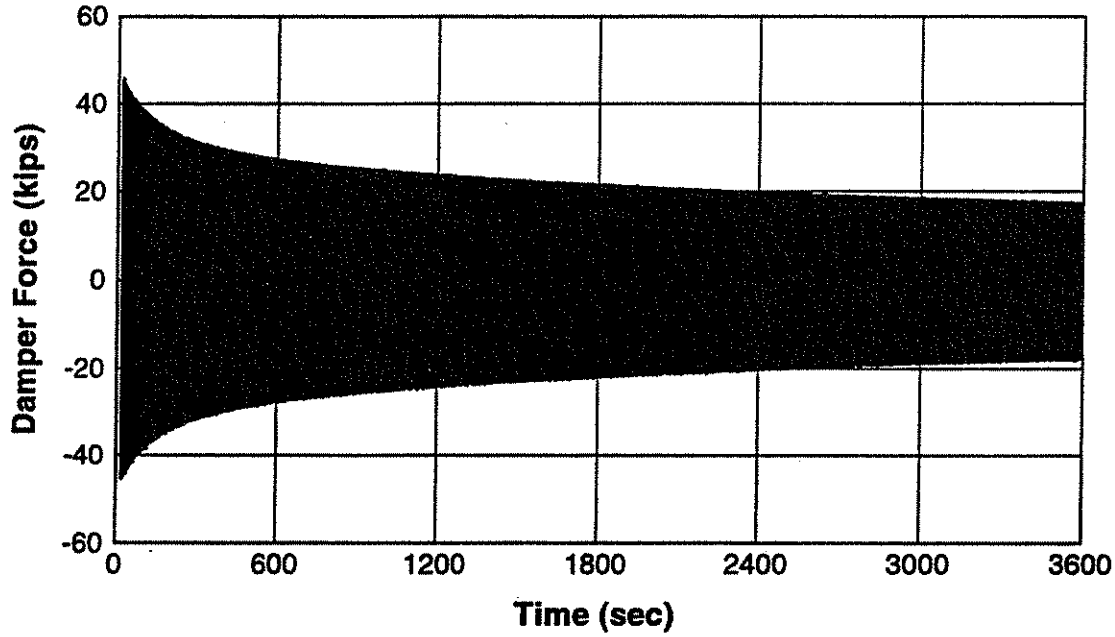

Fig. 3.31 - Measured damper force during hour-long constant amplitude sinusoidal loading at 0.37 hz and 19% strain.

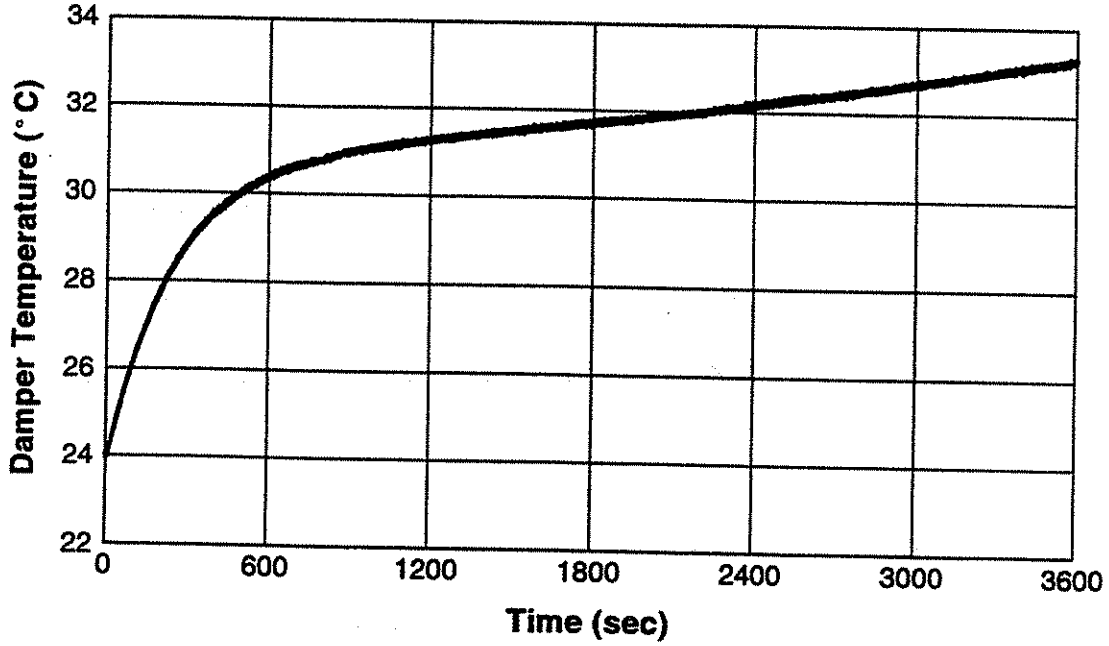

Fig. 3.32 - Measured damper temperature rise during hour-long constant amplitude sinusoidal loading at 0.37 hz and 19% strain.

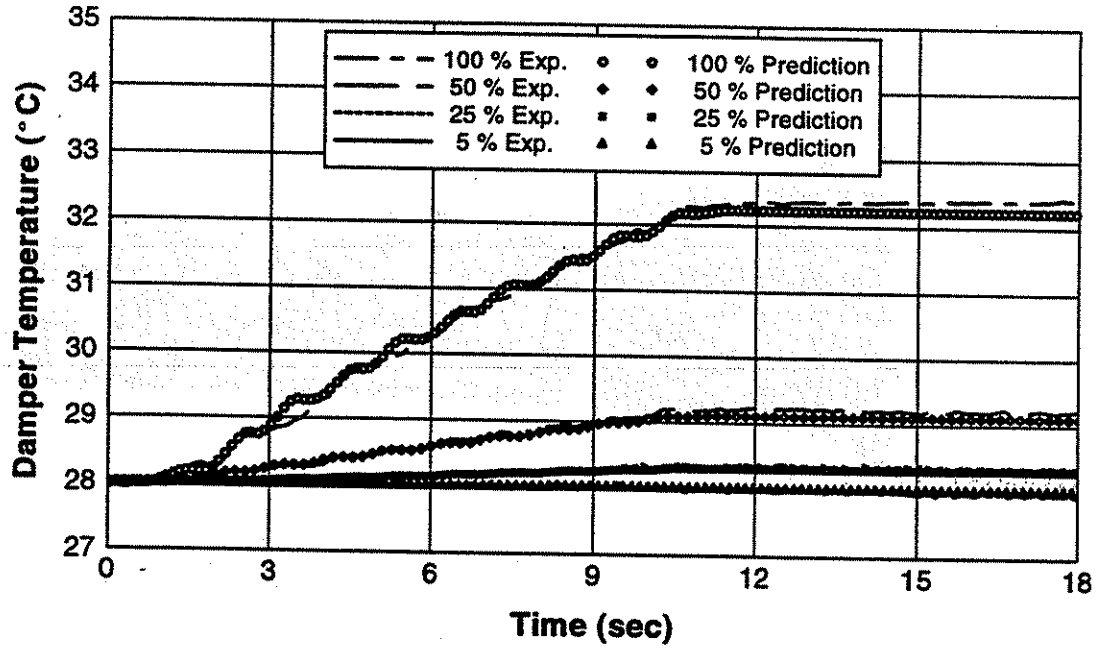

Fig. 3.33 - Comparison of measured and predicted damper temperature for stains of 5, 25, 50, and 100% with 0.5 hz loading frequency and 28 °C initial damper temperature.

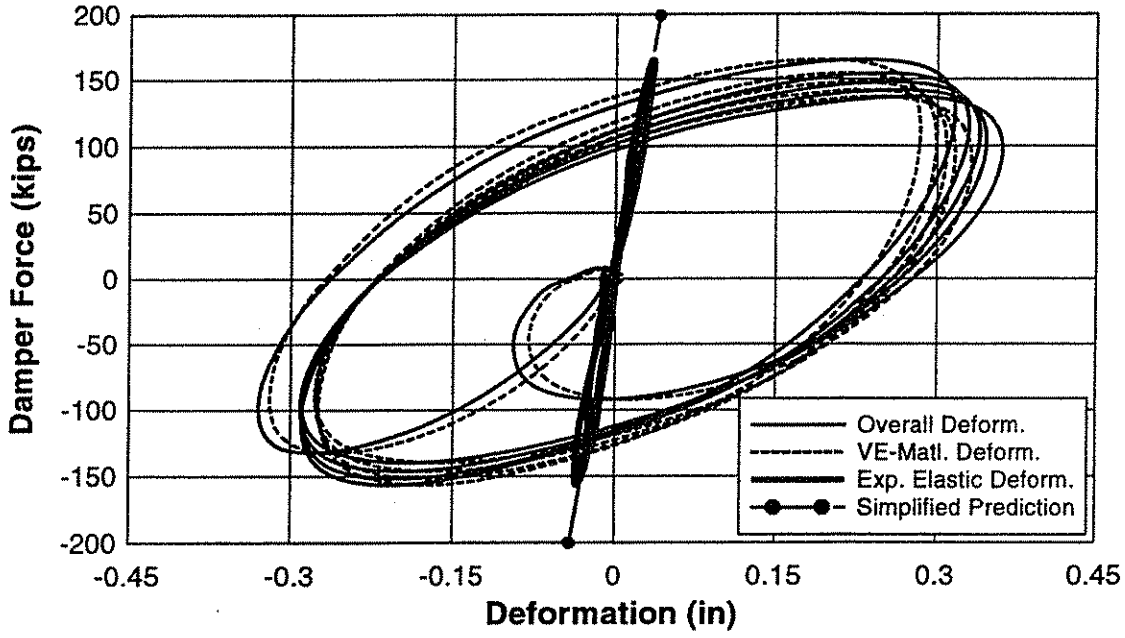

Fig. 3.34 - Measured overall added component deformation, damper deformation, and brace deformation shown with predicted brace stiffness from Eq. 3.11. Test was at 50% strain, 0.5 hz loading frequency, and 24 °C initial damper temperature.

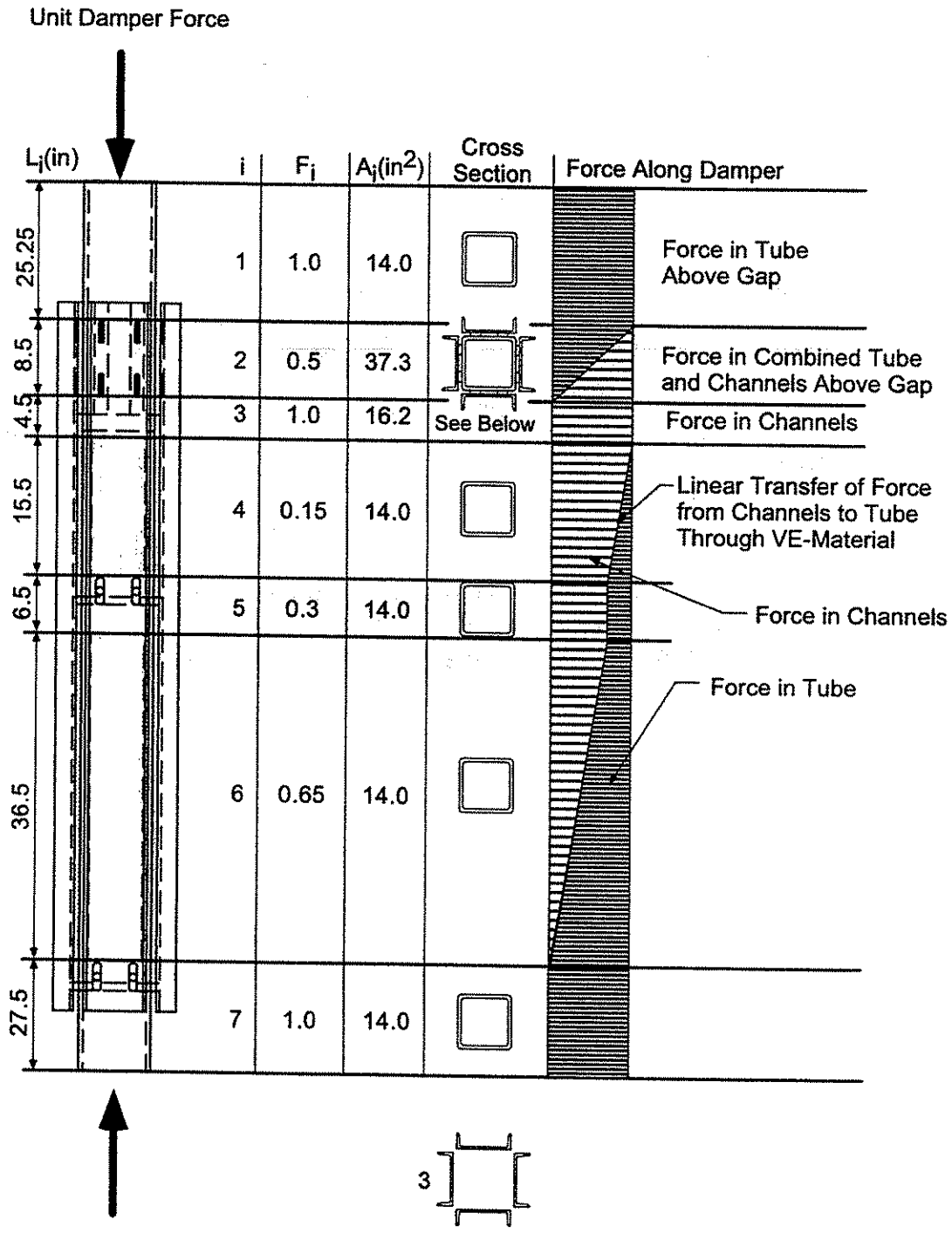

Fig. 3.35 - Method used to predict brace stiffness.

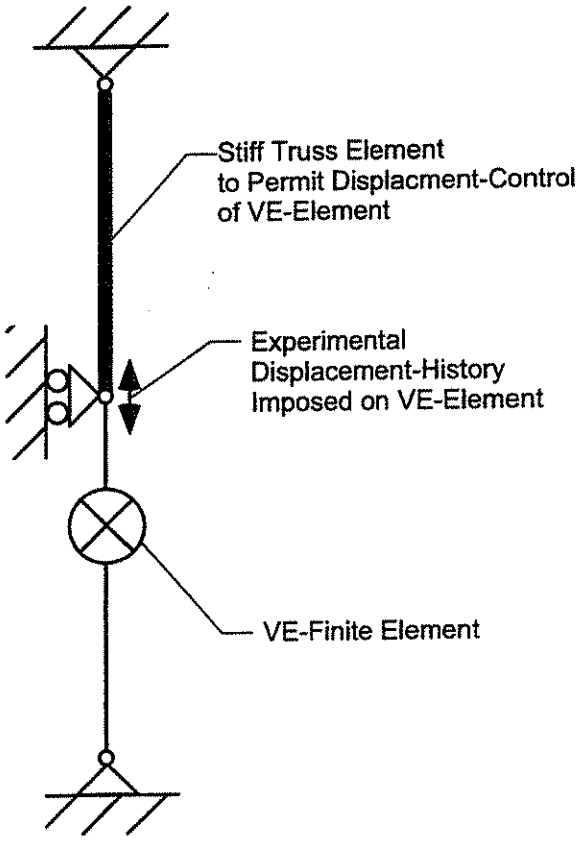

Fig. 3.36 - Schematic of individual damper test finite element model used to perform correlative analyses.

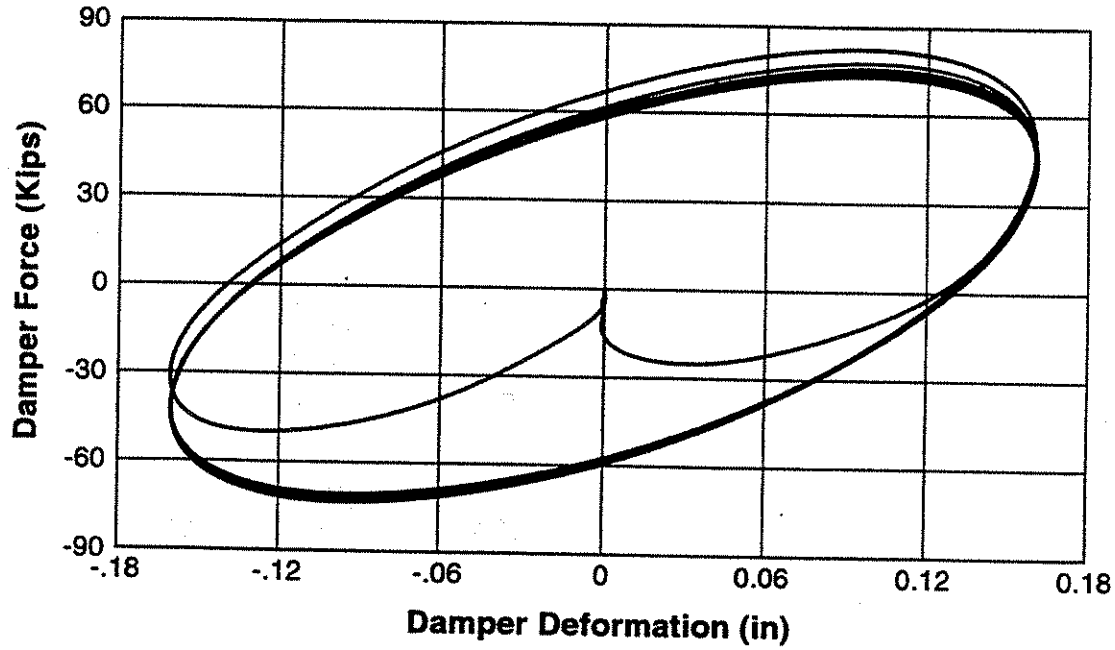

Fig. 3.37a - Measured damper force-deformation response for 25% strain, 0.1 hz loading frequency, and 16 °C initial damper temperature.

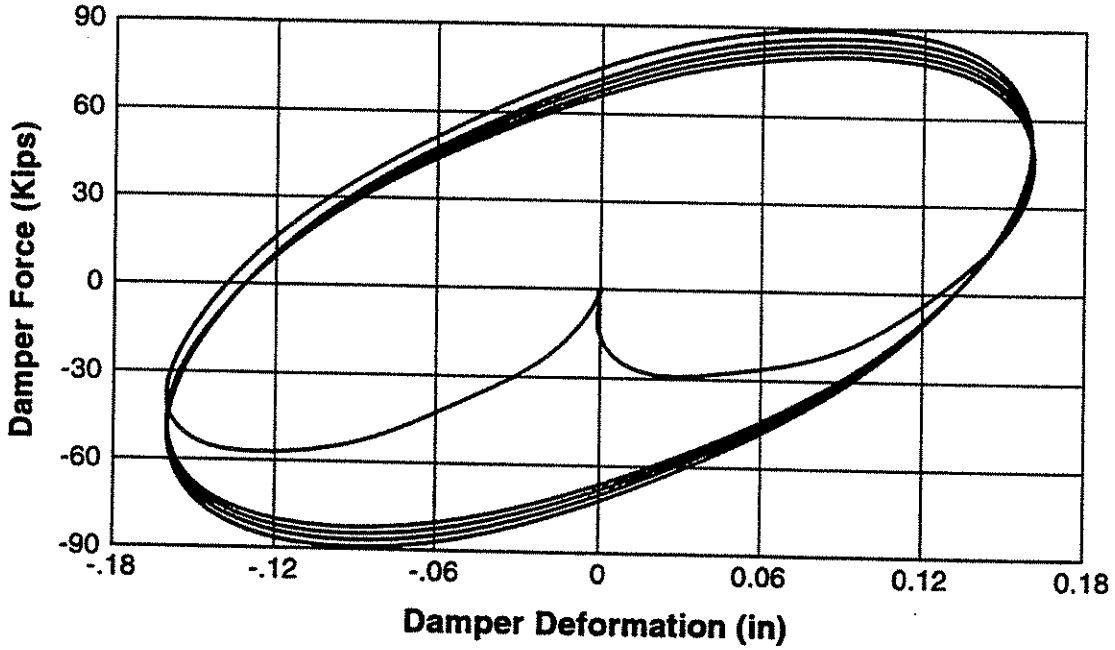

Fig. 3.37b - Analytically predicted damper force-deformation response for 25% strain, 0.1 hz loading frequency, and 16 °C initial damper temperature.

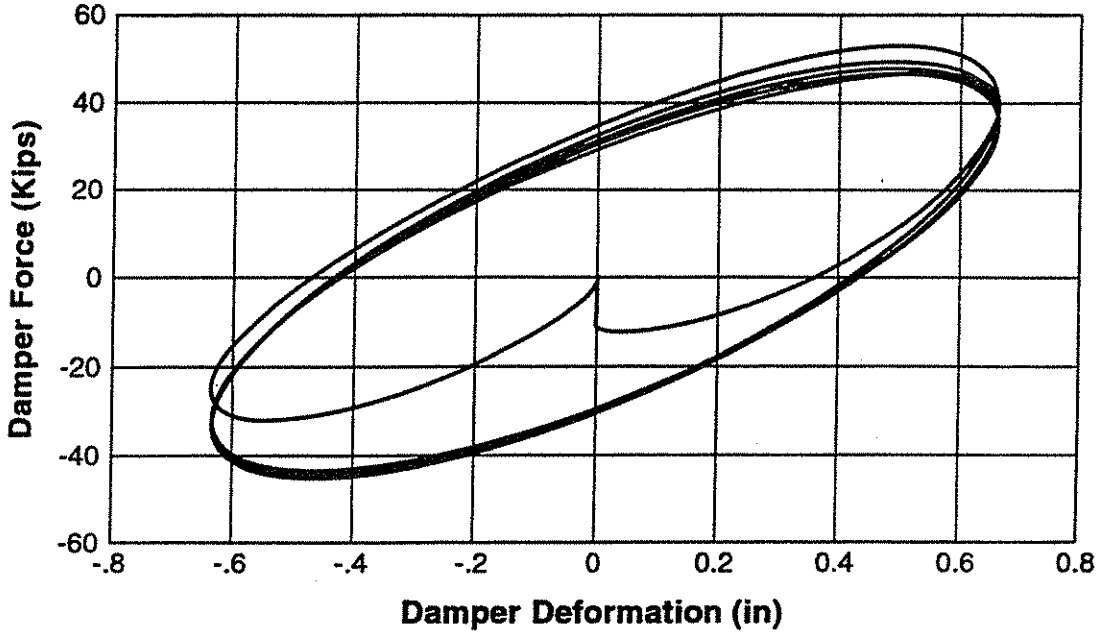

Fig. 3.38a - Measured damper force-deformation response for 100% strain, 0.1 hz loading frequency, and 32 °C initial damper temperature.

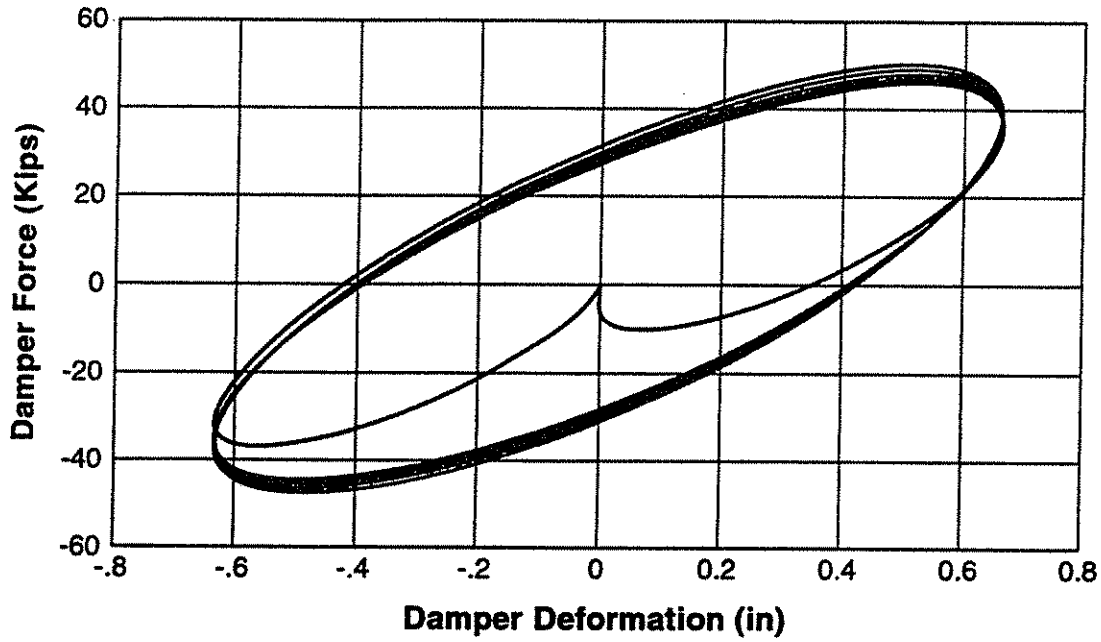

Fig. 3.38b - Analytically predicted damper force-deformation response for 100% strain, 0.1 hz loading frequency, and 32 °C initial damper temperature.

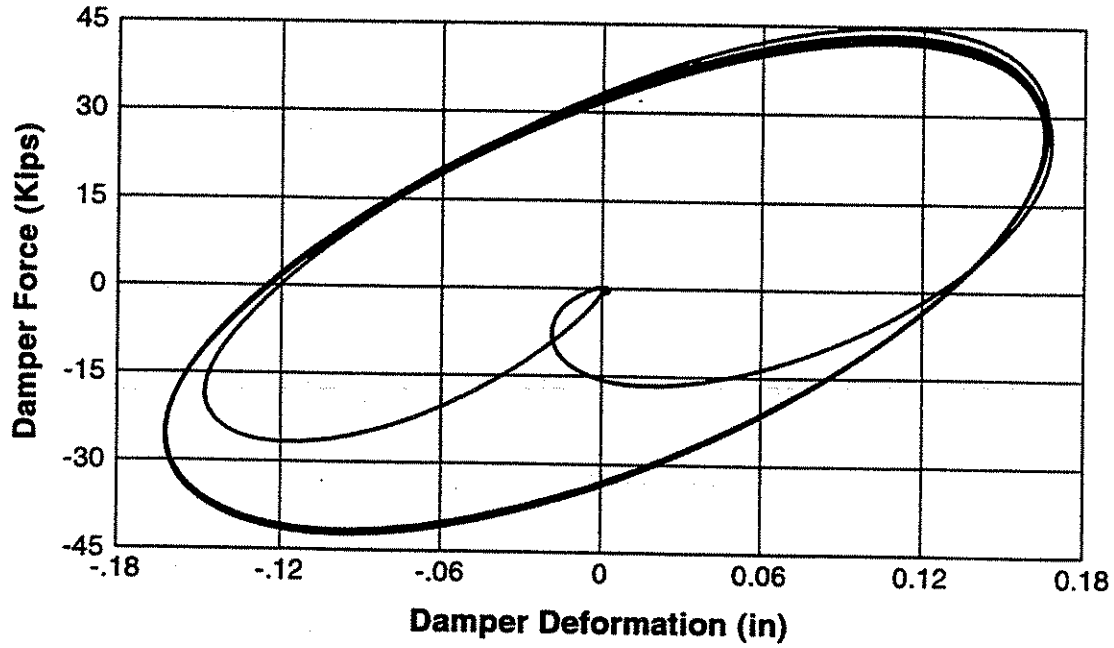

Fig. 3.39a - Measured damper force-deformation response for 25% strain, 1.0 hz loading frequency, and 32 °C initial damper temperature.

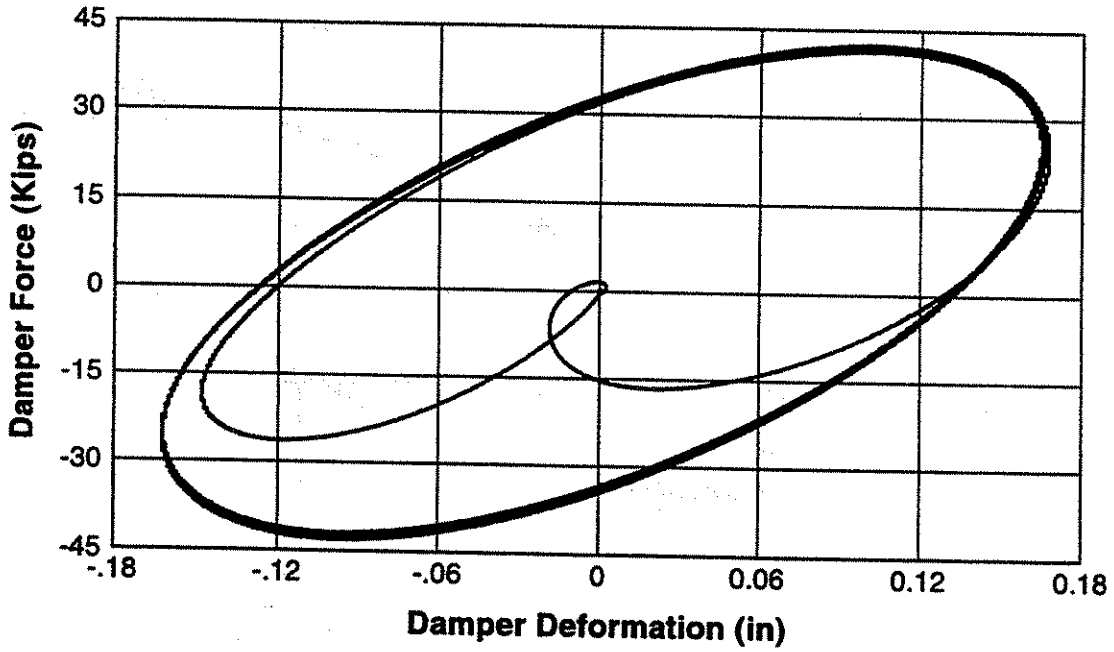

Fig. 3.39b - Analytically predicted damper force-deformation response for 25% strain, 1.0 hz loading frequency, and 32 °C initial damper temperature.

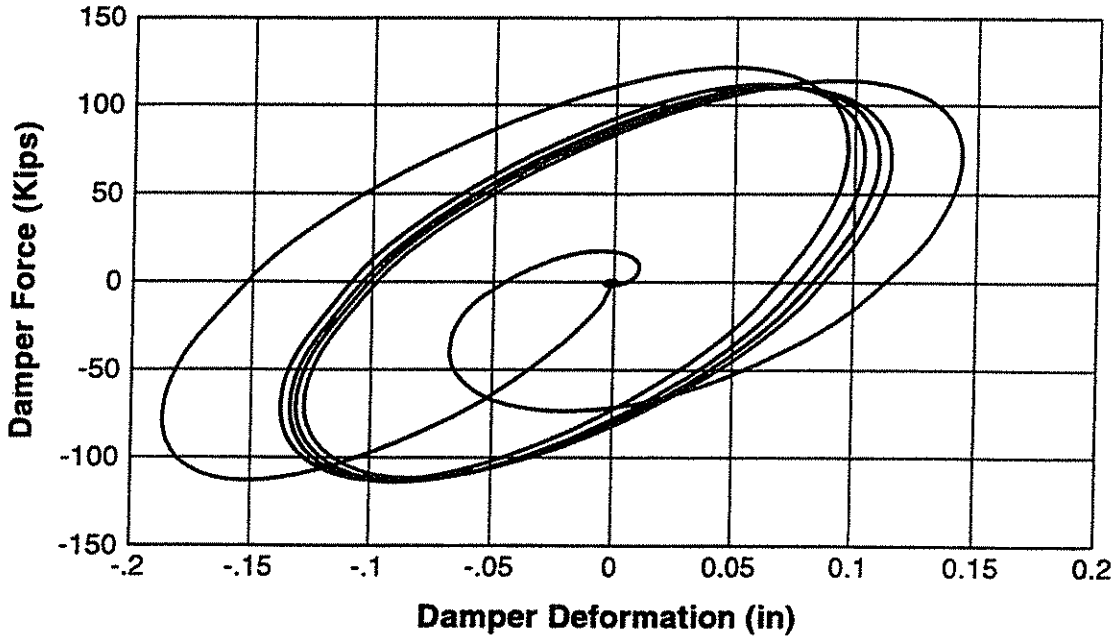

Fig. 3.40a - Measured damper force-deformation response for 25% strain, 2.0 hz loading frequency, and 24 °C initial damper temperature.

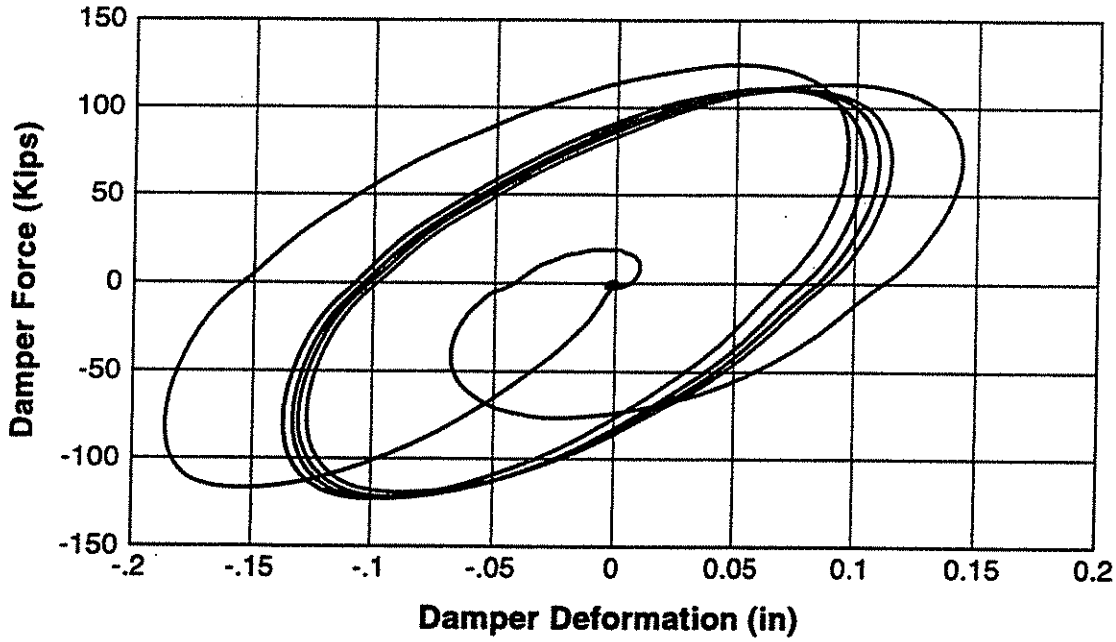

Fig. 3.40b - Analytically predicted damper force-deformation response for 25% strain, 2.0 hz loading frequency, and 24 °C initial damper temperature.

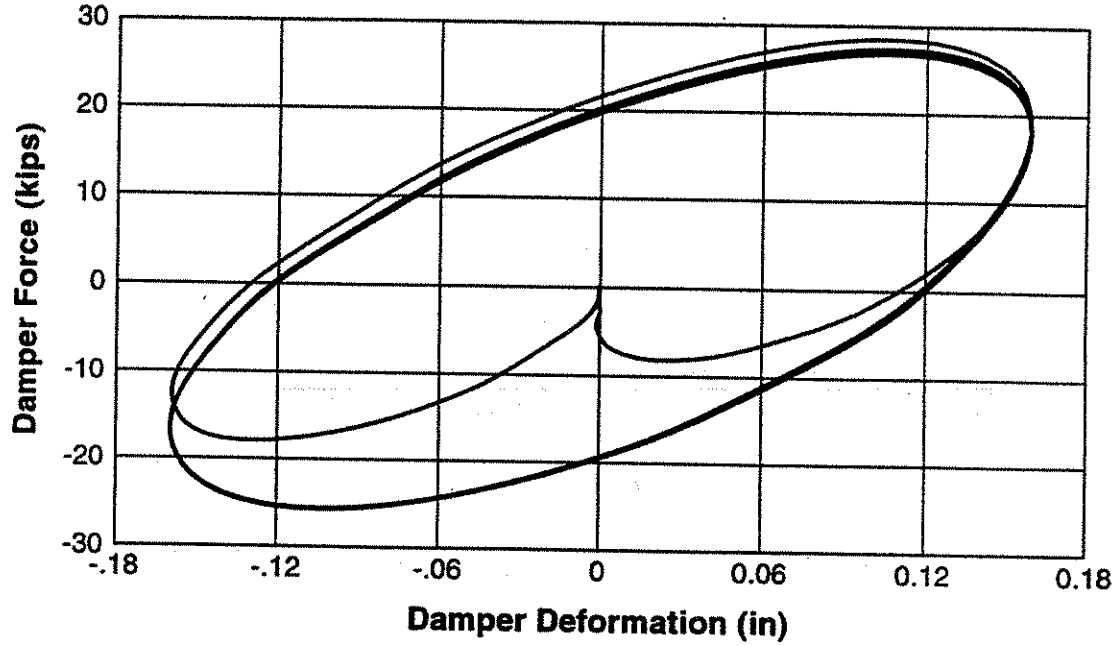

Fig. 3.41a - Measured damper force-deformation response for 25% strain, 0.1 hz loading frequency, and 24 °C initial damper temperature.

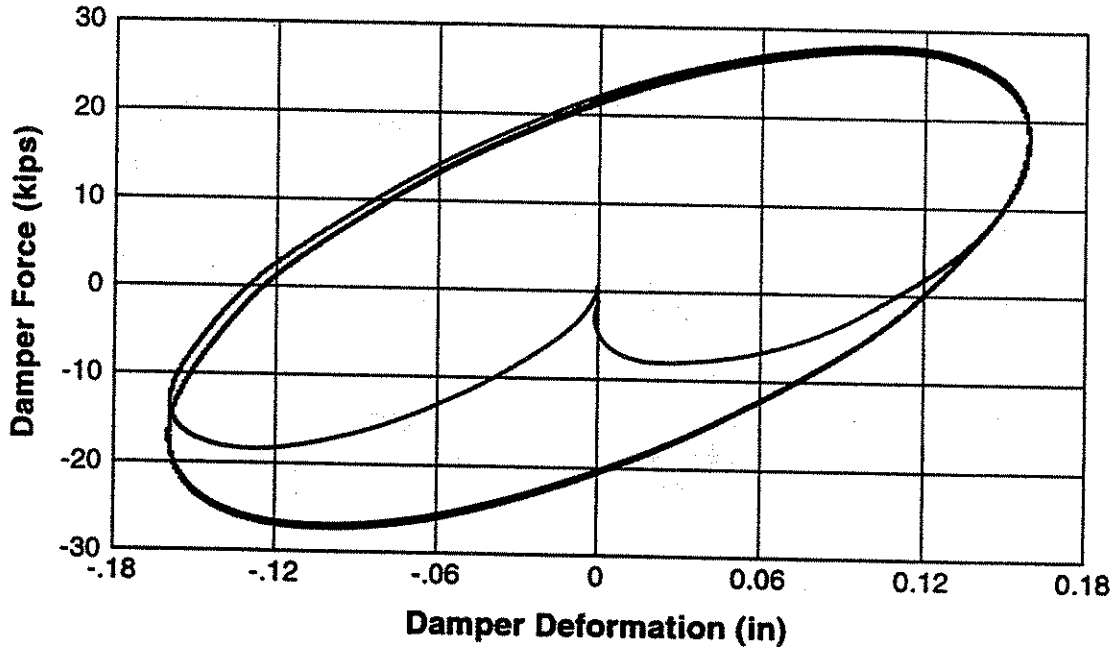

Fig. 3.41b - Analytically predicted damper force-deformation response for 25% strain, 0.1 hz loading frequency, and 24 °C initial damper temperature.

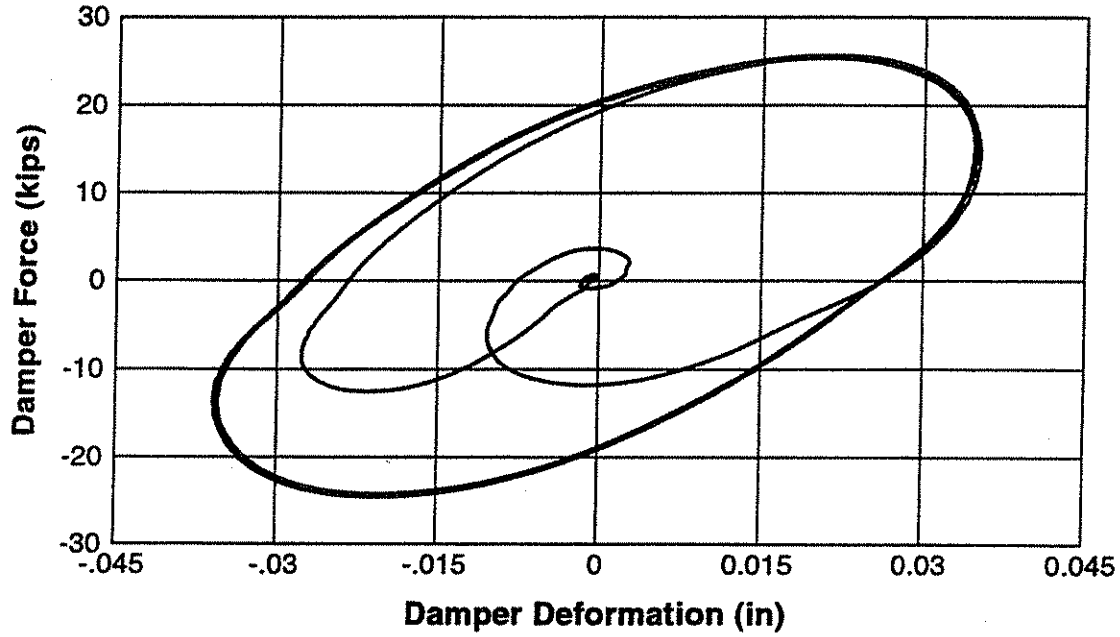

Fig. 3.42a - Measured damper force-deformation response for 5% strain, 1.0 hz loading frequency, and 24 °C initial damper temperature.

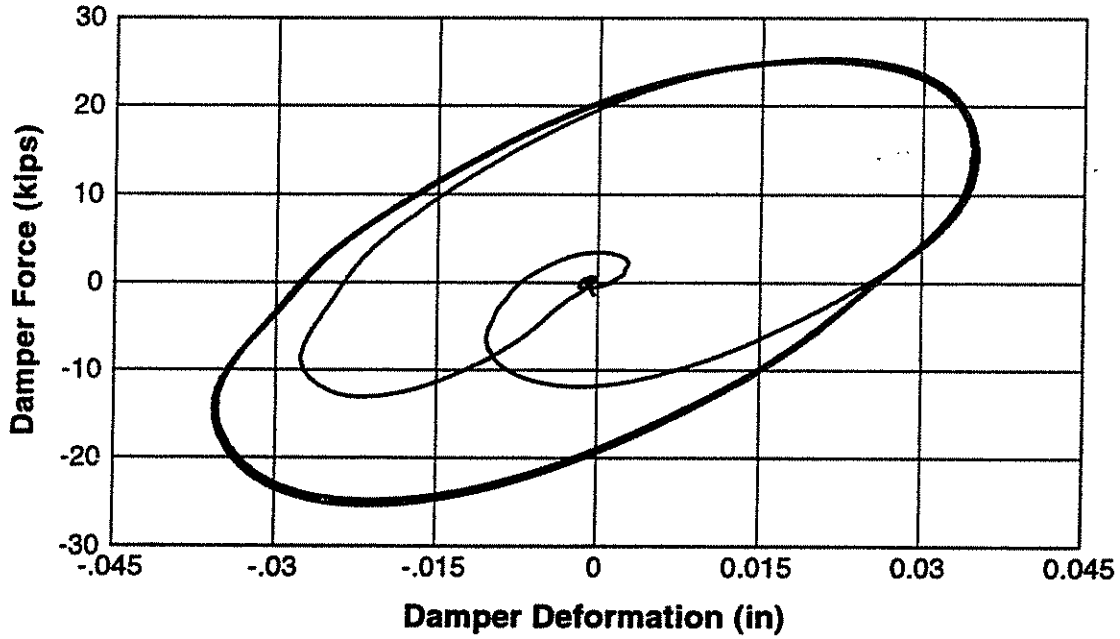

Fig. 3.42b - Analytically predicted damper force-deformation response for 5% strain, 1.0 hz loading frequency, and 24 °C initial damper temperature.

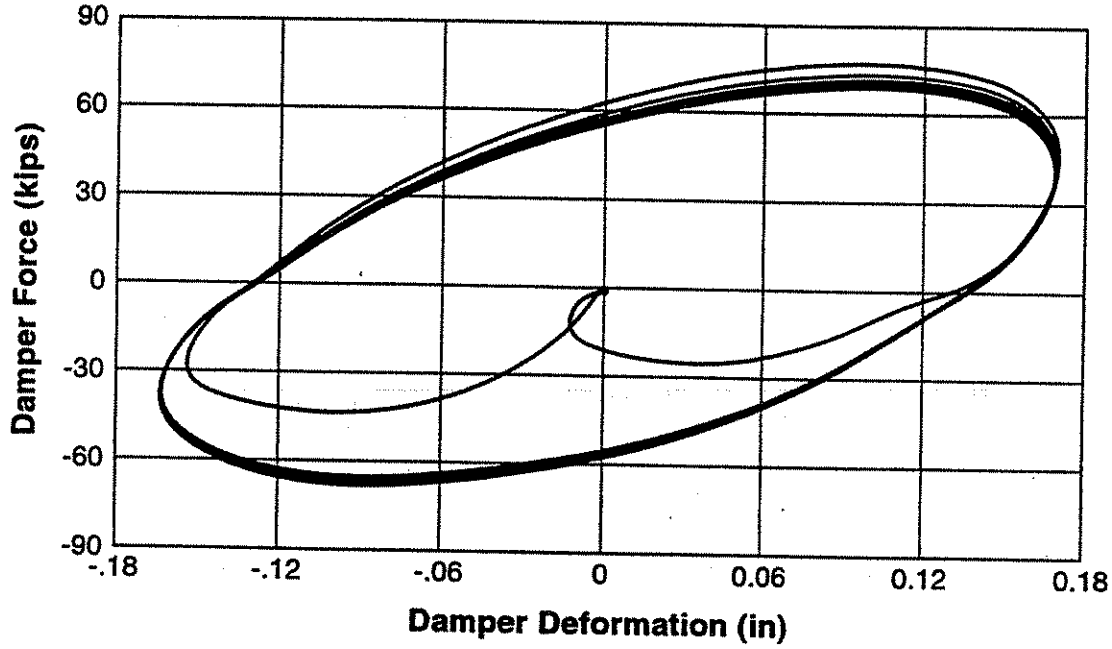

Fig. 3.43a - Measured damper force-deformation response for 25% strain, 0.5 hz loading frequency, and 24 °C initial damper temperature.

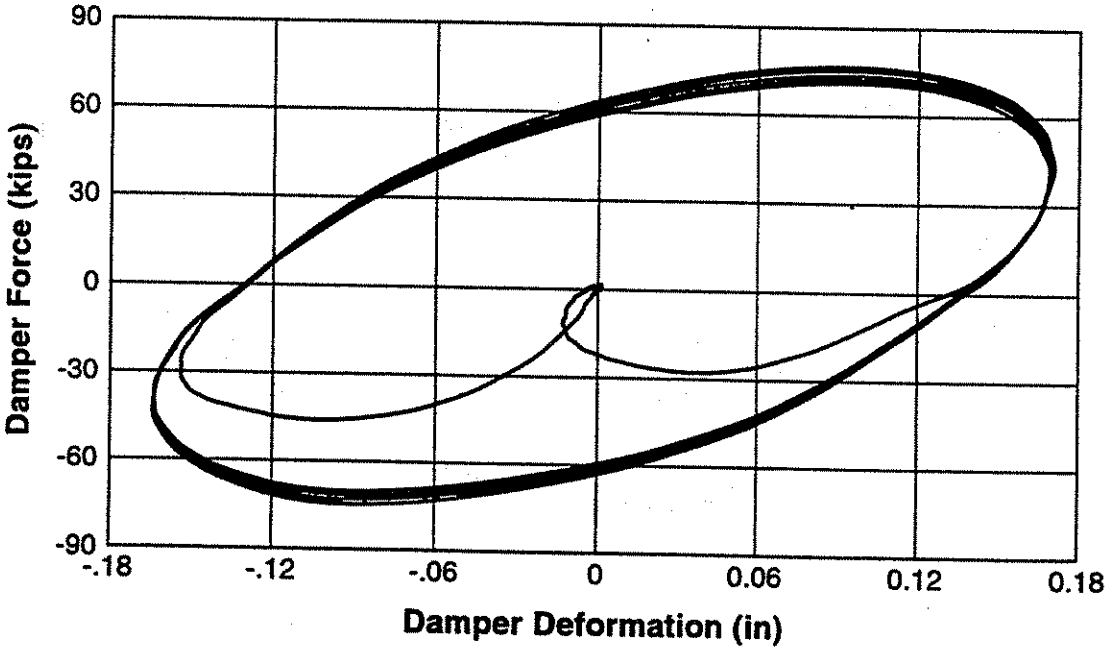

Fig. 3.43b - Analytically predicted damper force-deformation response for 25% strain, 0.5 hz loading frequency, and 24 °C initial damper temperature.

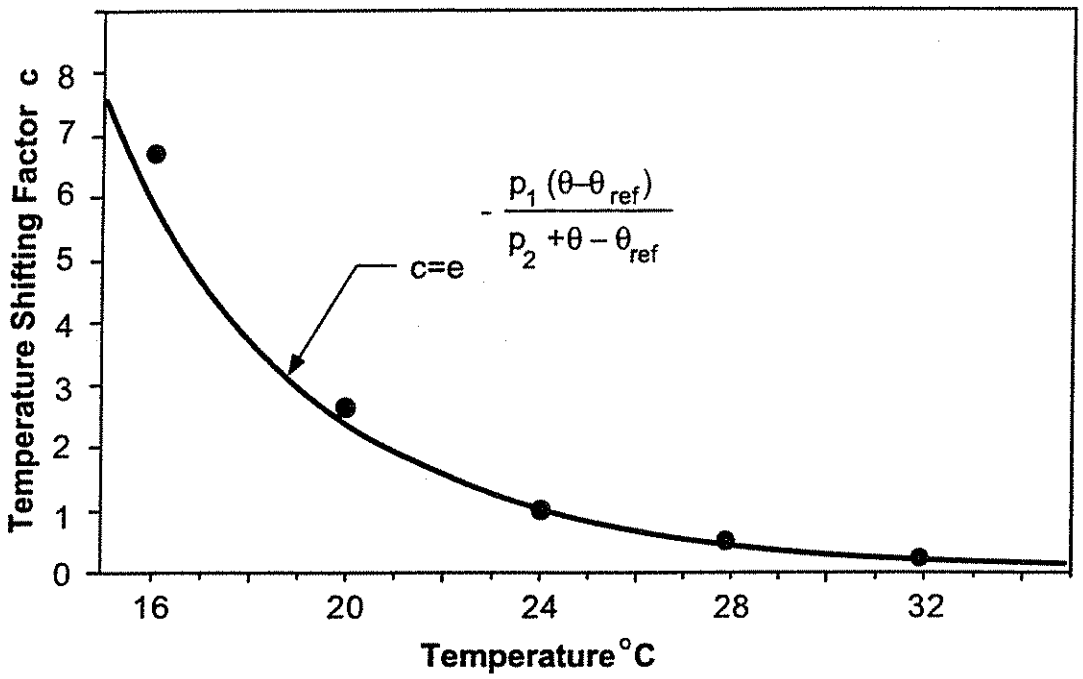

Fig. 3.44 - Temperature shifting coefficient as a function of temperature.

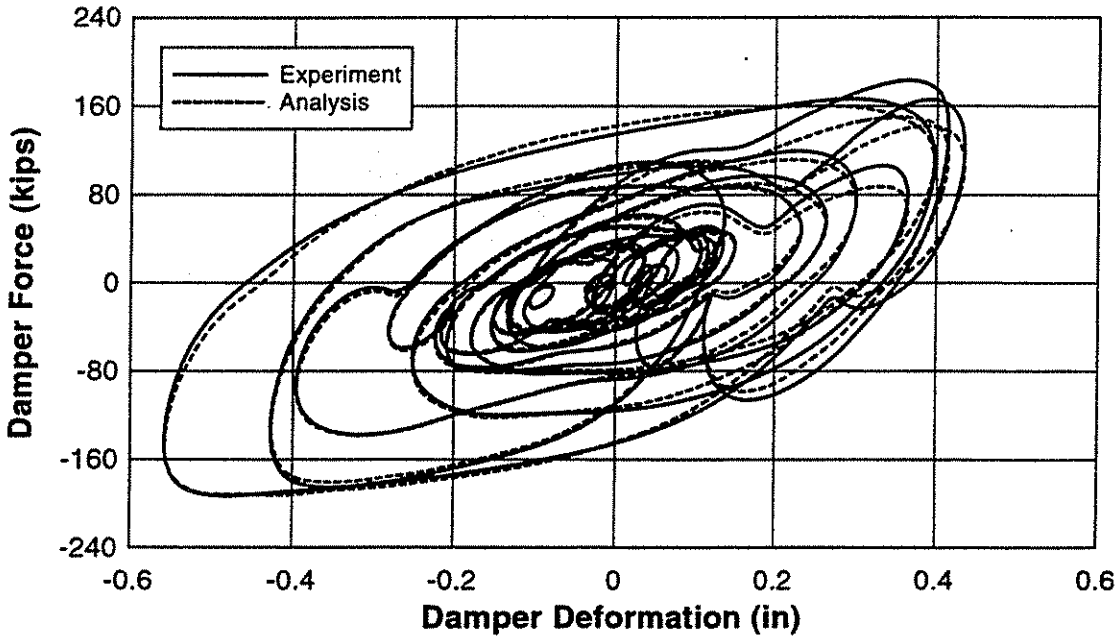

Fig. 3.45 - Comparison of measured and analytically predicted damper force-deformation response for 1.5 x El Centro 1940.

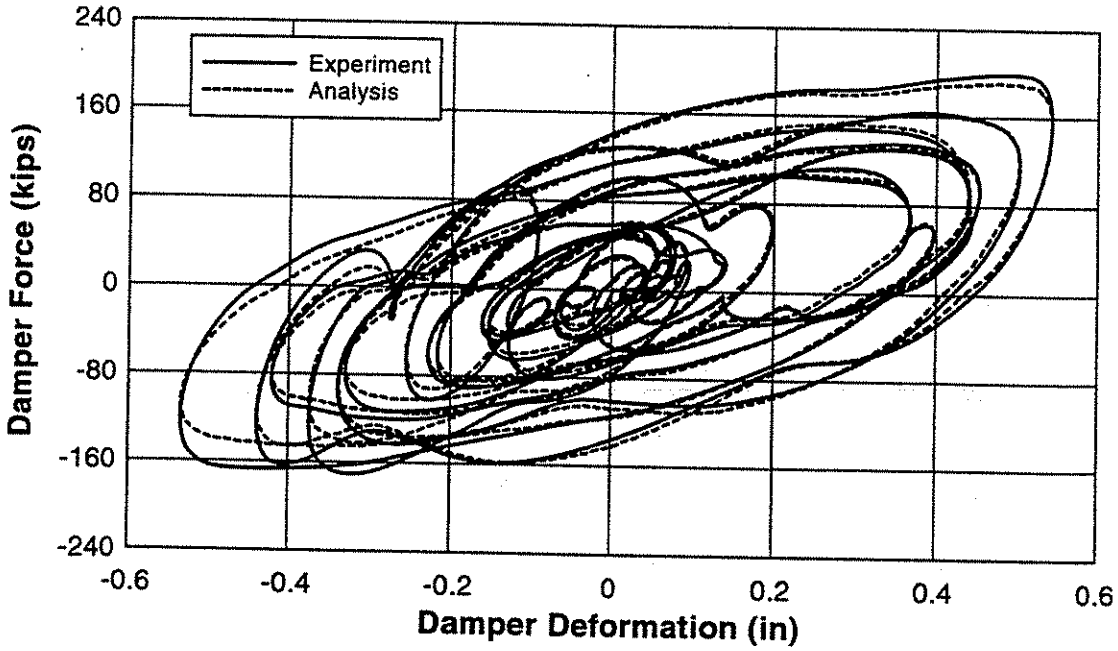

Fig. 3.46 - Comparison of measured and analytically predicted damper force-deformation response for 1.5 x Hachinohe.

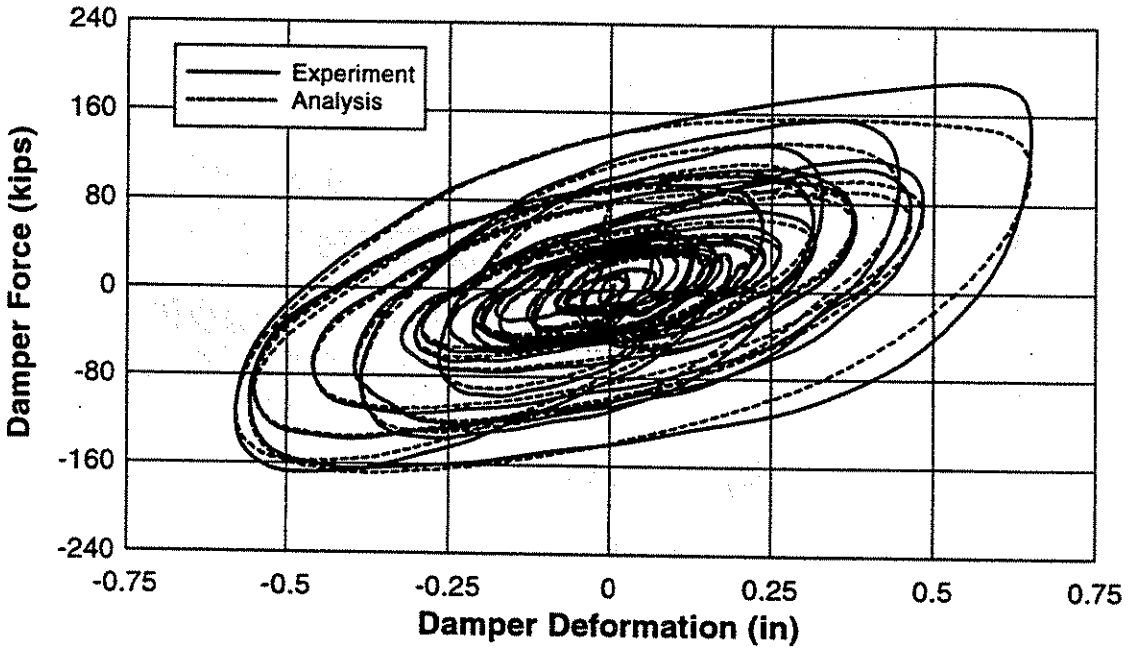

Fig. 3.47 - Comparison of measured and analytically predicted damper force-deformation response for 1985 Mexico City Central de Abastos - Frigorifico.

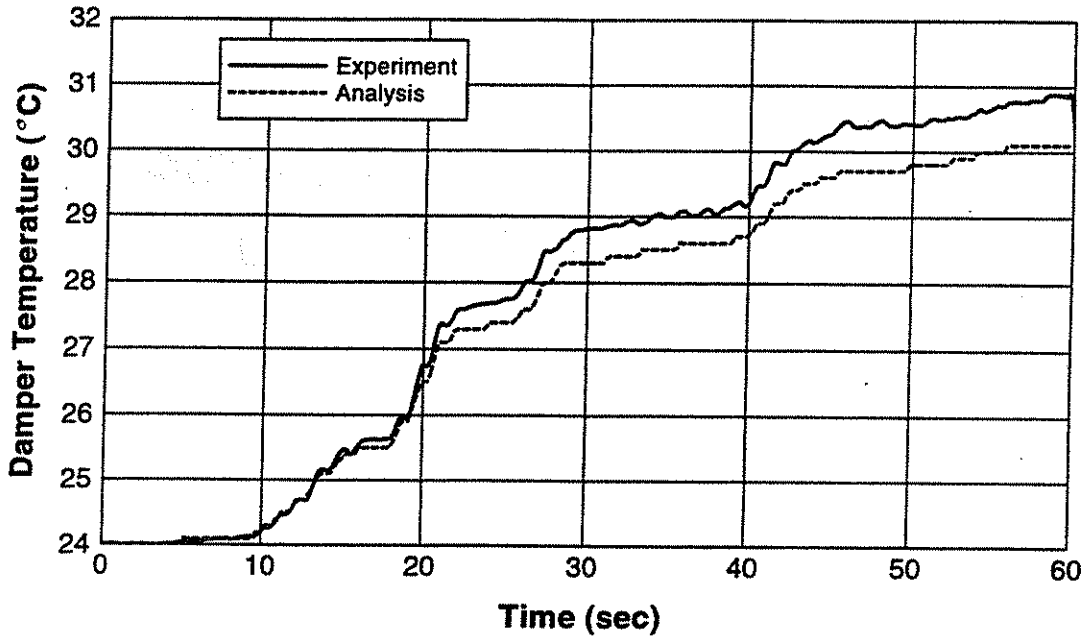

Fig. 3.48 - Comparison of experimental and analytically predicted temperature rise for 1985 Mexico City Central de Abastos - Frigorifico.

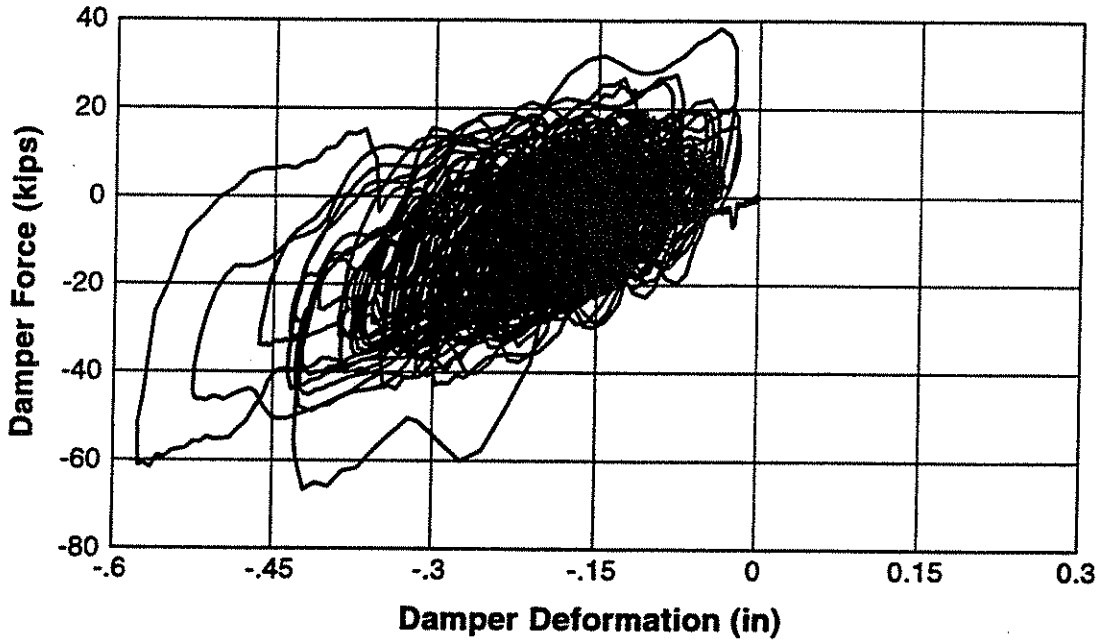

Fig. 3.49a - Analytically predicted damper force-deformation response at beginning of hour-long, simulated along-wind event with 500 year return period.

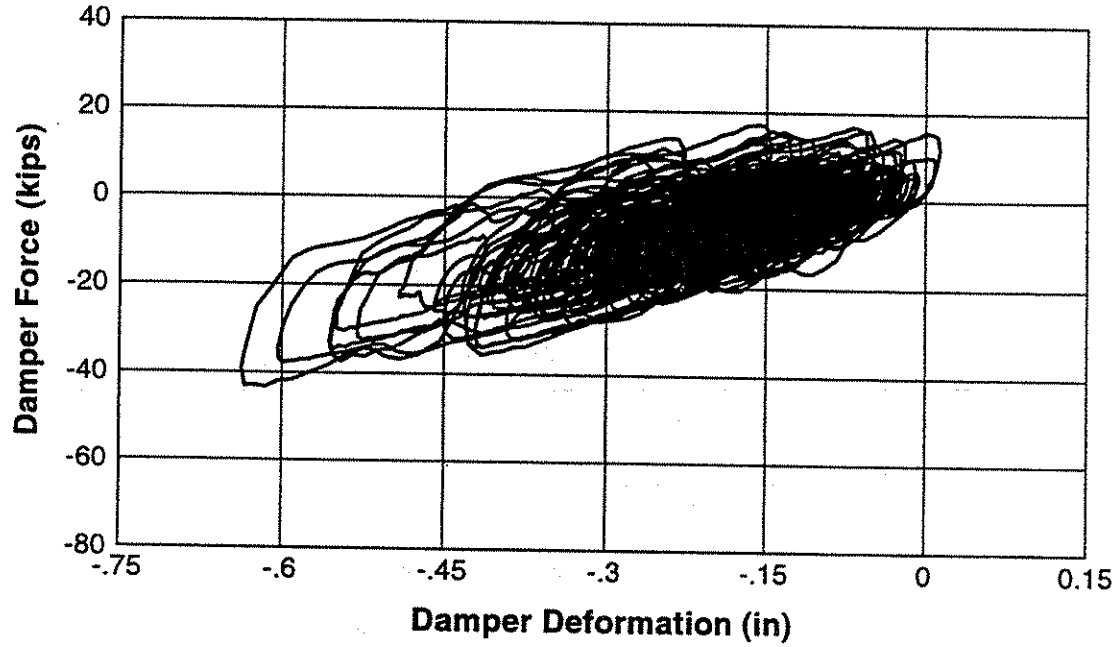

Fig. 3.49b - Analytically predicted damper force-deformation response at end of hour-long simulated along-wind event with 500 year return period.

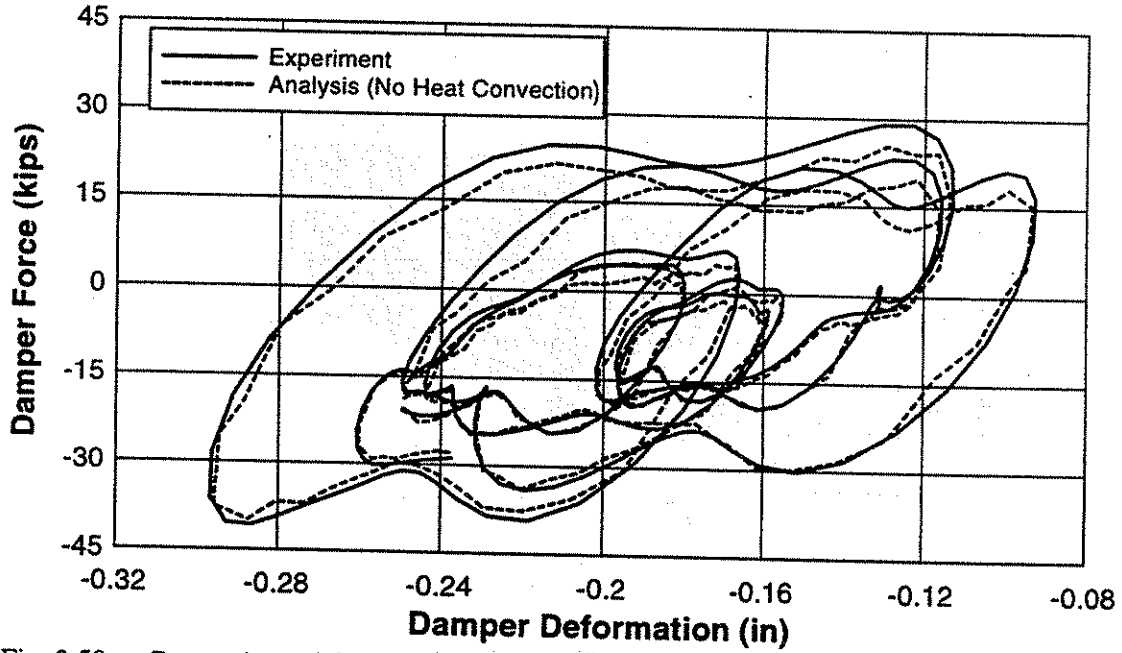

Fig. 3.50a - Comparison of experimental and analytically predicted force-deformation response at beginning of hour-long, simulated along-wind event with 500 year return period.

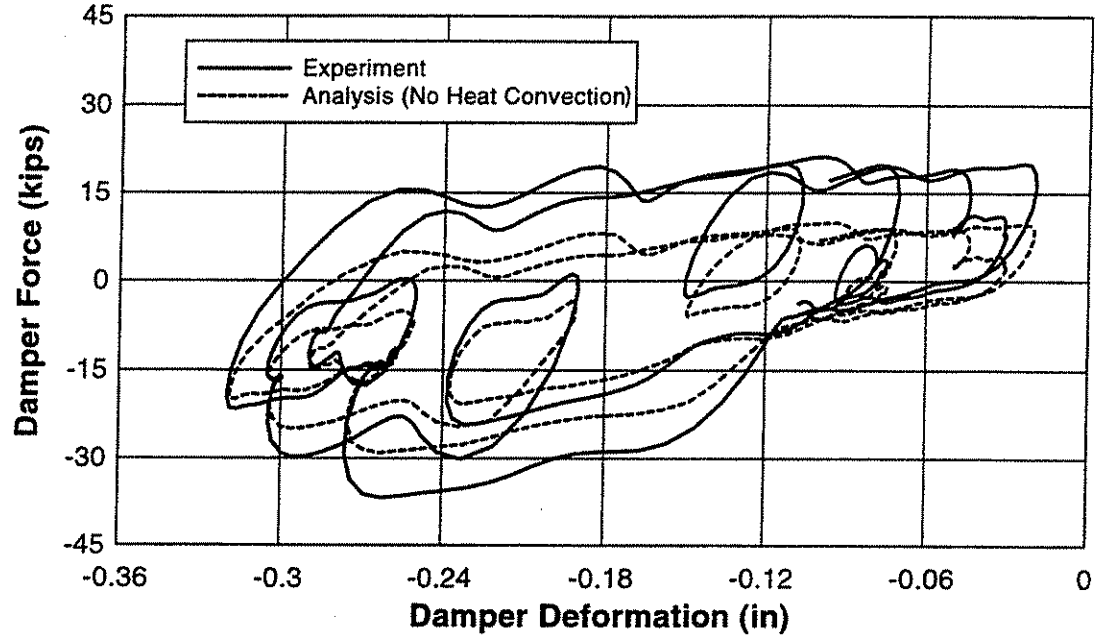

Fig. 3.50b - Comparison of experimental and analytically predicted force-deformation response at end of hour-long, simulated along-wind event with 500 year return period.

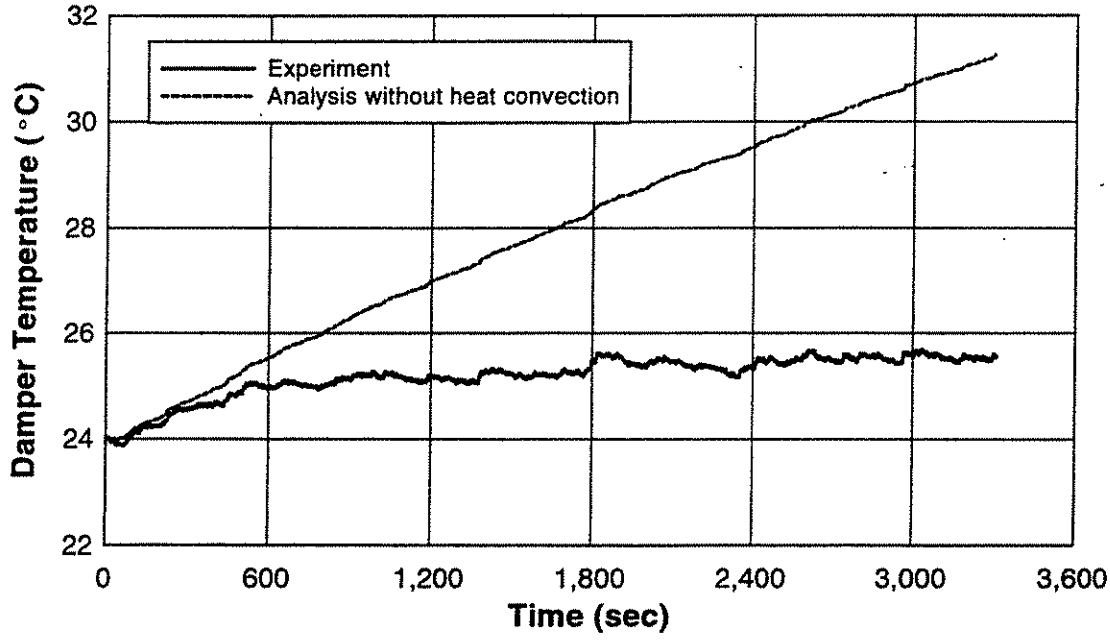

Fig. 3.51 - Comparison of experimental and analytically predicted damper temperature rise for hour-long, simulated along-wind event with 500 year return period.

CHAPTER 4.0 UNBRACED FRAME TESTS and ANALYSIS

4.1 Introduction

Proper design of VE-damped building structures requires knowledge of the frame stiffness before installation of the VE-dampers (unbraced frame stiffness). Unbraced frame stiffness is dependent on the stiffness of the beam-column connections and column base connections. This chapter presents results of experimental tests conducted to assess response of the test frame before installation of the VE-dampers. The test specimen is described, procedures for the experiments are presented, and test results are discussed. Correlative analysis of the test structure are also presented.

4.2 Test Specimen and Methodology

The test specimen is a portion of a larger prototype VE-damped frame. An important parameter used in the design of the prototype frame is the stiffness of the unbraced frame (frame without dampers). Because of the importance of the unbraced frame properties to the

prototype design, the frame without dampers was tested to verify design assumptions, assess the frame behavior, and develop an accurate analytical model of the frame.

The test specimen is a single bay, full-scale, lower three story portion of the 10-story prototype VE-damped building frame described in Chapter 6. Overall height of the test structure was 36 ft with a bay width of 20 ft. Relatively light member sizes were sufficient for the VE-frame. Columns were W14x159 and beams were W18x40 for the upper stories and W18x50 for the first story. Frame members were fabricated from A572-grade 50 steel. Actual material properties for the structural members are shown in Table 4.1. The experiment incorporated over 90% of the tall reaction wall in the ATLSS Multidirectional Testing Laboratory.

Actual design of the prototype VE-damped frame is described in detail in Chapter 6 for seismic forces and Chapter 7 for wind forces.

4.3 Individual Column Tests

Behavior of an unbraced frame is dependent upon the flexibility of the beam-column connections and the connection between the column and foundation. To assess the rotational stiffness of the column base connection, a series of tests were conducted on an individual column before erection of the beams which comprise the frame. Different magnitudes of

column axial load were investigated to determine the influence of pre-compression on the connection behavior.

The test specimen consisted of the east W14x159 column which was attached to the foundation beam with four 1-1/4 in. diameter A490 bolts as shown in Fig. 4.1a, 4.1b, and 4.1c. Lateral bracing was provided along the column length which permitted in-plane column displacement but prevented out-of-plane deformation. Bolts connecting the column base plate to foundation beam were pretensioned using a hydraulic torque wrench to the code prescribed pretension of 102 kips [AISC, 1994]. During installation, bolt forces were monitored through strain gages mounted on each bolt. Determination of bolt force was performed by first calibrating bolts from the same lot in tension to correlate actual bolt force with strain gage estimates of bolt force as shown in Fig. 4.2. Measured bolt strains during installation are shown in Fig. 4.3. As seen in this figure, the bolt exhibits some bending as one strain gage indicated compression and the opposite gage indicated tension at the onset of torque application. The average of the two measured strains was used to estimate bolt tension. Final average strain bolt strain was approximately 2900 $\mu\varepsilon$ (Fig. 4.3), which corresponds to approximately 102 kips of bolt pretension (Fig. 4.2).

Tests were conducted by applying axial load to the column top through a 3 in. diameter wire rope tensioned by a 340 kip capacity hydraulic actuator as shown in Fig. 4.4. The wire rope was attached to a clevis on the foundation beam at the north face of the column, ran around a 36 in. diameter shive at the column top and along the south column face to an axial force actuator which tensioned the rope. Static hydraulic pressure to the gravity force actuators was

provided by an Amsler pendulum-dynomometer. Tests were conducted for axial load levels of 0, 100, 200, 400 and 500 kips. After compressing the column, monotonic lateral load was applied by a 50 kip capacity hydraulic actuator located 17.5 ft. above the laboratory floor as shown in Fig. 4.1a.

Instrumentation for the individual column tests consisted of 22 channels of data, including strain gages, displacement transducers, and load cells. Instrumentation layout and channel identification for all sensors are illustrated in Fig. 4.5a. Strain gages were applied to the column at two locations along the column length as shown in Fig. 4.5a. At each location, 6 gages were installed on the column cross-section at each of the two elevations as shown in Fig. 4.5b. Column axial force and bending moment at the connection were determined from strain gage measurements. Displacement transducers were used to monitor the column base connection rotation, actuator displacement, column displacements, and to measure any slip at the base plate. Data were acquired using a PC-based Keithley Metrabyte DAS1802-ST-DA data acquisition board and 2 EXP-1800 multiplexing boards.

Connection rotations were computed from displacement transducers located on the column baseplate as illustrated in Fig. 4.5c. Column moments at the strain gage locations were determined from bending theory using strain measurements and nominal column cross sectional properties. Moment at the column base was determined from the moment gradient between the two strain gaged locations. Moment-rotation response for the column-to-foundation connection are shown in Fig. 4.6 for varying axial force levels. Connection stiffness was determined as the best-fit slope of the measured moment-rotation response. As

seen in Fig. 4.6, larger column axial force results in higher connection moment-rotation stiffness. Results from all tests indicate the connection rotational stiffness increases with column axial force, as illustrated in Fig. 4.7.

Behavior of the unbraced frame is influenced by the rotational stiffness of the column base connections. To accurately characterize the unbraced frame behavior, it was necessary to model the column-to-foundation connection stiffness in subsequent frame analyses. A complication arises in selection of a linear stiffness connection model due to the interrelationship between connection stiffness and column axial load (Fig. 4.7). During frame tests, column axial forces increase and decease depending upon the direction and magnitude of lateral loading. Due to this fluctuation of column axial force, an average stiffness value for the connection model was selected. The stiffness was chosen based on results of this test series and subsequent undamped frame experiments. The column base connection element was used in later analyses to model the connection flexibility at the foundation. It should be noted that the frame with dampers is much less sensitive to column base flexibility than the unbraced frame.

Bolt strains were also influenced by initial column axial forces. At higher column axial forces, the bending moment on the base plate due to lateral forces did not overcome the precompression of the connection until much larger applied moment as illustrated in Fig. 4.8 and the bolt forces were reduced as shown in Fig. 4.9. As a result, demand on the bolts due to column bending was reduced by application of higher initial column axial loads. When no

axial force was present in the column, bolt forces became large even for moderate column moments as shown in Fig. 4.9.

4.4 Unbraced Frame Tests

After characterization of the column-to-foundation connection behavior, the west column and beams were erected and connection pieces installed, completing the unbraced frame. The unbraced frame specimen is shown in Figs. 4.10. The beam-column connection details included web angles, top seat angle, and gusset plate for later attachment of the VE-damper as shown in Fig. 4.11. The gusset plate was welded to the beam flange in the shop and welded to the column angles after erection. Web angles were bolted to the column flange and beam web with A325 bolts. After initial tests, top-seat and web angles were welded to prevent slip between the connected parts.

Lateral bracing was constructed which permitted the frame to sway in-plane but prevented out-of-plane deformation. Beams were braced at quarter points along the span and columns were braced at each story level as shown in Fig. 4.10.

Testing of the unbraced frame was conducted using five different actuators to load the structure as illustrated in Fig. 4.10. Two 340 kip capacity actuators were used to produce axial load in the columns by tensioning 3 in. diameter wire ropes as described in section 4.3. The axial force actuators were not dynamically controlled during the experiments and

remained at a constant pressure after achieving the designated initial column force level. Two 110 kip capacity, dynamic double-acting hydraulic actuators were used to apply lateral forces to the frame at the third story level as shown in Fig. 4.12. The test specimen was subjected to displacement-controlled cyclic lateral forces. Fig. 4.13 shows the lateral top displacement history imposed during the test. Feedback for actuator control was provided by internal displacement transducers located within each actuator. Hydraulic oil was supplied to each of the two lateral force actuators by a 120 gpm, 3000 psi hydraulic supply, 40 gpm hydraulic service manifold, and two 40 gpm servo-valves. Servo-valves for the lateral force actuators were controlled using PC-based Vickers control software.

The use of wire rope to apply axial force to the columns required an additional actuator to correct for P-Δ effects. This is because as the frame sways due to lateral load, the wire rope, if uncorrected, would remain in a straight line as illustrated in Fig. 4.14. The wire rope in the displaced condition has both a vertical and horizontal component. The horizontal component provides a restoring force which acts to eliminate the P-Δ effect.

To include P-Δ effects during the experiments, the wire ropes were pulled with a P-Δ frame which was attached to a 50 kip capacity single acting hydraulic actuator. The P-Δ frame was displaced the same amount as the sheaves on the column tops which ensured that the vertical force remained vertical despite tilting of the frame as illustrated in Fig. 4.15. Due to the relatively low stiffness of wire rope, little additional axial force is applied to the column as a result of pulling on the wire ropes with the P-Δ actuator. Hydraulic oil was supplied to the P-Δ actuator by a 120 gpm, 3000 psi hydraulic supply, 40 gpm hydraulic service manifold, and

one 40 gpm servo-valve. The servo-valve for the P-Δ actuator was also controlled using PC-based Vickers control software.

Instrumentation for the unbraced frame experiments consisted of 164 channels of data, including strain gages, displacement transducers, and load cells. Instrumentation layout and channel identification for all sensors are illustrated in Figs. 4.16. Strain gages were used to determine local member forces and overall force equilibrium in the structure. Three strain gages were installed at each instrumented cross-section (Fig. 4.17a) to permit determination of member axial force and in-plane bending moment. Strain gages were located at least two times the member depth away from connections and points of inflection to ensure reliable strain measurements. Shear forces were determined by computing moment gradient in frame members from two or more strain gaged locations. Sign conventions used for bending moments in the columns and beams are shown in Fig. 4.17b. Displacement transducers were used to measure connection rotations, actuator displacements, story displacements, and to indicate slip at the base of the frame. Average connection rotation was determined from two or more displacement transducers at a connection as illustrated in Figs. 4.18a and 4.18b. Connection rotations were positive when in the direction of positive moment. Data were acquired using a PC-based Keithley Metrabyte DAS1802-ST-DA data acquisition board and eleven EXP-1800 multiplexing boards.

Test results included overall frame stiffness and damping as well as local member and connection behavior. Load-displacement response for the unbraced frame subjected to the displacement history of Fig. 4.13 is shown in Fig. 4.19 for small excursions (< 1.5 in.) and

Fig. 4.20 for large excursions (>1.5 in.). As seen in Fig. 4.19, there is little hysteresis at excursions below 1.5 in. of top displacement, and the equivalent frame stiffness was 17.9 kips/in. At larger excursions, the frame begins to show hysteretic behavior and slight softening as shown in Fig. 4.20 due to deformation of top seat and web angles (Fig. 4.21) and local connection yielding (Fig. 4.22). The equivalent frame stiffness, for the whole test, was determined from a best-fit line of the force-displacement response as 17.0 kips/in. The measured equivalent frame stiffness will be compared with the theoretical stiffness in section 4.5.

Equivalent viscous damping for the unbraced frame was estimated according to the Clough and Penzein [1993]:

$$\xi = \frac{ED}{4 \cdot \pi \cdot ES} \qquad [4.1]$$

Where ξ is the equivalent viscous damping ratio, ED is the energy dissipated during one full cycle = $\frac{1}{2}\sum F_i\left(\Delta_{i+1} - \Delta_{i-1}\right)$, and ES is the maximum strain energy stored. Damping ratios were computed for each cycle and are shown in Table 4.2. As seen in this table, the computed damping ratio was amplitude dependent. The larger damping ratios computed at the small displacement amplitudes were due mainly to the sensitivity of Eq. 4.1 to loading slip and electrical noise associated with the small measurements of ED and ES. Damping ratio was a minimum at 1.5 in. of top displacement and became larger at later excursions. This minimum occurs because there is little energy dissipation at small displacements while the energy stored increases at each subsequent cycle. At cycles greater than 1.5 in., energy dissipation begins to occur due to local connection yielding and prying, as shown by the

hysteresis in the load-displacement diagram and a reduction of the strain energy stored due to slight reduction in frame stiffness. These two effects result in increased damping ratios computed for the larger excursions. Despite the amplitude dependent damping ratios observed during the experiment, a constant damping ratio was used for all later analyses. A damping ratio of 2% was selected for the analytical models which is typical of the measured damping at larger displacement amplitudes and corresponds to the traditionally assumed value for steel frame buildings.

Local connection behavior was assessed by computing the moment-rotation response of each beam-column connection during the test. Average connection rotation was determined from displacement transducers and moments at connections were determined from strain measurements as described previously. Typical moment-rotation curves for the six beam-column connections are shown in Figs. 4.23a to 4.23f. Figs. 4.24a and 4.24b isolate the moment-rotation response at small (<1.5 in. top displacement) and large (>1.5 in. top displacement) excursions respectively for the East beam-column connection at level 2. As shown in these figures, the connections remain elastic at small excursions and only at larger excursions is there hysteresis in the moment-rotation response. The hysteretic behavior is a result of prying of the connection angles (Fig. 4.21) and local connection yielding (Fig. 4.22). As seen in Figs. 4.24a and b, the connections do not exhibit symmetric behavior. Connections were stiffer when the top flange is in compression and the gusset in tension. The increased stiffness in positive bending results from the top seat angle bearing directly on the column face while in negative bending, resistance is provided by the bending stiffness of the connection angle leg.

Upon completion of the unbraced frame tests, inspection of the connections revealed cracking along the fillet weld which attaches the gusset plates to the beam lower flange. All six gussets exhibited cracks which initiated at the weld root and propagated through the weld throat as shown in Figs. 4.25 and 4.26. These cracks resulted from stresses perpendicular to the lack of fusion along the gusset plate and the beam flange weld root, a large number of cycles, and significant stress range, as will be discussed in Chapter 5. Before welding the VE-dampers to the gusset plates, all cracks were repaired. Welds were air-arced to remove existing cracks and the plate was beveled to permit a full penetration weld along the first 3 in. of the gusset as shown in Fig. 4.27. Additionally, strain gages were installed on each gusset to measure the magnitude of stress perpendicular to the gusset plate weld in subsequent tests and presented in Chapter 5.

4.5 Analytical Correlation of Unbraced Frame Tests

Analytical correlation of the unbraced frame tests was performed using beam-column finite elements and an available computer analysis program PC-ANSR [Maison, 1992]. The analytical frame model used the center-line dimensions of the frame, nominal section properties, and column base connection flexibility. Column base connection flexibility was included by using a linear connection element at the column base with stiffness properties which could be adjusted to reflect the measured connection response discussed in section 4.3. Nominal cross-sectional properties were used for initial structural member stiffness properties

[AISC, 1994]. Member capacities were determined from tensile coupon data (Table 4.1) and nominal section properties.

Preliminary analyses were conducted which indicated a theoretical equivalent frame stiffness of 17.3 kips/in. The theoretical equivalent stiffness was less than the 17.9 kips/in measured for the small displacements discussed in section 4.3. This was a result of the rigid end-zones created by the gusset plates located at the beam-column connections. To include the stiffening influence of the gussett plates at the beam-column connections in the real structure, rigid end-zones were added to the beam elements in the analytical model.

Additional elastic analyses were performed and the model was calibrated to provide reasonable estimates of experimental global frame stiffness and local member forces for top displacements of approximately 2 in. This was performed by making minor adjustments to beam and column base connection element stiffness properties as well as varying the rigid end-zones lengths until achieving both reasonable global frame response and local member force estimates. The final analytical response is shown in Fig. 4.28 with the measured experimental frame response. Analytical member force distributions are shown in Fig. 4.29. Measured member force distributions are shown in Fig. 4.30. The final analytical model for the unbraced frame was used in all subsequent analyses without change, except for the addition of VE-damper elements as described in Chapter 5.

Equivalent viscous damping was included in the analytical model for future dynamic time history analyses using mass and stiffness proportional damping coefficients. From Clough

and Penzien [1993] a damping matrix **c** can be constructed of the mass **m** and stiffness **k** matices as:

$$\mathbf{c} = a_0\mathbf{m} + a_1\mathbf{k} \qquad [4.2]$$

where a_0 and a_1 are proportionality constants. For the unbraced frame structure, the damping matrix was determined only from the stiffness contribution because there was negligible mass ($\mathbf{m} \approx 0$). The stiffness proportional constant can be determined [Clough and Penzien, 1993] from:

$$a_1 = \frac{2\xi_o}{\omega_n} \qquad [4.3]$$

where ξ_o is the damping ratio of the unbraced frame (=2%), and ω_n is the natural frequency. Instead of the natural frequency ω_n, the loading frequency ω was used to compute the stiffness proportional constant for sinusoidal loading functions as will be discussed in Chapter 5. This results in different values of a_1 depending on the loading frequency used in the test.

4.6 Conclusions

Results of the individual column and unbraced frame experimental and analytical program are summarized below:

- Column base connection stiffness was dependent on the column axial force. The connection base stiffness was modeled using an average stiffness to account for varying axial force level in the column during frame tests.

- Bolt forces were influenced by column axial forces. There was less demand on the bolts with higher initial column axial compression.
- The bolted beam-column connections provided stiffness comparable to rigid all welded connections. This stiffness was a result of the rigid end-zones created by the gusset plates located at the beam-column connections.
- Damping ratios were dependent on frame displacement amplitude. A damping ratio of 2% was selected for analytical frame models which is typical of the measured damping at larger displacement amplitudes and corresponds to the traditionally assumed value for steel frame buildings.
- Cracking was observed along the fillet weld which attached the gusset plates to the beam flanges. The cracking was caused by significant stresses, a large number of cycles, and a weld detail which is susceptible to crack growth for cyclic stresses normal to the lack of fusion at the weld root.
- An analytical model of the unbraced frame was developed which included the effects of the column base connection stiffness and beam-column connection stiffness. Analyses were conducted which reasonably predicted the experimentally observed overall frame response and local member forces.

Member	Location	No. of Coupons	Type	Coupon Designation			Average Initial Area (in^2)	Fy (ksi)	Fu (ksi)	Final Elongation (in/in)
				No.	Section Location	Name				
Column W14x159	West	4	505	1)	Flange	WF1	0.501	54.01	73.76	0.362
				2)	Flange	WF2	0.500	53.34	76.25	0.357
				3)	Web	WW1	0.503	57.24	82.61	0.334
				4)	Web	WW2	0.501	59.32	83.87	0.323
							AVERAGE:	55.98	79.12	0.344
Column W14x159	East	4	505	1)	Flange	EF1	0.502	52.68	76.83	0.361
				2)	Flange	EF2	0.501	50.48	73.59	0.360
				3)	Web	EW1	0.500	57.31	81.87	0.319
				4)	Web	EW2	0.500	55.95	80.24	0.326
							AVERAGE:	54.11	78.13	0.342
Beam W18x50	Level 1	4	2 in. Gage	1)	Flange	L1F1	0.273	45.30	67.61	0.457
				2)	Flange	L1F2	0.264	44.25	68.63	0.385
				3)	Web	L1W1	0.185	50.10	73.68	0.357
				4)	Web	L1W2	0.182	49.93	72.20	0.381
							AVERAGE:	47.39	70.53	0.395
Beam W18x40	Level 2	4	2 in. Gage	1)	Flange	L2F1	0.261	57.38	78.02	0.393
				2)	Flange	L2F2	0.253	57.96	79.43	0.387
				3)	Web	L2W1	0.161	61.45	81.47	0.376
				4)	Web	L2W2	0.164	61.34	80.16	0.384
							AVERAGE:	59.53	79.77	0.385
Beam W18x40	Level 3	4	2 in. Gage	1)	Flange	L3F1	0.255	56.89	78.31	0.403
				2)	Flange	L3F2	0.261	55.46	77.19	0.391
				3)	Web	L3W1	0.162	56.02	74.47	0.404
				4)	Web	L3W2	0.164	57.74	75.76	0.389
							AVERAGE:	56.53	76.43	0.397

Table 4.1 - Tensile coupon data for frame members.

Cycle No.	Peak Force (kips)	Peak Displacment (in)	Equivalent Viscous Damping (%)
1	4.5	0.26	3.49
2	8.6	0.49	2.19
3	13.0	0.74	1.78
4	17.0	0.98	1.76
5	25.4	1.47	1.52
6	33.5	1.95	1.60
7	41.7	2.43	1.75
8	49.6	2.91	2.05
9	57.1	3.39	2.28
10	64.4	3.87	2.62

Table 4.2 - Equivalent viscous damping ratios for unbraced frame.

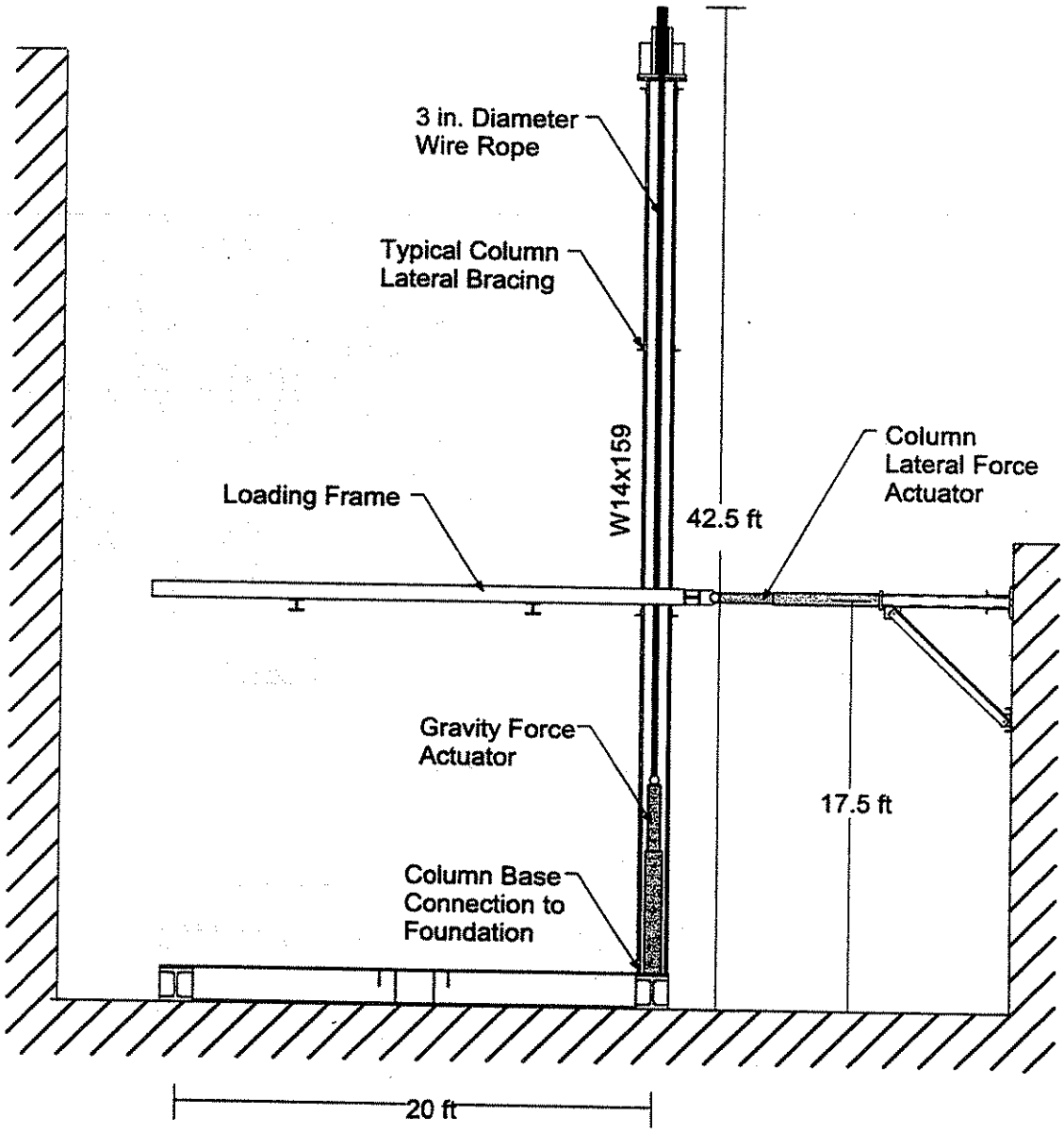

Fig. 4.1a - Individual column test configuration.

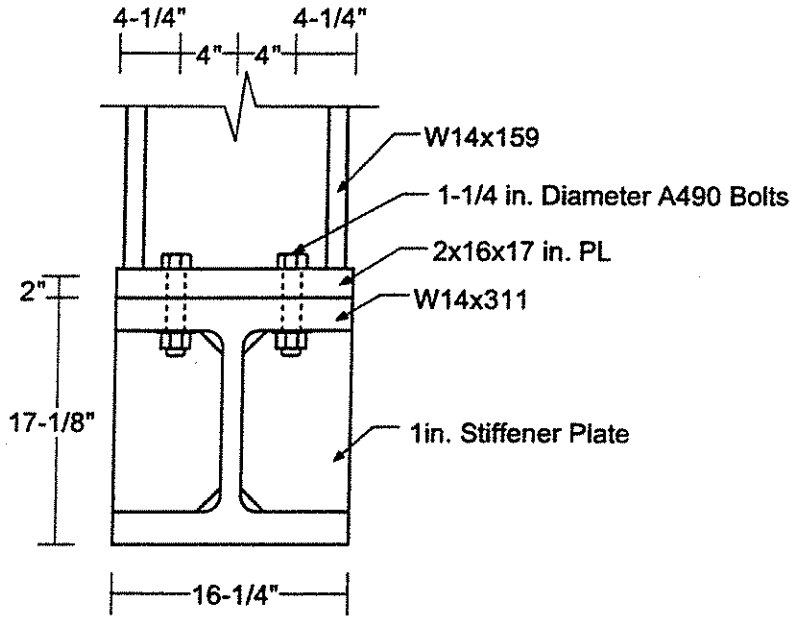

Fig. 4.1b - Elevation view of column base connection.

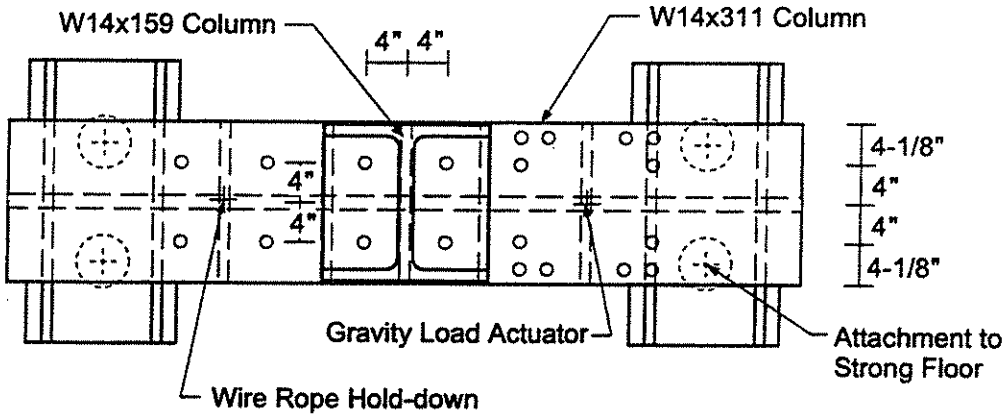

Fig. 4.1c - Plan view of column base connection.

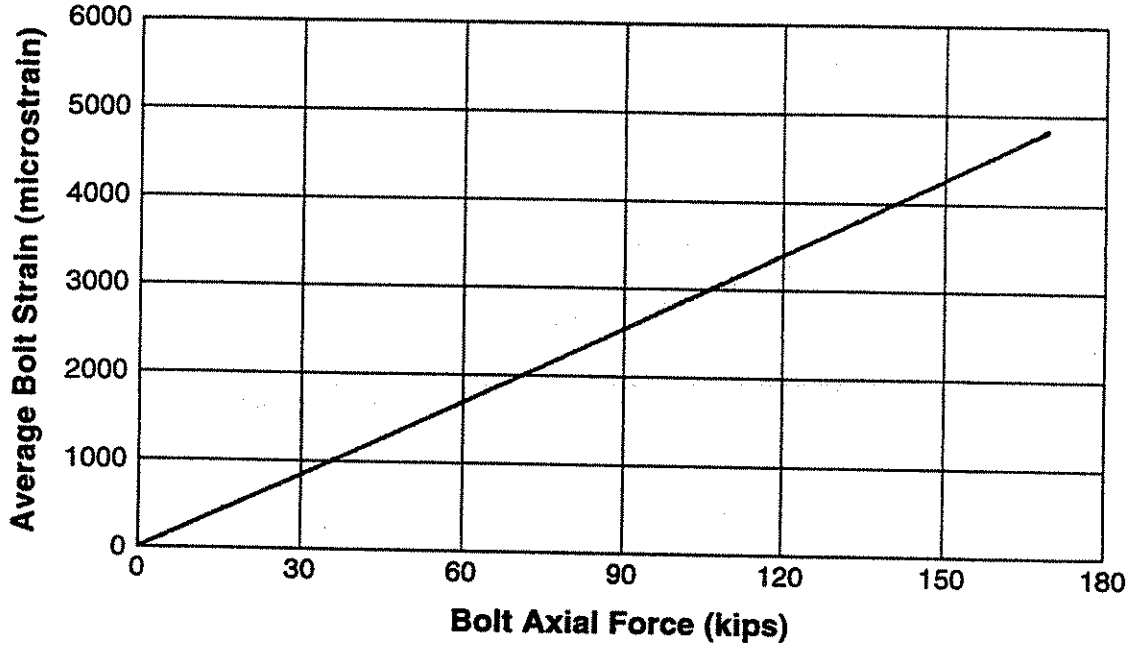

Fig. 4.2 - Relationship between connection bolt force and bolt strain.

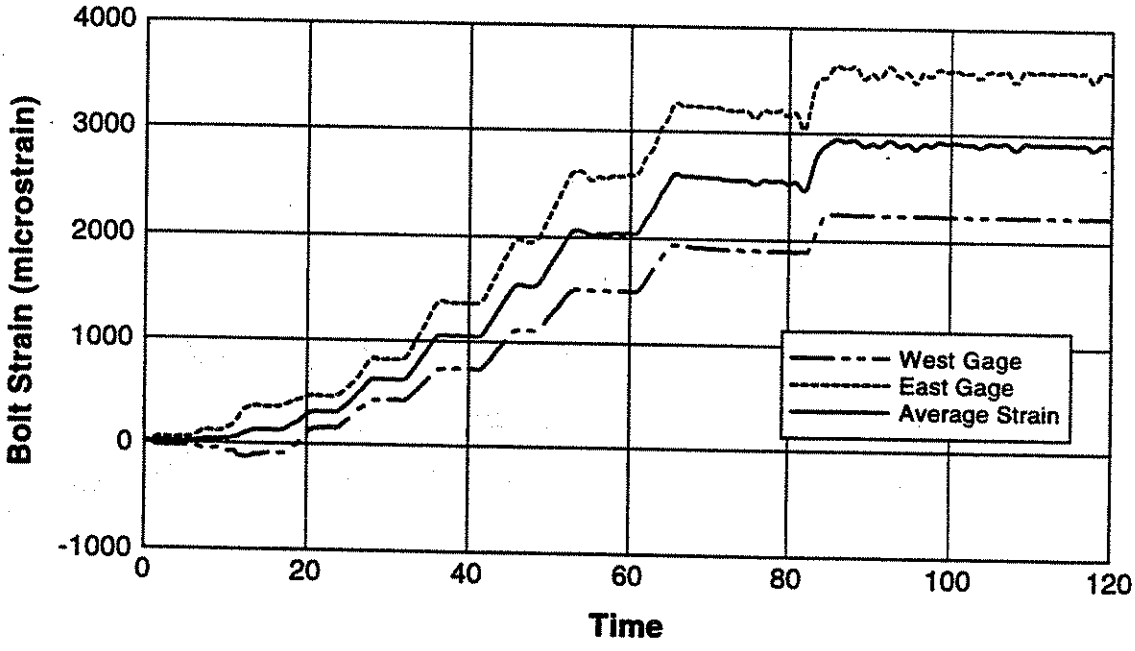

Fig. 4.3 - Measured bolt strain during bolt installation.

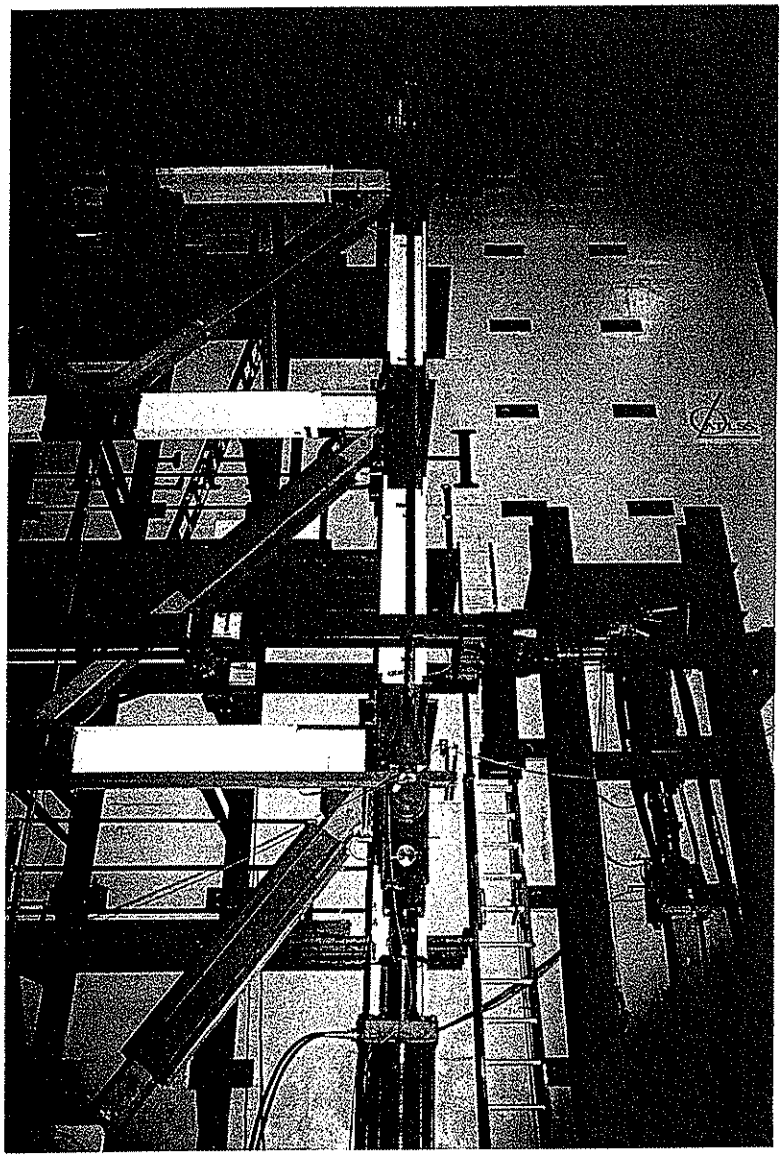

Fig. 4.4 - Actuator and wire rope assembly used to impose axial force in column.

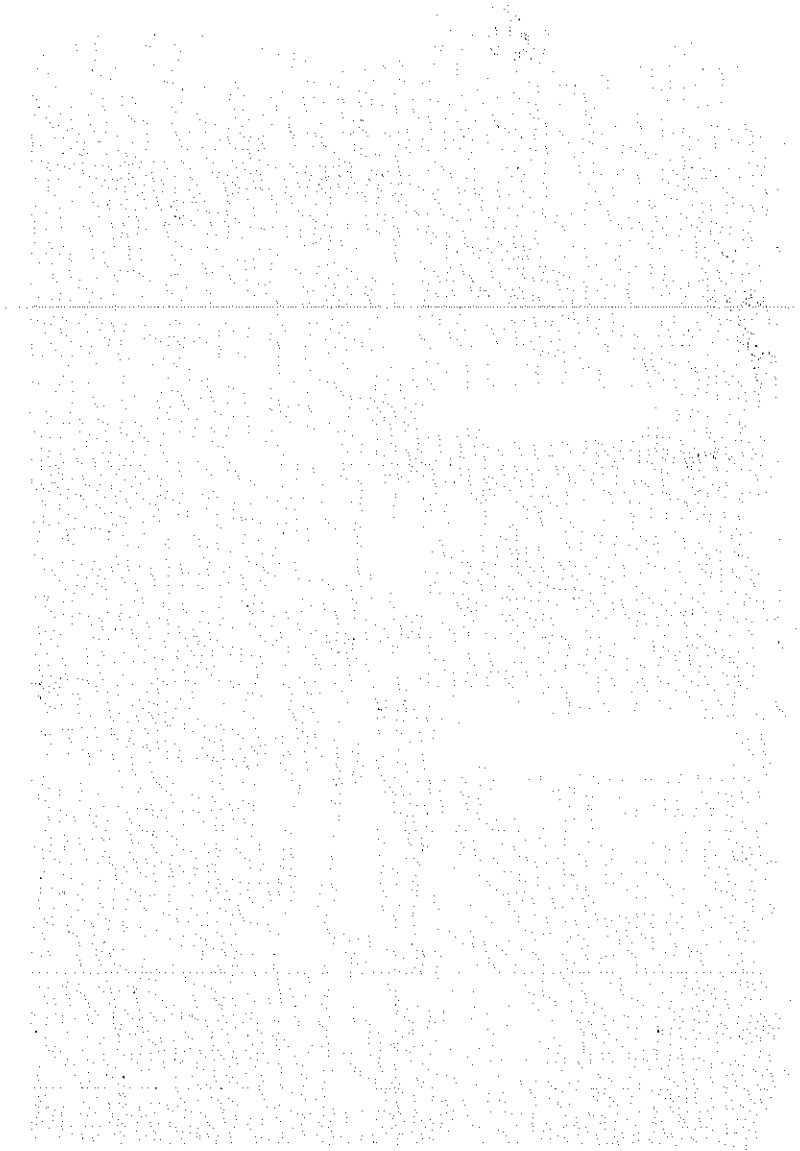

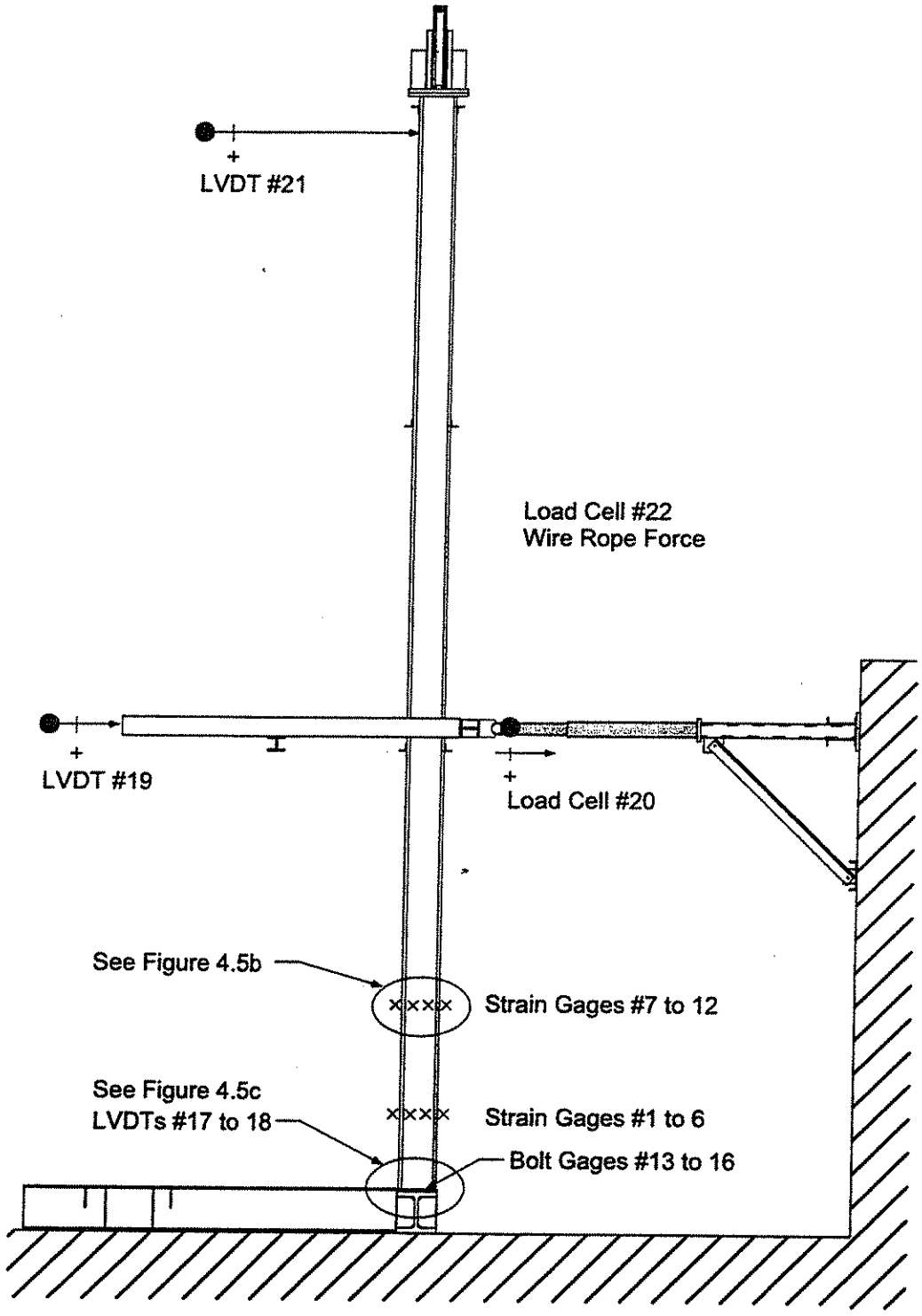

Fig. 4.5a - Instrumentation layout and channel identification for individual column test.

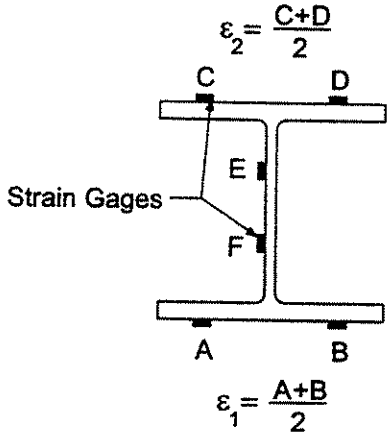

$$\text{Moment(kip-in)} = \frac{\varepsilon_1 - \varepsilon_2}{2} \frac{S\,E}{1000000}$$

$$\text{Axial Force(kips)} = \frac{\varepsilon_A+\varepsilon_B+\varepsilon_C+\varepsilon_D+\varepsilon_E+\varepsilon_F}{6} \frac{A\,E}{1000000}$$

Where S is the section modulus (in^3)
E is Modulus of Elasticity (29,000 ksi)
A is cross sectional area (in^2)
and strain readings in microstrain

Fig. 4.5b - Stain gage layout at each of the two instrumented column cross sections.

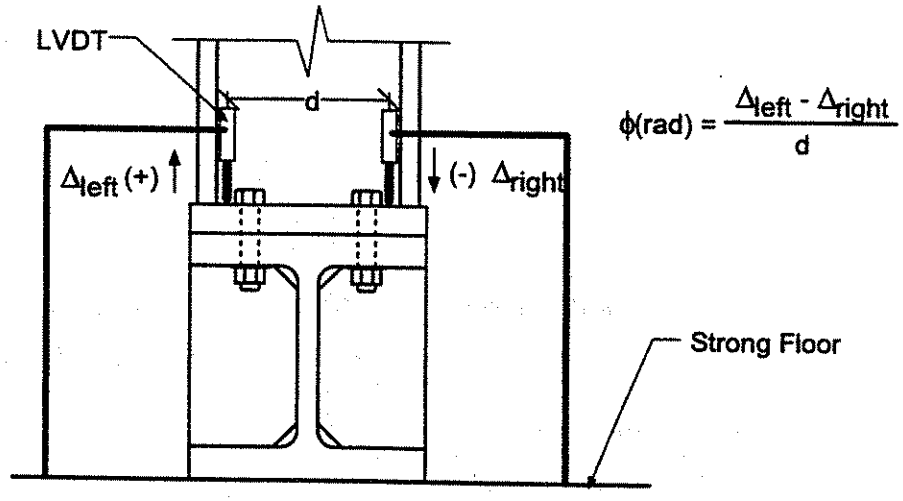

Fig. 4.5c - Method used to determine average column base connection rotation.

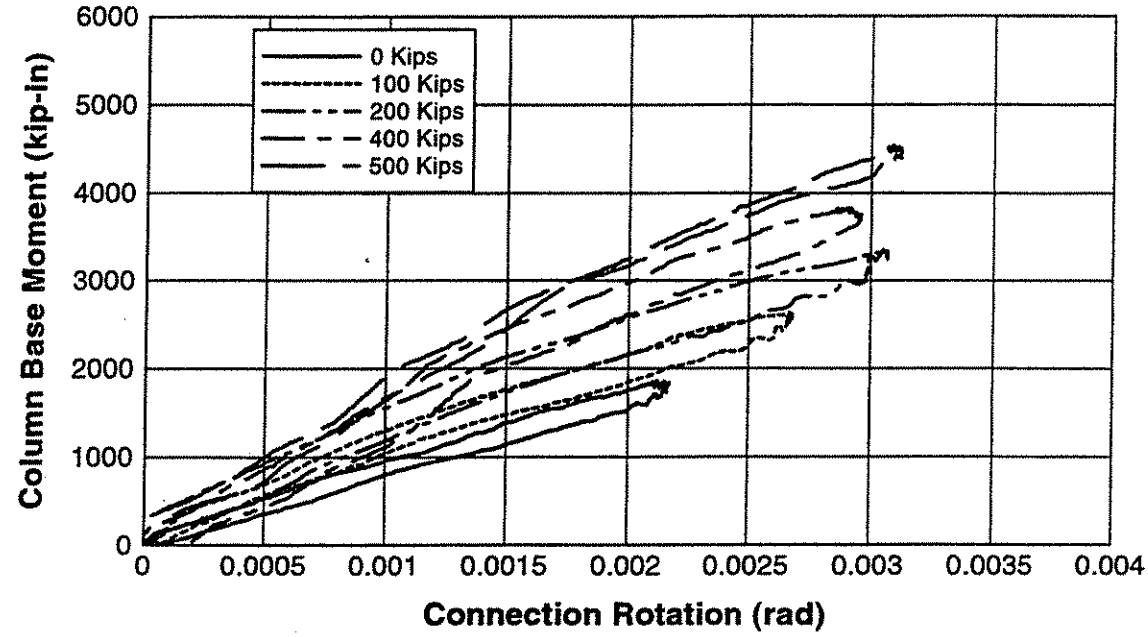

Fig. 4.6 - Column base connection moment-rotation response for different axial load levels.

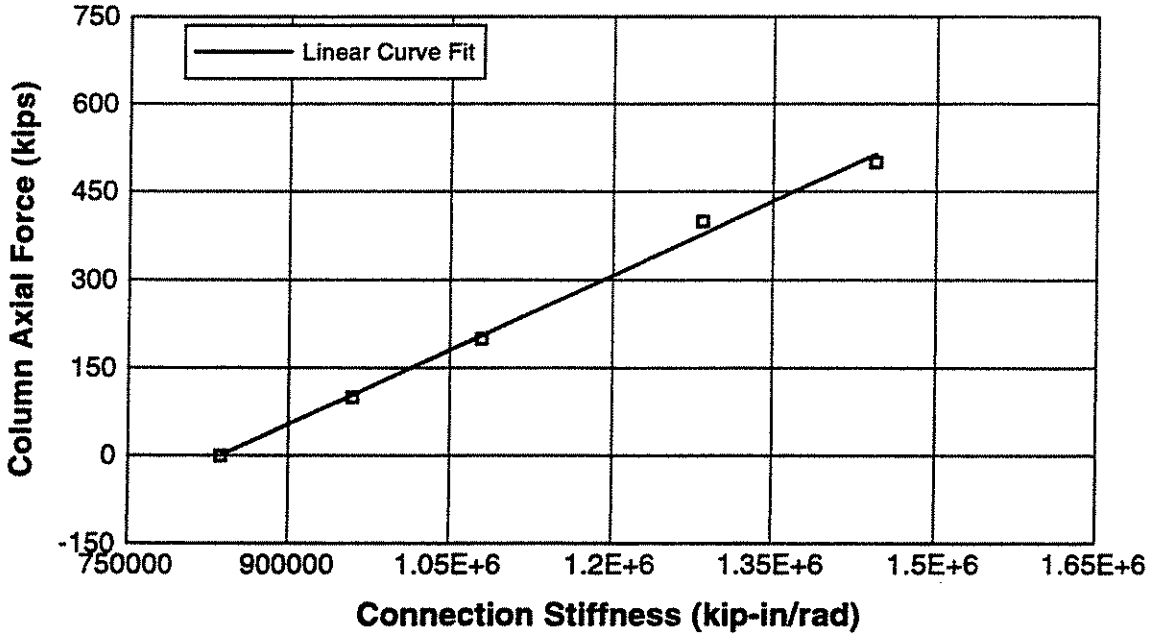

Fig. 4.7 - Influence of axial force on column base connection moment-rotation stiffness.

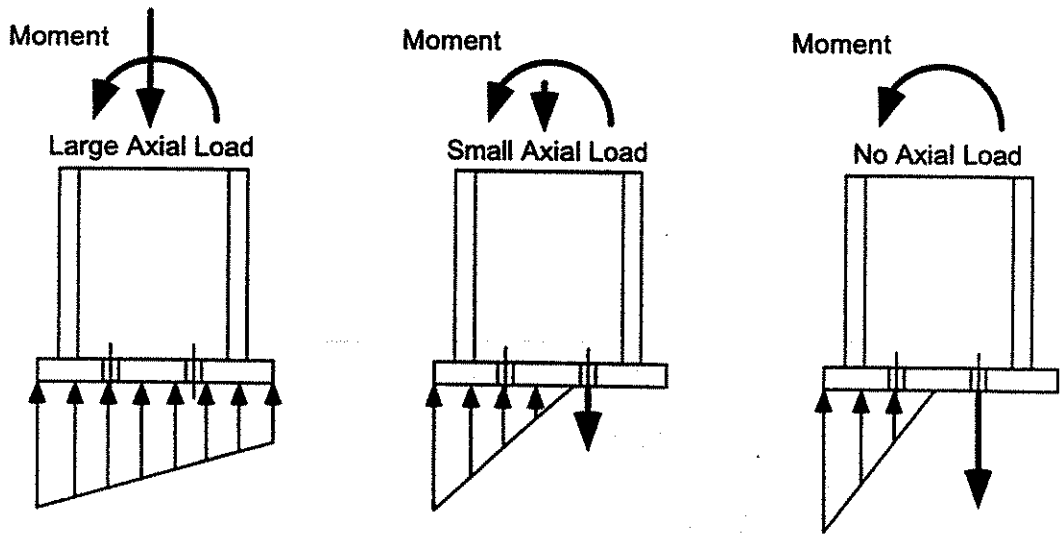

Fig. 4.8 - Schematic representation of role of axial force on bolt tension.

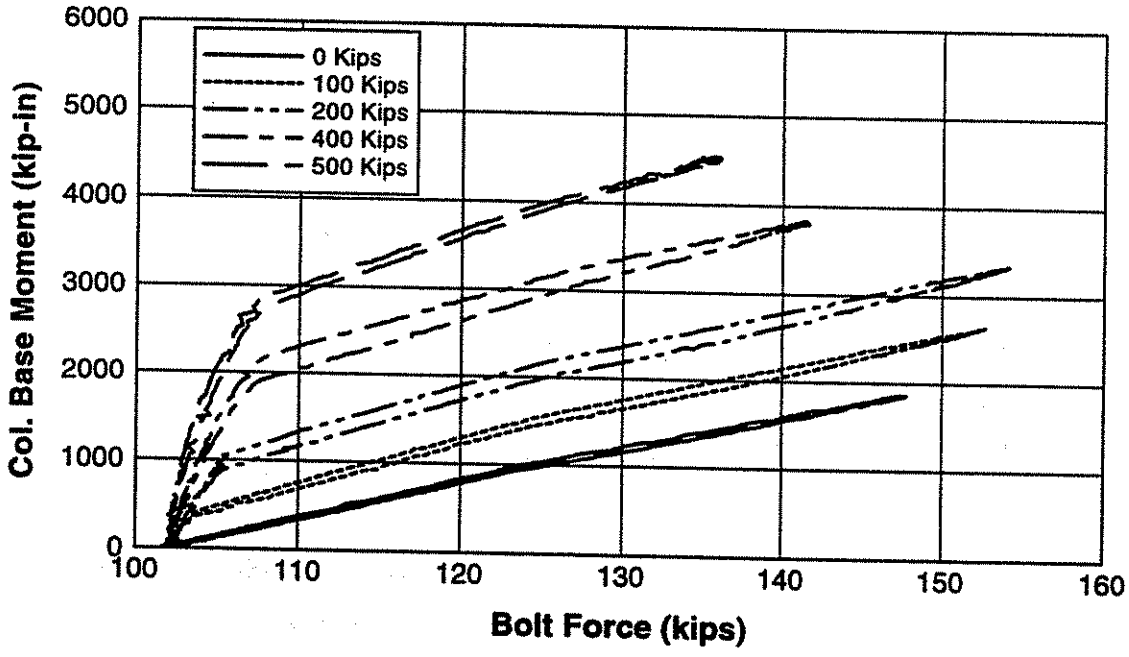

Fig. 4.9 - Bolt force as a function of moment for different column axial force levels.

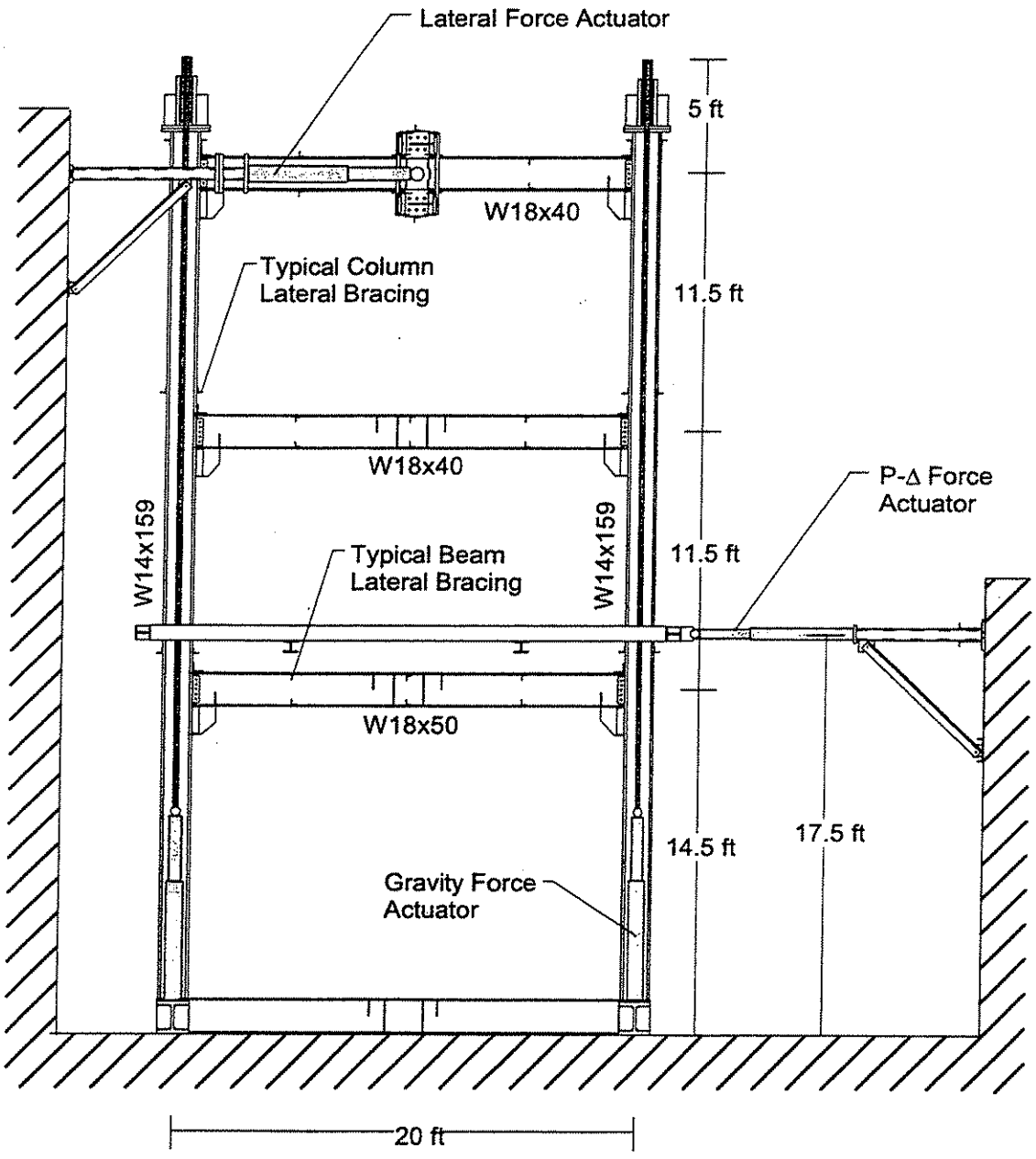

Fig. 4.10 - Unbraced frame test set-up.

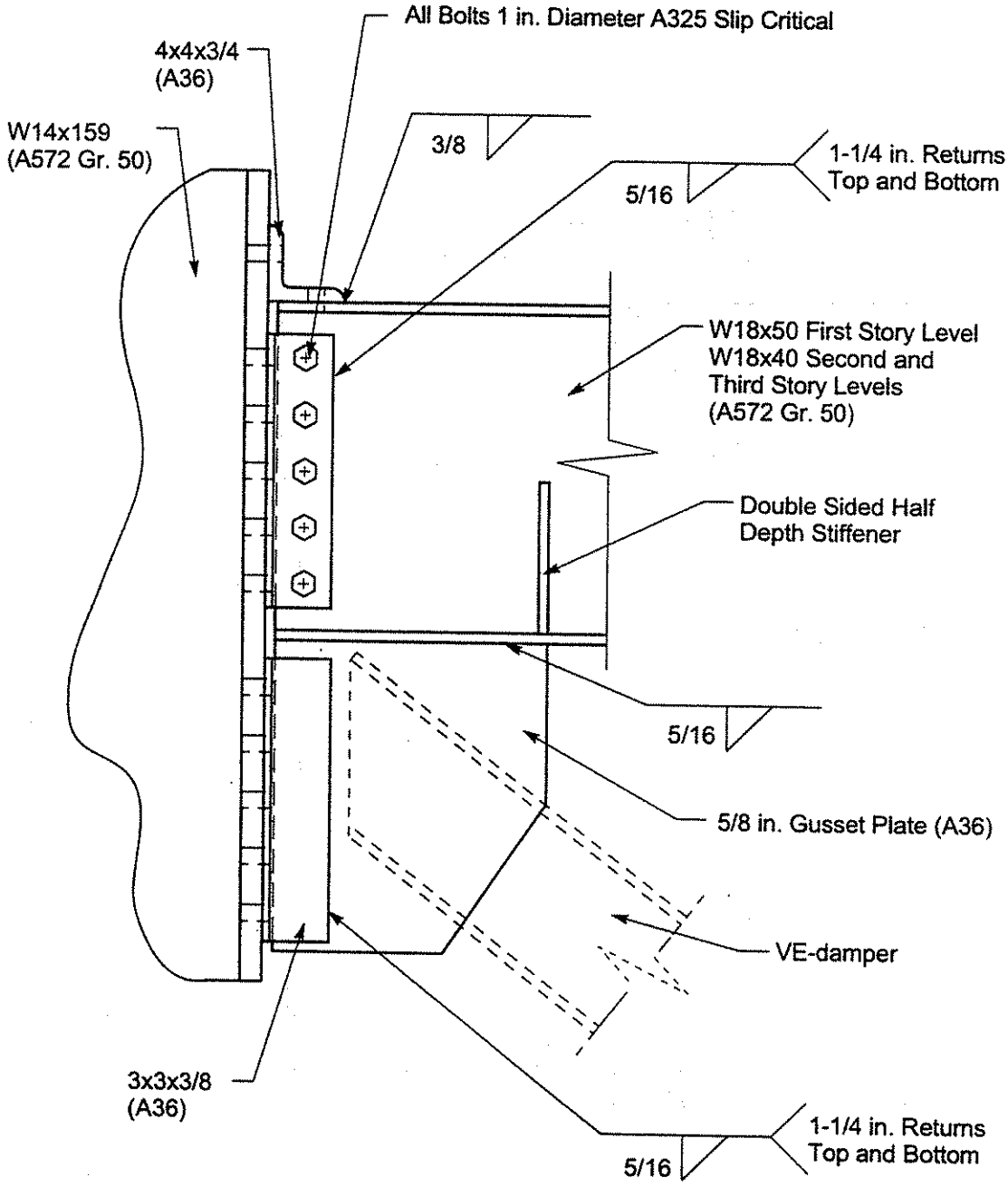

Fig. 4.11 - Beam-column connection detail.

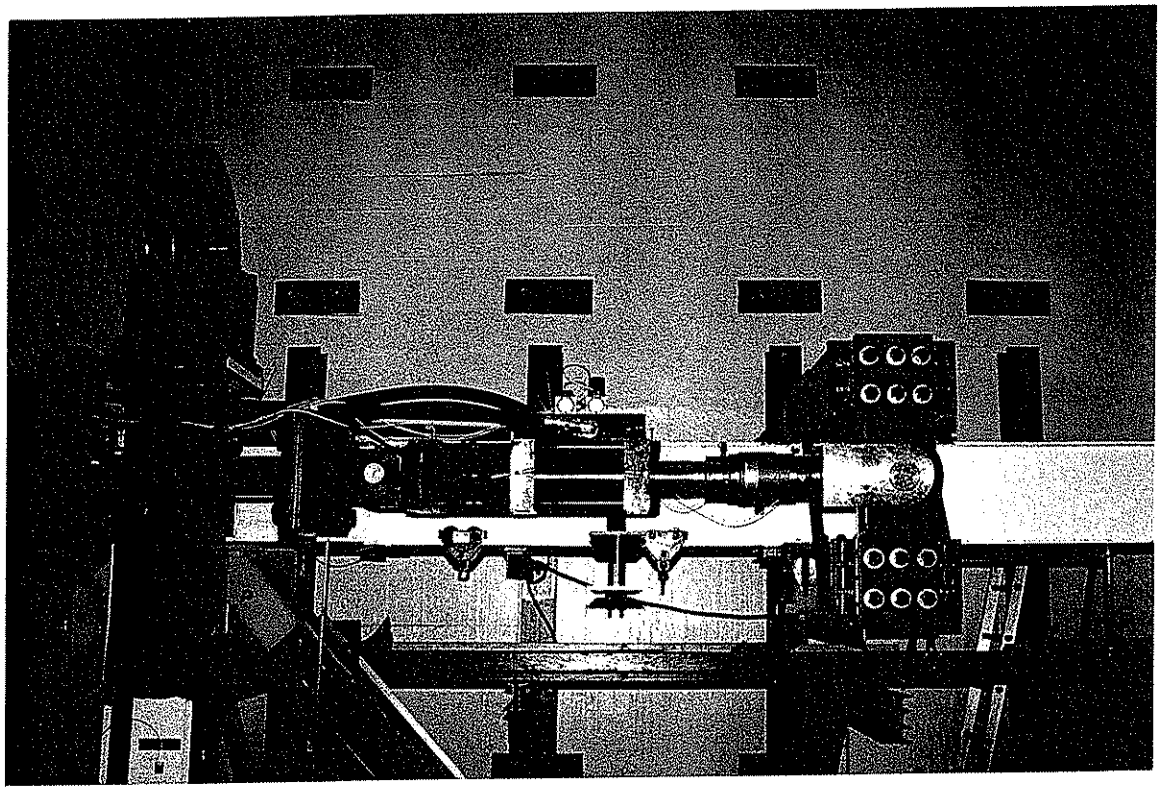

Fig. 4.12 - Hydraulic actuators at third story level.

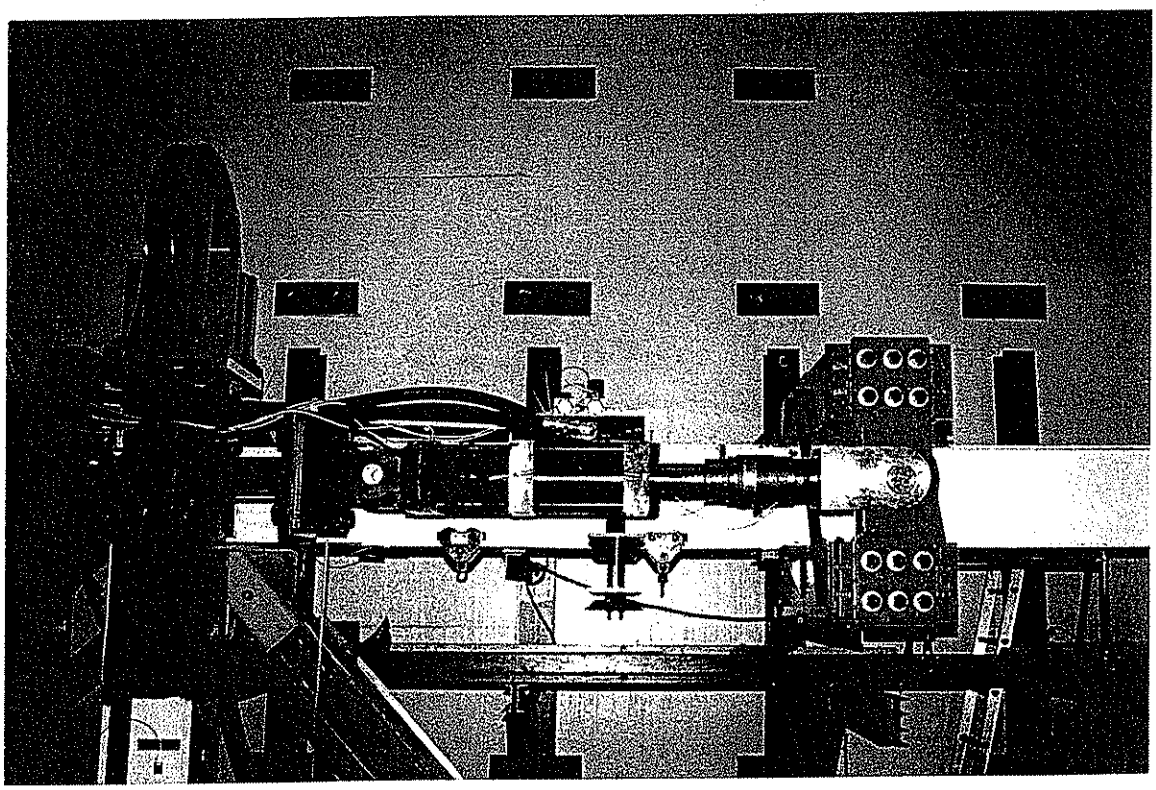

Fig. 4.12 - Hydraulic actuators at third story level.

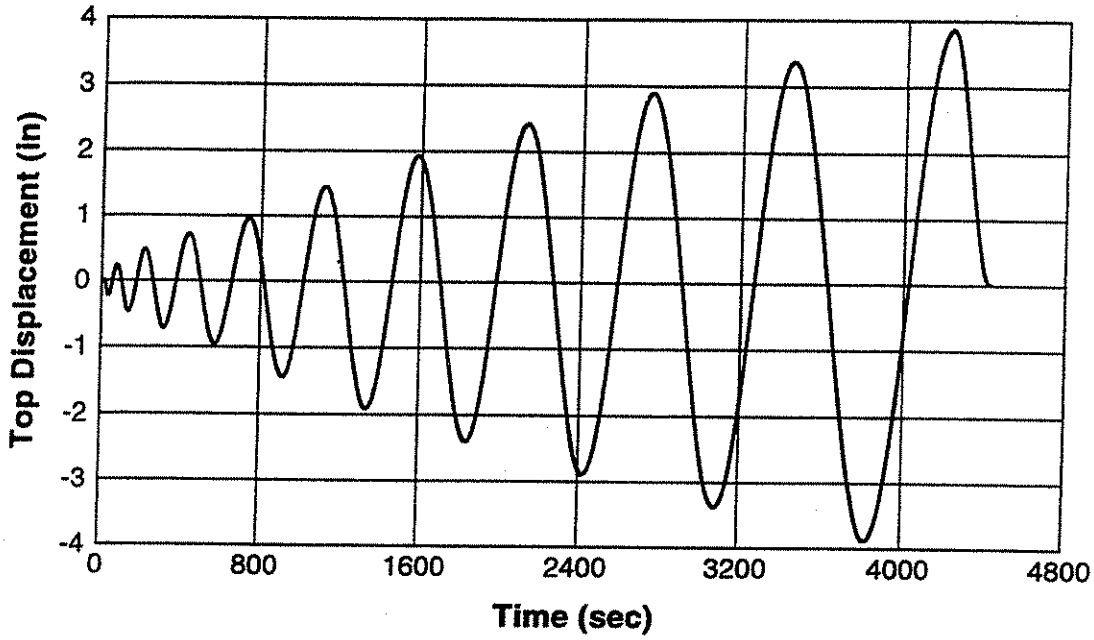

Fig. 4.13 - Loading history used to test unbraced frame.

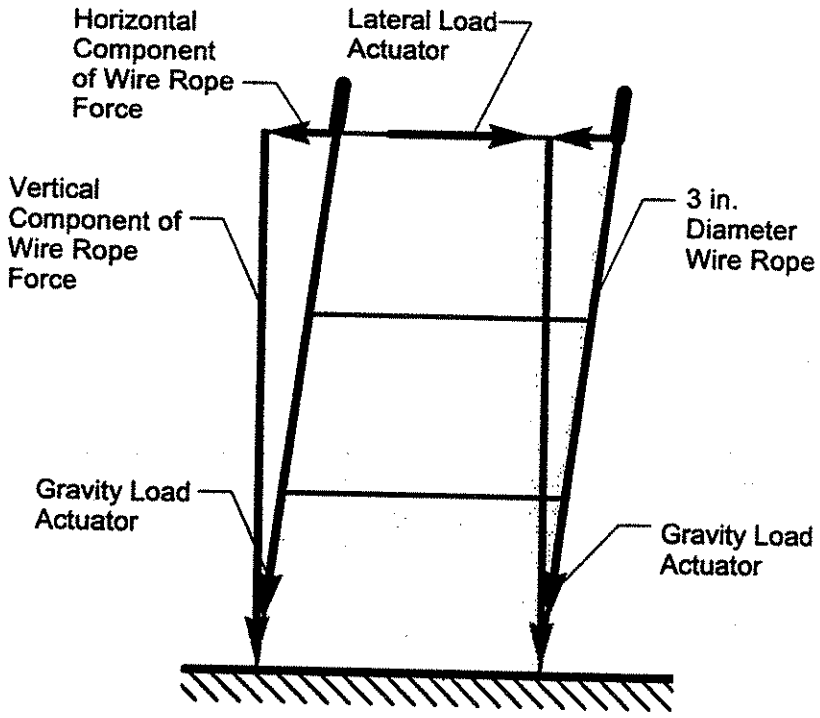

Fig. 4.14 - Force components provided by wire rope due to frame sway if uncorrected.

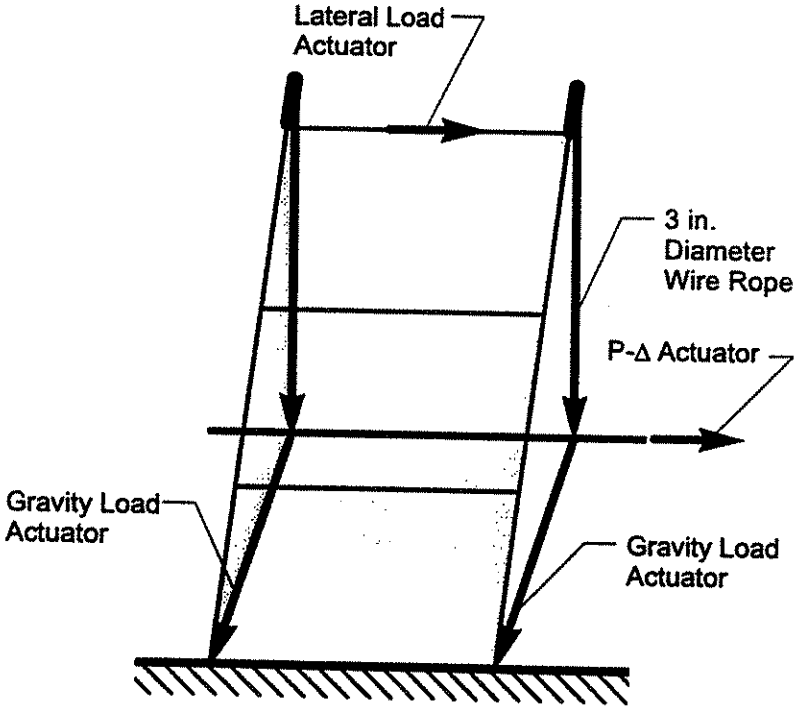

Fig. 4.15 - Axial force on columns remains vertical despite tilting of frame by controlling the P-Δ actuator.

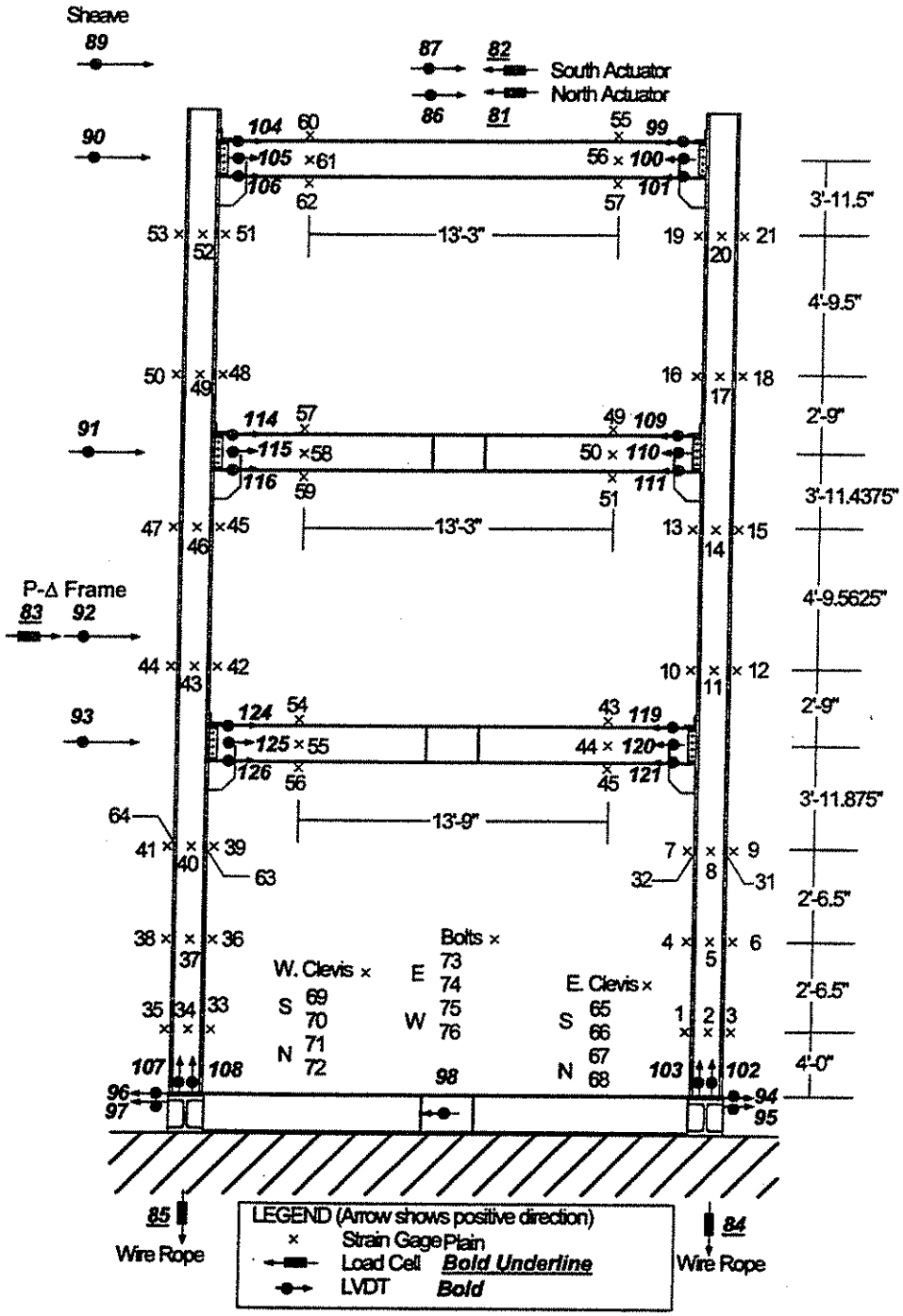

Fig. 4.16 - Instrumentation layout and channel identification for unbraced frame tests.

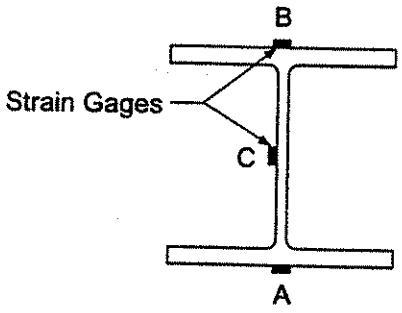

$$\text{Moment(kip-in)} = \frac{\varepsilon_A - \varepsilon_B}{2} \frac{S\,E}{1000000}$$

$$\text{Axial Force(kips)} = \frac{\varepsilon_A + \varepsilon_B + \varepsilon_C}{3} \frac{A\,E}{1000000}$$

Where S is the section modulus (in^3)
E is Modulus of Elasticity (29,000 ksi)
A is cross sectional area (in^2)
and strain readings in microstrain

Fig. 4.17a - Strain gage locations on each instrumented cross section.

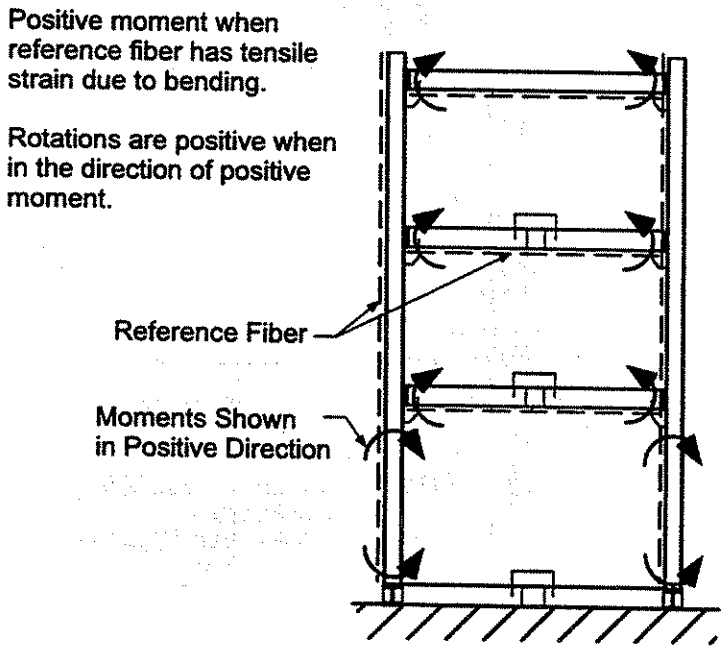

Fig. 4.17b - Sign convention for bending moments.

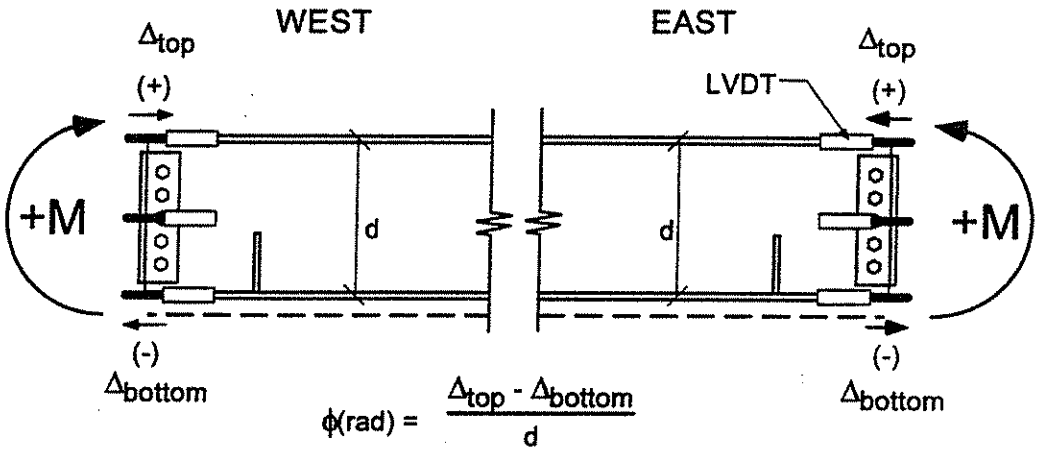

Fig. 4.18a - Method for determining beam-column connection rotations.

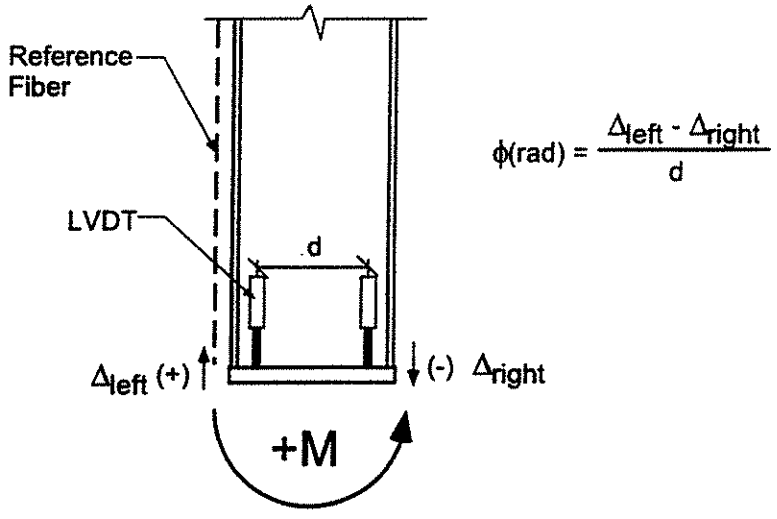

Fig. 4.18b - Method for determining column base connection rotations.

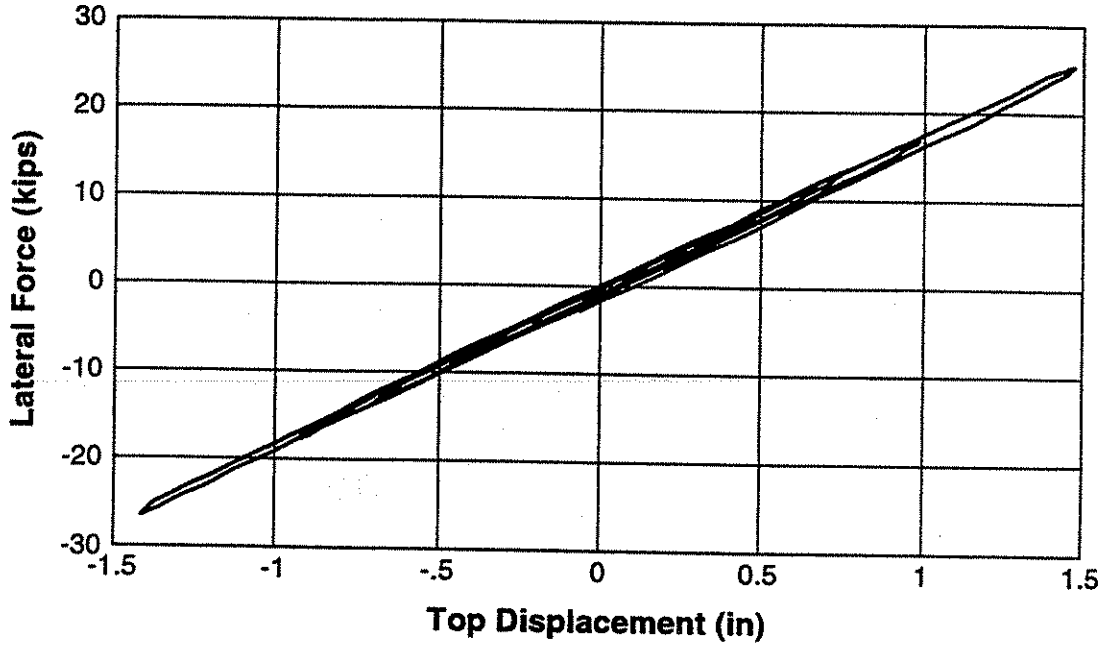

Fig. 4.19 - Overall unbraced frame load-displacement response at cycles below 1.5 in of top displacement.

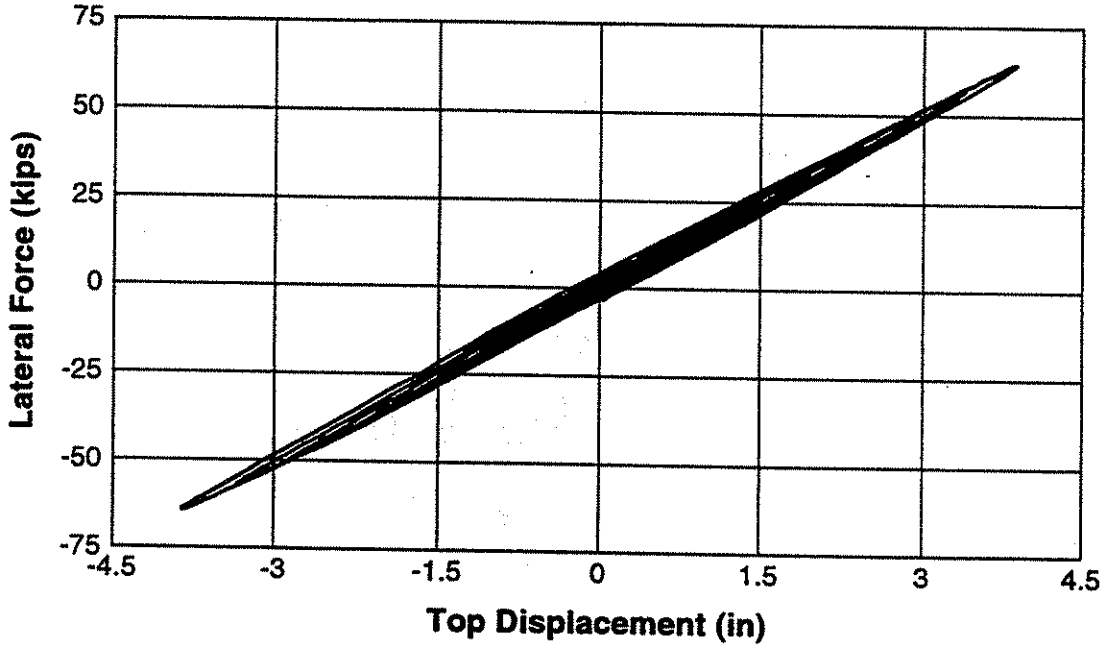

Fig. 4.20 - Overall unbraced frame load-displacement response at cycles above 1.5 in of top displacement.

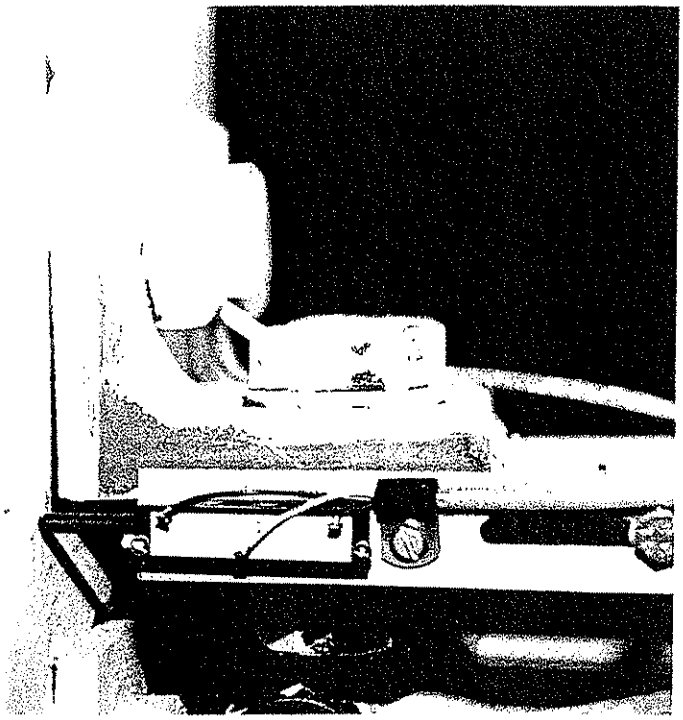

Fig. 4.21 - Prying of top seat connection at 4.0 in. of top displacement.

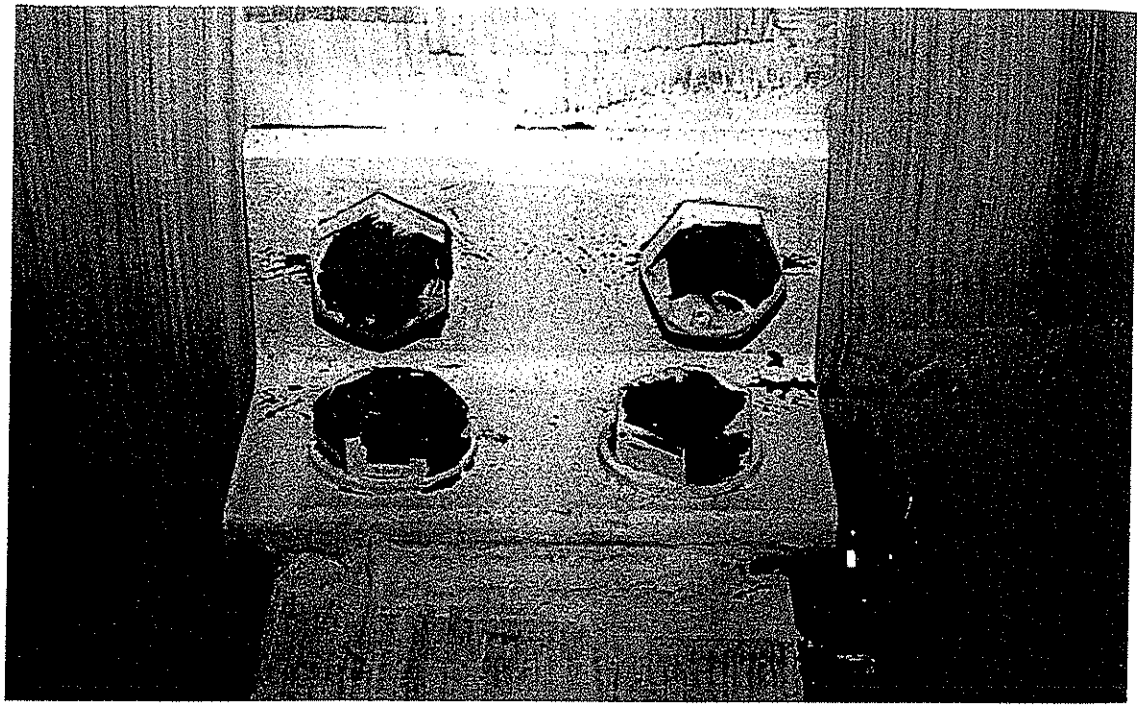

Fig. 4.22 - Local connection yielding.

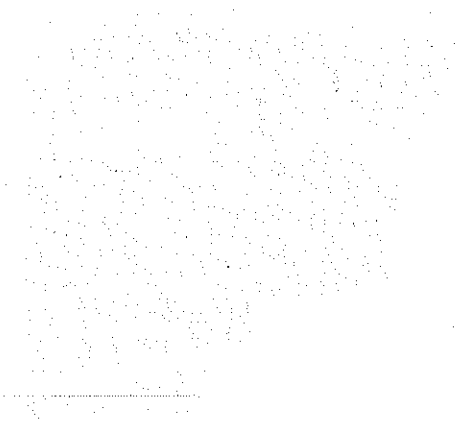

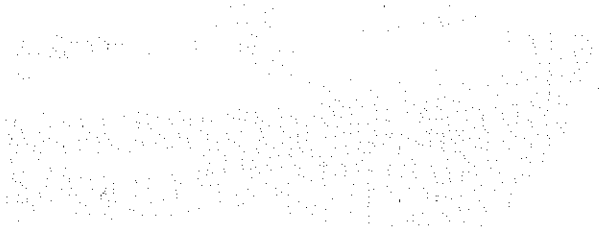

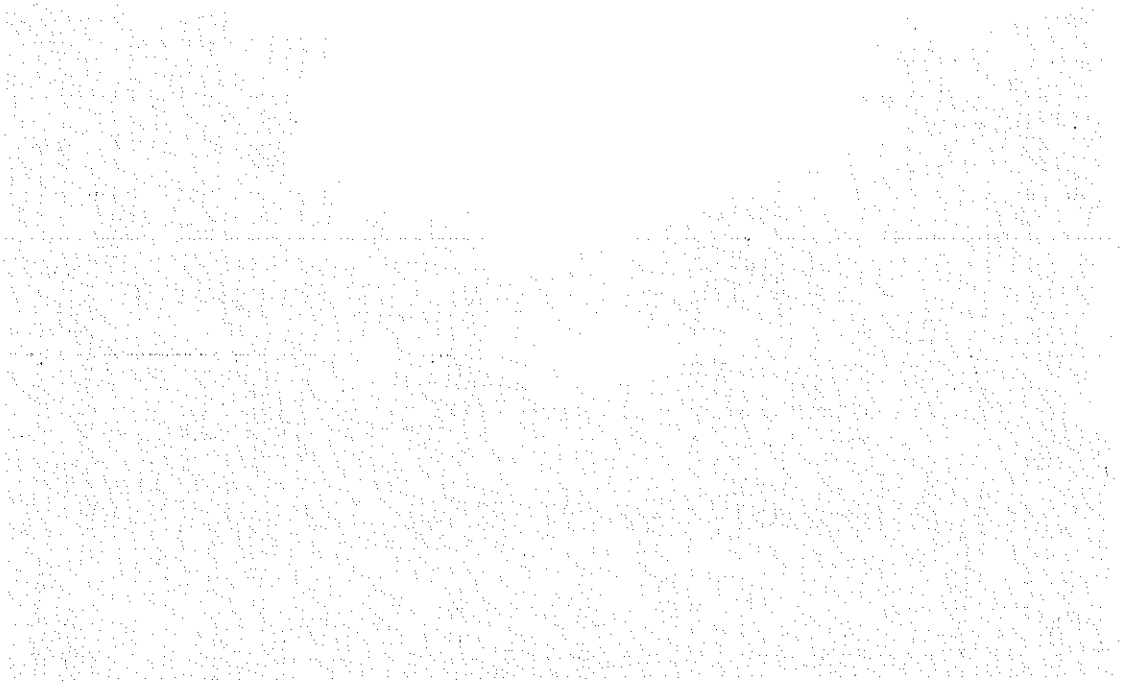

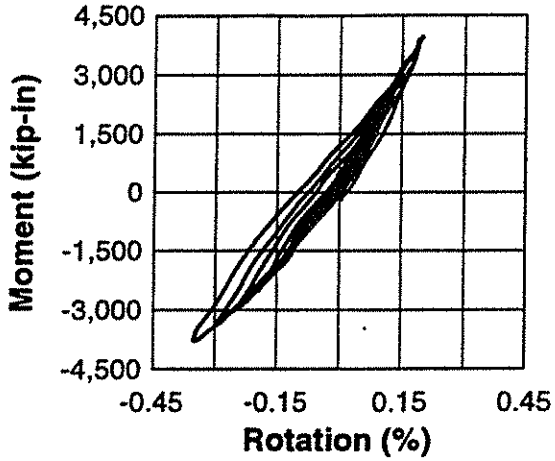

Fig. 4.23a - Connection Level 1 East moment-rotation response.

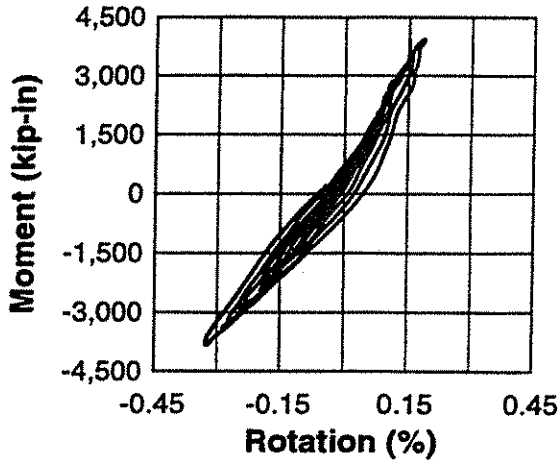

Fig. 4.23b - Connection Level 1 West moment-rotation response.

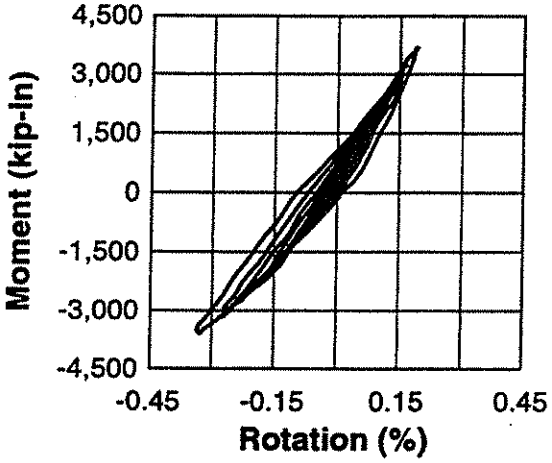

Fig. 4.23c - Connection Level 2 East moment-rotation response.

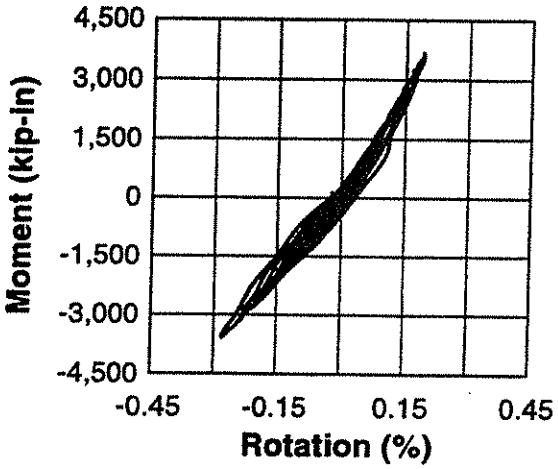

Fig. 4.23d - Connection Level 2 West moment-rotation response.

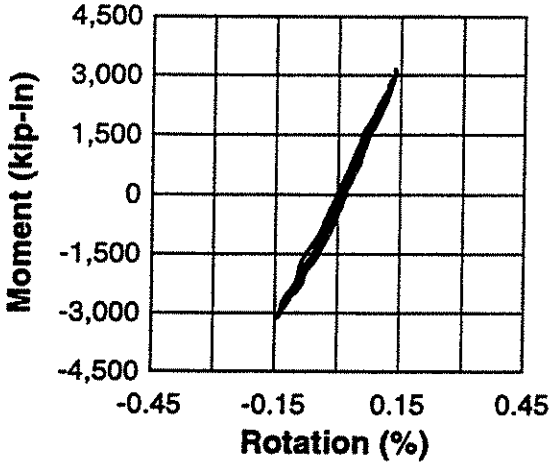

Fig. 4.23e - Connection Level 3 East moment-rotation response.

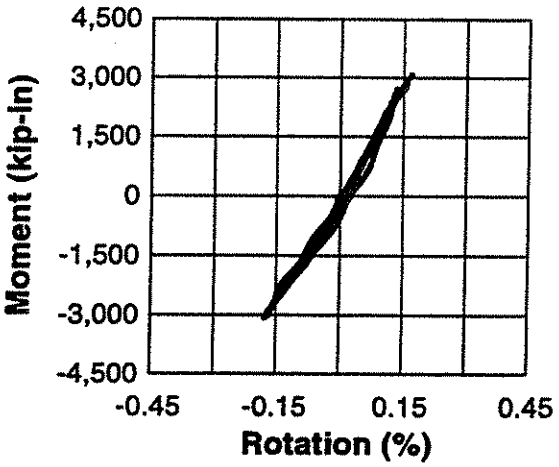

Fig. 4.23f - Connection Level 3 West moment-rotation response.

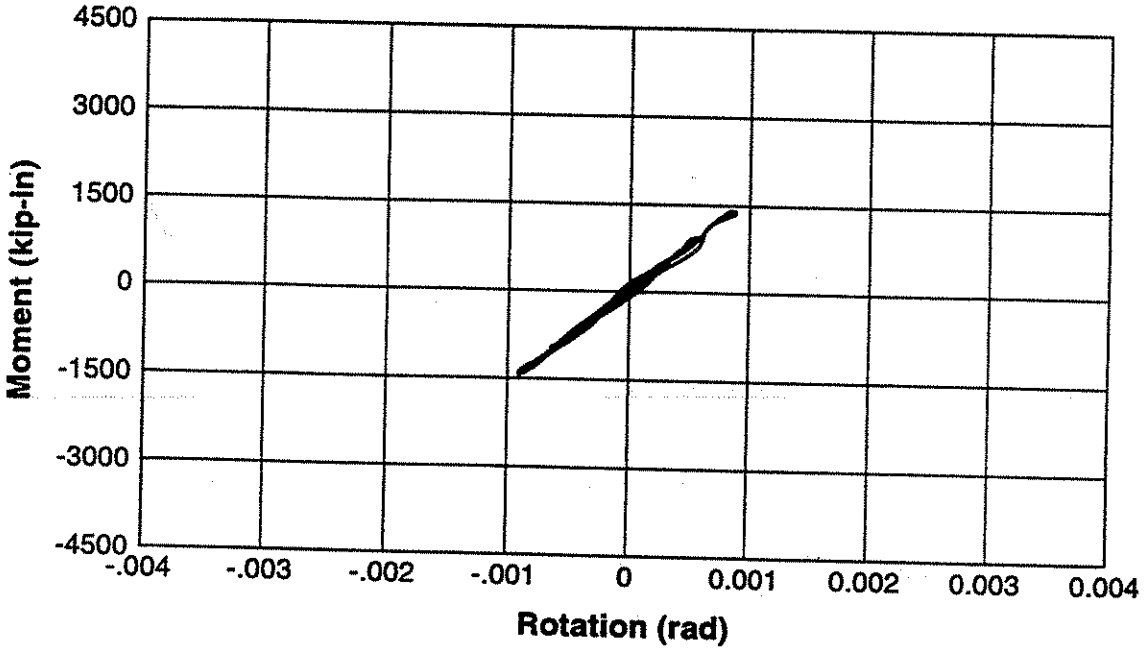

Fig. 4.24a - Example beam-column connection moment-rotation response at small excursions (Level 2 East).

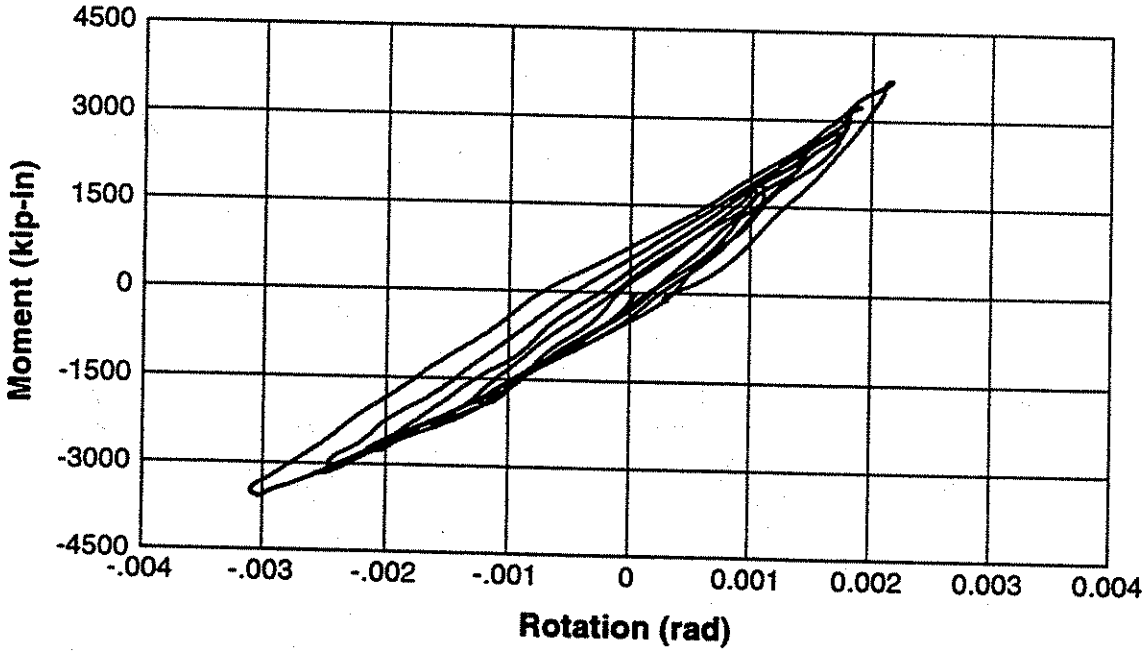

Fig. 4.24b - Example beam-column connection moment-rotation response at larger excursions (Level 2 East).

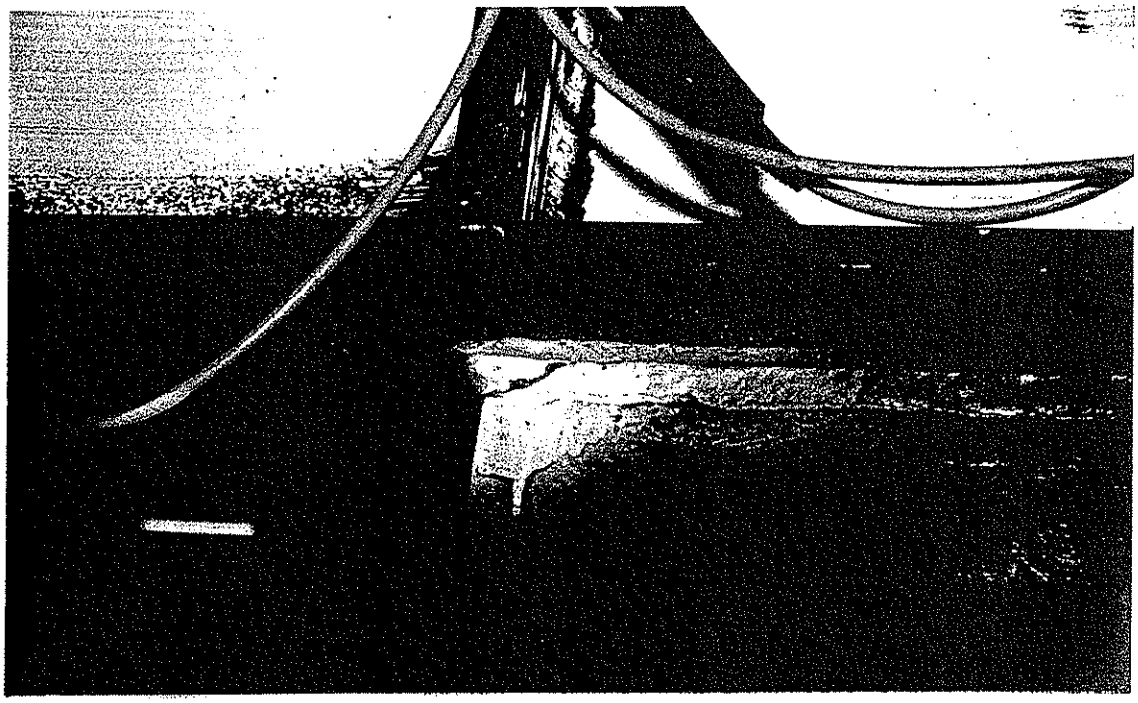

Fig. 4.25 - Example of cracks observed at fillet weld connection between gusset plate and beam bottom flange.

Fig. 4.26 - Example of cracks observed at fillet weld connection between gusset plate and beam bottom flange.

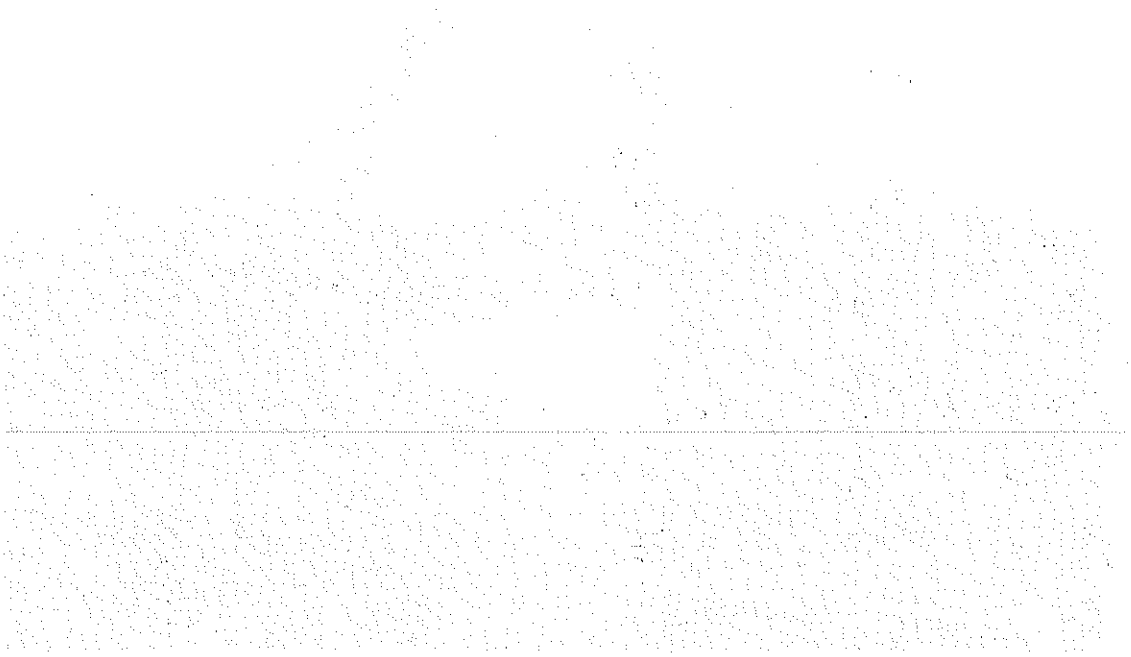

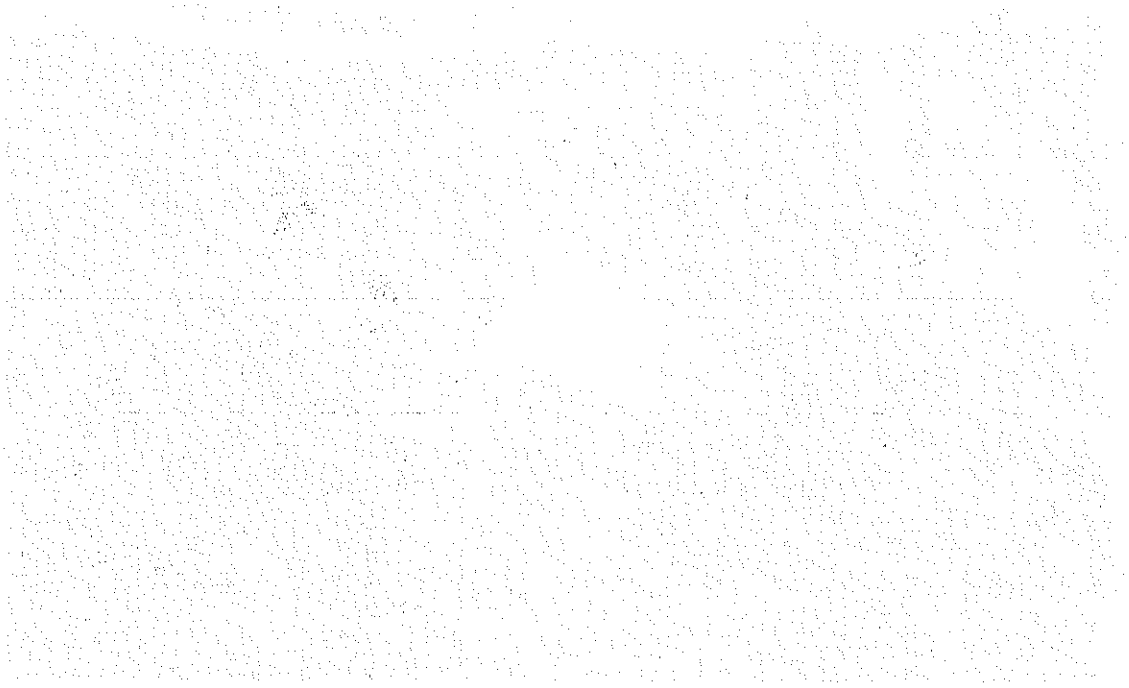

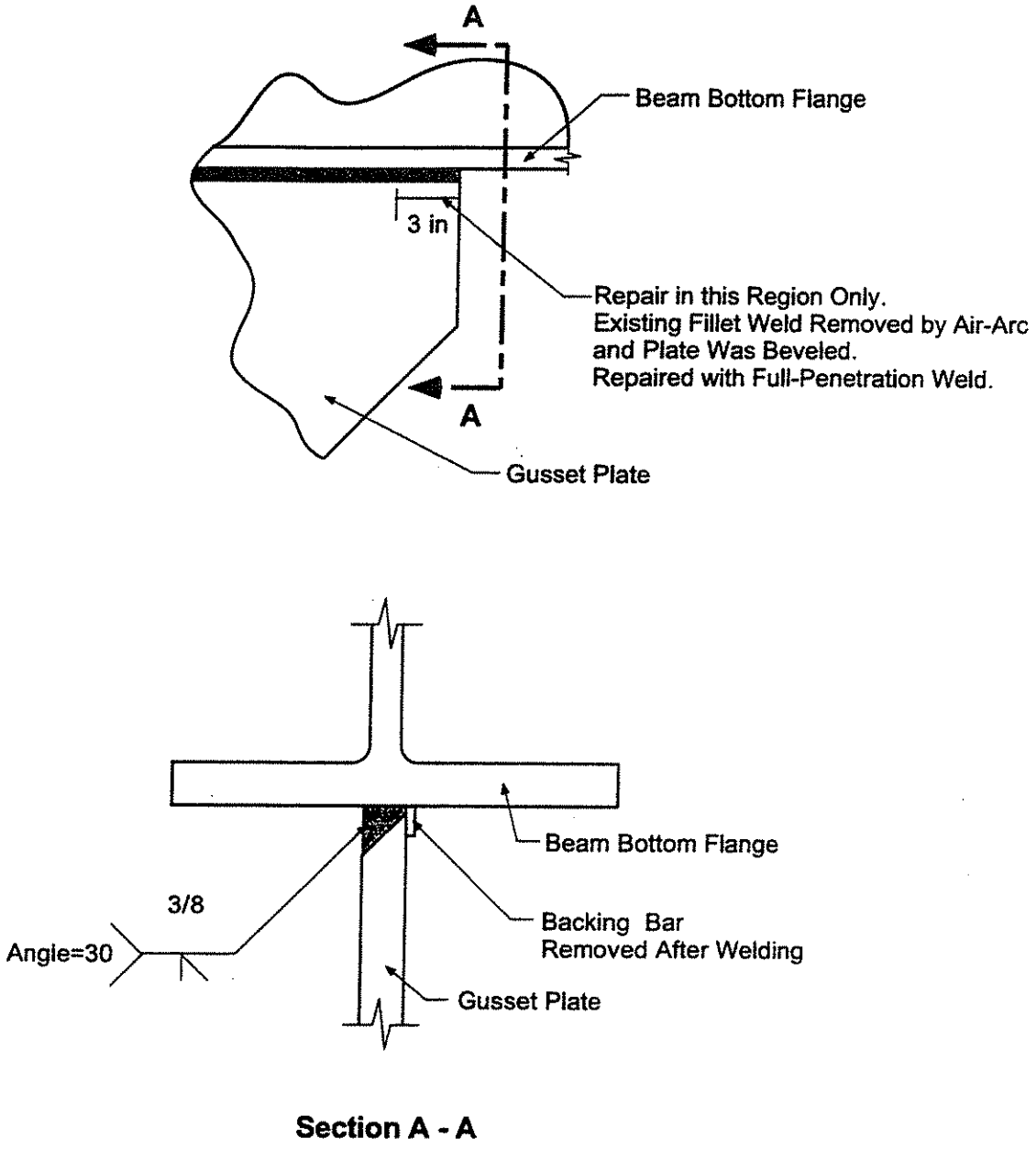

Fig. 4.27 - Repair detail for weld connection between gusset plate and beam bottom flange.

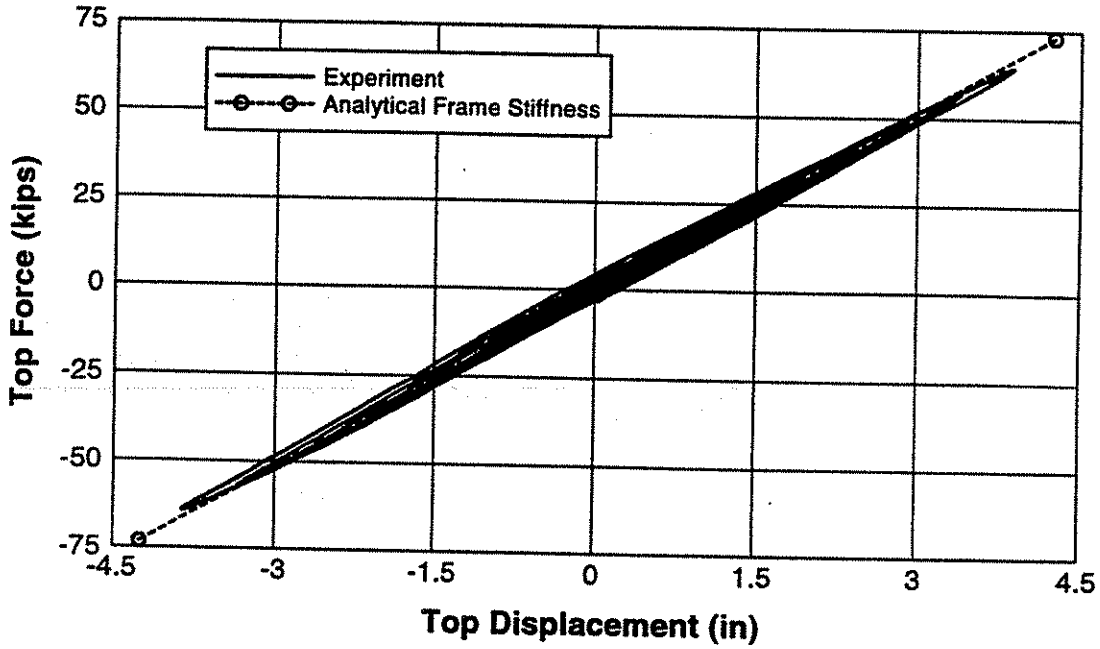

Fig. 4.28 - Analytically predicted frame stiffness and measured frame response.

Bold represents beam force or moment.

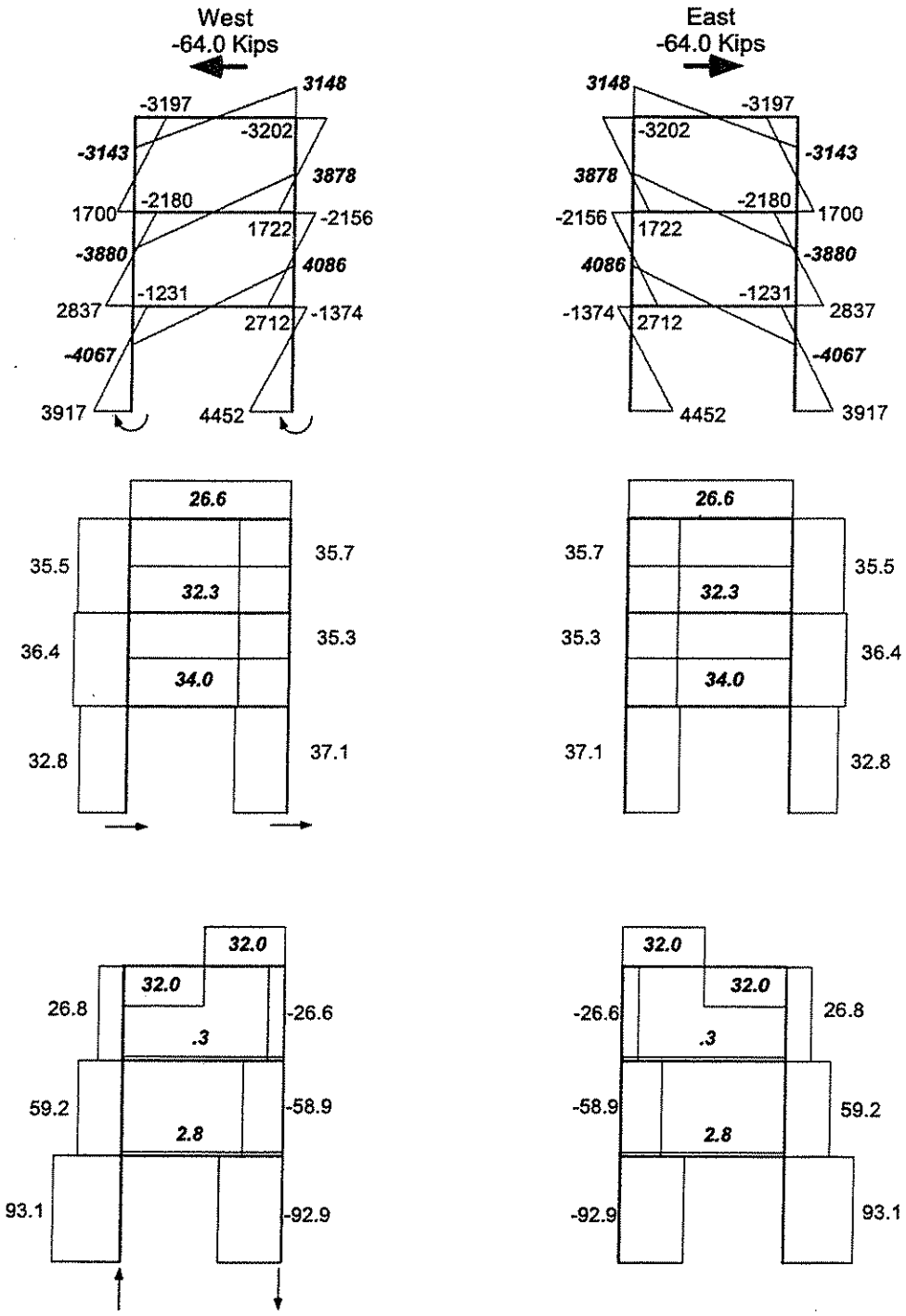

Fig. 4.29 - Analytically predicted local member forces at peak applied force.

Bold represents beam force or moment.

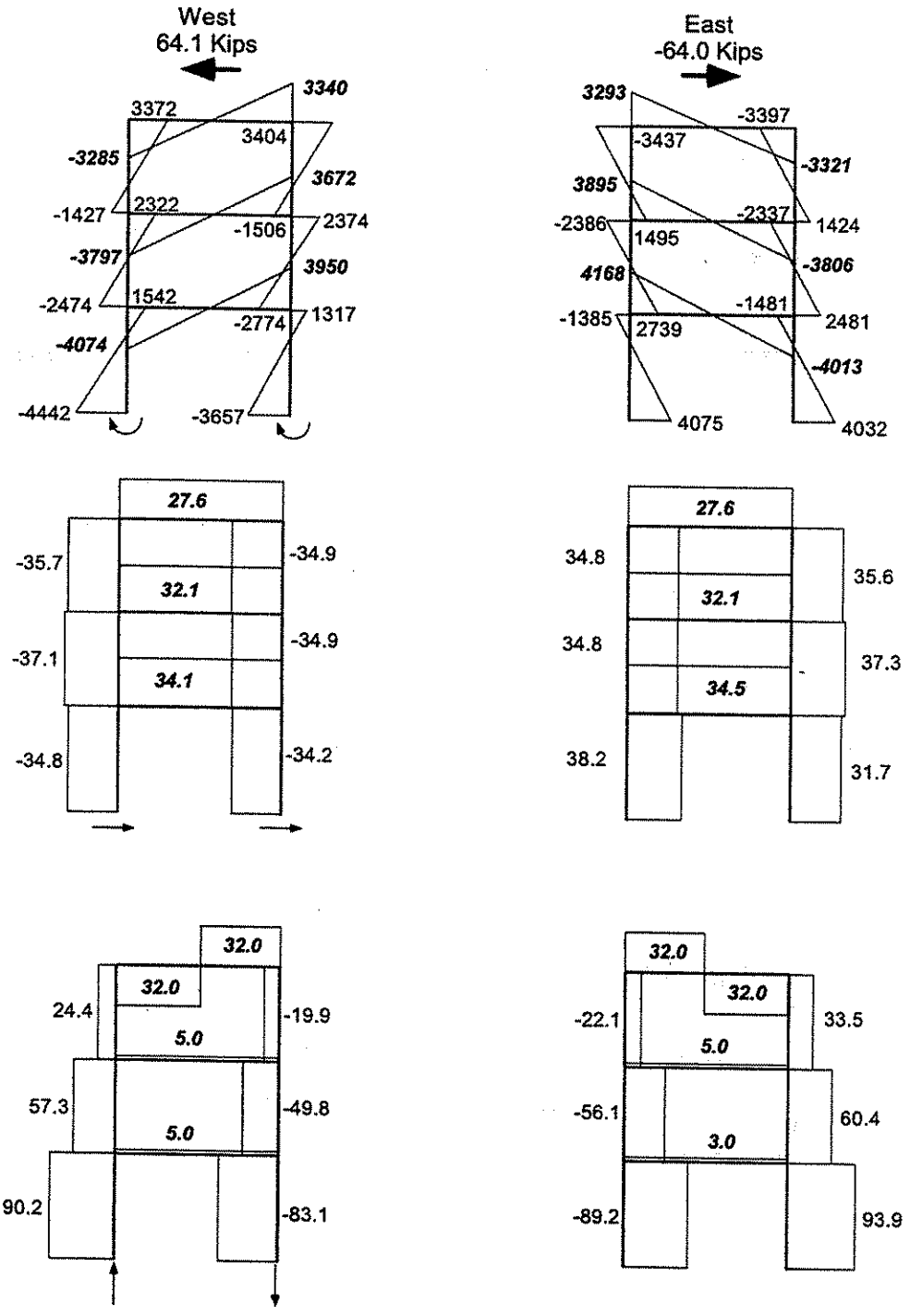

Fig. 4.30 - Measured local member forces at peak applied force.

CHAPTER 5.0 VE-FRAME BASIC LOADING TESTS and ANALYSIS

5.1 Introduction

This chapter presents experimental results and analytical correlation of basic tests performed on the test structure after installation of the VE-dampers. These basic tests included constant amplitude sinusoidal and relaxation tests. Testing methods and instrumentation are described. Experimental results, including global frame stiffness and damping, as well as local member response and damper interaction are presented. Analytical correlation of the VE-damped structure is performed using several analytical methods. These analytical methods are described and analyses results are presented.

5.2 Test Specimen and Instrumentation

The test specimen was a VE-damped steel frame consisting of the unbraced frame (Chapter 4) with VE-dampers (Chapter 3) installed in each story level as shown in Figs. 5.1 and 5.2. The VE-frame was specifically designed as a VE-damped structure and the dampers and structure were designed to achieve specific seismic performance criteria as will be described in Chapter 6.

VE-dampers were installed in the unbraced frame by welding the damper tube ends to gusset plates located at beam-column connection and beam midspan. The damper tube was slotted to fit on the gusset plates. A 1 in. diameter erection bolt was used to temporarily hold the damper during erection and welding. Fillet welds were used to permanently fasten the tube to the gusset plates as shown in Fig. 5.3.

Instrumentation for the basic tests included all channels used in the unbraced frame tests, as described in Chapter 4 and 32 additional sensors. The additional instrumentation was used to measure the damper forces, temperature rise, VE-material deformation, and brace deformation. A total of 196 channels were recorded for each test, and instrumentation layout and channel identification for all sensors are illustrated in Fig. 5.4. Damper force was measured using four strain gages on the tube cross-section as illustrated in Fig. 5.4. These strain measurements provided axial force, in-plane bending and out-of-plane bending of the damper. Thermocouples were installed in each of the six VE-dampers using the procedure described in Chapter 3 and provided continuous measurement of the VE-material temperature. Two LVDTs were used to measure the VE-material deformation on each damper as shown in Fig. 5.6. Overall deformation of the damper was measured using a string pot oriented along the brace axis as illustrated in Fig. 5.5a. Data were acquired using a PC-based Keithley Metrabyte DAS1802-ST-DA data acquisition board and 13 EXP-1800 multiplexing boards. Acquisition rates were varied according to loading frequency as shown in Table 5.1.

Data sampling time was determined using an external analog clock. The analog clock consisted of a continuous direct-current sawtooth waveform produced by a Stanford Research Systems Model DS335 synthesized function generator. Voltage signal from the function generator was recorded by the data acquisition system. Amplitude of the waveform was ± 9 volts at a frequency of 0.27778 hz. These settings permitted time to be measured with a resolution of 0.001 seconds.

To investigate the influence of temperature on damper performance, the VE-material internal temperature was varied from 16 to 32 °C as shown in the test matrix. Insulated enclosures were built around each damper to permit temperature control as shown in Fig. 5.7. Both heaters and air conditioners were located at each story level to achieve the desired initial damper temperatures. A thermocouple, inserted within the VE-material, was used for control of the forced air heating or cooling. All initial temperatures were controlled within a selected tolerance of ±0.1 °C. A handheld multiple input digital thermometer, was used to measure initial temperatures from the control thermocouples.

Testing of the VE-damped frame was conducted using five actuators to load the specimen as described in Chapter 4. At the beginning of each test, 400 kips of axial force was applied to each column with the axial force actuators. Initial damper temperatures at all three story levels were adjusted until achieving the desired temperature. Lateral loads were then applied dynamically to the frame with the lateral force actuators and data were acquired.

5.3 Sinusoidal VE-Frame Tests

A series of sinusoidal tests were performed to characterize the VE-damped frame response under different loading frequencies, initial temperatures, and frame displacement amplitudes. Five cycles were applied for each sinusoidal test. Four loading frequencies were investigated: 0.1, 0.5, 1.0, and 2.0 hz. Initial damper temperatures were: 16, 20, 24, 28, and 32 °C. Nominal frame top displacement amplitudes ranged from 0.25 to 4.0 in. The complete matrix for the sinusoidal tests is shown in Table 5.2. Test results included overall frame stiffness and damping, local member force magnitudes, overall force equilibrium for the structure, damper stiffness and force-deformation response, and interaction of damper forces with elastic frame member forces.

5.3.1 Global VE-Frame Response

Results of the short duration sinusoidal tests indicated the VE-damped frame exhibits frequency and temperature sensitivities typical of VE-materials. Typical measured overall VE-frame response is shown in Fig. 5.8. Examples of overall VE-frame response are shown in Fig. 5.9 for constant loading frequency of 0.5 hz and frame displacement amplitude of 0.5 in., at different initial temperatures of 16, 20, 24, 28, 32 °C. Example overall VE-frame responses are shown in Fig. 5.10 for a constant initial temperature of 32 °C and frame displacement amplitude of 0.25 in., at different loading frequencies of 0.1, 0.5, 1.0, and 2.0 hz. Example overall VE-frame responses are shown in Fig. 5.11 for constant initial

temperature of 20 °C and loading frequency of 0.1 hz, at different frame displacement amplitudes of 0.25, 0.5, 1.0, 2.0, and 4.0 in.

Frame stiffness and damping were computed from overall frame load-deformation curves. The elastic frame stiffness was computed:

$$K' = \sqrt{|K^*|^2 - K''^2} \qquad [5.1]$$

Where K'', K' are defined in Fig. 5.12. Frame stiffnesses for each test are summarized in Tables 5.3a to 5.3e. The frame exhibited marked changes in stiffness for different initial temperatures (Fig. 5.13) and frequencies (Fig. 5.14). At lower temperatures and higher frequencies, the frame was stiffer than at higher temperatures and lower frequencies.

Equivalent viscous damping ratios were computed for each test using Eq. 4.1. The second cycle was used for computing the damping ratio because the first cycle did not achieve the target displacement. The strain energy term in Eq. 4.1 was computed using K' determined from Eq. 5.1. Damping ratios for each test are summarized in Tables 5.3a to 5.3e. At 0.25 nominal top displacement amplitude, the frame damping ratio was dependent on temperature and frequency as shown in Figs. 5.15 and 5.16. Damping ratio trends observed for small frame displacements were also found for larger displacement amplitudes as shown in Fig. 5.17. While the VE-frame stiffness exhibited temperature sensitivity, the damping ratio was fairly stable through the range of temperatures for the 0.5 hz frequency (the natural frequency of the seismic prototype structure, Chapter 6) as shown in Fig. 5.15. Damping ratio was also

fairly stable through different frequencies, at 24 °C (the reference temperature of the seismic prototype structure, Chapter 6), as shown in Fig. 5.16.

Temperature rise within the VE-material was monitored continuously for each of the six dampers in the frame. Typical temperature rise for the second story west damper is shown in Fig. 5.18 for an initial temperature of 24 °C and a 0.5 hz loading frequency with different magnitude frame displacement amplitudes of 0.25, 0.5, 1.0, and 2.0 in. As seen in this figure, larger frame displacements resulted in increased temperature rise within the VE-dampers. Temperature rise within dampers at each story level for all sinusoidal tests are summarized in Tables 5.4a to 5.4e.

Current design guidelines recommend limiting damper strains to below 100%, however, this may be unnecessarily over-conservative. Two tests were performed with damper strains of up to 130% to determine if significant changes occur in behavior or performance when the dampers undergo strains over 100%. Overall load-deformation response for these tests are shown in Figs. 5.19 and 5.20. No adverse effects were observed for these tests and the dampers provided predicted stiffness and damping as discussed later in section 5.5.

5.3.2 Local Member Response

Sufficient data was recorded for the 69 sinusoidal tests to permit assessment of all local member force and connection response. Comprehensive results from only one test are presented in this section for brevity. The presented results illustrate the detailed response data collected and highlight the local behavior and interaction of structural members. The sinusoidal test at 0.5 hz, 24 °C initial damper temperature, and ±2 in. nominal top displacement was selected for this purpose. This test contained a combination of significant damper forces and lateral displacement permitting elucidation of interactions between frame member and VE-dampers.

Overall frame response is shown in Fig. 5.21 for this test. This type of hysteresis results from out-of-phase response between force and displacement as illustrated in Fig. 5.22. As seen in this figure, the force leads displacement by approximately 0.2 seconds. As seen in both Figs. 5.21 and 5.22, the top force at later cycles becomes progressively smaller while the displacement remains unchanged. A reduction in damper stiffness caused by temperatures rise in the dampers from energy dissipation results in reduced actuator force required to produce the specified frame displacement.

The hysteresis shown in Fig. 5.21 exhibits some distortion because forces generated during the test (peak = 222 kips) actually exceeded the nominal capacity of the lateral force actuators (220 kips). While the majority of tests did not exhibit this type of distortion, as shown in Figs. 5.9 to 5.11, distortion was observed for tests which approached frequency, stroke, or force capacities of the actuators and servo-valves.

Frame displacements at each story level were in-phase as shown in Fig. 5.23. Interstory drifts are shown in Fig. 5.24. Level 1 exhibited slightly more drift than the upper stories because of the larger first story height. Interstory drifts for the upper stories were similar.

Bending moments for frame members were determined from strain gage measurements as described in Chapter 4. Time history responses of computed moments, from strain measurements, for the east and west columns are shown in Figs. 5.25a to 5.25c and 5.26a to 5.26c respectively. The moment presented in these figures is for the column moment just above the lower connection (base) and just below the upper connection (top) for the particular column segment. Moment gradient in the column was linear between the base and top. All column segments were in reverse curvature, and the west column carried slightly higher moment than the east column. Column moments did not change during the test indicating a strong dependence on top displacement.

As seen in Figs. 5.25a and 5.26a, both the east and west column foundation connections exhibit unsymmetric behavior. Each column base carries higher moment when subjected to additional axial compression. Columns are subjected to additional compression force on opposite cycles and while one column carries less moment as its axial force reduces, the other carries higher moment as its axial force increases. As a result, the combined moment resistance provided by the two columns remains almost unchanged as shown in Fig. 5.27.

Points of inflection in the first story column shifted depending on the direction of loading, due to axial force-connection stiffness interaction described in Chapter 4. Inflection points were located in the upper half of the column and on opposite cycles are as high as 0.65 times the story height as shown in Fig. 5.28. There is no column moment above the third story connection because the column terminates above this level. As a result of this boundary effect, inflection points in the third story column were located in the lower half of the member. Only the inflection points in the second story columns were located at midheight.

Time history responses of computed column axial forces for the east and west columns are shown in Figs. 5.29 and 5.30 respectively. East and west column segments carried equal and opposite axial forces. Column axial force magnitudes became progressively smaller during the test indicating a strong dependence on the VE-damper forces.

Shear forces were determined from the moment gradient in each column segment. Time history responses of the computed column shear forces for the east and west columns are shown in Figs. 5.31 and 5.32 respectively. The west column carried higher shear forces than the east column. Larger shear forces in the west column resulted from the larger west column moments described previously. Column shear force magnitudes remained unchanged during the test indicating a strong dependence on displacement.

Time history of computed beam moment response is shown in Figs. 5.33a, 5.33b, and 5.33c for the first, second, and third story levels respectively. Beams were in reverse curvature and moments were symmetric indicating points of inflection were located at midspan. The first

story beam carried slightly higher moment than the upper story beams. Beam moments at each cycle remained unchanged during the test indicating a strong association with displacement.

Time history of beam axial force response is shown in Figs. 5.34a, 5.34b, and 5.34c for the first, second, and third story levels respectively. Upper story axial forces were symmetrical while the first story exhibited slightly symmetrical behavior. Beam axial forces became progressively smaller during the test indicating a strong dependence on the VE-damper forces.

Beam shear force response is shown in Fig. 5.35 for the three story levels. All shear forces were symmetrical. The first story beam carried more shear force than the upper story beams. The larger shear force resulted from the larger beam moment described above. Beam shears at each cycle remained unchanged during the test indicating a strong dependence on the top displacement.

Damper response for each of the six dampers in the frame are shown in Figs. 5.36a to 5.38b. As seen in these figures, eastern dampers begin in tension while the western dampers begin in compression. The response of the two dampers in each story are similar in displacement amplitude and only slightly unequal in force magnitude. Imbalance in the two damper force magnitudes within a story level or misalignment of the line of action between dampers would result in addition bending moment in the beam. No significant behavior of this type was observed in the beam bending moments discussed above. If the dampers were at significantly different initial temperatures, serious bending could be imposed on the beam due to a

concentrated force at midspan from the imbalance of damper forces. A single damper could be used in each bay to ensure this situation does not occur.

Damper forces in later cycles became progressively smaller as shown in the force-deformation response curves. Damper stiffness reduced as temperature increased due to energy dissipation by the VE-material. Measured temperature rise for dampers in each story level are shown in Fig. 5.39. As shown in Fig. 5.39, temperature rise begins at the onset of loading and increases almost linearly during loading. Initial and final measured temperatures for this and all tests is presented in Tables 5.4a to 5.4 e.

Phase relationships between member and damper forces were determined from normalized responses. Normalizing of member responses was performed by dividing the measured response at each time by the maximum response. Normalized response time histories were then plotted for a single cycle to determine the magnitude of time lag between the member forces. As member forces become more out-of-phase with each other, time history responses indicate a larger time lag. Additionally, the normalized member forces were plotted against the normalized damper deformation to determine the shape of the response. Here, as member forces become more out-of-phase with each other they exhibit fatter elliptical force-damper deformation response.

The phase relationship between frame top force and displacement and the level 2 East VE-damper force and deformation is shown in Figs. 5.40a and 5.40b. The damper force exhibited the greatest time lag from the top displacement. Top force was only slightly out-of-phase

with the damper force. This slight phase shift is due to the contribution of the unbraced frame force which acts in-phase with top displacement. Top displacement and damper deformation are out-of-phase with the damper and top frame forces due to viscous component from the VE-material.

The phase relationships between level 2 East VE-damper response and the East second story column forces are shown in Figs. 5.41a and 5.41b and phase relationships between level 2 East VE-damper response and second story beam forces are shown in Figs. 5.42a and 5.42b. Column and beam moments and shear forces are more in-phase with frame lateral displacements while the column and beam axial forces are more in-phase with the damper force. Slight phase differences between frame deformation and beam and column moments and shears are due to imperfect force balance between the two dampers within a story. The small imbalance in damper forces results in slight beam bending due to damper imposed midspan force. The damper imposed moments contain out-of-phase components which results in a slight time lag for the beam moments. These small time lagged beam moments are then transferred into the columns and resulting column shear forces.

Beams and columns in the VE-frame must be designed to resist both moment and axial force. Moments have been shown to be produced mainly by frame lateral displacement while axial forces are mainly generated by VE-damper forces as demonstrated by the force-deformation response. As shown in Figs. 5.43a and 5.43b, the maximum axial force and maximum moments occur at different instances of time. As a result, the axial force-moment interaction exhibits hysteresis as shown in Fig. 5.44a and 5.44b. This presents a complication when

predicting the most critical load combination for design of the member. A proposed simplification would conservatively design the member assuming both peak moment and axial force occur at the same instant. Gravity loads also contribute to column axial forces and must be considered simultaneously with the dynamically generated axial forces. However, gravity forces do not change during lateral displacement of the frame and can be directly superimposed on the dynamic forces.

5.5.3 Elastic Stiffness of Brace

As discussed in Chapter 3, VE-dampers, like those used in this study, are typically attached to a steel brace and the interaction between the brace and damper affects the behavior of the VE system. The combined damper and brace assembly is termed *'added component'*. The brace and damper are connected in series and the complex stiffness of the added component K^*_a contains in-phase stiffness K'_a and out-of-phase stiffness $\eta_a K'_a$:

$$K^*_a = K'_a(1 + i\eta_a) = \frac{K_b K^*_d}{K_b + K^*_d} \qquad [5.2]$$

where η_a is the loss factor of the added component, K^*_d is the complex damper stiffness, and K_b is the brace in-phase elastic stiffness. From Chapter 2, $K^*_d = K'_d(1 + i\eta_d)$ and $K'_d = G'A/t$. Damping provided by the brace is assumed negligible and the complex brace stiffness then contains only in-phase parts. K'_a and η_a are determined according to Eqs. 5.3 and 5.4 respectively [Kasai and Fu, 1995]:

$$K'_a = \frac{K_b K'_d}{(K_b/\Gamma) + K'_d} \qquad [5.3]$$

$$\eta_a = \frac{\eta_d}{\left[1 + \left(1 + \eta_d^2\right) K'_d / K_b\right]} \qquad [5.4]$$

$$\Gamma = 1 + \frac{\eta_d^2}{(1 + K_b/K'_d)} \qquad [5.5]$$

where η_d is the loss factor for the damper, K'_d is the in-phase stiffness of the VE-damper, $\eta_d K'_d$ is the out-of-phase stiffness of the VE-damper.

To illustrate the influence of the brace stiffness, Eq. 5.3 was used to compute the added component stiffness and Eq. 5.4 was used to compute the added component loss factor for different amounts of brace stiffness and an assumed η_d =1.36 and K'_d =222 kips/in. Results are shown in Figs. 5.45 and 5.46. The in-phase added component stiffness is not particularly sensitive to the brace stiffness (Fig. 5.45) when the brace stiffness is above 1000 kips/in. The amount of damping provided by the VE-dampers is seriously diminished when a soft brace is used (Fig. 5.46). An important result of the sinusoidal tests was the measurement of the brace in-phase stiffness for the added components in the frame. Measured in-phase brace stiffness included the influence of both the steel brace members and connections of the brace to the frame.

Brace in-phase stiffness was determined by measuring the local VE-material deformation and overall deformation of the added component with displacement transducers and subtracting the local VE-material deformation from the overall deformation. Typical force-deformation

response for the added component, VE-material, and brace at story levels 1 and 2 are shown in Figs. 5.47 and 5.48 respectively. Brace stiffness, along the axis of the added component, was estimated at 3000 kips/in for the first story level and 3500 kips/in for the second and third story levels. The first story damper was less stiff than the dampers in the upper stories due to the longer brace length in the first story. As seen in Figs. 5.47 and 5.48, there is a slight difference in the tension and compression behavior of the brace. In compression, the brace is slightly stiffer than when in tension due to the flexibility of the gusset angles. When the brace is in tension, the connection stiffness is dependent on the bending stiffness of the column-to-gusset angle legs. In contrast, when the brace is in compression, the angles bear directly on the column face.

Elastic brace stiffness was also predicted using the simplified procedure described in Chapter 3 for a typical damper. The overall length of the tube centerline was used for computing the brace stiffness as illustrated in Figs. 5.49. Brace stiffness was determined by computing the elastic deformation to a unit damper force and included the varying cross sectional areas along the damper length. The path considered for the deformation calculation included the tube above the channels (Fig. 5.49 section 1), combined tube and channels (section 2), channels (section 3), and tube (sections 4, 5, 6, and 7). Computed brace stiffness using this method was 3002 kips/in for the first story and 3565 kips/in for the upper stories. This simplified procedure reasonably predicted the experimentally measured brace stiffness. It should be noted that the connections used to connect the VE-dampers to the frame were stiff and no significant reduction in damper stiffness resulted from connection flexibility. If connections are used which are not stiff, the simplified method would over-predict brace

stiffness. A more conservative brace stiffness can be determined by using the centerline dimensions for the bay length and story height. Using bay and story height centerline dimensions, predicted brace stiffness was 2569 kips/in for the first story and 2817 kips/in for the upper stories.

Measured added component loss factor η_a and stiffness K'_a were compared with calculated values (Eqs. 5.3 and 5.4) using the measured brace stiffness, in-phase stiffness K'_d, and loss factor η_d. As shown in Figs. 5.50 and 5.51, computed added component loss factor and stiffness compared well with measured values.

5.3.4 Bending Behavior of VE-Dampers

Previous experimental work has used reduced scale models for the structure and dampers. Brace details and connections for these models may not adequately reflect actual brace stiffness and connection conditions. The tests conducted as part of this study were able to identify some of the implications of realistic size dampers, frame members, and connections on actual damper and frame performance. Two such findings were in-plane and out-of-plane bending of the brace.

A damper rigidly connected to a gusset plate results in bending of the damper as the frame undergoes lateral displacement, due to rotation of the connections. To quantify the amount of in-plane bending moment in the dampers, additional strain gages were placed on the tube face

at uniform spacing as shown in Fig. 5.52. The additional gages permitted calculation of the moment gradient in the damper.

The in-plane bending moment was significant as shown in Figs. 5.53 for the first and second story dampers respectively. Moment diagrams for the first and second story dampers, at peak frame displacement, are shown in Fig. 5.54. The damper moments were largest at the base of the brace. In-plane bending moment in the first story dampers was less than that of the dampers in the upper stories. Ends of the first story dampers are welded to a beam which does not exhibit midspan rotation due to frame sway, resulting in reduced damper bending. Measured damper moments were out-of-phase with the damper axial force and in-phase with the deformation of the structure as shown in Fig. 5.55, indicating the bending is caused by beam bending, connection rotations, and end translations due to frame sway.

The observed in-plane bending is of practical significance to damper design. VE-dampers are typically designed for shear deformation in the VE-material. Bending of the damper would introduce tensile and compressive stresses perpendicular to the pads of VE-material. This could potentially affect damper performance from both a low and high cycle fatigue perspective by initiating or propagating cracks at the edges of the VE-pads. Damper designs, like that used for the tested VE-dampers, should provide guide bolts which minimize through thickness direction stresses on the VE-material due to brace bending.

Misalignment of the damper ends could result in out-of-plane bending of the dampers. The test structure exhibited negligible out-of-plane bending (approximately 2% of in-plane

moment) as shown in Fig. 5.56. While minimal out-of-plane bending was observed, guide bolts should be provided in damper designs to minimize through thickness direction stresses on the VE-material from out-of-plane bending due to possible misalignments.

5.4 Relaxation Tests

In addition to sinusoidal tests, relaxation tests were performed to determine the proportion of frame stiffness provided by the VE-dampers at large time intervals and to isolate the interaction between the damper force and connection stresses. Relaxation tests were conducted by specifying a top story actuator displacement as a single step and holding the displacement fixed as shown in Fig. 5.57. When the structure is displaced quickly, the VE-dampers pick-up force, as the displacement is held constant, the damper force decays as shown in Fig. 5.58. Overall force and displacement responses to a 1 in. step displacement are shown in Fig. 5.57 for the first six seconds after application of the displacement, Fig. 5.59 for a relaxation time of one minute, Fig. 5.60 for a relaxation time of five minutes, and Fig. 5.61 for a relaxation time of 17 hours. As shown in these figures, the majority of the frame stiffness was contributed by the dampers just after application of the step displacement. The frame stiffness at peak lateral force was 149.8 kips/in. As time increased, the damper forces decreased due to relaxation of the VE-material and the overall frame stiffness reduced. The frame stiffness reduced to 34.9 kips/in after 6.8 seconds, 27.7 kips/in after one minute, 25.9 kips/in after 5 minutes, and 23.1 kips/in after 17 hours. While the VE-frame exhibited significant stiffness reduction due to damper relaxation, the VE-frame remained stiffer than

the unbraced frame. Even at very large relaxation time the dampers still contributed to lateral frame stiffness. The unbraced frame exhibited a stiffness of 17.9 kips/in for a 1.0 in. top displacement. Even after a relaxation time of 17 hours, the VE-frame was 1.3 times stiffer than the unbraced frame. This would indicate VE-dampers contribute stiffness to the structure even for lower frequency forces, such as wind, and static forces.

The influence of damper forces on individual frame member forces has been shown in section 5.3. Similar interactions between damper forces and member forces were found from relaxation tests.

Effects of damper force on connection stresses were determined from the relaxation tests. In particular, stresses in the gusset plate perpendicular to the beam flange, beam web angles, and top seat angle were examined. Of primary interest was determination of the magnitude of stress at the weld attaching the gusset plates to the beam bottom flanges. This weld experienced fatigue cracking during unbraced frame tests as described in Chapter 4. Addition of the dampers was thought to reduce demand on the weld because the damper induced stresses act in opposition to the beam bending induced stresses as illustrated in Fig. 5.62. Typical recorded stresses at the gusset connection during the relaxation tests are shown in Fig. 5.63. As shown in this figure, stresses in the gusset plate increased as the damper forces decayed. Predicted stress at the gusset-to-beam weld was 10 ksi/in of frame displacement when no damper force is present. Actual magnitude of stress in the gusset plate depends on the phase relationship between damper induced stresses and beam bending induced stresses. Beam bending induced stresses are in-phase and damper induced stresses are out-of-phase

with frame displacement. The degree of phase lag depends on the particular loading frequency and VE-material temperature. In general, larger damper forces reduced the magnitude of stress at the weld. The largest measured stress in the gusset plate was 38.6 ksi. This value was above the nominal yield stress of the gusset plate (36 ksi) and occurred for the top displacement of 4 in. and an initial damper temperature of 32 °C. The large measured stresses are confirmed by observed flaking of the white wash in the gusset plate as shown in Fig. 5.64. Additionally, there is a large stress range due to load reversals which can contribute to crack growth from the lack of fusion line along the gusset plate and beam bottom flange weld root.

Damper forces also influenced stresses in the top seat and beam web connection angles. The beam-column connection must carry both the beam axial force due to damper forces and beam bending moments and shears due to frame sway. Fig. 5.65 shows the interaction of these two forces on the beam web connection angle. Just after displacement of the frame, the connection angles are in tension due to the large damper induced beam axial force. As the damper forces decay, beam axial forces reduce and beam bending induced stresses dominate the connection response. Top seat angles also demonstrated this interaction between beam axial force and beam bending. As shown in Fig. 5.66, demand on the top seat angle increased as damper force decreased.

In general, measured stresses on the beam shear angles were relatively small. Maximum stress measured in the shear angle was only 5.9 ksi. Maximum stress measured in the top seat angle was 23.2 ksi for a peak top displacement of 4 in. and an initial damper temperature of

32 °C. Larger damper forces result in larger beam axial forces and reduce the demand on the top seat angles. This is because beam axial forces act in opposition to the connection stress from beam bending as illustrated in Fig. 5.62.

5.5 Analytical Correlation of Sinusoidal VE-Frame Tests

This section presents analytical correlation of the experimental sinusoidal response for the VE-damped frame. Analytical methods included both time history and simplified analysis procedures. Time history analyses were conducted using three approaches to model the effect of the VE-dampers: a global Rayleigh damping model, a local Rayleigh damping model, and a fractional derivative model. Simplified analyses methods included static analysis and a hand calculation portal method. Both of the simplified analysis methods incorporated corrections for prediction of peak member force due to damper induced out-of-phase response. Corrections for peak member forces were also required for the global Rayleigh damping method.

Five different sinusoidal tests were used for correlative analyses. The selected test parameters included a full range of initial damper temperatures, loading rates, and displacement amplitudes as shown in Table 5.5. Analyses results, including global frame response, peak member forces for all members, and time history response of selected members, were compared with experimental results.

To permit direct comparison of all the analysis methods, experimental frame response was numerically adjusted to remove P-Δ effects from the measured third story actuator forces. This was done because several of the analysis methods neglect second order P-Δ effects.

5.5.1 Global Rayleigh Damping Model

The global Rayleigh damping model (GRD) is a practical analysis procedure currently being applied to the analysis of VE-frames (Chang *et al.*, 1991). The amount of global damping is based on the modal strain energy method (MSE), originally developed in the aerospace/mechanical engineering field. The GRD approximates the VE-damper as a member having in-phase stiffness only, and the damping provided by the VE-dampers is applied to the entire structure as equivalent viscous damping as illustrated in Fig. 5.67a.

The VE-frame analytical model consisted of the unbraced frame model developed in Chapter 4 and elastic truss elements to simulate the added components. In-phase stiffness of the added components for analysis was determined by applying Eqs. 5.3 and 5.4. The damper loss factor η_d and stiffness K'_d were determined from experimental force-deformation response for the six VE-dampers in the frame as shown in Table 5.6. Average properties for two dampers within a story level were used for analysis purposes.

Equivalent viscous damping ξ_{tot} for the VE-frame was calculated using an energy approach and static analysis [Kasai *et al.*, 1994][Sause *et al.*, 1994] as follows:

$$\xi_{tot} = \frac{\sum \eta_a \cdot F_a \cdot u_a}{2\sum F \cdot u} + \xi_o \qquad [5.6]$$

where $\sum F \cdot u$ is the total work done by external lateral forces, $\sum \eta_a \cdot F_a \cdot u_a$ is the total energy dissipated by the VE-dampers, and ξ_o is the unbraced frame damping ratio (2%). When performing the static analysis for computation of ξ_{tot}, P-Δ effects were neglected and a single external force applied at the third story level was used load the model. Computed ξ_{tot} values for the correlation tests are summarized in Table 5.7.

Equivalent viscous damping ratios were used to determine a proportional damping matrix **c** for dynamic analyses [Clough and Penzein, 1993]:

$$\mathbf{c} = a_0\mathbf{m} + a_1\mathbf{k} \qquad [5.7]$$

where **m** is the mass matrix, **k** is the stiffness matrix, a_0 is a mass proportional damping coefficient, and a_1 is a stiffness proportional damping coefficient. Mass proportional damping factors were not used because the test structure had no consequential mass. The stiffness proportional damping factor a_1 was computed using the particular test forcing frequency ω (rad/sec) and computed damping ratio from Eq. 5.6 [Clough and Penzein, 1993]:

$$a_1 = \frac{2\xi_{tot}}{\omega} \qquad [5.8]$$

where ω is the excitation frequency instead of the natural frequency. Dynamic time history analysis of the VE-frame analytical model was performed using a general purpose computer program, PC-ANSR [Maison, 1992], and applying the experimentally measured displacement

history at the third story level. Element forces and nodal displacements were stored after each time step for comparison with experimental responses.

Analytically predicted overall frame response are shown in Figs. 5.68b to 5.72b. Analytically predicted peak frame member forces are shown in Table 5.8 for all five test cases considered. Predicted peak member forces are illustrated in Figs. 5.73, 5.74, and 5.75 for three cases: small frame displacement at 16 °C and 32 °C, and large frame displacements at 28 °C. Analytically determined time history for the eastern column axial force and bending moment just above the second story is shown in Fig. 5.76 for 0.5 hz loading frequency, top displacement of 0.5 in., and 32 °C initial damper temperature case.

In general, the models reasonably predicted overall frame stiffness. This was observed for all analysis methods considered. Some under-estimation of the column base moment was caused by the connection flexibilities developed from individual column and unbraced frame tests. The analytical model employed column base connection stiffnesses (kip-in/rad) which were tailored to describe moment-rotation behavior from the individual column and unbraced frame tests (Chapter 4). The column base connection stiffness was observed to be dependent on column axial force. Peak column axial forces in the individual column and unbraced frame tests were lower than those of the VE-frame tests. Because the analytical connection model was tailored for smaller axial force levels, they were softer than the actual connection stiffness of the experiment resulting in some under-estimation of frame stiffness and column moments particularly near the foundation.

Analyses results, before correction, indicate the VE-frame response over the frequency, amplitude, and temperature range was not reasonably predicted by the GRD method. Overall frame stiffness was reasonably predicted, however the GRD method assumes all forces are in-phase with displacement and thus out-of-phase response are not included. Local member forces which are in-phase with displacement (bending moments and shear forces) were well predicted. Axial member forces (Fig. 5.41a), which are significantly affected by the out-of-phase VE-damper forces, were seriously underestimated. Individual VE-damper response was also not well predicted for this same reason.

To account for the out-of-phase response, GRD member forces required modification to predict actual peak forces in the VE-system. This was accomplished by adding a viscous force component to the in-phase member forces computed from the analysis as described in section 5.5.4. Corrected GRD member forces are shown in Table 5.8 and figures already show the corrected axial forces. The GRD, with correction for time-lagged peak member response, can reasonably predict member forces.

The GRD method did not include VE-damper temperature rise effects. As a result, the GRD method would tend to over-estimate frame stiffness at later cycles when significant temperature rise occurs in the dampers.

5.5.2 Local Rayleigh Damping Model

Some dynamic analysis programs, such as PC-ANSR, permit stiffness proportional equivalent viscous damping to be applied at the element level. The local Rayleigh damping model (LRD) utilizes this feature to approximate both in-phase and out-of-phase stiffness of the VE-damper as illustrated in Fig. 5.67b.

The VE-frame analytical model consisted of the unbraced frame model developed in Chapter 4 and elastic truss elements to simulate the added components. In-phase stiffness of the added components was determined by the procedure described for the GRD method. Out-of-phase stiffness as well as high local damping of the added component are approximated by applying element level stiffness proportional damping to the truss element. The damping coefficient for the truss element was chosen proportional to the added component stiffness and estimated as:

$$\mathbf{c} = \frac{\eta_a K'_a}{\omega} \qquad [5.9]$$

where ω is the forcing frequency (rad/sec). Considering each brace individually $\mathbf{k}=K'_a$, neglecting the mass contribution $\mathbf{m}=0$, and substituting Eq. 5.9 into Eq. 5.7 provides the stiffness proportional damping coefficient for the truss element:

$$a_1 = \frac{\eta_a}{\omega} \qquad [5.10]$$

Stiffness proportional damping factors a_1 were computed for the experimental added component loss factors and forcing frequencies ω (rad/sec). Dynamic time history analysis of the VE-frame analytical model was performed using PC-ANSR and applying the

experimentally measured displacement history at the third story level. Element forces and nodal displacements were stored after each time step for comparison with experimental response.

Analytically predicted overall frame response are shown in Figs. 5.68c to 5.72c. Analytically predicted peak frame member forces are shown in Table 5.8 for all five test cases considered. Predicted peak member forces are illustrated in Figs. 5.73, 5.74, and 5.75 for three cases: small frame displacement at 16 °C and 32 °C, and large frame displacements at 28 °C. Analytically determined time history for the eastern column axial force and bending moment just above the second story is shown in Fig. 5.77 for 0.5 hz loading frequency, top displacement of 0.5 in., and 32 °C initial damper temperature case.

The LRD analyses results indicate the method reasonably predicts the VE-frame response over the frequency, amplitude, and temperature range considered. Overall frame stiffness was well predicted while overall damping was slightly under-estimated. Local member forces, including time lagged response for peak axial forces in the beams and columns, were reasonably predicted by the method.

The LRD method did not include VE-damper temperature rise effects. As a result, LRD method tends to over-estimate frame stiffness at later cycles when significant temperature rise occurs in the dampers as shown in Figs. 5.71 and 5.72.

5.5.3 Fractional Derivative Model

An analytical finite element which models VE-damper behavior has been developed which employs a fractional derivative model (FDM) for the stress-strain relationship [Kasai *et al.*, 1994]. The material constitutive rule simulates the nonlinear cyclic behavior for a VE-damper, including temperature and excitation frequency effects, as described in Chapter 3. Linear aspects of the model are illustrated in Fig. 5.67c.

The VE-frame analytical model consisted of the unbraced frame model developed in Chapter 4 and viscoelastic damper elements in each story to simulate the VE-dampers. Parameters for the VE-element were determined from individual VE-damper experiments described in Chapter 3 and Appendix A. Dynamic time history analysis of the VE-frame analytical model was performed using PC-ANSR and applying the experimentally measured displacement history at the third story level. Element forces and nodal displacements were stored after each time step for comparison with experimental response.

Analytically predicted overall frame response are shown in Figs. 5.68d to 5.72d. Analytically predicted peak frame member forces are shown in Table 5.8 for all five test cases considered. Predicted peak member forces are illustrated in Figs. 5.73, 5.74, and 5.75 for three cases: small frame displacement at 16 °C and 32 °C, and large frame displacements at 28 °C. Analytically determined time history for the eastern column axial force and bending moment just above the second story is shown in Fig. 5.76 for 0.5 hz loading frequency, top displacement of 0.5 in., and 32 °C initial damper temperature case. Example measured and

predicted individual damper response is shown in Figs. 5.77a and 5.77b. Example measured and predicted damper temperature rise is shown in Fig. 5.78.

The FDM analyses results indicate the method is capable of predicting the VE-frame response over the frequency, amplitude, and temperature range considered. The model reasonably predicted overall frame stiffness and damping as well as local member forces including time lagged response for peak axial forces in the beams and columns. Individual force-deformation response for a typical VE-damper as shown in Fig. 5.77b, was also reasonably predicted by the method.

An additional advantage with the FDM is the ability to predict VE-damper temperature rise and resulting VE-material property changes in stiffness and damping. This capability enabled the FDM to predict structural response at later cycles when temperature dependent changes become significant.

5.5.4 Static Analysis Method with Correction for Time-Lagged Response

An elastic static analysis method was used to predict frame stiffness, damping ratio, and peak member forces. The static analysis method assumes all forces are in-phase (i.e. no time lag) with displacement, and thus require modification to predict actual peak forces in the VE-system. This is accomplished by adding a viscous force component to the member forces computed from analysis.

The VE-frame analytical model consisted of the unbraced frame model developed in Chapter 4 and linear elastic truss elements to simulate the added components. Using the experimental results, added component stiffnesses were calculated according to Eq. 5.3 as summarized in Table 5.6. Static analysis was performed on the model with a specified top force equal to the experimental force obtained at maximum displacement on the second sinusoidal cycle.

The obtained member forces from static analysis included: the added component axial forces P'_a, moment, shear, and axial forces of each column; M'_{col}, V'_{col}, and P'_{col} respectively, as well as moment, shear, and axial forces of each beam; M'_{beam}, V'_{beam}, and P'_{beam} respectively. Peak forces were determined by modifying the forces from static analysis to include the viscous force contribution as [Kasai and Fu, 1995]:

$$P_{a_{max}} = P'_a\sqrt{1+\eta_a{}^2} \qquad [5.11]$$

$$M_{col_{max}} = M'_{col} \qquad [5.12]$$

$$V_{col_{max}} = V'_{col} \qquad [5.13]$$

$$P_{col_{max}} = P'_{col}\sqrt{1+\eta_{p,col}{}^2} \qquad [5.14]$$

$$M_{beam_{max}} = M'_{beam} \qquad [5.15]$$

$$V_{beam_{max}} = V'_{beam} \qquad [5.16]$$

where $\tan^{-1}\eta_{p,col}$ is the lag angle of the column axial force with respect to the frame displacement. An approximate expression for $\eta_{p,col}$ is [Kasai and Fu, 1995]:

$$\eta_{p,col} = \frac{\eta_a\left[1-\frac{h}{L}\frac{V'_{col}}{P'_{col}}\right]}{\left(1+K_f/K'_a\right)} \qquad [5.17]$$

where K_f = shear drift stiffness of the frame without dampers, and h and L = height and span length at the corresponding story level of the VE-damped bay. Additionally, the peak beam axial force can be determined:

$$P_{beam_{max}} = P'_{beam}\sqrt{1+\eta_a{}^2} \qquad [5.18]$$

As shown in Eqs. 5.11 to 5.18, only member axial forces and added component forces must be corrected for viscous force contributions. Bending moments and shear forces are considered in-phase with frame lateral displacements and do not require correction.

Analytically predicted member forces, corrected for peak response, for all frame members are shown in Tables 5.8. As shown in these tables, the static analysis method with correction for time lagged response reasonably predicted peak member forces for the test cases considered.

5.5.5 Portal Analysis Method with Correction for Time-Lagged Response

The final method considered is a portal method modified for time-lagged peak member response. Unlike the previous methods, it does not require knowledge of the specific member sizes and is appropriate for preliminary design of VE-frames [Kasai and Fu, 1995].

This method uses the unbraced frame and VE-frame stiffness ratio as well as experimental points of inflection in columns to predict member force distributions. For a given in-phase lateral force, set equal to the experimental force at maximum displacement, a free-body diagram for the structure is drawn as shown in Fig. 5.79. Actual inflection point locations

from column strain measurements were determined and used to compute moment equilibrium of the free-body. The horizontal component of the in-phase added components V_a' can be determined [Kasai and Fu, 1995]:

$$V_a' = \frac{V_{story}'}{\left(1 + \frac{K_f}{K_a'}\right)} \qquad [5.19]$$

where K_f is the shear drift stiffness of the frame without dampers and V_{story}' is the in-phase lateral force. The shear force in each column V_{col}' can be computed:

$$V_{col}' = \frac{V_{story}' - V_a'}{2} \qquad [5.20]$$

Column axial forces P_{col}' are calculated from moment equilibrium equations at each inflection point. Column moments M_{col}' are determined from column shear forces and appropriate lever arms. After determination of column moments, beam moments M_{beam}' are determined from moment equilibrium at joints. Shear forces in the beams V_{beam}' are determined from the beam moments. Beam axial forces P_{beam}' are equal to the horizontal component of the added components which are connected to the beam. All member forces obtained through the above procedure are in-phase components and must be modified by adding the out-of-phase (i.e. viscous) component using Eqs. 5.11 to 5.18.

Predicted member forces, corrected for peak response, for all frame members are shown in Table 5.8. Considering the simplicity of the portal method with correction for time lagged response, peak member forces for the test cases considered were reasonably predicted as shown in the tables.

Actual measured inflection points were used to compute force distribution in the structure. This was done to permit direct comparison with the other analysis methods. For practical preliminary design and analysis of VE-frames, inflection points would be assumed at midheight of the columns. This assumption would appear be adequate for most buildings which do not have the boundary effects of the test structure.

5.5.6 Discussion of Measured Loss Factors for Frame VE-dampers

The analysis methods described were implemented using experimentally measured damper stiffness and loss factors for the six frame VE-dampers. Damper stiffness measured for the frame dampers was similar to that determined from the individual damper tests and manufacturer's data described in Chapter 3. However, loss factors measured for the frame damper were typically much smaller than those from the individual damper. The smaller loss factors measured in the frame VE-dampers was caused by imperfect sinusoidal displacement history imposed on the test structure as shown in Fig. 5.80. This imperfect sinusoidal displacement resulted in distorted velocities which directly influence the damper forces, particularly as the structure passed through zero displacement.

This was further verified by performing analysis of the VE-frame with an ideal sinusoidal displacement history at the third story. Analysis of the VE-frame was conducted using the fractional derivative model described in section 5.5.3 and model parameters determined from the individual damper tests (Chapter 3 and Appendix A) with a perfect sinusoidal

displacement amplitude of 2 in. and frequency of 0.5 hz. The initial damper temperature was 24 °C. Analytically predicted global force-deformation response for the VE-frame is shown in Fig. 5.81. The analysis exhibited much fuller hysteresis than the experimental response (Fig. 5.71a) while the analytical frame stiffness was similar to the measured stiffness.

Individual damper responses from the ideal sinusoidal analysis were used to compute damper stiffness K'_d and loss factors η_d for dampers in each story. The ideal sinusoidal damper stiffness and loss factors were compared with those measured from the individual damper experiment described in Chapter 3, and those measured from the frame experiment as shown in Table 5.8. As seen in this table, the perfect sinusoidal displacement input produced similar loss factors to those of the individual damper tests and larger than the measured values from the VE-frame tests. Stiffness values were comparable between the analysis and experiments.

Additionally, VE-properties were computed assuming perfect elliptical force-deformation behavior. Actual measured VE-damper force-deformation response was not truly elliptical and error in estimating stiffness and loss factors based on the geometrical relationships (Chapter 3) may result from this source. This is particularly true for loss factors which are quite sensitive to the peak force and force at zero displacement values used.

It is valuable to note that the fractional derivative model was able to accurately capture the VE-damper behavior even with the imperfect sinusoidal displacement history.

5.6 Conclusions

Results of the sinusoidal and relaxation tests and correlative analyses are summarized below:

- Sinusoidal and relaxation tests provided detailed comprehensive data for global frame response as well as local member forces and connection response.
- The overall VE-frame response exhibited frequency and temperature dependent behavior typical of VE-materials.
- Higher temperatures and lower frequencies resulted in lower VE-frame stiffness. Equivalent viscous damping was more complex and depending on initial damper temperature and frequency would increase or decrease.
- The VE-frame exhibited fairly stable damping ratio through the range of initial temperatures investigated (16 to 32 °C) for the 0.5 hz loading frequency. This frequency is the natural frequency of the seismic prototype frame used as the basis for design of the test specimen as presented in Chapter 6.
- The VE-frame also exhibited fairly stable damping ratio through the range of loading frequencies investigated for the initial damper temperature of 24 °C.
- Inflection points in the beams were located at midspan. Column inflection points varied depending on story level. Due to boundary effects, the inflection point in the third story column was below midheight, and the first story column inflection point was above midheight. Only the second story column exhibited inflection points at midheight.

- Bending moments and shear forces for frame members were typically in-phase with frame displacements. Axial forces in the beams and columns had significant out-of-phase components due to VE-damper forces.
- The phase lag between moment and axial force in the beams and columns results in peak forces occurring at different instances of time. As a result, determining the critical design load combination can be difficult. A proposed simplification would conservatively design members assuming the peaks occur simultaneously.
- Elastic brace stiffness was measured and could be reasonably predicted using the simplified method presented in Chapter 3. Accuracy of Eqs. 5.3 and 5.4 for computing the stiffness and loss factor of the added components were verified by experimental measurements. Added component stiffness was not sensitive to the brace stiffness but the added component loss factor was sensitive to the brace stiffness.
- In-plane bending of the added components was measured. Bending was induced by frame drift and connection rotation and is out-of-phase with damper force. Guide bolts provided in the damper design limited through-thickness direction stresses in the VE-material and no apparent adverse effect on damper performance was noted. Brace bending should be considered in design of VE-dampers to limit through-thickness direction stresses on the VE-material.
- Negligible out-of-plane bending of the added components was observed. Accidental out-of-plane brace bending due to misalignment should be considered in design of VE-dampers to limit through-thickness direction stresses on the VE-material by providing guide bolts.

- The VE-dampers contribute to frame stiffness even after very long relaxation times. This indicates the dampers can provide some level of stiffness for slowly applied loads such as wind and gravity forces.
- Significant secondary stresses were measured at the interface between the gusset plate and beam lower flange. The peak measured stress at the weld between the gusset plate and beam flange was 38.6 ksi. Damper forces tended to reduce the demand on the gusset plate and beam flange weld.
- Results of the analytical correlations indicated all methods (some only after correction) were reasonably able to predict the frame response and member forces.
- The GRD method tended to slightly over-predict the equivalent viscous damping of the VE-frame.
- The GRD, static, and portal methods assume all member forces are in-phase with displacement and required corrections to predict peak member forces.
- The LRD and FDM were able to model out-of-phase damper forces directly.
- The FDM had the added advantage of being able to capture the temperature rise effect in the dampers.
- The portal method with correction for peak member force provides an excellent means for preliminary design and analysis of VE-frames considering the simplicity and reasonable results.
- Loss factors determined from the sinusoidal frame tests were lower than those determined from individual damper tests described in Chapter 3. This resulted from imperfect sinusoidal frame displacements imposed by the hydraulic actuators. When an ideal

sinusoidal displacement history is used, the analytically predicted loss factors are similar to those of the individual damper tests and published by the manufacturer.

Loading Frequency (hz)	Data Acquisition Sampling Frequency (hz)	Time Between Samples (sec)	Time Between Channels (μsec)
0.1	33	0.0303	155
0.5	165	0.0061	31
1.0	331	0.0030	15
2.0	399	0.0025	13

Table 5.1 - Data acquisition sampling rates.

Frequency (hz)	16℃ Amplitude (in)	20℃ Amplitude (in)	24℃ Amplitude (in)	28℃ Amplitude (in)	32℃ Amplitude (in)	Summary
0.1	0.25	0.25	0.25	0.25	0.25	5
	-	0.50	0.50	-	-	2
	1.00	1.00	1.00	1.00	1.00	5
	-	2.00	2.00	2.00	2.00	4
	-	3.00	3.00	3.00	3.00	4
	-	-	-	4.00	4.00	2
					Frequency Total=	22
0.5	0.25	0.25	0.25	0.25	0.25	5
	0.50	0.50	0.50	0.50	0.50	5
	-	1.00	1.00	1.00	1.00	4
	-	-	2.00	2.00	2.00	3
	-	-	-	3.00	3.00	2
					Frequency Total=	19
1.0	0.25	0.25	0.25	0.25	0.25	5
	0.50	0.50	0.50	0.50	0.50	5
	-	1.00	1.00	1.00	1.00	4
	-	-	-	2.00	2.00	2
	-	-	-	-	3.00	1
					Frequency Total=	17
2.0	0.25	0.25	0.25	0.25	0.25	5
	-	0.50	0.50	0.50	0.50	4
	-	-	-	1.00	1.00	2
					Frequency Total=	11
Temp. Totals=	7	13	14	17	18	
					Grand Total=	69

Table 5.2 - Equivalent viscous damping ratios for unbraced frame.

Initial VE-Temp. (°C)	Loading Freq. (hz)	Nominal Top Disp. (in)	K' (kip/in)	K" (kip/in)	|K*| (kip/in)	η	Equiv. Viscous Damping Ratio (%)
16	0.1	0.25	100.9	64.5	119.8	0.64	27.1%
16	0.1	1.00	92.1	61.3	110.6	0.67	28.1%
16	0.5	0.25	191.9	85.6	210.1	0.45	20.8%
16	0.5	0.50	182.1	84.8	200.9	0.47	21.3%
16	1.0	0.25	230.6	76.9	243.1	0.33	16.8%
16	1.0	0.50	221.1	74.9	233.4	0.34	16.9%
16	2.0	0.25	253.7	71.2	263.4	0.28	13.0%

Table 5.3a - VE-frame properties for 16 °C sinusoidal tests.

Initial VE-Temp. (°C)	Loading Freq. (hz)	Nominal Top Disp. (in)	K' (kip/in)	K" (kip/in)	|K*| (kip/in)	η	Equiv. Viscous Damping Ratio (%)
20	0.1	0.25	65.5	42.5	78.1	0.65	26.8%
20	0.1	0.50	67.6	44.1	80.7	0.65	27.3%
20	0.1	1.00	63.2	40.8	75.2	0.65	26.8%
20	0.1	2.00	61.2	39.9	73.1	0.65	27.1%
20	0.1	3.00	57.6	37.2	68.6	0.65	27.0%
20	0.5	0.25	130.8	75.8	151.2	0.58	25.0%
20	0.5	0.50	131.1	77.4	152.3	0.59	25.7%
20	0.5	1.00	123.8	76.2	145.4	0.62	26.1%
20	0.5	2.00					
20	1.0	0.25	175.8	83.4	194.6	0.47	22.1%
20	1.0	0.50	166.3	90.1	189.1	0.54	22.7%
20	1.0	1.00	159.7	83.1	180.0	0.52	21.8%
20	2.0	0.25	203.0	81.6	218.8	0.40	18.5%
20	2.0	0.25	197.8	80.6	213.5	0.41	19.1%

Table 5.3b - VE-frame properties for 20 °C sinusoidal tests.

Initial VE Temp. (°C)	Loading Freq. (hz)	Nominal Top Disp. (in)	K' (kip/in)	K" (kip/in)	|K*| (kip/in)	η	Equiv. Viscous Damping Ratio (%)
24	0.1	0.25	51.8	30.7	60.2	0.59	25.2%
24	0.1	0.50	52.5	29.1	60.0	0.55	24.8%
24	0.1	1.00	52.0	30.0	60.1	0.58	25.1%
24	0.1	2.00	50.6	29.4	58.6	0.58	25.3%
24	0.1	3.00	47.9	28.4	55.7	0.59	25.1%
24	0.5	0.25	95.0	60.8	112.8	0.64	27.7%
24	0.5	0.50	94.1	63.2	113.3	0.67	28.0%
24	0.5	1.00	90.1	60.8	108.7	0.67	28.0%
24	0.5	2.00	86.1	57.5	103.6	0.67	27.3%
24	1.0	0.25	129.1	78.9	151.3	0.61	26.2%
24	1.0	0.50	127.4	78.4	149.6	0.62	26.4%
24	1.0	1.00	124.9	75.0	145.7	0.60	25.4%
24	2.0	0.25	166.2	84.5	186.4	0.51	23.1%
24	2.0	0.50	162.2	81.2	181.4	0.50	22.2%

Table 5.3c - VE-frame properties for 24 °C sinusoidal tests.

Initial VE Temp. (°C)	Loading Freq. (hz)	Nominal Top Disp. (in)	K' (kip/in)	K'' (kip/in)	|K*| (kip/in)	η	Equiv. Viscous Damping Ratio (%)
28	0.1	0.25	42.4	21.1	47.3	0.50	22.3%
28	0.1	1.00	41.6	19.0	45.7	0.46	21.1%
28	0.1	2.00	40.5	18.9	44.7	0.47	21.3%
28	0.1	3.00	39.9	19.2	44.3	0.48	21.8%
28	0.1	4.00	38.5	18.4	42.7	0.48	21.6%
28	0.5	0.25	67.6	43.9	80.6	0.65	28.1%
28	0.5	0.50	67.2	43.1	79.8	0.64	27.4%
28	0.5	1.00	66.9	44.8	80.5	0.67	27.8%
28	0.5	2.00	66.0	42.3	78.4	0.64	27.2%
28	0.5	3.00	***	***	***	***	***
28	1.0	0.25	91.6	63.0	111.2	0.69	28.6%
28	1.0	0.50	88.9	60.5	107.6	0.68	28.4%
28	1.0	1.00	90.6	60.9	109.1	0.67	27.9%
28	1.0	2.00	***	***	***	***	***
28	2.0	0.25	119.7	79.1	143.5	0.66	27.4%
28	2.0	0.50	117.3	74.9	139.2	0.64	26.4%
28	2.0	1.00	114.9	67.8	133.4	0.59	24.4%

*** Poor actuator control.

Table 5.3d -VE-frame properties for 28 °C sinusoidal tests.

Initial VE Temp. (°C)	Loading Freq. (hz)	Nominal Top Disp. (in)	K' (kip/in)	K" (kip/in)	|K*| (kip/in)	η	Equiv. Viscous Damping Ratio (%)
32	0.1	0.25	37.1	14.7	39.9	0.40	18.1%
32	0.1	1.00	36.2	13.3	38.6	0.37	17.5%
32	0.1	2.00	35.4	13.4	37.8	0.38	17.8%
32	0.1	3.00	34.1	13.0	36.5	0.38	17.9%
32	0.1	4.00	33.2	13.4	35.8	0.40	18.7%
32	0.5	0.25	51.8	31.2	60.5	0.60	26.0%
32	0.5	0.50	52.9	31.4	61.5	0.59	25.6%
32	0.5	1.00	52.1	31.3	60.8	0.60	25.8%
32	0.5	2.00	50.4	29.8	58.5	0.59	25.4%
32	0.5	3.00	***	***	***	***	***
32	1.0	0.25	66.5	45.2	80.4	0.68	28.7%
32	1.0	0.50	66.6	44.9	80.3	0.67	28.4%
32	1.0	1.00	65.4	43.3	78.4	0.66	27.9%
32	1.0	2.00	***	***	***	***	***
32	1.0	3.00	***	***	***	***	***
32	2.0	0.25	81.8	61.2	102.2	0.75	29.9%
32	2.0	0.50	82.5	59.5	101.7	0.72	28.7%
32	2.0	1.00	85.1	49.8	98.6	0.59	26.2%

*** Poor actuator control.

Table 5.3e - VE-frame properties for 32 °C sinusoidal tests.

Loading Rate (hz)	Sampling Rate (hz)	Nominal Frame Displacement (in)	Damper Location (Story Level)	Initial Temperature (°C)	Final Temperature (°C)
0.1	33	0.25	1	15.9	15.9
			2	15.9	15.9
			3	16.1	16.1
0.1	33	1	1	16.0	16.5
			2	16.0	16.6
			3	16.0	16.6
0.5	165	0.25	1	16.0	16.1
			2	15.9	16.0
			3	16.0	16.0
0.5	165	0.5	1	16.0	16.1
			2	16.1	16.1
			3	16.0	16.1
1	331	0.25	1	16.0	16.0
			2	16.0	16.0
			3	16.0	16.0
1	331	0.5	1	16.0	16.1
			2	15.9	16.1
			3	15.9	16.1
2	399	0.25	1	16.1	16.1
			2	16.1	16.1
			3	16.0	16.0

Table 5.4a -Measured damper temperature rise for 16 °C sinusoidal tests.

Loading Rate (hz)	Nominal Frame Displacement (in)	Damper Location (Story Level)	Initial Temperature (°C)	Final Temperature (°C)
0.1	0.25	1	20.0	20.0
		2	20.1	20.1
		3	20.0	20.0
0.1	0.5	1	20.0	20.1
		2	19.9	20.0
		3	19.9	20.0
0.1	1	1	20.0	20.4
		2	20.0	20.3
		3	20.1	20.4
0.1	2	1	20.0	21.2
		2	20.0	21.3
		3	19.9	21.4
0.1	3	1	19.9	23.1
		2	19.9	23.2
		3	20.0	23.6
0.5	0.25	1	20.1	20.1
		2	20.1	20.1
		3	20.1	20.1
0.5	0.5	1	20.1	20.2
		2	19.9	20.1
		3	20.1	20.3
0.5	1	1	19.9	20.7
		2	19.9	20.4
		3	19.9	20.7
1	0.25	1	20.0	20.0
		2	20.0	20.0
		3	20.0	20.0
1	0.5	1	20.0	20.1
		2	19.9	20.0
		3	19.9	20.0
1	1	1	20.1	21.3
		2	20.1	20.8
		3	20.0	21.1

Table 5.4b1 - Measured damper temperature rise for 20 °C sinusoidal tests.

Loading Rate (hz)	Nominal Frame Displacement (in)	Damper Location (Story Level)	Initial Temperature (°C)	Final Temperature (°C)
2	0.25	1	20.0	19.9
		2	20.1	20.1
		3	20.1	20.1
2	0.5	1	20.0	20.1
		2	19.9	20.1
		3	19.9	20.1

Table 5.4b2 - Measured damper temperature rise for 20 °C sinusoidal tests.

Loading Rate (hz)	Nominal Frame Displacement (in)	Damper Location (Story Level)	Initial Temperature (°C)	Final Temperature (°C)
0.1	0.25	1	24.1	24.1
		2	24.1	24.1
		3	24.1	24.1
0.1	0.5	1	23.9	24.0
		2	23.9	24.0
		3	24.0	24.1
0.1	1	1	24.1	24.3
		2	24.0	24.2
		3	24.0	24.3
0.1	2	1	24.1	25.3
		2	24.1	25.3
		3	24.0	25.3
0.1	3	1	24.1	26.3
		2	24.1	26.6
		3	24.1	26.7
0.5	0.25	1	24.1	24.2
		2	24.1	24.2
		3	24.1	24.2
0.5	0.5	1	24.1	24.3
		2	24.0	24.2
		3	24.0	24.2
0.5	1	1	24.1	25.0
		2	24.1	24.8
		3	24.1	24.8
0.5	2	1	23.9	26.3
		2	23.9	26.1
		3	23.9	26.2

Table 5.4c1 - Measured damper temperature rise for 24 °C sinusoidal tests.

Loading Rate (hz)	Nominal Frame Displacement (in)	Damper Location (Story Level)	Initial Temperature (°C)	Final Temperature (°C)
1	0.25	1	24.1	24.1
		2	24.1	24.1
		3	24.1	24.1
1	0.5	1	24.1	24.3
		2	24.1	24.1
		3	24.1	24.2
1	1	1	23.9	24.7
		2	23.9	24.6
		3	23.9	24.7
2	0.25	1	24.1	24.2
		2	24.1	24.2
		3	24.0	24.1
2	0.5	1	24.1	24.3
		2	24.0	24.2
		3	24.0	24.2

Table 5.4c2 - Measured damper temperature rise for 24 °C sinusoidal tests.

Loading Rate (hz)	Nominal Frame Displacement (in)	Damper Location (Story Level)	Initial Temperature (°C)	Final Temperature (°C)
0.1	0.25	1	28.1	28.2
		2	28.1	28.1
		3	28.0	28.0
0.1	1.0	1	28.1	28.3
		2	28.0	28.2
		3	27.9	28.1
0.1	2.0	1	28.1	28.8
		2	28.0	28.8
		3	27.9	28.7
0.1	3.0	1	27.9	29.4
		2	27.9	29.7
		3	27.9	29.7
0.1	4.0	1	28.0	31.3
		2	28.0	31.2
		3	28.0	30.9
0.5	0.25	1	28.0	28.0
		2	27.9	27.9
		3	27.9	27.9
0.5	0.5	1	28.1	28.2
		2	28.0	28.1
		3	28.1	28.2
0.5	1.0	1	28.1	28.6
		2	28.1	28.5
		3	28.0	28.6
0.5	2.0	1	27.9	29.6
		2	28.0	29.7
		3	27.9	29.8
0.5	3.0	1	27.9	30.9
		2	27.9	30.8
		3	27.9	31.1

Table 5.4d1 - Measured damper temperature rise for 28 °C sinusoidal tests.

Loading Rate (hz)	Nominal Frame Displacement (in)	Damper Location (Story Level)	Initial Temperature (°C)	Final Temperature (°C)
1	0.25	1	27.9	27.9
		2	28.1	28.1
		3	28.1	28.1
1	0.5	1	28.1	28.3
		2	28.1	28.4
		3	28.1	28.3
1	1.0	1	27.9	28.6
		2	27.9	28.4
		3	27.9	28.5
1	2.0	1	27.9	29.4
		2	27.9	29.2
		3	27.9	29.4
2	0.25	1	28.1	28.2
		2	28.1	28.2
		3	28.0	28.1
	0.5	1	28.1	28.4
		2	28.1	28.3
		3	28.0	28.3
2	1.0	1	28.1	28.6
		2	28.0	28.4
		3	28.1	28.6

Table 5.4d2 - Measured damper temperature rise for 28 °C sinusoidal tests.

Loading Rate (hz)	Nominal Frame Displacement (in)	Damper Location (Story Level)	Initial Temperature (°C)	Final Temperature (°C)
0.1	0.25	1	32.1	32.1
		2	32.0	32.0
		3	31.9	31.9
0.1	1	1	32.1	32.1
		2	32.1	32.2
		3	32.1	32.1
0.1	2	1	31.9	32.4
		2	31.9	32.5
		3	31.9	32.5
0.1	3	1	31.9	33.1
		2	31.9	33.1
		3	31.9	33.1
0.1	4	1	32.0	33.9
		2	31.9	34.0
		3	31.9	34.0
0.5	0.25	1	32.1	32.1
		2	32.0	32.0
		3	31.9	31.9
0.5	0.5	1	31.9	32.1
		2	31.9	32.1
		3	32.0	32.2
0.5	1.0	1	32.0	32.3
		2	31.9	32.3
		3	32.0	32.4
0.5	2.0	1	32.1	33.3
		2	32.0	33.3
		3	32.0	33.4
0.5	3.0	1	32.0	34.3
		2	31.9	34.2
		3	31.9	34.3

Table 5.4e1 - Measured damper temperature rise for 32 °C sinusoidal tests.

Loading Rate (hz)	Nominal Frame Displacement (in)	Damper Location (Story Level)	Initial Temperature (°C)	Final Temperature (°C)
1	0.25	1	32.1	32.2
		2	32.1	32.2
		3	32.1	32.2
1	0.5	1	32.1	32.1
		2	32.0	32.1
		3	31.9	31.9
1	1.0	1	32.0	32.4
		2	32.0	32.4
		3	32.0	32.4
1	2.0	1	31.9	33.1
		2	31.9	33.0
		3	31.9	33.1
1	3.0	1	31.9	33.2
		2	31.9	33.2
		3	31.9	33.2
2	0.25	1	32.0	32.1
		2	32.0	32.1
		3	31.9	31.9
	0.5	1	32.1	32.2
		2	32.1	32.2
		3	32.0	32.1
2	1.0	1	32.1	32.5
		2	32.1	32.4
		3	32.0	32.3

Table 5.4e2 - Measured damper temperature rise for 32 °C sinusoidal tests.

Initial VE Temperature (°C)	Loading Frequency (hz)	Nominal Top Disp. (in)	Equiv. Viscous Damping Ratio (%) **
16	0.5	0.50	23.0%
32	0.5	0.50	29.4%
28	0.1	4.00	23.0%
24	0.5	2.00	30.8%
24	2.0	0.25	26.9%

** Damping ratio computed by neglecting P-Δ effects.

Table 5.5 - Equivalent viscous damping ratios for selected tests used for correlative analyses.

Initial VE-Temp. (°C)	Loading Freq. (hz)	Nominal Top Disp. (in)	Story Level	VE-Strain (%)	K'd (kip/in)	K" (kip/in)	|K*| (kip/in)	η d	Kb (kip/in)	Eq. 5.5 Γ	Eq. 5.3 K'a (kip/in)	Eq. 5.4 η a
16	0.5	0.50	1	10.0%	756.0	870.6	1153.1	1.15	3000	1.27	726.0	0.73
			2	8.3%	851.9	996.1	1310.7	1.17	3500	1.27	825.3	0.74
			3	9.0%	754.5	876.6	1156.6	1.16	3500	1.24	738.0	0.77
32	0.5	0.50	1	15.3%	128.5	135.4	186.7	1.05	3000	1.05	128.6	0.97
			2	16.6%	129.8	138.8	190.1	1.07	3500	1.04	130.1	0.99
			3	16.0%	124.8	132.5	182.0	1.06	3500	1.04	125.0	0.99
28	0.1	4.00	1	121.4%	87.2	80.4	118.6	0.92	3000	1.02	86.7	0.87
			2	133.6%	79.8	73.0	108.2	0.92	3500	1.02	79.5	0.88
			3	129.5%	77.0	70.2	104.2	0.91	3500	1.02	76.6	0.88
24	2.0	0.25	1	5.8%	694.0	757.5	1027.4	1.09	3000	1.22	662.0	0.72
			2	5.2%	731.1	790.8	1076.9	1.08	3500	1.20	702.5	0.74
			3	5.2%	732.6	753.1	1050.7	1.03	3500	1.18	694.6	0.72
24	0.5	2.00	1	56.5%	277.0	328.6	429.7	1.19	3000	1.12	280.9	0.97
			2	56.7%	274.3	322.8	423.6	1.18	3500	1.10	278.0	0.99
			3	57.3%	251.1	295.7	387.9	1.18	3500	1.09	254.5	1.01

Table 5.6 - Measured VE-damper properties for selected tests used for correlative analyses.

Initial VE Temperature (°C)	Loading Frequency (hz)	Nominal Top Disp. (in)	GRD Equiv. Viscous Damping Ratio (%)
16	0.5	0.50	27.2%
32	0.5	0.50	31.1%
24	2.0	0.25	26.9%
24	0.5	2.00	36.1%
28	0.1	4.00	24.0%

Table 5.7 - Computed equivalent viscous damping ratios from Eq. 5.6 for selected tests used for correlative analyses.

Member Force Location	Experiment	GRD	GRD Corrected	LRD	FRD	Static Corrected	Portal
Column Moments (kip-in)							
E Col. 0-1 Base	619	530	530	532	528	568	385
E Col. 0-1 Top	421	277	277	285	257	276	279
E Col. 1-2 Base	188	188	188	180	249	174	256
E Col. 1-2 Top	205	98	98	94	167	101	256
E Col. 2-3 Base	250	273	273	273	258	298	234
E Col. 2-3 Top	363	337	337	333	340	363	333
W Col. 0-1 Base	707	605	605	607	601	646	385
W Col. 0-1 Top	458	302	302	310	279	299	279
W Col. 1-2 Base	167	171	171	164	230	159	256
W Col. 1-2 Top	196	93	93	89	162	98	256
W Col. 2-3 Base	227	277	277	277	262	300	234
W Col. 2-3 Top	356	337	337	333	340	363	333
Beam Moments (kip-in)							
Beam L1 E	510	465	465	461	493	450	535
Beam L1 W	518	472	472	469	496	458	535
Beam L2 E	422	372	372	366	391	399	634
Beam L2 W	420	370	370	365	390	398	634
Beam L3 E	363	331	331	327	334	357	333
Beam L3 W	356	331	331	327	335	357	333
Axial Forces (kips)							
E Col. 0-1	154.0	137.8	162.6	165.3	180.6	175.1	163.5
E Col. 1-2	97.0	89.4	106.4	106.8	116.2	114.8	113.2
E Col. 2-3	42.0	43.1	50.6	52.0	57.2	54.5	47.7
W Col. 0-1	156.0	137.8	162.6	165.4	180.4	175.0	163.5
W Col. 1-2	99.0	89.3	106.4	106.8	116.0	114.7	113.2
W Col. 2-3	45.0	43.1	50.6	52.0	57.0	54.5	47.7
Beam E L1	46.0	37.5	46.7	45.4	49.7	50.1	47.3
Beam W L1	47.0	37.5	46.7	45.4	49.7	51.0	47.3
Beam E L2	41.0	35.1	44.2	43.2	47.9	47.7	48.3
Beam W L2	42.0	35.1	44.2	43.2	47.9	47.4	48.3
Beam E L3	48.0	39.5	49.2	47.0	51.2	53.0	48.5
Beam W L3	47.0	39.5	49.2	47.0	51.2	53.0	48.5
Shear Forces (kips)							
Col. E 0-1	6.0	5.1	5.1	5.2	5.0	5.4	4.3
Col. W 0-1	7.0	5.8	5.8	5.8	5.6	6.0	4.3
Col. E 1-2	2.9	2.1	2.1	2.0	3.0	2.0	3.7
Col. W 1-2	2.8	1.9	1.9	1.8	2.9	1.9	3.7
Col. E 2-3	4.7	4.4	4.4	4.4	4.2	4.8	4.1
Col. W 2-3	4.7	4.5	4.5	4.4	4.3	4.8	4.1
Beam L1	4.4	3.9	3.9	3.8	4.1	3.7	4.5
Beam L2	3.6	3.1	3.1	3.1	3.3	3.3	5.3
Beam L3	3.5	2.8	2.8	2.8	2.8	3.1	2.8

Table 5.8a -Peak member forces from experiment and analyses for sinusoidal test at 16 °C, 0.5 hz with a top frame displacement of 0.5 in.

Member Force Location	Experiment	GRD	GRD Corrected	LRD	FRD	Static Corrected	Portal
Column Moments (kip-in)							
E Col 0-1 Base	670	568	568	580	581	580	461
E Col 0-1 Top	333	259	259	279	273	266	334
E Col 1-2 Base	275	331	331	320	341	336	344
E Col 1-2 Top	285	244	244	240	262	247	344
E Col 2-3 Base	223	245	245	245	226	251	290
E Col 2-3 Top	438	411	411	408	404	419	414
W Col 0-1 Base	794	647	647	661	662	659	461
W Col 0-1 Top	421	284	284	304	297	288	334
W Col 1-2 Base	319	311	311	300	321	319	344
W Col 1-2 Top	334	238	238	234	257	244	344
W Col 2-3 Base	295	249	249	250	231	253	290
W Col 2-3 Top	445	412	412	408	405	420	414
Beam Moments (kip-in)							
Beam L1 E	560	590	590	591	597	601	678
Beam L1 W	579	595	595	596	600	607	678
Beam L2 E	501	488	488	483	487	497	634
Beam L2 W	505	487	487	482	487	497	634
Beam L3 E	438	405	405	401	398	412	414
Beam L3 W	445	405	405	401	398	413	414
Axial Forces (kips)							
E Col 0-1	49.6	41.7	46.5	51.3	53.7	47.4	46.1
E Col 1-2	32.6	27.1	30.4	33.6	35.1	31.0	35.2
E Col 2-3	17.5	12.8	13.4	16.0	17.1	13.6	11.9
W Col 0-1	50.7	41.7	46.5	51.3	53.5	47.4	46.1
W Col 1-2	34.2	27.1	30.4	33.6	34.9	30.9	35.2
W Col 2-3	18.9	12.9	13.4	16.0	16.9	13.7	11.9
Beam E 1	15.3	8.9	12.5	12.6	12.9	12.2	13.8
Beam W 1	15.7	8.9	12.5	12.6	12.7	13.3	13.8
Beam E 2	12	8.2	11.6	11.5	12.7	12.0	15.3
Beam W 2	12.2	8.2	11.6	11.5	12.7	11.7	15.3
Beam E 3	17.6	12.9	18.2	15.5	16.1	18.5	17.1
Beam W 3	16.3	12.9	18.2	15.5	16.0	18.5	17.1
Shear Forces (kips)							
Col E 0-1	6.4	5.3	5.3	5.5	5.4	5.4	5.1
Col W 0-1	6.8	5.9	5.9	6.1	6.1	6.0	5.1
Col E 1-2	4.3	4.2	4.2	4.1	4.4	4.2	5.0
Col W 1-2	4.4	4.0	4.0	3.9	4.2	4.1	5.0
Col E 2-3	4.8	4.8	4.8	4.7	4.6	4.9	5.1
Col W 2-3	5	4.8	4.8	4.8	4.6	4.9	5.1
Beam L1	4.7	4.9	4.9	4.9	5.0	5.0	5.6
Beam L2	4.2	4.1	4.1	4.0	4.1	4.1	5.3
Beam L3	3.8	3.4	3.4	3.4	3.4	3.5	3.5

Table 5.8b -Peak member forces from experiment and analyses for sinusoidal test at 32 °C, 0.5 hz with a top frame displacement of 0.5 in.

Member Force Location	Experiment	GRD	GRD Corrected	LRD	FRD	Static Corrected	Portal
Column Moments (kip-in)							
E Col. 0-1 Base	344	287	287	289	285	287	197
E Col. 0-1 Top	200	140	140	145	138	140	142
E Col. 1-2 Base	110	123	123	114	139	122	140
E Col. 1-2 Top	126	82	82	76	93	81	140
E Col. 2-3 Base	131	125	125	130	131	125	116
E Col. 2-3 Top	190	178	178	176	181	178	166
W Col. 0-1 Base	385	327	327	329	324	326	197
W Col. 0-1 Top	268	153	153	159	149	152	142
W Col. 1-2 Base	104	114	114	105	129	115	140
W Col. 1-2 Top	115	79	79	73	91	80	140
W Col. 2-3 Base	112	127	127	132	133	126	116
W Col. 2-3 Top	192	178	178	176	181	178	166
Beam Moments (kip-in)							
Beam L1 E	271	263	263	259	265	262	282
Beam L1 W	284	267	267	263	266	266	282
Beam L2 E	232	207	207	203	209	206	256
Beam L2 W	242	206	206	202	209	206	256
Beam L3 E	190	175	175	173	178	175	166
Beam L3 W	192	175	175	174	178	175	166
Axial Forces (kips)							
E Col. 0-1	84	69.8	82.0	84.1	85.6	81.8	76.5
E Col. 1-2	51	45.2	53.4	54.2	55.1	53.3	48.8
E Col. 2-3	21	22.0	25.3	26.5	27.2	25.2	22.0
W Col. 0-1	84	69.8	82.0	84.1	85.4	81.8	76.5
W Col. 1-2	51	45.1	53.3	54.2	54.9	53.2	48.8
W Col. 2-3	20	22.0	25.3	26.5	27.0	25.2	22.0
Beam E 1	24	18.6	23.2	22.8	23.2	22.9	22.0
Beam W 1	25	18.6	23.2	22.8	23.2	23.4	22.0
Beam E 2	22	17.9	22.0	22.0	22.6	22.0	22.4
Beam W 2	22	17.9	22.0	22.0	22.6	21.9	22.4
Beam E 3	26	19.9	24.7	23.8	24.1	24.8	22.2
Beam W 3	24	19.9	24.7	23.8	24.1	24.8	22.2
Shear Forces (kips)							
Col. E 0-1	3.8	2.7	2.7	2.8	2.7	2.7	2.2
Col. W 0-1	4.2	3.1	3.1	3.1	3.0	3.0	2.2
Col. E 1-2	1.7	1.5	1.5	1.4	1.6	1.5	2.0
Col. W 1-2	1.6	1.4	1.4	1.3	1.5	1.4	2.0
Col. E 2-3	2.3	2.2	2.2	2.2	2.2	2.2	2.0
Col. W 2-3	2.2	2.2	2.2	2.2	2.3	2.2	2.0
Beam L1	2.3	2.2	2.2	2.2	2.2	2.2	2.3
Beam L2	1.9	1.7	1.7	1.7	1.7	1.7	2.1
Beam L3	1.9	1.5	1.5	1.5	1.5	1.5	1.4

Table 5.8c -Peak member forces from experiment and analyses for sinusoidal test at 24 °C, 2.0 hz with a top frame displacement of 0.25 in.

Member Force Location	Experiment	GRD	GRD Corrected	LRD	FRD	Static Corrected	Portal
Column Moments (kip-in)							
E Col. 0-1 Base	2844	2271	2271	2321	2363	2480	1888
E Col. 0-1 Top	1612	961	961	1058	1140	1055	1367
E Col. 1-2 Base	994	1095	1095	1002	1129	1188	1440
E Col. 1-2 Top	967	785	785	737	916	851	1440
E Col. 2-3 Base	1013	1113	1113	1151	965	1219	1309
E Col. 2-3 Top	1619	1649	1649	1631	1542	1799	1763
W Col. 0-1 Base	3143	2589	2589	2647	2692	2821	1888
W Col. 0-1 Top	1804	1062	1062	1163	1238	1152	1367
W Col. 1-2 Base	1076	1018	1018	928	1046	1117	1440
W Col. 1-2 Top	1081	763	763	715	893	838	1440
W Col. 2-3 Base	1026	1130	1130	1167	985	1228	1309
W Col. 2-3 Top	1649	1650	1650	1632	1543	1800	1763
Beam Moments (kip-in)							
Beam L1 E	2245	2056	2056	2038	2201	2243	2807
Beam L1 W	2315	2080	2080	2065	2213	2269	2807
Beam L2 E	1927	1898	1898	1856	1831	2069	2749
Beam L2 W	1965	1893	1893	1850	1828	2066	2749
Beam L3 E	1619	1622	1622	1604	1516	1769	1763
Beam L3 W	1649	1623	1623	1605	1517	1770	1763
Axial Forces (kips)							
E Col. 0-1	354.5	285.7	340.2	375.4	336.9	371.1	352.1
E Col. 1-2	218.8	186.4	220.5	244.5	219.6	240.6	215.5
E Col. 2-3	95.2	88.2	98.5	116.7	106.4	107.5	92.2
W Col. 0-1	367.5	285.7	340.2	375.3	336.7	370.9	352.1
W Col. 1-2	223.8	186.1	220.2	244.2	219.4	240.1	215.5
W Col. 2-3	101.8	88.2	98.6	116.8	106.2	107.5	92.2
Beam E L1	102.6	71.5	97.0	99.8	88.3	103.6	94.4
Beam W L1	114.7	71.5	97.0	99.8	88.3	108.1	94.4
Beam E L2	89.6	64.7	87.6	91.7	84.1	96.2	93.7
Beam W L2	90.4	64.7	87.6	91.7	84.1	94.9	93.7
Beam E L3	112.8	84.7	114.7	109.0	98.3	125.2	100.5
Beam W L3	110.5	84.7	114.7	109.0	98.3	125.2	100.5
Shear Forces (kips)							
Col. E 0-1	28.2	20.6	20.6	21.5	22.3	22.6	20.9
Col. W 0-1	31.3	23.3	23.3	24.3	25.0	25.3	20.9
Col. E 1-2	14.5	13.6	13.6	12.5	14.8	14.8	20.9
Col. W 1-2	15.6	12.9	12.9	11.8	14.0	14.2	20.9
Col. E 2-3	19.0	20.0	20.0	20.1	18.2	21.8	22.3
Col. W 2-3	19.2	20.1	20.1	20.3	18.3	22.0	22.3
Beam L1	19.0	17.1	17.1	16.9	18.4	18.7	23.4
Beam L2	16.6	15.8	15.8	15.5	15.3	17.2	22.9
Beam L3	15.3	13.8	13.8	13.6	12.9	15.0	14.7

Table 5.8d -Peak member forces from experiment and analyses for sinusoidal test at 24 °C, 0.5 hz with a top frame displacement of 2.0 in.

Member Force Location	Experiment	GRD	GRD Corrected	LRD	FRD	Static Corrected	Portal
Column Moments (kip-in)							
E Col. 0-1 Base	4674	4353	4353	4382	4488	4462	3577
E Col. 0-1 Top	2233	1576	1576	1622	1774	1620	2590
E Col. 1-2 Base	2600	2729	2729	2696	2682	2774	2820
E Col. 1-2 Top	2350	2119	2119	2102	2221	2152	2820
E Col. 2-3 Base	1650	1910	1910	1914	1792	1961	2367
E Col. 2-3 Top	3200	3355	3355	3349	3293	3436	3375
W Col. 0-1 Base	5030	4959	4959	4994	5113	5073	3577
W Col. 0-1 Top	2000	1754	1754	1812	1959	1789	2590
W Col. 1-2 Base	2620	2561	2561	2542	2520	2639	2820
W Col. 1-2 Top	2412	2065	2065	2060	2177	2128	2820
W Col. 2-3 Base	1644	1939	1939	1949	1831	1980	2367
W Col. 2-3 Top	3150	3356	3356	3351	3295	3436	3375
Beam Moments (kip-in)							
Beam L1 E	4327	4304	4304	4293	4357	4395	5410
Beam L1 W	4404	4314	4314	4327	4378	4429	5410
Beam L2 E	3866	4029	4029	4009	3985	4113	5186
Beam L2 W	3979	4000	4000	4001	3980	4108	5186
Beam L3 E	3200	3299	3299	3293	3238	3378	3375
Beam L3 W	3150	3300	3300	3295	3240	3379	3375
Axial Forces (kips)							
E Col. 0-1	270.5	248.1	263.7	281.9	285.5	270.5	268.8
E Col. 1-2	172.3	160.9	168.5	183.6	187.6	172.7	164.3
E Col. 2-3	79.6	75.3	75.9	86.3	89.3	77.9	68.5
W Col. 0-1	298.0	248.7	264.3	281.9	285.3	270.3	268.8
W Col. 1-2	179.5	161.2	168.7	183.3	187.4	172.5	164.3
W Col. 2-3	84.0	75.7	76.3	86.4	89.1	77.9	68.5
Beam E L1	52.9	45.3	60.4	60.3	62.4	57.8	54.9
Beam W L1	61.0	45.3	60.4	60.3	62.4	65.9	54.9
Beam E L2	61.8	41.3	54.9	55.0	58.7	57.2	53.7
Beam W L2	61.4	41.3	54.9	55.0	58.7	55.2	53.7
Beam E L3	103.0	79.6	105.9	88.0	89.2	108.4	82.0
Beam W L3	95.0	79.6	105.9	88.0	89.2	108.6	82.0
Shear Forces (kips)							
Col. E 0-1	45.7	37.8	37.8	38.2	39.8	38.8	39.5
Col. W 0-1	47.7	42.8	42.8	43.3	45.0	43.7	39.5
Col. E 1-2	34.1	35.1	35.1	34.8	35.5	35.7	40.9
Col. W 1-2	36.7	33.5	33.5	33.3	34.0	34.6	40.9
Col. E 2-3	35.3	38.2	38.2	38.1	36.8	39.1	41.6
Col. W 2-3	34.9	38.4	38.4	38.4	37.2	39.3	41.6
Beam L1	36.4	36.0	36.0	35.8	36.4	36.7	45.1
Beam L2	32.7	33.7	33.7	33.4	33.2	34.2	43.2
Beam L3	29.6	28.0	28.0	27.9	27.5	28.7	28.1

Table 5.8e -Peak member forces from experiment and analyses for sinusoidal test at 28 °C, 0.1 hz with a top frame displacement of 4.0 in.

Story Level	K'd Ideal Sinusoidal (kip/in)	K'd Individual Damper (kip/in)	K'd Frame Damper	ηd Ideal Sinusoidal (kip/in)	ηd Individual Damper	ηd Frame Damper
1	247	241	277	1.36	1.31	1.19
2	245	241	274	1.37	1.31	1.18
3	249	241	251	1.35	1.31	1.18

Table 5.9 - Comparison of VE-damper properties from individual damper tests (Chapter 3), imperfect sinusoidal displacement history, and an ideal sinusoidal displacement history.

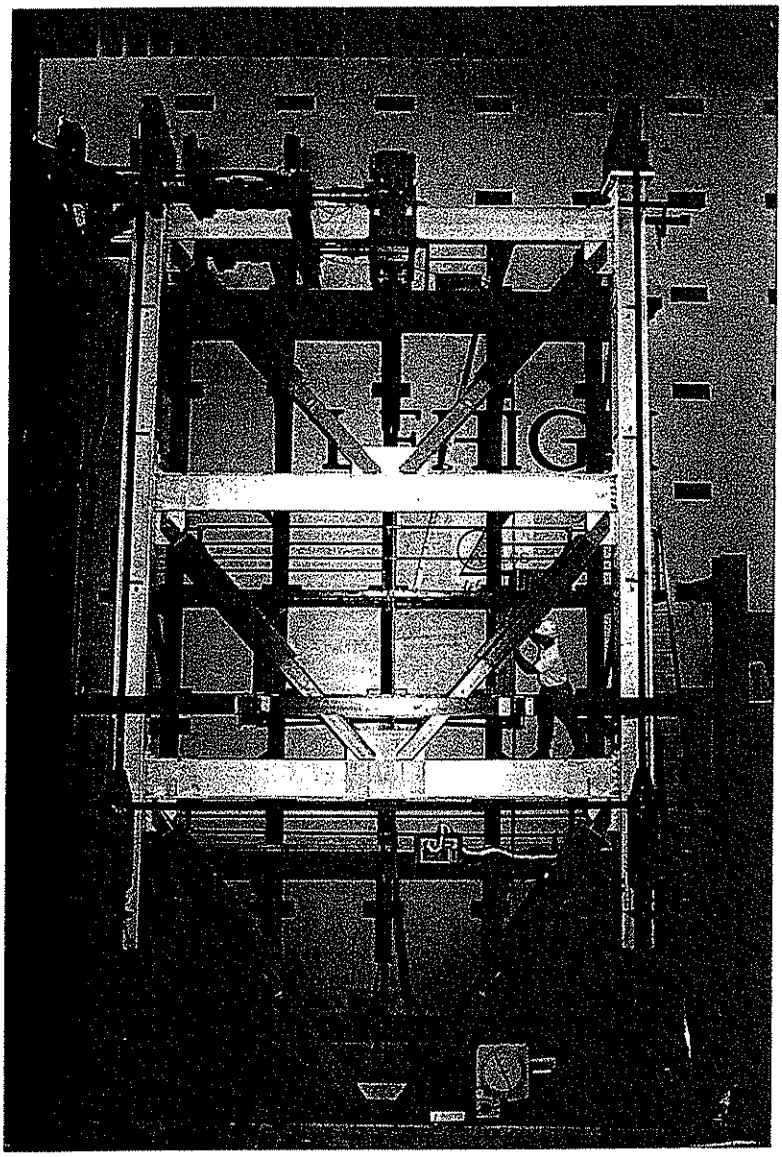

Fig. 5.1 - VE-frame test specimen.

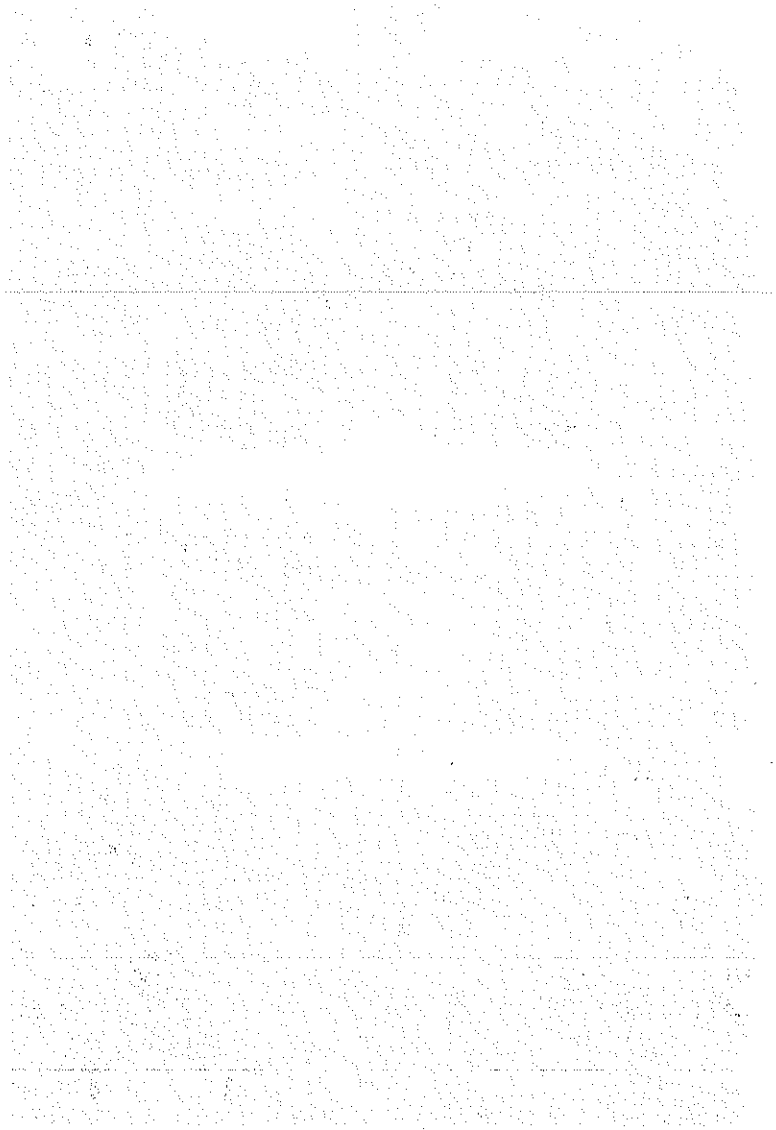

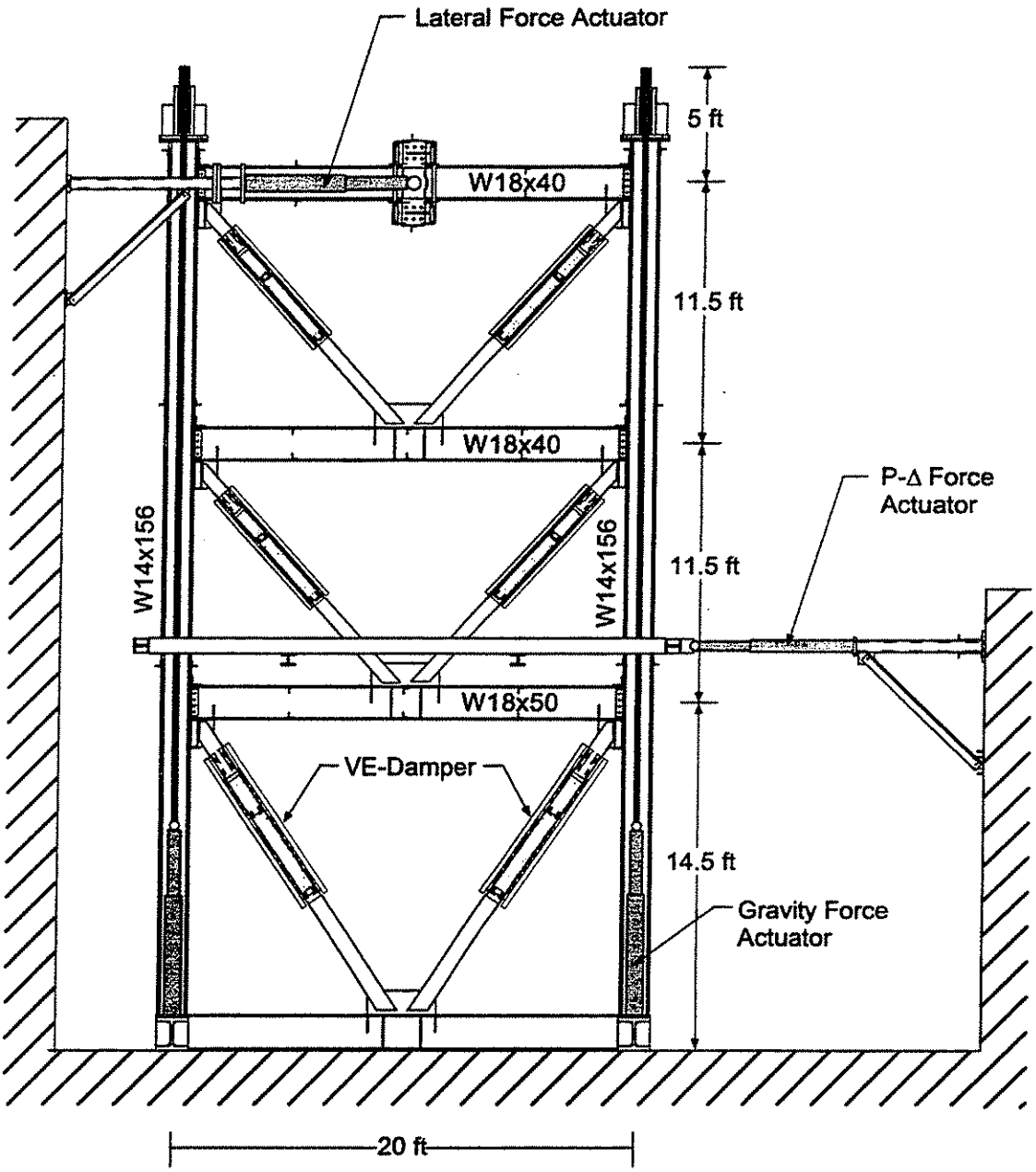

Fig. 5.2 - Schematic of test specimen and set-up.

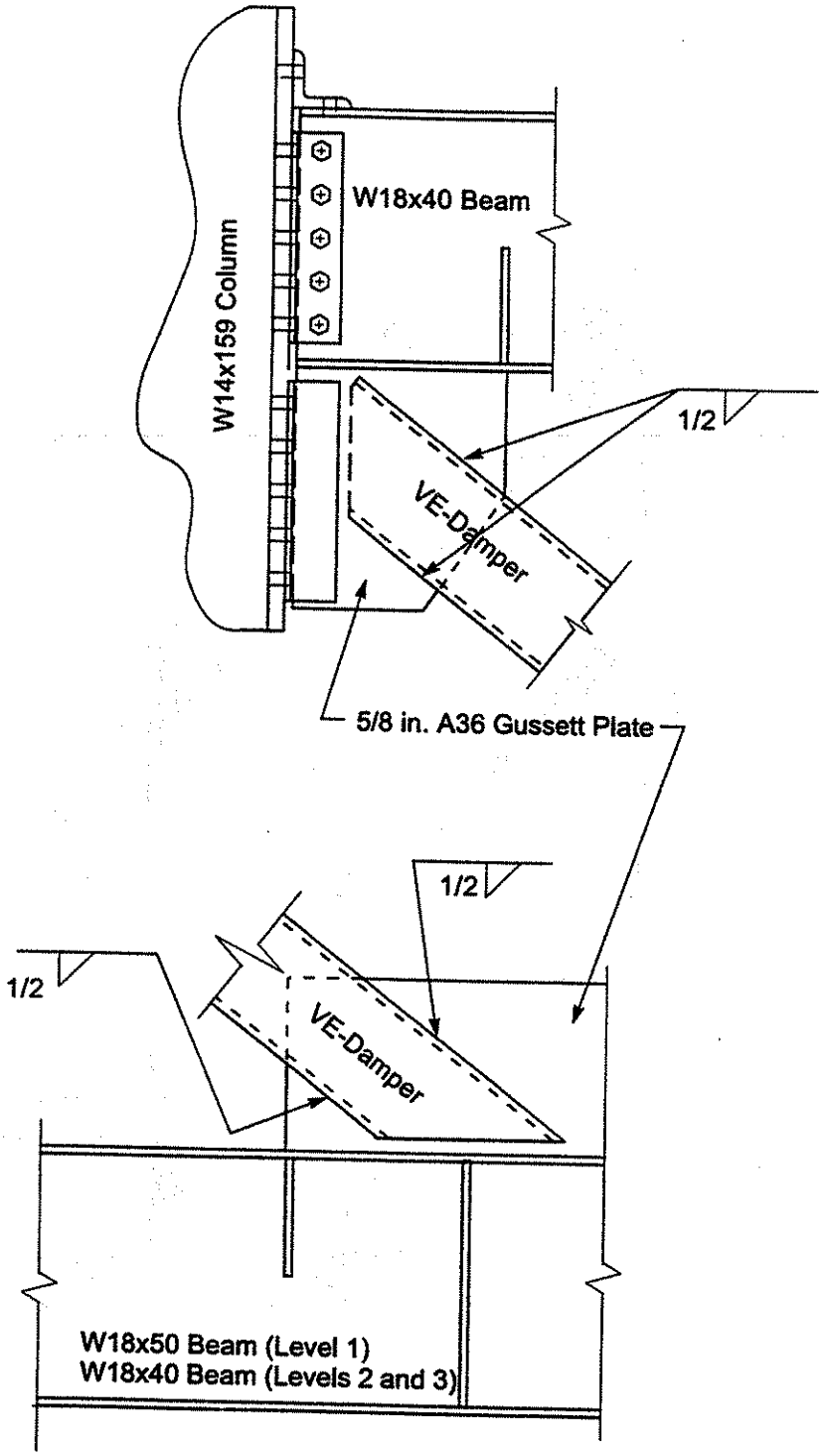

Fig. 5.3 - Damper connections to beam-column and beam at midspan.

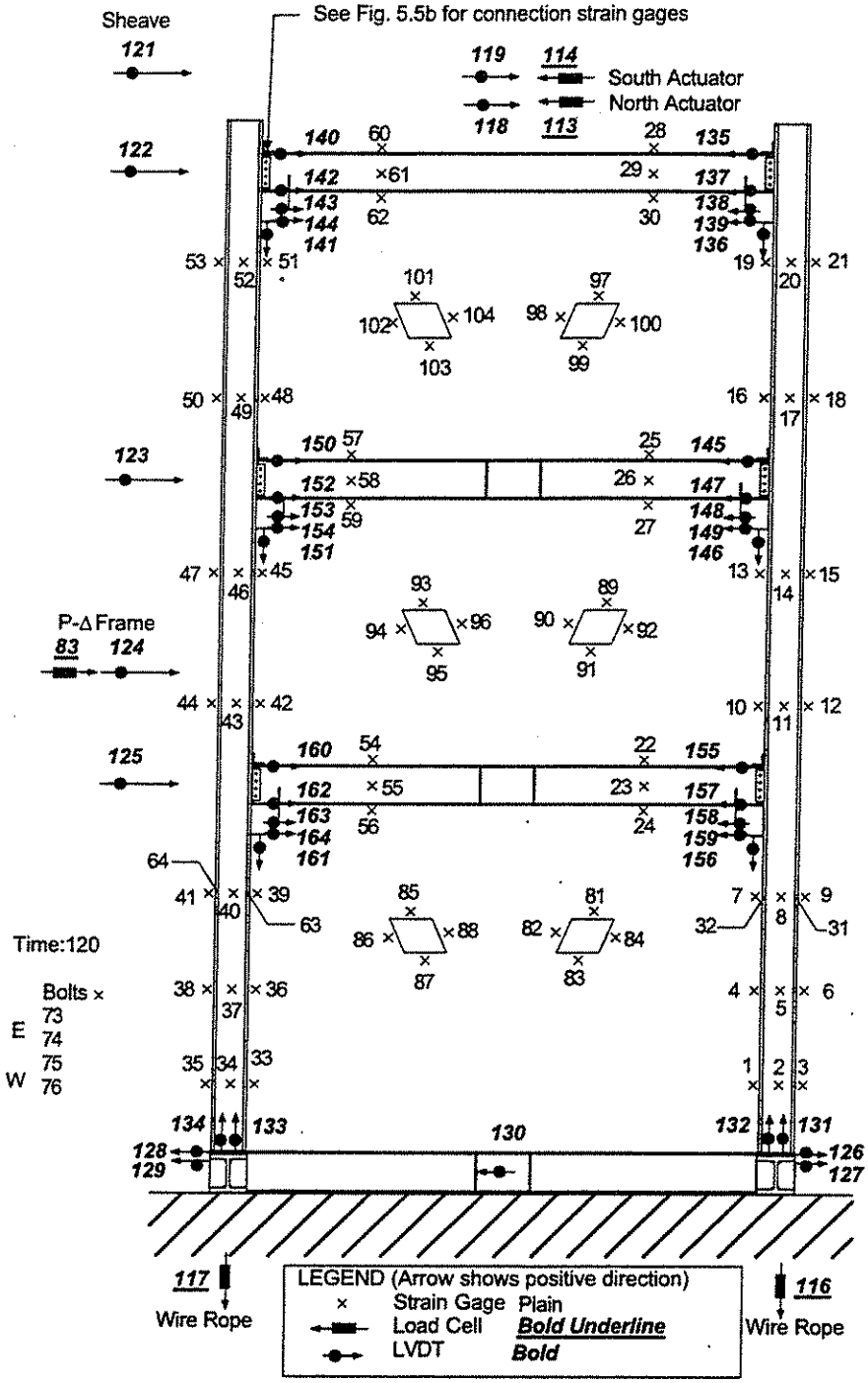

Fig. 5.4 - Instrumentation layout and channel identification for VE-frame.

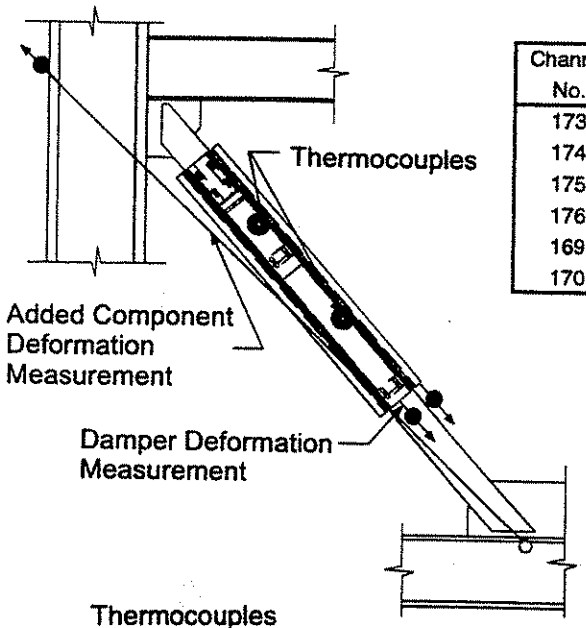

Damper Deformation

Channel No.	Damper Location	Channel No.	Damper Location
173	Level 3 East Top	171	Level 2 West Top
174	Level 3 East Side	172	Level 2 West Side
175	Level 3 West Top	165	Level 1 East Top
176	Level 3 West Side	166	Level 1 East Side
169	Level 2 East Top	167	Level 1 West Top
170	Level 2 East Side	168	Level 1 West Side

Added Component Deformation

Channel No.	Damper Location
177	Level 3 East
178	Level 3 West
179	Level 2 East
180	Level 2 West
181	Level 1 East
182	Level 1 West

Thermocouples

Channel No.	Damper Location	Channel No.	Damper Location	Channel No.	Damper Location
185	Level 3 East Top	189	Level 2 East Top	193	Level 1 East Top
186	Level 3 East Bottom	190	Level 2 East Bottom	194	Level 1 East Bottom
187	Level 3 West Top	191	Level 2 West Top	195	Level 1 West Top
188	Level 3 West Bottom	192	Level 2 West Bottom	196	Level 1 West Bottom

Fig. 5.5a - Instrumentation used to determine damper and added component response.

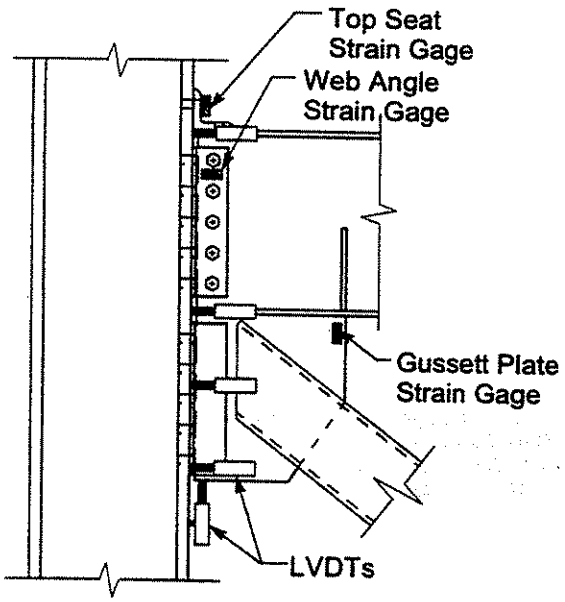

Channel No.	Location
65	Level 3 West Top Seat
66	Level 3 West Web
67	Level 3 West Gusset
68	Level 2 West Top Seat
69	Level 2 West Web
70	Level 2 West Gusset
71	Level 1 West Top Seat
72	Level 1 West Web
80	Level 1 West Gusset
105	Level 3 East Top Seat
106	Level 3 East Web
107	Level 3 East Gusset
108	Level 2 East Top Seat
109	Level 2 East Web
110	Level 2 East Gusset
111	Level 1 East Top Seat
112	Level 1 East Web
79	Level 1 East Gusset

Fig. 5.5b - Instrumentation used for local connection response measurement.

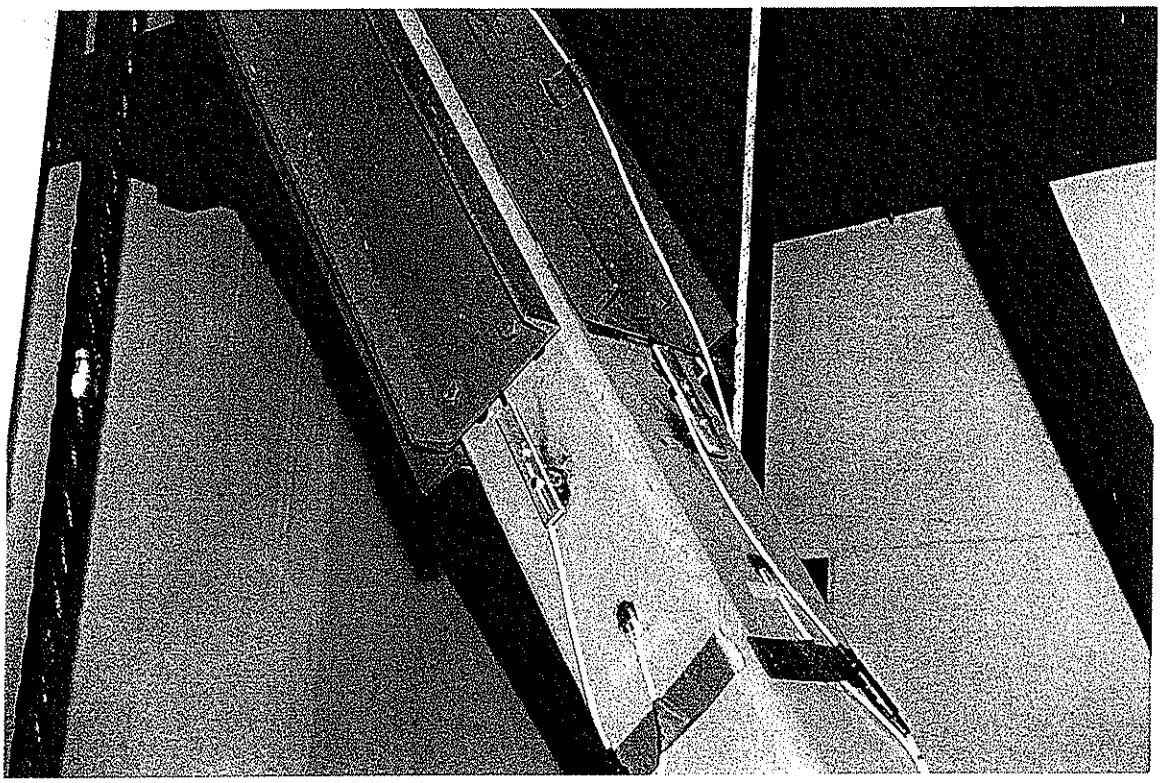

Fig. 5.6 - Displacement transducers used to measure damper deformation and strain gages used to measure damper force (two shown and two on opposite faces).

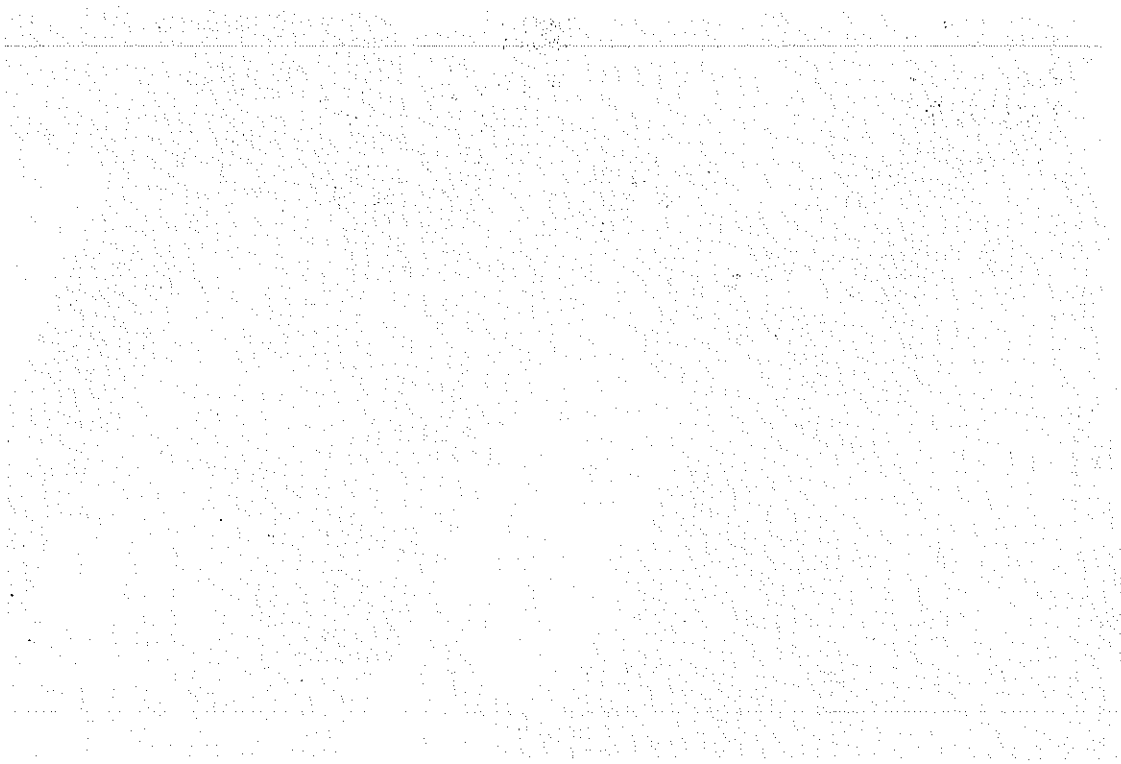

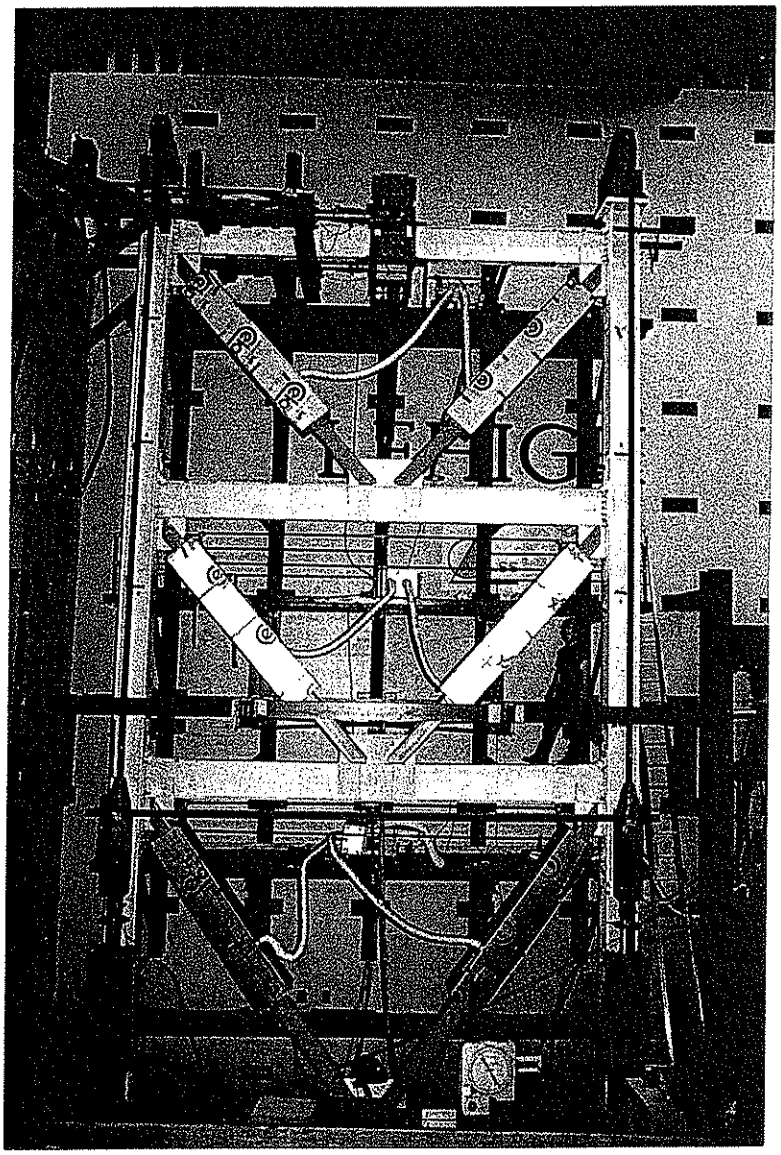

Fig. 5.7 - Insulated enclosures around each damper used to control initial temperature.

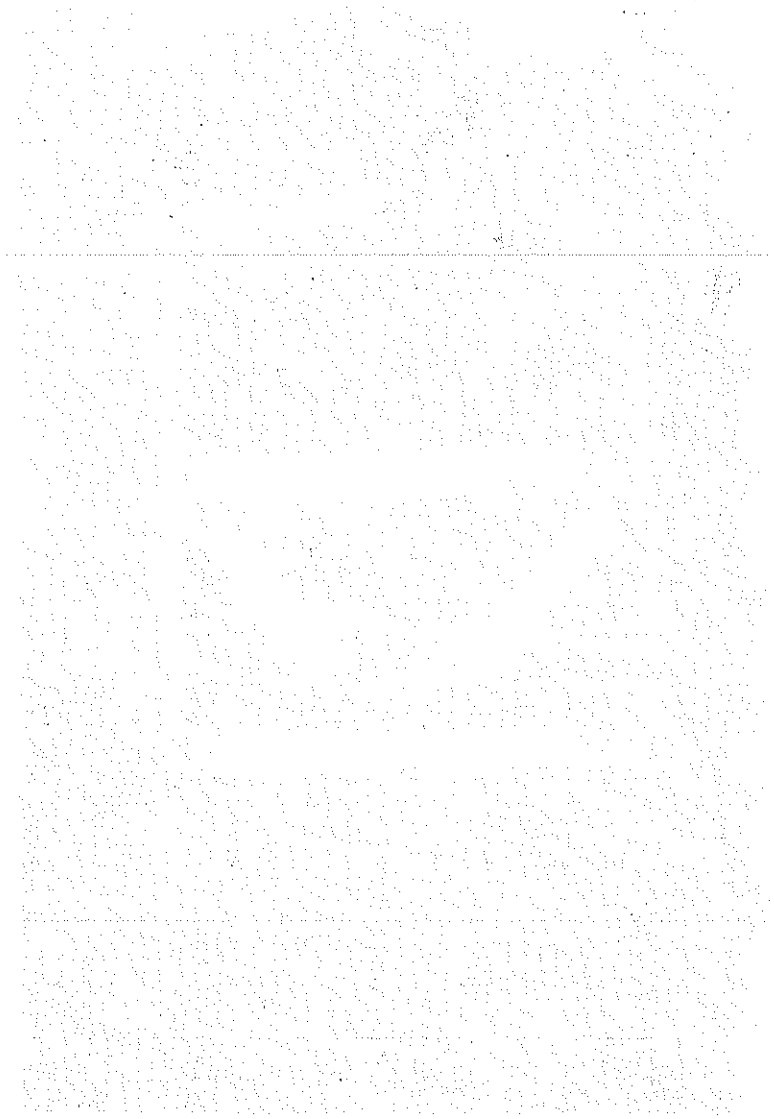

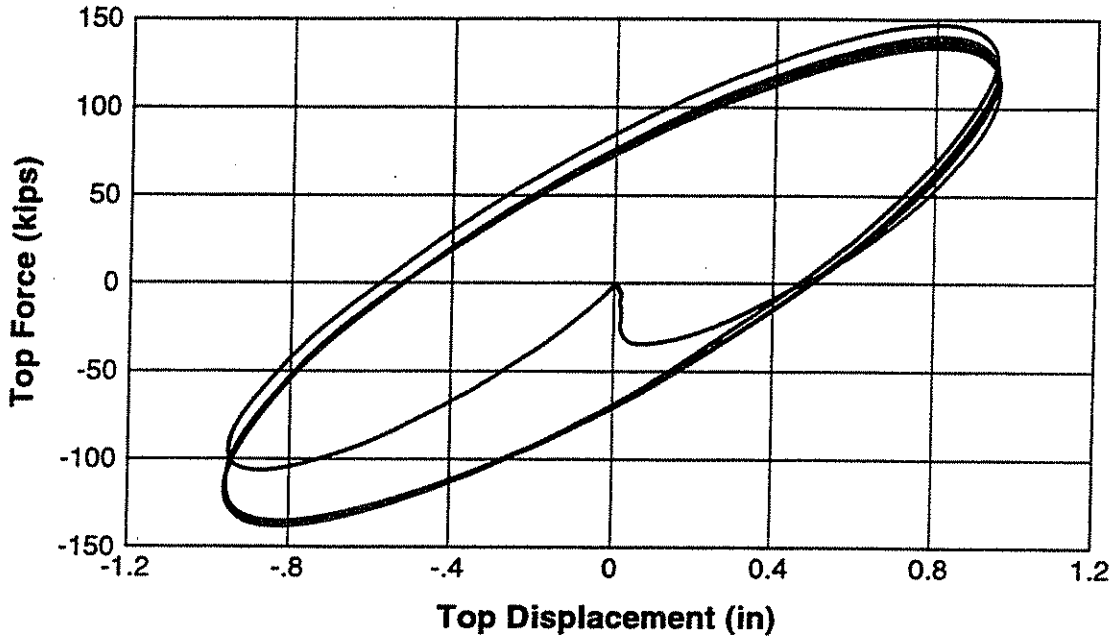

Fig. 5.8 - Typical overall frame force-displacement response for harmonic excitation.

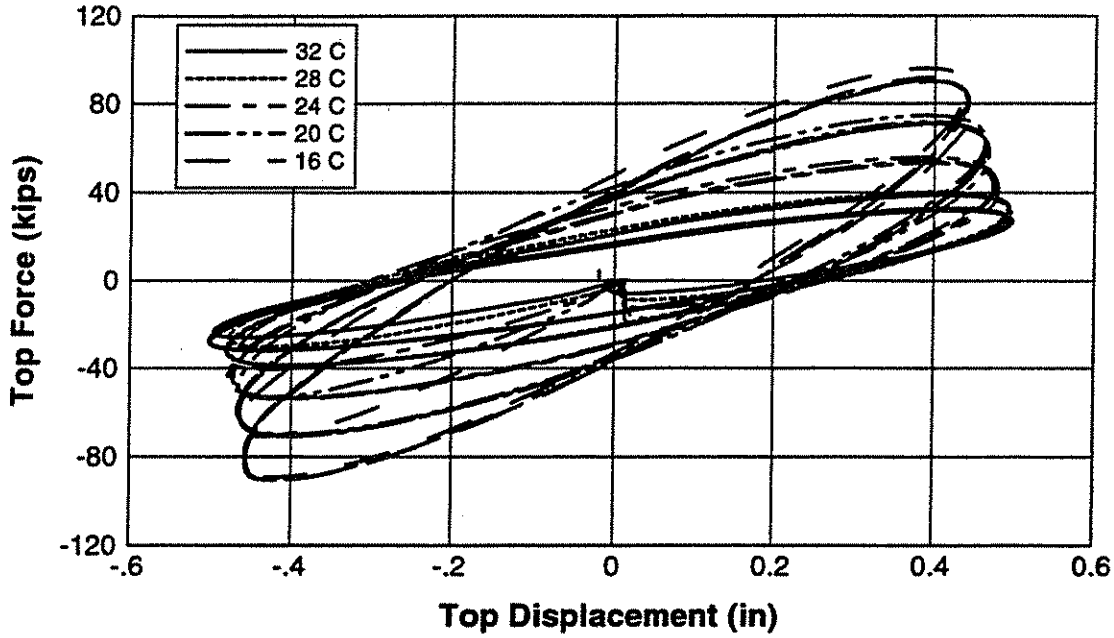

Fig. 5.9 - Example overall frame force-displacement response for loading frequency of 0.5 hz, nominal displacement amplitude of 0.5 in. and varying initial temperatures of 16, 20, 24, 28, and 32 °C.

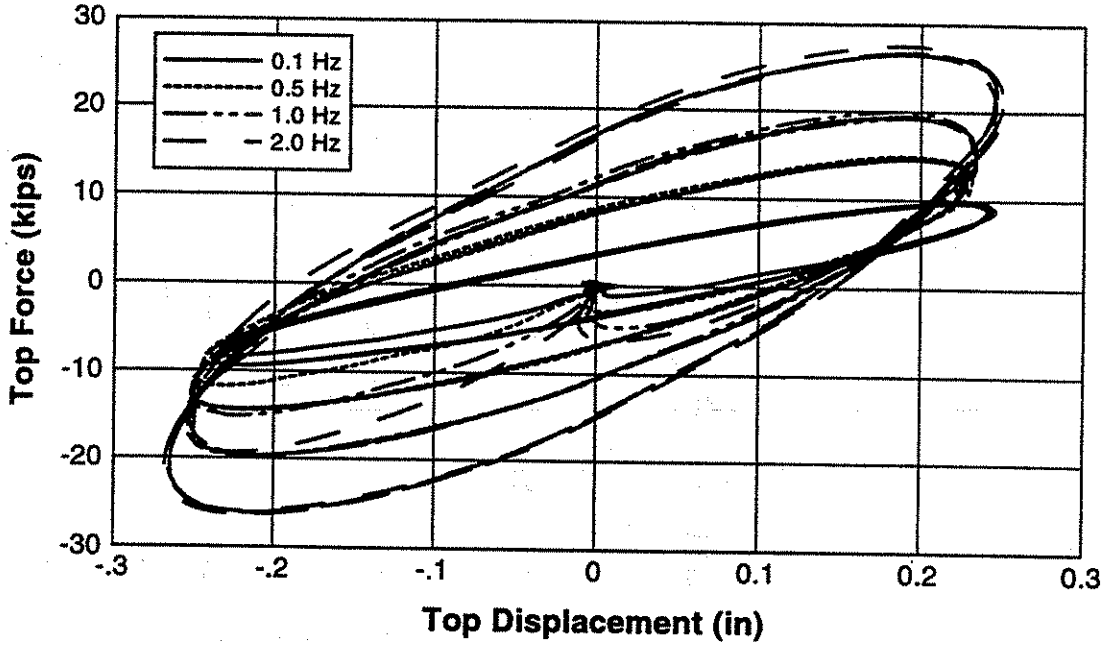

Fig. 5.10 - Example overall frame force-displacement response for initial temperature of 32 °C, nominal displacement amplitude of 0.5 in., and varying loading frequencies of 0.1, 0.5, 1.0, and 2.0 hz.

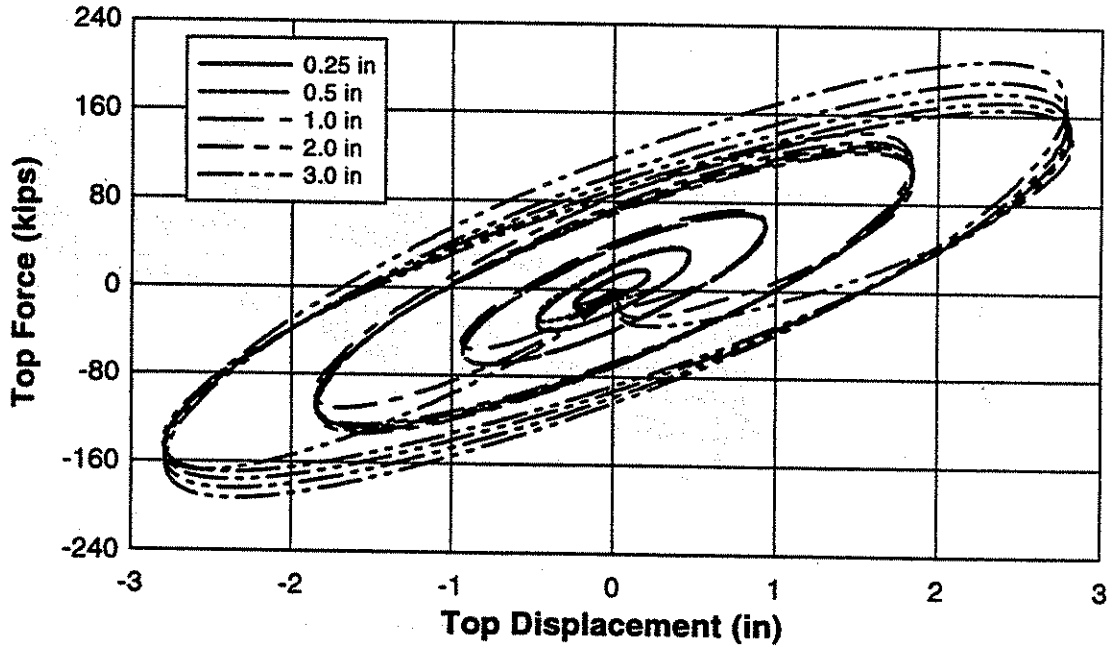

Fig. 5.11 - Example overall frame force-displacement response for initial temperature of 20 °C, loading frequency of 0.1 hz, and varying nominal displacement amplitudes of 0.25, 0.5, 1.0, 2.0, and 3.0 in.

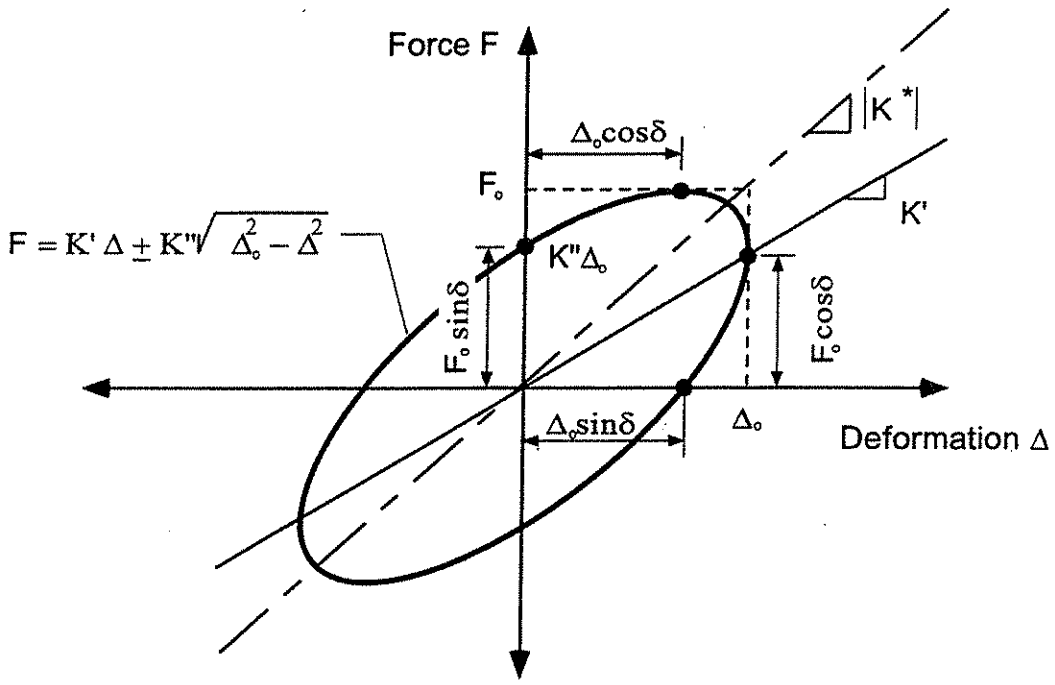

Fig. 5.12 - Ideal harmonic force-displacement response for the VE-frame.

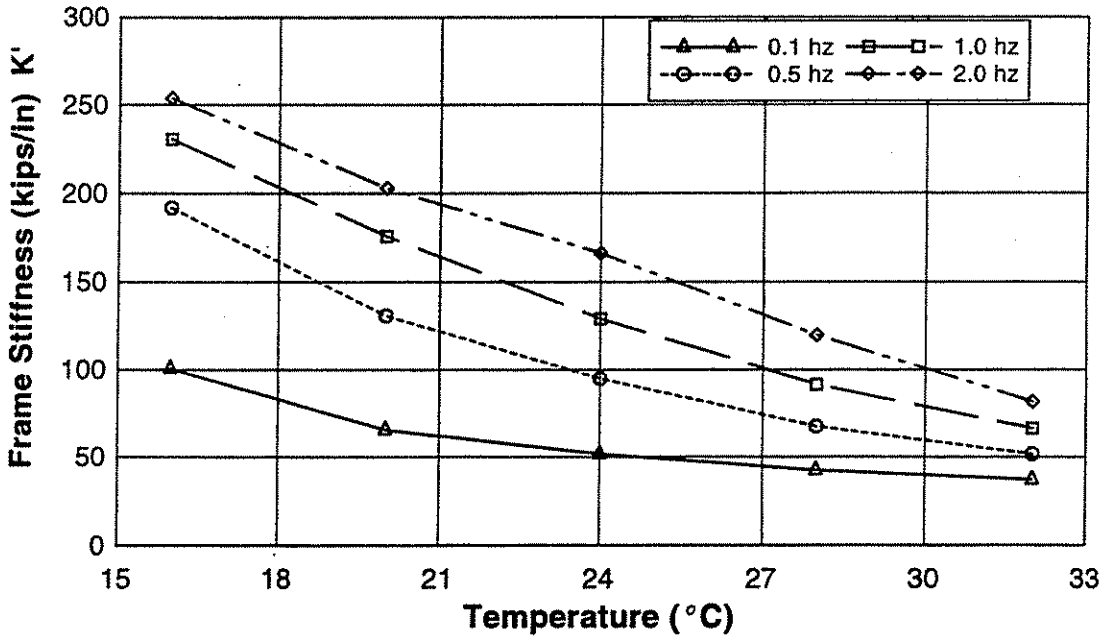

Fig. 5.13 - Influence of temperature on VE-frame stiffness for loading frequencies of 0.1, 0.5, 1.0 and 2.0 hz at 0.25 in. nominal frame displacement.

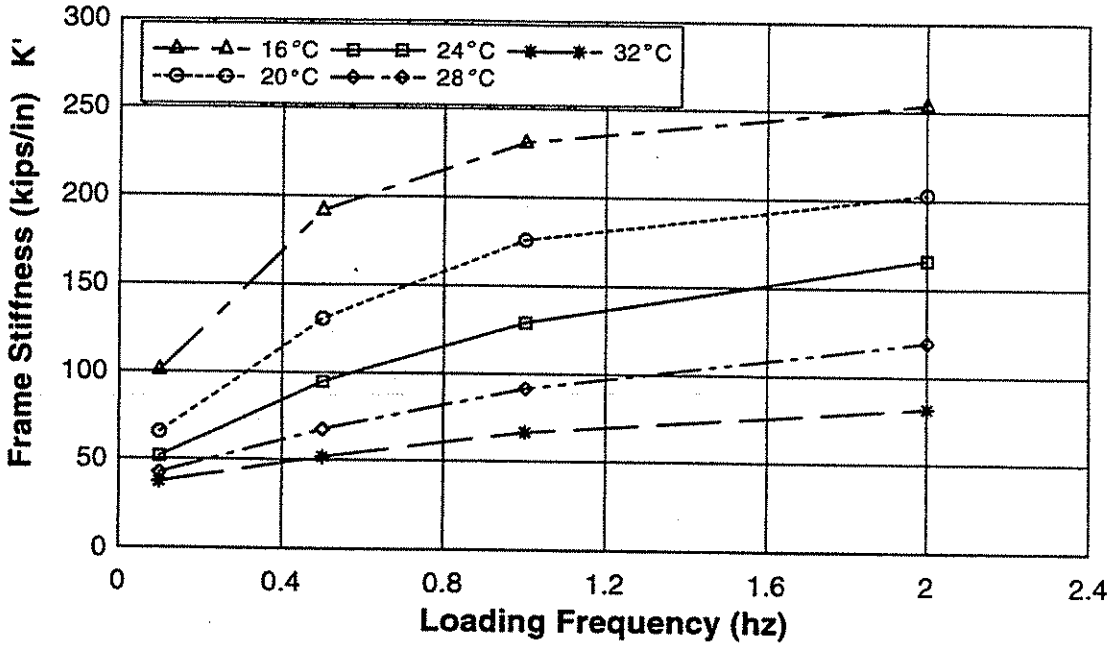

Fig. 5.14 - Influence of loading frequency on VE-frame stiffness for initial damper temperatures of 16, 20, 24, 28 and 32 °C at 0.25 in. nominal frame displacement.

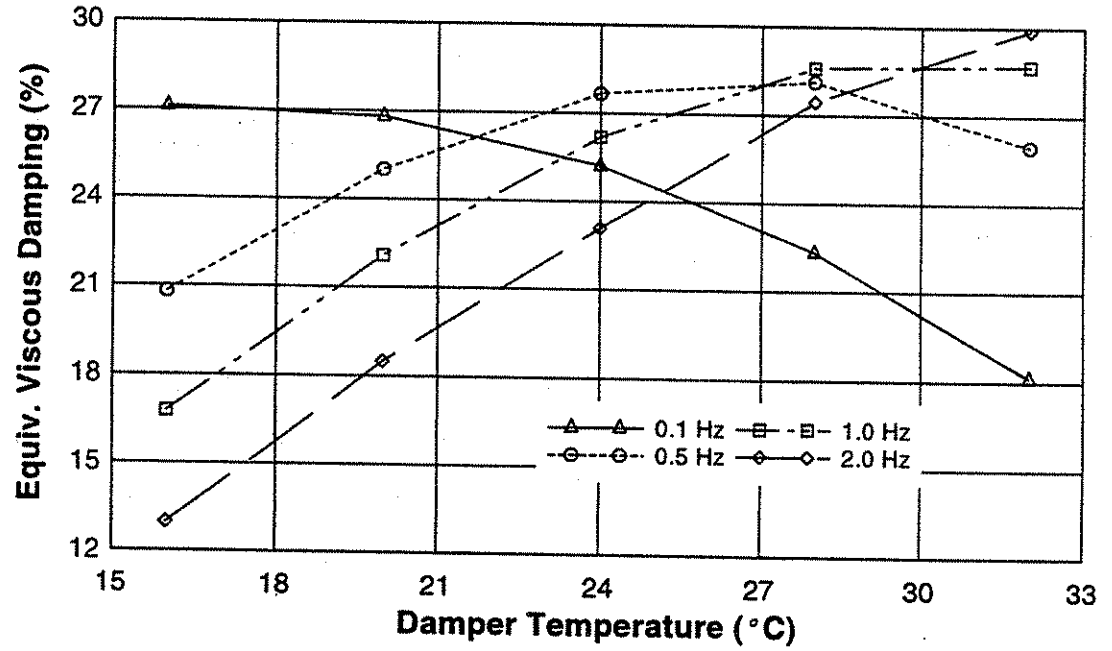

Fig. 5.15 - Influence of temperature on VE-frame equivalent viscous damping ratio for loading frequencies of 0.1, 0.5, 1.0 and 2.0 hz at 0.25 in. nominal frame displacement.

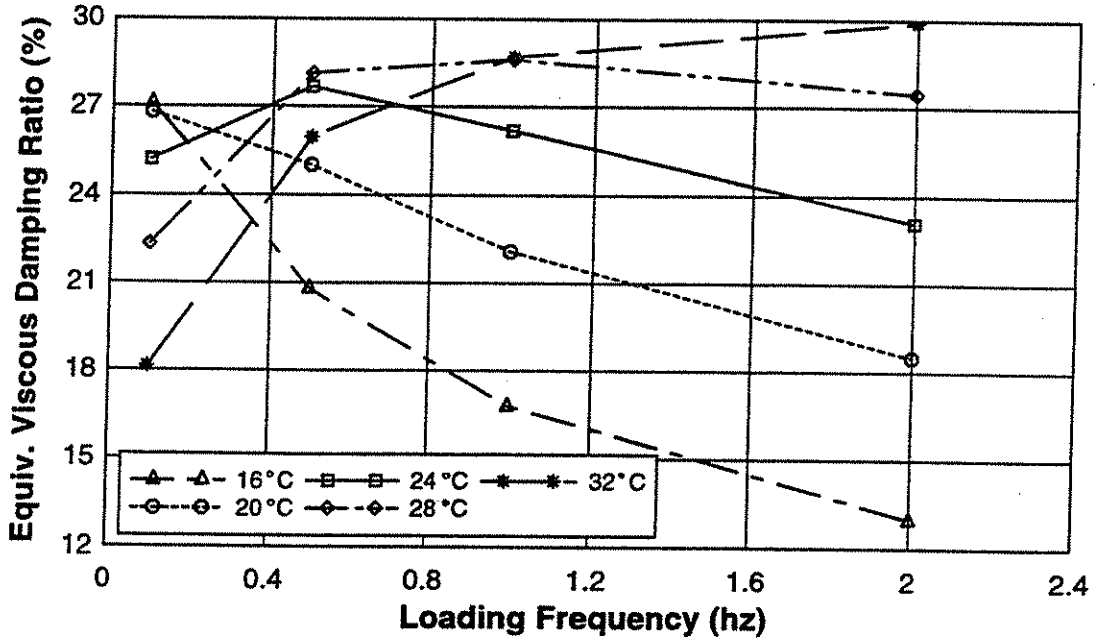

Fig. 5.16 - Influence of loading frequency on VE-frame equivalent viscous damping ratio for initial damper temperatures of 16, 20, 24, 28 and 32 °C at 0.25 in. nominal frame displacement.

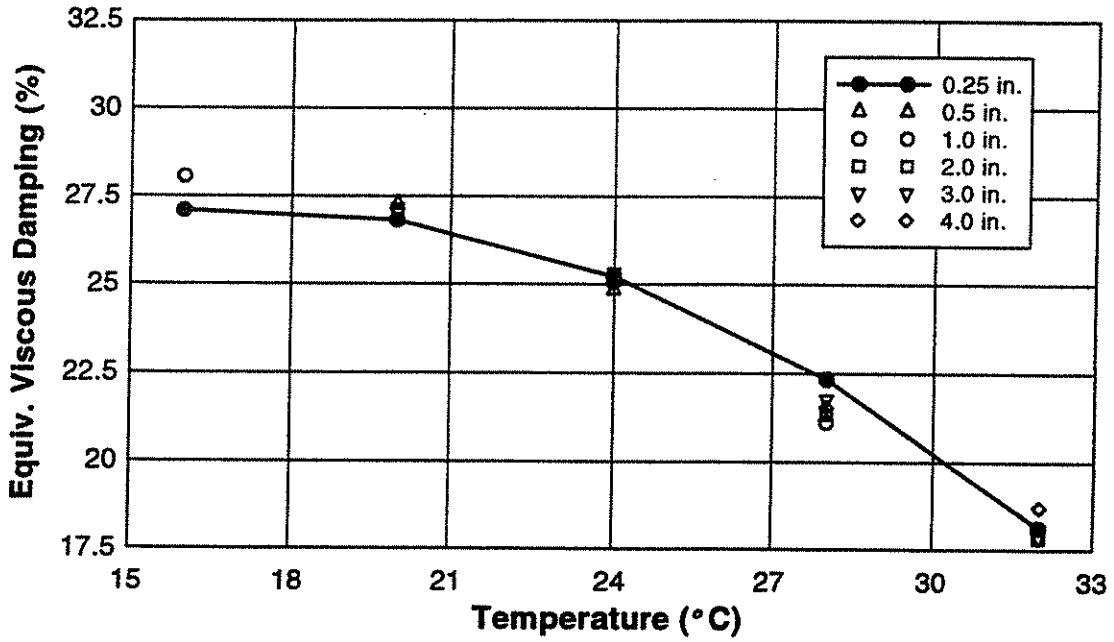

Fig. 5.17 - Similar trend of temperature effect on VE-frame equivalent viscous damping ratio for different nominal frame displacements for constant loading frequency of 0.1 hz.

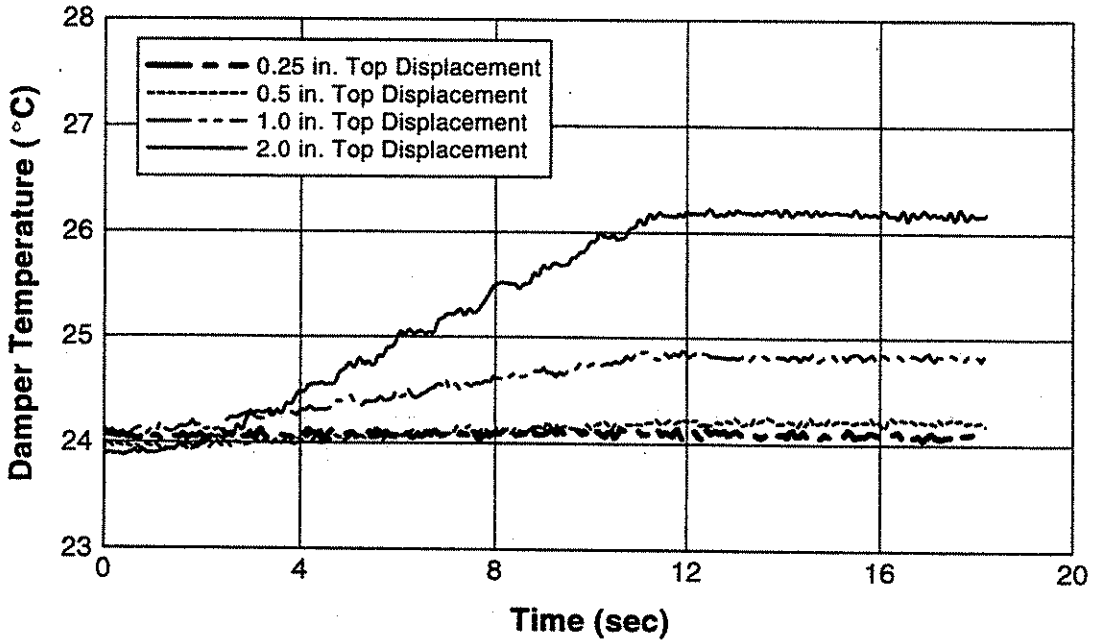

Fig. 5.18 - Examples of measured temperature rise in second story East VE-damper for 0.5 hz loading frequency, 24 °C initial damper temperature, and nominal frame displacements of 0.25, 0.5, 1.0, and 2.0 in.

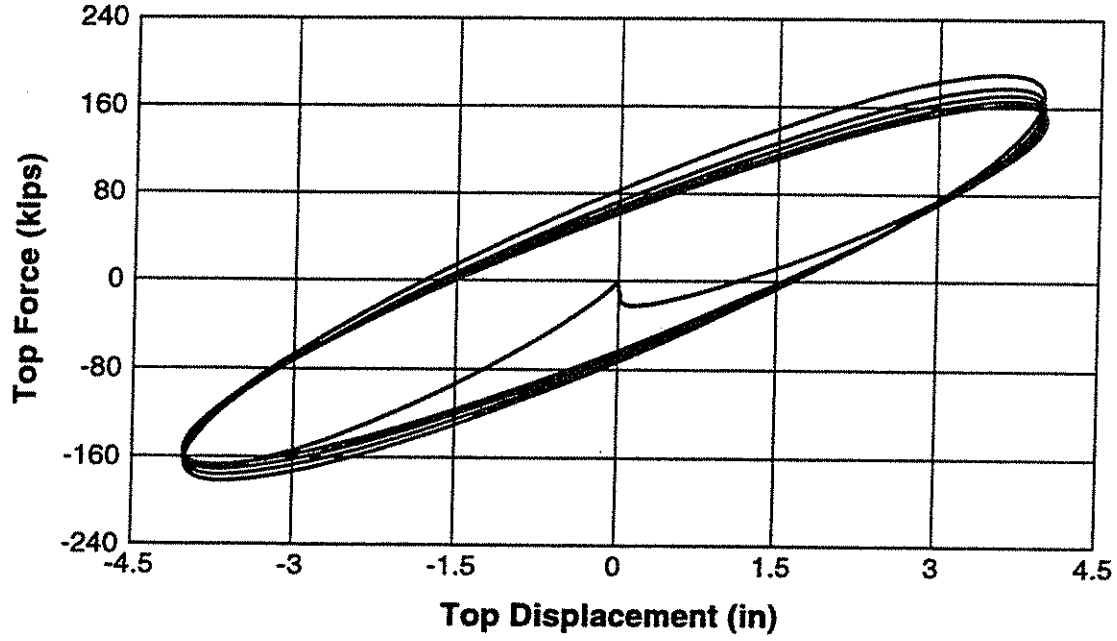

Fig. 5.19 - Measured VE-frame force-deformation response for nominal frame displacement of 4.0 in., loading frequency of 0.1 hz, and initial temperature of 28 °C (130% VE-material strain).

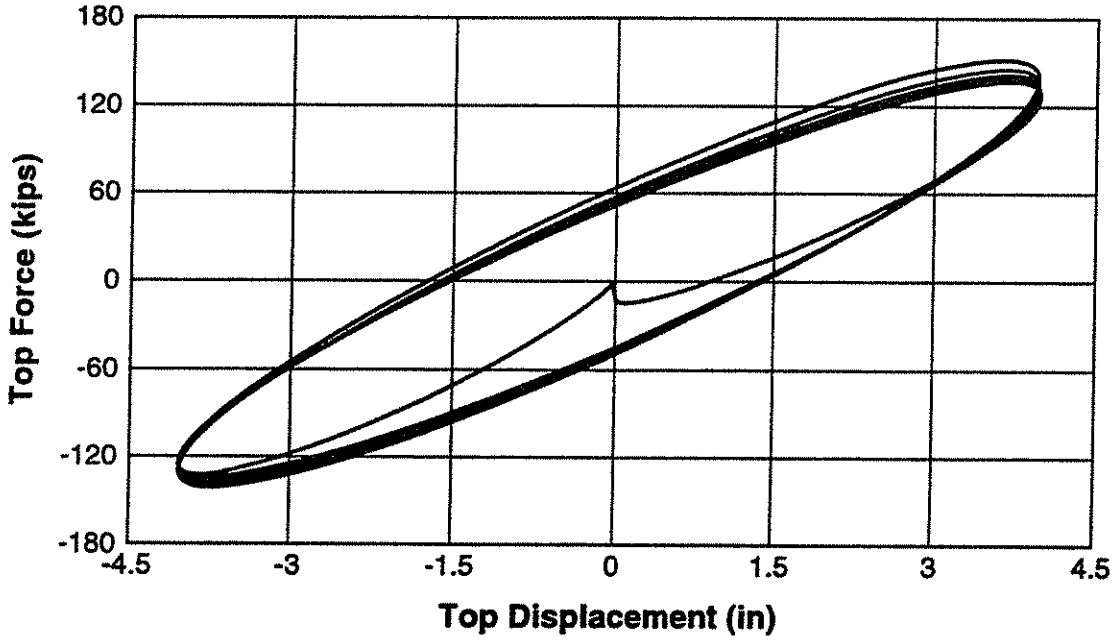

Fig. 5.20 - Measured VE-frame force-deformation response for nominal frame displacement of 4.0 in., loading frequency of 0.1 hz, and initial temperature of 32 °C (130% VE-material strain).

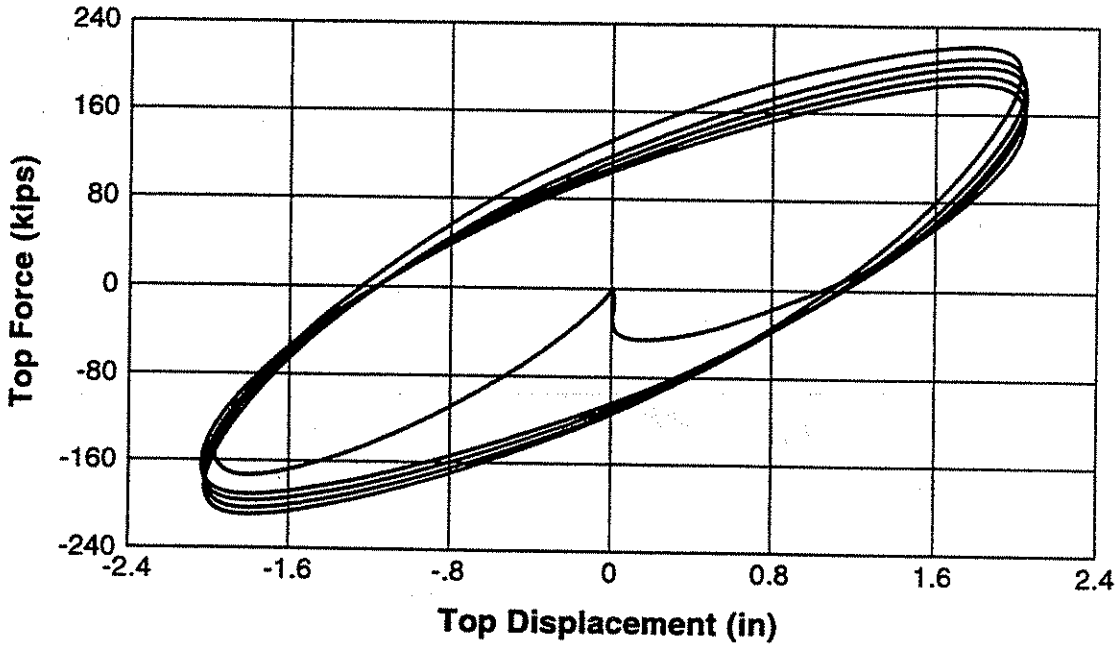

Fig. 5.21 - Measured VE-frame force-deformation response for nominal frame displacement of 2.0 in., loading frequency of 0.5 hz, and initial temperature of 24 °C.

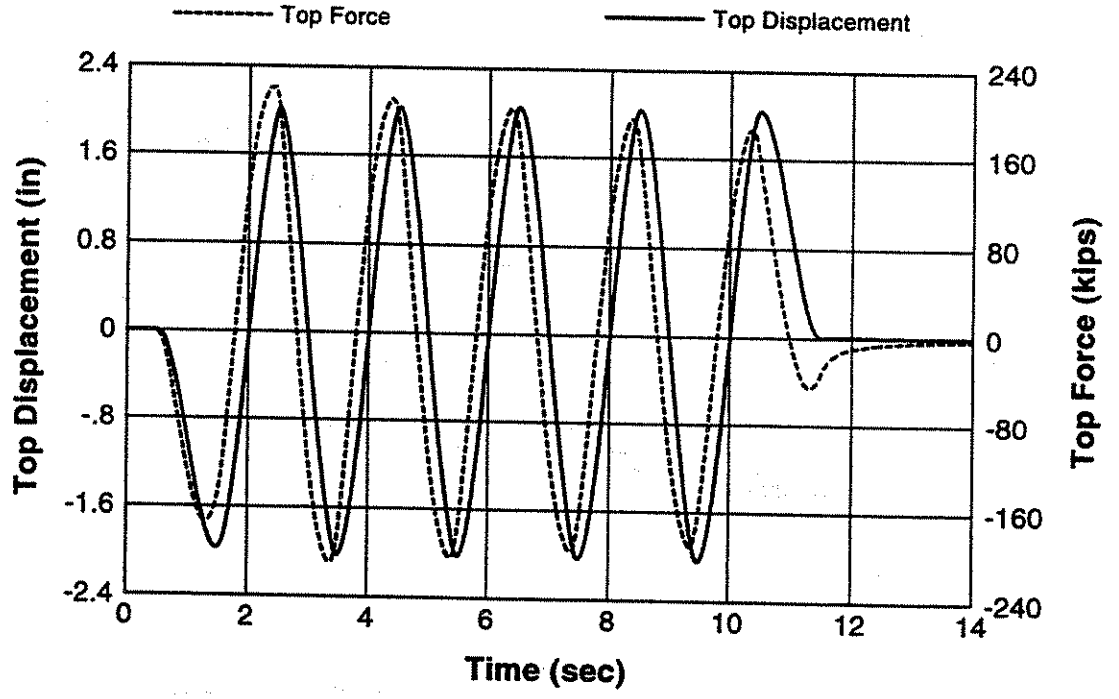

Fig. 5.22 - Time lag between applied force at top of frame and frame displacement.

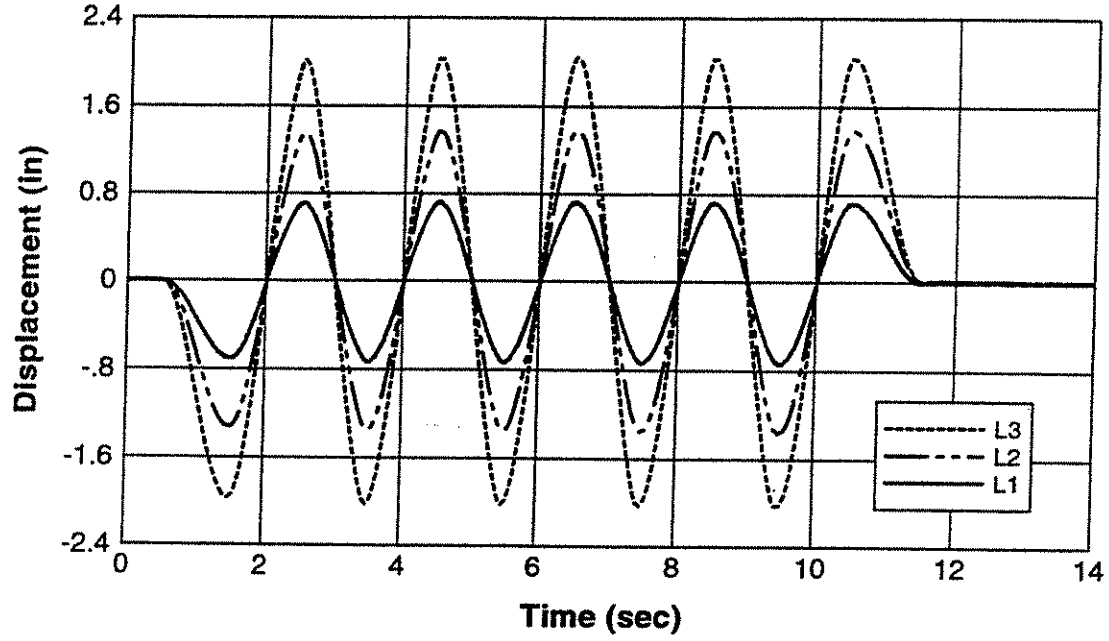

Fig. 5.23 - Measured displacements at each story level.

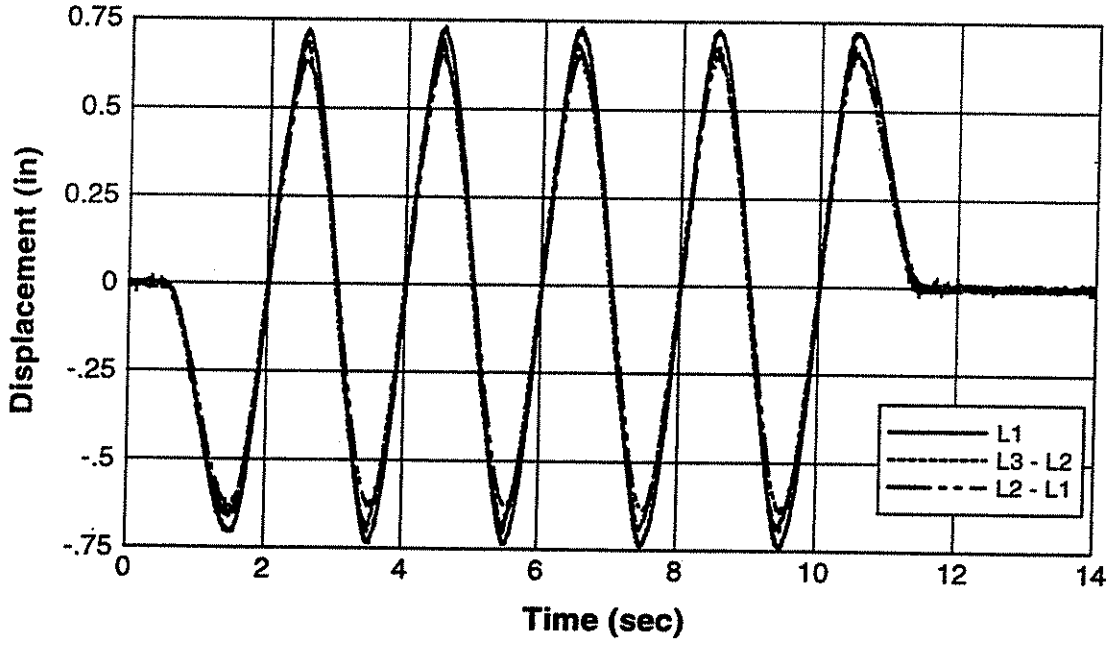

Fig. 5.24 - Interstory displacements.

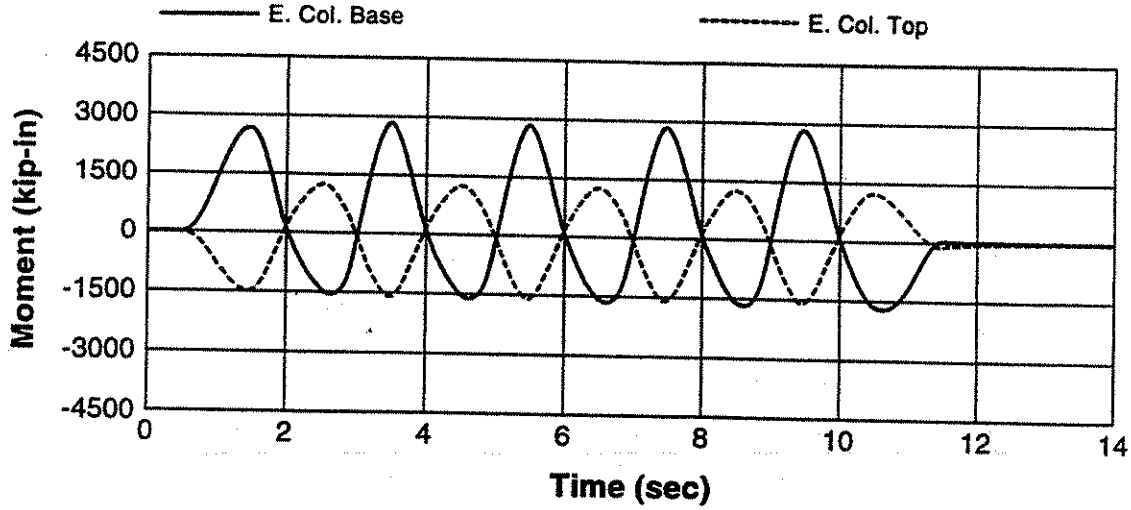

Fig. 5.25a - Moments at top and bottom of first story East column.

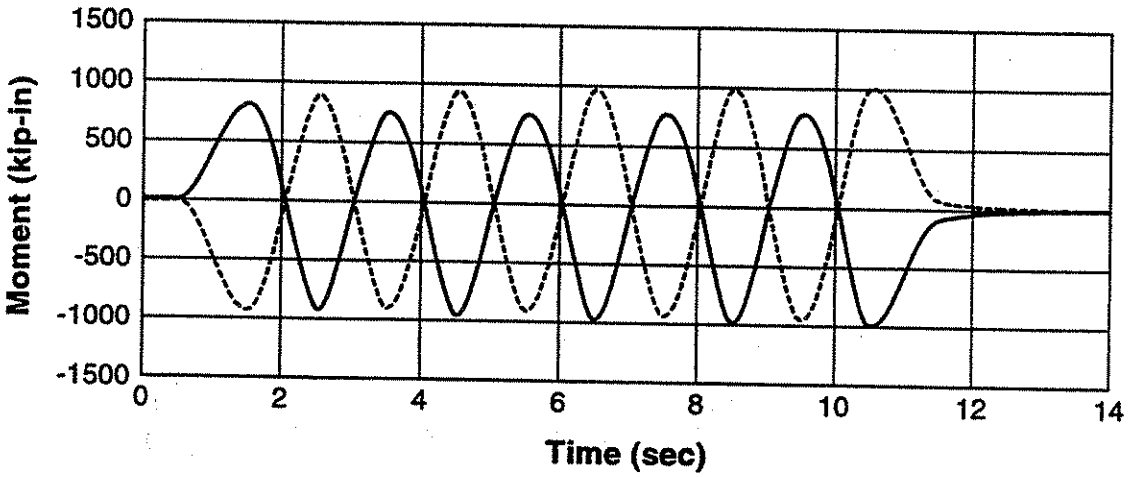

Fig. 5.25b - Moments at top and bottom of second story East column.

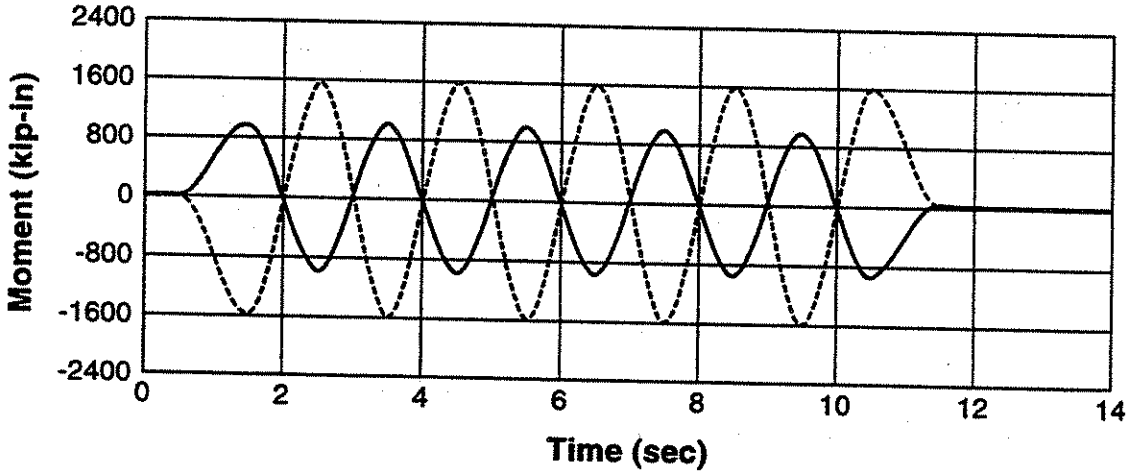

Fig. 5.25c - Moments at top and bottom of third story East column.

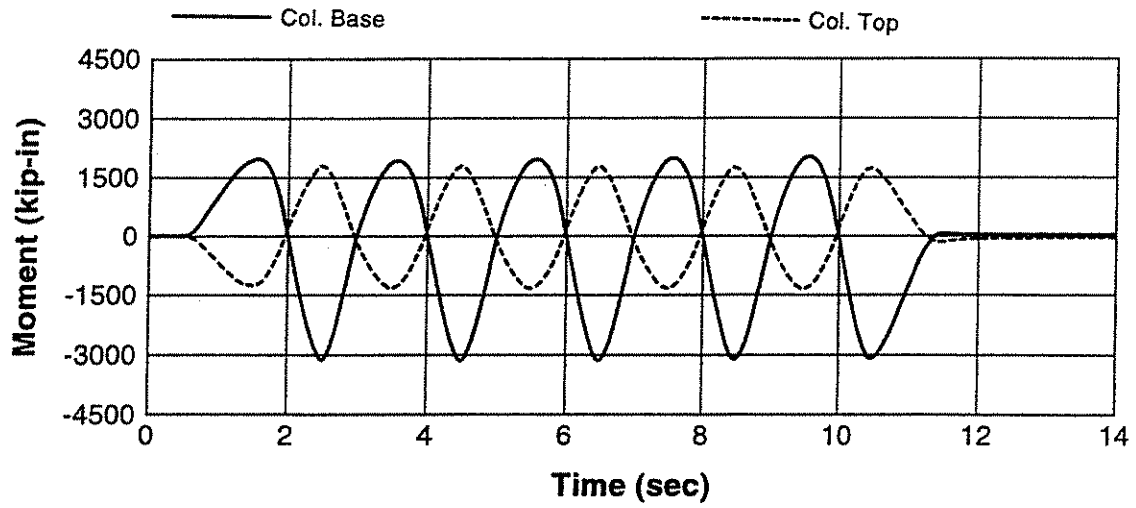

Fig. 5.26a - Moments at top and bottom of first story West column.

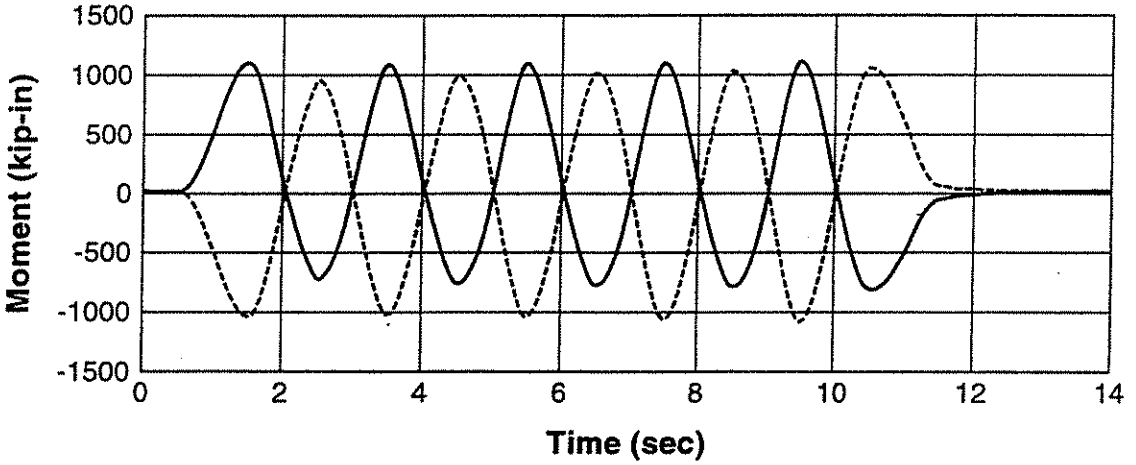

Fig. 5.26b - Moments at top and bottom of second story West column.

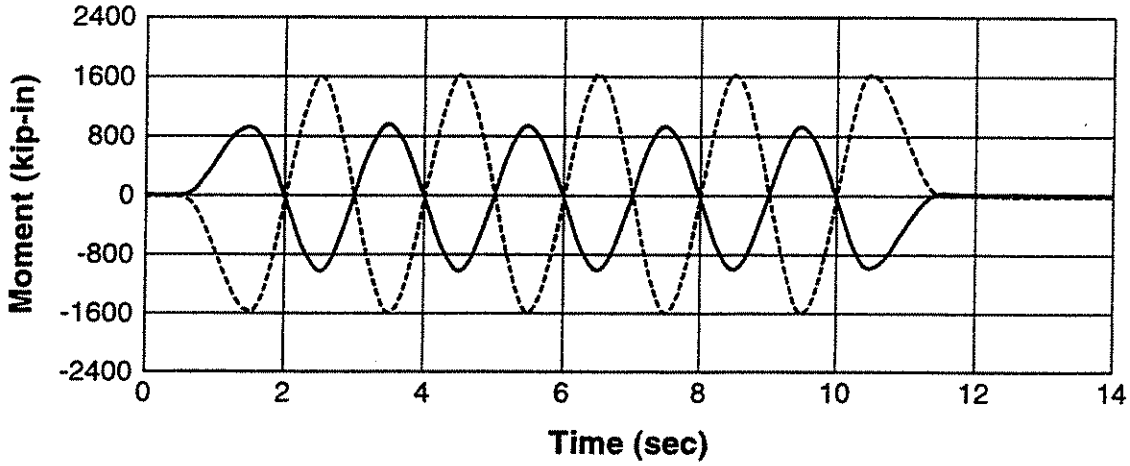

Fig. 5.26c - Moments at top and bottom of third story West column.

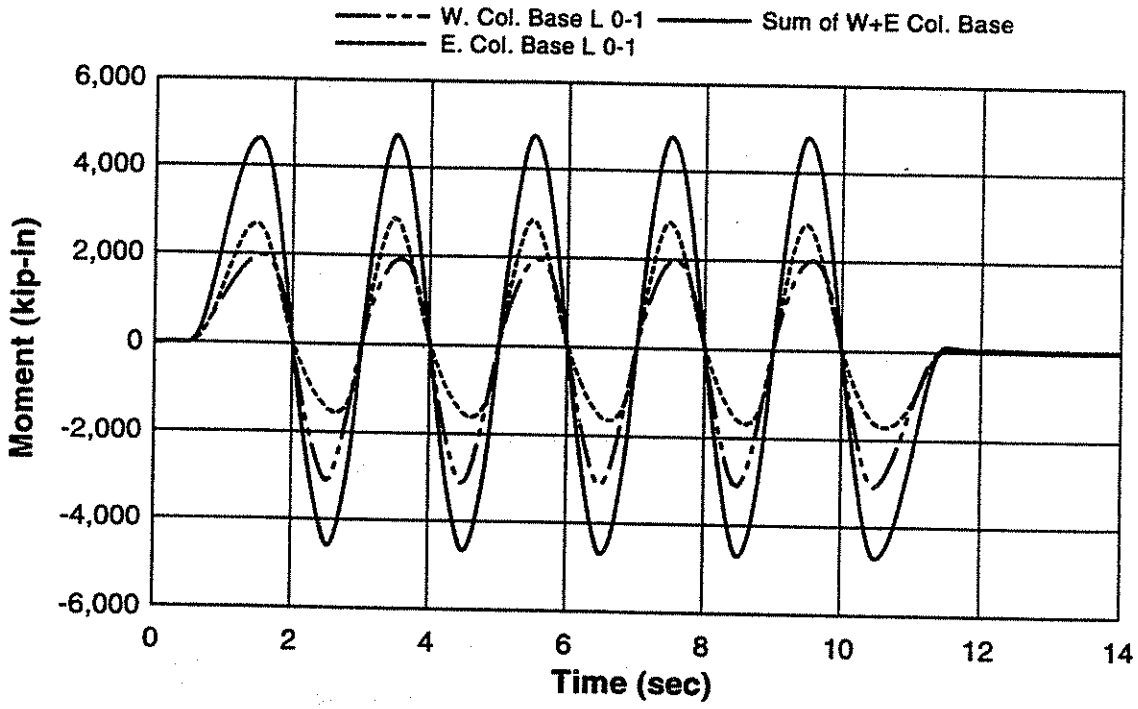

Fig. 5.27 - Combined moment resistance provided by both East and West column base connections.

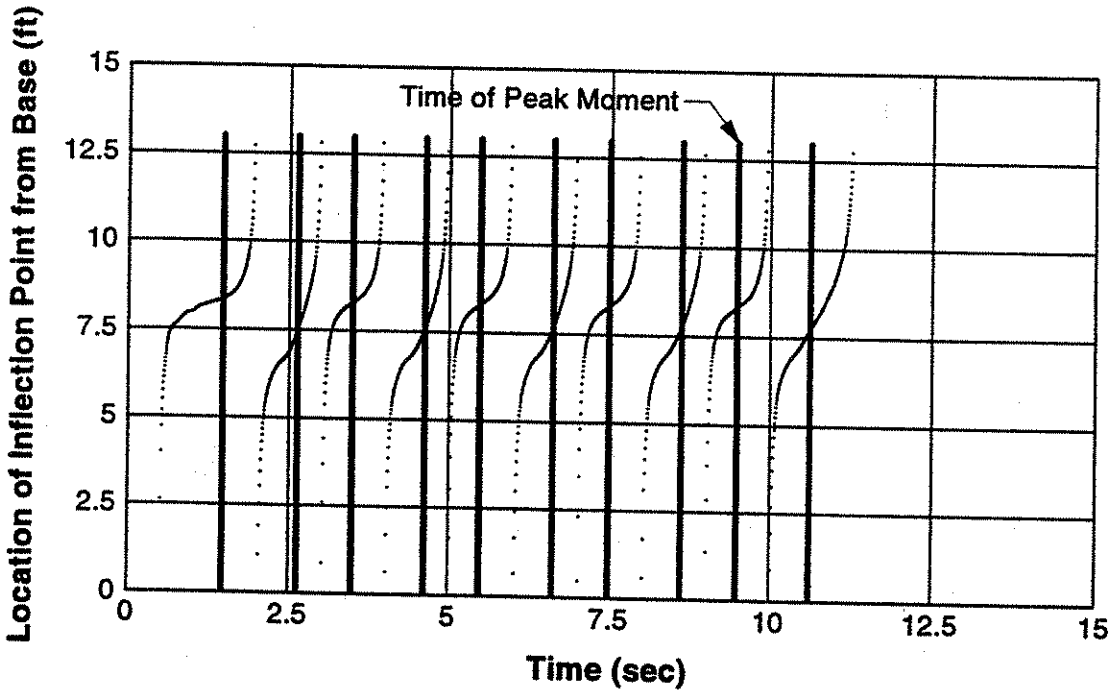

Fig. 5.28 - Inflection point location in East first story column, measured from base.

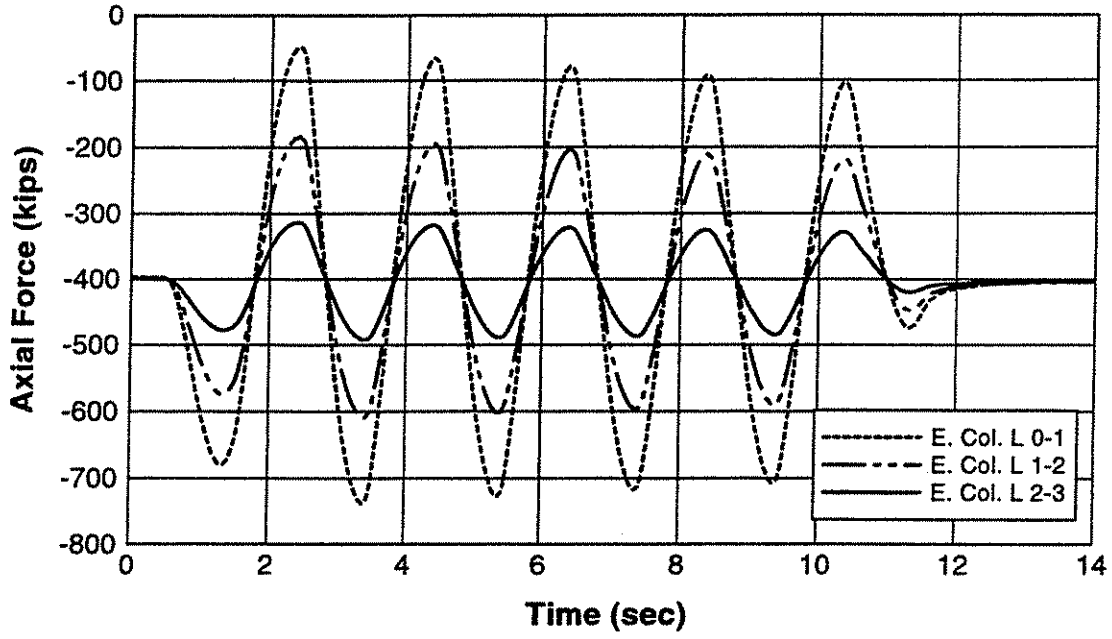

Fig. 5.29 - Axial forces in East column story segments.

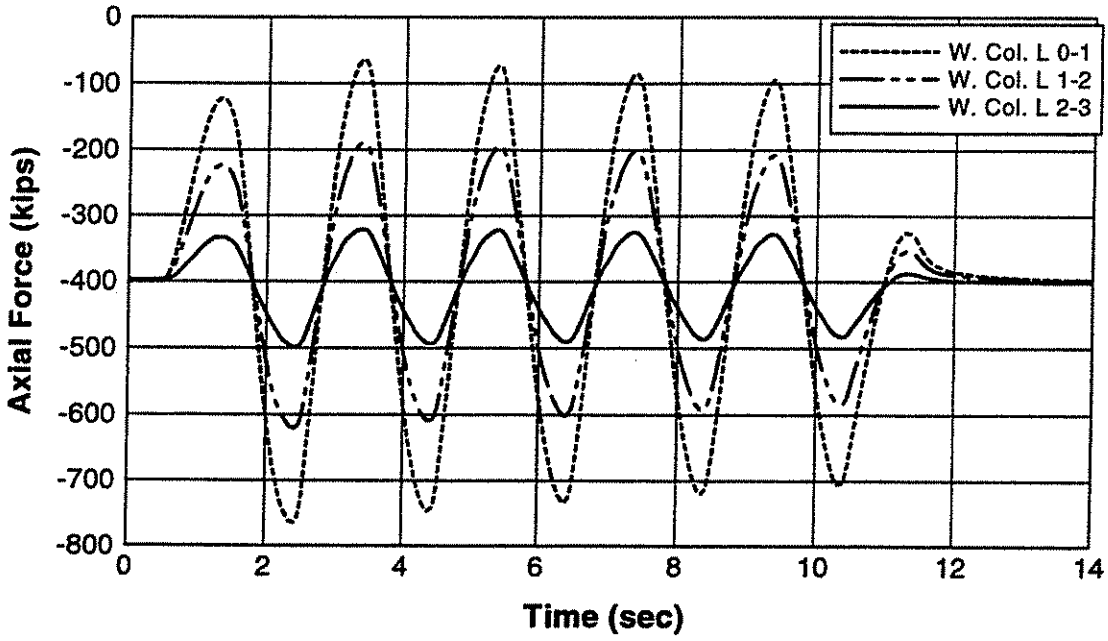

Fig. 5.30 - Axial forces in West column story segments.

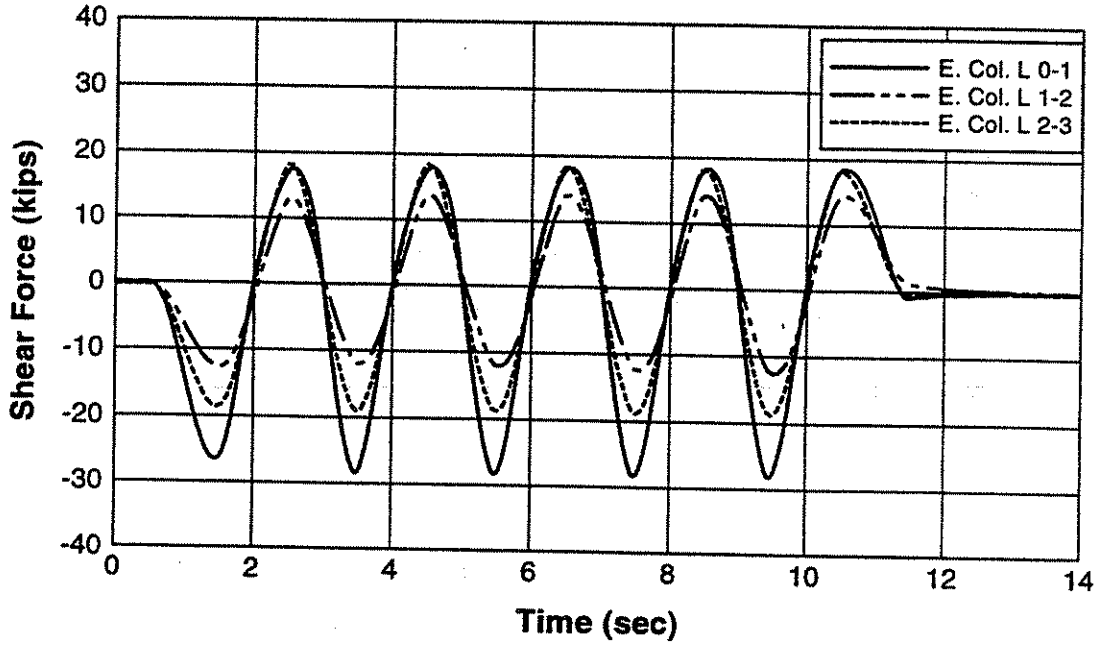

Fig. 5.31 - Shear forces in East column story segments.

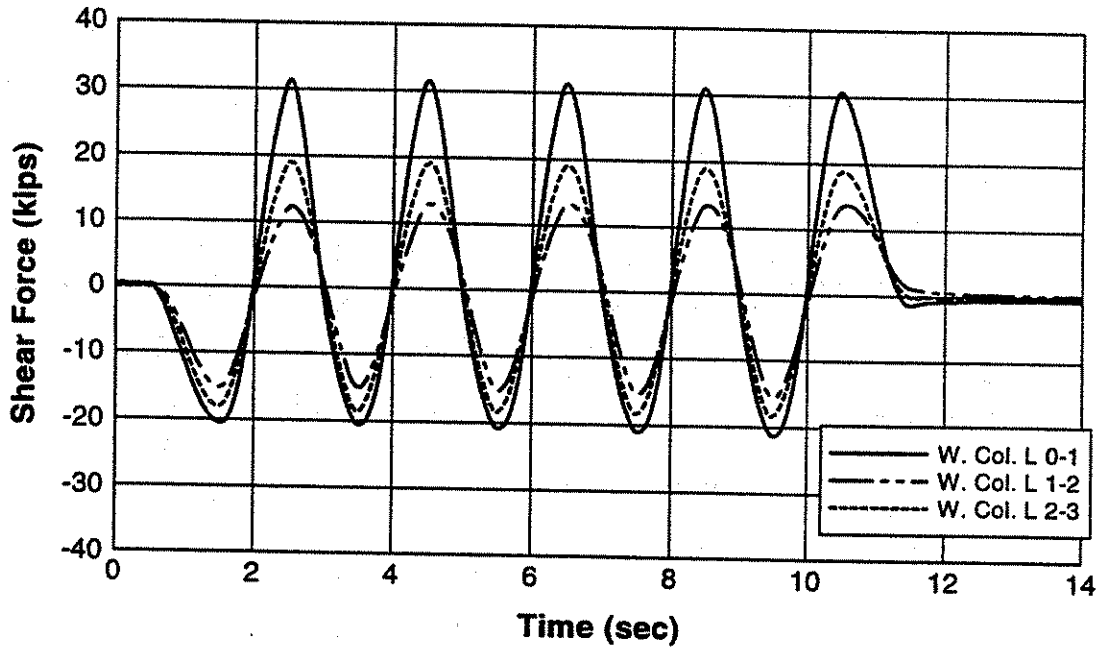

Fig. 5.32 - Shear forces in West column story segments.

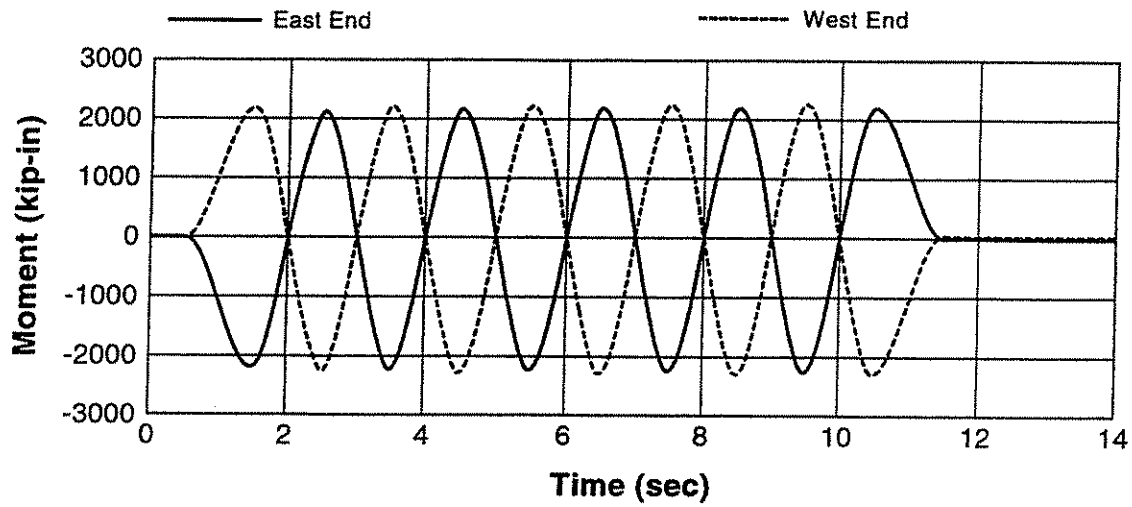

Fig. 5.33a - Moments at East and West ends of first story beam (at column centerline).

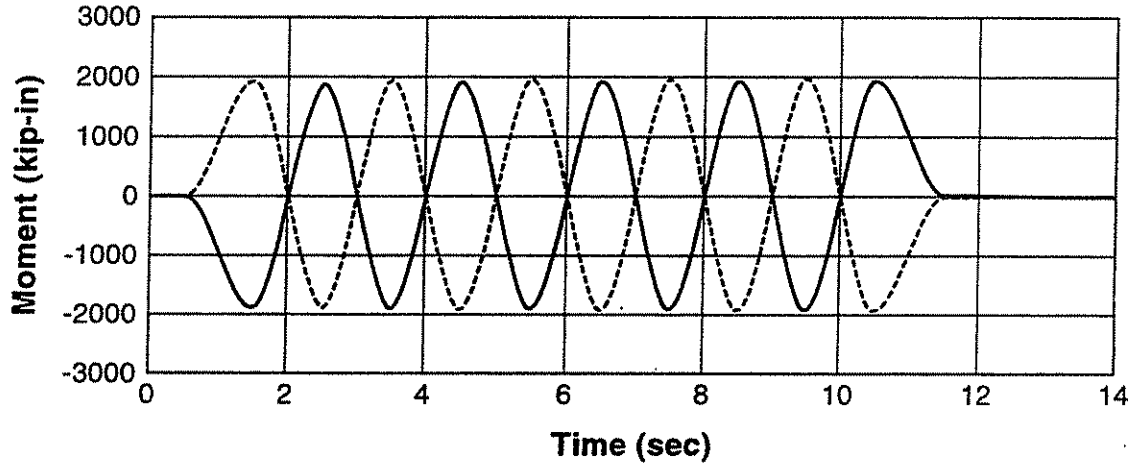

Fig. 5.33b - Moments at East and West ends of second story beam (at column centerline).

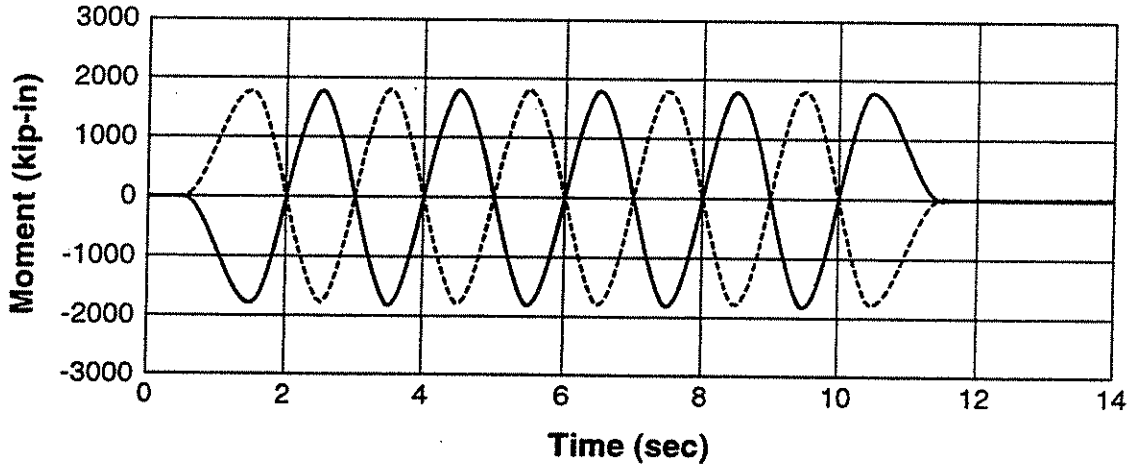

Fig. 5.33c - Moments at East and West ends of third story beam (at column centerline).

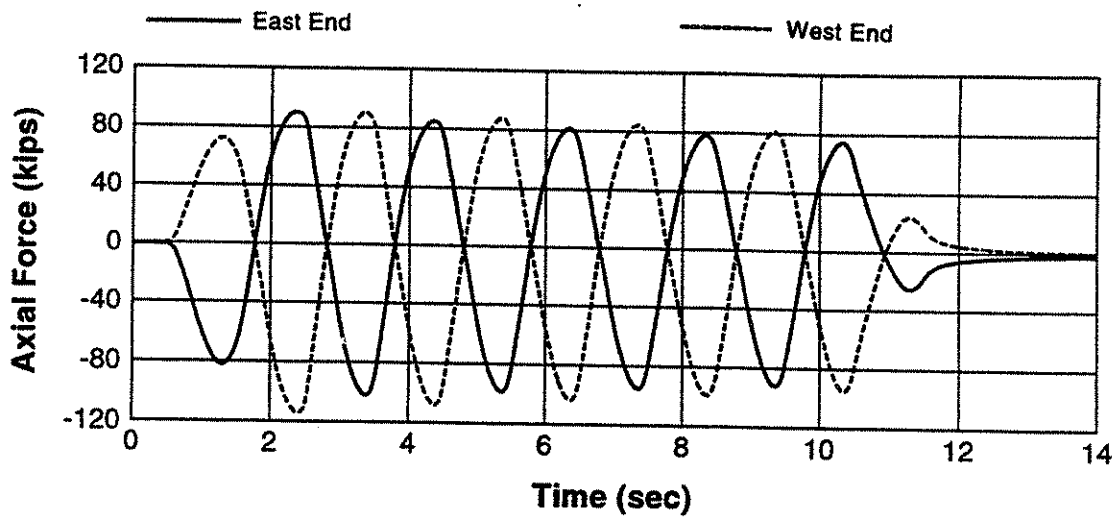

Fig. 5.34a - Axial forces in East and West ends of first story beam.

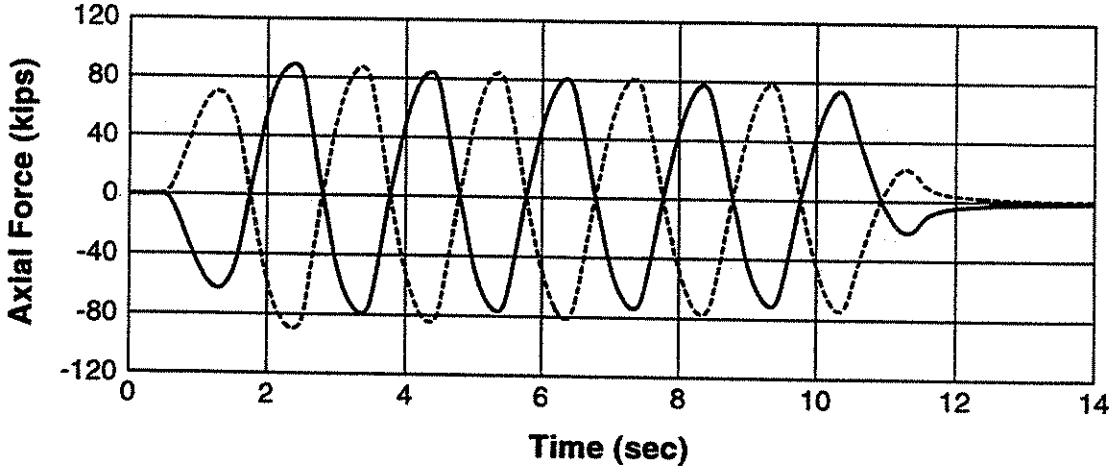

Fig. 5.34b - Axial forces in East and West ends of second story beam.

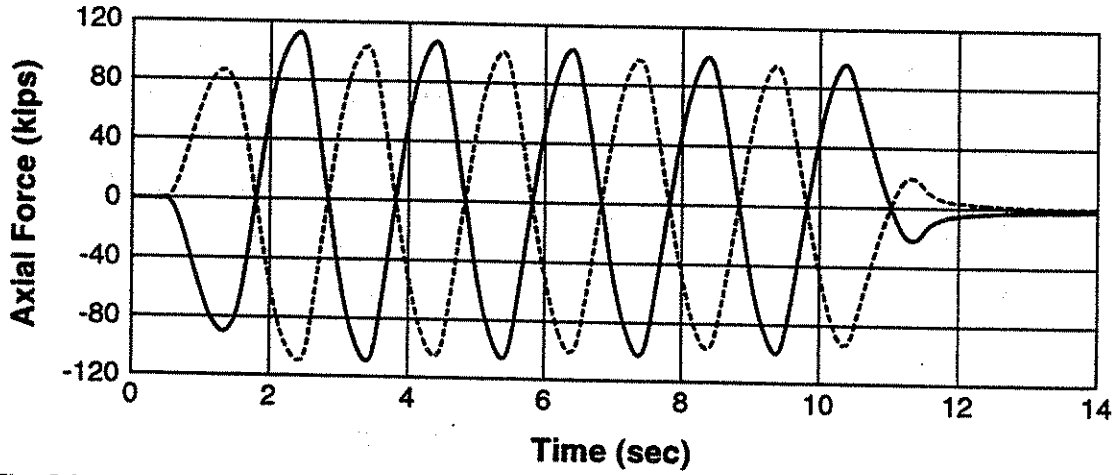

Fig. 5.34c - Axial forces in East and West ends of third story beam.

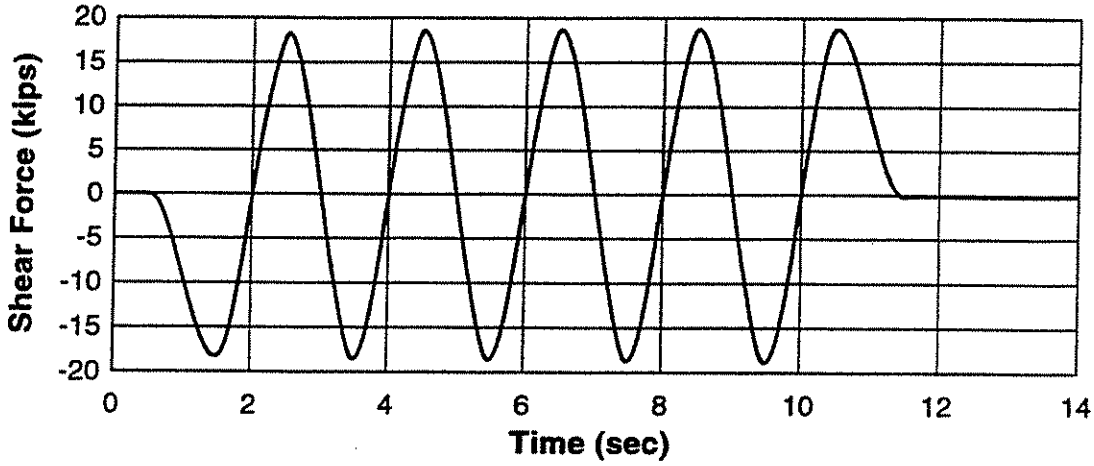

Fig. 5.35a - Shear force in first story beam.

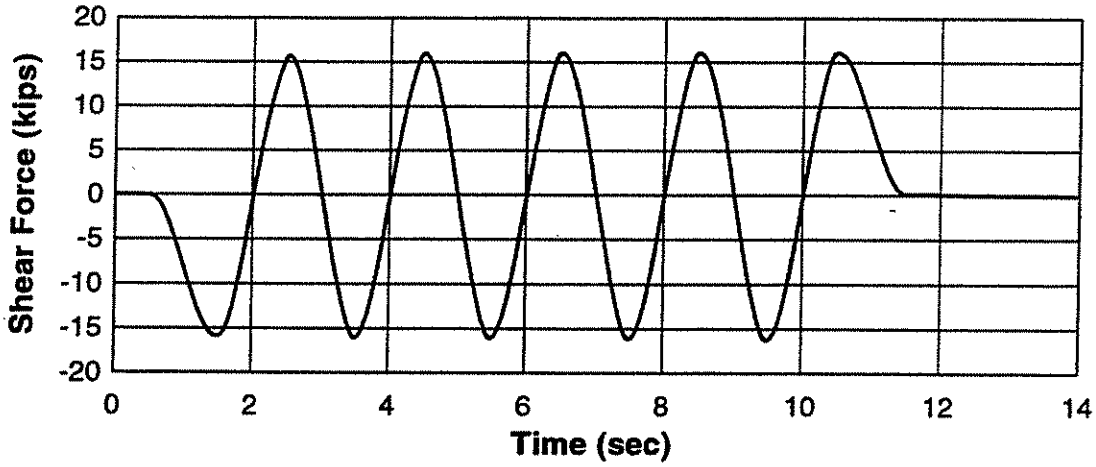

Fig. 5.35b - Shear forces in second story beam.

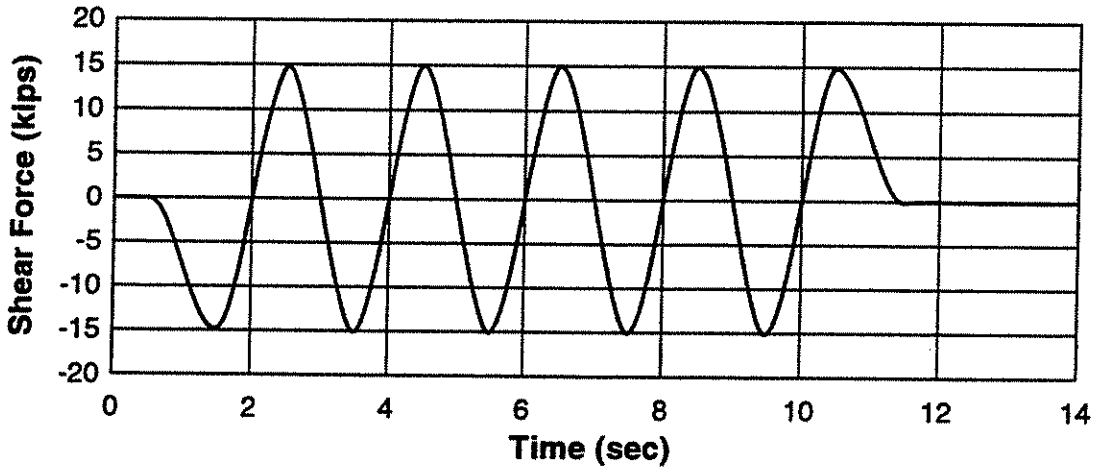

Fig. 5.35c - Shear force in third story beam.

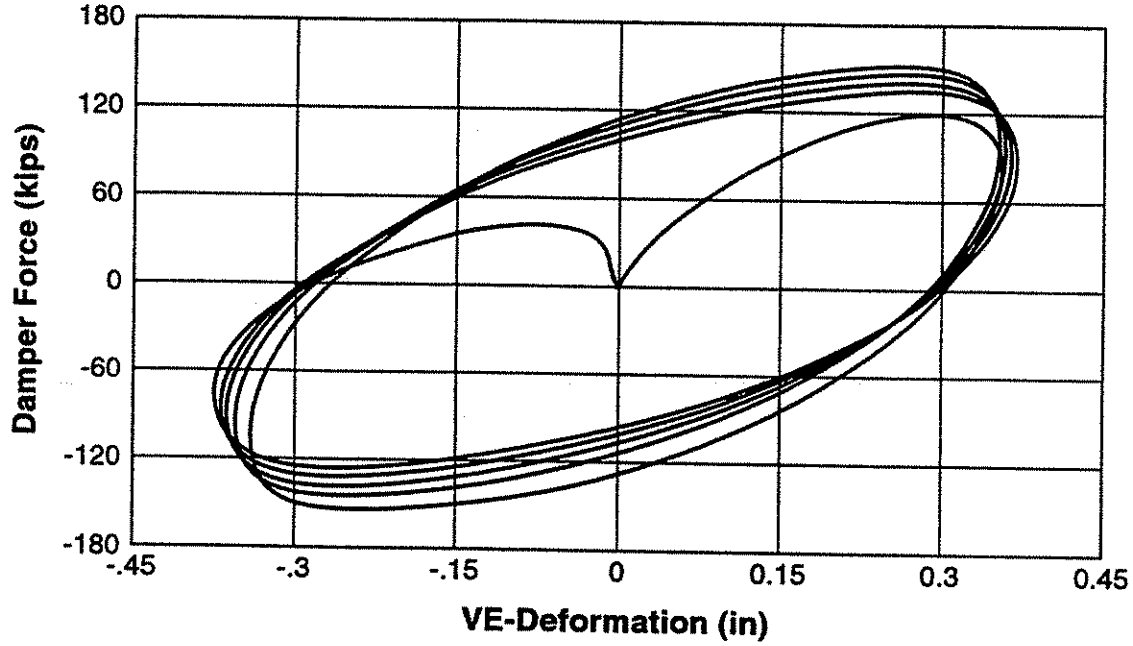

Fig. 5.36a - VE-damper force-deformation response in East first story level.

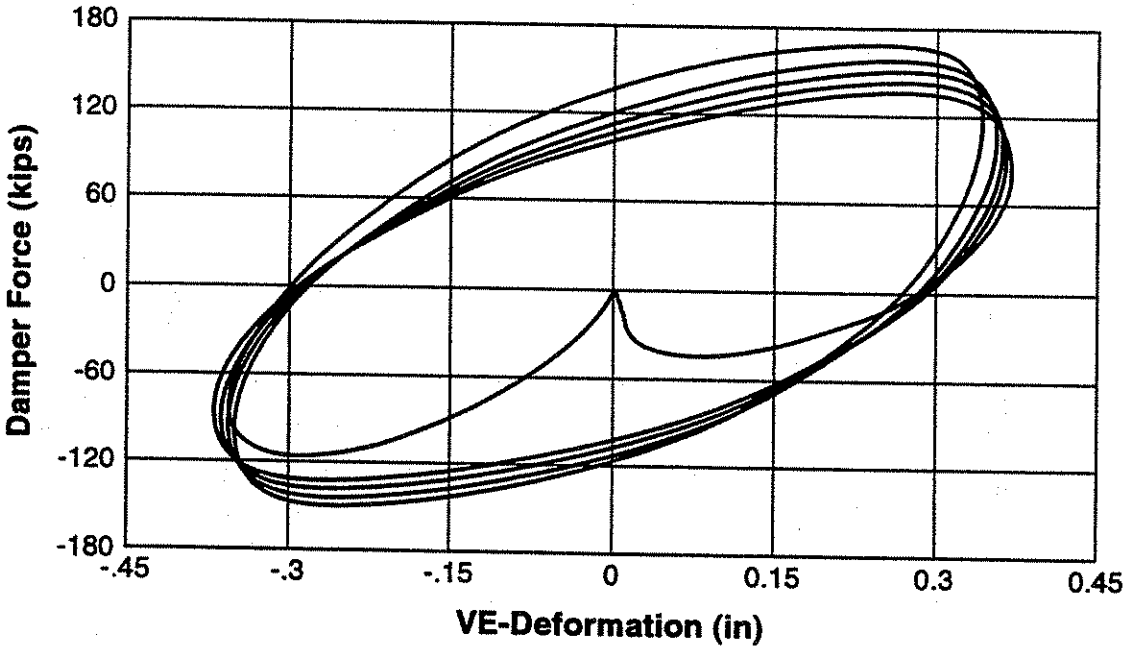

Fig. 5.36b - VE-damper force-deformation response in West first story level.

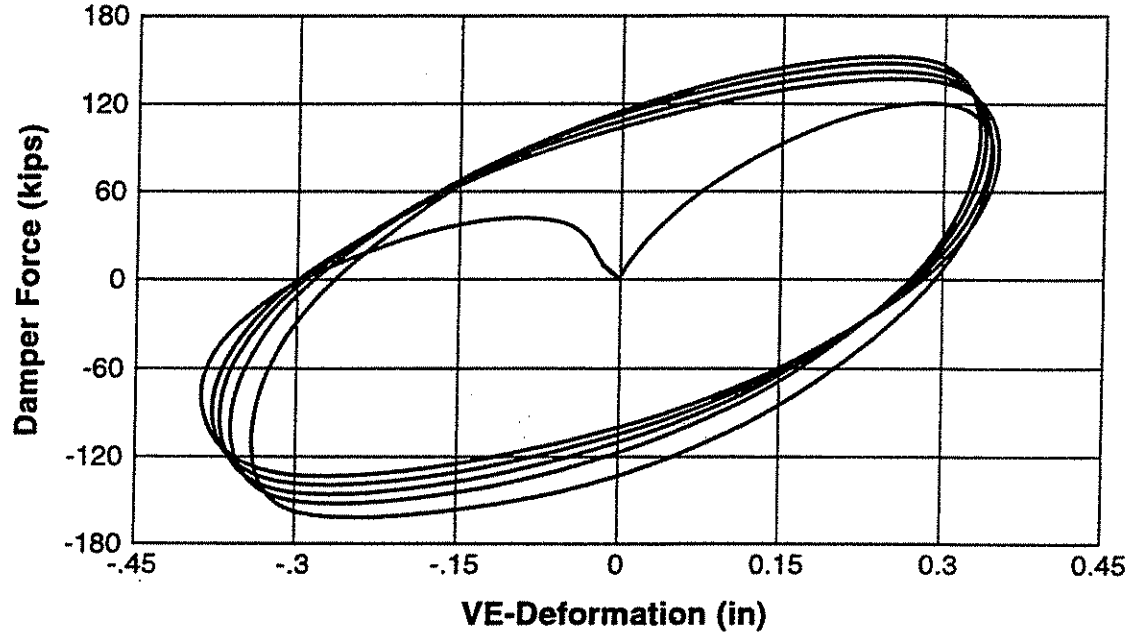

Fig. 5.37a - VE-damper force-deformation response in East second story level.

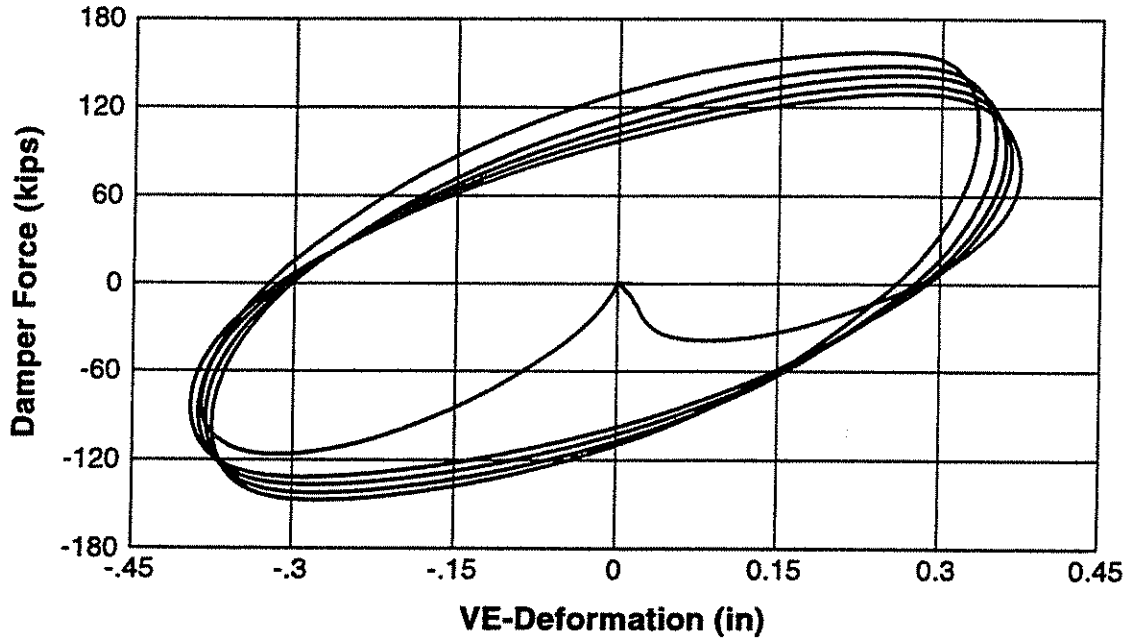

Fig. 5.37b - VE-damper force-deformation response in West second story level.

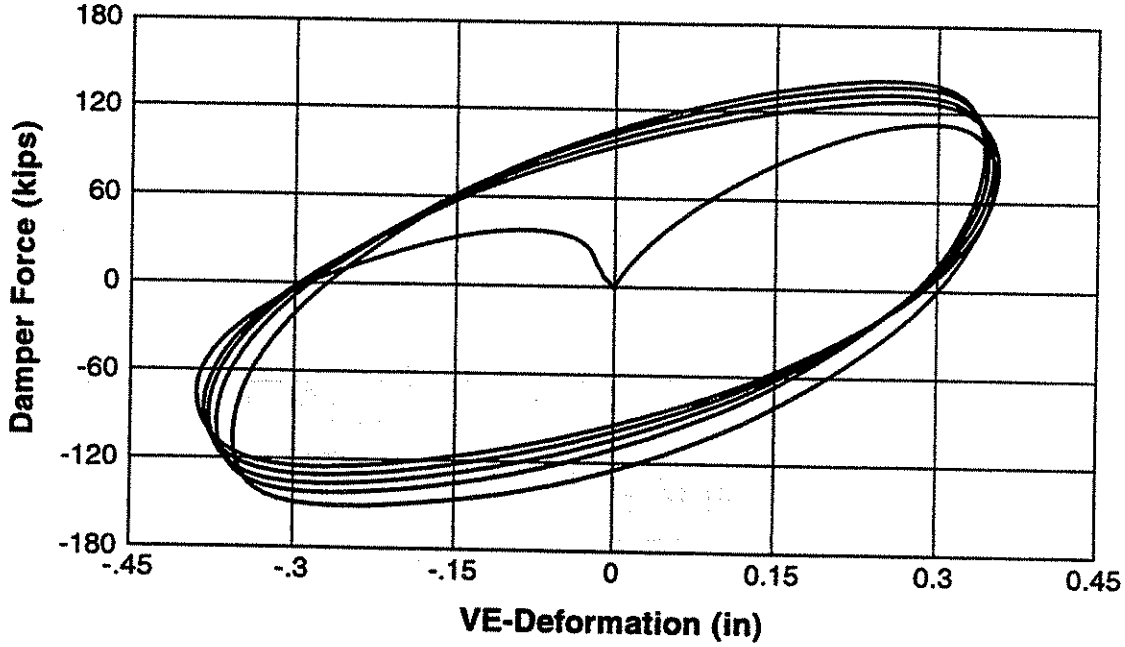

Fig. 5.38a - VE-damper force-deformation response in East third story level.

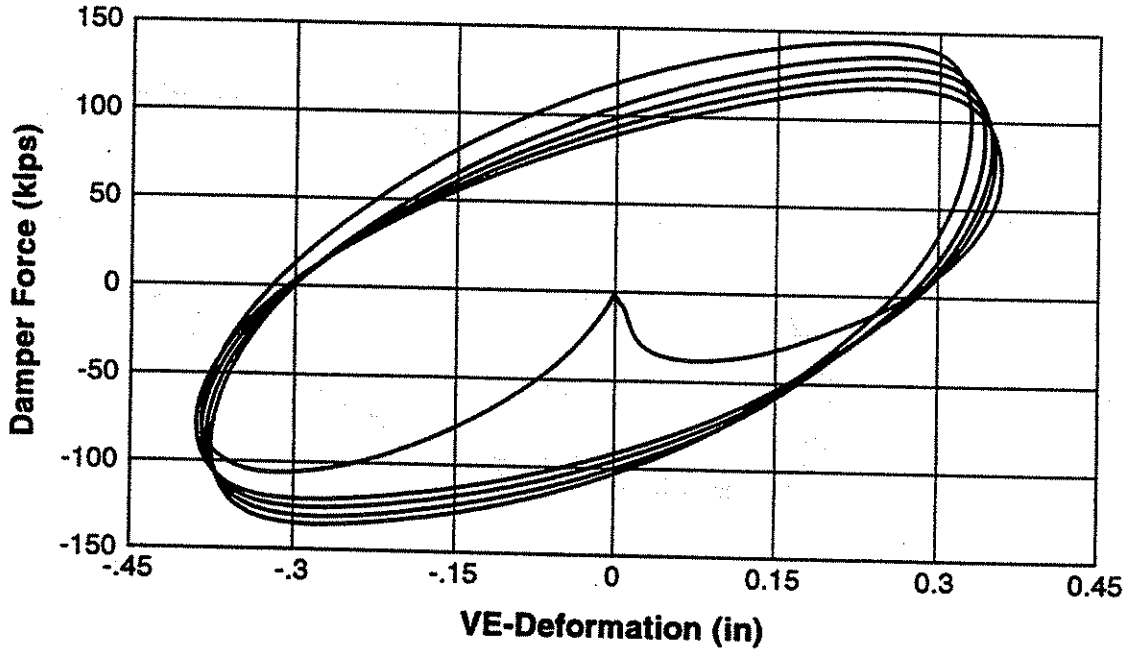

Fig. 5.38b - VE-damper force-deformation response in West third story level.

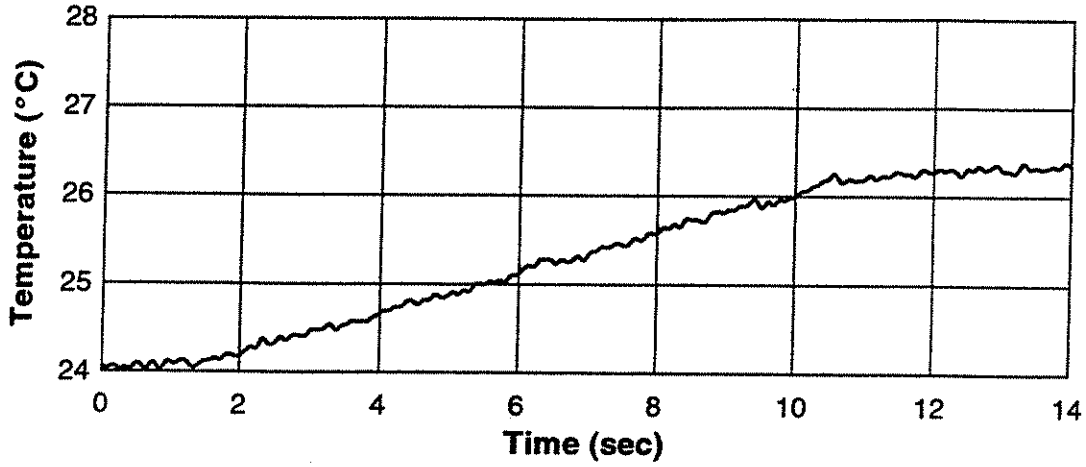

Fig. 5.39a - Temperature rise in first story VE-damper.

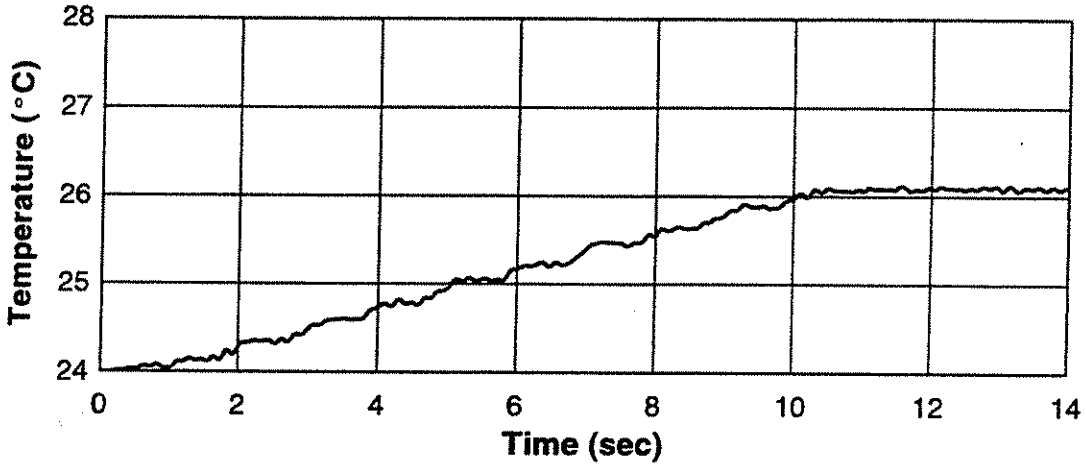

Fig. 5.39b - Temperature rise in second story VE-damper.

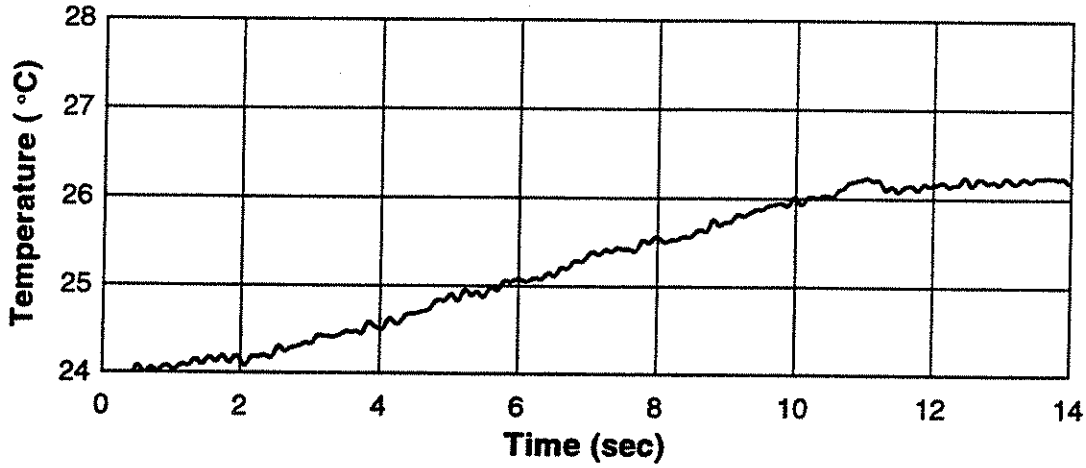

Fig. 5.39c - Temperature rise in third story VE-damper.

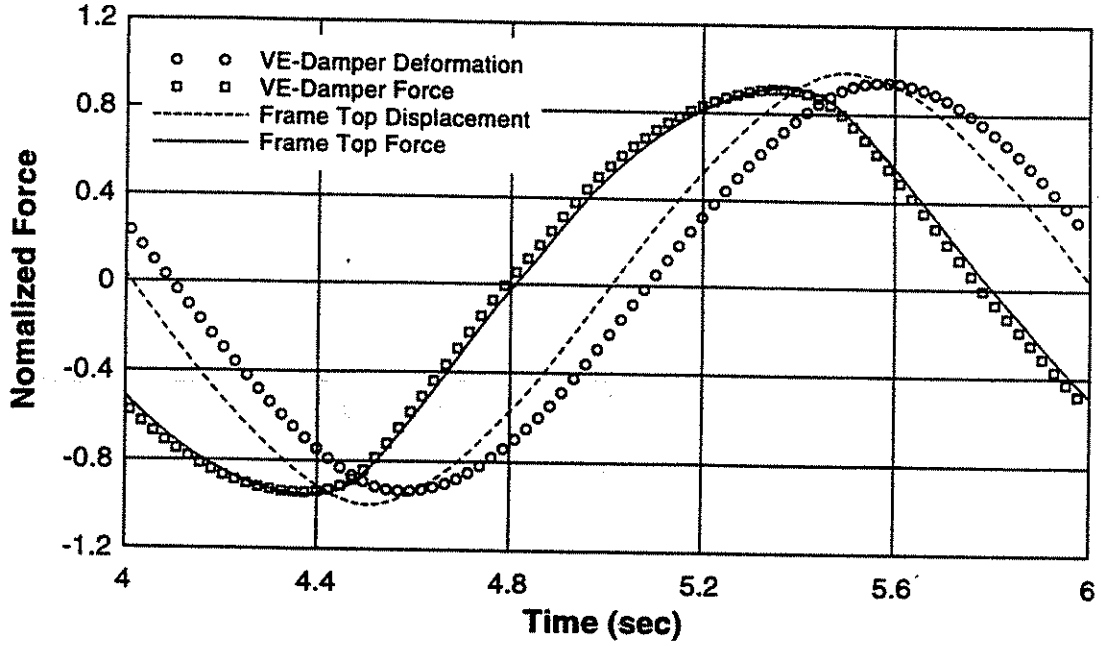

Fig. 5.40a - Time lag between normalized frame and damper (second story East) responses.

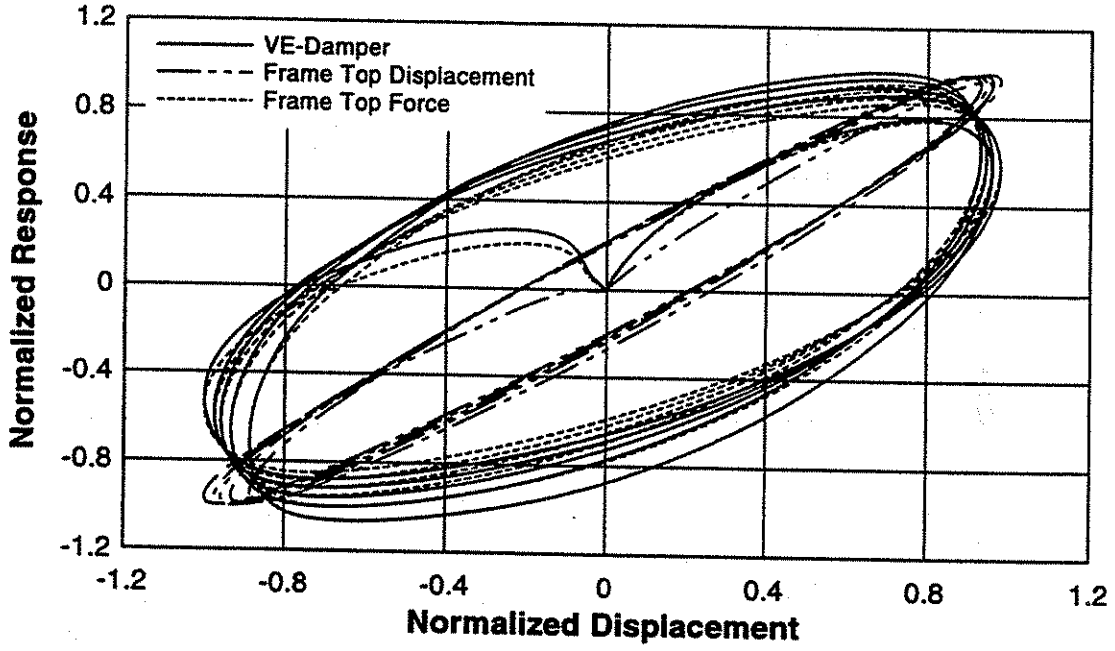

Fig. 5.40b - Normalized frame and damper (second story East) responses.

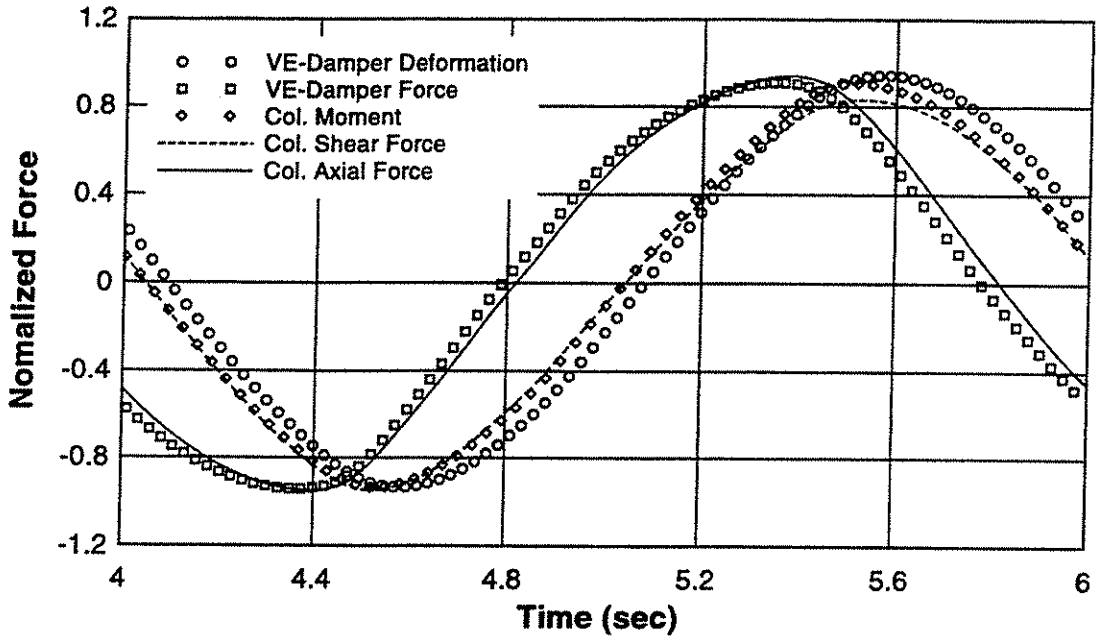

Fig. 5.41a - Time lag between normalized column (top of second story East) and damper (second story East) responses.

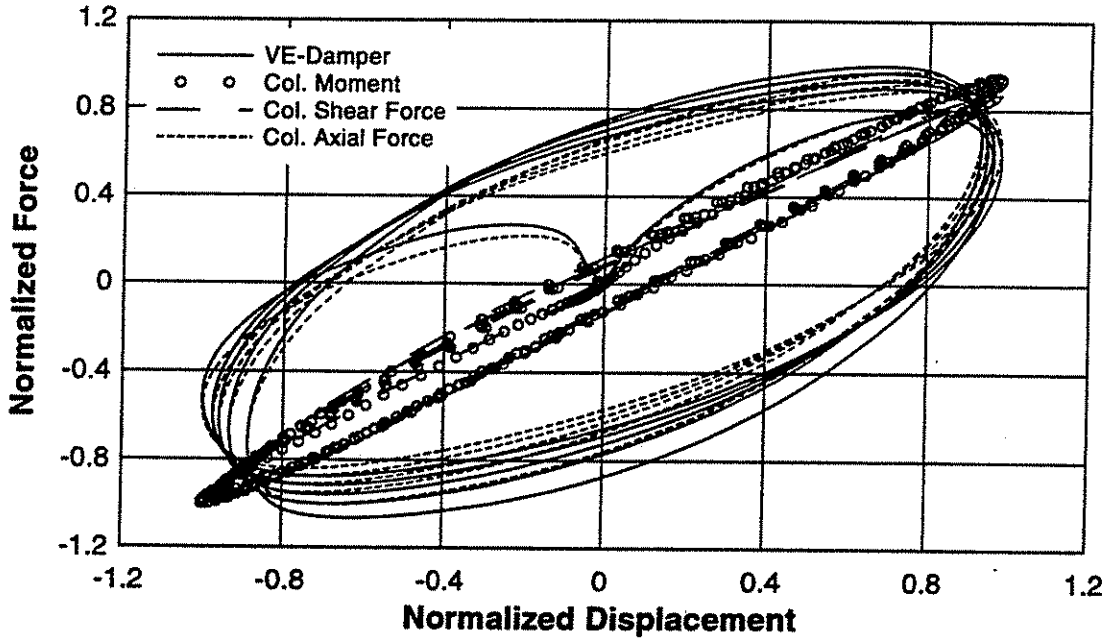

Fig. 5.41b - Normalized column (top of second story East) and damper (second story East) responses.

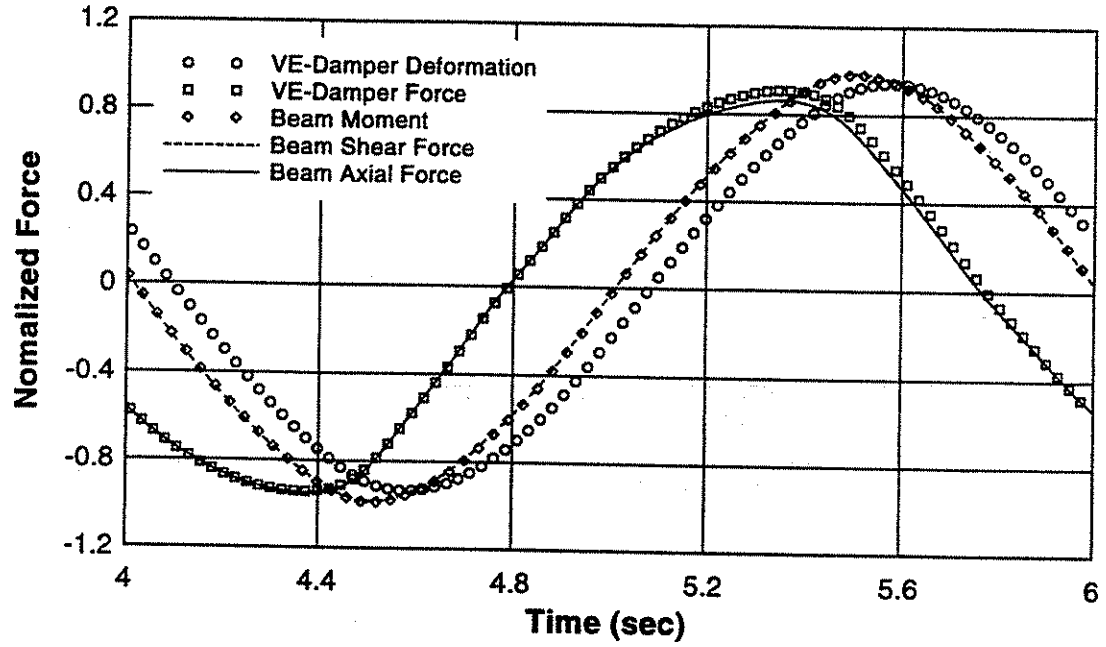

Fig. 5.42a - Time lag between normalized beam (second story East) and damper (second story East) responses.

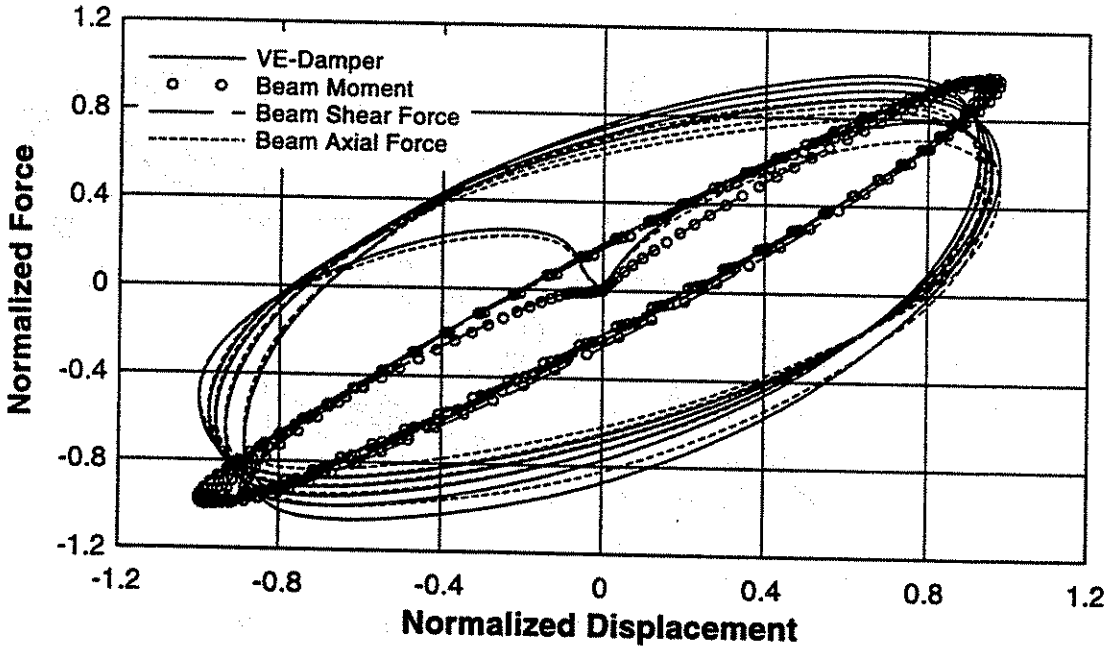

Fig. 5.42b - Normalized beam (second story East) and damper (second story East) responses.

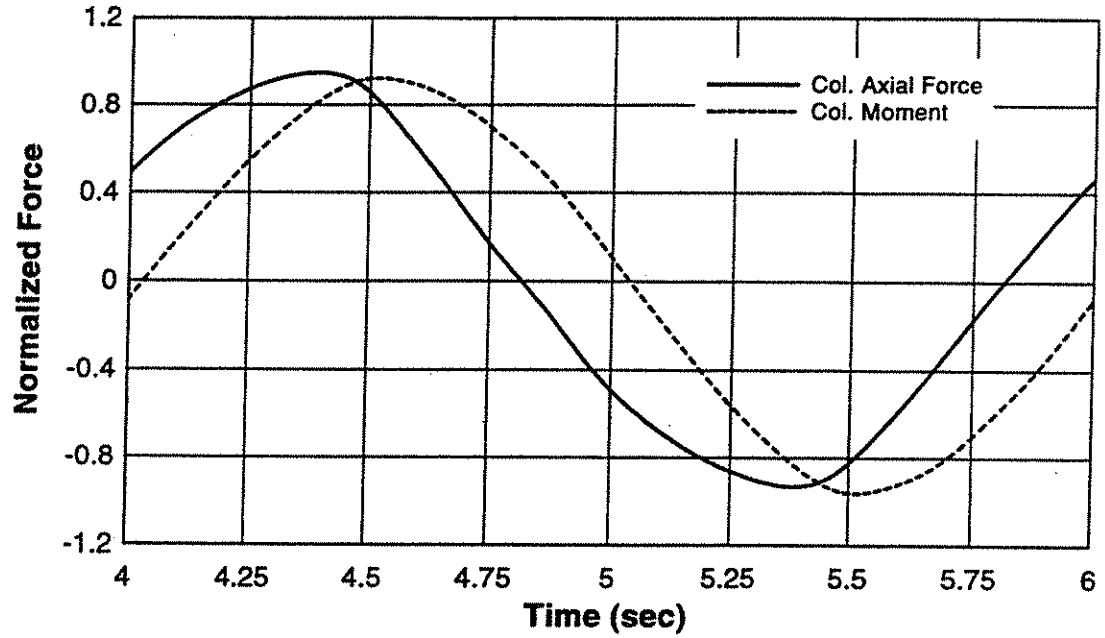

Fig. 5.43a - Time lag between normalized axial force and moment in column.

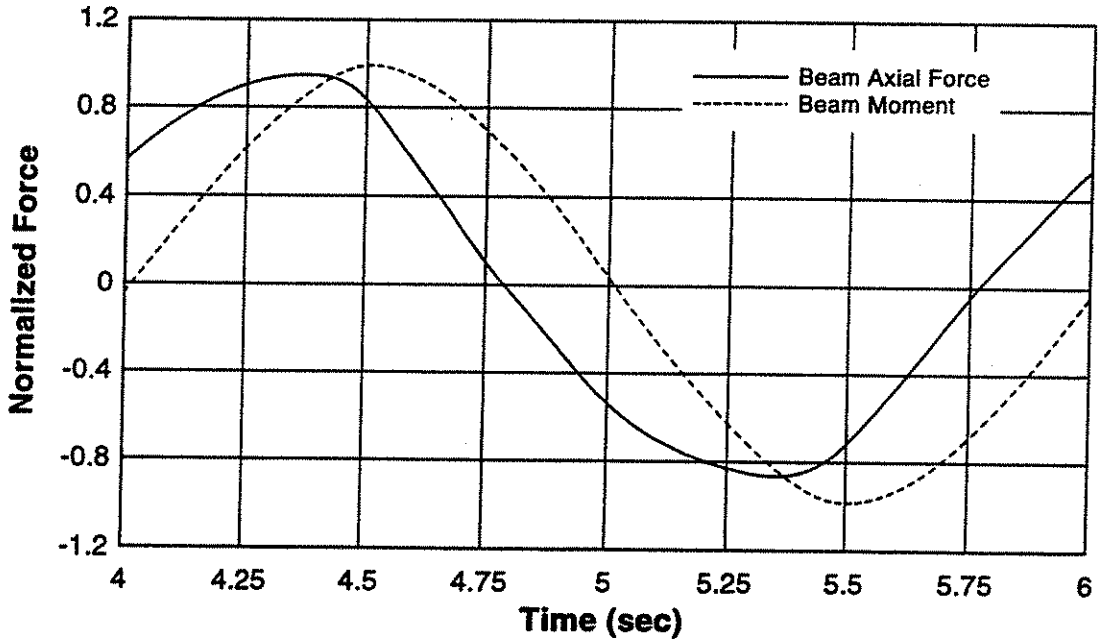

Fig. 5.43b - Time lag between normalized axial force and moment in beam.

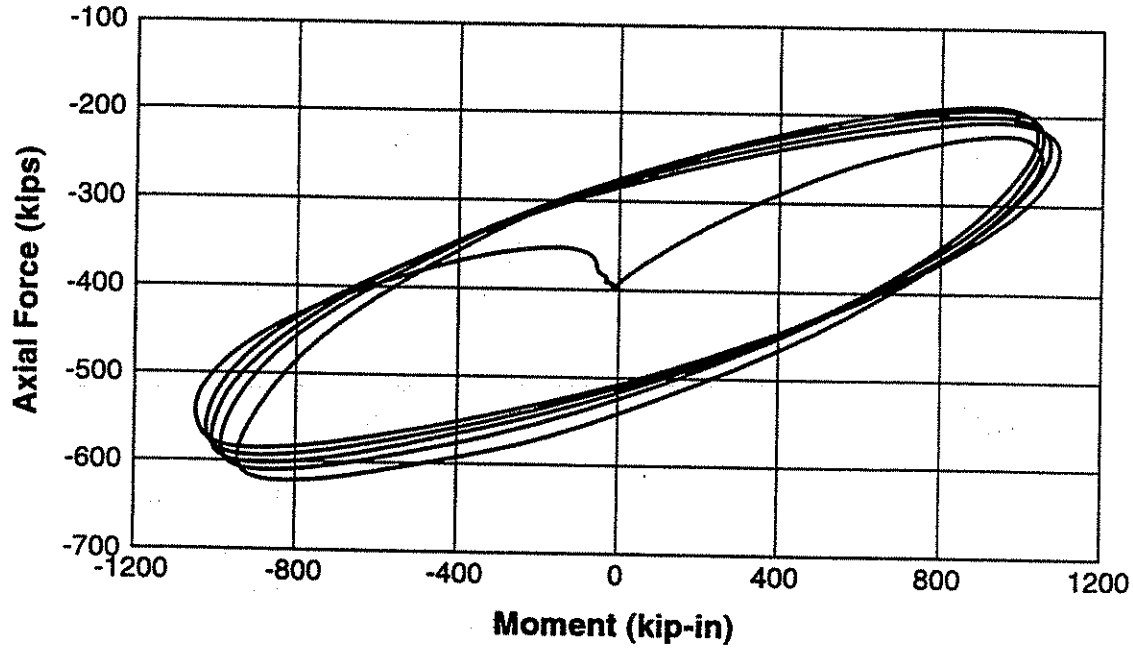

Fig. 5.44a - Moment-axial force interaction for column.

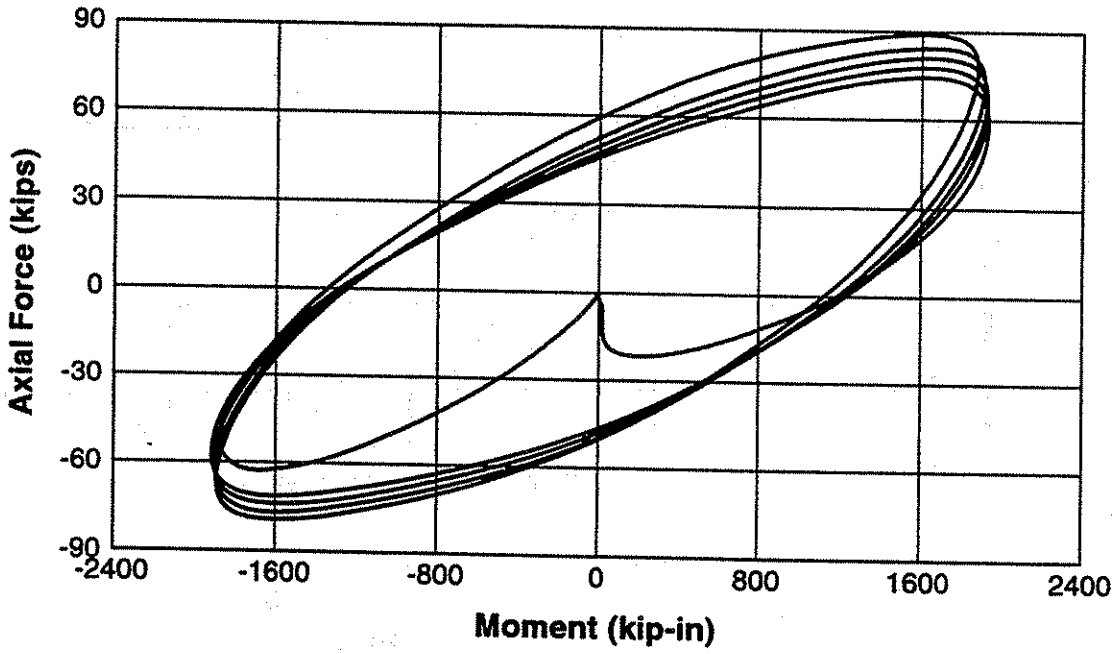

Fig. 5.44b - Moment-axial force interaction for beam.

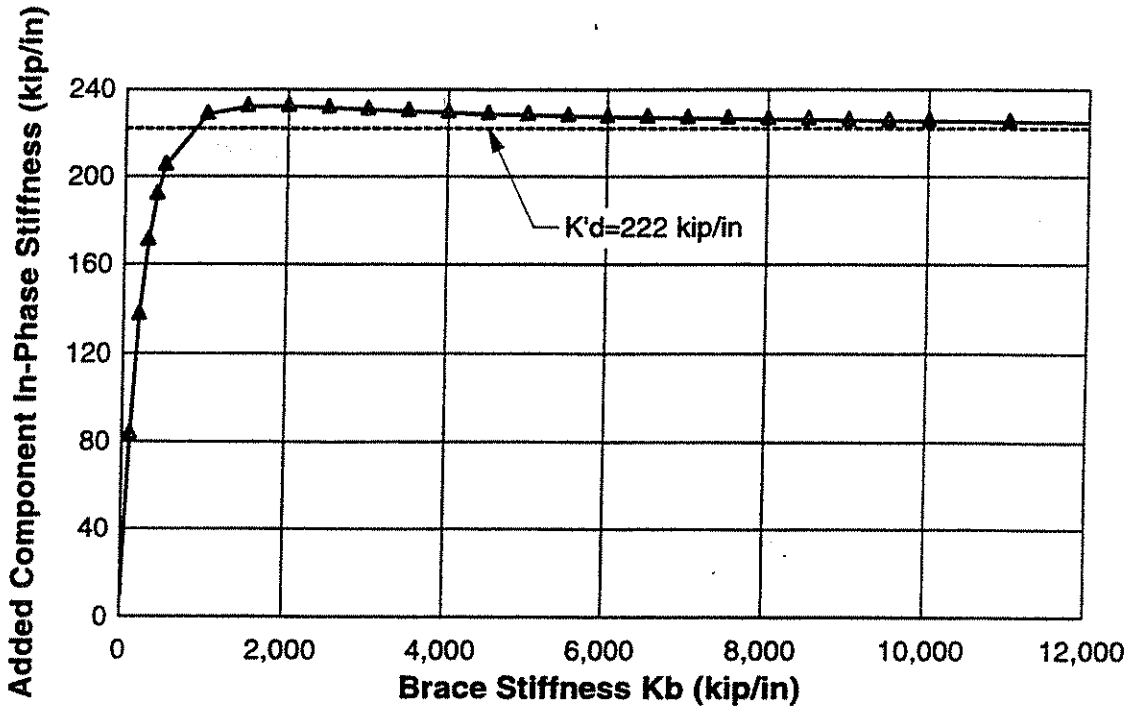

Fig. 5.45 - Influence of brace stiffness on added component stiffness.

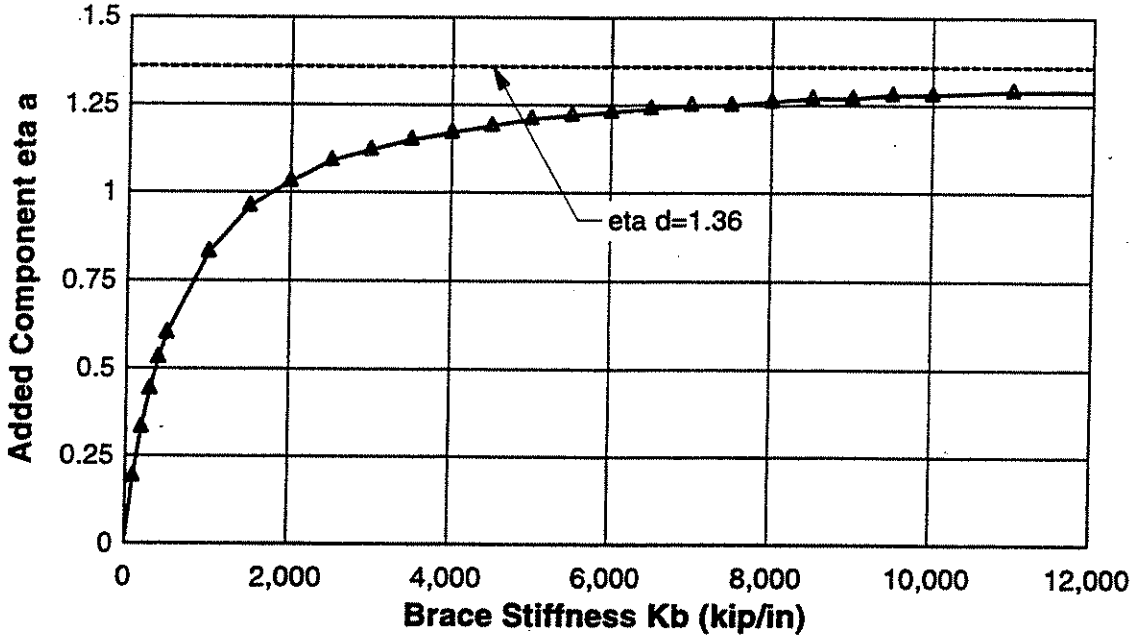

Fig. 5.46 - Influence of brace stiffness on added component η_a.

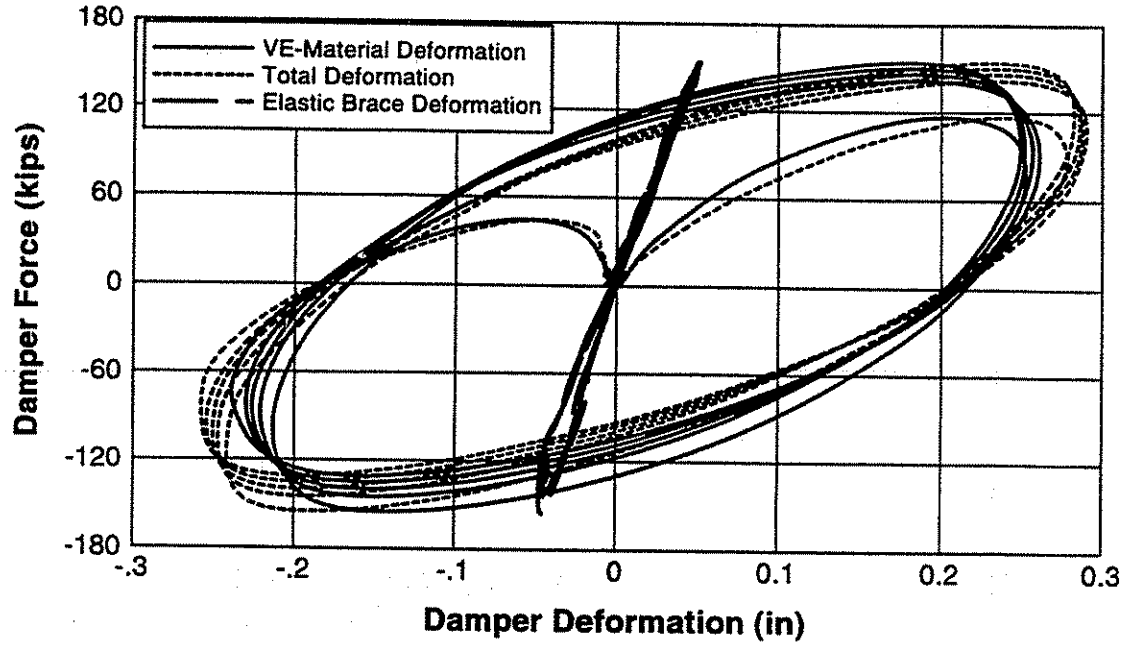

Fig. 5.47 - Example measured added component, damper, and brace force-deformation response for first story VE-dampers.

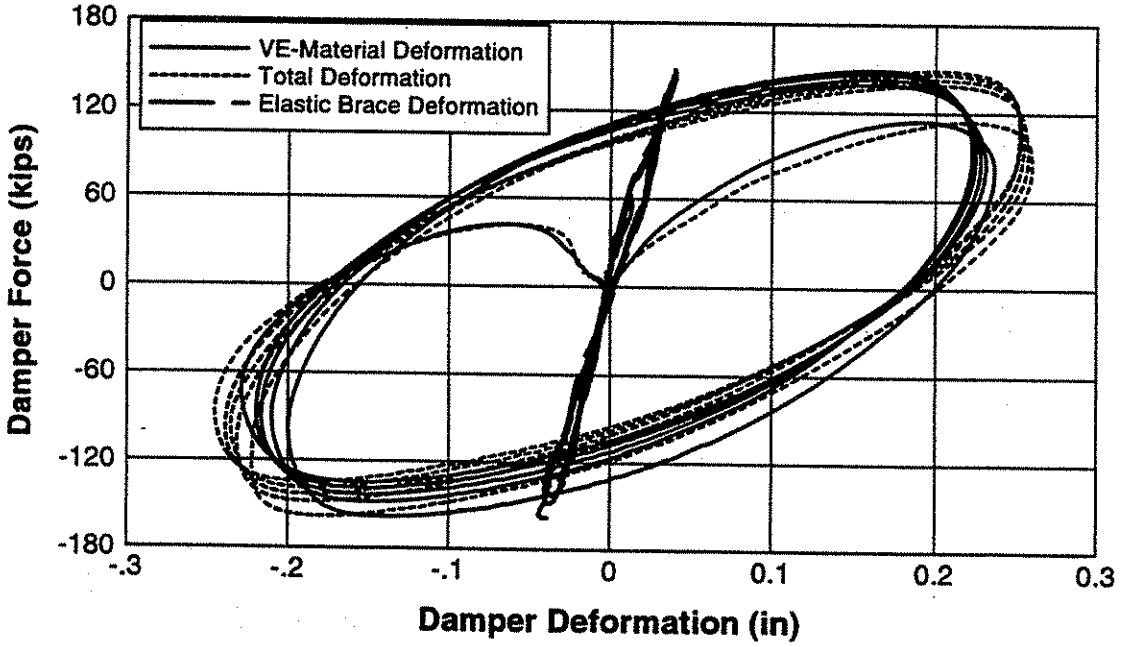

Fig. 5.48 - Example measured added component, damper, and brace force-deformation response for second and third story VE-dampers.

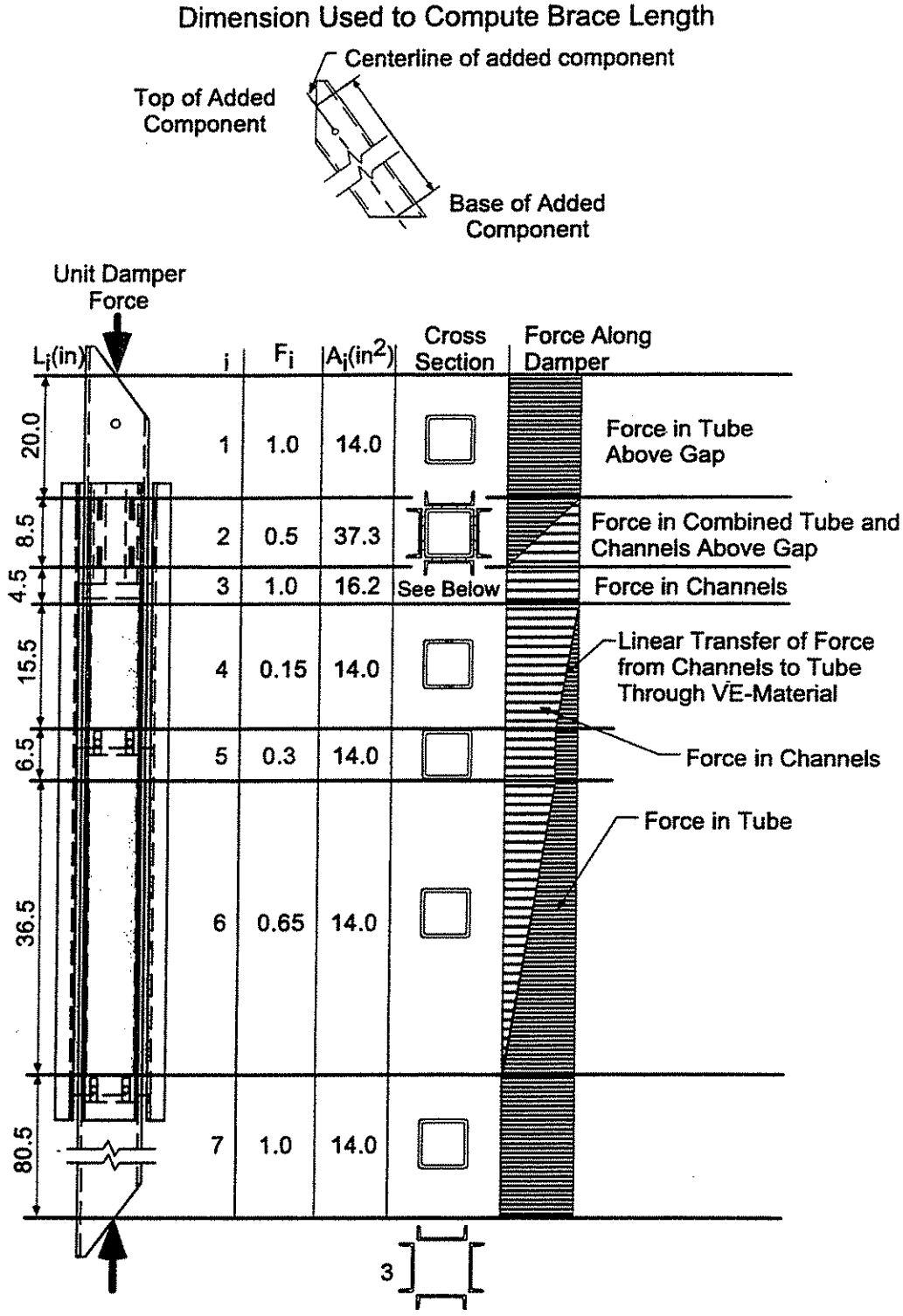

Fig. 5.49 - Length of brace and method used for computing brace stiffness.

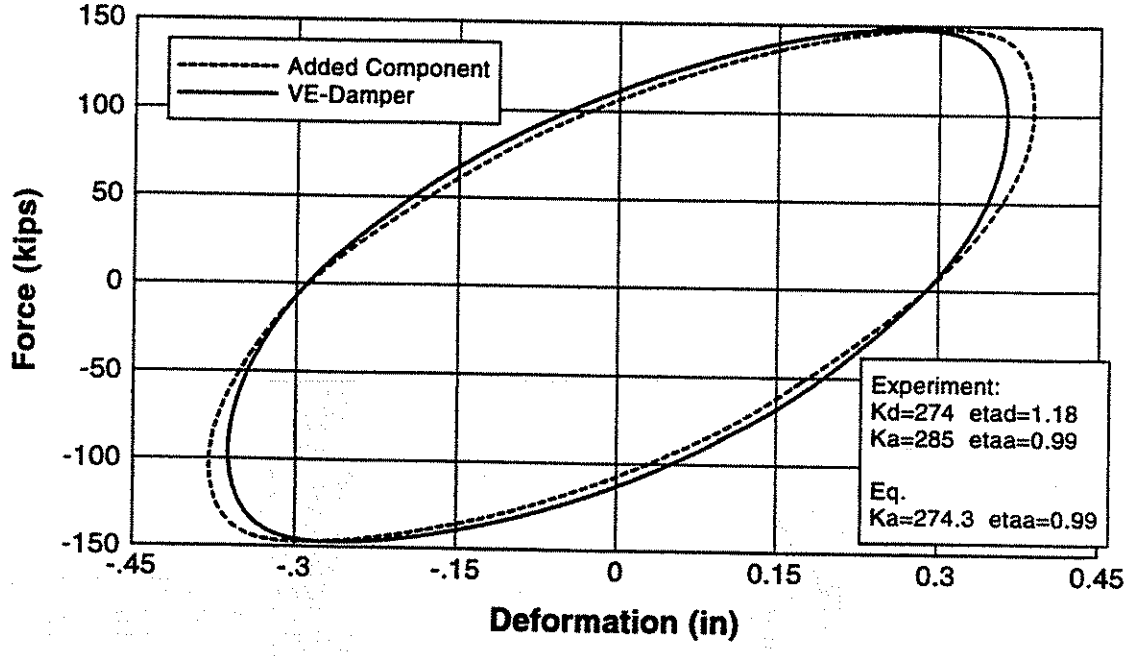

Fig. 5.50 - Comparison of measured and computed added component properties.

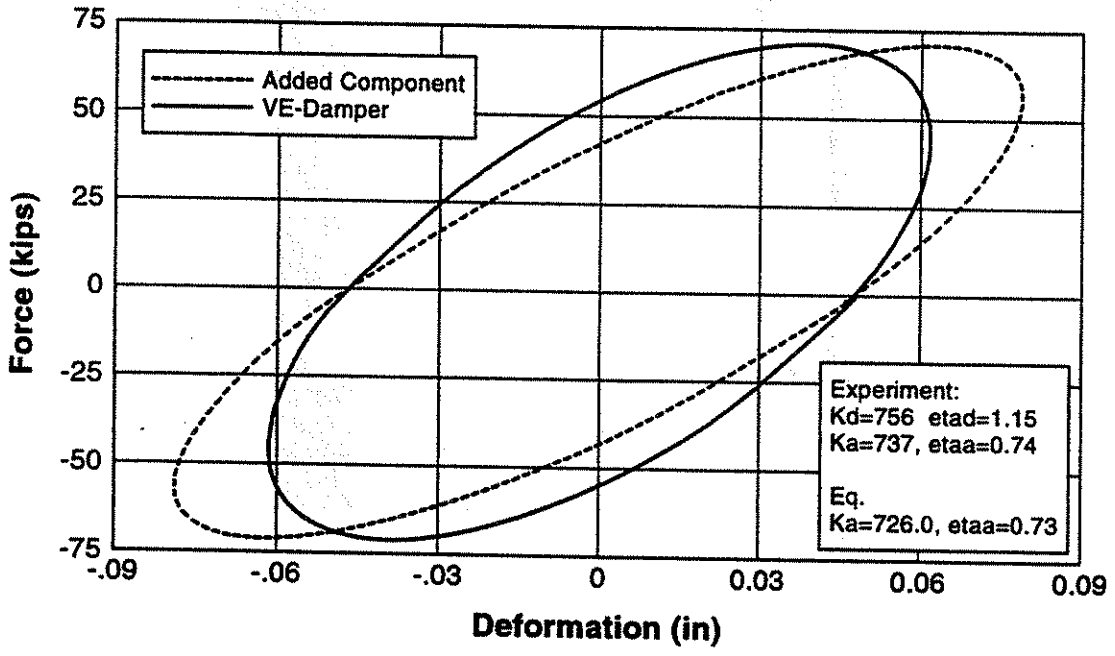

Fig. 5.51 - Comparison of measured and computed added component properties.

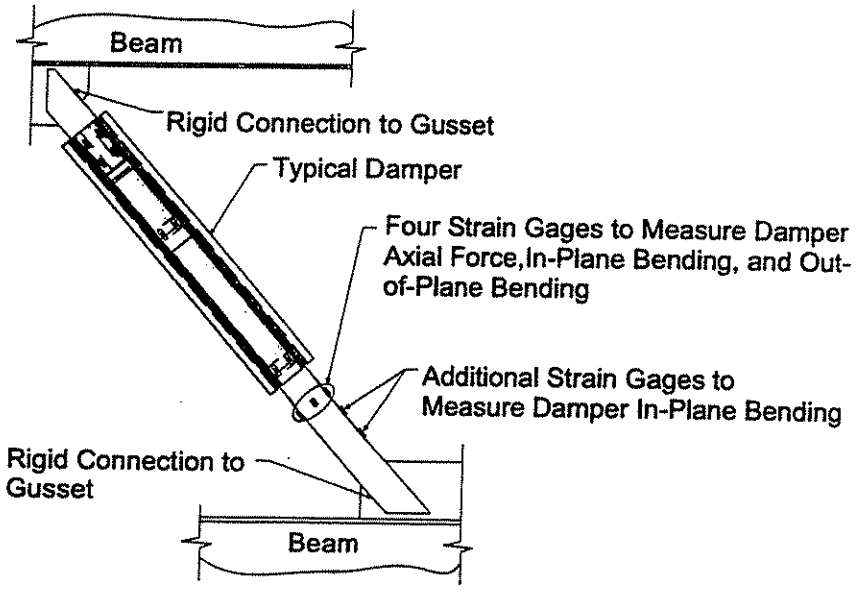

Fig. 5.52 - Additional strain gages on brace to determine moment gradient in added component.

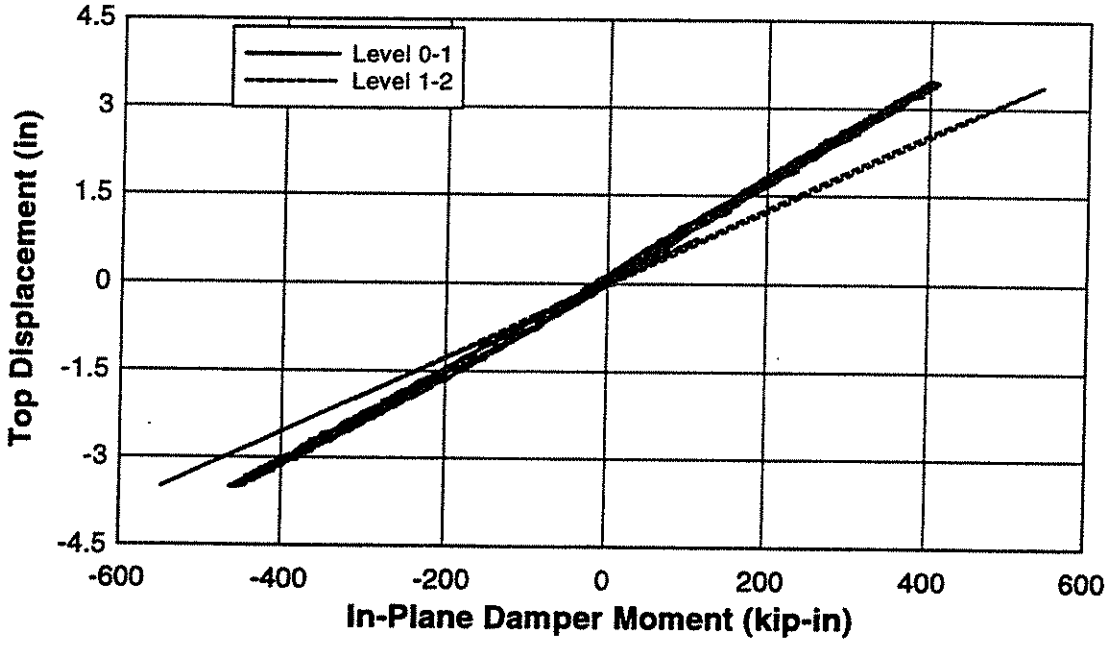

Fig. 5.53 - In-plane moment at bottom of added components.

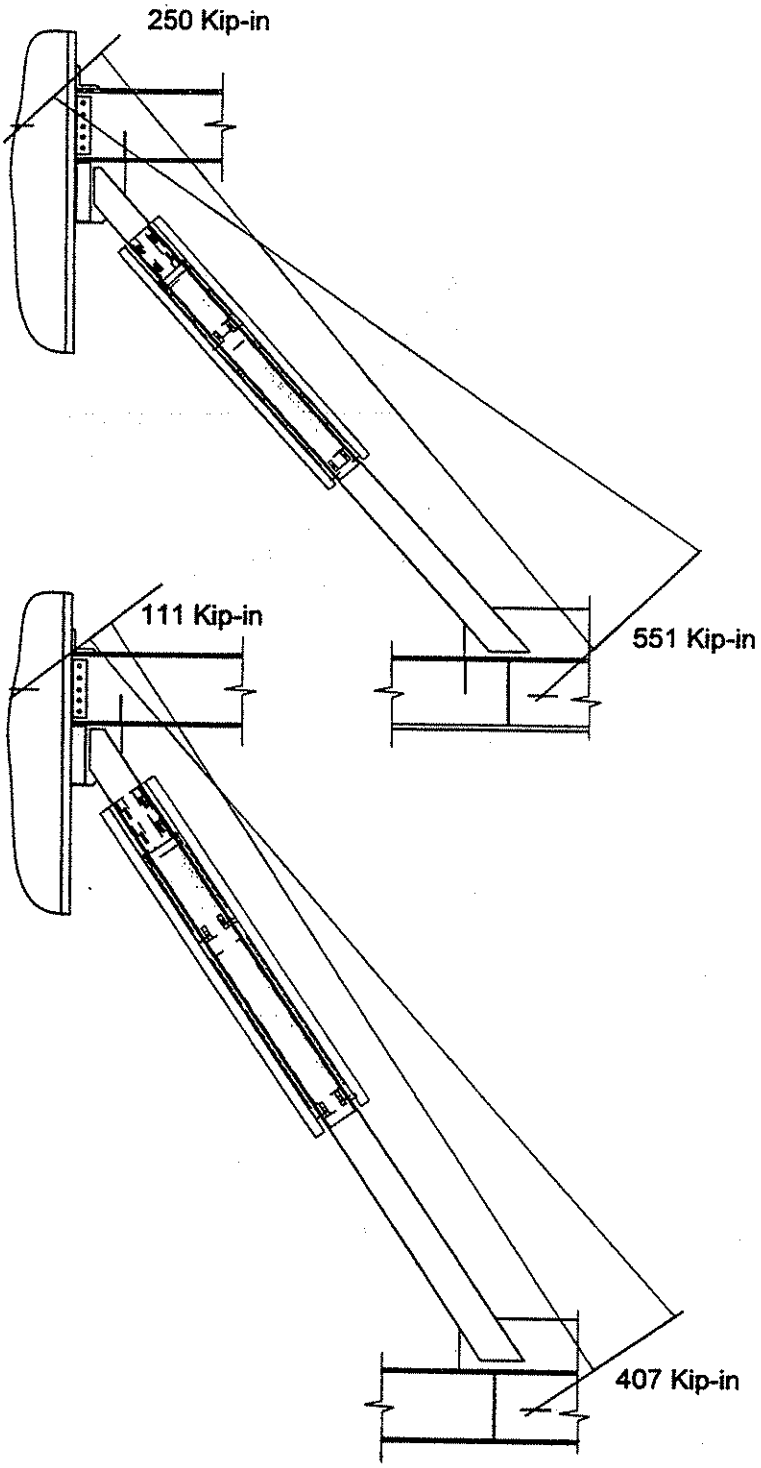

Fig. 5.54 - Moment distribution in added components.

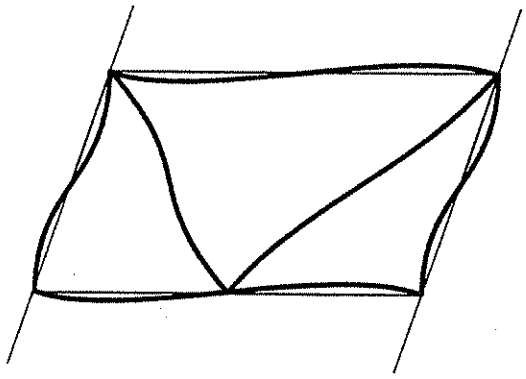

Exagerated Frame Deformations

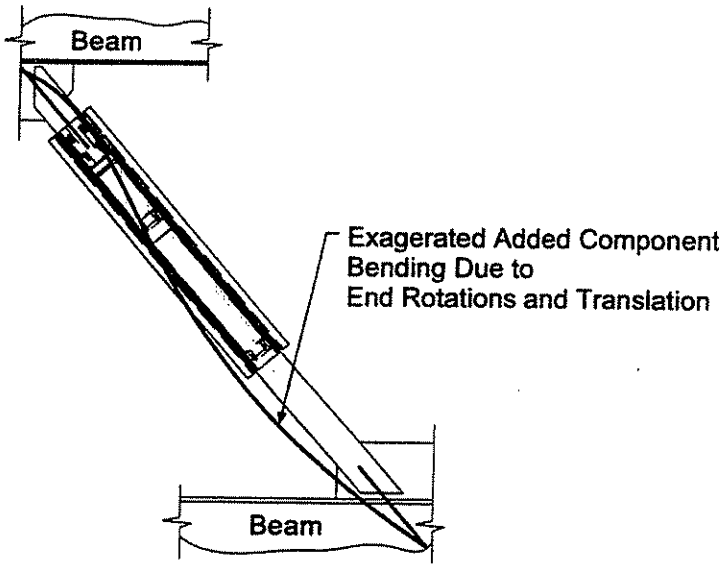

Exagerated Added Component Deformations

Fig. 5.55 - Schematic of bending in added component.

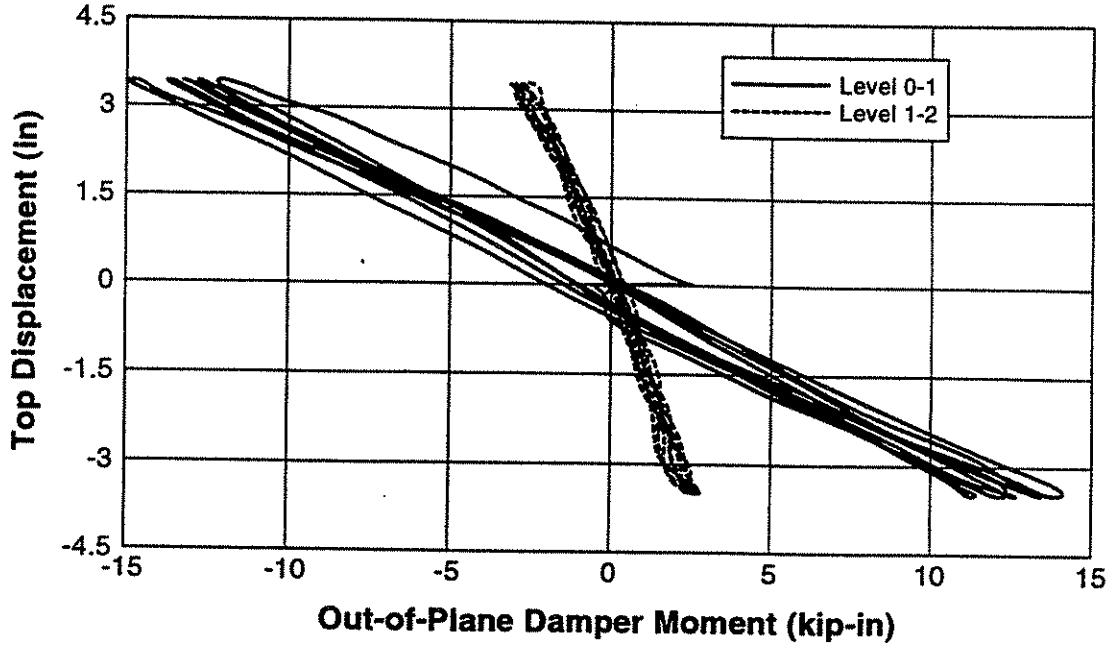

Fig. 5.56 - Out-of-plane moment at bottom of added components.

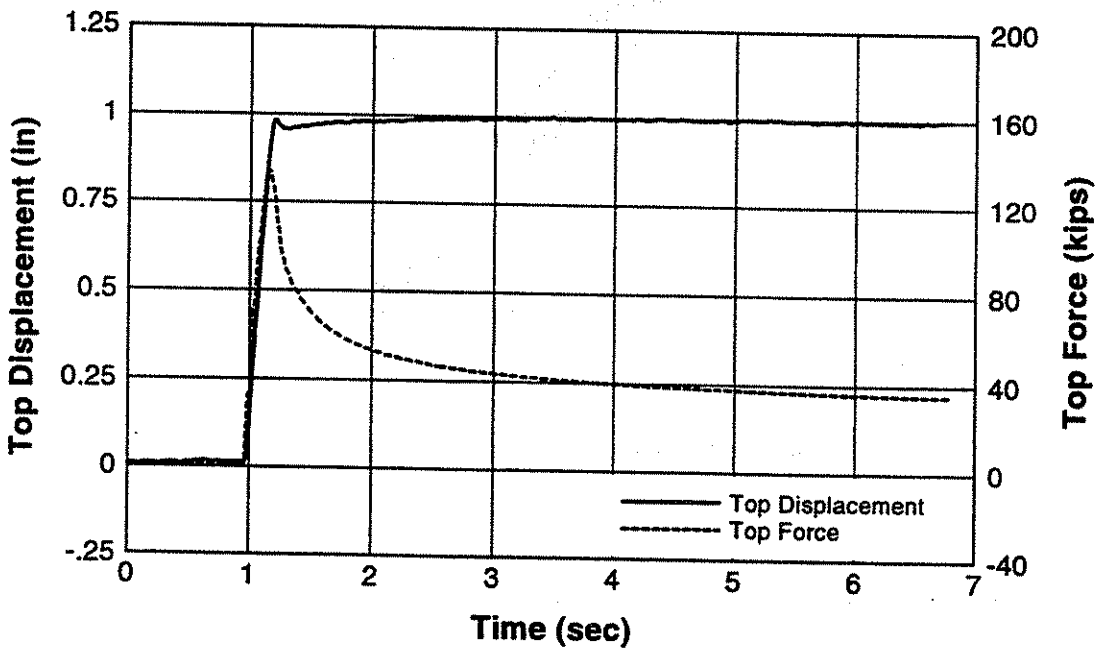

Fig. 5.57 - Measured frame force and displacement response for first 6 seconds of a step 1 in. top displacement.

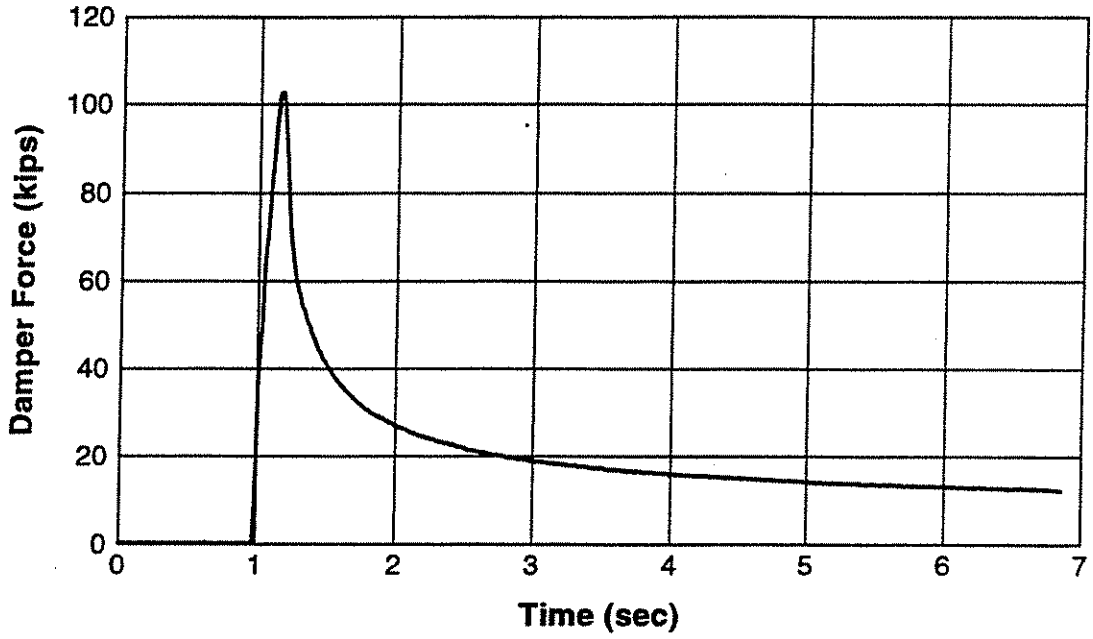

Fig. 5.58 - Measured damper force decay as frame is held in displaced position.

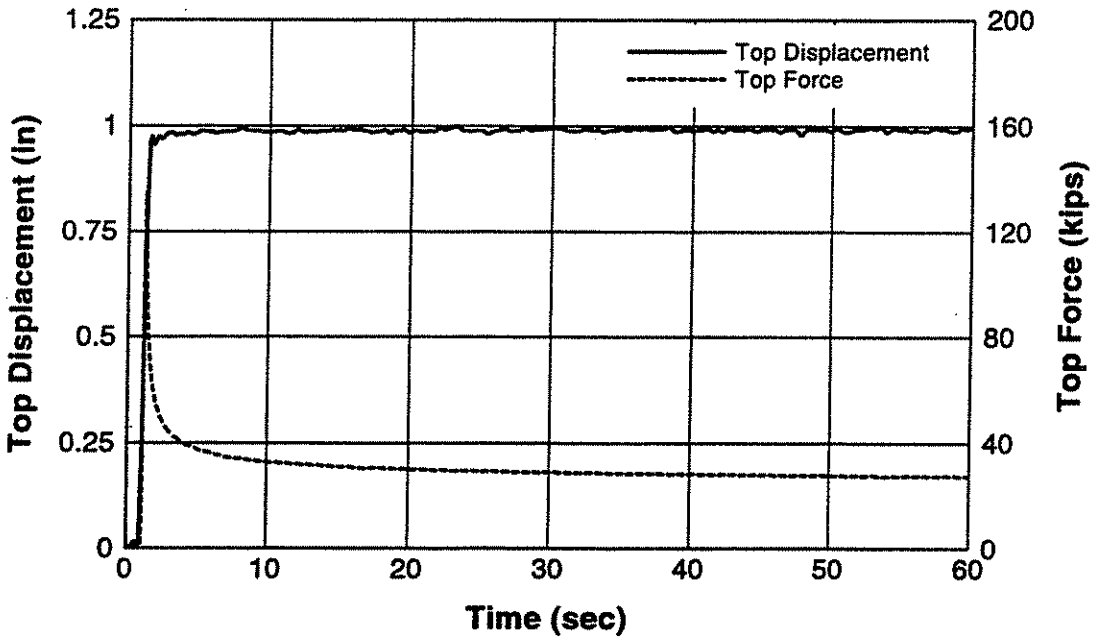

Fig. 5.59 - Measured frame force and displacement response for first minute of a step 1 in. top displacement.

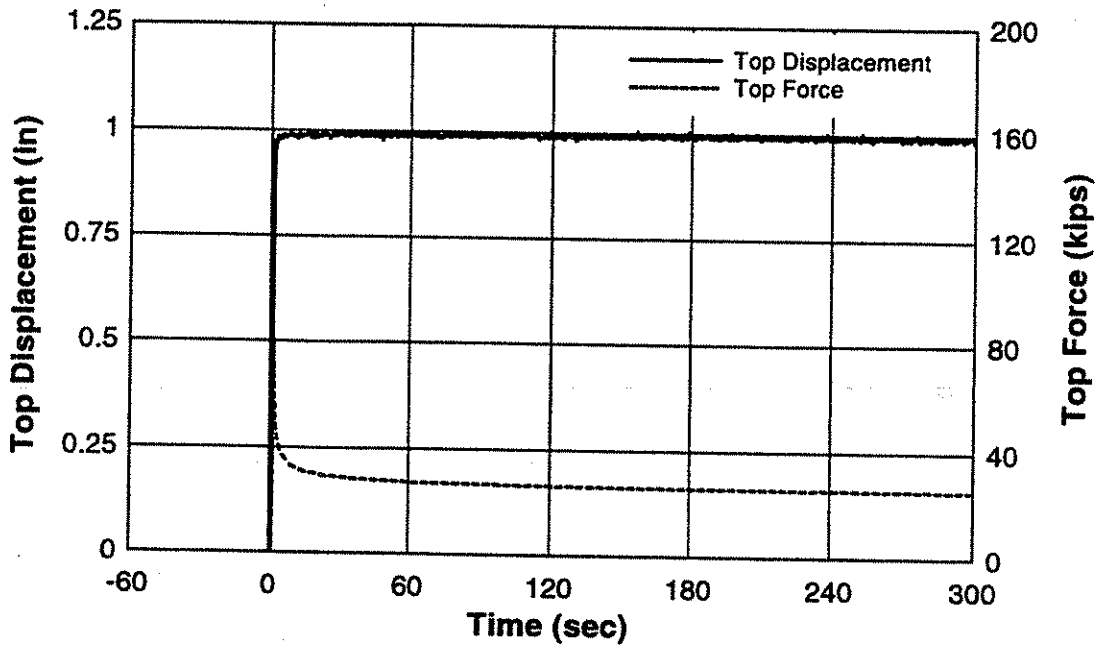

Fig. 5.60 - Measured frame force and displacement response for first 5 minutes of a step 1 in. top displacement.

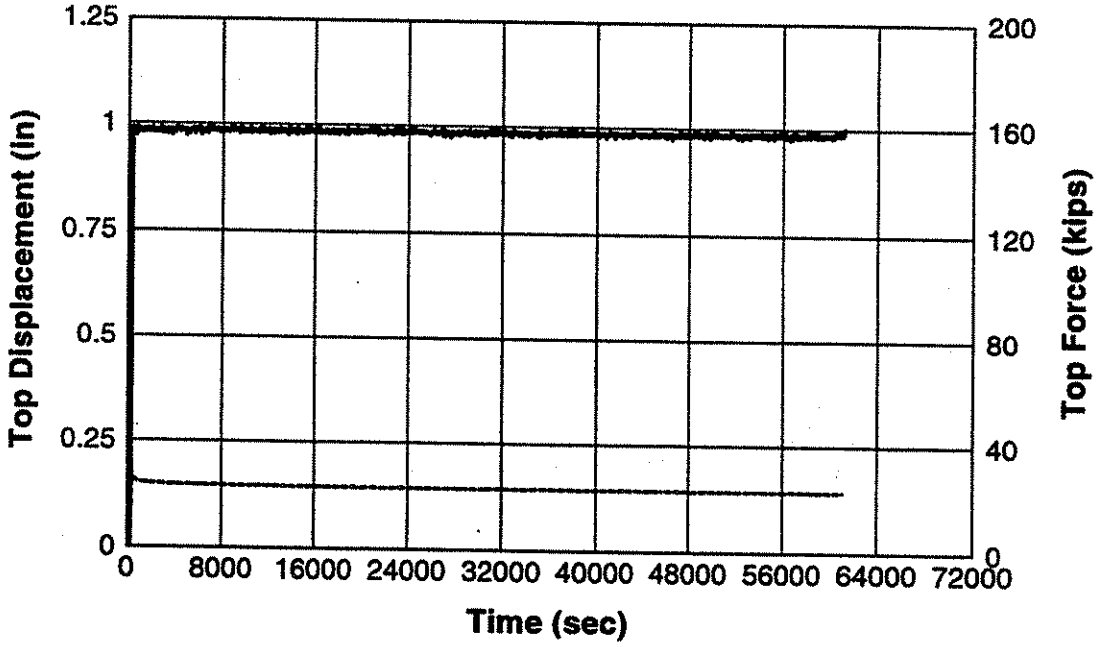

Fig. 5.61 - Measured frame force and displacement response for first 17 hours of a step 1 in. top displacement.

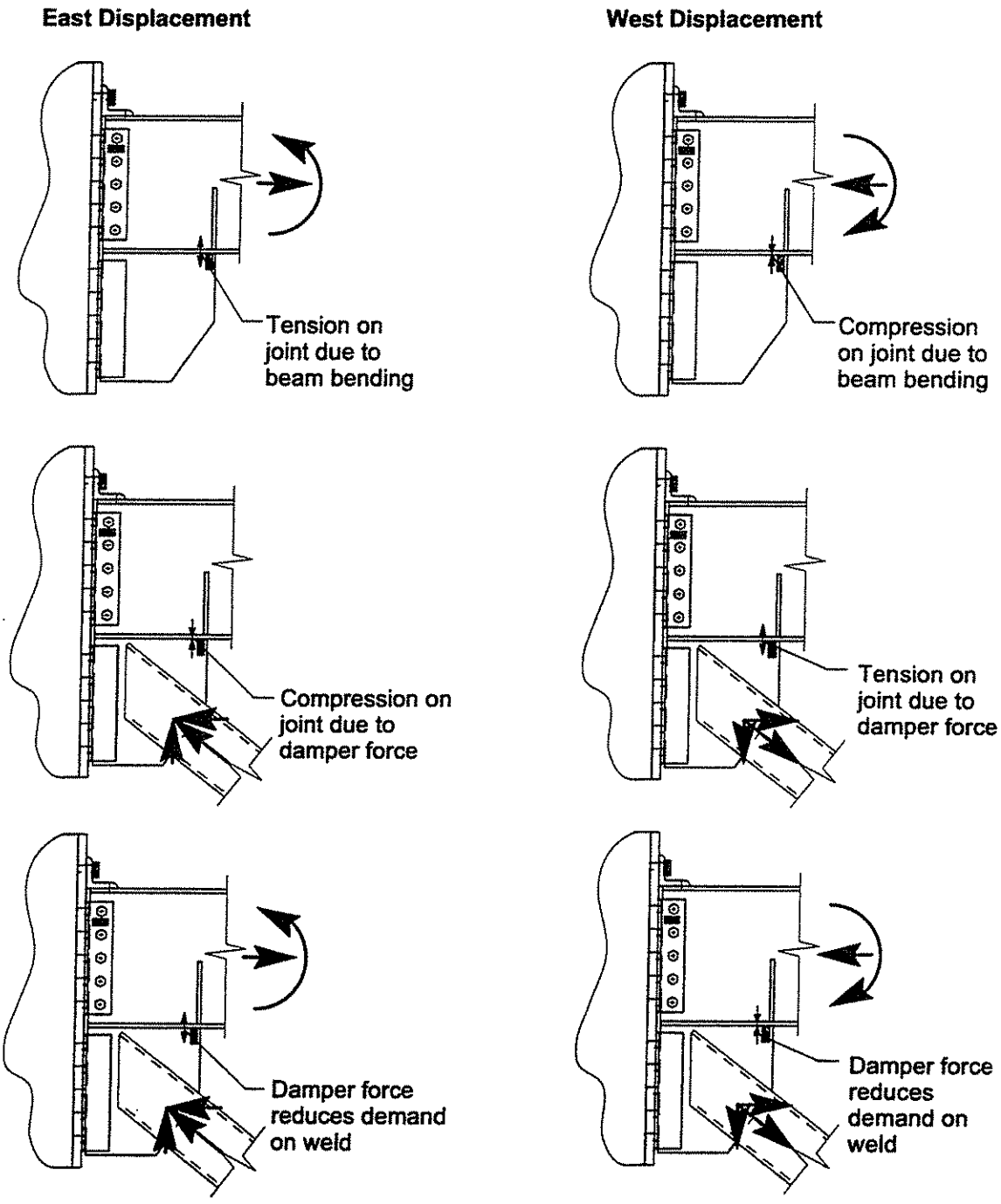

Fig. 5.62 - Influence of VE-damper force on welded connection between beam bottom flange and gusset plate.

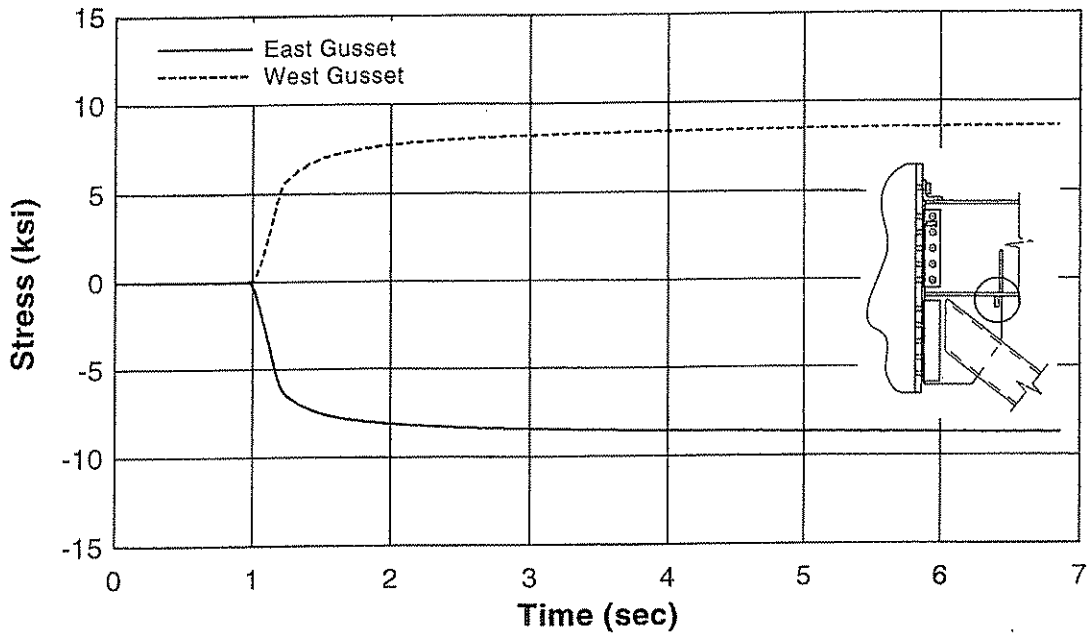

Fig. 5.63 - Measured stress at welded connection between beam bottom flange and gusset plate as damper forces decay during relaxation test at 1 in. top displacement.

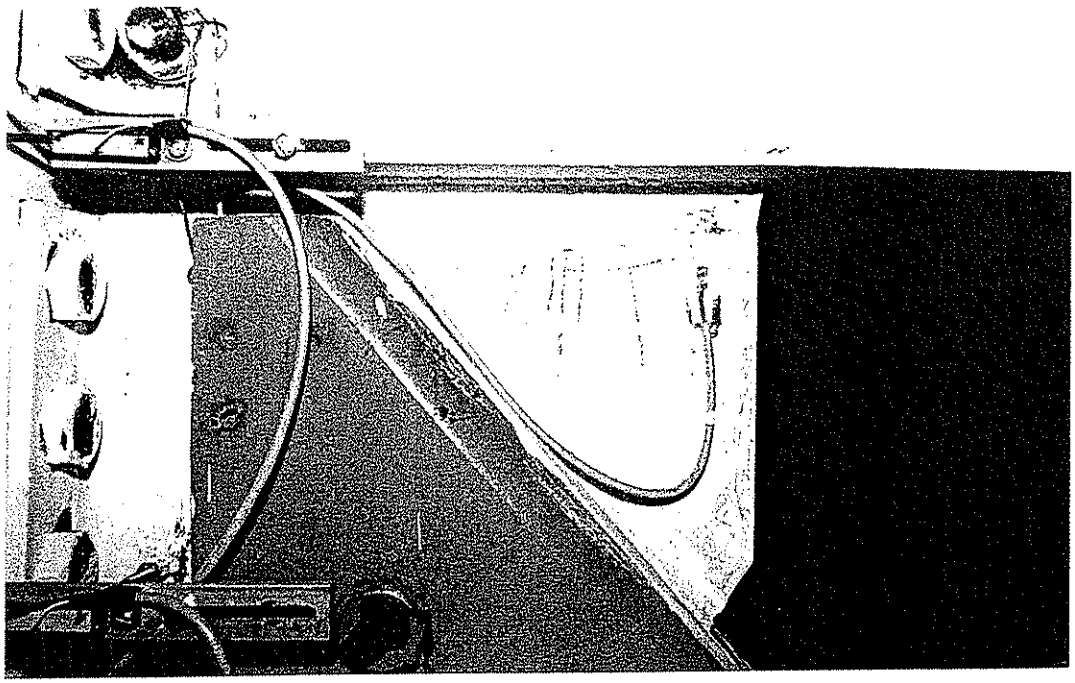

Fig. 5.64 - Example of observed flaking of white wash on gusset plates.

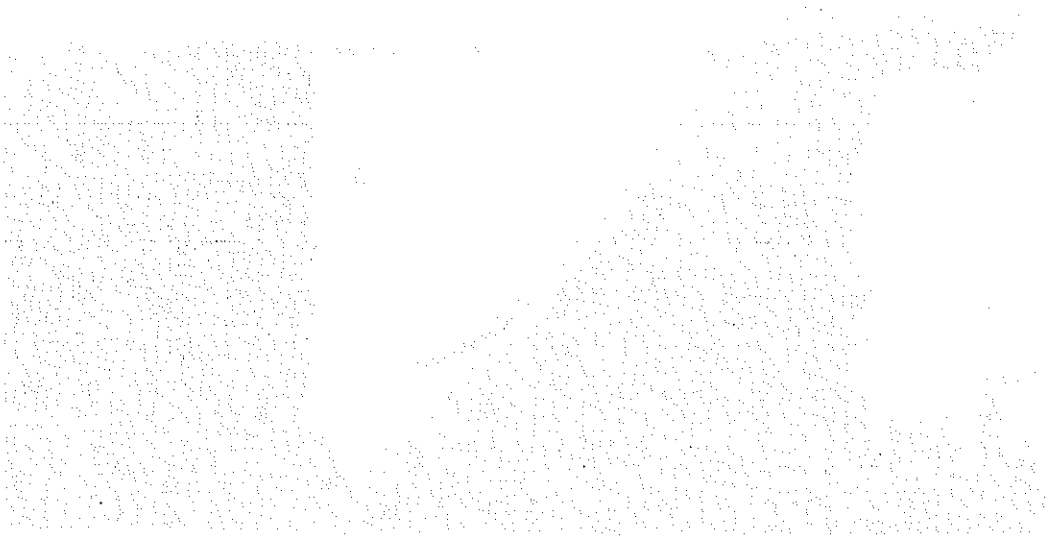

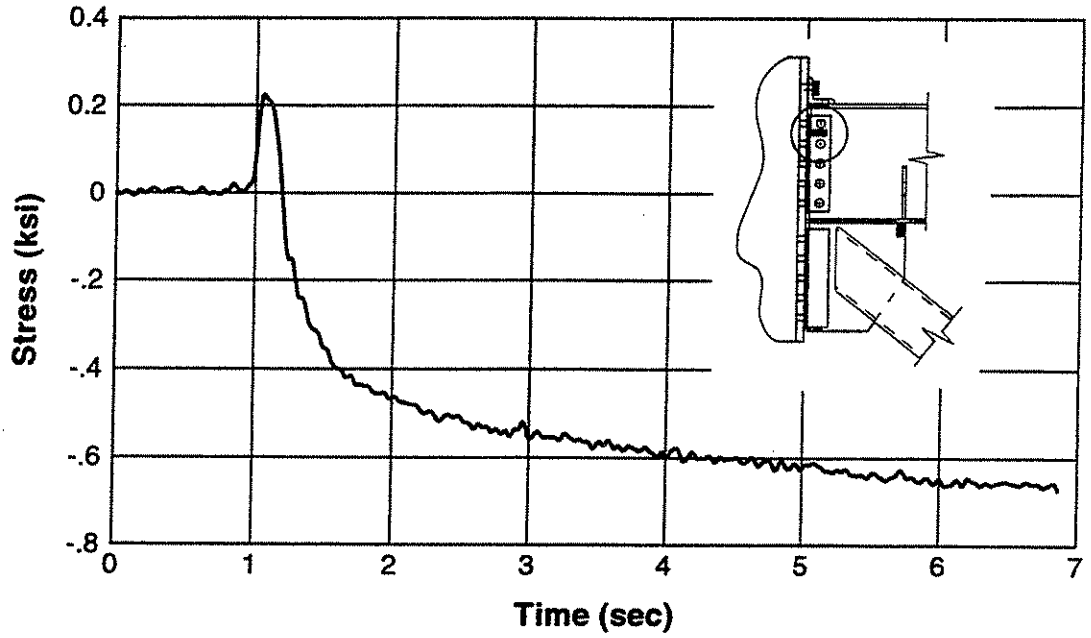

Fig. 5.65 - Measured stress at beam web connection angle as damper forces decay during relaxation test at 1 in. top displacement.

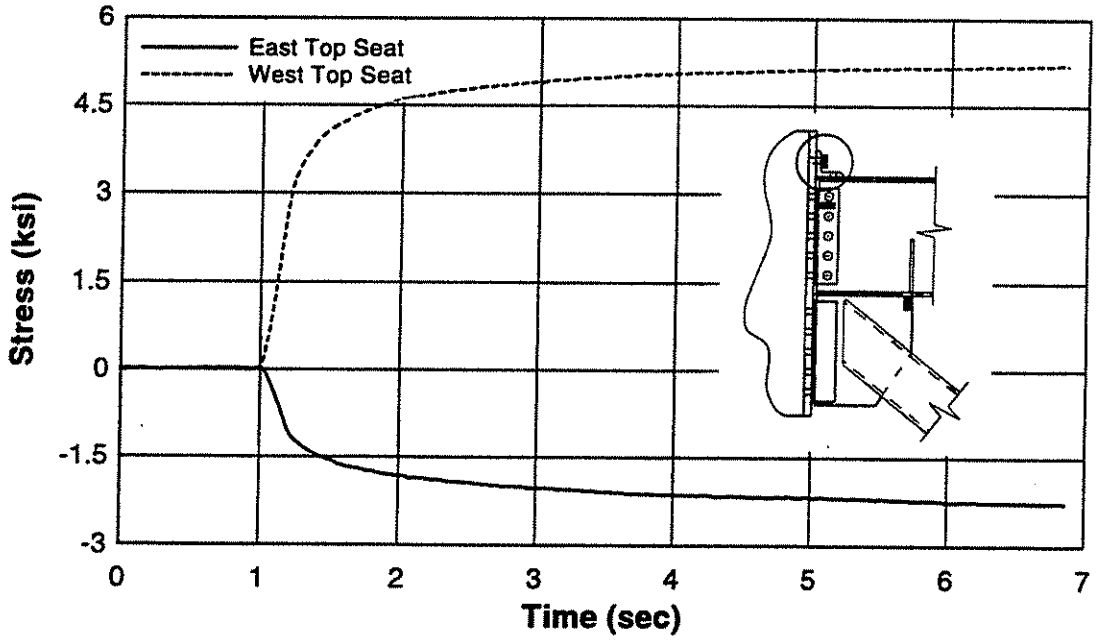

Fig. 5.66 - Measured stress at beam top-seat connection angle as damper forces decay during relaxation test at 1 in. top displacement.

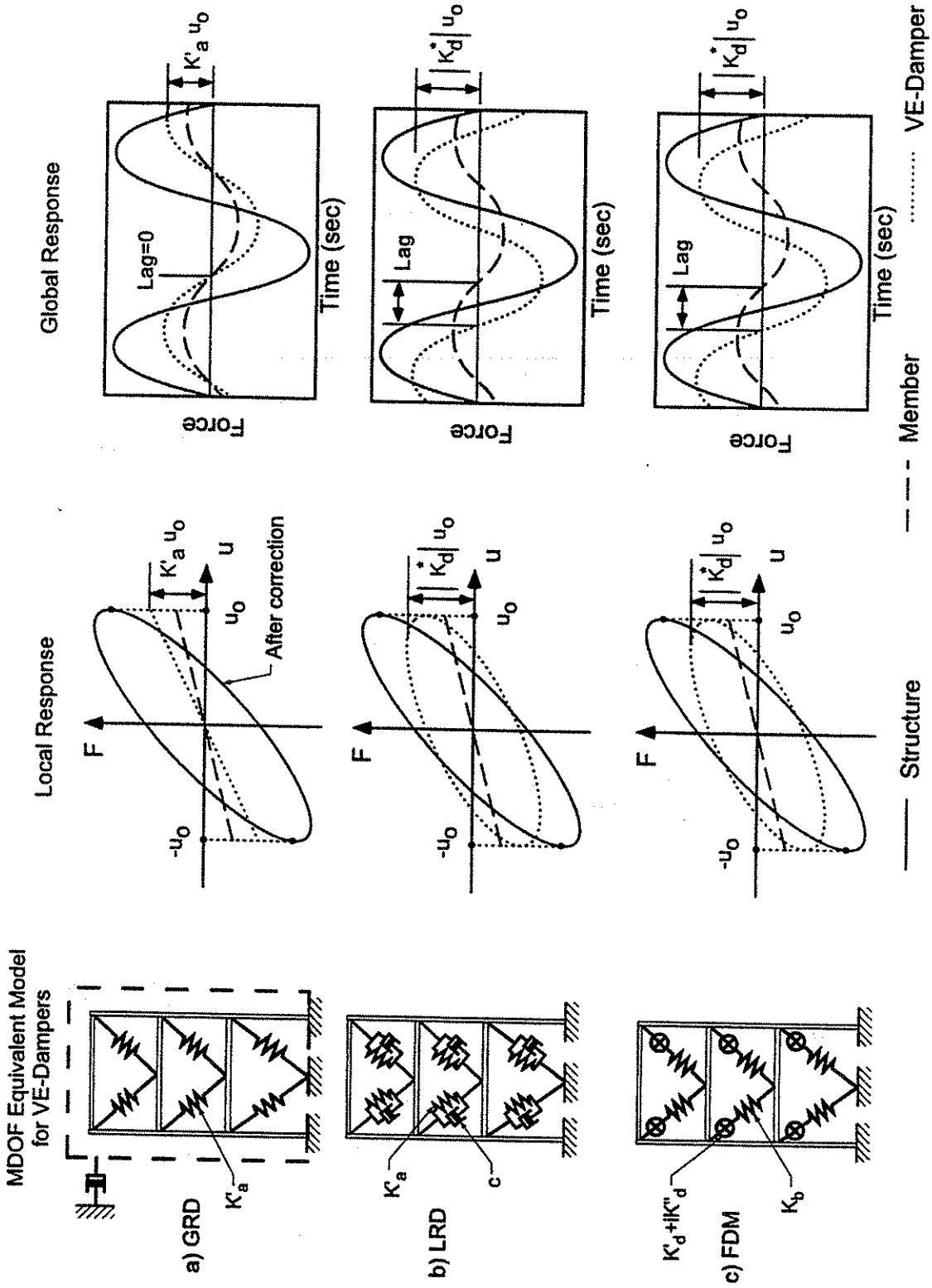

Fig. 5.67 - Equivalent models and examples of response for the three time-history analysis methods used to model VE-dampers.

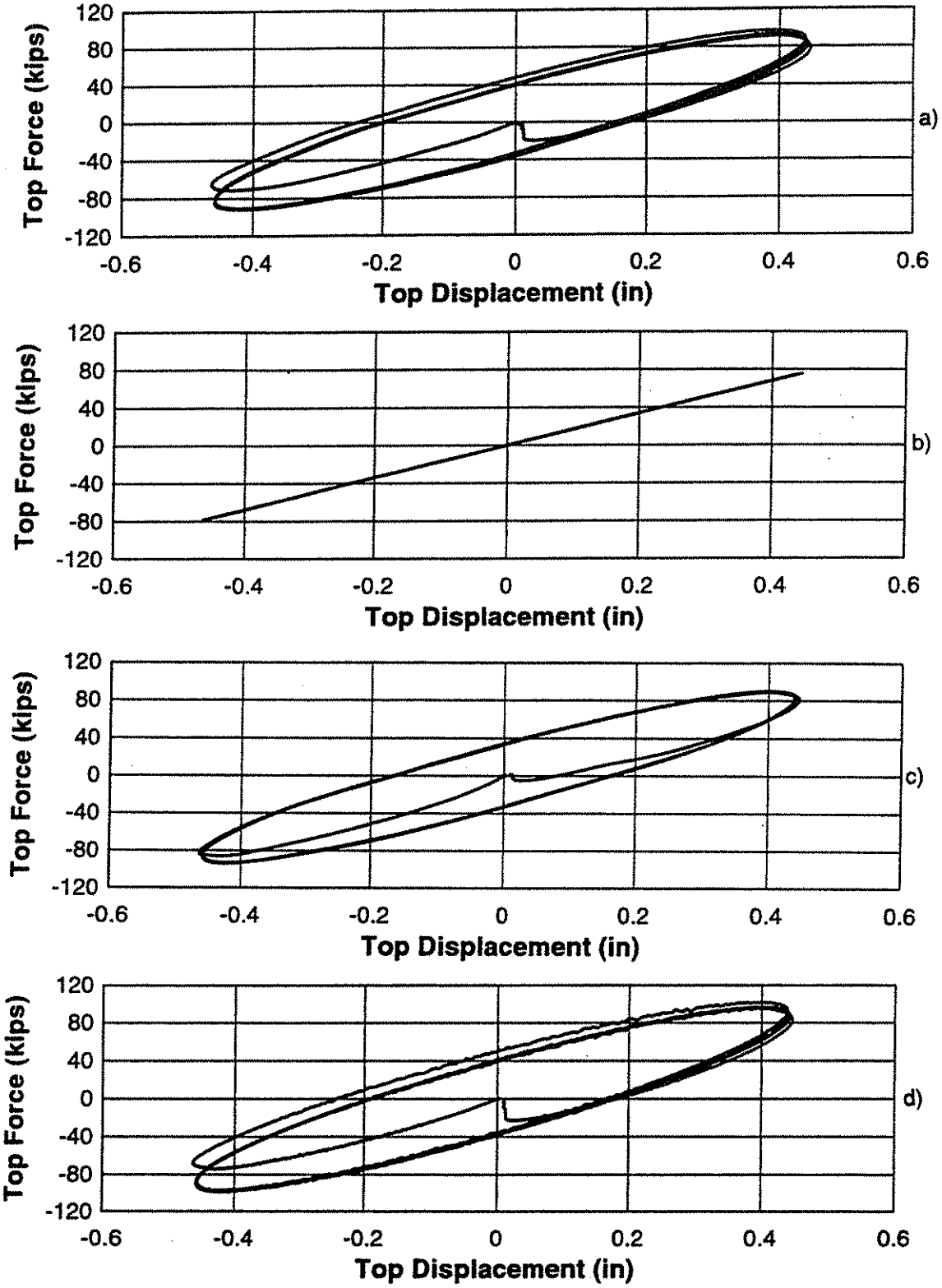

Fig. 5.68 - Force-deformation response for 16 °C, 0.5 hz, and 0.5 in. nominal displacement amplitude a) Experimental, b) GRD, c) LRD, d) FDM.

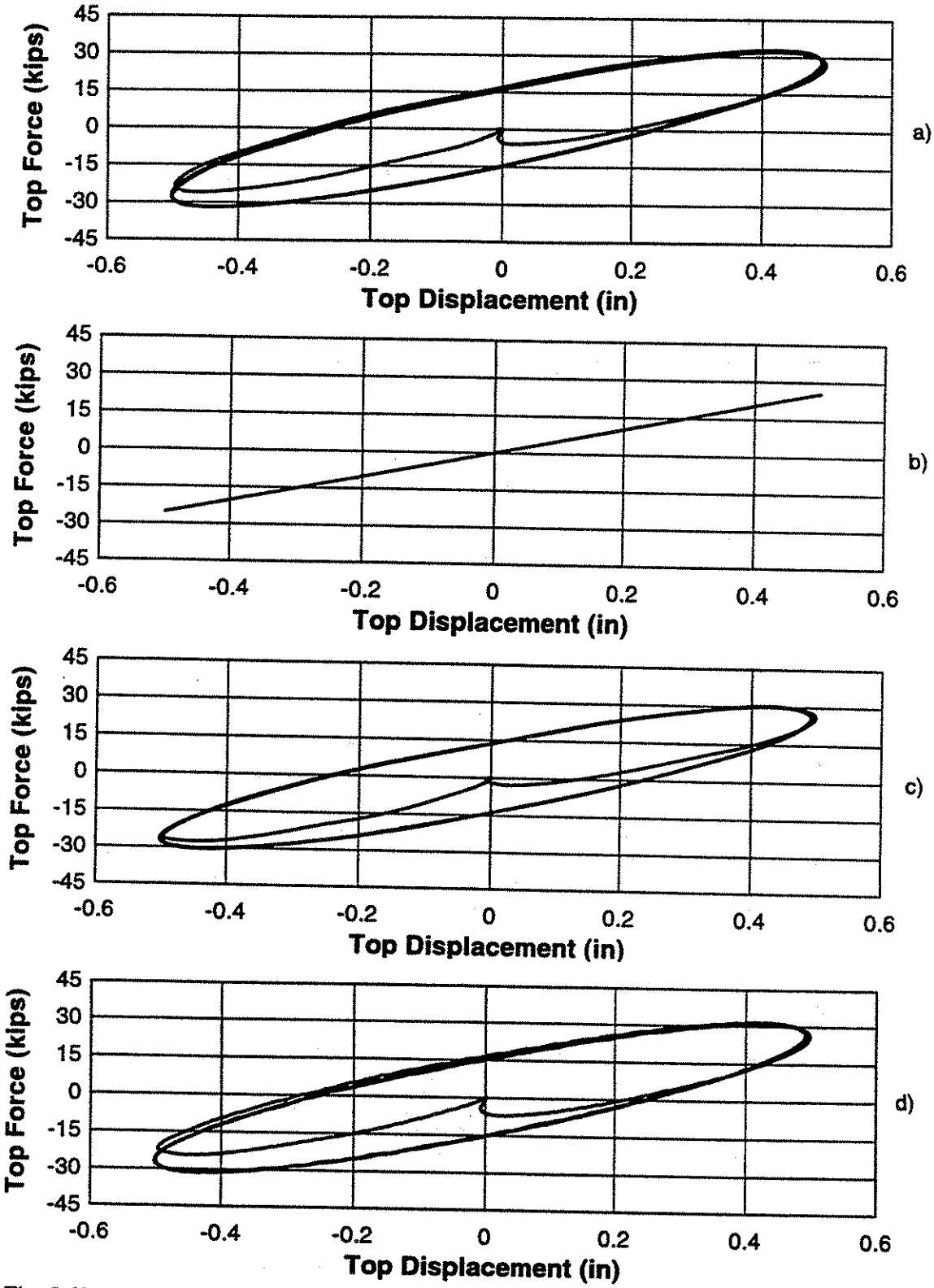

Fig. 5.69 - Force-deformation response for 32 °C, 0.5 hz, and 0.5 in. nominal displacement amplitude a) Experimental, b) GRD, c) LRD, d) FDM.

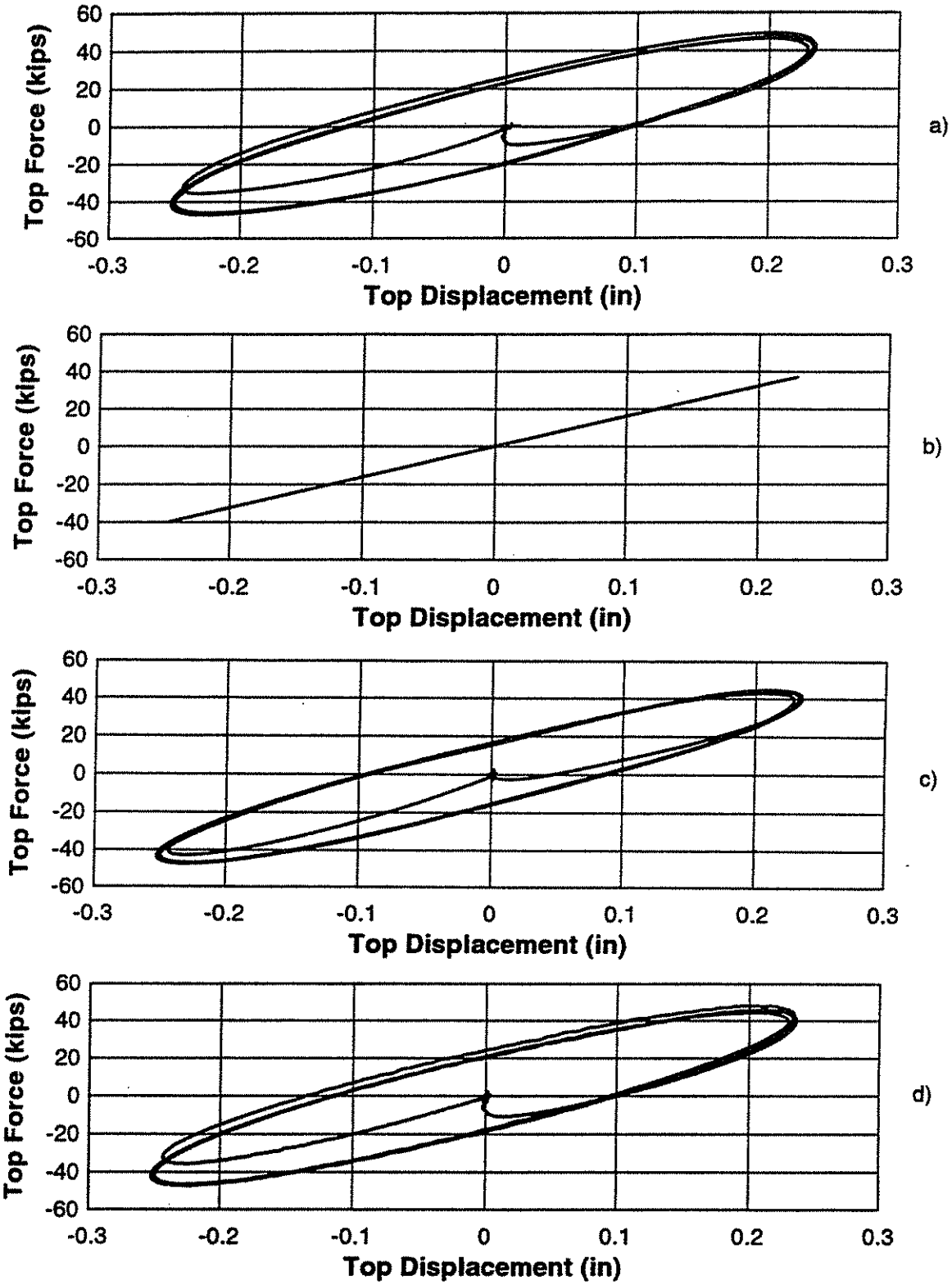

Fig. 5.70 - Force-deformation response for 24 °C, 2.0 hz, and 0.25 in. nominal displacement amplitude a) Experimental, b) GRD, c) LRD, d) FDM.

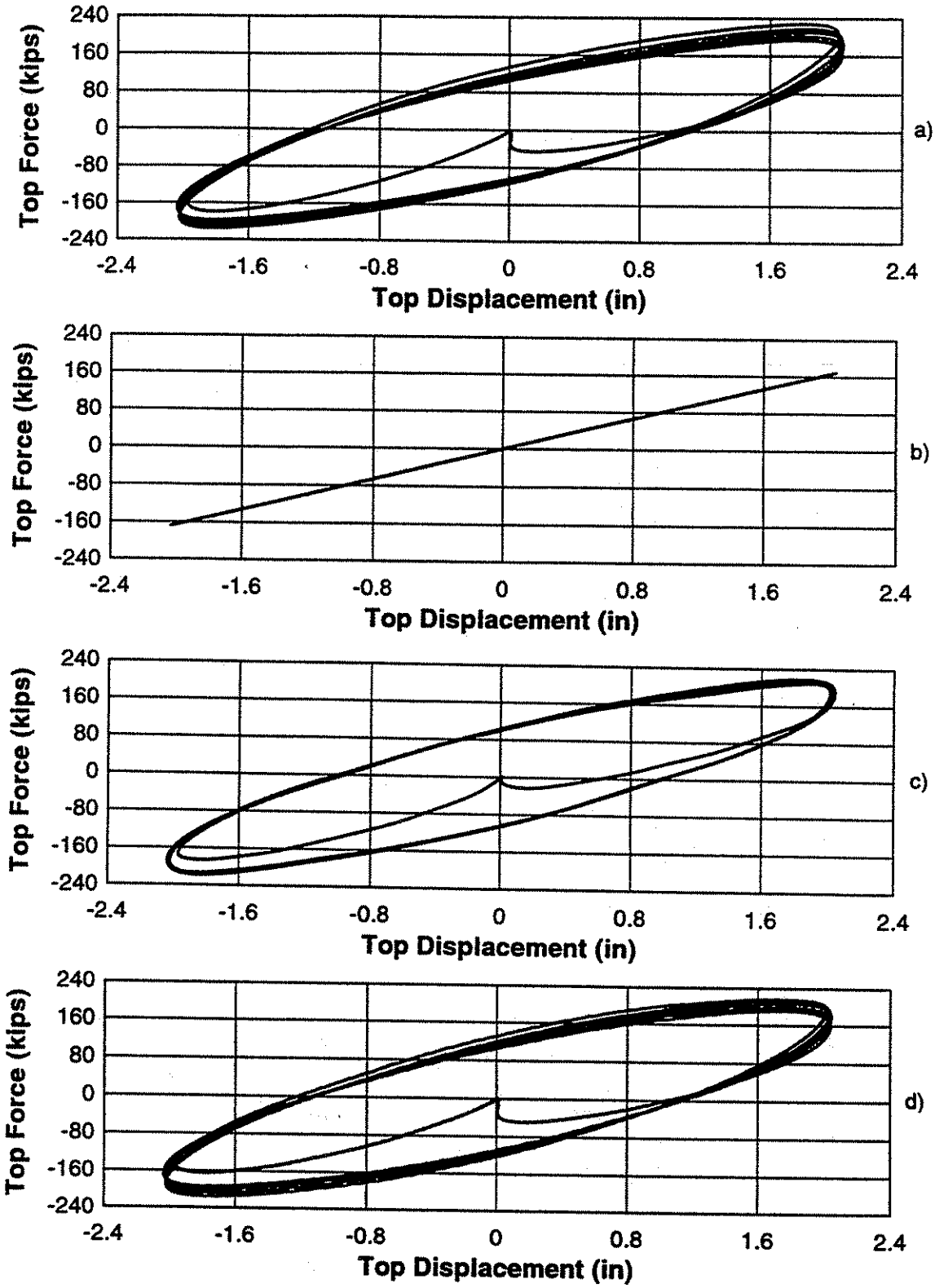

Fig. 5.71 - Force-deformation response for 24 °C, 0.5 hz, and 2.0 in. nominal displacement amplitude a) Experimental, b) GRD, c) LRD, d) FDM.

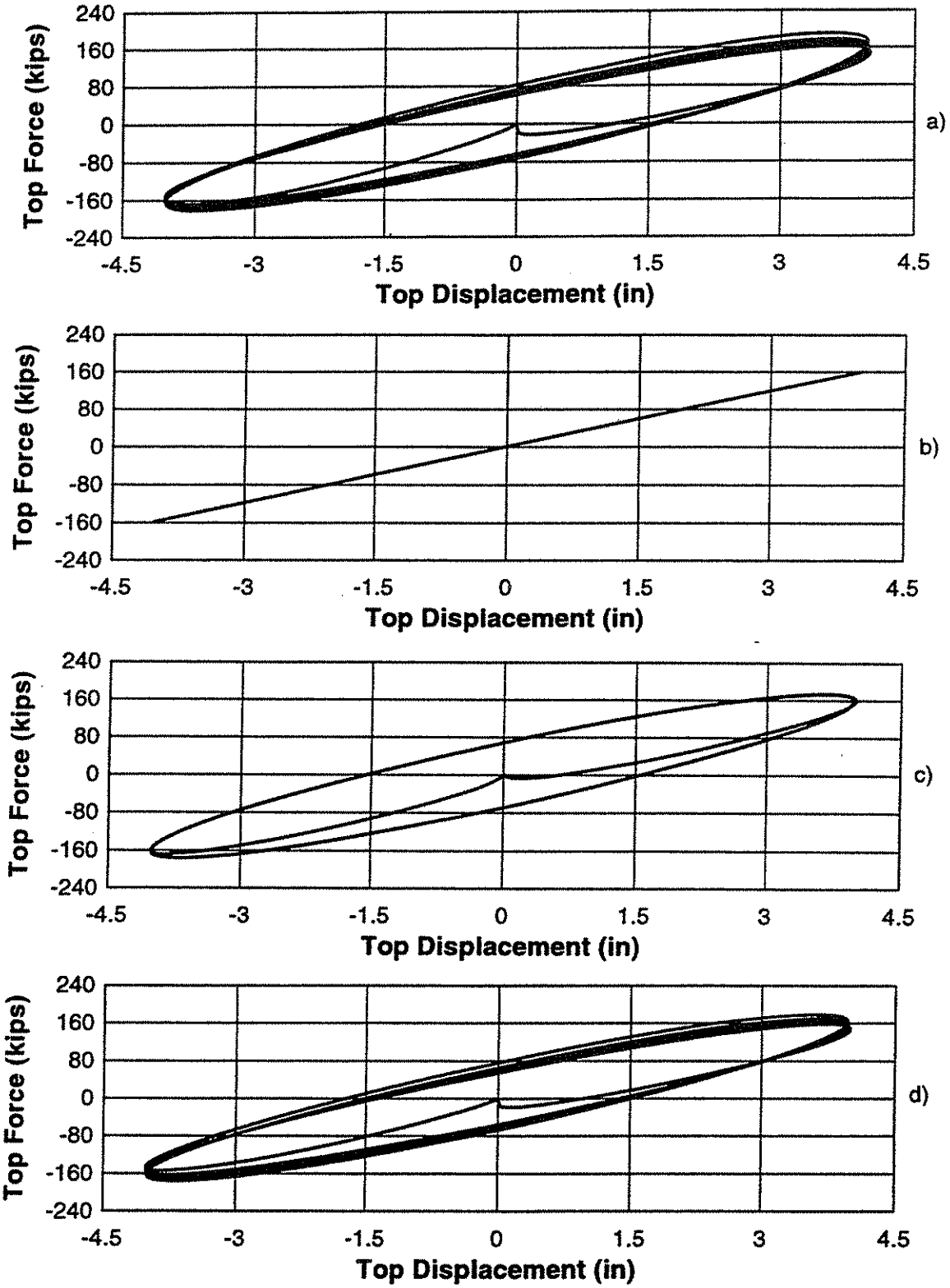

Fig. 5.72 - Force-deformation response for 28 °C, 0.1 hz, and 4.0 in. nominal displacement amplitude a) Experimental, b) GRD, c) LRD, d) FDM.

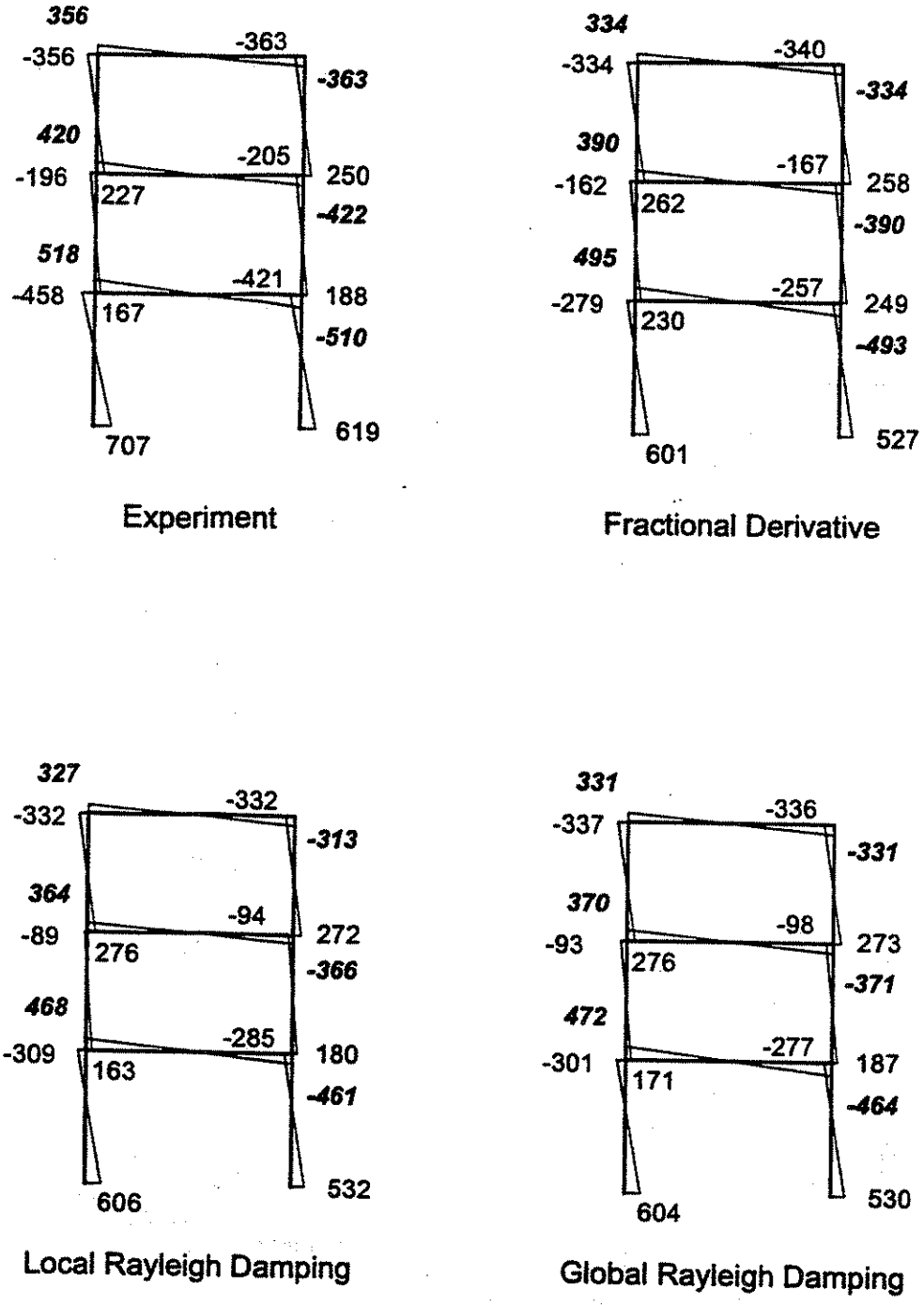

Fig. 5.73a - Peak member bending moments for 16 °C, 0.5 hz, and 0.5 in. nominal displacement amplitude for all time-history analysis methods.

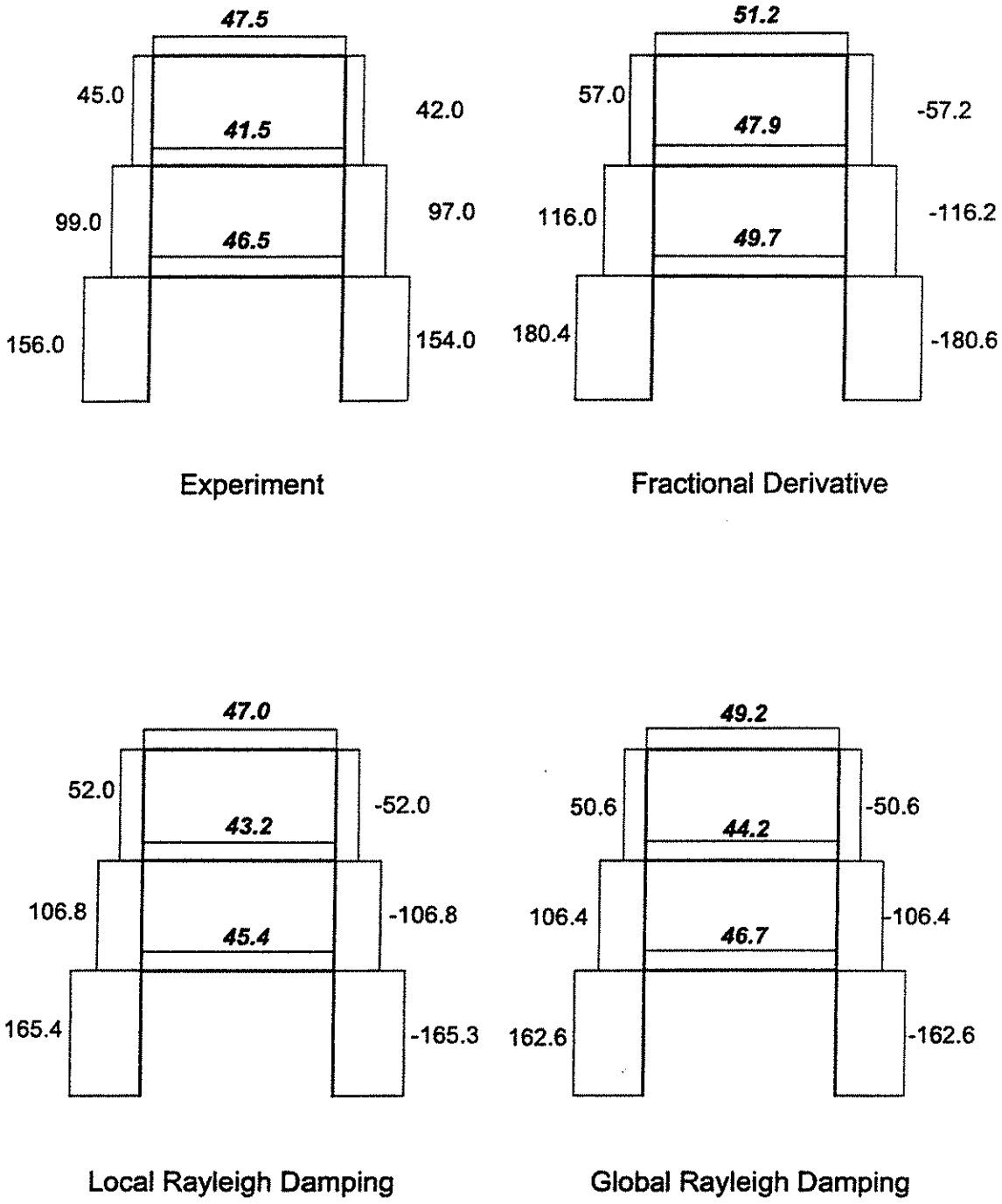

Fig. 5.73b - Peak member axial forces for 16 °C, 0.5 hz, and 0.5 in. nominal displacement amplitude for all time-history analysis methods.

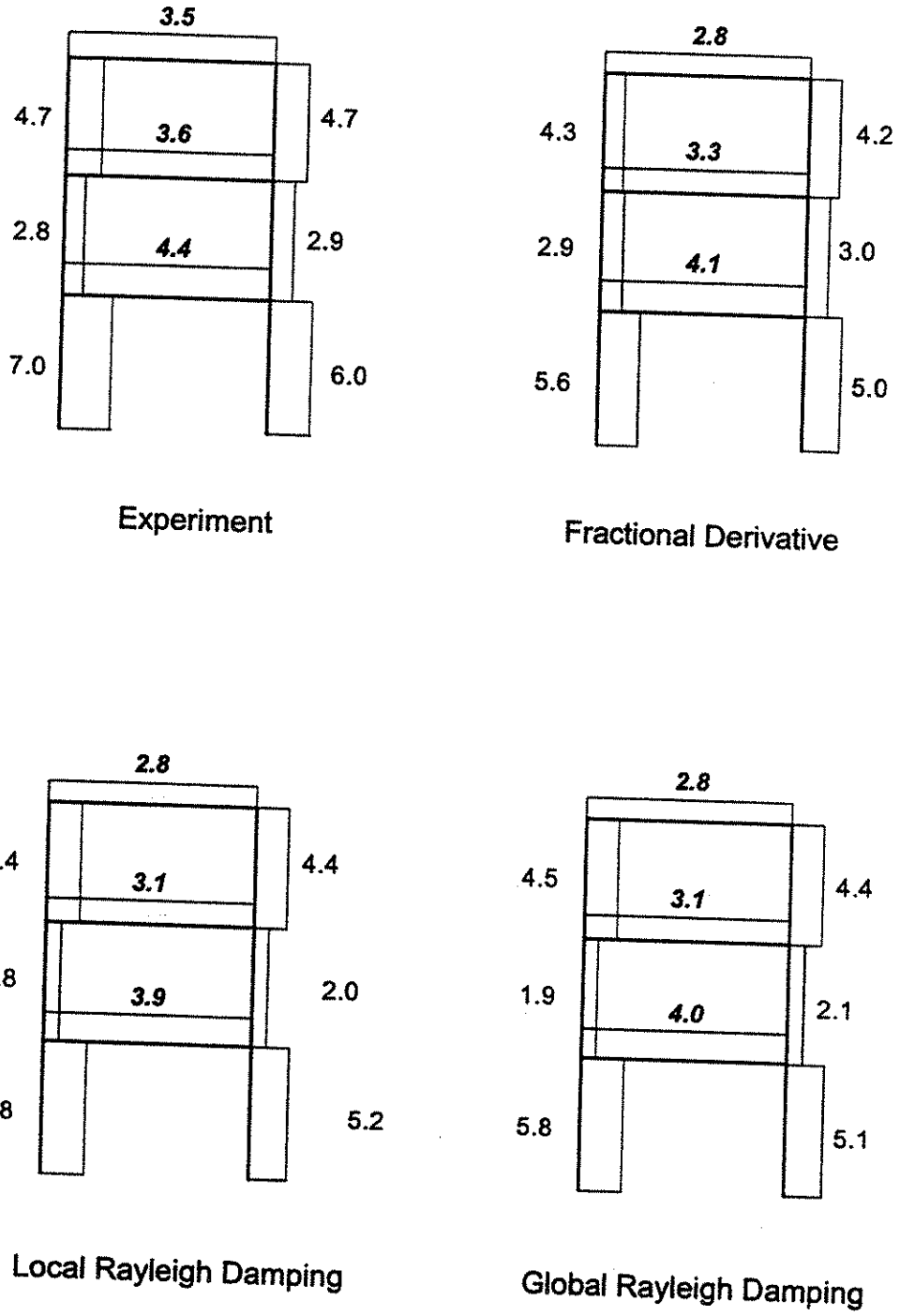

Fig. 5.73c - Peak member shear forces for 16 °C, 0.5 hz, and 0.5 in. nominal displacement amplitude for all time-history analysis methods.

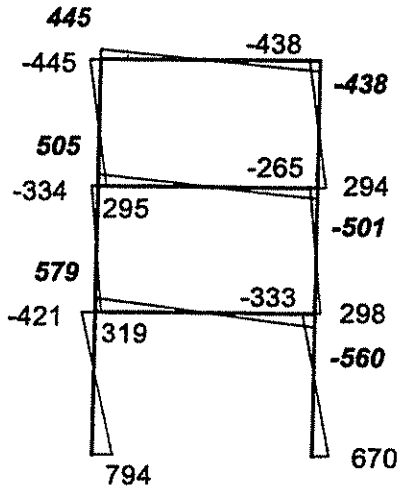

Experiment

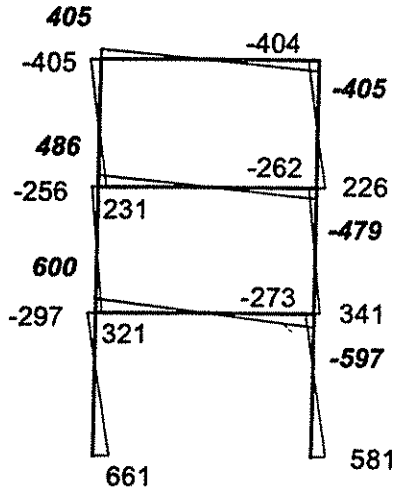

Fractional Derivative

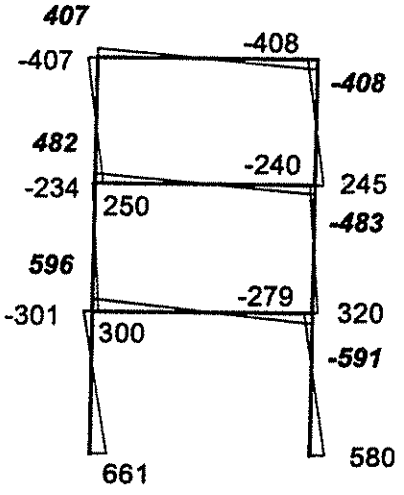

Local Rayleigh Damping

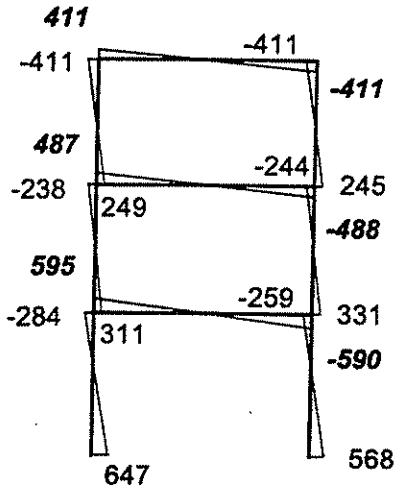

Global Rayleigh Damping

Bold represents beam member forces

Fig. 5.74a - Peak member bending moments for 32 °C, 0.5 hz, and 0.5 in. nominal displacement amplitude for all time-history analysis methods.

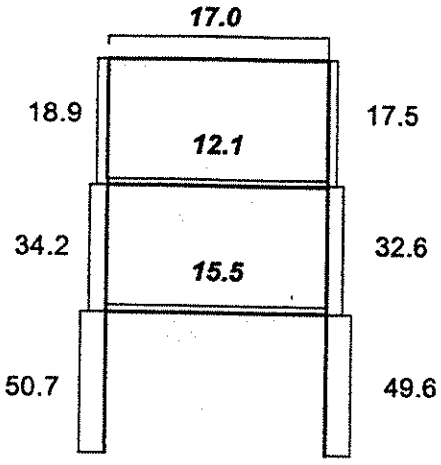

Experiment

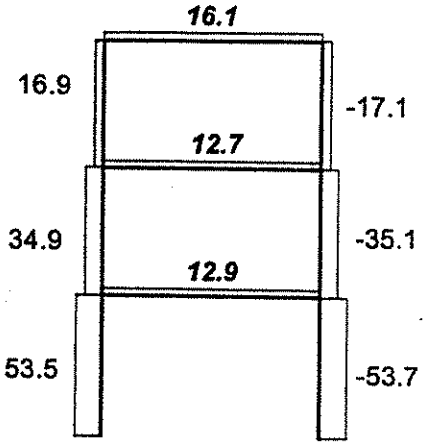

Fractional Derivative

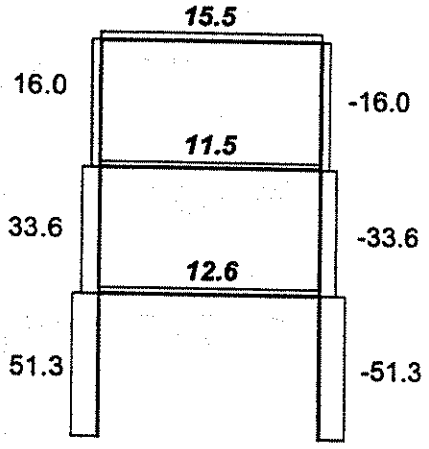

Local Rayleigh Damping

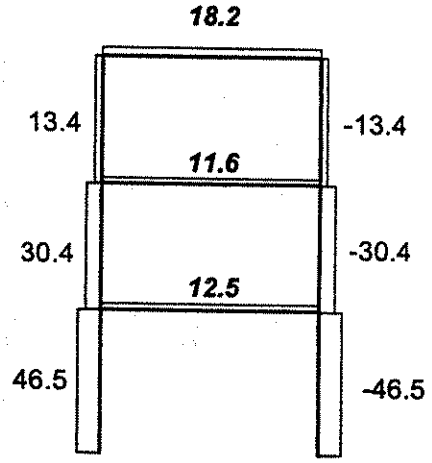

Global Rayleigh Damping

Bold represents beam member forces

Fig. 5.74b - Peak member axial forces for 32 °C, 0.5 hz, and 0.5 in. nominal displacement amplitude for all time-history analysis methods.

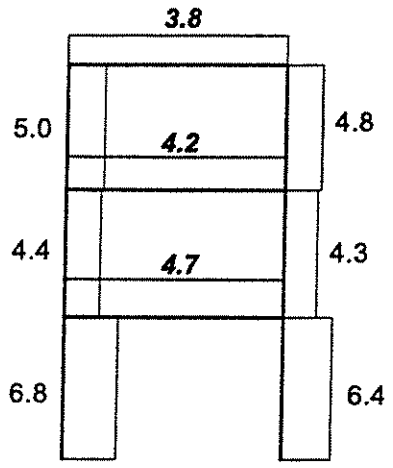

Experiment

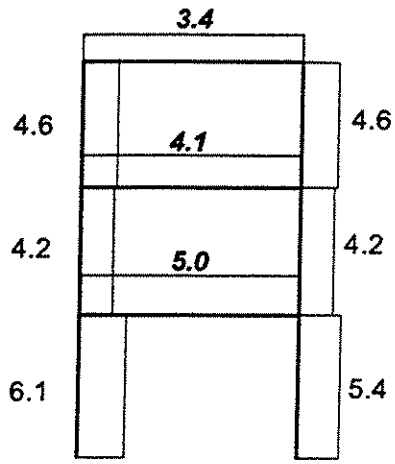

Fractional Derivative

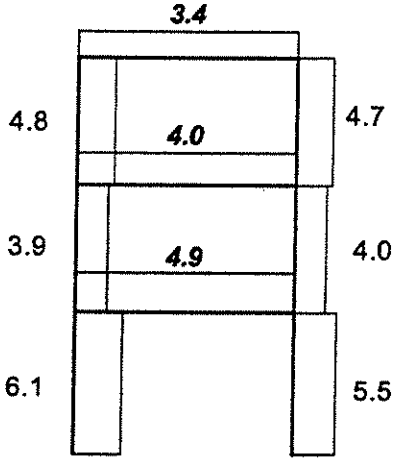

Local Rayleigh Damping

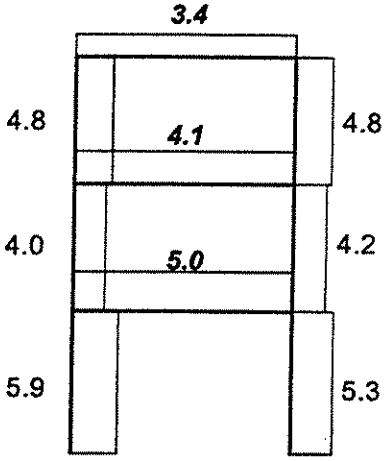

Global Rayleigh Damping

Bold represents beam member forces

Fig. 5.74c - Peak member shear forces for 32 °C, 0.5 hz, and 0.5 in. nominal displacement amplitude for all time-history analysis methods.

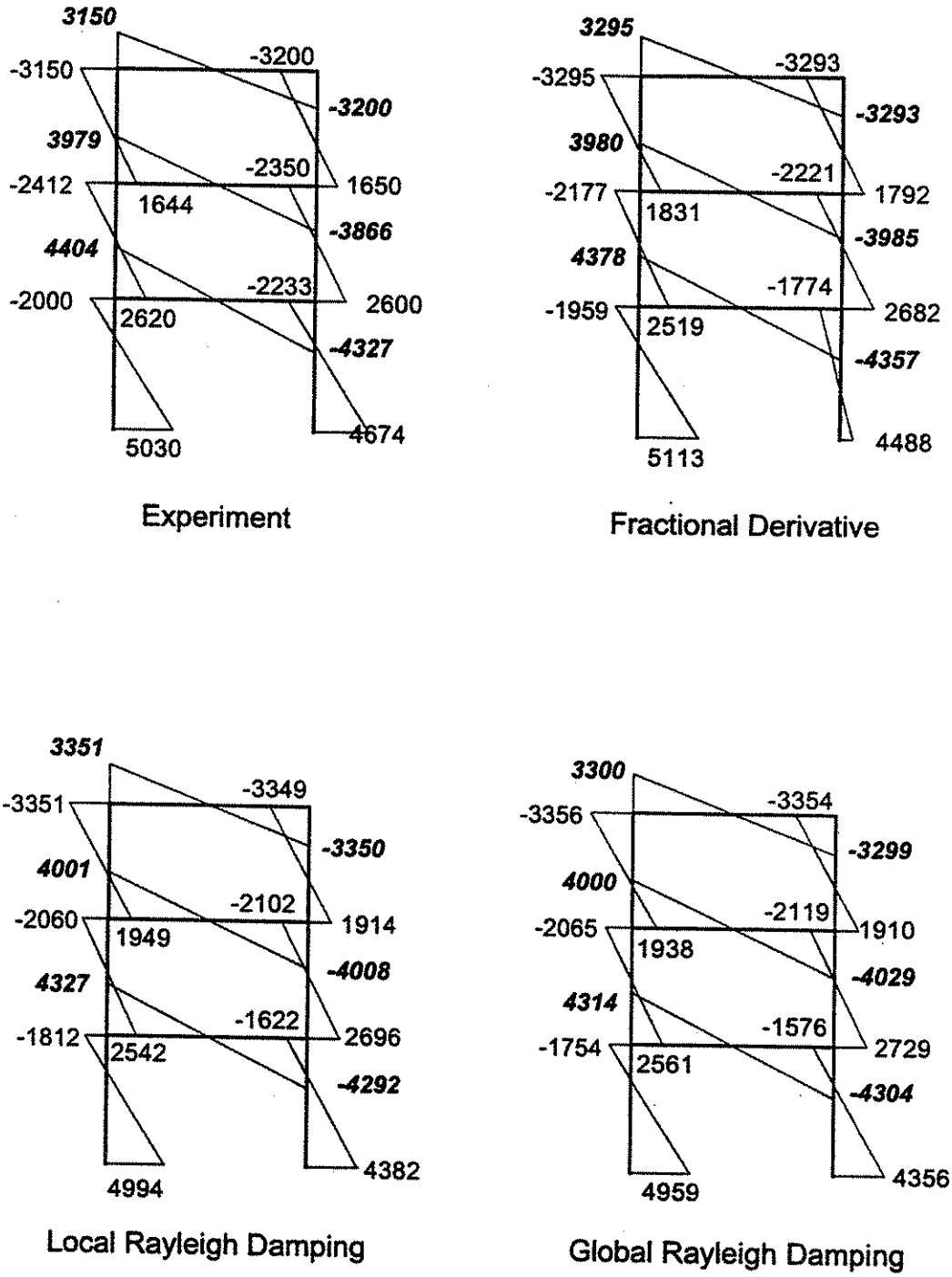

Fig. 5.75a - Peak member bending moments for 28 °C, 0.1 hz, and 4.0 in. nominal displacement amplitude for all time-history analysis methods.

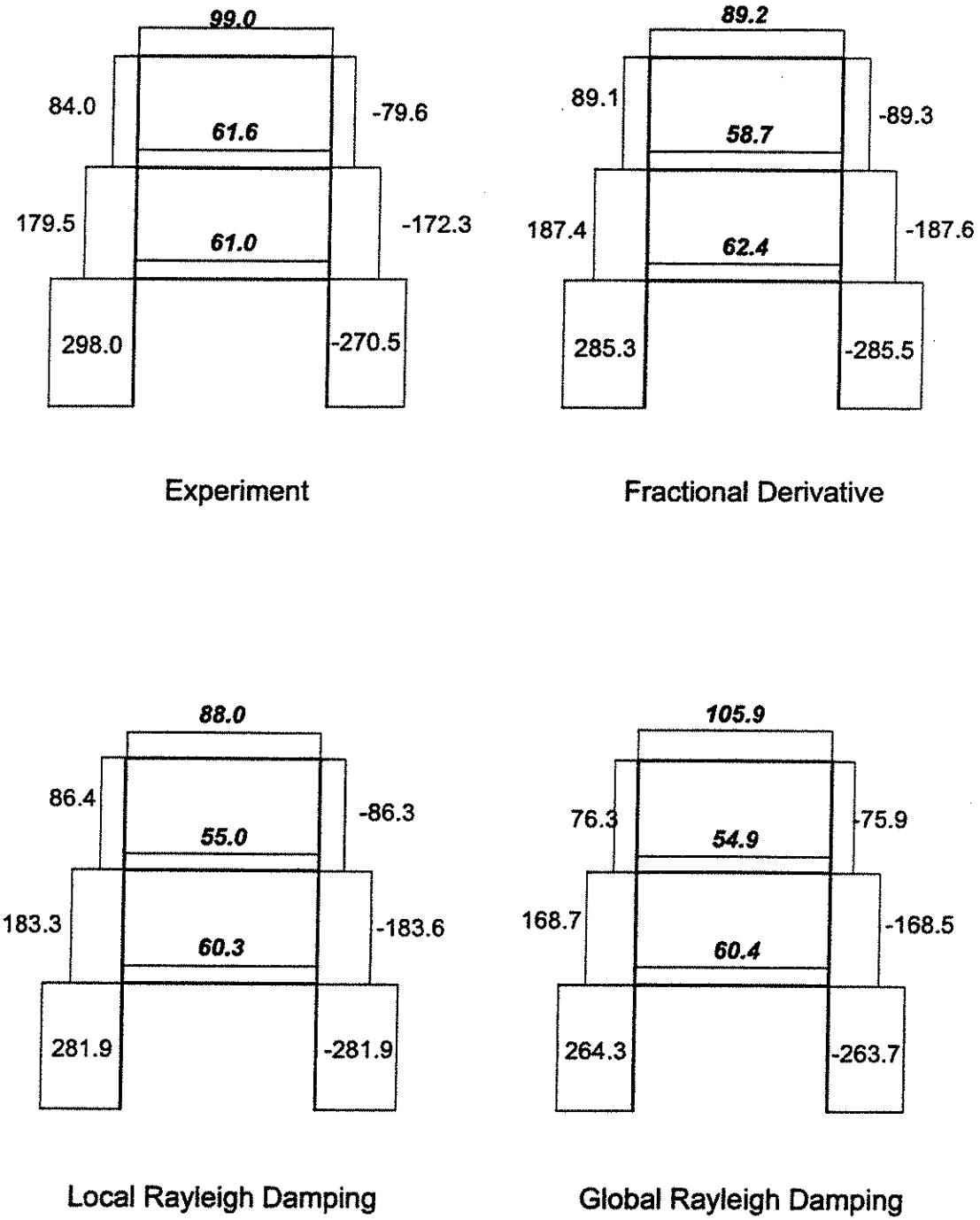

Fig. 5.75b - Peak member axial forces for 28 °C, 0.1 hz, and 4.0 in. nominal displacement amplitude for all time-history analysis methods.

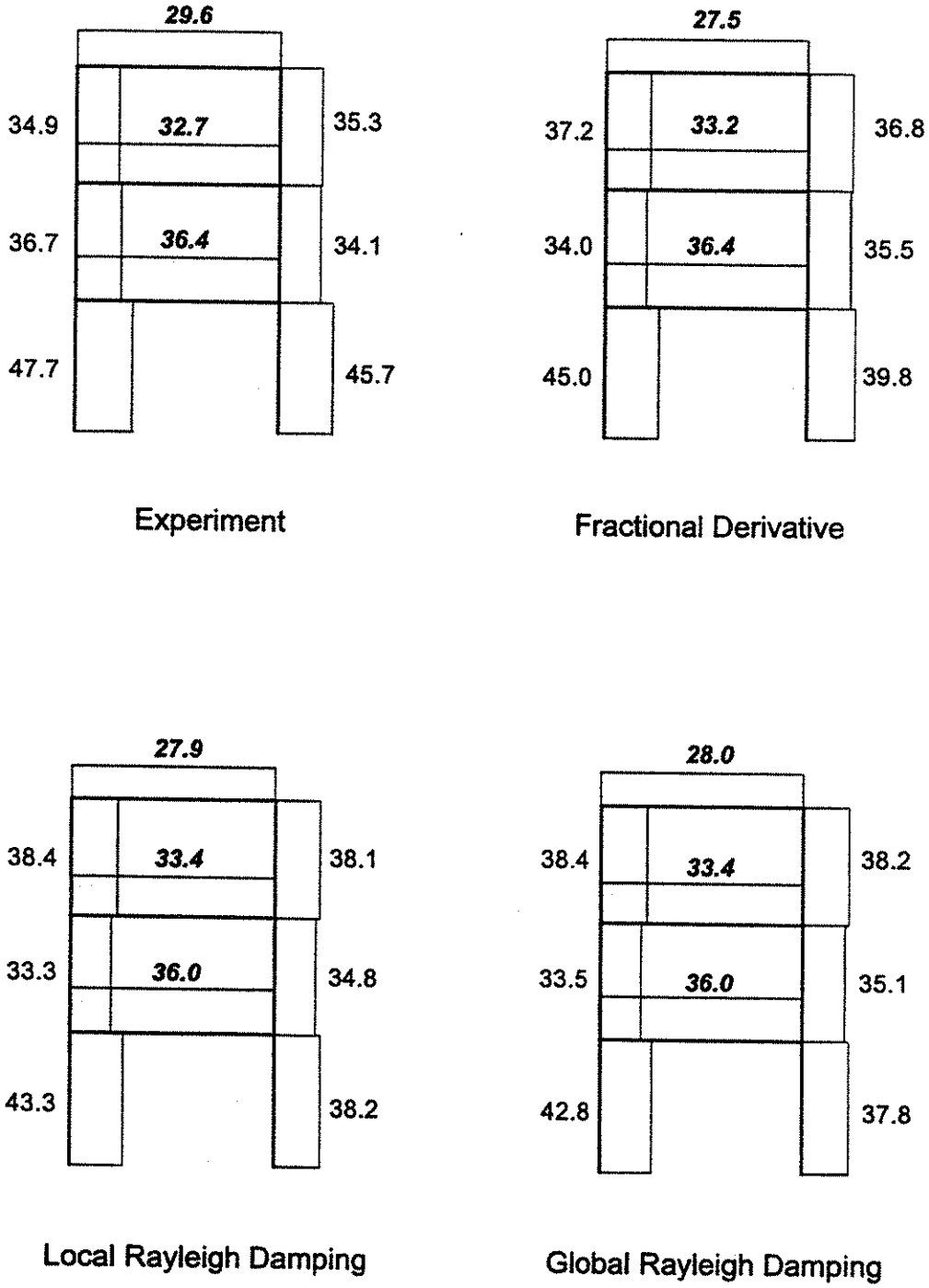

Fig. 5.75c - Peak member shear forces for 28 °C, 0.1 hz, and 4.0 in. nominal displacement amplitude for all time-history analysis methods.

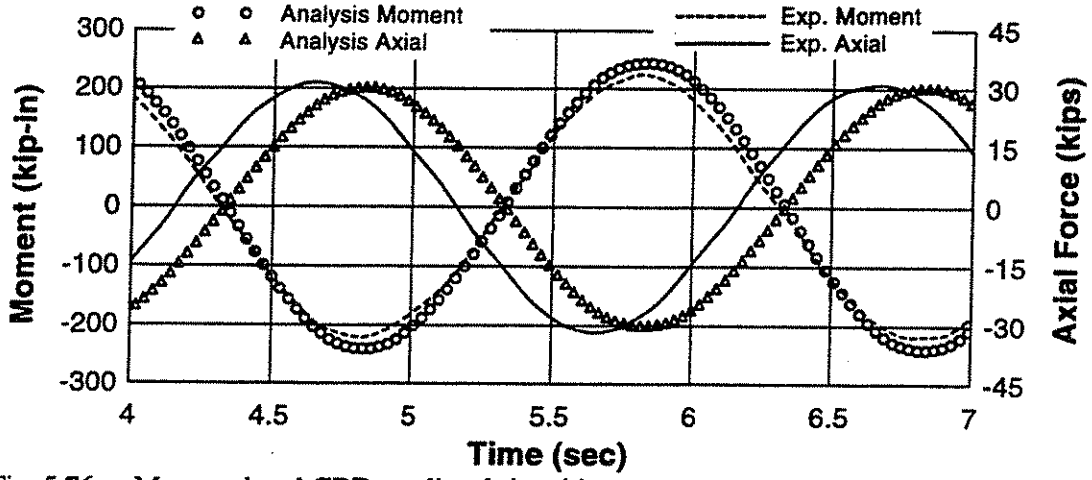

Fig. 5.76a - Measured and GRD predicted time history response at second story East column for 32 °C, 0.5 hz, and 0.5 in. nominal displacement amplitude test.

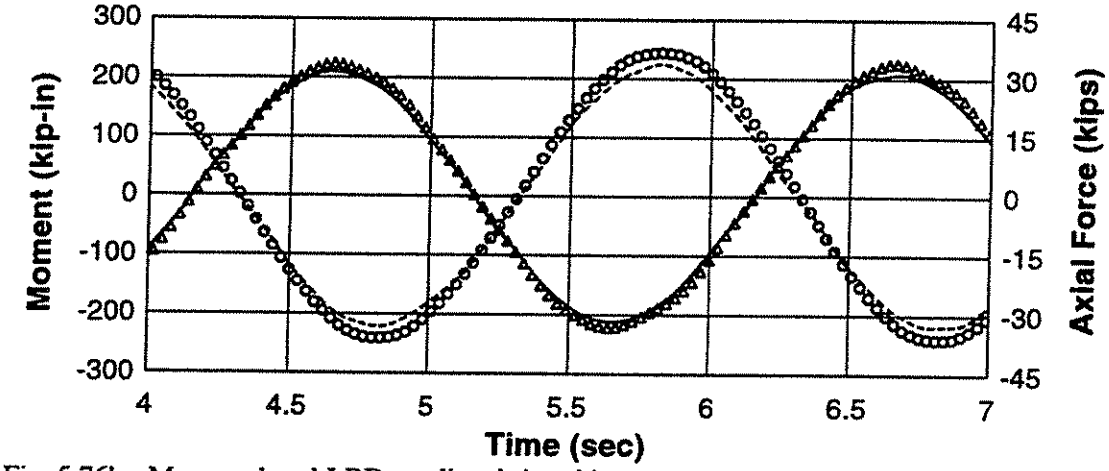

Fig. 5.76b - Measured and LRD predicted time history response at second story East column for 32 °C, 0.5 hz, and 0.5 in. nominal displacement amplitude test.

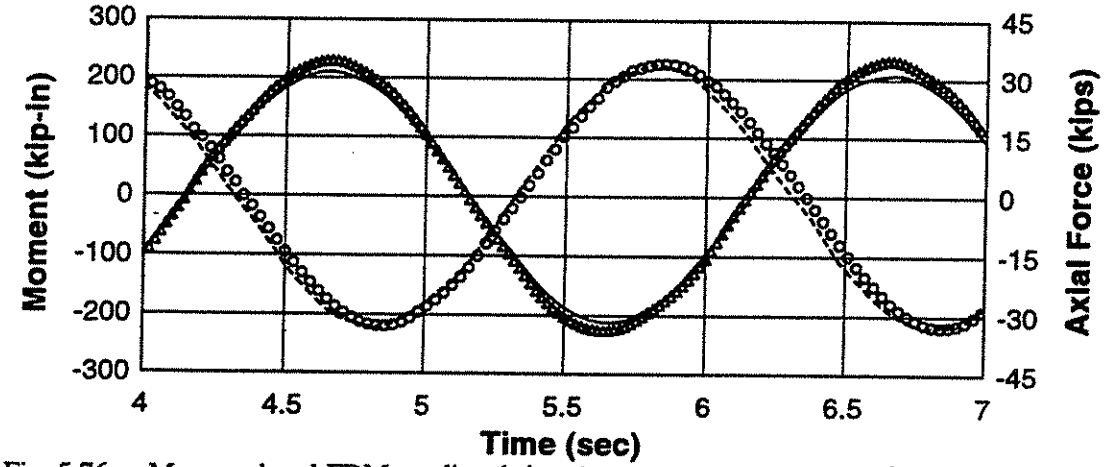

Fig. 5.76c - Measured and FDM predicted time history response at second story East column for 32 °C, 0.5 hz, and 0.5 in. nominal displacement amplitude test.

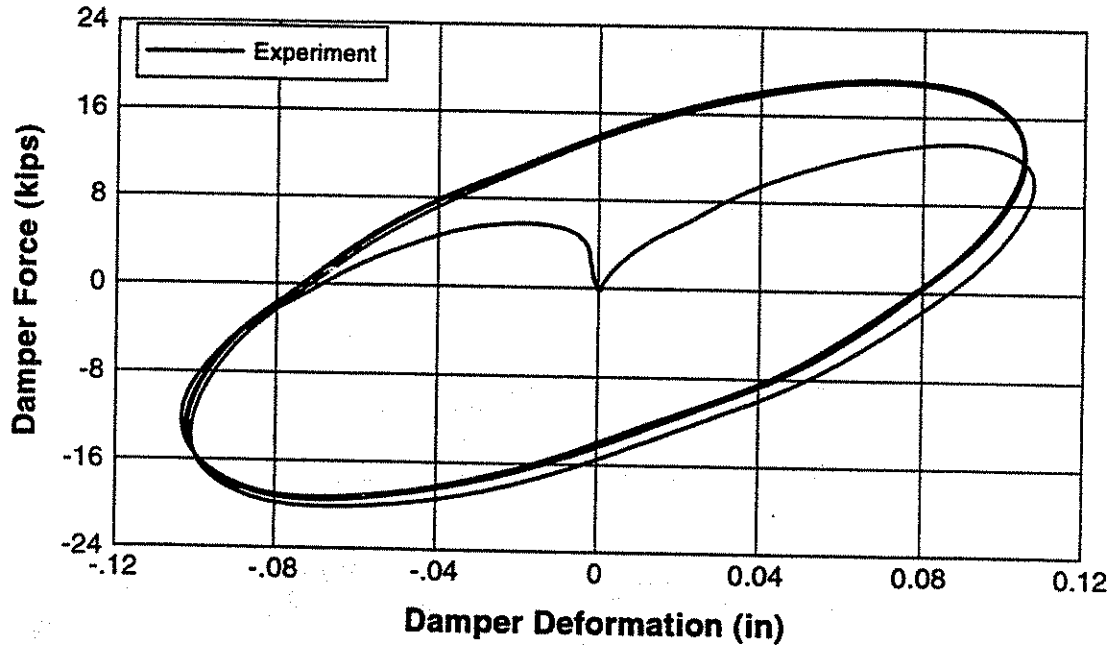

Fig. 5.77a - Measured damper response at second story East damper for 32 °C, 0.5 hz, and 0.5 in. nominal displacement amplitude test.

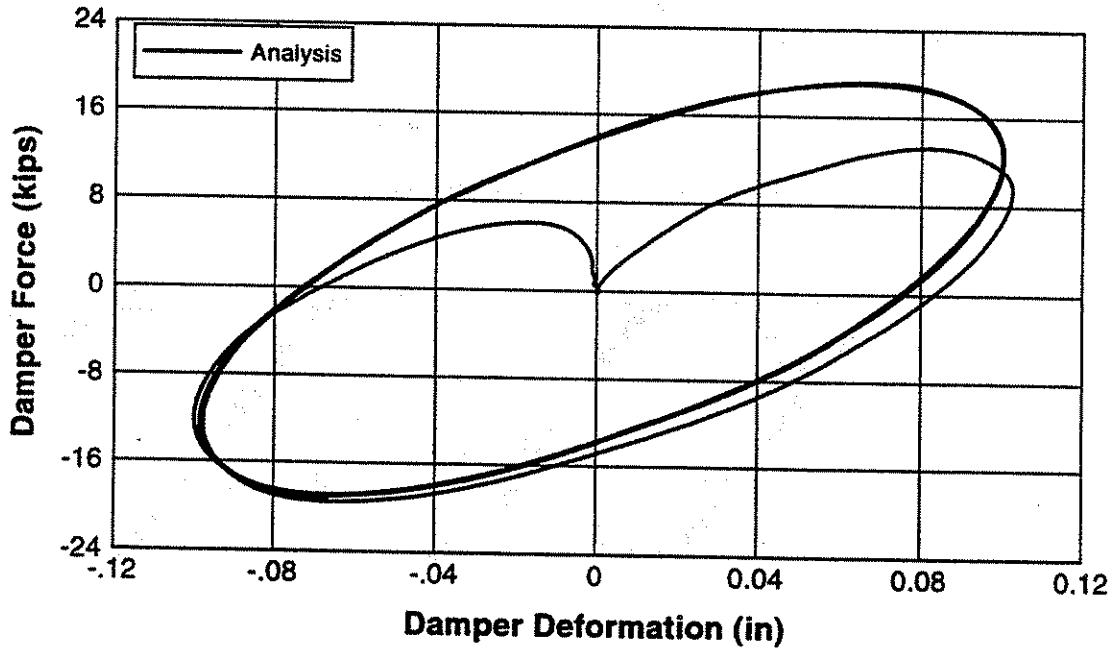

Fig. 5.77b - FDM predicted damper response at second story East damper for 32 °C, 0.5 hz, and 0.5 in. nominal displacement amplitude test.

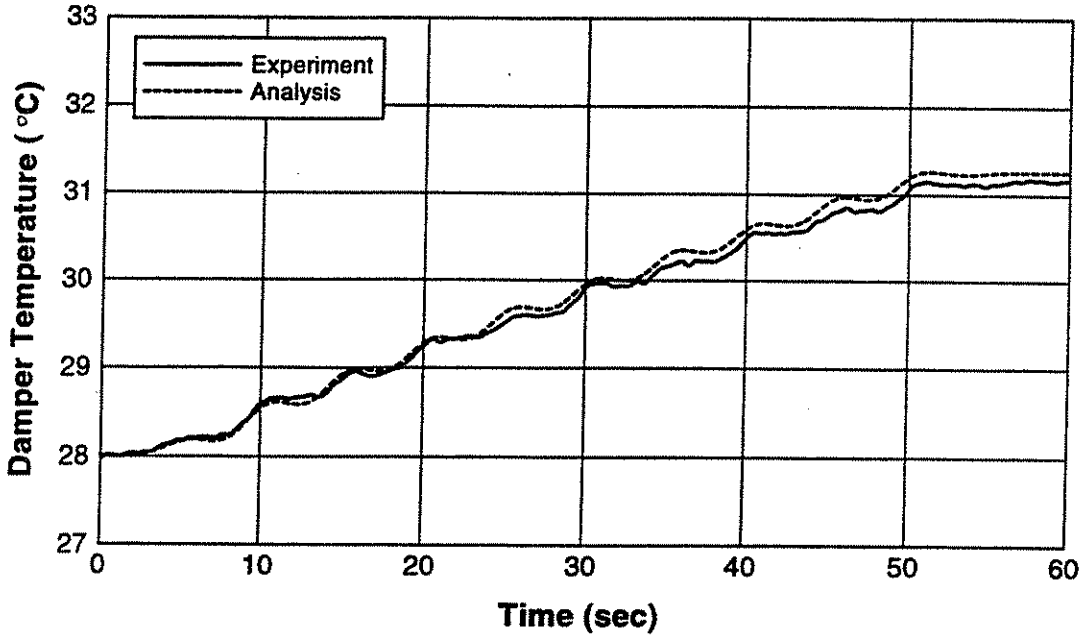

Fig. 5.78 - Measured and FDM predicted damper temperature rise at second story East damper for 28 °C, 0.1 hz, and 4.0 in. nominal displacement amplitude test.

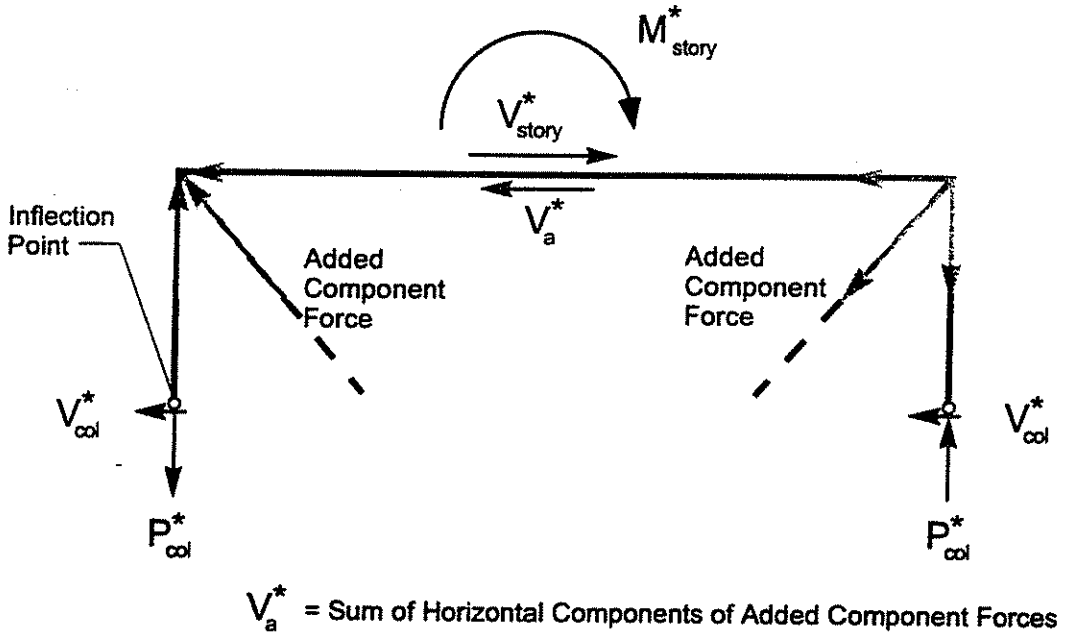

Fig. 5.79 - Free-body of frame segment used to determine member forces.

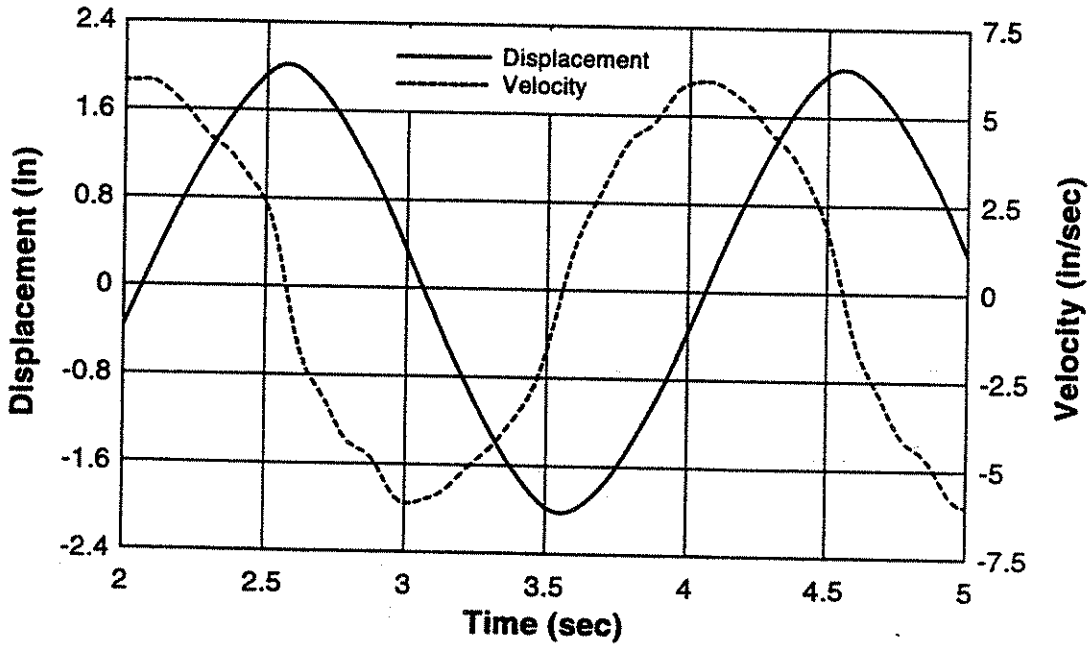

Fig. 5.80 - Distorted shape of imposed displacement and velocity history.

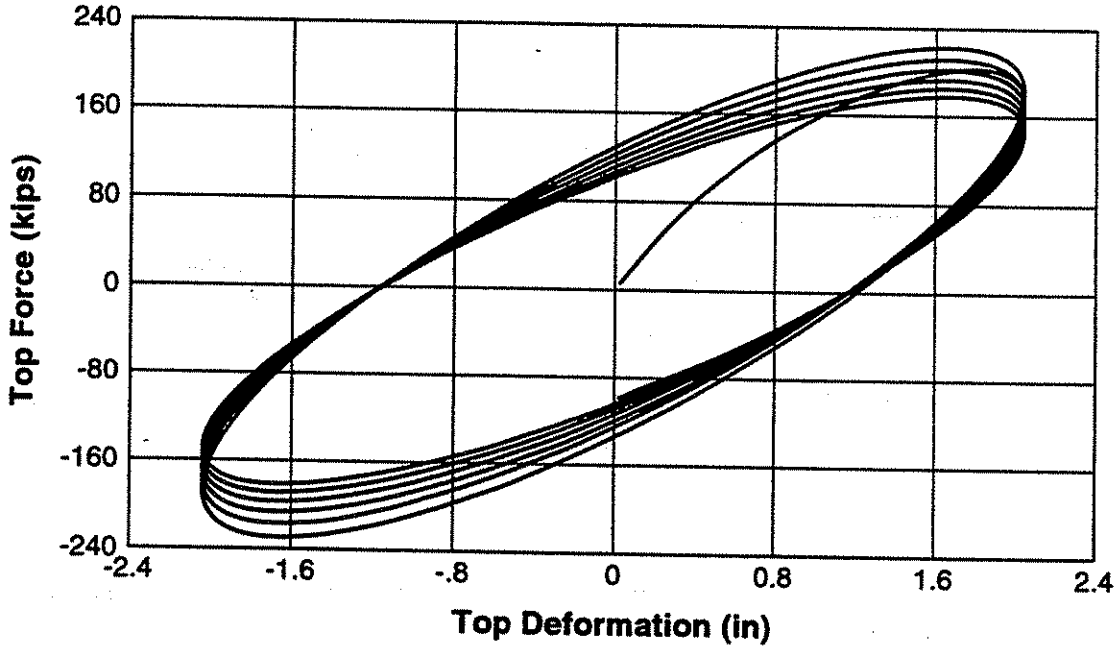

Fig. 5.81 - Analytically predicted force-displacement response of VE-frame when subjected to an ideal sinusoidal loading history.

CHAPTER 6.0 EARTHQUAKE RESPONSE: SIMULATION, TESTING, AND ANALYSIS

6.1 Introduction

This chapter presents results of the experimental and analytical program for a VE-damped steel frame building subjected to earthquake forces. Design of a prototype VE-frame for seismic forces is described. A testing methodology for the full-scale frame experiment is presented and the analytical procedure, used as the basis for the methodology, is verified through correlation of small-scale shaking table tests. Experimental response of the structure to nine different earthquake motions is presented including: global frame response, local member forces, VE-damper response, and temperature rise. Analytical correlation of earthquake induced structural response was conducted using fractional derivative, global Rayleigh damping, and local Rayleigh damping methods. Influence of initial damper temperature and damper temperature rise on structural response are addressed. Finally, conclusions are presented.

6.2 Seismic Prototype Frame Design

A prototype steel frame was designed to permit assessment of the seismic behavior for a full-scale VE-damped steel frame. A building layout was established which attempted to reflect an actual structure and met additional requirements for testing such as the force, displacement, and loading frequency capabilities of the hydraulic actuators as well as available space and hold-down spacing in the laboratory. The selected plan and elevation of the seismic prototype building are shown in Fig. 6.1. Building response was considered for the east-west direction only. Frames and members in the north-south direction were assumed to be appropriately designed and no torsional response was considered. As seen in this figure, there are six VE-damped frames in the east-west direction. All VE-frames in the east-west direction are identical and other framing members carry gravity load only.

6.2.1 Design Criteria

Design of the VE-frame was performed using an NEHRP based equivalent static force design procedure developed by Kasai and Fu [1995]. The VE-frame is located in San Francisco, California on very dense soil. The frame was designed to satisfy two criteria:

- The structure should remain elastic against the design based earthquake (DBE) at 24 °C.
- The building should protect non-structural components for the DBE by limiting the drift to 0.0075 radians at the reference temperature of 24 °C.

To economically achieve this level of seismic performance, the structure must use some type of supplemental damping device. For this study, VE-dampers are considered.

Frame members were of A572 grade 50 steel and connection pieces were of A36 steel. Square tube sections corresponding to A500 Grade B (F_y=46 ksi) were used for the brace, which attaches the VE-damper to the frame.

6.2.2 Design Forces

The design base shear spectrum from the National Earthquake Hazard Reduction Program (NEHRP) Recommended Provisions for Seismic Regulations for New Buildings [1995] is:

$$V_{DBE} = \frac{1.2C_v}{T^{2/3}}W \leq 2.5C_aW \qquad [6.1]$$

where V_{DBE} is the base shear for an elastic building subjected to the DBE, T is the building period, W is the total weight of the building, C_v is a seismic coefficient which depends on the soil type and effective peak velocity-related acceleration (A_v=0.4), and C_a is a seismic coefficient which depends on the soil type and effective peak acceleration (A_a=0.4). The prototype frame is located on a site with very dense soil corresponding to NEHRP soil profile B/C, which results in C_v =0.48 and C_a =0.40. The required NEHRP yield base shear strength is:

$$V_{yield} = \frac{V_{DBE}}{R} \qquad [6.2]$$

where R is a strength reduction factor which depends on the type of framing used by the structure. Eq. 6.2 anticipates yielding and ductility of the frame when subjected to the DBE. For an elastic structure R=1.0, and a conventional structure would require a large V_{yield} and consequently large members and connections. The VE-frame uses VE-dampers to reduce the earthquake forces by providing high damping. To include the beneficial effects of higher damping, the yield base shear strength becomes:

$$V_{yield} = D_\xi V_{DBE} \qquad [6.3]$$

where D_ξ is a parameter which indicates the effect of the higher damping in reducing the DBE base shear. The damping effect parameter is defined [Kasai and Fu, 1995] as:

$$D_\xi = \frac{1.5}{\sqrt{1+25\xi}} \qquad [6.4]$$

where ξ is the frame damping ratio. Note the NEHRP spectrum (Eq. 6.1) uses a ξ of 5% for which D_ξ=1.0. The design pseudo-acceleration spectrum $S_{pa}(T,\xi)$ for a highly damped VE-frame is:

$$S_{pa}(T,\xi) = D_\xi \frac{1.2C_v}{T^{2/3}} \le D_\xi 2.5C_a \qquad [6.5]$$

The design pseudo-acceleration spectrum is shown in Fig. 6.2 for damping ratios of 5, 10, 20, and 30%. As seen in this figure, the DBE acceleration decreases as the damping ratio increases, resulting in lower required base shear. The design displacement spectrum $S_d(T,\xi)$ is:

$$S_d(T,\xi) = \frac{4\pi^2}{T^2} D_\xi \frac{1.2C_v}{T^{2/3}} \le \frac{4\pi^2}{T^2} D_\xi 2.5C_a \qquad [6.6]$$

The design displacement spectrum is shown in Fig. 6.3 for damping ratios of 5, 10, 20, and 30%.

Many different combinations of building period and damping ratio are possible for the prototype frame. The building period was initially estimated from the NEHRP approximate formula for the fundamental period [NEHRP, 1995] as:

$$T_a = C_T h_n^{3/4} \qquad [6.7]$$

where C_T is a coefficient which is related to the framing system, and h_n is the height of the building in feet. C_T coefficient of 0.03, specified for an eccentrically braced frame, is used for the VE-frame with stiff dampers. The building period estimate from Eq. 6.7 is typically lower than the actual period, which is generally conservative from the perspective of strength requirement. However, Eq. 6.7 would result in an unconservative estimate of lateral drift. For the prototype frame, T_a was 1.06 seconds (Eq. 6.7) for which the required $S_{pa}(1.06,\xi)$=0.553, 0.443, 0.338, and 0.284 g for ξ=5, 10, 20, and 30%. A target damping ratio of 30% was selected to minimize the DBE base shear. From Eq. 6.6, the actual building period T must be below 1.17, 1.38, 1.69, and 1.94 seconds for ξ=5, 10, 20, and 30% to keep the frame drift below 0.0075 rad. Limits on actual building period were estimated by noting that $S_d(T,\xi)$ is the maximum displacement of a multi-story building at the 2/3-height when the fundamental mode shape is a straight-line. Highly damped VE-structures tend to exhibit straight-line fundamental mode shapes [Kasai *et al.*, 1994]. For the target damping ratio of 30%, the actual building period must be below 1.94 seconds.

Dead load on the floors was 78 psf and curtain wall dead load was 15 psf. The total dead weight of the building was 9139.2 kips. Traditionally, building code specifications compute the required base shear as $S_{pa}M_{tot}$. For the multi-degree of freedom (MDOF) VE-frame, which exhibits a straight line fundamental mode shape, the theoretical base shear is $S_{pa}M_{tot}/1.33$. Thus, the theoretical required yield strength for the seismic prototype frame is:

$$V_{yield} = \frac{S_{pa}(T = T_a = 1.06, \xi = 30\%)M_{tot}}{1.33} \qquad [6.8]$$

From Eq. 6.8, the required yield strength was 1949.2 kips for the prototype frame. This total base shear was shared equally among the six VE-frames in the east-west direction (Fig. 6.1).

The total base shear was distributed vertically to each story level according to the NEHRP formula:

$$F_i = V_{yield} \frac{w_i h_i^k}{\sum_{i=1}^{N} w_i h_i^k} \qquad [6.9]$$

where w_i is the portion of the gravity load at level i (kips), h_i is the height from the base to level i (ft), k is a coefficient which is related to the building period, and N is the number of stories. The coefficient k is 1.0 for a building with a period of 0.5 seconds or less, 2.0 for a building with a period of 2.5 seconds or more, and is determined by interpolation for a building with a period between 0.5 and 2.5 seconds.

6.2.3 Preliminary Analysis and Member Selection

The key to controlling temperature sensitivity for a VE-frame is to provide a stiff damper and a stiff brace relative to the frame stiffness without dampers. A stiff damper is desirable because it attracts force. A stiff brace is desirable because it permits the force attracted by the damper to be dissipated by enabling deformation to take place in the VE-material instead of in elastic deformation of the brace. The role of damper and brace stiffness on the equivalent damping ratio for a single degree of freedom (SDOF) system is shown in Fig. 6.4 for an assumed η_d=1.32 at the reference temperature of 24 °C, a loading frequency of 0.5 hz, and strain of 50%. A target damper to frame stiffness ratio K'_d/K_f =3 in the lower three stories was selected and brace to frame stiffness ratio $K_b/K_f \geq 20$. From Fig. 6.4, this would lead to ξ of 33% which is relatively stable even as K'_d/K_f varies due to temperature changes in the VE-material. Although the damping ratio of a MDOF VE-frame is typically less than that of a SDOF system, due to chord drift which does not promote energy dissipation in the VE-

dampers, the final damping ratio for the MDOF VE-frame should be close to the target of 30%.

Using the computed lateral loads (Eq. 6.9) and the stiffness ratios above, the portal method, as described in Chapter 5, was used to obtain the maximum member forces. The maximum member forces included the effect of the out-of-phase forces from the dampers. In addition to seismic forces, gravity forces were included using the AISC LRFD [1993] load combination $1.2DL + 0.5LL \pm E$, where DL is the dead load, LL is the live load, and E is the earthquake lateral load. Live load on the floors was 50 psf and live load reduction factors were used for beams and columns as permitted by ASCE 7-95.

Members were sized based on the computed maximum forces described above. Beams and columns were designed considering the combined axial force and moment interaction using the AISC LRDF [1993] interaction equations:

$$\text{for} \quad \frac{P_u}{\phi_c P_n} \geq 0.2 \qquad \frac{P_u}{\phi_c P_n} + \frac{8}{9}\left(\frac{M_u}{\phi_b M_n}\right) \leq 1.0 \qquad [6.10a]$$

$$\text{for} \quad \frac{P_u}{\phi_c P_n} < 0.2 \qquad \frac{P_u}{2\phi_c P_n} + \frac{M_u}{\phi_b M_n} \leq 1.0 \qquad [6.10b]$$

where P_u and M_u are the maximum axial force and moment on the member from the applied loads, and P_n and M_n are the nominal axial force and moment capacities of the member, ϕ_c=0.85 is the axial force strength reduction factor and ϕ_b=0.9 is moment strength reduction factor. As discussed in Chapter 5, the maximum axial load and moment occur at different instances of time, however for conservative design, peaks are assumed to occur simultaneously.

Brace size for the added component was determined using the computed axial forces from the portal analysis described previously. For additional conservatism, the axial force in the brace was amplified by a factor of 1.5 to prevent possible brace buckling [Kasai and Popov, 1986]. Effective length factors of $k_x=k_y=0.8$ and strength reduction factor $\phi=0.85$ were used for design of the braces.

6.2.4 Period and Damping Estimates from Elastic Static Analysis

With the member sizes obtained above, elastic static analysis was performed for the frame without dampers. This analysis was performed to determine the shear stiffness of the frame K_f. Beam-column and column base connections were assumed rigid and center-line frame dimensions were used for the model. To isolate the frame shear stiffness, axial deformations in the columns were suppressed by artificially increasing the cross sectional area. Suppression of column axial deformation was done for this analysis only. Lateral forces determined from Eq. 6.9 were used to load the unbraced frame model. The computed frame stiffness was ≈ 72 kips/in in the lower stories. Using the target ratio $K'_d/K_f = 3$ at each story level, the required damper stiffness K'_d was determined. Similarly, the brace stiffness K_b was determined for the brace sizes selected in the previous section assuming center-line dimensions for the member and axial area of the tube only. With the computed K'_d and K_b at each story, the added component stiffness K'_a was determined from Eq. 5.3 assuming $\eta_d=1.32$. An analytical model of the VE-frame was then developed. The added components were modeled with linear elastic truss elements with in-phase stiffness K'_a. The fundamental building period T was calculated using Rayleigh's method as:

$$T = 2\pi \sqrt{\frac{\sum_{i=1}^{N} W_i \Delta_i^2}{g \sum_{i=1}^{N} F_i \Delta_i}} \qquad [6.11]$$

where Δ_i are the i-th story lateral displacements which correspond to story forces F_i (Eq. 6.9), and g is the gravitational acceleration. The period was 2.0 seconds which is larger than the T_a=1.06 used in preliminary design. The period is also very close to the limit for drift control at ξ=30%.

Equivalent viscous damping ξ_{tot} for the VE-frame was calculated using an energy approach and static analysis [Kasai *et al.*, 1994][Sause *et al.*, 1994] as:

$$\xi_{tot} = \frac{\sum \eta_a F_a u_a}{2 \sum_{i=1}^{N} F_i \Delta_i} + \xi_o \qquad [6.12]$$

where $\sum_{i=1}^{N} F_i \Delta_i$ is the total work done by external lateral forces with Δ_i and F_i defined previously, $\sum \eta_a F_a u_a$ is the total energy dissipated by the VE-dampers where F_a and u_a are the force and deformation of the added component respectively, ξ_o is the unbraced frame damping ratio (2%) and N is the number of stories. The computed damping ratio ξ_{tot} was 30.2% which is very close to the 30% assumed during initial design.

6.2.5 VE-Damper Design

The VE-damper was designed based on deformation calculations from static analysis performed to estimate the period and damping ratio of the VE-frame in the previous section.

Thickness of the VE-layer h=0.625 in. was selected so as to limit the maximum shear strain γ to approximately 100%. An average γ of 0.7 times the maximum shear strain was considered as an average VE-material strain during a random earthquake event. For the selected damper thickness h=0.625 in., reference temperature of 24 °C, VE-frame building period of 2.0 seconds, and average strain of 70%, storage modulus G'=114 psi (determined from manufacturer's data), and the damper area A was determined by:

$$A = \frac{K'_d h}{G'} \qquad [6.13]$$

to provide the required damper stiffness. The required area of VE-material was 1248 in^2. The final damper design is illustrated in Figs. 3.1a and 3.1b.

6.2.6 Final Design for Test Specimen

After completing the design steps in the previous sections, the initial frame design was refined to include lateral forces for the actual building period as well as actual damper stiffness and loss factors. This was done to provide frame member sizes which were as small as possible to permit applied laboratory forces and displacements to be within testing capabilities and to enable application of significant stress in members during the tests. The final design was performed iteratively following the design procedure in sections 6.2.1 to 6.2.5. The final fundamental period was 2.0 seconds which results in $S_{pa}(2.0,\xi)$= 0.186 g for ξ=30.2% which was the final damping ratio. The corresponding base shear V_{yield} was 1275.9 kips for each VE-frame. Final design distributed lateral forces at each story level and overturning moment are shown in Table 6.1. Using the portal method, computed maximum member forces are shown in Table 6.2. Final member and brace sizes are shown in Table 6.3. The computed damping

ratio for the frame was 30.2% from Eq. 6.12. The final design achieved the strength requirement of elastic performance and the drift requirement less than 0.0075 rad. at the reference temperature for the DBE. Time-history analysis of the frame subjected to selected earthquake ground motions indicates the frame drift was below 0.005 rad. as will be shown in section 6.3.

6.2.7 Check of Design for Wind Forces

After the seismic design was complete, the frame was checked for strength against code wind forces prescribed in ASCE 7-95. The design wind speed was 85 mph for San Francisco, California. Code wind forces were computed according to the procedure available in the commentary for a building with a fundamental frequency below 1 hz. To compute the strength of the frame for wind forces, the AISC LRFD [1993] load combination $1.2DL + 0.5LL \pm 1.3W$ was used, where DL is the dead load, LL is the live load, and W is the wind lateral load. The contribution of the VE-dampers was conservatively neglected for wind analyses and the VE-frames were modeled as unbraced frames. Member forces and frame drifts were evaluated from static analysis of the unbraced frames subjected to code wind forces. The unbraced frames exhibited sufficient strength and stiffness for the code prescribed wind forces and gravity loads, including second order effects. Computed frame drifts, including second-order effects, were below 1/500 for short term effects [ASCE 7-95]. Additional work related to wind effects on VE-frames is contained in Chapter 7.

6.2.8 Special Design Considerations for VE-Frame Test

Actual steel framed buildings would typically have dampers which are inverse to the layout used for the test specimen as illustrated in Fig. 6.5a. This would be done to reduce the number of foundation locations. The inverted placement of the dampers in the prototype frame was required to permit attachment of a loading fixture at the third story elevation as illustrated in Fig. 6.5b.

6.3 Testing Methodology and Verification

6.3.1 Testing Methodology

Due to specimen size and limitations in laboratory testing capabilities, it is currently prohibitive to test a ten story structure at full-scale. However, a unique methodology was developed to test a portion of the full-scale prototype 10-story VE-frame developed in section 6.2 subjected to large magnitude vertical and lateral earthquake or wind forces. This was possible by taking advantage of several structural characteristics. Lower stories contribute the least to lateral forces on the prototype building, from both wind and seismic forces. As a result, neglecting lateral force contributions of the lower stories will not dramatically change the response behavior of the frame. Higher modes do not typically contribute to the structural response for a highly damped VE-frame. This permits lateral forces to be applied only at the top of the specimen to accurately reflect the dynamic straight line deformed shape of the frame. Finally, structural members within the lower stories carry the largest forces, from both cumulative gravity load and lateral forces. This permits assessment of frame member response

to realistic forces of large magnitude. Using these features, the lower three story portion, of the 10-story prototype frame, can used as the test specimen to investigate the behavior of a VE-damped steel frame to gravity, seismic, and wind loading of large magnitude as illustrated in Fig. 6.6. The lower three story test specimen of the larger 10-story prototype VE-frame is illustrated in Fig. 5.2.

Although only the lower three story portion was used in the experiment, the response of the full 10-story structure was reflected in the displacement response imposed on the three story portion. This was carried out in several ways:

- The cumulative axial forces from gravity loads from the complete 10-story structure were applied to the columns of the frame test specimen.
- Second order or P-Δ effects were included by the method described in Chapter 5.
- In general, highly damped structures, like the VE-damped prototype frames, behave predominantly in the first mode. The first mode has a straight line displaced shape and as a result, the test structure only requires lateral force actuators at the third story location to accurately simulate the displacement response within all three lower stories.
- Contribution of the first three stories to the dynamic response, for both wind and seismic events, is minimal. Thus, there is little difference between member forces and frame displacements in the 3-story test specimen and the 10-story prototype frame by neglecting lower story contributions.
- Dynamic response of the 10 story frame including the influence of the VE-dampers is accurately captured using the finite element described in Chapters 3 and 5. Therefore,

prediction of dynamic response for the frame using the VE-element is reasonable as described further in section 6.3.2.

- The mass, stiffness, and damping for the full 10-story frame are included in the analytical model. Damping and frame stiffness inherent in the unbraced frame, as described in Chapter 4, were included in the 10-story analytical model. Nonlinear dynamic time-history analysis of the 10-story model was performed for base accelerations. Computed analytical displacement response at the third story was imposed on the test specimen in real-time as illustrated in Fig. 6.7.
- The real-time displacement history imposed on the test specimen generates equivalent forces in members and dampers to those in the 10-story prototype with one exception. One limitation of the testing method is the inability to impose sufficient axial force in columns of the laboratory specimen from overturning moment. Overturning moment from lateral forces on the 10-story frame generates significant axial forces in the lower story columns due to larger moment arms of the forces. The laboratory specimen only produces overturning moment from the third story, and as a result column axial forces in the test specimen are smaller than those in the prototype frame. Other column forces in the prototype frame, such as bending moments and shears, are adequately captured.

6.3.2 Verification of Testing Methodology

The testing methodology for both earthquake and wind hazards is based on analytical prediction of frame response using beam-column finite elements and a sophisticated VE-damper finite element described in Chapter 3. Previously described validation of the VE-damper finite element, demonstrated the effectiveness of the element in predicting individual

VE-damper response to sinusoidal and random inputs, and VE-frame response to sinusoidal excitations. To further assess the methodology used to test the full-scale frame portion, the FDM analysis method was used to predict seismic response of a reduced scale VE-frame.

A 2/5 scale three-story steel moment resisting frame with and without VE-dampers was recently subjected to shaking table earthquake simulations at the National Taiwan Institute of Technology (NTIT), Taipei, Taiwan [Chou, 1994]. Two frames were tested at NTIT: a moment resisting frame without VE-dampers (MRF) and an identical MRF with added VE-dampers (VE-frame). The frame was designed to satisfy strength requirements of NEHRP 1988, but largely violates code specified drift requirements. Frames consisted of a single bay with columns spaced at 2.4 m and story elevations of 1.6 and 1.4 m as illustrated in Figs. 6.8a and 6.8b. Section properties for members are shown in Table 6.4. Steel plates were used to provide lumped mass at each story as shown in Fig. 6.8b. Except for the VE-dampers installed at each story, the VE-frame was identical to the MRF. The viscoelastic material used in the dampers was ISD 110, manufactured by 3M Corporation, the same material used in the dampers tested at Lehigh. Damper dimensions and configuration are illustrated in Fig. 6.8c.

The MRF was subjected to El Centro table accelerations with scaled peak ground accelerations (PGA) from 0.05g to 0.5g. Experimental results from the MRF indicated yielding of some members at 0.1g El Centro and severe damage to the frame after 0.5g El Centro. The VE-frame was subjected to El Centro table accelerations with scaled PGA from 0.05g to 0.8g. Initial temperatures of the VE-dampers were 30 °C ± 1 °C and torsional response of the MRF and VE-frames was negligible.

Before analysis of the VE-frame, an analytical finite element model was developed to calibrate the response of the MRF without dampers to the experimental response. Elastic free vibration properties of the analytical MRF model were calibrated to the experimentally reported values using static analysis and employing an improved Rayleigh procedure Eq. 6.11.

Dynamic analysis of the MRF was conducted using PC-ANSR [Maison, 1992] and NTIT shaking table acceleration records. Table motions corresponding to El Centro with PGA of 0.05g were selected to correlate structural response when the frame remains elastic. Proportional viscous damping values for the frame were adjusted until the experimental and analytical response were comparable. Damping ratios determined from analysis corresponded well with experimentally reported values. Analytical displacement time history at the roof elevation and experimental response are shown in Figs. 6.9a and 6.9b respectively.

Dynamic analysis of the VE-frame was conducted using table motions corresponding to El Centro with PGA of 0.5g. Analysis of the VE-damped frame was performed utilizing the material, stiffness, and frame damping properties determined from the earlier analytical correlation of the MRF. No modifications were made to the frame members after completion of the MRF analyses. The only changes were to introduce VE-dampers to the MRF model. Analytical VE-frame response was determined using the fractional derivative model [Kasai *et al.*, 1993] to model the VE-dampers. Element parameters were determined using the VE-material properties from experimental damper response under sinusoidal loading at 28 °C. Analytical displacement time history at the roof elevation and experimental response for El

Centro 0.5g are shown in Figs. 6.10a and 6.10b respectively. As seen in this figure, analysis using the VE-finite element reasonably predicts actual VE-frame response.

Results of this series of analyses indicate the methodology used to test the VE-damped frame (i.e. using analysis to predict actual frame response to ground shaking) is reasonable and the predicted response of the 10-story prototype frame would reflect actual structural behavior if subjected to the earthquake ground motions considered as part of this study.

6.4 Simulated Earthquake Tests

6.4.1 Earthquake Ground Motions Investigated

Nine different earthquake ground motions were included in the test program and significant characteristics are presented in Table 6.5. The selected earthquake records reflect many different characteristics including duration, intensity, frequency content, and soil conditions. Acceleration time-histories and response spectra for the nine records are shown in Figs. 6.11a to 6.19c. Three of the records (1.5xEl Centro, 1.5xHachinohe, and 2.824xTaft) are considered design level earthquakes for Japanese seismic design practice [AIJ, 1990].

6.4.2 Experimental Procedure

The response of the VE-damped frame to the nine earthquakes was investigated by performing nonlinear time-history analysis of the seismic prototype frame described in section 6.3 using the fractional derivative method described in Chapter 5. The analytical model of the 10-story

prototype VE-frame incorporated many earlier experimental findings which were important to the frame behavior. The fractional derivative parameters used in the VE-damper finite element were those determined from individual damper tests as presented in Chapter 3 and Appendix A. The frame model included column base connection flexibility and beam-column rigid end-zones as described in Chapter 4. Equivalent damping assigned to the unbraced frame was 2%, as discussed in Chapter 4. Analytically predicted frame response at the third story for the nine earthquakes is shown in Figs. 6.20a to 6.28a.

Analytically computed response at the third story was imposed on the test specimen in real-time. The analytical third story displacement response was discretized into displacement-time pairs equally spaced at 0.14 seconds for lateral actuator displacement commands. This fairly coarse spacing of displacement commands was required due to limitations in communication rates between the control computer and DCLs located in the actuators. Displacement control of the actuators was performed using ramp functions from point to point of the discretized analytical displacement history. Instrumentation layout for the earthquake tests was the same as that described in Chapter 5. Data were acquired for the 196 channels of instrumentation at an acquisition rate of 100 hz (separation of 0.01 seconds between samples) for all tests except the two Mexico City earthquakes which used acquisition rates of 50 and 25 hz as shown in Table 6.6. These acquisition rates permitted continuous measurement of overall frame behavior, member response, and damper temperature rise as well as assessment of the interaction of between the frame member forces and damper forces.

6.4.3 Experimental Results

Measured displacement time histories at the third story from the experiment are shown in Figs. 6.20b to 6.28b for the nine earthquakes. The specimen remained elastic during all tests with the exception of minor local yielding at near beam-column connections. As a result of the coarse spacing of actuator commands described above, some of the small detail of the response record is lost, however, in general the displacement response is well captured. Additionally, the peak displacements tend to be slightly lower than the predicted displacement, particularly on the second half cycle of a large excursion as illustrated in Figs. 6.20a and 6.20b. Some distortion is also evident in the peak displacement cycles of some records (Figs. 6.20a and 6.20b). This distortion is caused by the physical limitations in the hydraulic control system including pressure drop across the servo-valves and instantaneous flow capacity at the peak demand. Finally, there was some stretching of the time scale between the actuator command and actual displacements. This was a limitation of the control system. In general, however, the peak response portion of the displacement history was well captured. It should be noted that the testing capabilities in the ATLSS laboratory are outstanding and the observed limitations resulted from the very demanding test requirements related to specimen size as well as actuator force, displacement, and velocity capacities.

Measured overall force-deformation response for the frame is shown in Figs. 6.29a to 6.36a for eight of the nine earthquakes. The ninth earthquake (1.5xEl Centro) is described in section 6.4.4. Overall responses indicated the dampers provided significant energy dissipation for all the earthquakes. The California and Japanese earthquakes exhibit more random response with

a few large cycles and many small cycles while the Mexico City earthquakes exhibit almost harmonic response with many moderate cycles or small cycles.

Example force-deformation response for the second story East VE-damper during each test is shown in Figs. 6.29b to 6.38b. These response curves exhibit significant energy dissipation. As shown in these figures, the damper stiffness slightly decreases during the test, indicating temperature rise. Typical temperature rise measured in the second story East damper is shown in Figs. 6.29c to 6.36c. During large excursions, dampers exhibited the largest temperature increases. Final measured temperatures for dampers in each story for each earthquake are shown in Table 6.6. The largest temperature rise (3.4 °C) was observed for the Mexico City Central de Abastos-Frigorifico earthquake record. This earthquake was of 60 second duration with many significant excursions (Fig. 6.27a). Additionally, the Mexico City Central de Abastos-Oficina record produced a temperature rise of 2.2 °C with only moderate excursions and duration of almost 2 minutes. Damper temperatures were predicted, as shown in Figs. 6.29c to 6.36c, by integrating the damper stress-strain response and dividing by the specific heat and density of the VE-material (Eq. 3.6). As shown in these figures, damper temperature rise was reasonably predicted for the earthquakes. This indicates that for short duration seismic events (even those that last 2 minutes), heat transfer can be neglected when determining damper temperature rise.

Phase relationships between members and dampers for the seismic response were similar to those described in Chapter 5. Column moments were in-phase with displacements and axial forces were in-phase with the damper force. As a result, the axial force-moment interaction

exhibits hysteresis as shown in Figs. 6.37 to 6.44. The phase lag causes maximum axial force and maximum moment to occur at different instances of time as described in Chapter 5.

6.4.4 Comparison of Predicted 10-Story and Measured 3-Story Response

Experimental VE-frame response was determined from time history analysis of the 10-story prototype frame as described in section 6.4.2. The analytically computed displacement response was imposed on the test specimen which ensured the overall experimental and analytical displacement responses are similar as shown in Figs. 6.20a to 6.28b. Local member responses were compared to determine if the predicted and measured responses were also similar. The El Centro earthquake response was selected for this comparison. The computed and actual measured displacement response at the third story level were shown previously in Fig. 6.20a and 6.20b. The second story beam at the west beam-column joint and third story west column were chosen for comparison between 10-story analytically predicted response and measured 3-story specimen response.

The predicted and measured moment in the west beam-column joint are shown in Figs. 6.45a and 6.45b respectively. Predicted and measured axial force at the west beam-column joint are shown in Figs. 6.46a and 6.46b respectively. As seen in these figures, the measured responses corresponded well with the predicted values. The predicted and measured moment in the third story west column are shown in Figs. 6.47a and 6.47b respectively. Predicted and measured axial force in the third story west column are shown in Figs. 6.48a and 6.48b respectively. As seen in these figures, the measured column moment response corresponded with the predicted. However, the measured axial force response is significantly smaller than the predicted

response. This is a result of the overturning moment on the frame, which in the experiment is generated by actuators located at the third story elevation. In the 10-story prototype building, overturning moment is generated by lateral forces on all the stories. Lateral forces on the upper stories have much larger moment-arms, resulting in much higher column axial forces than those produced by laterally loading at the third story only as done in the experiment. This large difference in column axial force from overturning moment does significantly not impact VE-damper response.

6.4.5 Correlation of Experimental Frame Response

Analytical correlation of the experimental seismic response for the VE-damped frame was conducted using the fractional derivative model for the VE-dampers. The 1.5xEl Centro response was chosen for these correlative analyses. Analysis results, including global frame response and time history response of selected members were compared with experimental results.

The VE-frame analytical model consisted of the unbraced frame model developed in Chapter 4 with VE-damper elements. Parameters for the VE-element were determined in Chapter 3 and Appendix A. Dynamic time history analysis of the VE-frame analytical model was performed using PC-ANSR and applying the experimentally measured displacement history at the third story level. Element forces and nodal displacements were stored after each time step for comparison with experimental response.

Analytically predicted and measured overall frame response are shown in Fig. 6.49. Examples of the analytically predicted and measured damper response are shown in Fig. 6.50 or the second story East damper. Predicted and measured temperature rise for the second story East damper is shown in Fig. 6.51. Analytically determined and measured moment time history for the East second story beam is shown in Fig. 6.52. Analytically predicted and measured axial force time history for the East second story beam is shown in Fig. 6.53. As shown in these figures, the FDM reasonably predicted the overall frame response, local member response, VE-damper response, and temperature rise for the random displacement history.

6.5 Seismic Analysis of VE-Damped Frame

Using the global Rayleigh damping and local Rayleigh damping methods presented in Chapter 5, the 10-story prototype VE-frame response was predicted for three of the nine earthquake ground motions (1.5xEl Centro, Northridge: Santa Monica, and Mexico City: Central de Abastos-Frigorifico) and the responses were compared with the response from the fractional derivative method (FDM). The FDM predicted responses are repeated in Figs. 6.54a, 6.55a, and 6.56a for comparison with response predictions from the other methods. Additionally, the influence of initial damper temperature and temperature rise for long duration earthquakes were investigated using the fractional derivative method.

6.5.1 Global Rayleigh Damping (GRD) Method

The global Rayleigh damping method (GRD) was described previously in Chapter 5. The GRD analytical model for the seismic prototype frame consisted of beam-column elements for the frame members and elastic truss elements to simulate in-phase stiffness of the added components. In-phase stiffness of the added components for analysis was determined from Eq. 5.3. The brace stiffness was 3000 kips/in for the first story and 3500 kips/in for the second and third stories based on actual measurements for the frame added components (Chapter 5). The natural frequency of vibration for the prototype frame (0.5 hz) was used as the loading frequency, 24 °C was the initial damper temperature, and average shear strain was assumed to be 50% to determine damper loss factor η_d and stiffness K'_d. Values for the loss factor and storage modulus were determined from experimental force-deformation response for the individual damper presented in Chapter 3.

Equivalent viscous damping for the VE-frame was calculated using an energy approach and static analysis (Eq. 6.12). The frame damping ratio without VE-dampers was 2% based on measured values (Chapter 4). Total equivalent damping ratio for the VE-frame was computed as 30.2%. Equivalent viscous damping ratios were used to determine a mass and stiffness proportional damping matrix (Eq. 5.7). Mass and stiffness proportional coefficients were determined according to Clough and Penzien [1993].

Using the GRD model, analytically predicted VE-frame response at the third story is shown in Figs. 6.54b, 6.55b, and 6.56b for three of the nine earthquakes (1.5xEl Centro, Northridge: Santa Monica, and Mexico City: Central de Abastos-Frigorifico). From these figures, it can be

seen that the GRD method reasonably predicted the overall VE-frame response. At later parts of the displacement response records, the GRD method tends to underestimate the deflection. This was particularly true for the long duration Mexico City earthquake (Figs. 6.56). This is because the GRD method neglects temperature rise in the dampers which results in overestimation of the damper stiffness at later portions of the record. Also, as demonstrated in Chapter 5, local member axial forces would require correction to determine the predict peak force (Eqs. 5.11 to 5.18) because the GRD assumes all forces are in-phase with displacement.

6.5.2 Local Rayleigh Damping Method

The local Rayleigh damping method (LRD) is described in Chapter 5. The LRD analytical model for the seismic prototype frame consisted beam-column elements for the frame members and elastic truss elements with high local damping to simulate both the in-phase and out-of-phase stiffness the added components. In-phase stiffness of the added components was determined from Eqs. 5.3 as described in section 6.5.1. The damping coefficient for the truss element was chosen proportional to the added component stiffness and estimated according to Eq. 5.10 using the natural frequency of the seismic prototype frame.

Using this model, analytically predicted VE-frame response at the third story is shown in Figs. 6.54c, 6.55c, and 6.56c for three of the nine earthquakes (1.5xEl Centro, Northridge:Santa Monica, and Mexico City: Central de Abastos-Frigorifico). From these figures, it can be seen that the LRD method does an excellent job of predicting the overall VE-frame response. At later parts of the displacement response records, the LRD method, like the GRD method, tends to underestimate deflections. This was particularly true for the longer duration Mexico City

earthquake (Figs. 6.56). This is because the LRD method also neglects temperature rise in the dampers which results in overestimation of the damper stiffness at later portions of the record. Local member forces, including time lagged response for peak axial forces in the beams and columns, are reasonably predicted by the method, as described in Chapter 5.

6.5.3 Influence of Initial Damper Temperature

Temperature has been shown to have an influence on the stiffness and damping of a VE-frame (Chapter 5). To determine the influence of initial damper temperature on the prototype structural response, FMD analyses of the frame were performed at temperatures of 16, 24 and 32 °C for the 1.5xEl Centro ground motion. The displacement response at the third story and axial force in the first story column were used to identify the influence of the initial damper temperature. Displacement of the frame at the third story is shown in Fig. 6.57 for initial damper temperatures of 16, 24 and 32 °C. As seen in this figure, as the damper initial temperature increases, the frame drift increases, and the period increases. These effects are due primarily to damper stiffness decrease at higher temperatures. Column axial force in the first story is shown in Fig. 6.58 for initial damper temperatures of 16, 24 and 32 °C. Column axial forces mainly result from overturning moment and thus provide an indication of the total lateral force attracted by the structure.

The prototype building period and damping ratio were computed for the initial damper temperatures of 16 and 32 °C. Building period was determined from static analysis and Eq. 6.11. Lower temperatures cause increased damper stiffness and shorter natural period. Higher temperatures cause reduced damper stiffness and longer natural period. The computed natural

period was 1.61 and 2.63 seconds for the initial damper temperatures of 16 and 32 °C respectively. Equivalent viscous damping was estimated from static analysis and Eq. 6.12. The computed damping ratio was 21.4% and 26.2% for the initial damper temperatures of 16 and 32 °C respectively. The damping ratio was relatively stable, particularly in through the higher range of temperatures. The influence of damper initial temperature on the required base shear is shown in Fig. 6.59. This figure illustrates the required base shear for the prototype frame for initial temperatures of 16, 24, and 32 °C. The influence of initial damper temperature on deflections is shown in Fig. 6.60 which illustrates the spectral displacement for the prototype frame for initial temperatures of 16, 24, and 32 °C. From Figs. 6.59 and 6.60, it can be seen that seismic forces are reduced as frame stiffness decreases due to higher initial damper temperatures. However, as the frame stiffness decreases, the drift increases. Based on these interactions between frame displacements and lateral forces, there should be an ideal damper configuration which can produce an optimum level of VE-frame performance for both strength and drift criteria. This optimum VE-frame performance is currently being investigated [Kasai *et. al.*, 1997c].

From this series of analyses, it is clear the VE-frame exhibits some temperature sensitivity, particularly related to building stiffness. The observed temperature sensitivity for the VE-frame was due to the sensitivity of the VE-material available at the time this work began (3M ISD-110). Adequate structural performance was achieved by selection of a stiff damper and brace relative to the unbraced frame stiffness which minimized the temperature sensitivity of the damping ratio. While the design goals were met with the ISD-110 material, more stable VE-frame performance could be achieved with a less temperature sensitive material.

Currently, a new VE-material is available which exhibits reduced temperature sensitivity. The experimental technique and measured behavior trends as well as analysis tools which have been developed and applied to the temperature sensitive material are applicable to this new material.

6.5.4 Influence of Temperature Rise for Long Duration Ground Motions

One concern of structural designers regarding use of VE-dampers is the temperature rise which occurs during a seismic event and alters the dynamic properties of the structure. As seen in section 6.4.3, VE-damper temperatures do increase during significant seismic events. For the design level earthquakes (1.5xEl Centro, 1.5xHachinohe, and 2.824xTaft) the typical temperature rise was approximately 2.0 °C. This relatively small increase in temperature results in only moderate changes the damper stiffness and negligible changes in damping ratio. Based on Fig. 6.59, the base shear for the VE-frame does not change significantly as the period increases from the reference temperature. There would however, be an increase in frame drift as seen in Fig. 6.60 as the period becomes longer.

For shorter duration ground motions on stiff soil, typical of California earthquakes, the greatest demand on the structure occurs near the beginning of the record when the dampers are close to the initial temperature (Figs. 6.20 to 6.26). After this peak demand, there is typically only minor shaking, and the fact that the damper temperature is higher makes little difference in determining the peak response, as the dampers have already absorbed the significant energy from the event. To illustrate this behavior, analysis was conducted which suppressed the temperature rise in the VE-dampers for the 2.824xTaft ground motion. Displacement response

at the third story is shown for the analyses with and without damper temperature rise in Fig. 6.61. Superimposed on the response is the second story VE-damper temperature rise. As shown in the figure, the damper temperature rises during the large excursions in the first half of the response (1.8 °C after 12 seconds). However, the displacements between the two cases do not differ significantly and there is no strong shaking late in the record which would cause damage to the structure as a result of its slightly softened state.

This is not the case for longer duration earthquakes where there is strong motion late in the record. Ground motion records of this type are generally associated with soft soils or clays. The two Mexico City earthquake records used in this study exemplify ground shaking of this type (Figs. 6.18a and 6.19a). To determine the influence of temperature rise, analyses were conducted which suppressed the temperature rise in the VE-dampers for the two Mexico City ground motion records. Displacement response at the third story is shown for these cases with and without damper temperature rise in Figs. 6.62 and 6.63. As shown in these figures, the VE-frames with temperature rise exhibited larger displacements during the later half of the records. For the Mexico City-Frigorifico response, the peak deflection in the second half of the record (30 to 60 seconds) would be underestimated by 16% if temperature rise were not considered. For the Mexico City-Oficina response, the peak deflection in the second half of the record (75 to 150 seconds) would be underestimated by 14% if temperature rise were not considered.

To further illustrate the effect of temperature rise for these types of ground motions, the Mexico City-Oficina record was scaled by a factor of two and the analyses repeated for the

VE-frame with and without damper temperature rise. Displacement response at the third story is shown in Fig. 6.64. As seen in this figure, the responses are similar through the first half of the record. After 75 seconds, the dampers have heated to 27.2 °C. During the second part of the response, the effect of damper temperature rise becomes clear. An FFT of the second portion of the earthquake record from 75 to 140 seconds, indicates the seismic energy is concentrated near 0.3 hz or 3.3 seconds period as shown in Fig. 6.65. The continued strong motion during the second half of the record causes additional temperature rise which further softens the VE-dampers and shifts the period toward the energy rich frequency range. While period increase due to softening did not significantly increase the member forces as shown in Fig. 6.65, it did significantly increase frame drift. Analysis conducted without considering temperature rise for this ground motion would underestimate displacements by over 100% (Fig. 6.64) during the second half of the response. Additionally, the VE-frame analysis with temperature rise exhibited limited yielding at the beam column locations in the first two story levels. The VE-frame analysis without temperature rise falsely indicated elastic behavior. Based on these findings, damper temperature rise should be considered to determine VE-frame response for long duration earthquake motions. New less temperature sensitive VE-materials may reduce the significant softening observed for the current material when subjected to intense long duration motions.

6.6 Conclusions

Results of the simulated earthquake tests and analyses are summarized below:

- A prototype 10-story VE-frame was designed using an equivalent lateral force procedure. Design criteria included elastic performance and small drift (<0.0075 rad.) at the reference temperature. Subsequent analysis and testing indicated these goals were achieved and the design methodology provides a practical means of designing VE-damped steel frames.
- A unique methodology was developed which permitted testing of the full-scale lower three story portion of the 10-story prototype VE-damped frame subjected to significant seismic and gravity forces.
- The testing methodology relies on analysis to predict structural response to earthquake ground motions. Correlative analyses of small-scale shaking table studies indicate the analysis method reasonably predicts the frame response.
- Measured overall frame response indicated significant energy dissipation by the VE-dampers and elastic response of the steel members.
- Local member forces and damper behavior were in general reasonably captured by the test method. Column axial forces were significantly lower in the test specimen than the 10-story prototype frame due to overturning moment contributions from lateral forces at the upper stories which could not be implemented by the testing method.
- Measured temperature rise in the dampers corresponded reasonably well with predicted values.
- Analytical correlation of the measured VE-frame seismic response was performed using the FDM. The FDM method reasonably predicted the overall frame response, local member response, VE-damper response, and temperature rise for the random displacement history.

- Analytical prediction of seismic response for the VE-frame can also be adequately performed for short duration earthquake motions using both the local Rayleigh damping and global Rayleigh damping methods.
- Temperature rise, which may occur during long or intense motions, is not considered by either the LRD or GRD method. As a result, these procedures can seriously under-predict frame response when significant temperature rise occurs.
- Temperature rise during an earthquake does not appear to be a significant factor in determining the VE-frame response for the short duration ground motions investigated as part of this study.
- The VE-frame exhibited some degree of temperature sensitivity, particularly related to frame stiffness. Damping ratio was less sensitive to temperature changes in the dampers.
- Adequate structural performance of the VE-frame was achieved by selection of a stiff damper and brace relative to the unbraced frame stiffness which minimized the temperature sensitivity. More stable VE-frame performance could be achieved with a less temperature sensitive material, which is currently under development. The experimental technique and measured behavior trends as well as analysis tools which have been developed and applied to the temperature sensitive material will be applicable to these new materials.
- Seismic forces and frame drift vary due to shifting of the fundamental period and damping ratio caused by damper temperature changes. An ideal damper design should optimize the VE-frame performance by minimizing the influence of these two factors. This is currently being studied by Kasai *et al.* [1997c].

Story Level	Height (ft)	Floor Weight# (kips)	Lateral Force (kips)	Shear (kips)	Overturning Moment (kip-ft)
1	13.0	152.3	1.1	212.6	228346
2	24.5	152.3	3.3	211.6	195173
3	36.0	152.3	6.5	208.2	165979
4	47.5	152.3	10.5	201.8	137241
5	59.0	152.3	15.4	191.2	109399
6	70.5	152.3	21.0	175.8	83011
7	82.0	152.3	27.4	154.8	58749
8	93.5	152.3	34.5	127.4	37389
9	105.0	152.3	42.2	92.9	19811
10	116.5	152.3	50.7	50.7	6991

Contribution assigned to each of the six VE-frames.

Table 6.1 - Equivalent lateral forces for VE-prototype frame.

Member Forces from Seismic Forces E						
Story Level	Beam Axial P* (kips)	Beam Moment M' (kip-ft)	Column Axial P* (kips)	Column Moment M' (kip-ft)	Column Shear V' (kips)	1.5xDamper Axial P* (kips)
1	231	325	1204	173	27	352
2	230	302	1034	152	26	351
3	226	295	876	150	26	345
4	219	282	720	145	25	334
5	208	264	570	137	24	317
6	191	238	428	126	22	291
7	168	203	299	111	19	257
8	139	158	187	92	16	211
9	101	103	96	67	12	154
10	55	36	31	36	6	84

Member Forces from 1.2 DL + 0.5 LL						
Story Level	Beam Axial (kips)	Beam Moment (kip-ft)	Column Axial (kips)	Column Moment (kip-ft)	Column Shear (kips)	Damper Axial (kips)
1		17	296			
2		17	267			
3		17	237			
4		17	207			
5		17	178			
6		17	148			
7		17	119			
8		17	89			
9		17	59			
10		17	30			

Summation of Member Forces from 1.2 DL + 0.5 LL+ E						
Story Level	Beam Axial (kips)	Beam Moment (kip-ft)	Column Axial (kips)	Column Moment (kip-ft)	Column Shear (kips)	Damper Axial (kips)
1	231	342	1500	173	27	352
2	230	319	1301	152	26	351
3	226	312	1113	150	26	345
4	219	299	927	145	25	334
5	208	281	748	137	24	317
6	191	255	577	126	22	291
7	168	220	418	111	19	257
8	139	175	276	92	16	211
9	101	120	155	67	12	154
10	55	53	61	36	6	84

Table 6.2 - Member forces for prototype VE-frame.

Story Level	Beam Member	Column Member	Brace Member
1	W18x50	W14x159	TS8x8x1/2
2	W18x40	W14x159	TS8x8x1/2
3	W18x40	W14x159	TS8x8x1/2
4	W18x40	W14x145	TS8x8x3/8
5	W18x35	W14x145	TS8x8x3/8
6	W18x35	W14x145	TS8x8x3/8
7	W16x31	W14x82	TS8x8x1/4
8	W16x31	W14x82	TS8x8x1/4
9	W10x19	W14x48	TS7x7x3/16
10	W10x19	W14x48	TS7x7x3/16

Table 6.3 - Member sizes for prototype VE-frame.

Location	Area (cm^2)	Ix (cm^4)	Zx (cm^3)
Beam Level 1	7.00	135.3	28.5
Beam Level 2	6.85	121.5	26.8
Beam Level 3	6.10	64.9	18.7
Column Level 0-1	9.10	107.1	29.9
Column Level 1-2	7.60	86.0	24.3
Column Level 2-3	7.60	86.0	24.3

Table 6.4 - NTIT Small-scale shaking table VE-frame properties.

Earthquake	Year	Location	Soil Type	PGA (g)	Duration# (sec)
1.5 x El Centro (N-S)	1940	El Centro, California	Alluvium+	0.52	30
1.5 x Tokachi-Oki (N-S)	1968	Hachinohe, Japan	Deep Cohesionless-	0.34	30
2.824 x Taft (S69E)	1952	Kern County, Califonia	Alluvium+	0.51	30
Oakland (CSMIP 58224 Chan.6) E-W	1989	Loma Prieta, California	Alluvium+	0.25	20
Treasure Island (90)	1989	Loma Prieta, California	Fill+	0.16	15
Castaic Old Ridge Route (360)	1994	Northridge, California	Unknown	0.51	20
Santa Monica City Hall Grounds (90)	1994	Northridge, California	Unknown	0.88	15
Central de Abastos-Frigorifico (E-W)	1985	Mexico City	Soft Clay+	0.10	60
Central de Abastos-Oficina (N-S)	1985	Mexico City	Soft Clay+	0.07	120

Length of record with significant ground shaking.
-[Seed *et al*., 1974] +[Miranda, 1993]

Table 6.5 - Characteristics of earthquake ground motions considered.

Earthquake Loading, 24 C Initial Temperature

Sampling Rate (hz)	Damper Location (Story Level)	Initial Temperature (°C)	Final Temperature (°C)
1.5 x El Centro			
100	L1	24.1	25.8
	L2	23.9	25.7
	L3	24.1	25.7
Hachinohe x 1.5			
100	L1	24.1	26.0
	L2	23.9	26.1
	L3	24.0	26.1
2.824 x Taft			
100	L1	24.1	26.1
	L2	23.9	26.1
	L3	24.1	26.2
Loma Prieta 1989: Oakland			
100	L1	24.1	24.9
	L2	23.9	24.9
	L3	23.9	24.9
Loma Prieta 1989: Treasure Island			
100	L1	24.1	24.8
	L2	23.9	24.7
	L3	23.9	24.6
Northridge 1994: Castaic Old Ridge Route			
100	L1	24.0	25.8
	L2	23.9	25.7
	L3	23.9	25.6
Northridge 1994: Santa Monica City Hall Grounds			
100	L1	24.0	25.3
	L2	23.9	25.4
	L3	24.0	25.4
Mexico City 1985: Central de Abastos-Frigorifico			
50	L1	24.0	27.1
	L2	23.9	27.3
	L3	23.9	27.3
Mexico City 1985: Central de Abastos-Oficina			
24	L1	24.1	26.1
	L2	24.0	26.2
	L3	24.1	26.3

Table 6.6 - Sampling rates and measured damper temperature rise for earthquake tests.

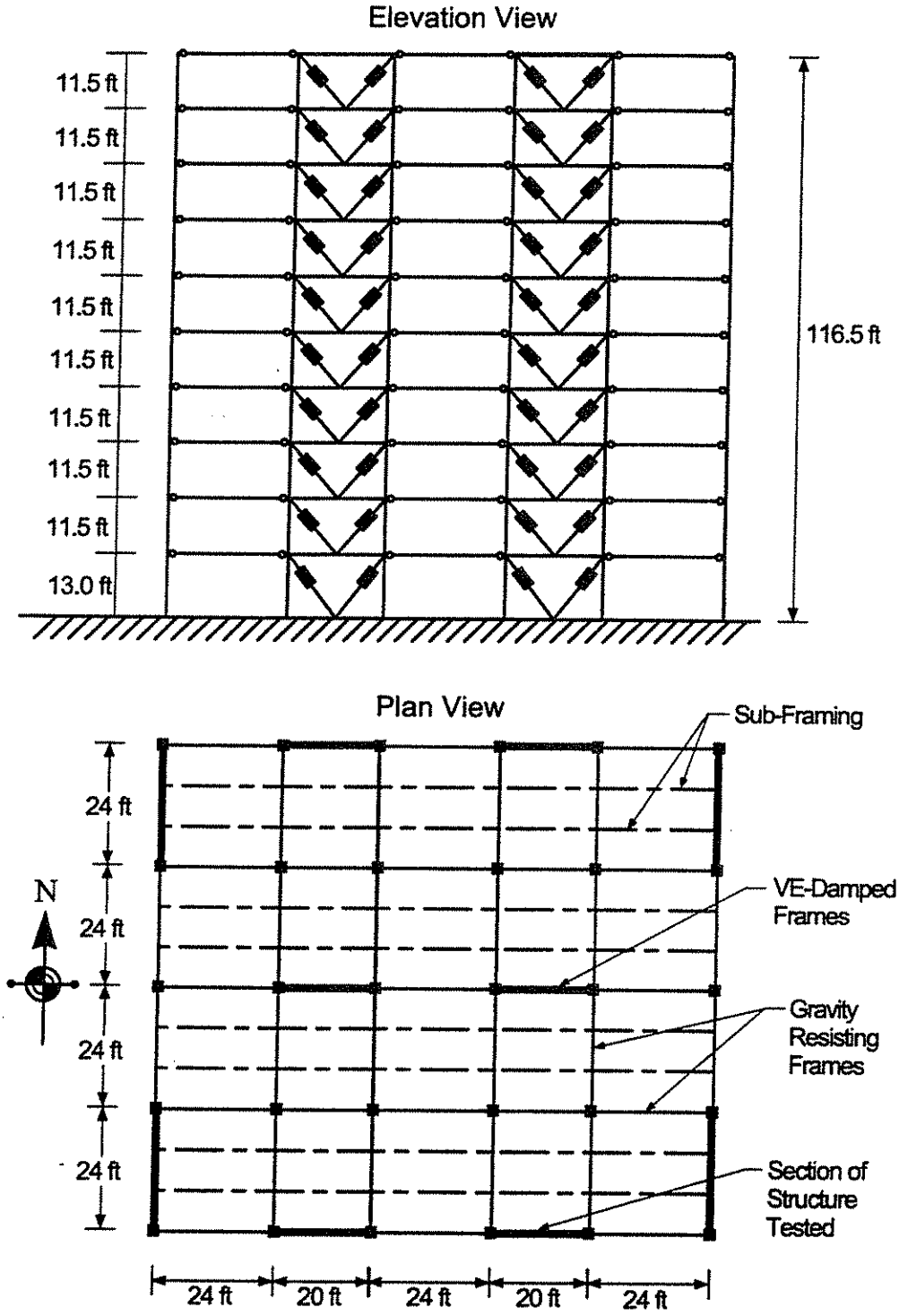

Fig. 6.1 - Seismic prototype frame VE-frame.

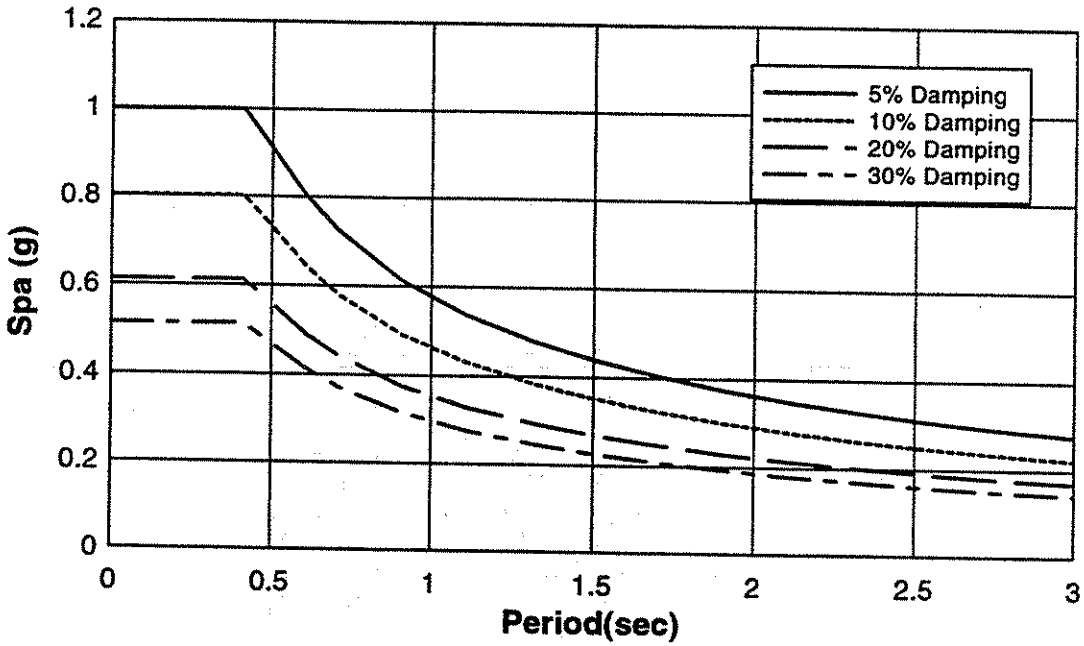

Fig. 6.2 - NEHRP pseudo-acceleration spectrum (C_v=0.48, C_s=0.40) for various damping ratios.

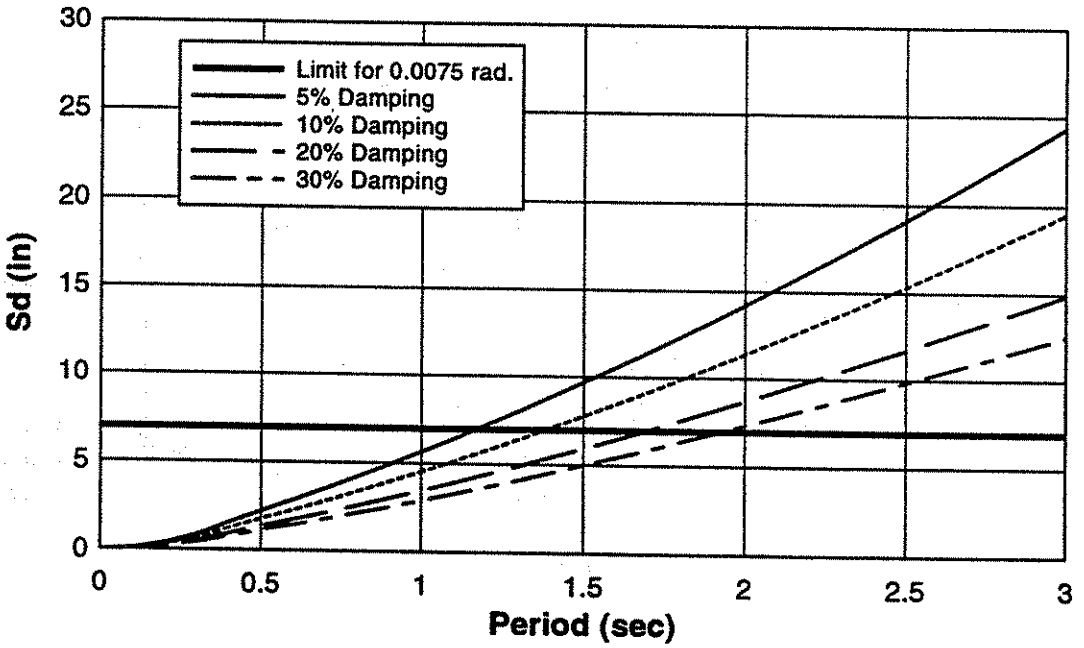

Fig. 6.3 - NEHRP displacement spectrum (C_v=0.48, C_s=0.40) for various damping ratios.

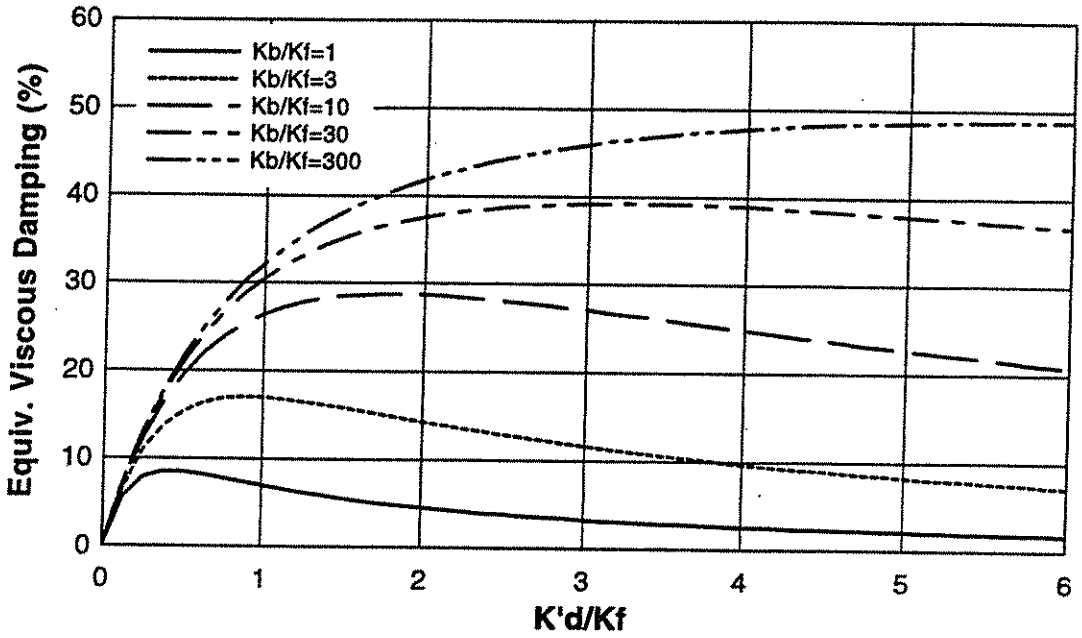

Fig. 6.4 - Equivalent viscous damping ratio for a SDOF system (η_d=1.32) for various damper to frame and brace to frame stiffness ratios.

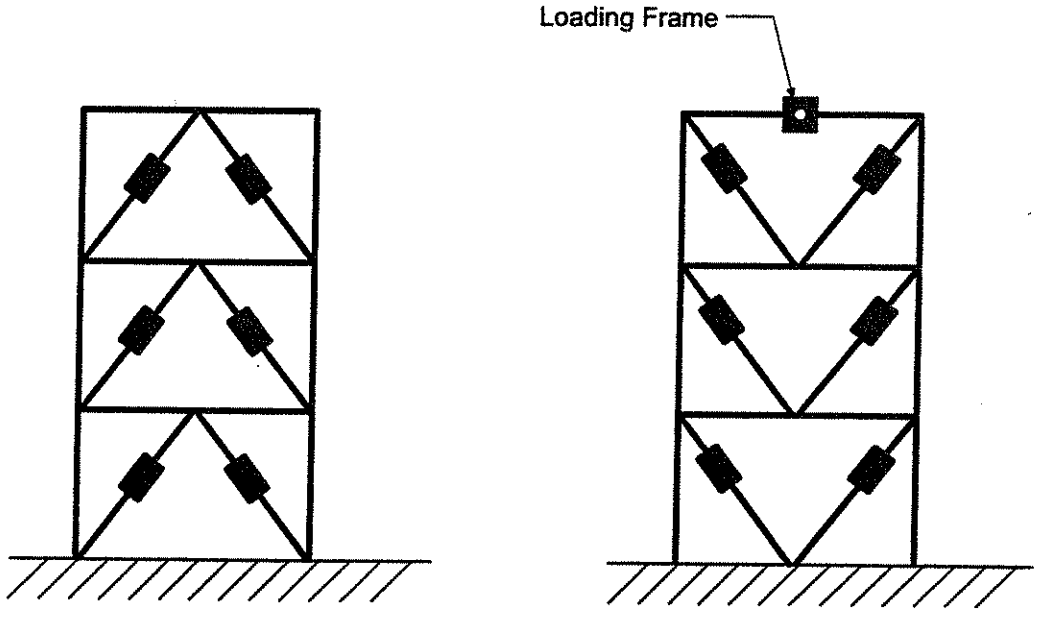

Fig. 6.5 - Typical VE-damper layout for actual structure and layout required for test specimen for loading frame attachment.

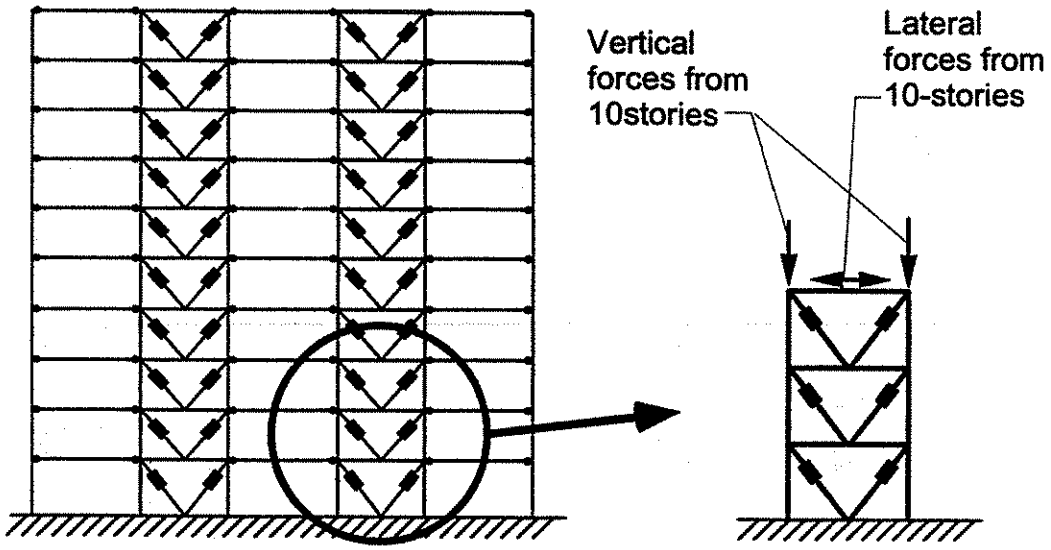

Fig. 6.6 - Schematic of methodology for testing lower three story portion of 10-story prototype VE-frame.

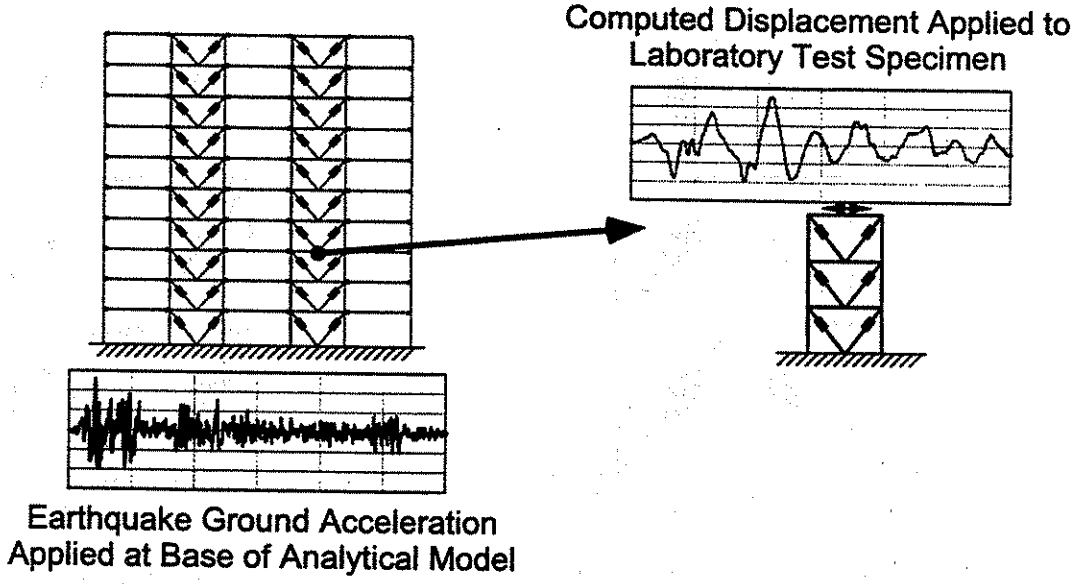

Fig. 6.7 - Schematic of testing methodology which uses analysis of 10-story prototype to determine laboratory imposed displacement history on VE-frame test specimen.

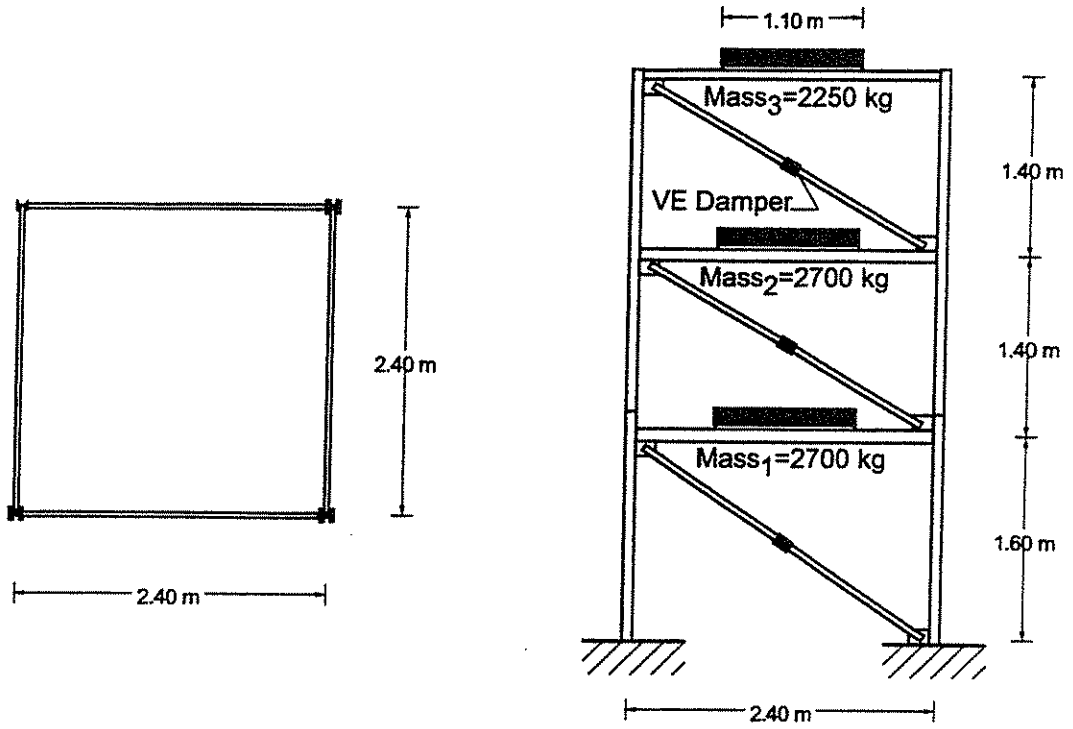

Fig. 6.8a, b - NTIT small-scale shaking table frame specimen.

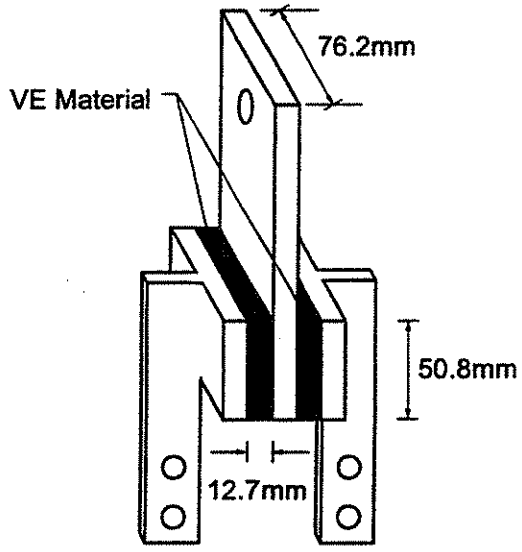

Fig. 6.8c- VE-damper contained in NTIT small-scale shaking table test specimen.

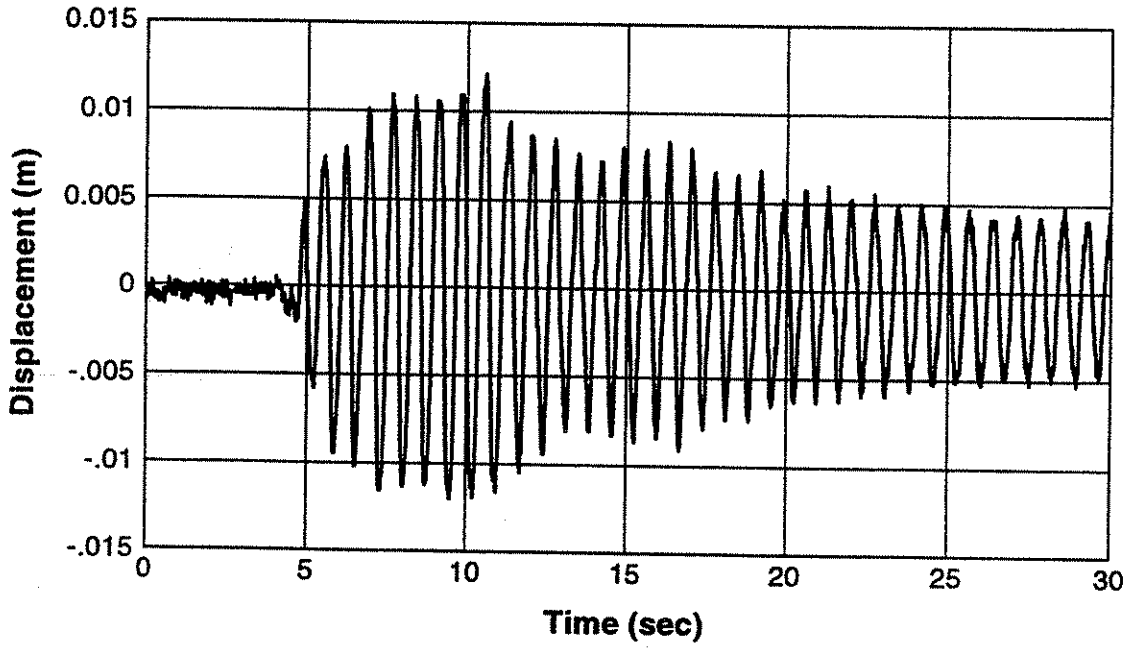

Fig. 6.9a - Measured MRF shaking table response at roof level for El Centro with peak acceleration of 0.05g .

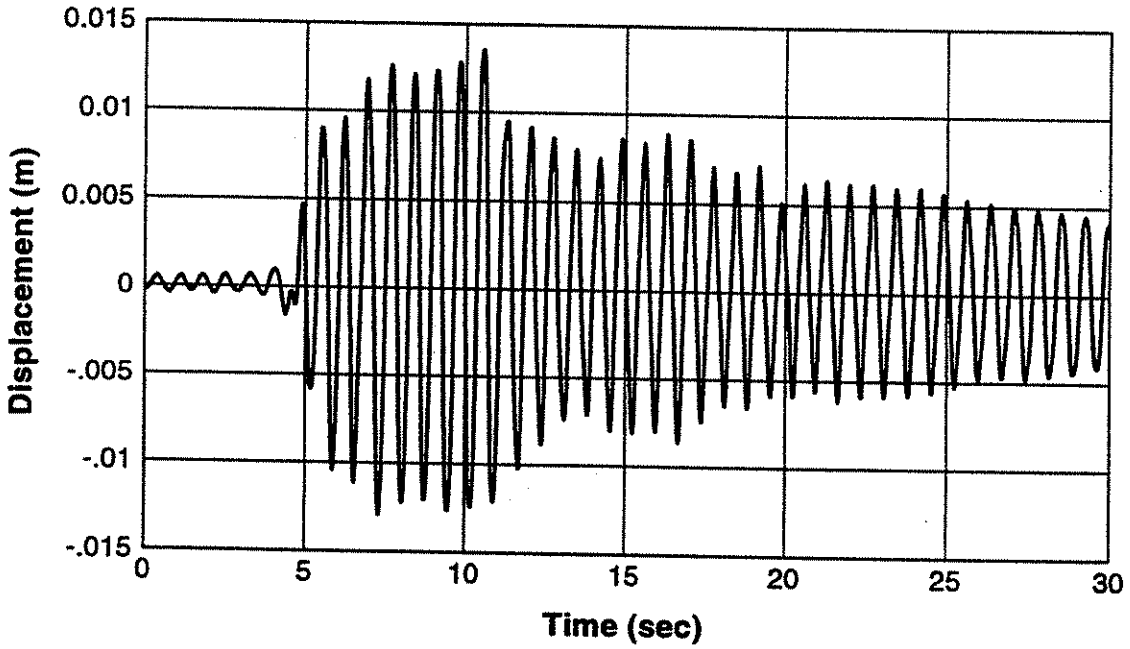

Fig. 6.9b - Predicted MRF shaking table response at roof level for El Centro with peak acceleration of 0.05 g.

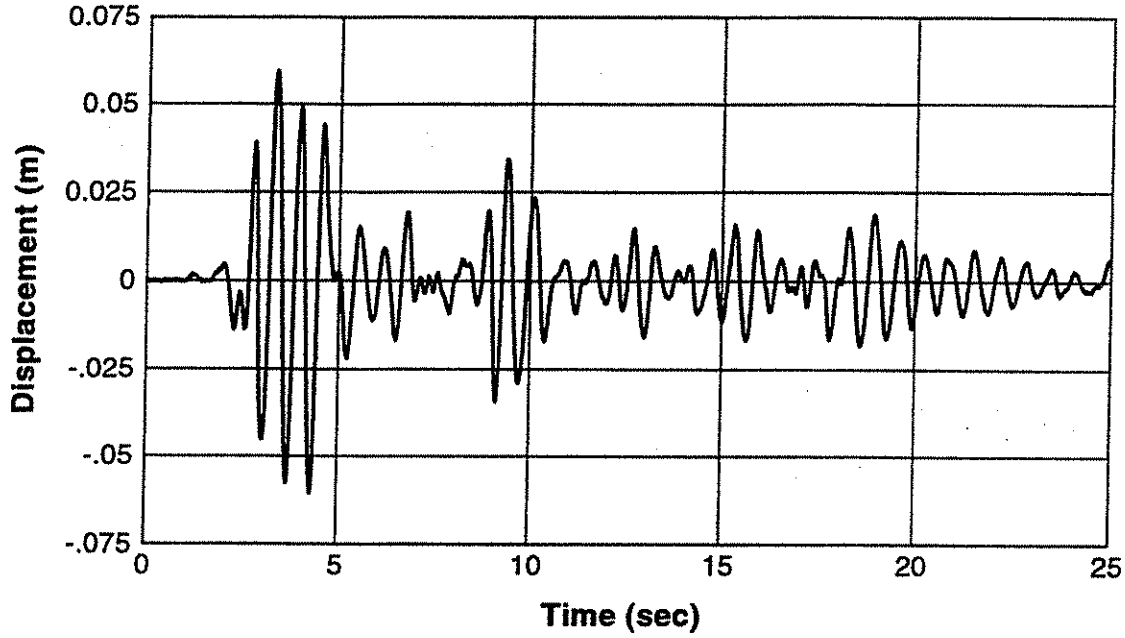

Fig. 6.10a - Measured VE-frame shaking table response at roof level for El Centro with peak acceleration of 0.5 g.

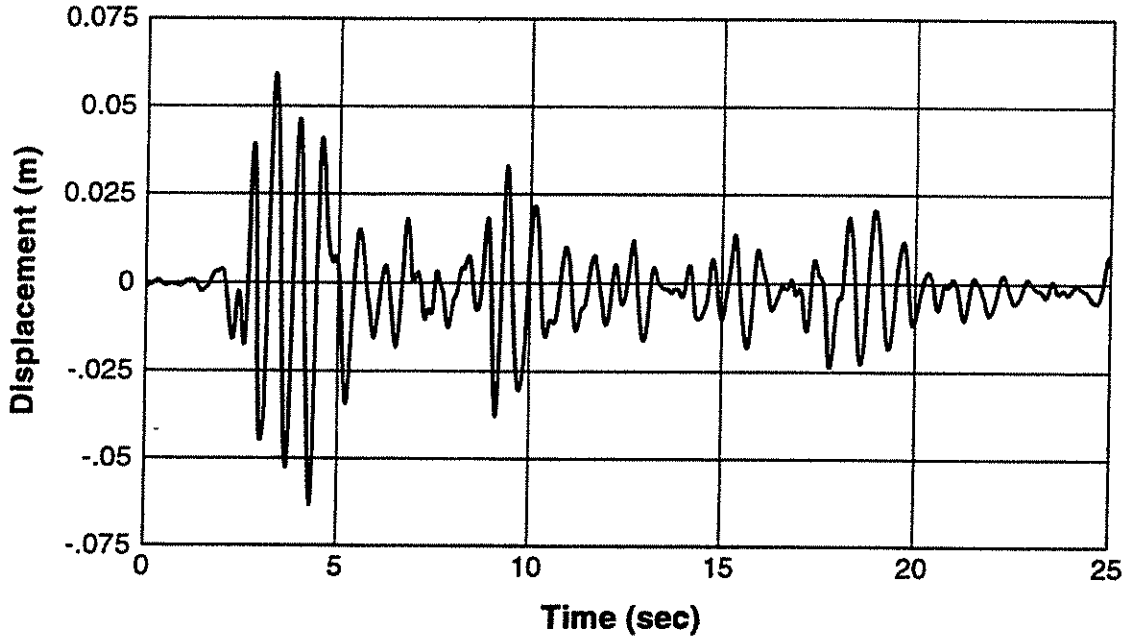

Fig. 6.10b - Predicted VE-frame shaking table response at roof level for El Centro with peak acceleration of 0.5 g.

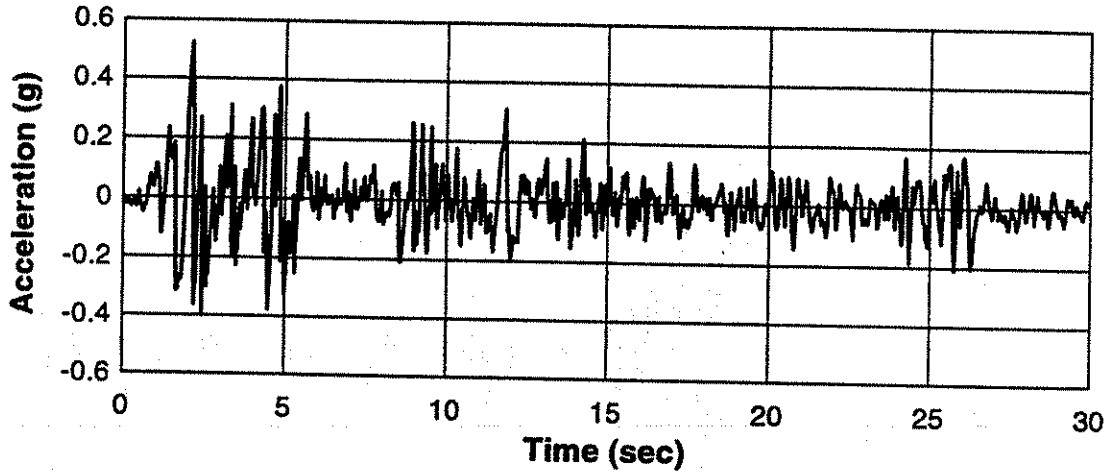

Fig. 6.11a - 1.5 x El Centro ground acceleration time history.

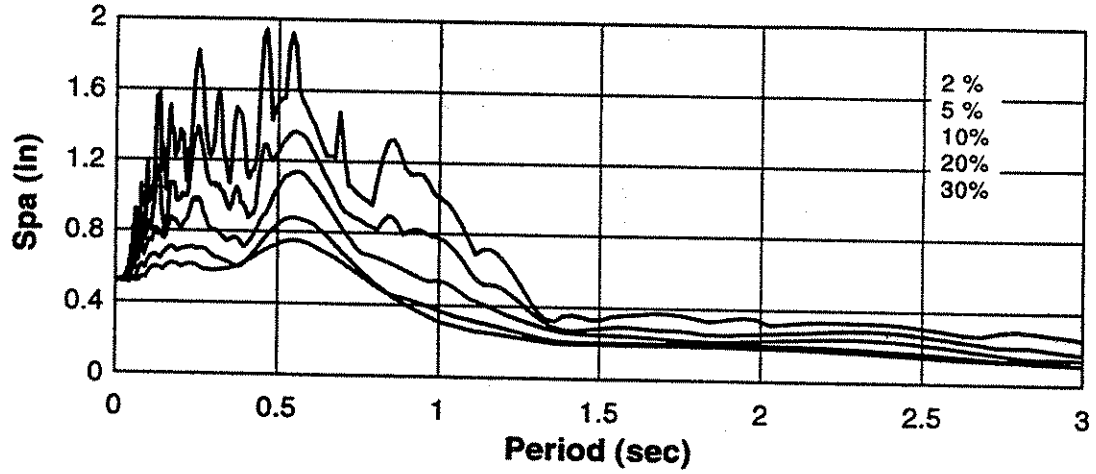

Fig. 6.11b - 1.5 x El Centro pseudo-acceleration response spectra.

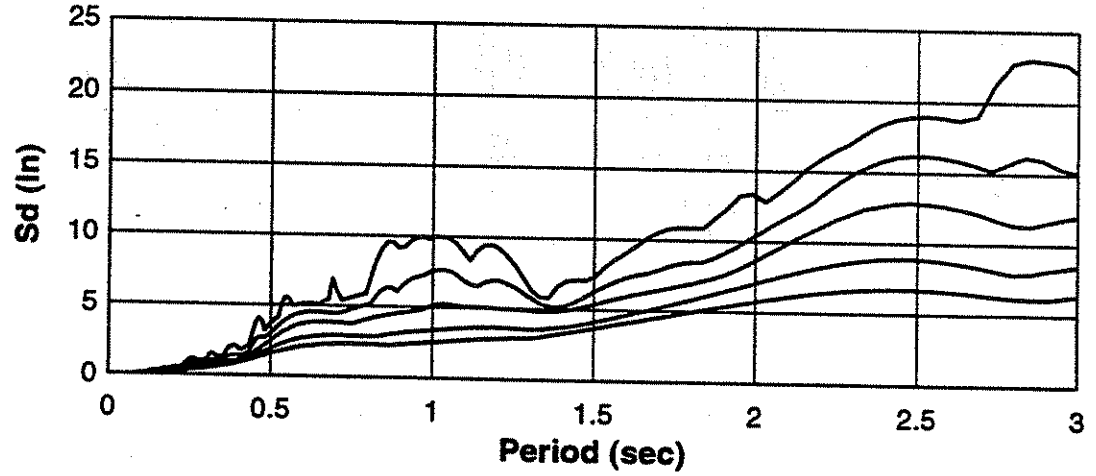

Fig. 6.11c - 1.5 x El Centro displacement response spectra.

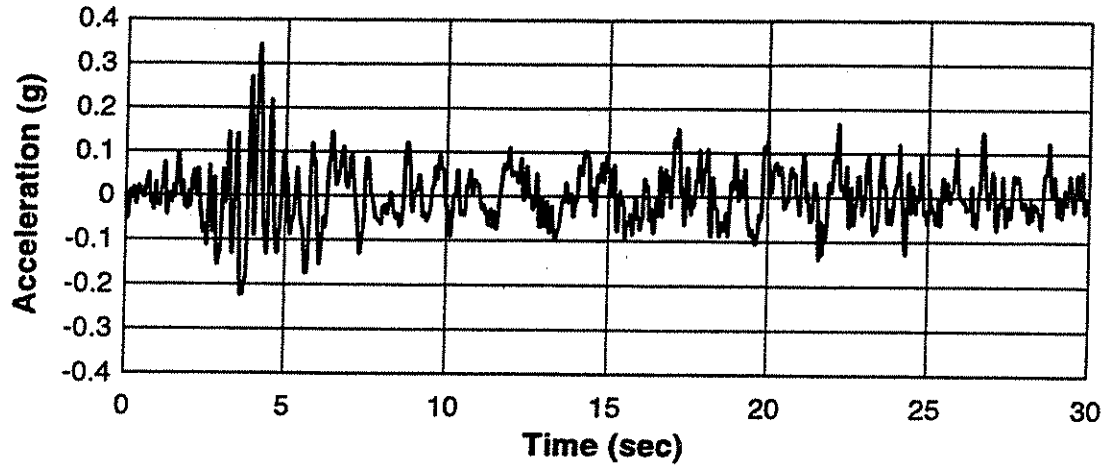

Fig. 6.12a - 1.5 x Hachinohe ground acceleration time history.

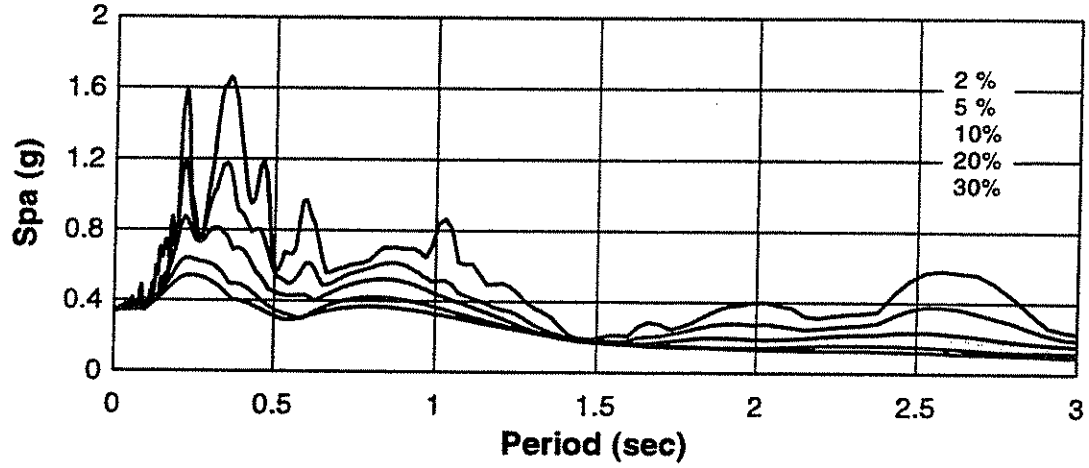

Fig. 6.12b - 1.5 x Hachinohe pseudo-acceleration response spectra.

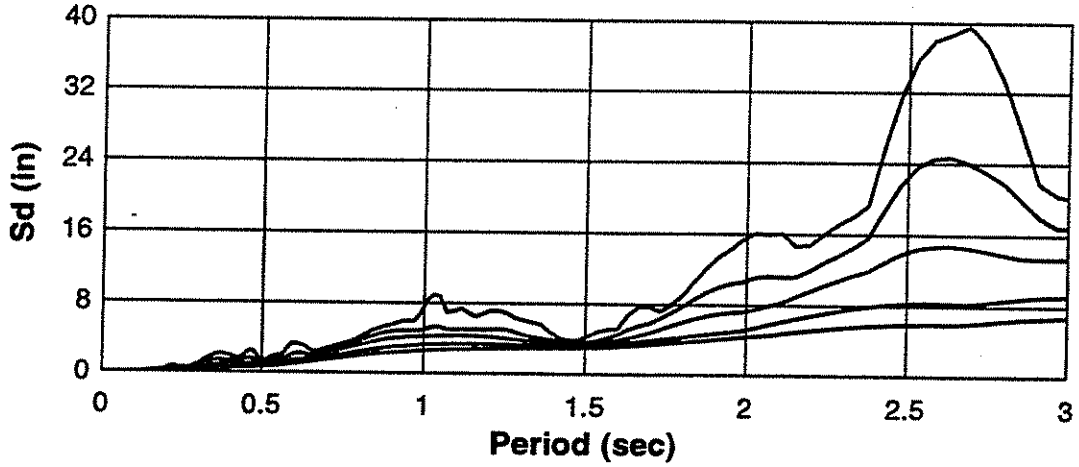

Fig. 6.12c - 1.5 x Hachinohe displacement response spectra.

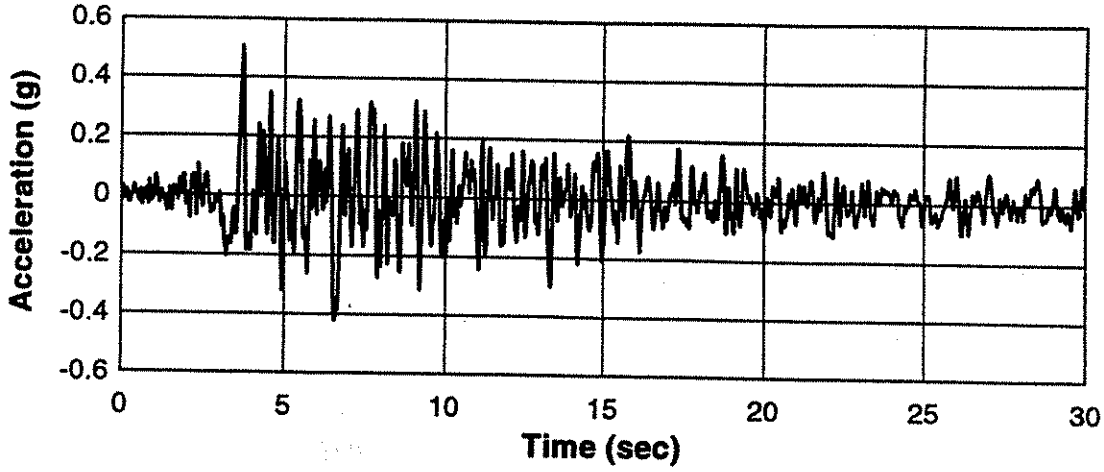

Fig. 6.13a - 2.824 x Taft ground acceleration time history.

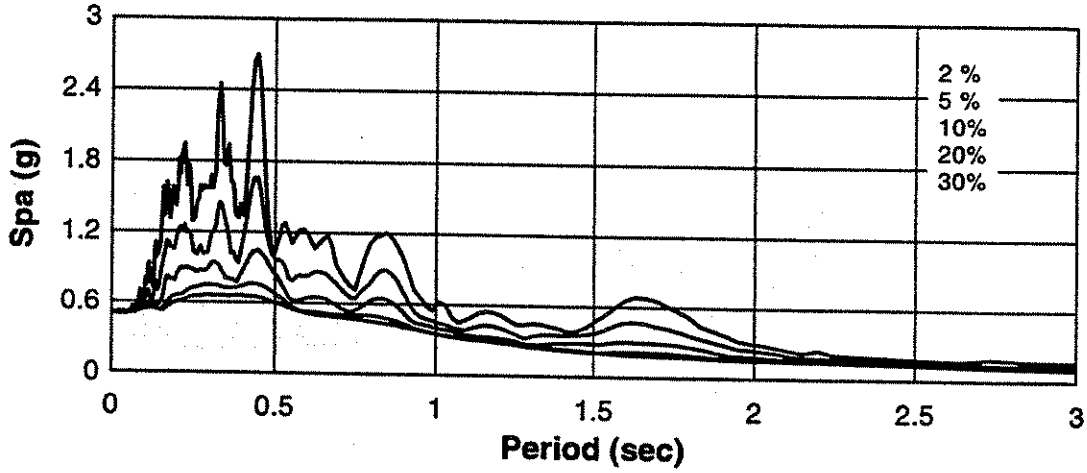

Fig. 6.13b - 2.824 x Taft pseudo-acceleration response spectra.

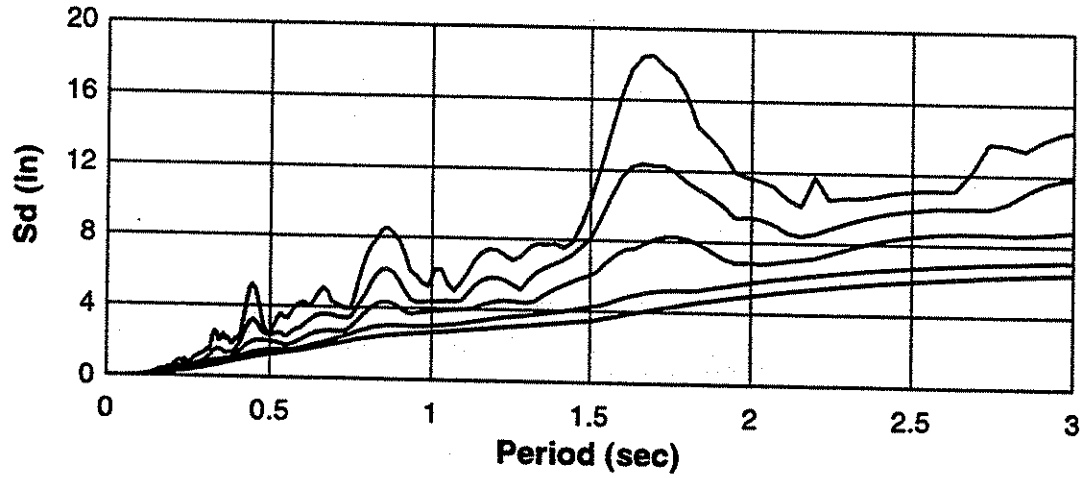

Fig. 6.13c - 2.824 x Taft displacement response spectra.

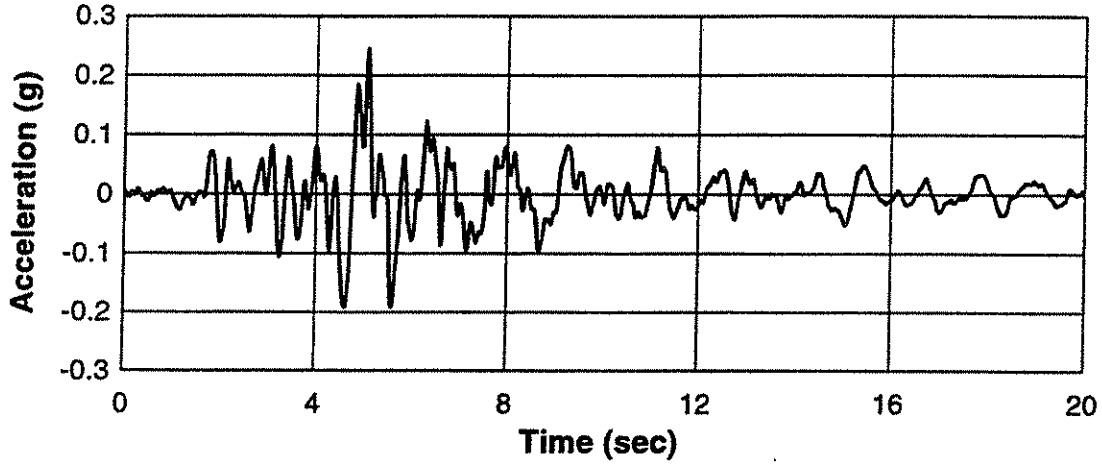

Fig. 6.14a - Loma Prieta: Oakland ground acceleration time history.

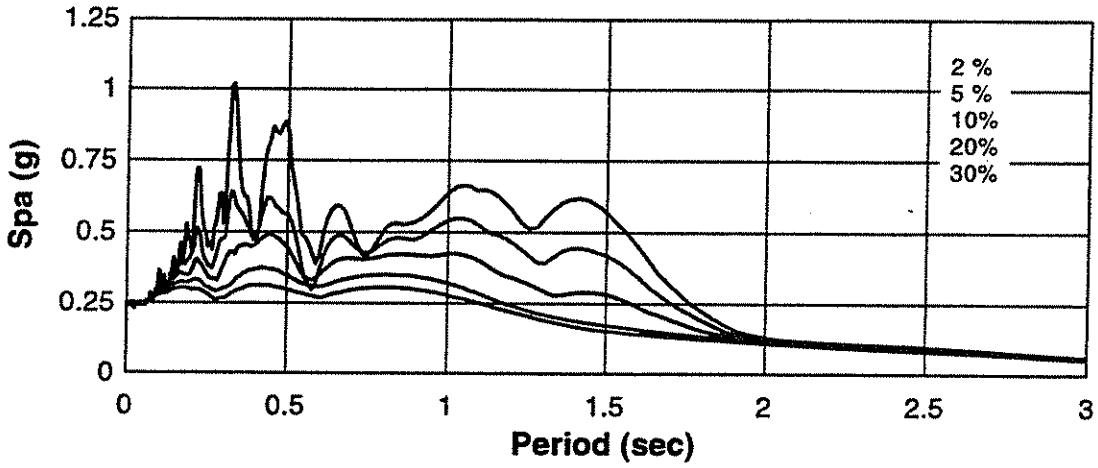

Fig. 6.14b - Loma Prieta: Oakland pseudo-acceleration response spectra.

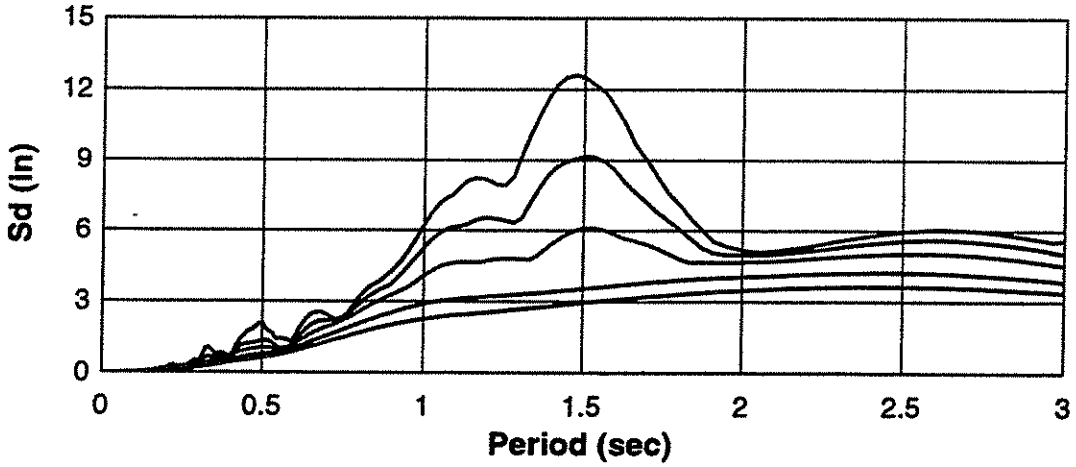

Fig. 6.14c - Loma Prieta: Oakland Island displacement response spectra.

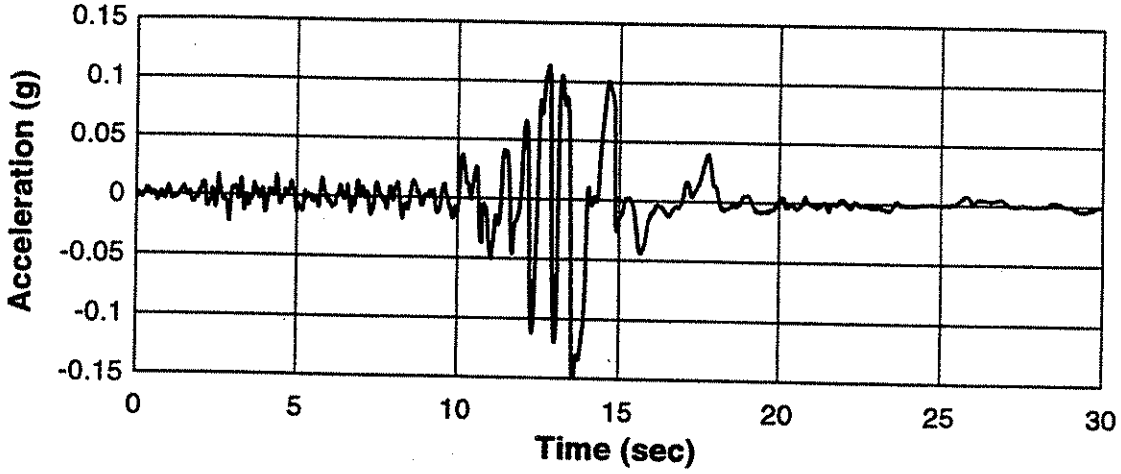

Fig. 6.15a - Loma Prieta: Treasure Island ground acceleration time history.

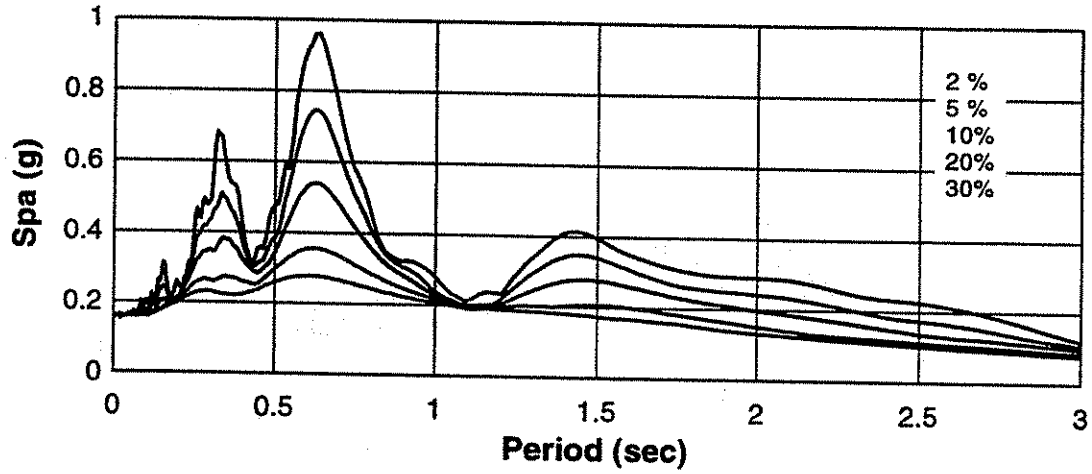

Fig. 6.15b - Loma Prieta: Treasure Island pseudo-acceleration response spectra.

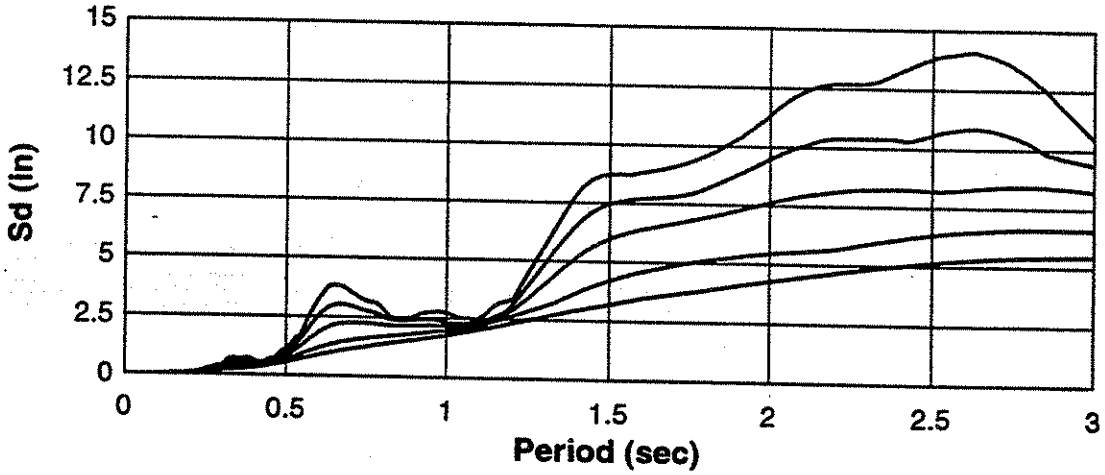

Fig. 6.15c - Loma Prieta: Treasure Island displacement response spectra.

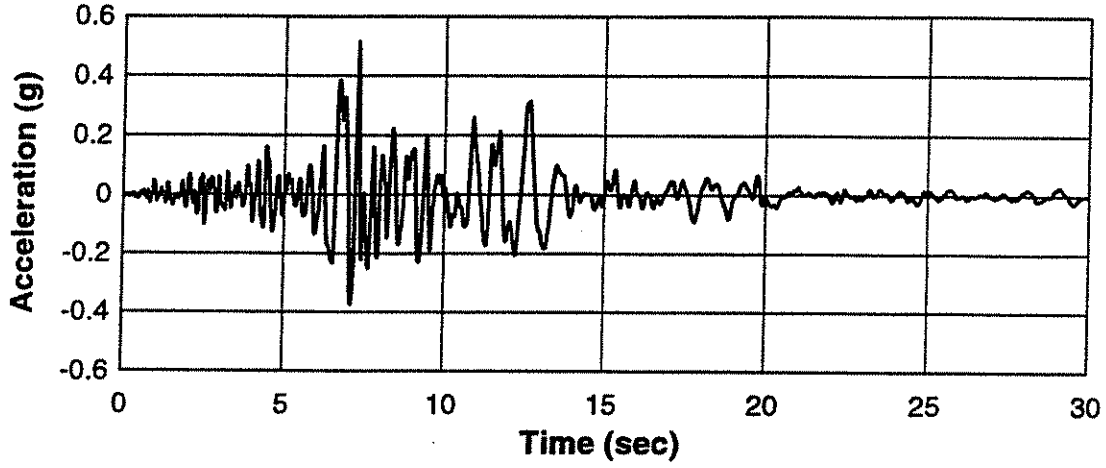

Fig. 6.16a - Northridge: Castaic Old Ridge Route ground acceleration time history.

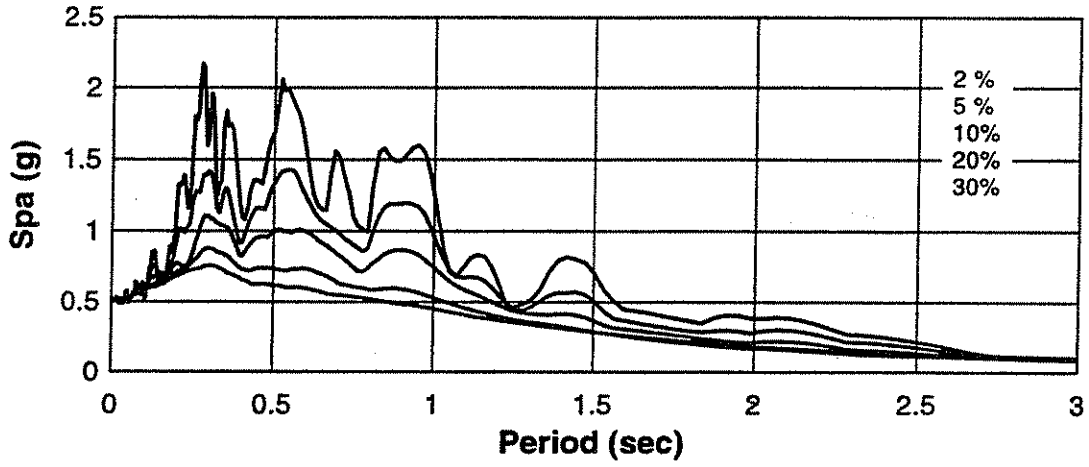

Fig. 6.16b - Northridge: Castaic Old Ridge Route pseudo-acceleration response spectra.

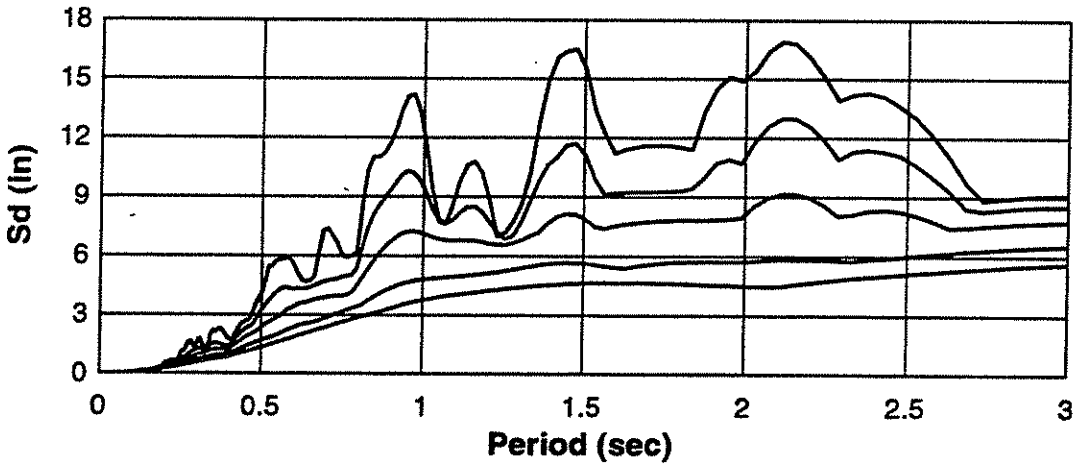

Fig. 6.16c - Northridge: Castaic Old Ridge Route displacement response spectra.

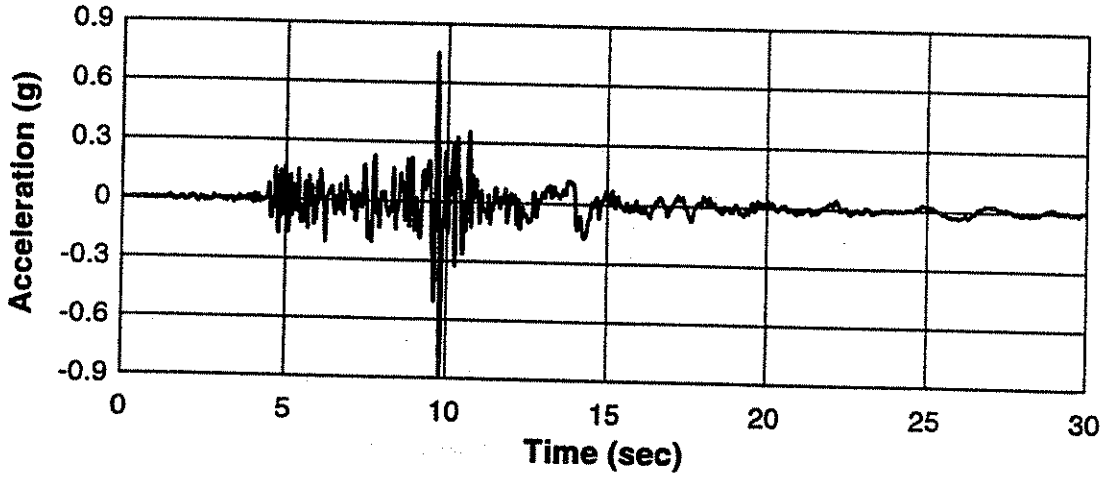

Fig. 6.17a - Northridge: Santa Monica City Hall Grounds ground acceleration time history.

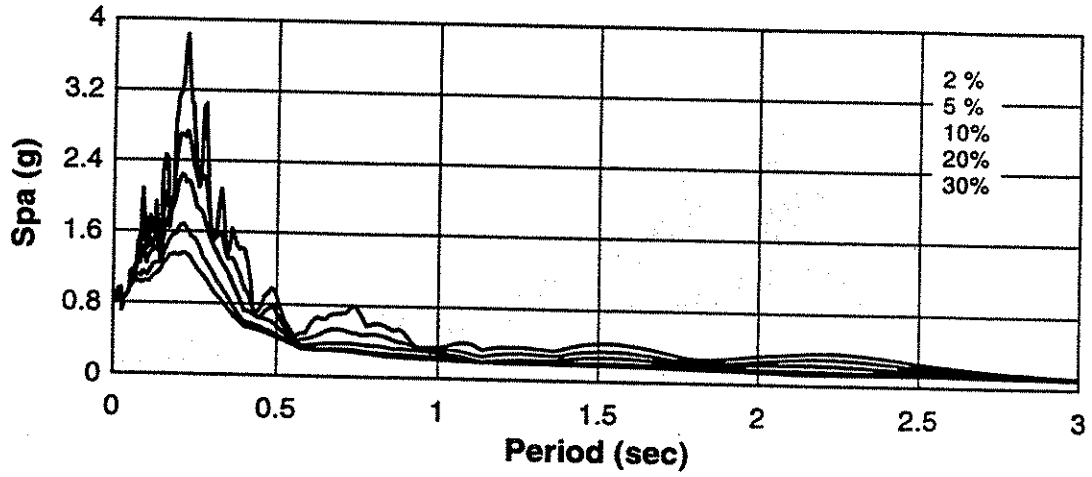

Fig. 6.17b - Northridge: Santa Monica City Hall Grounds pseudo-acceleration spectra.

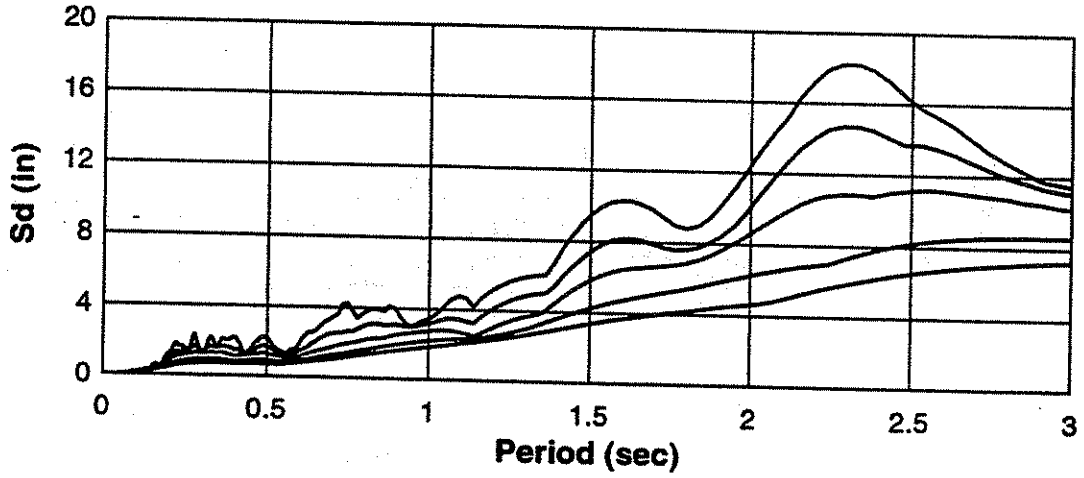

Fig. 6.17c - Northridge: Santa Monica City Hall Grounds displacement response spectra.

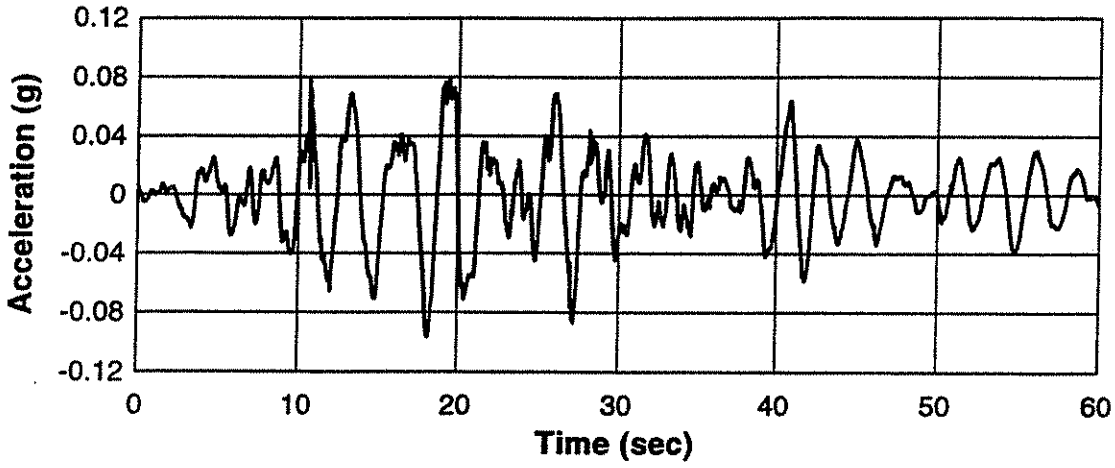

Fig. 6.18a - Mexico City: Central de Abastos-Frigorifico ground acceleration time history.

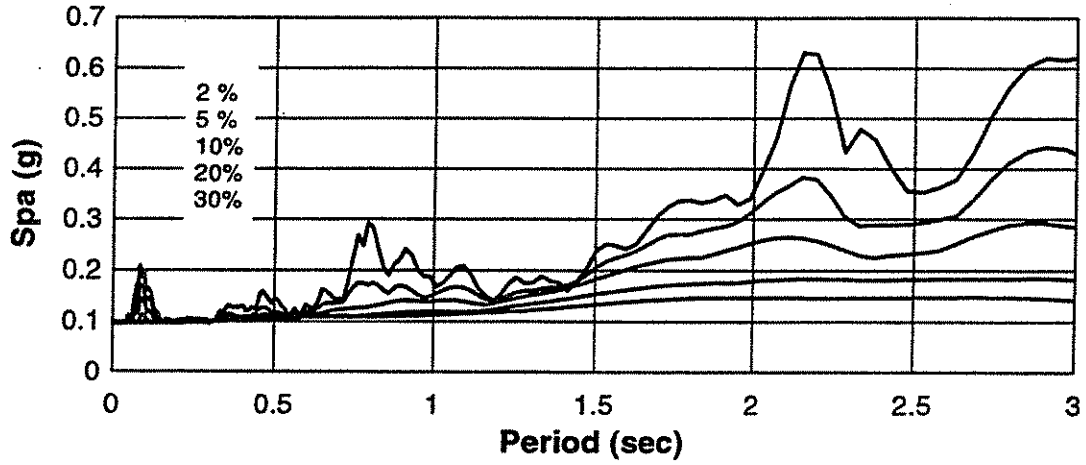

Fig. 6.18b - Mexico City: Central de Abastos-Frigorifico pseudo-acceleration spectra.

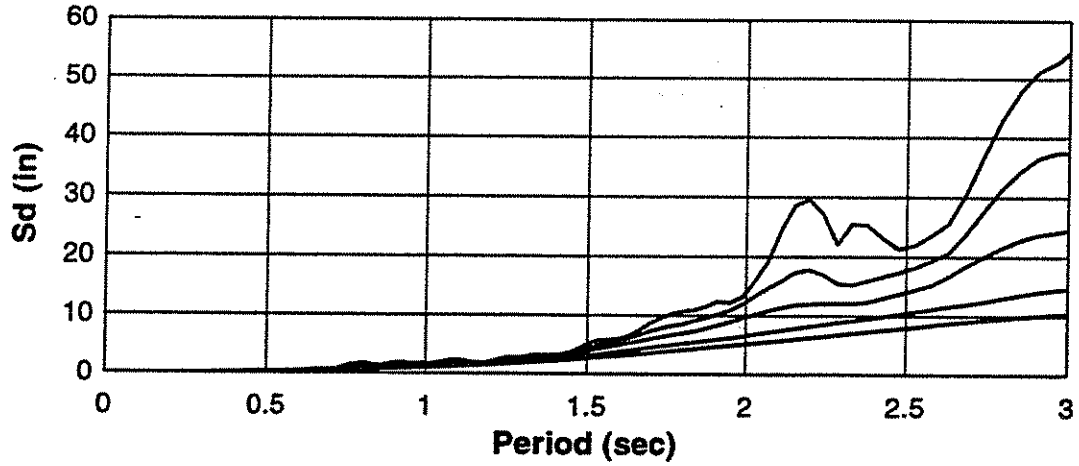

Fig. 6.18c - Mexico City: Central de Abastos- Frigorifico displacement response spectra.

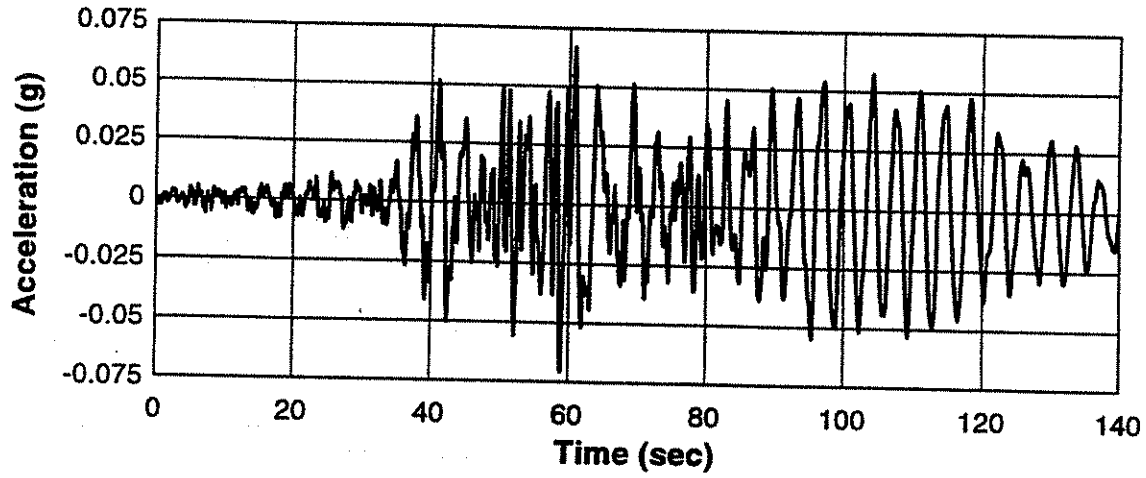

Fig. 6.19c - Mexico City: Central de Abastos- Oficina displacement response spectra.

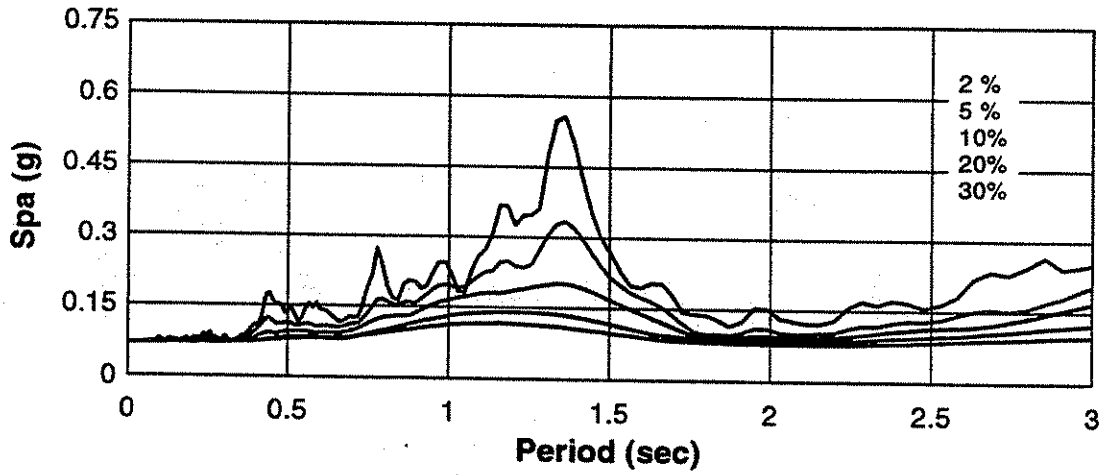

Fig. 6.19a - Mexico City: Central de Abastos- Oficina ground acceleration time history.

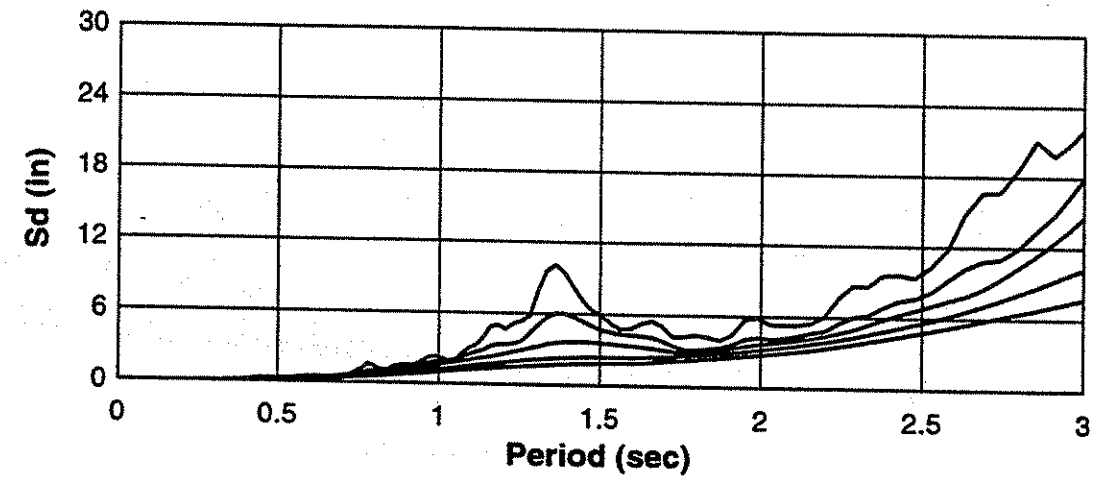

Fig. 6.19b - Mexico City: Central de Abastos- Oficina pseudo-acceleration response spectra.

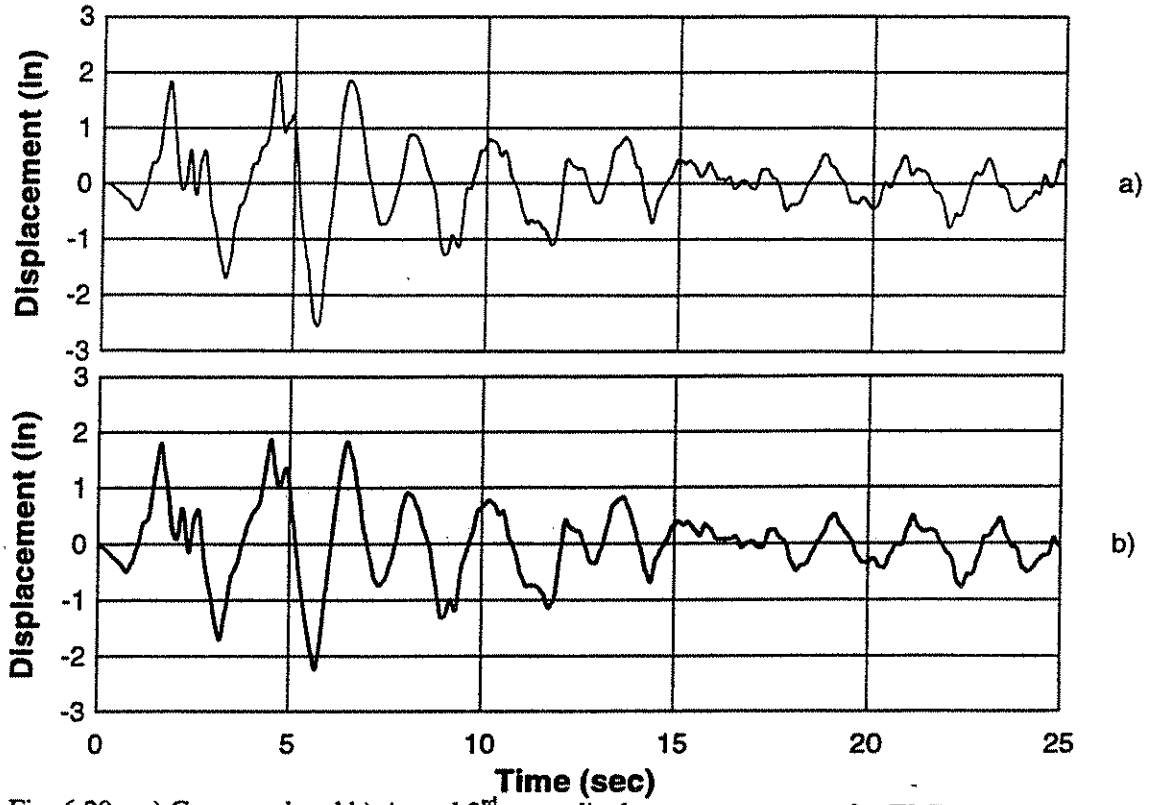

Fig. 6.20 - a) Command and b) Actual 3rd story displacement response for El Centro.

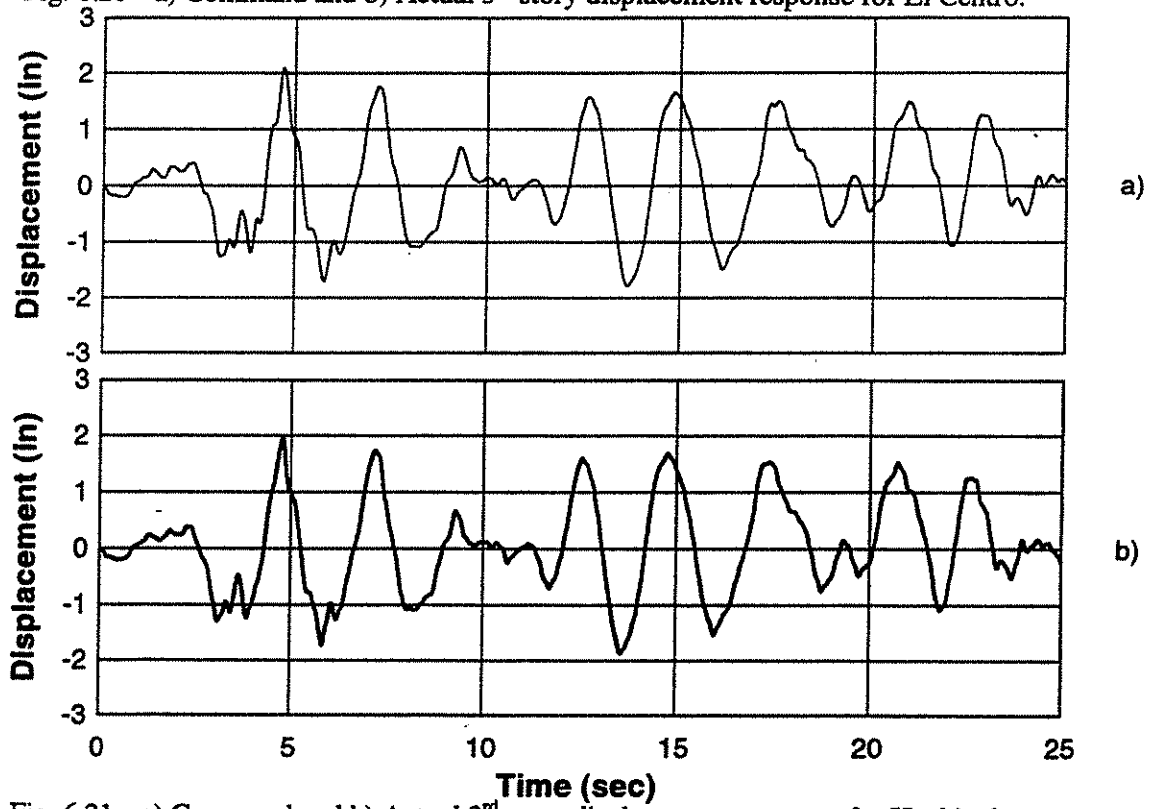

Fig. 6.21 - a) Command and b) Actual 3rd story displacement response for Hachinohe.

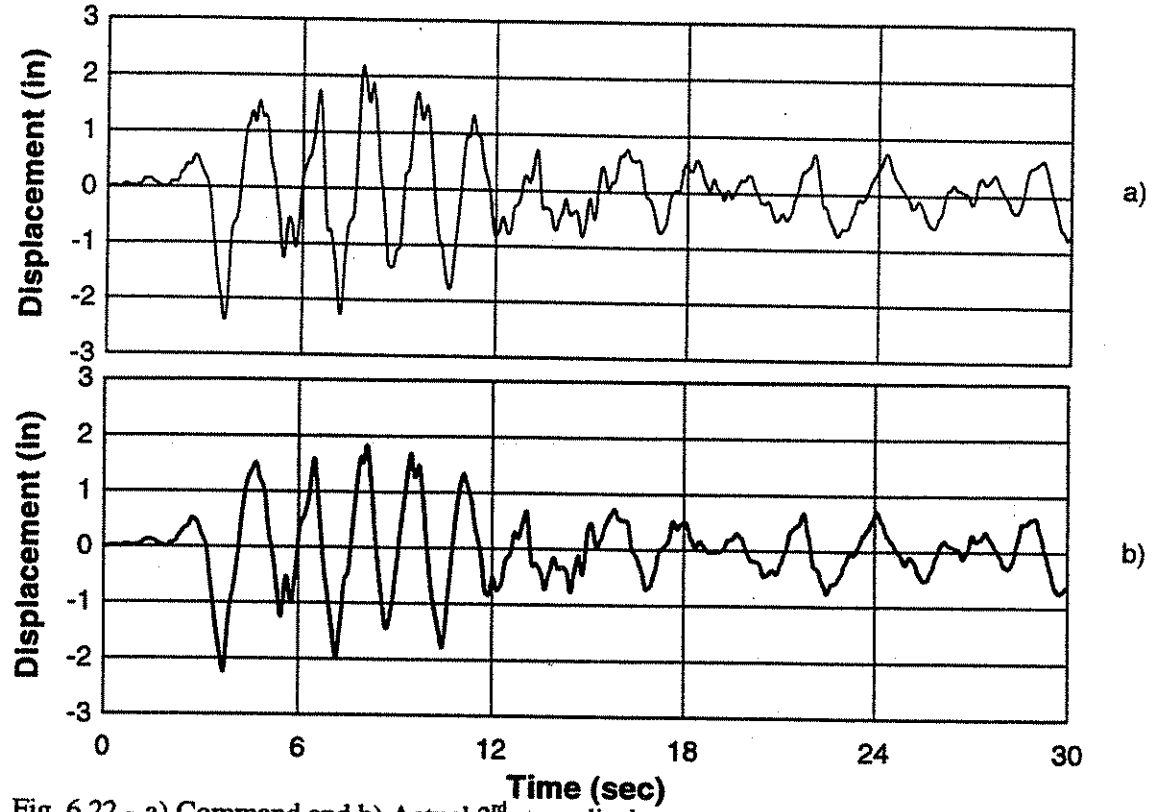

Fig. 6.22 - a) Command and b) Actual 3rd story displacement response for Taft.

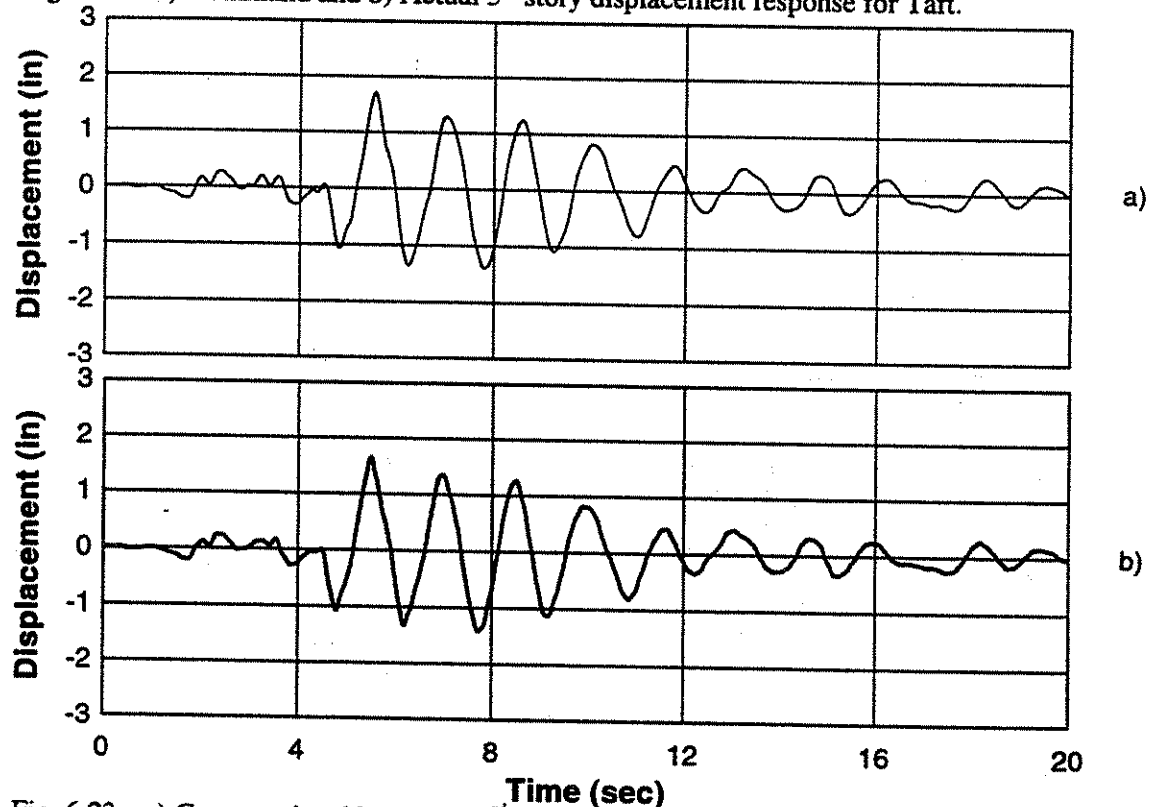

Fig. 6.23 - a) Command and b) Actual 3rd story displacement response for Oakland.

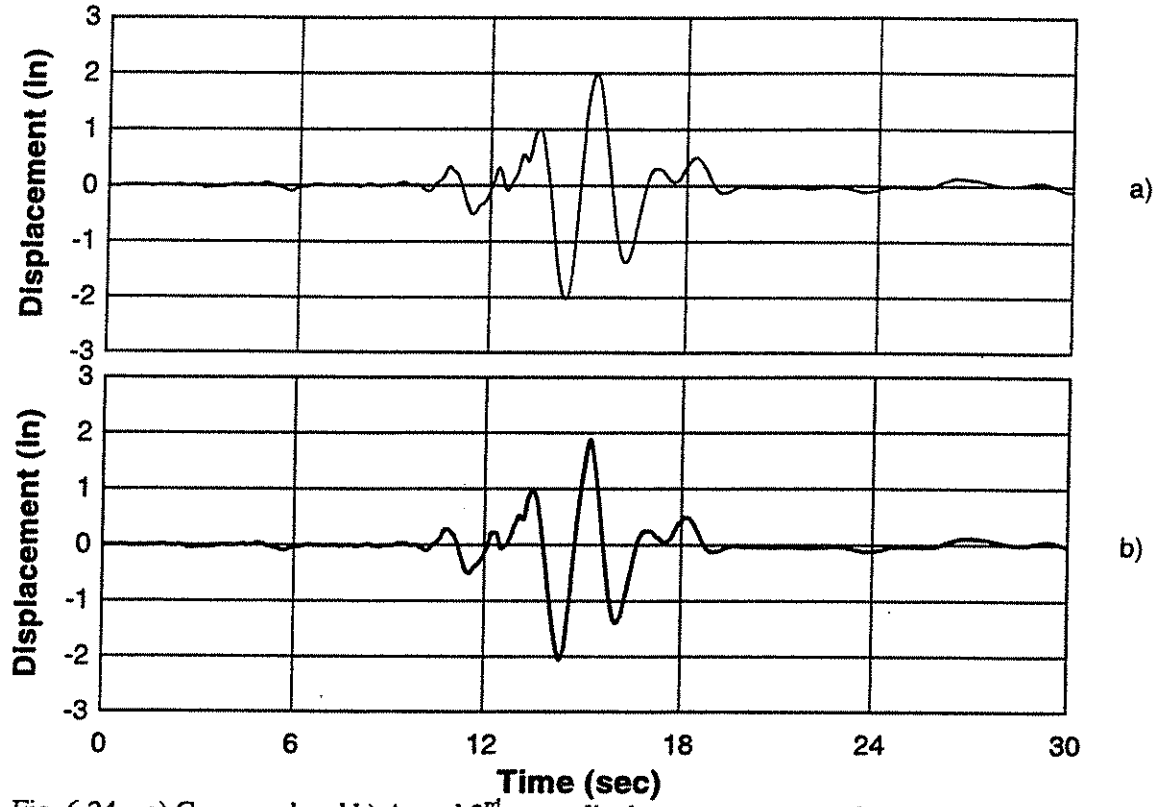

Fig. 6.24 - a) Command and b) Actual 3rd story displacement response for Treasure Island.

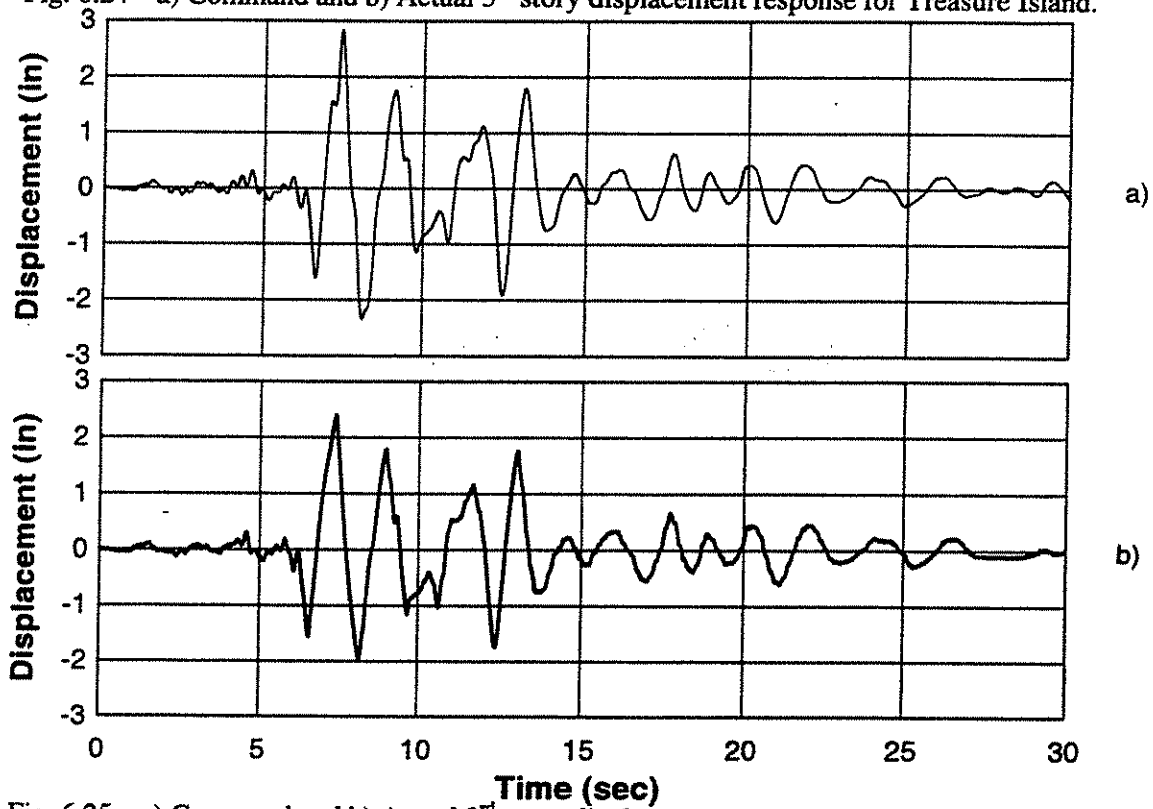

Fig. 6.25 - a) Command and b) Actual 3rd story displacement response for Castaic.

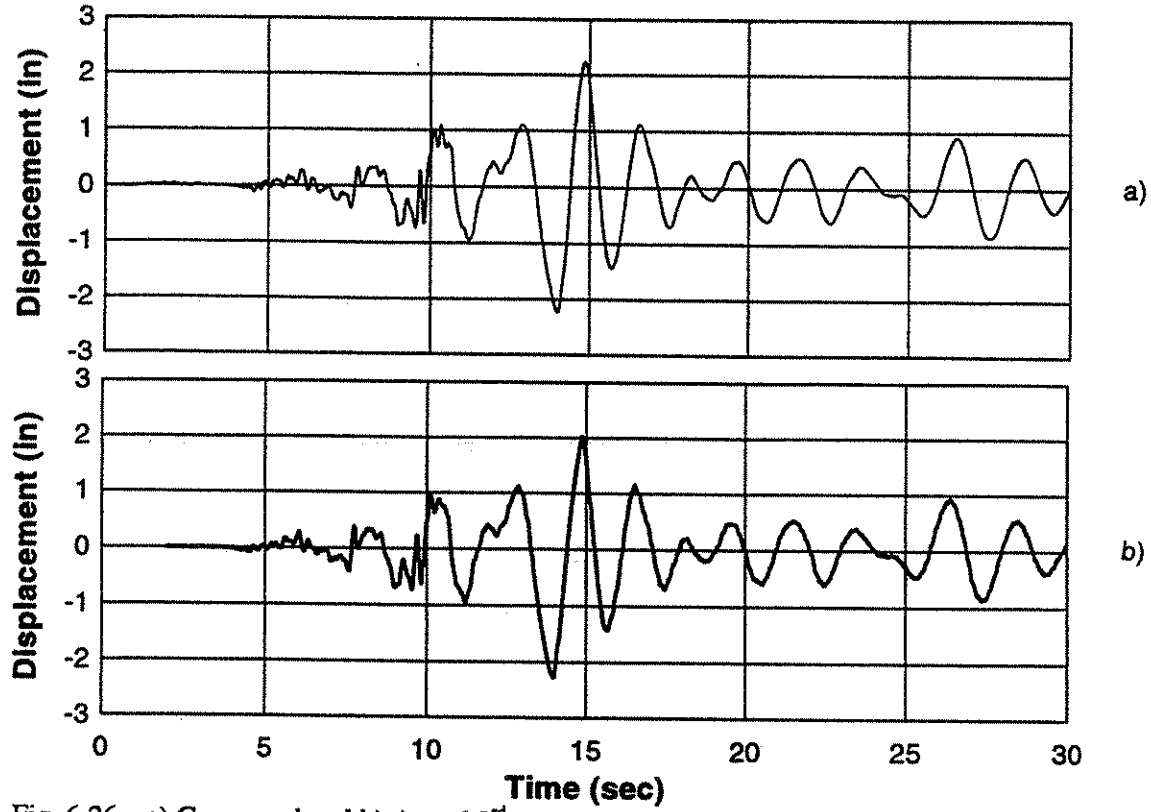

Fig. 6.26 - a) Command and b) Actual 3rd story displacement response for Santa Monica.

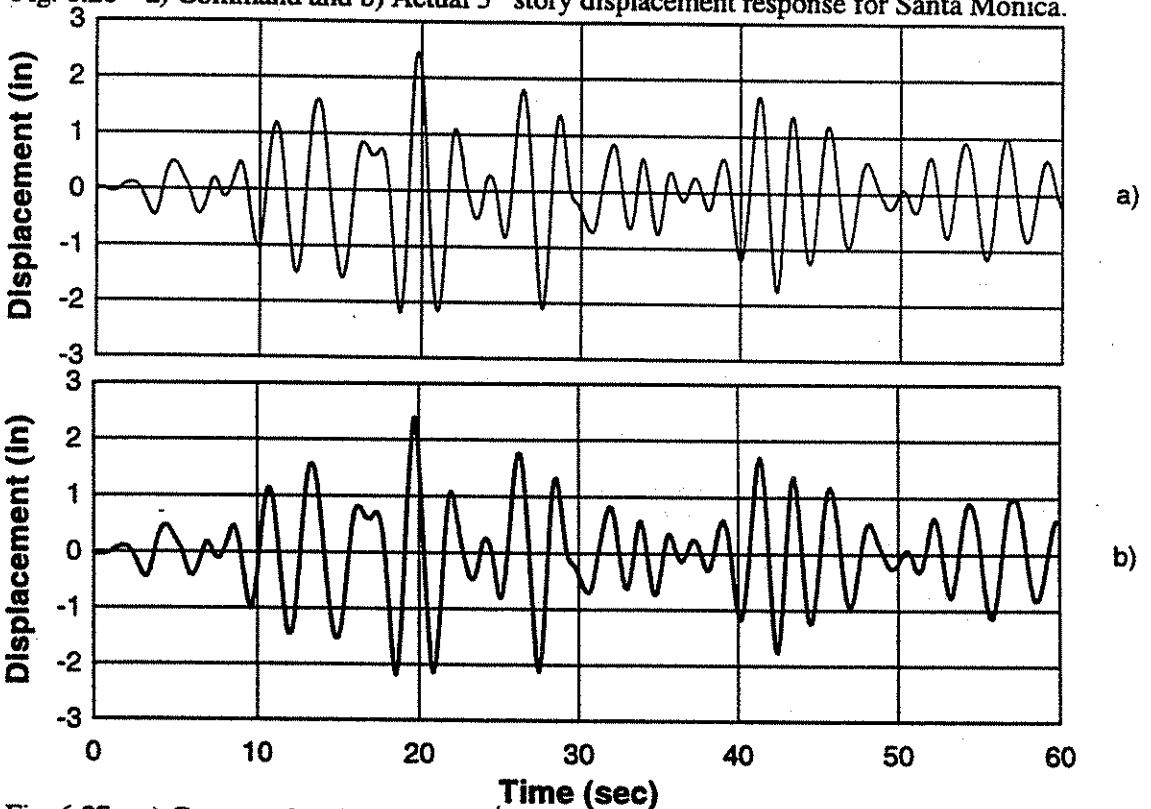

Fig. 6.27 - a) Command and b) Actual 3rd story displacement response for Frigorifico.

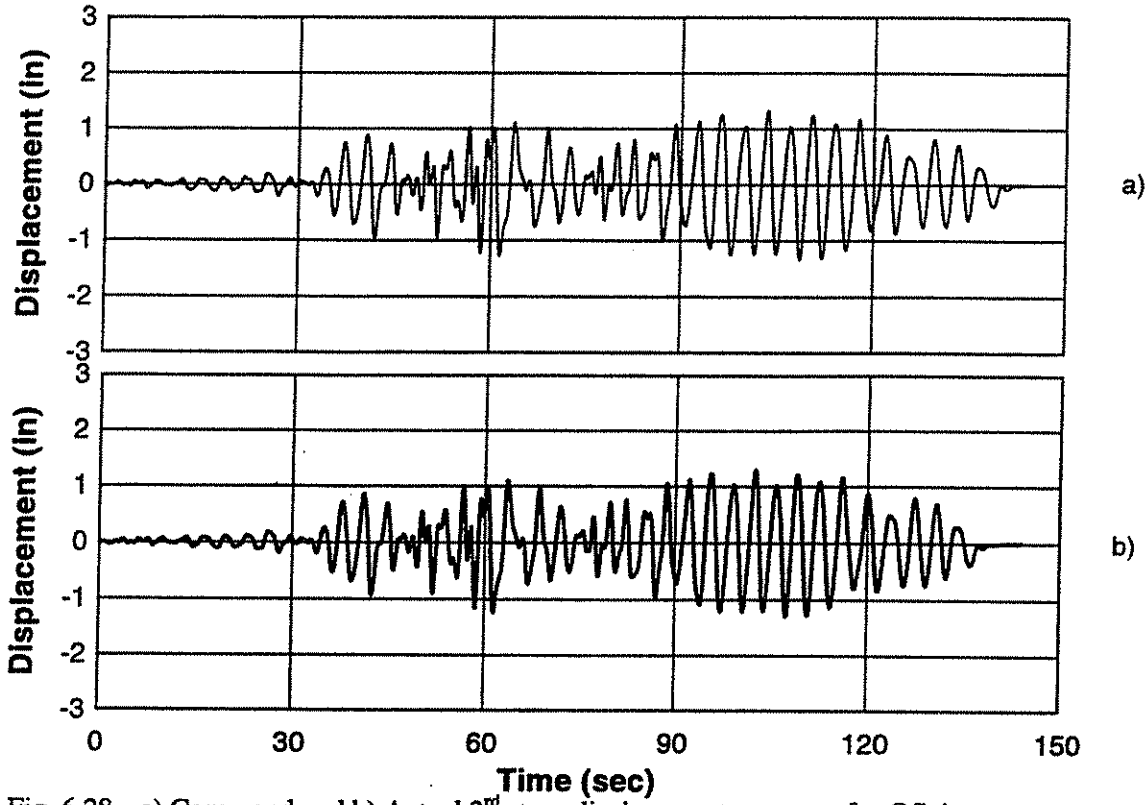

Fig. 6.28 - a) Command and b) Actual 3rd story displacement response for Oficina.

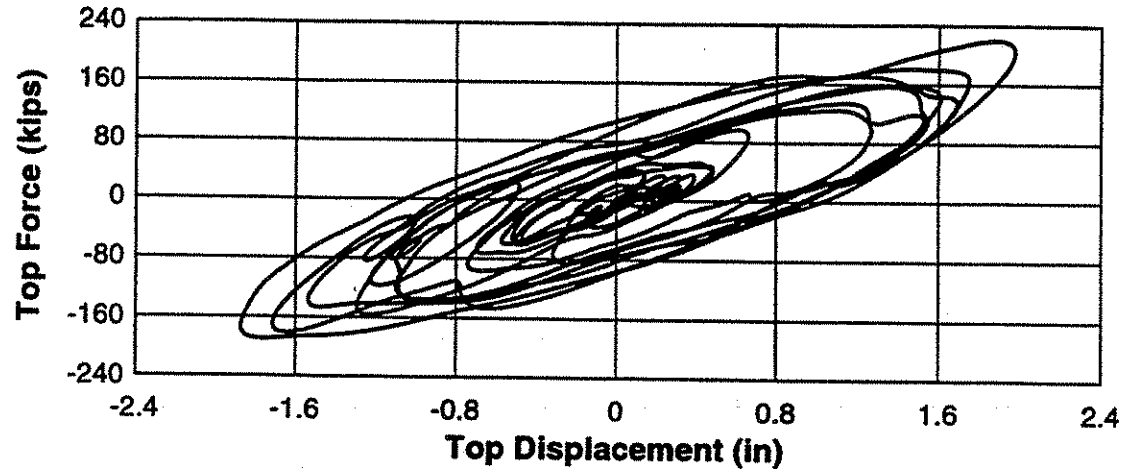

Fig. 6.29a - Measured overall force-displacement response for Hachinohe.

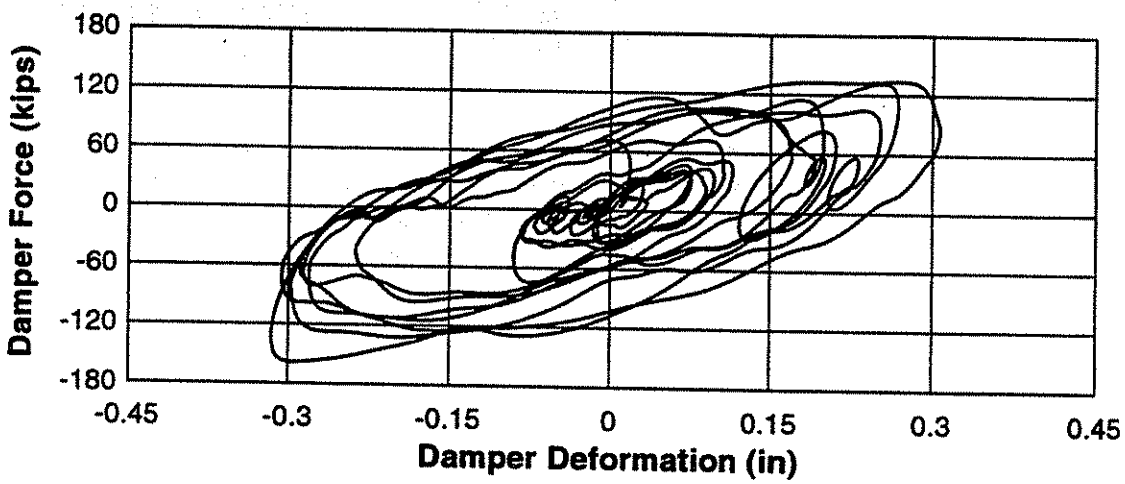

Fig. 6.29b - Example measured damper force-deformation response for Hachinohe.

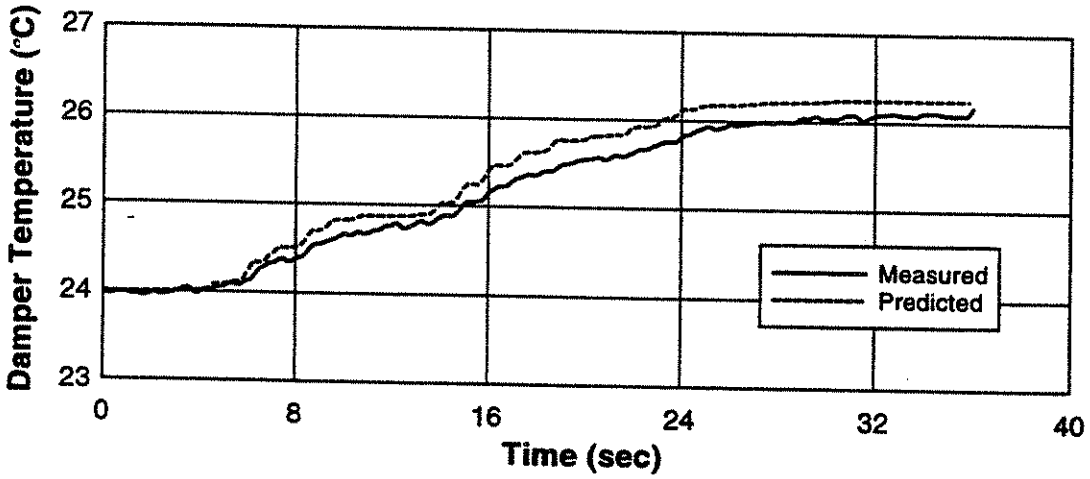

Fig. 6.29c - Example measured and predicted damper temperature rise for Hachinohe.

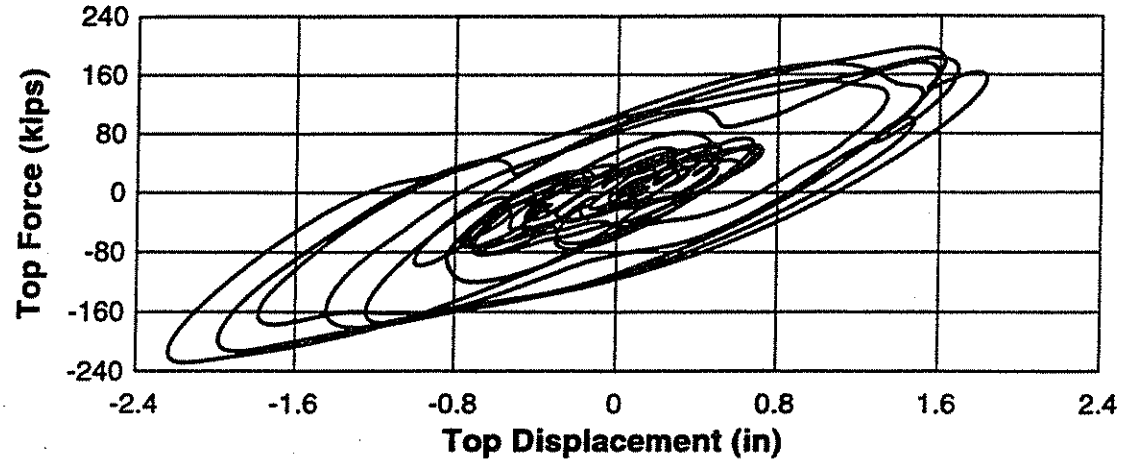

Fig. 6.30a - Measured overall force-displacement response for Taft.

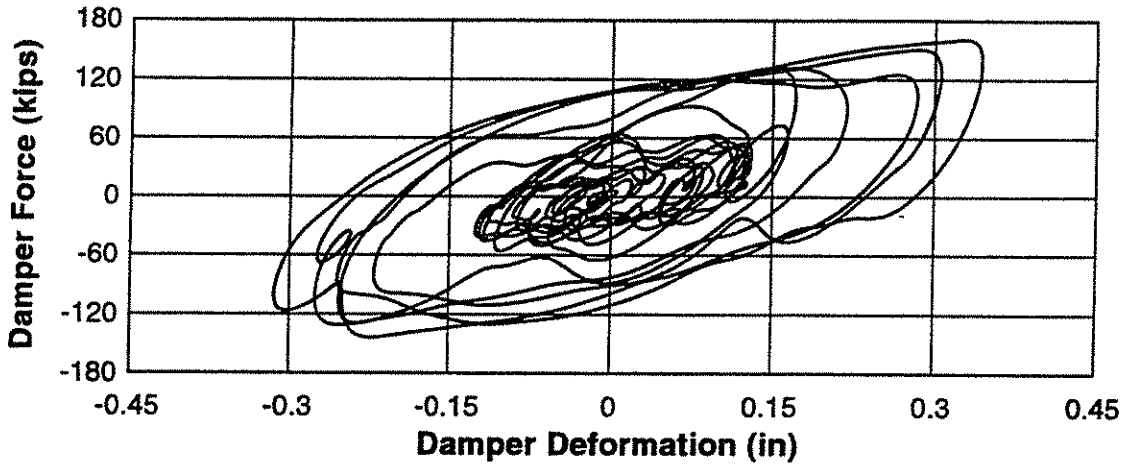

Fig. 6.30b - Example measured damper force-deformation response for Taft.

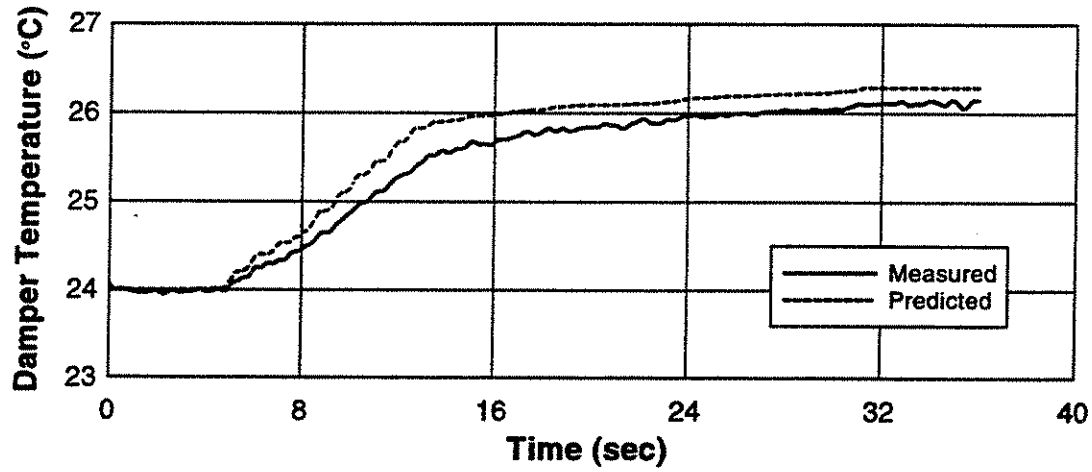

Fig. 6.30c - Example measured and predicted damper temperature rise for Taft.

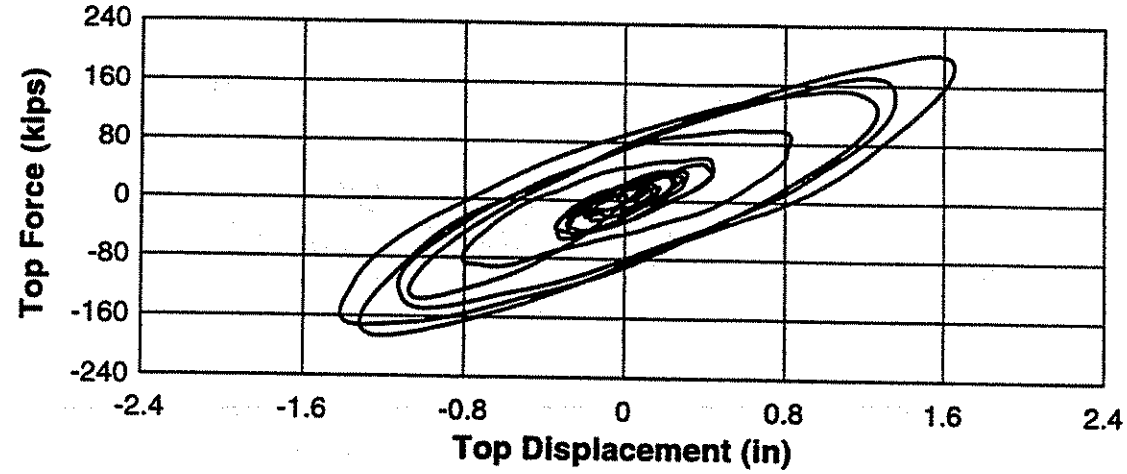

Fig. 6.31a - Measured overall force-displacement response for Oakland.

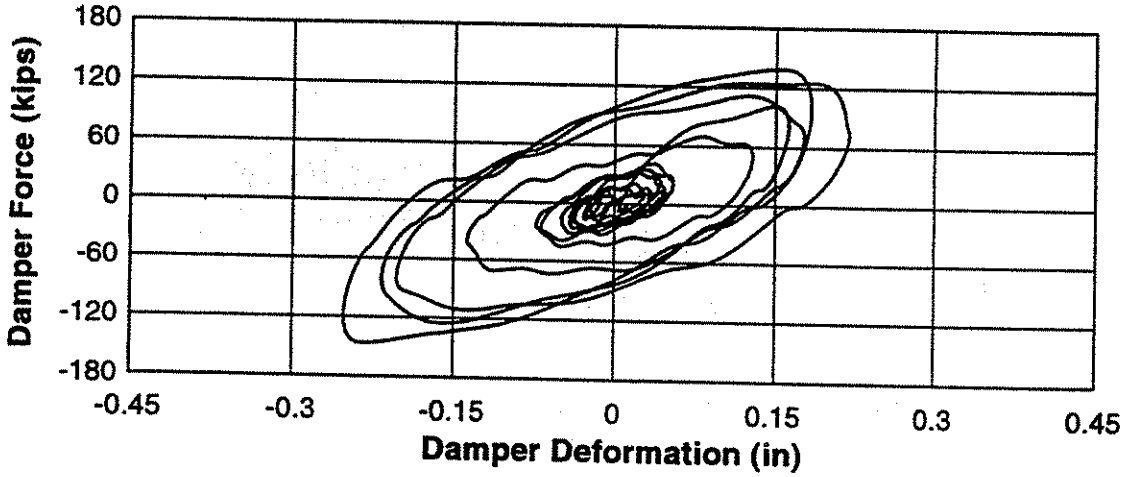

Fig. 6.31b - Example measured damper force-deformation response for Oakland.

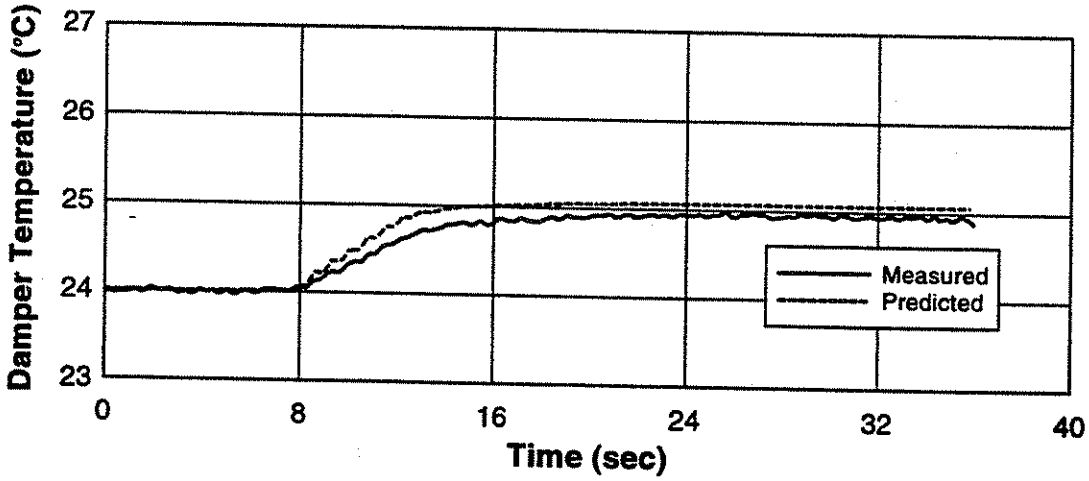

Fig. 6.31c - Example measured and predicted damper temperature rise for Oakland.

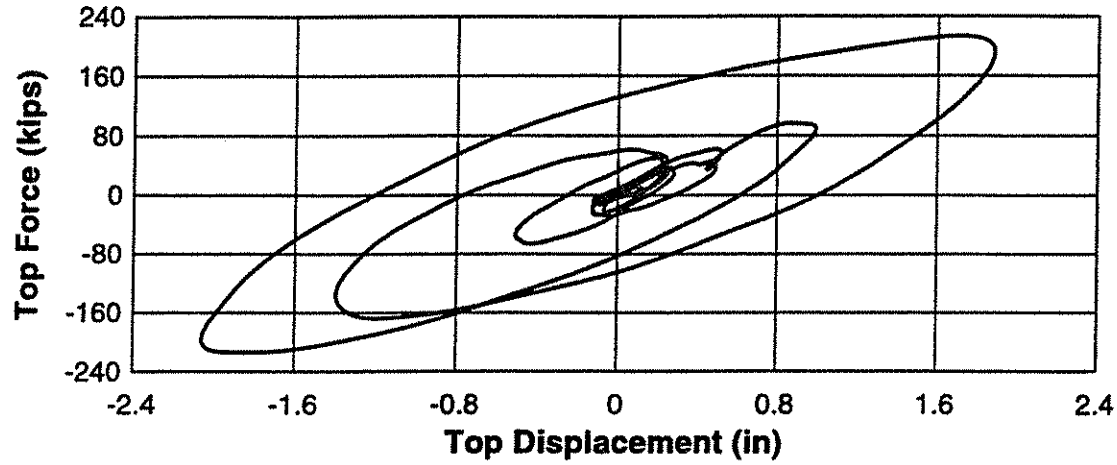

Fig. 6.32a - Measured overall force-displacement response for Treasure Island.

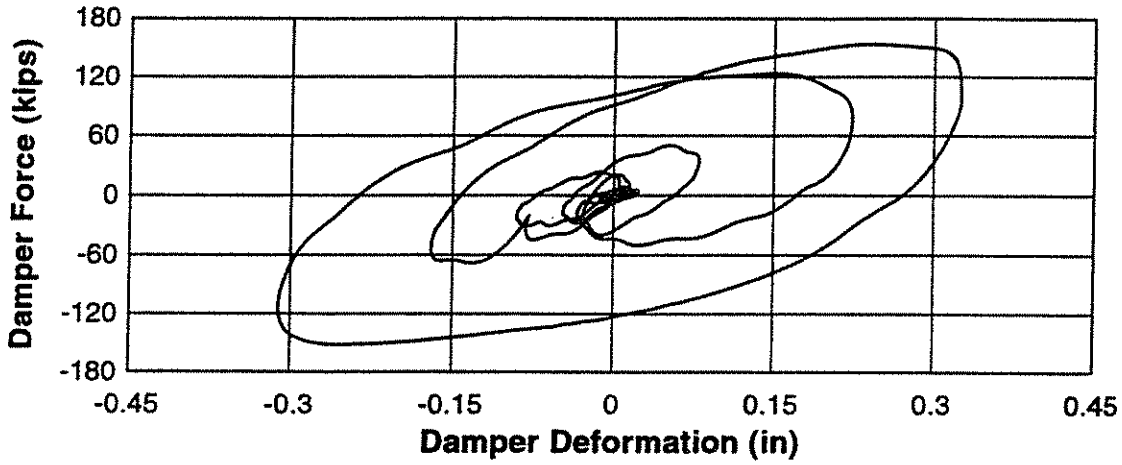

Fig. 6.32b - Example measured damper force-deformation response for Treasure Island.

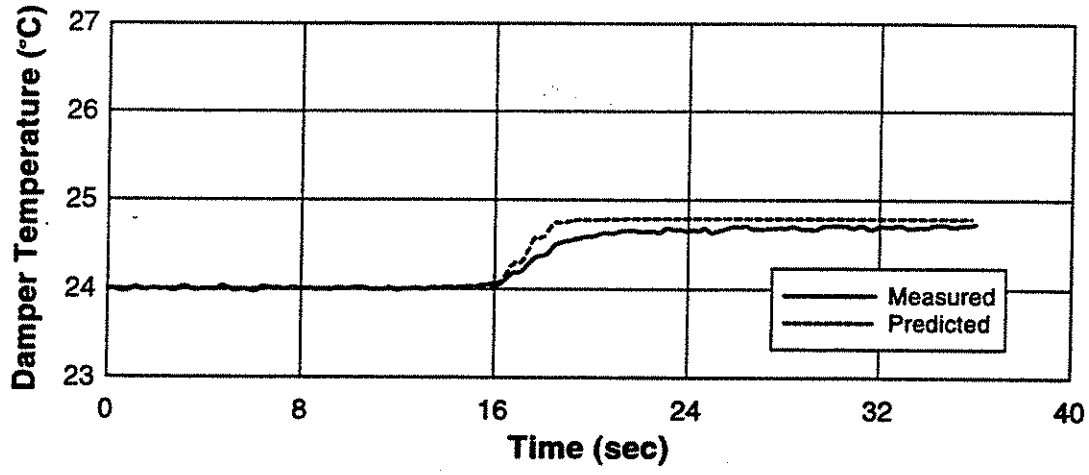

Fig. 6.32c - Example measured and predicted damper temperature rise for Treasure Island.

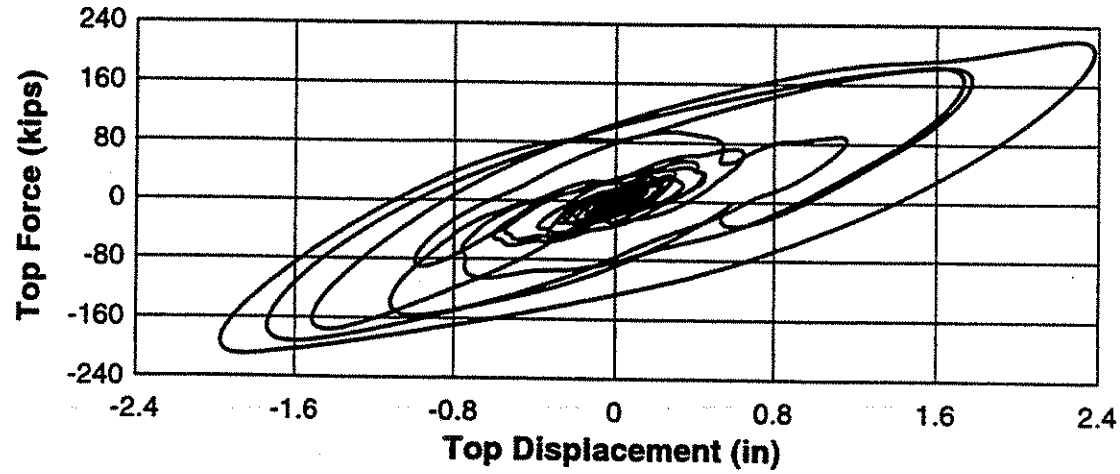

Fig. 6.33a - Measured overall force-displacement response for Castaic.

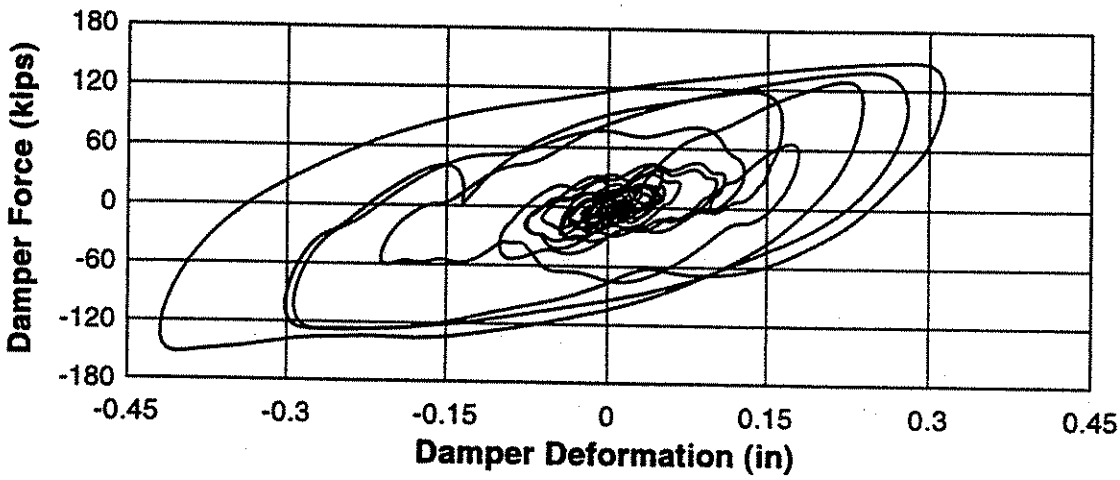

Fig. 6.33b - Example measured damper force-deformation response for Castaic.

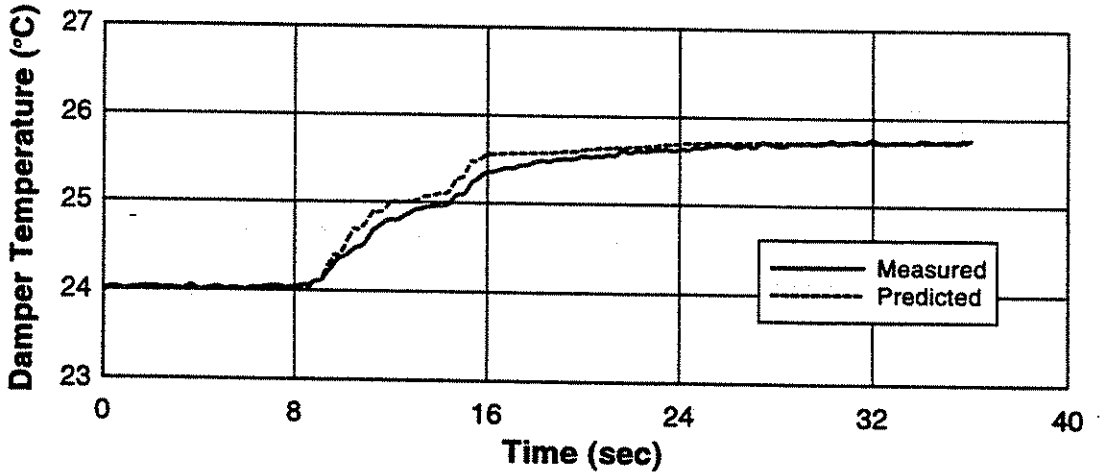

Fig. 6.33c - Example measured and predicted damper temperature rise for Castaic.

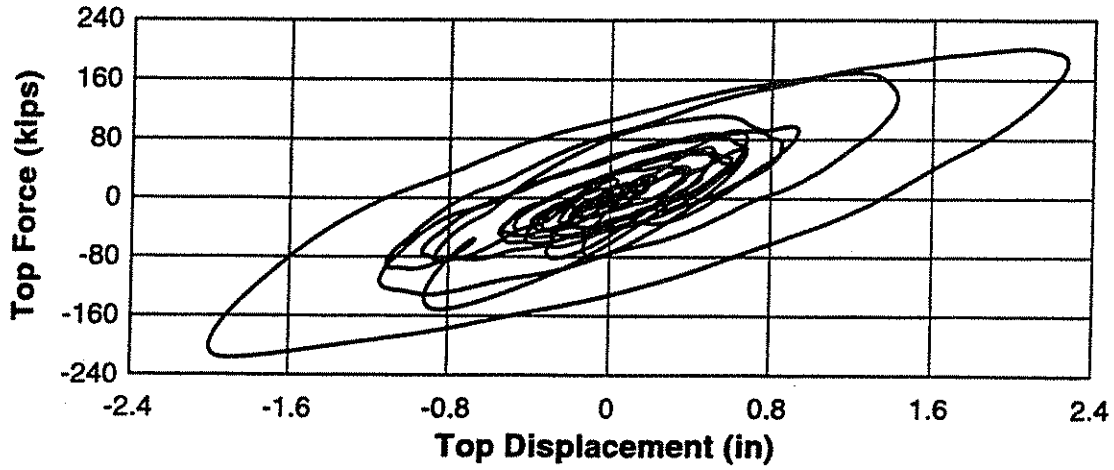

Fig. 6.34a - Measured overall force-displacement response for Santa Monica.

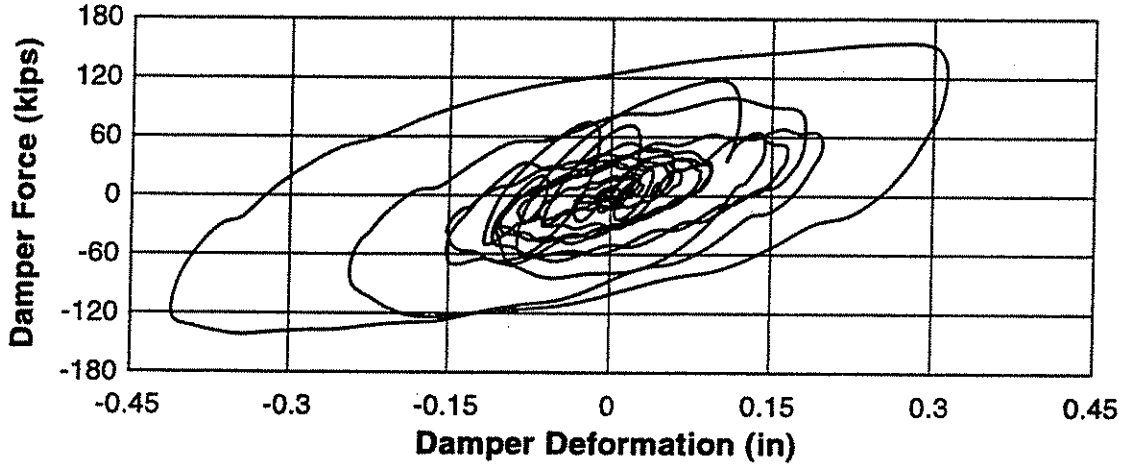

Fig. 6.34b - Example measured damper force-deformation response for Santa Monica.

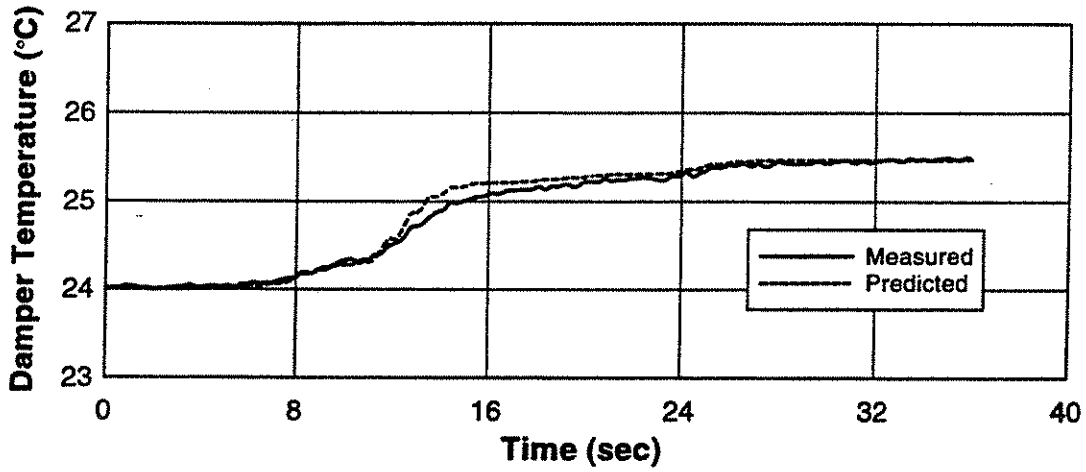

Fig. 6.34c - Example measured and predicted damper temperature rise for Santa Monica.

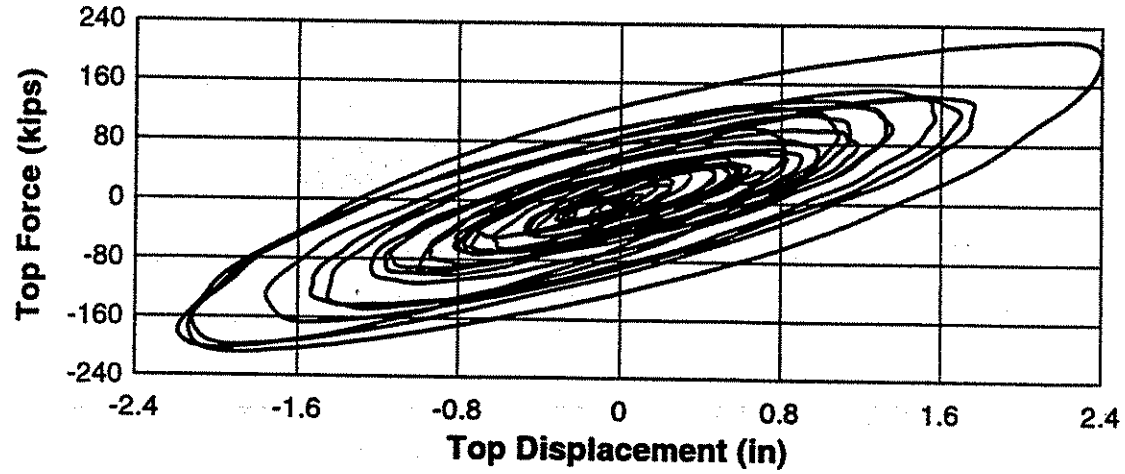

Fig. 6.35a - Measured overall force-displacement response for Frigorifico.

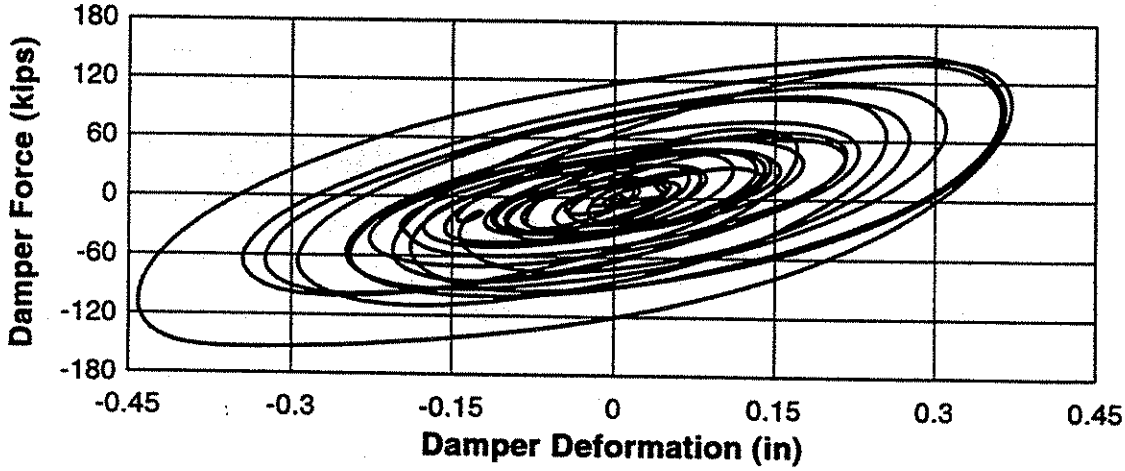

Fig. 6.35b - Example measured damper force-deformation response for Frigorifico.

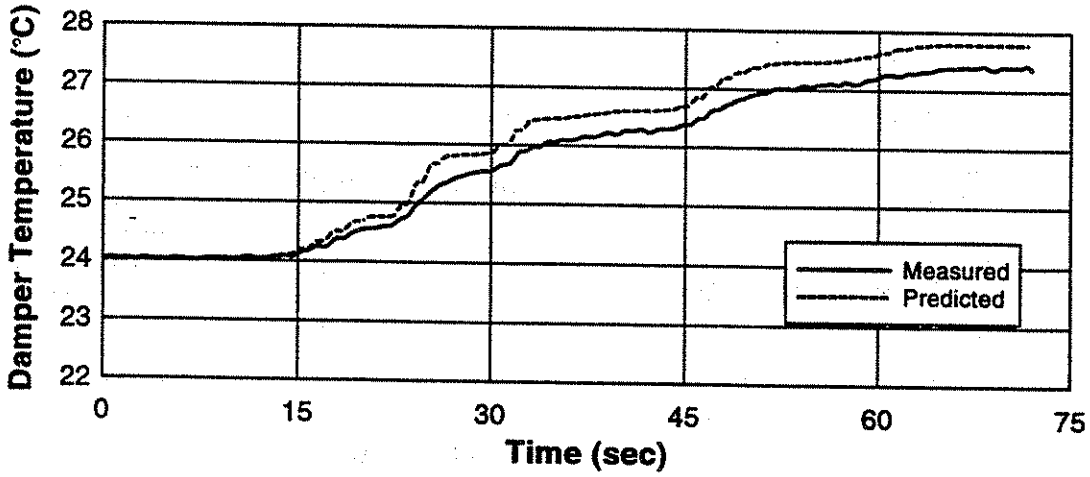

Fig. 6.35c - Example measured and predicted damper temperature rise for Frigorifico.

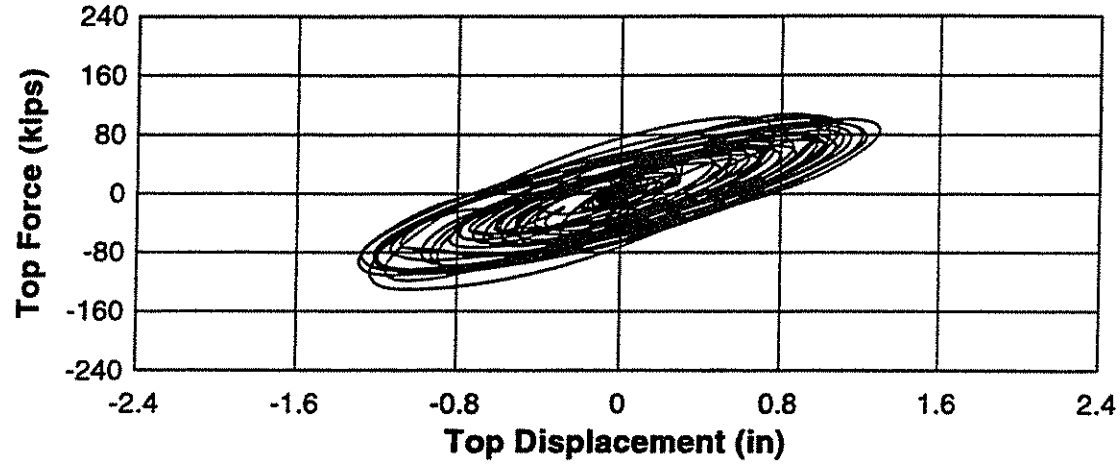

Fig. 6.36a - Measured overall force-displacement response for Oficina.

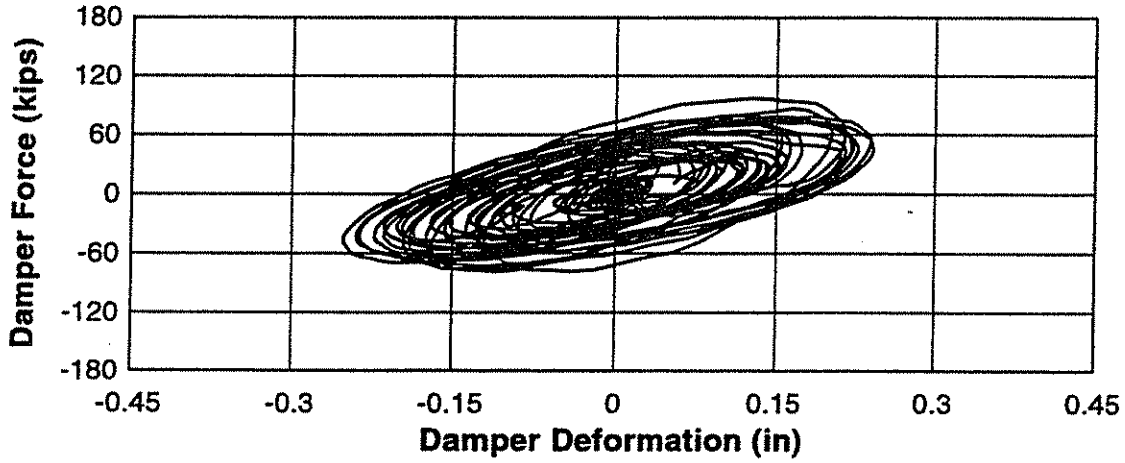

Fig. 6.36b - Example measured damper force-deformation response for Oficina.

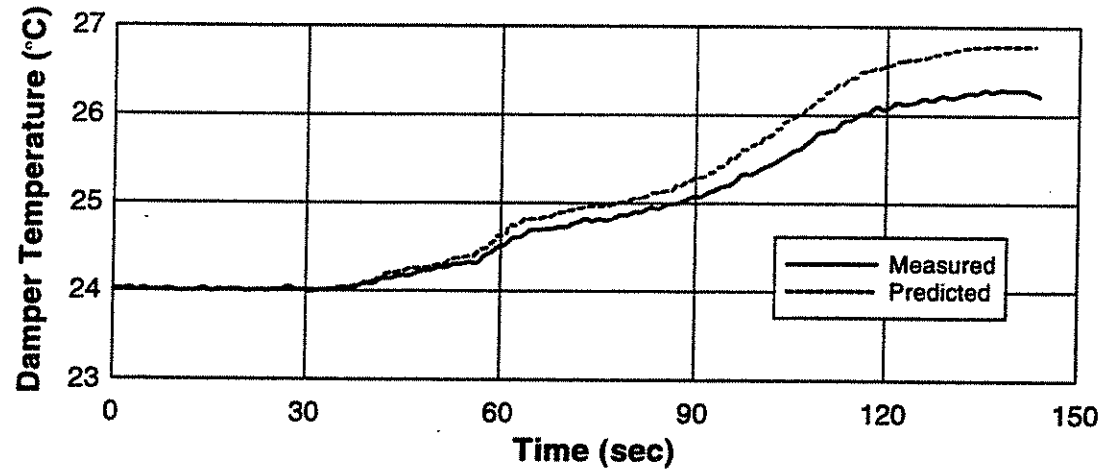

Fig. 6.36c - Example measured and predicted damper temperature rise for Oficina.

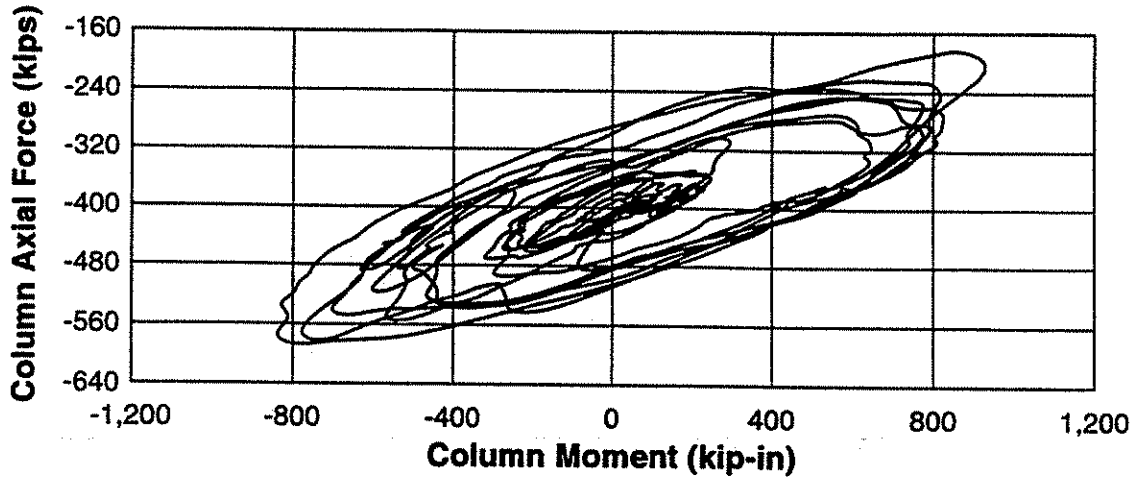

Fig. 6.37 - Measured axial force-moment interaction in East second story column for Hachinohe.

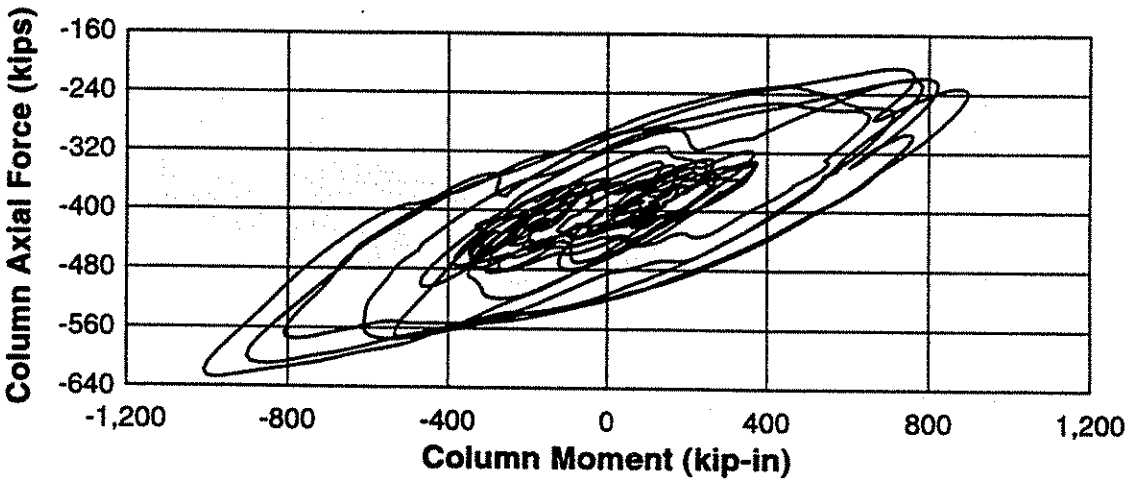

Fig. 6.38 - Measured axial force-moment interaction in East second story column for Taft.

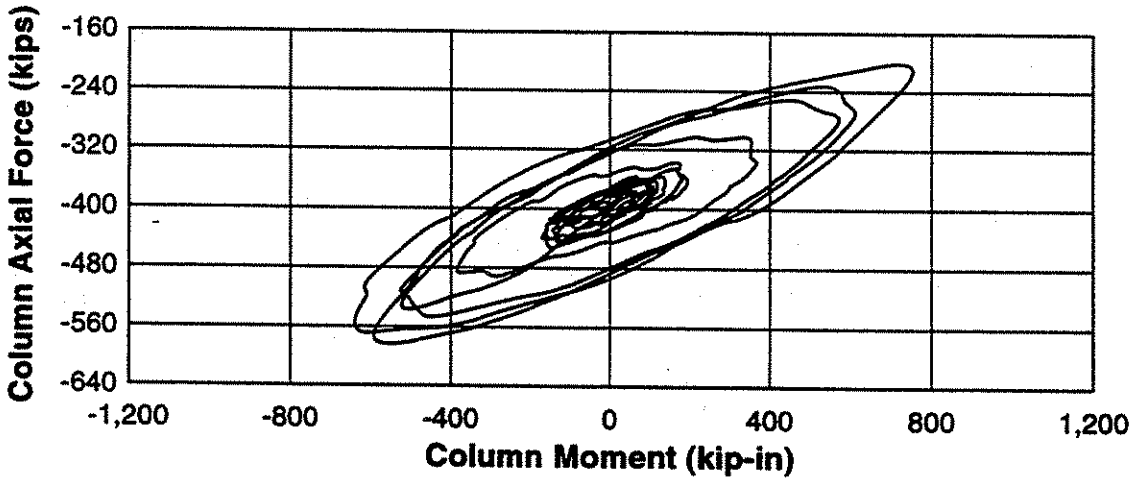

Fig. 6.39 - Measured axial force-moment interaction in East second story column for Oakland.

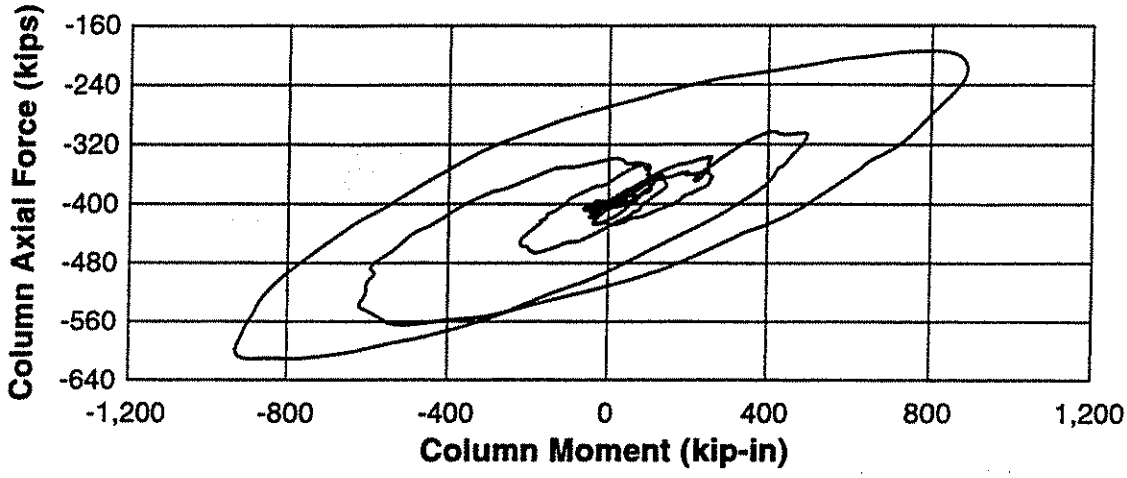

Fig. 6.40 - Measured axial force-moment interaction in East second story column for Treasure Island.

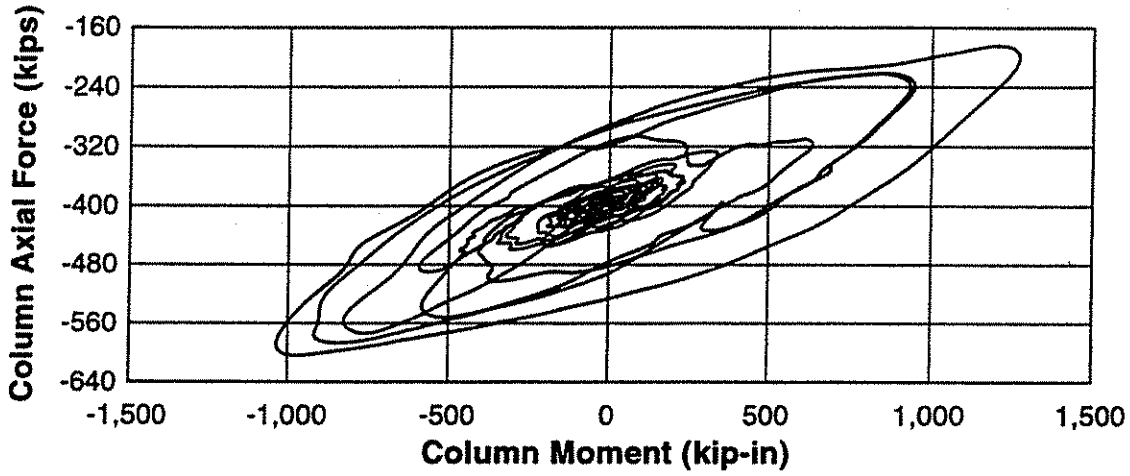

Fig. 6.41 - Measured axial force-moment interaction in East second story column for Castaic.

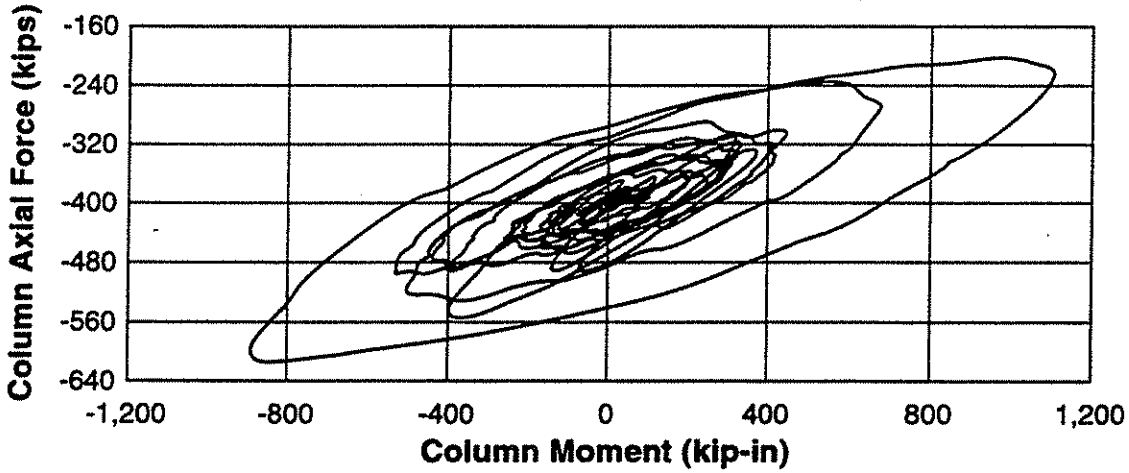

Fig. 6.42 - Measured axial force-moment interaction in East second story column for Santa Monica.

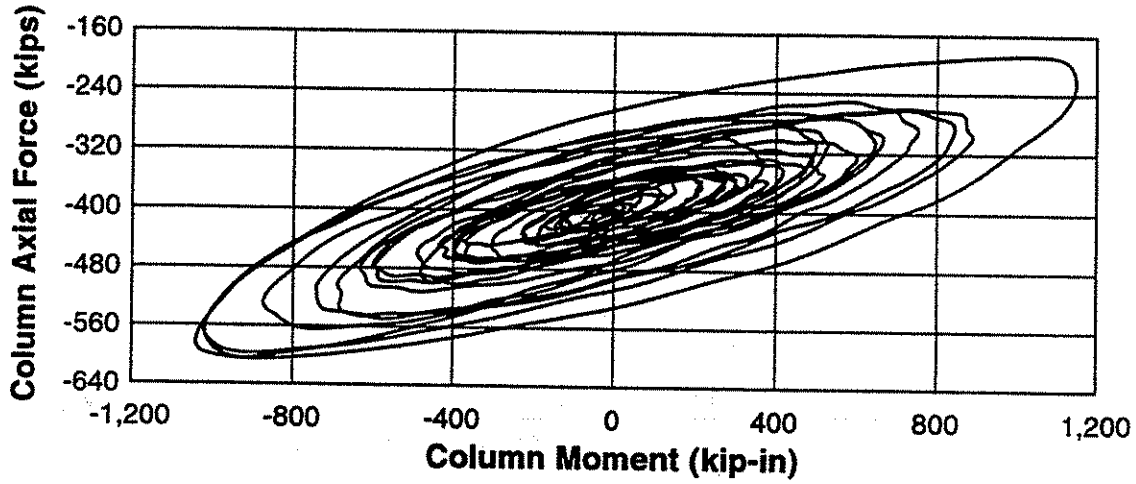

Fig. 6.43 - Measured axial force-moment interaction in East second story column for Frigorifico.

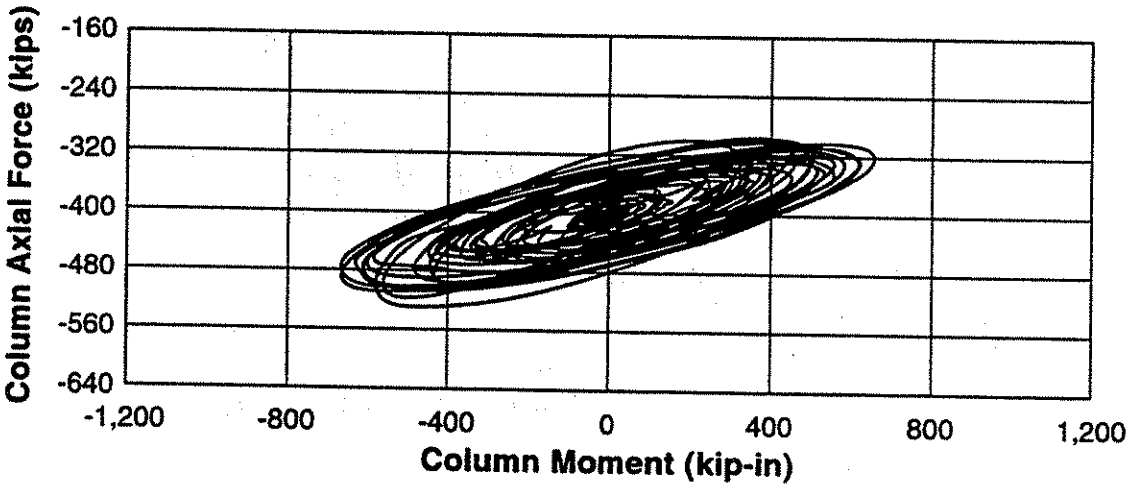

Fig. 6.44 - Measured axial force-moment interaction in East second story column for Oficina.

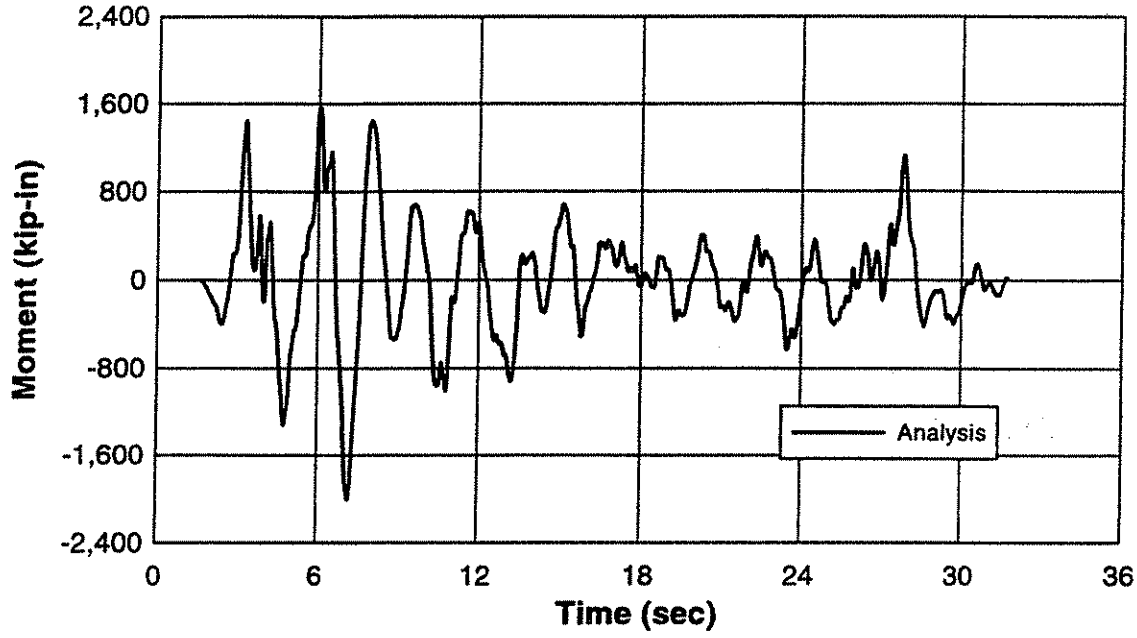

Fig. 6.45a - Predicted moment response at second story West beam for El Centro.

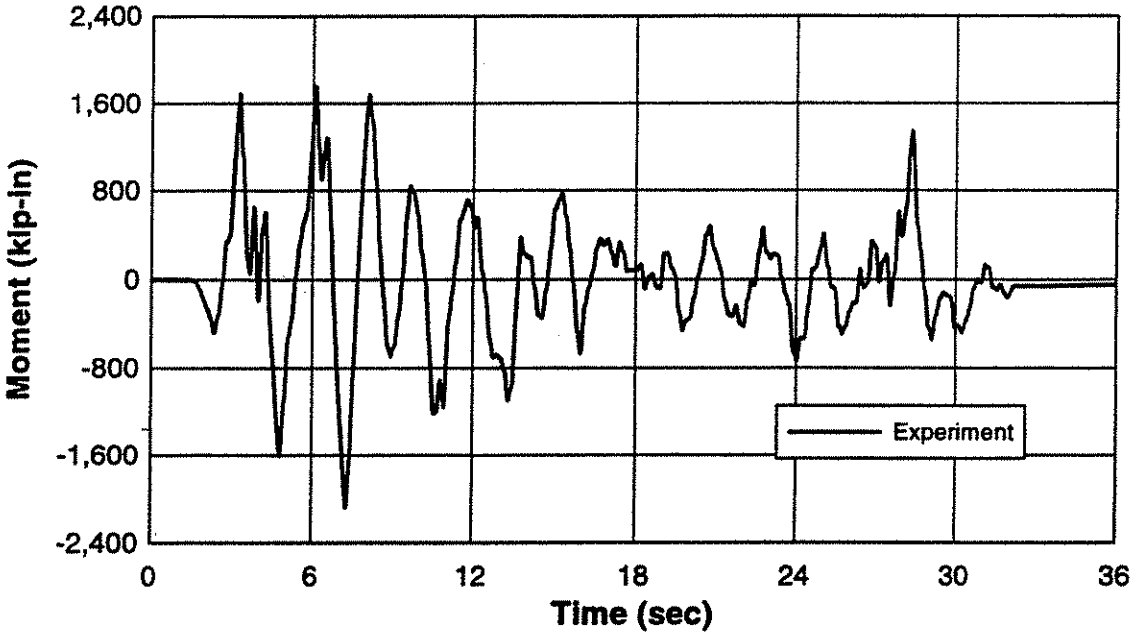

Fig. 6.45b - Measured moment response at second story West beam for El Centro.

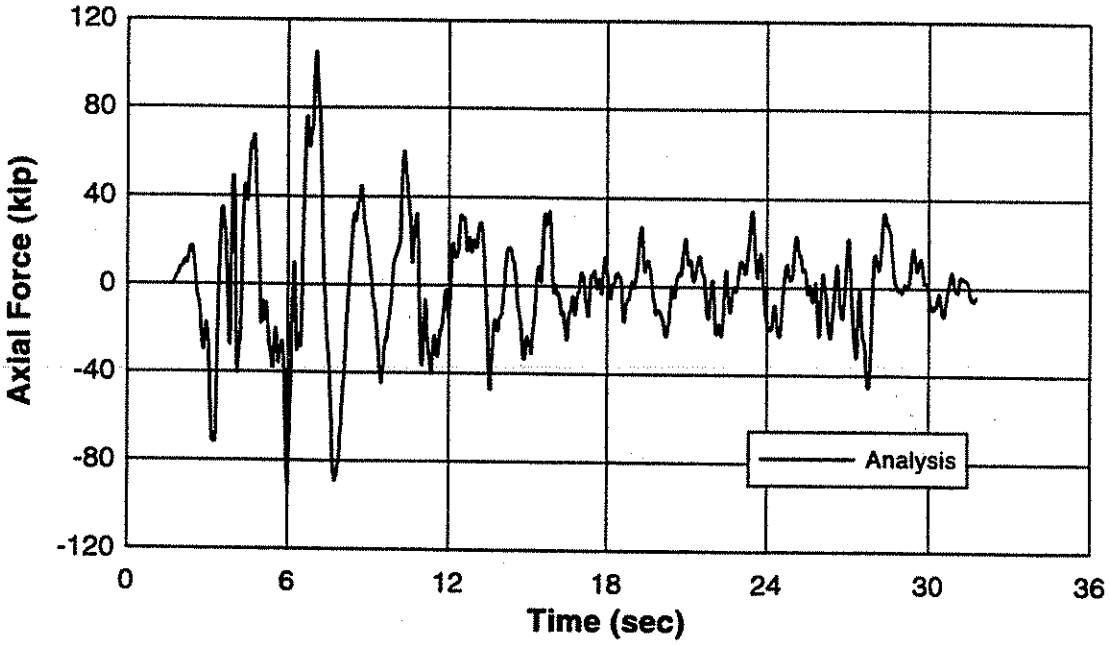

Fig. 6.46a - Predicted axial force response at second story West beam for El Centro.

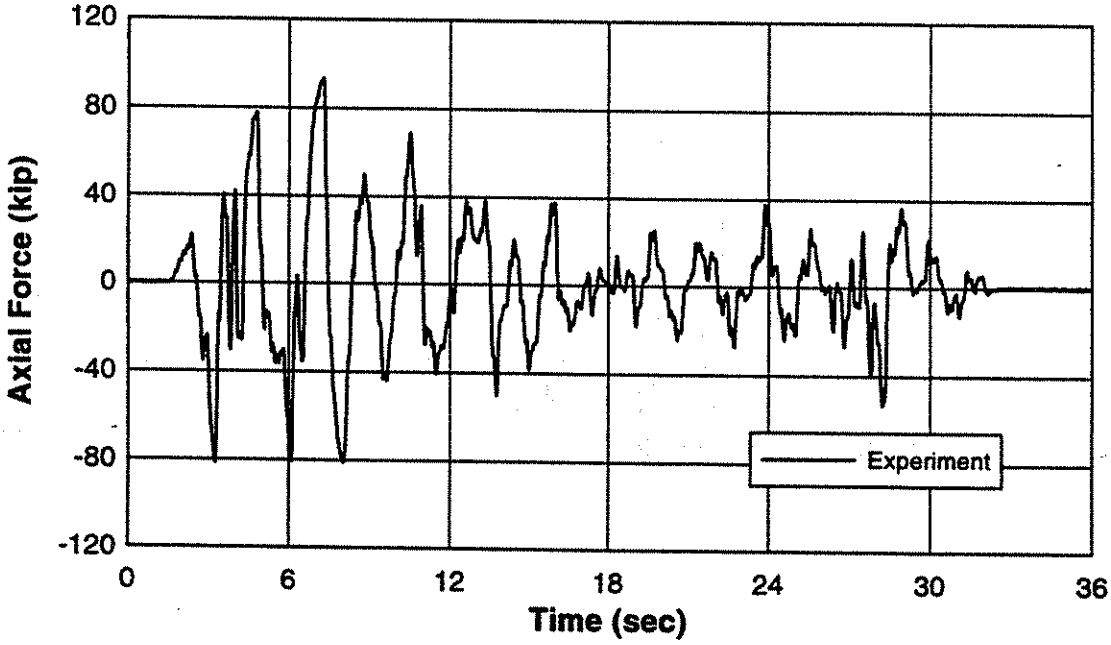

Fig. 6.46b - Measured axial force response at second story West beam for El Centro.

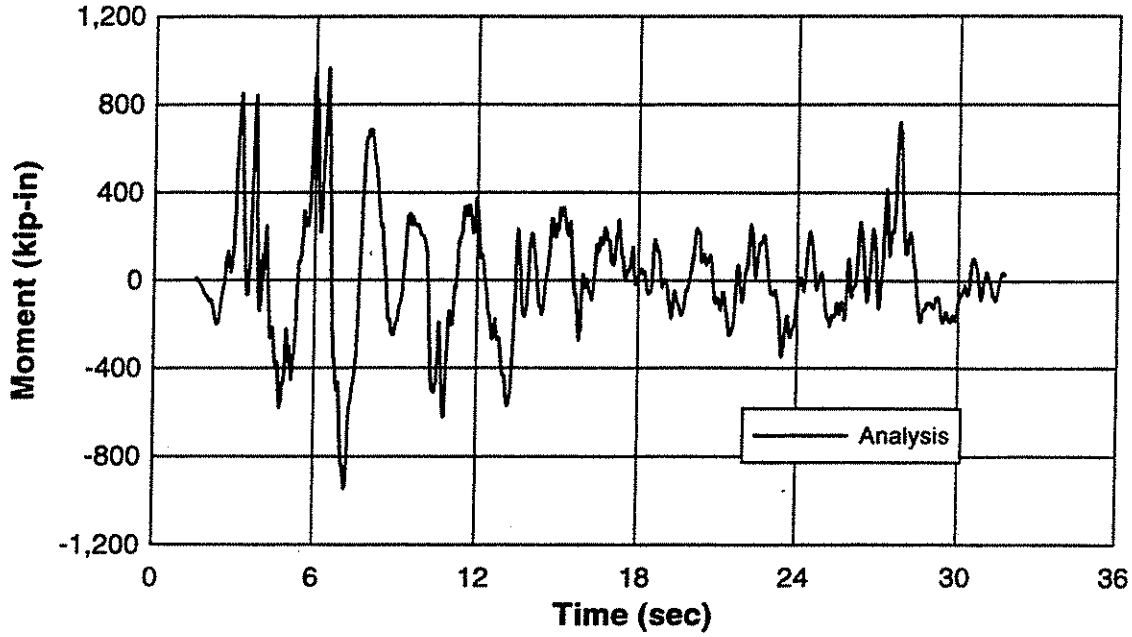

Fig. 6.47a - Predicted moment response at second story West column for El Centro.

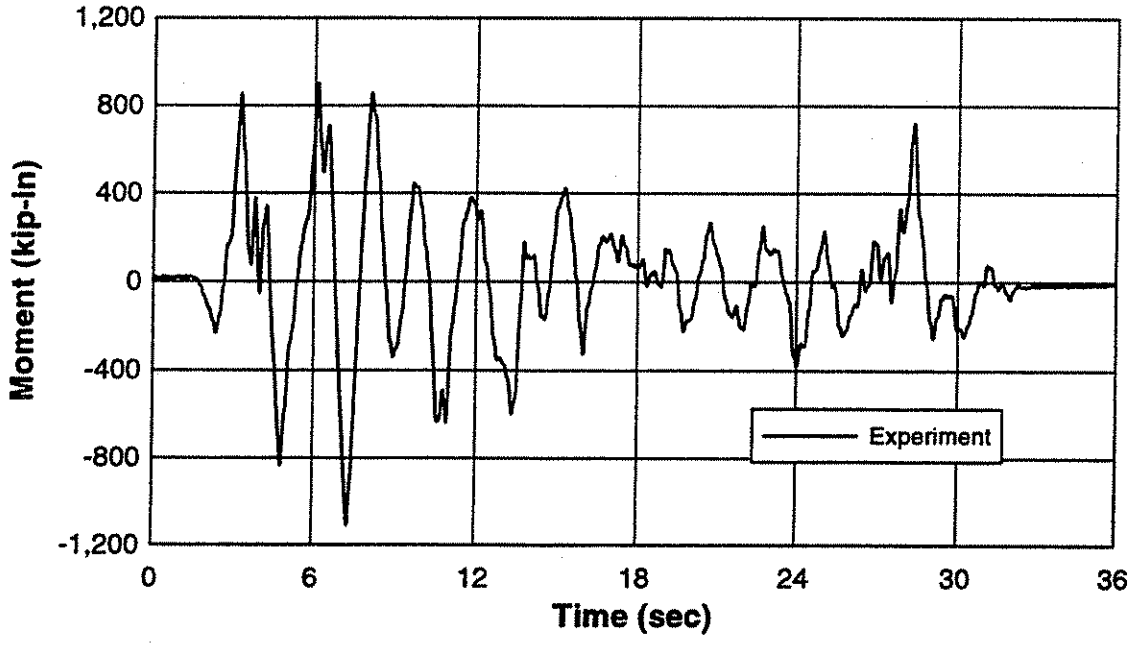

Fig. 6.47b - Measured moment response at second story West column for El Centro.

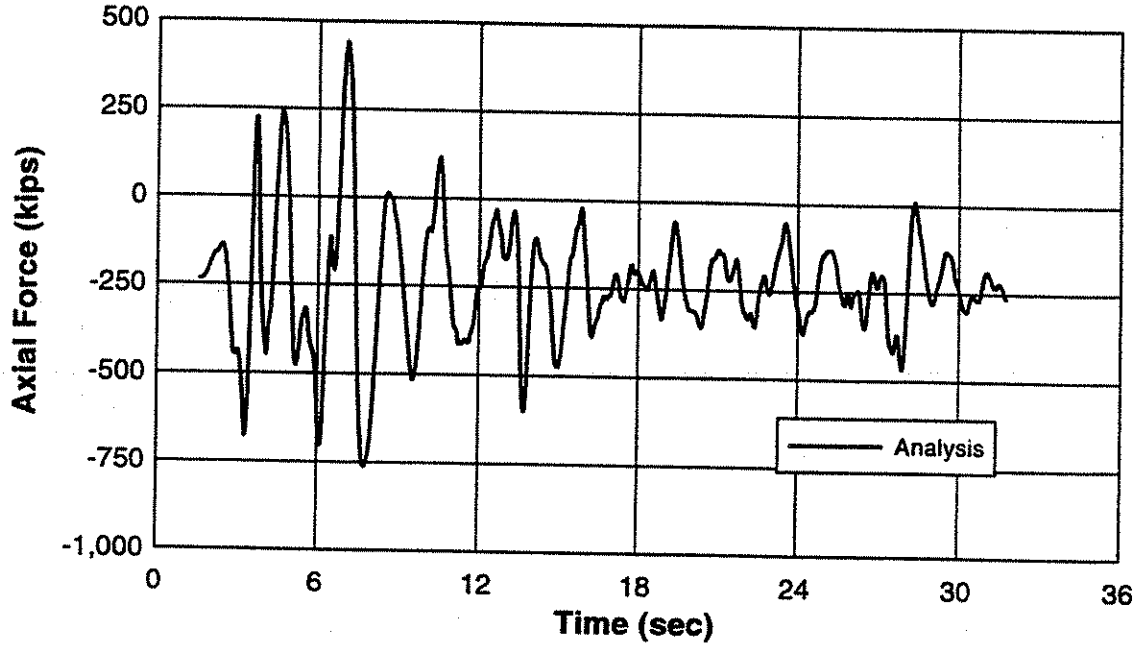

Fig. 6.48a - Predicted axial force response at third story West column for El Centro.

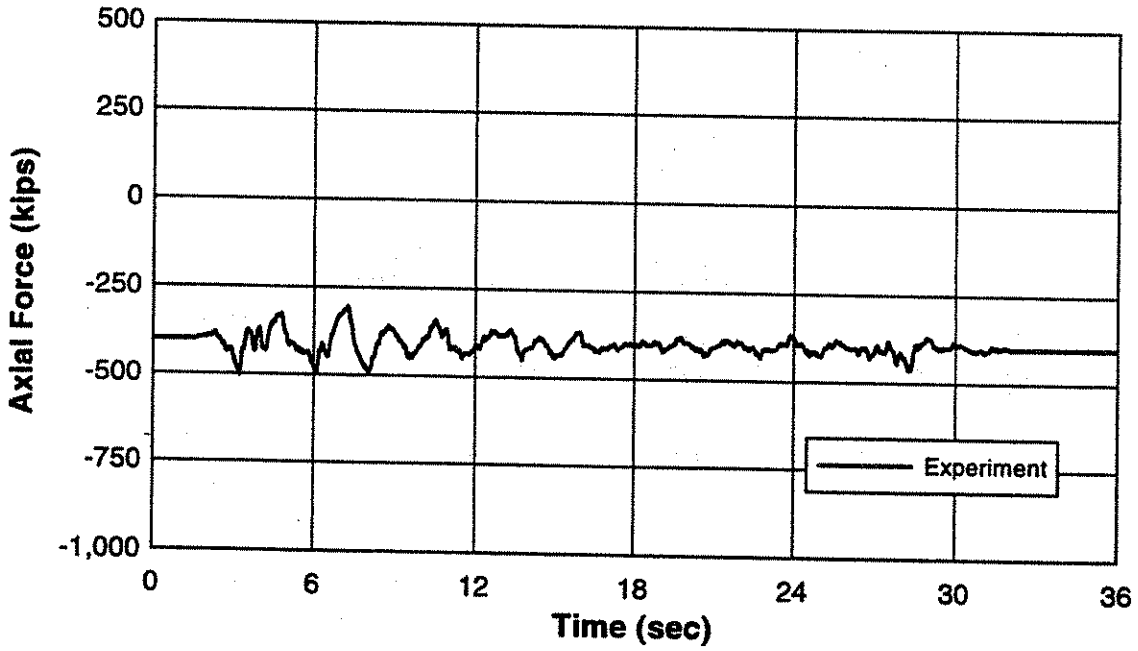

Fig. 6.48b - Measured axial force response at third story West column for El Centro.

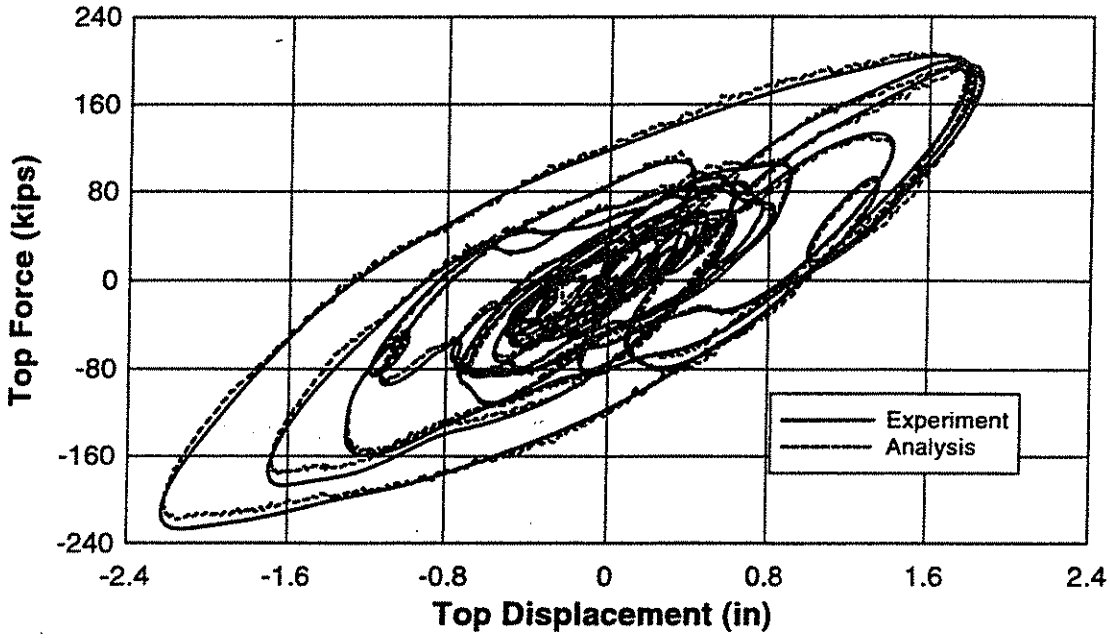

Fig. 6.49 - Measured and predicted overall force-displacement response for El Centro.

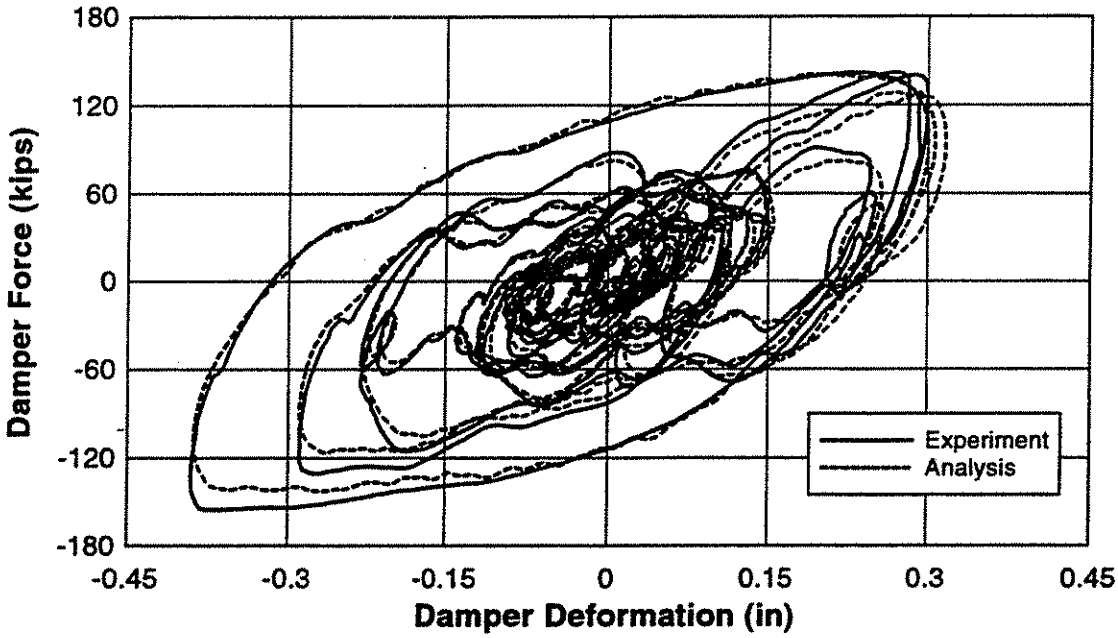

Fig. 6.50 - Measured and predicted force-deformation response at second story East damper for El Centro.

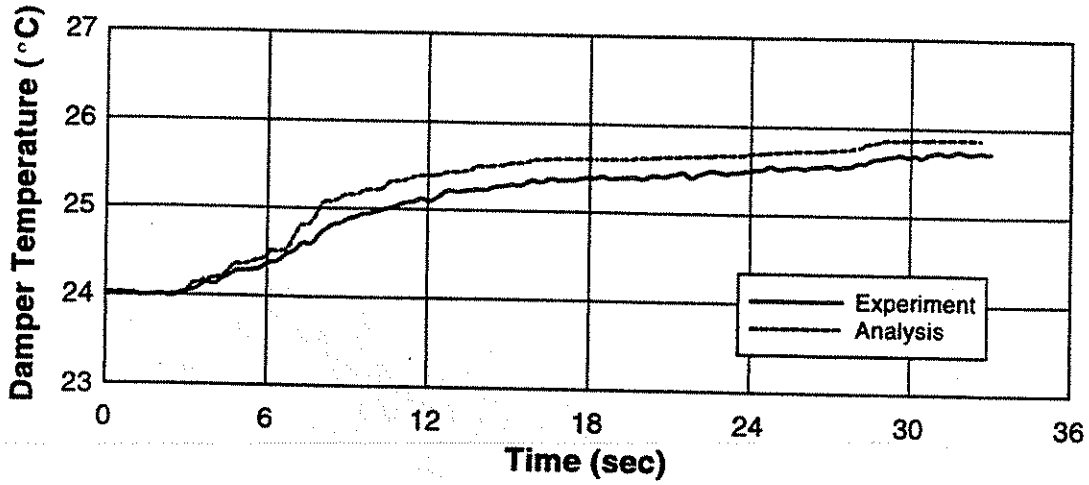

Fig. 6.51 - Measured and predicted temperature rise in second story East damper for El Centro.

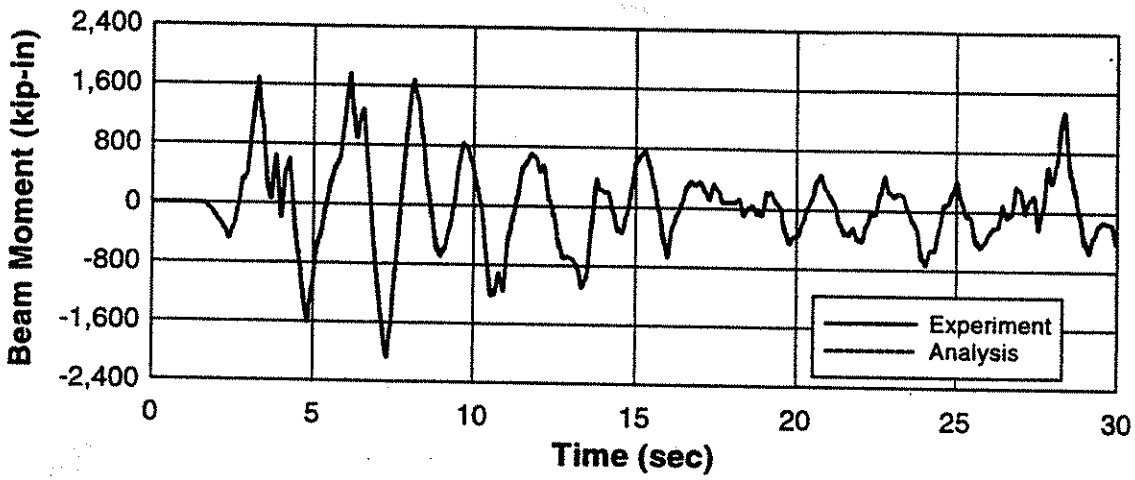

Fig. 6.52 - Measured and predicted moment response in second story East beam for El Centro.

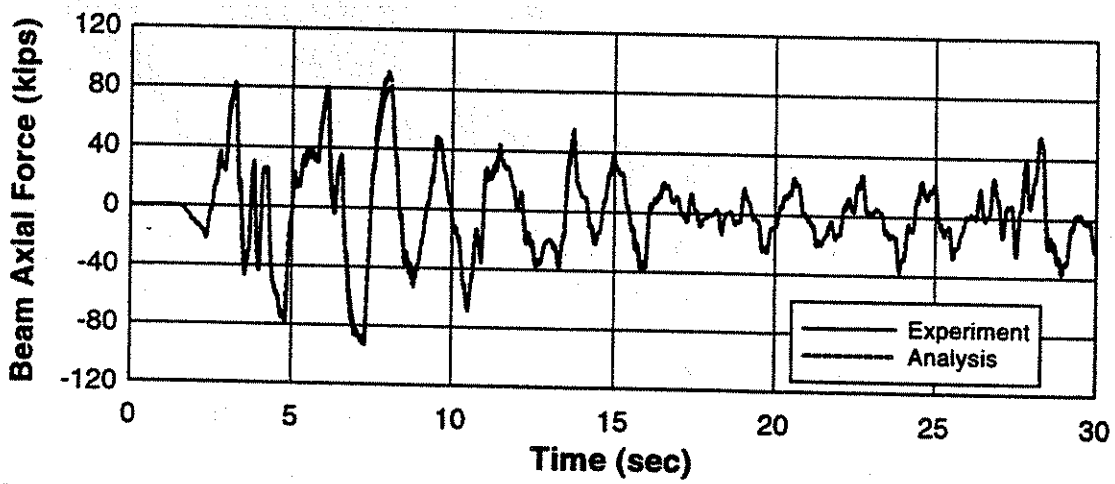

Fig. 6.53 - Measured and predicted axial force response in second story East beam for El Centro.

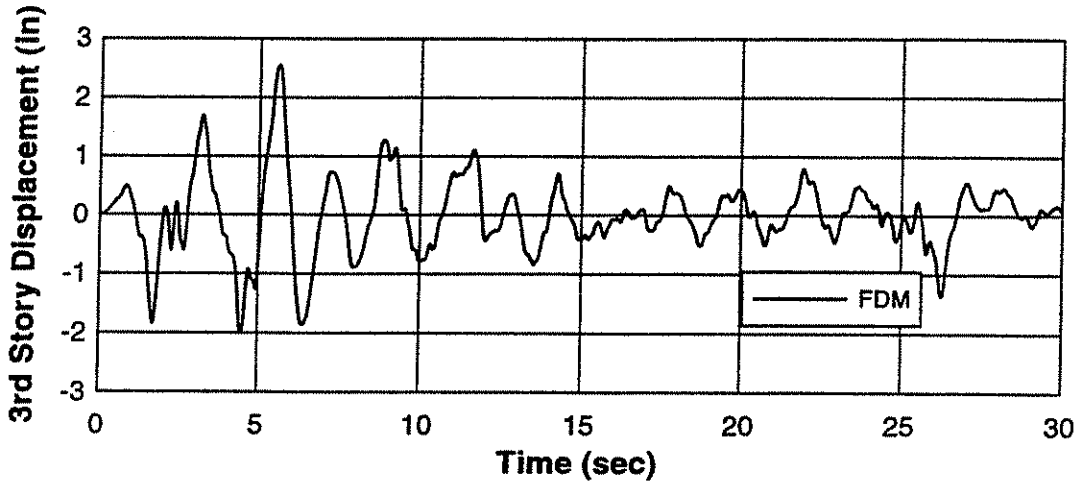

Fig. 6.54a - FDM predicted displacement response at third story for El Centro.

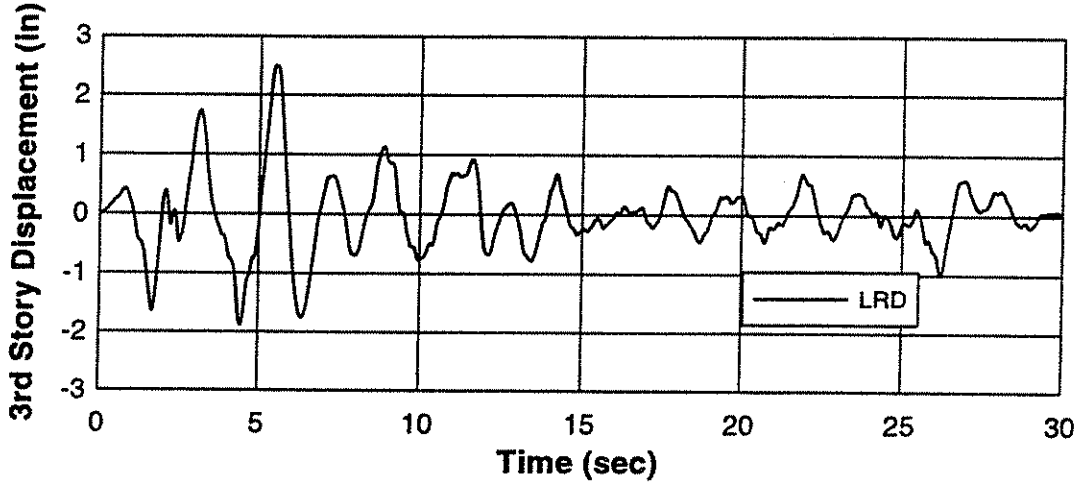

Fig. 6.54b - LRD predicted displacement response at third story for El Centro.

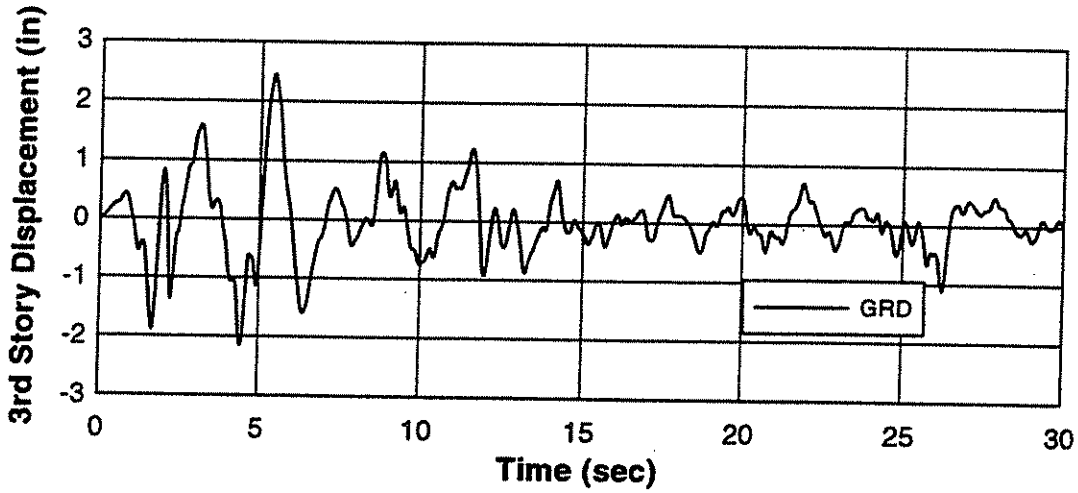

Fig. 6.54c - GRD predicted displacement response at third story for El Centro.

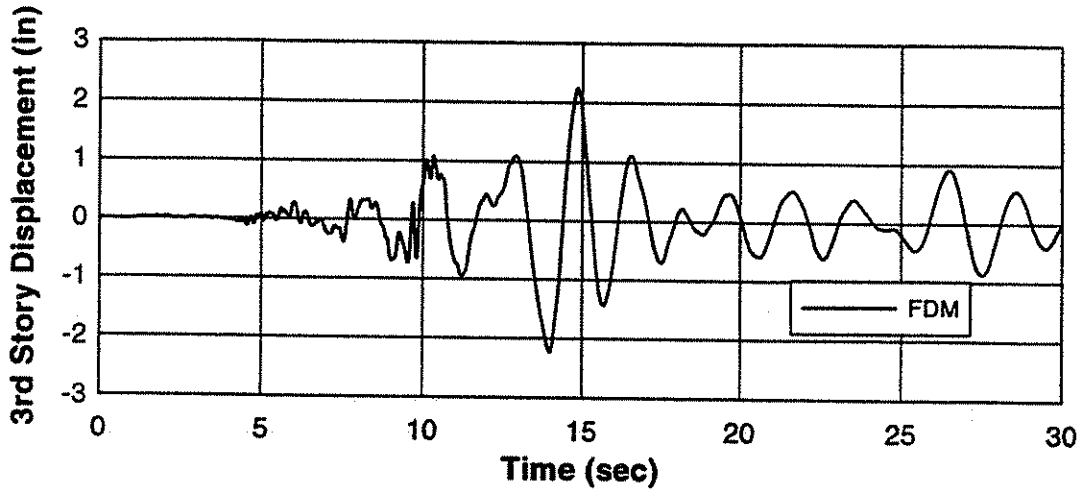

Fig. 6.55a - FDM predicted displacement response at third story for Santa Monica.

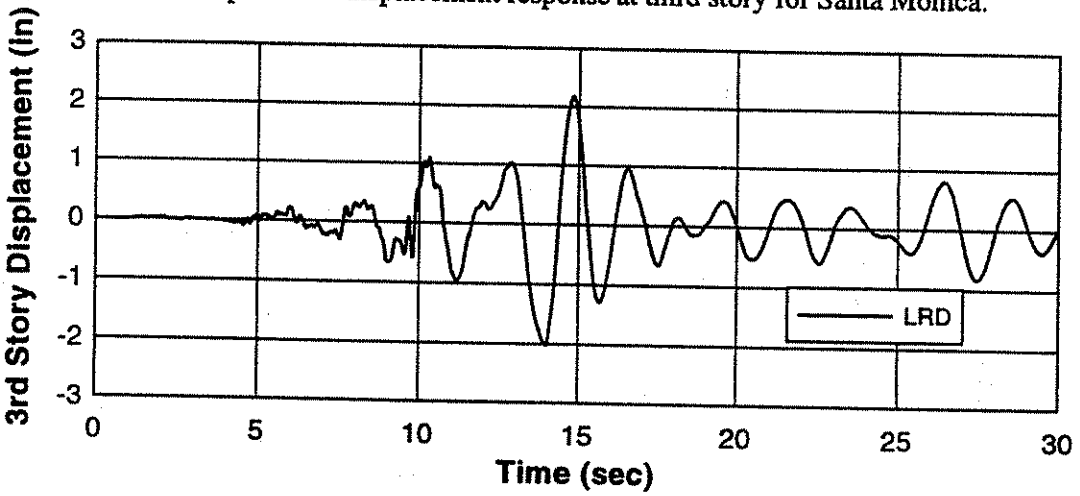

Fig. 6.55b - LRD predicted displacement response at third story for Santa Monica.

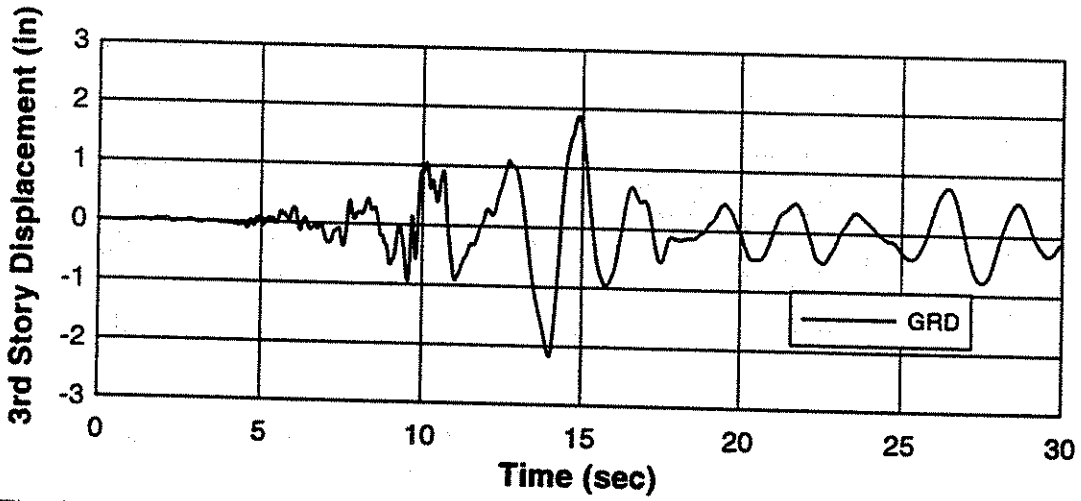

Fig. 6.55c - GRD predicted displacement response at third story for Santa Monica.

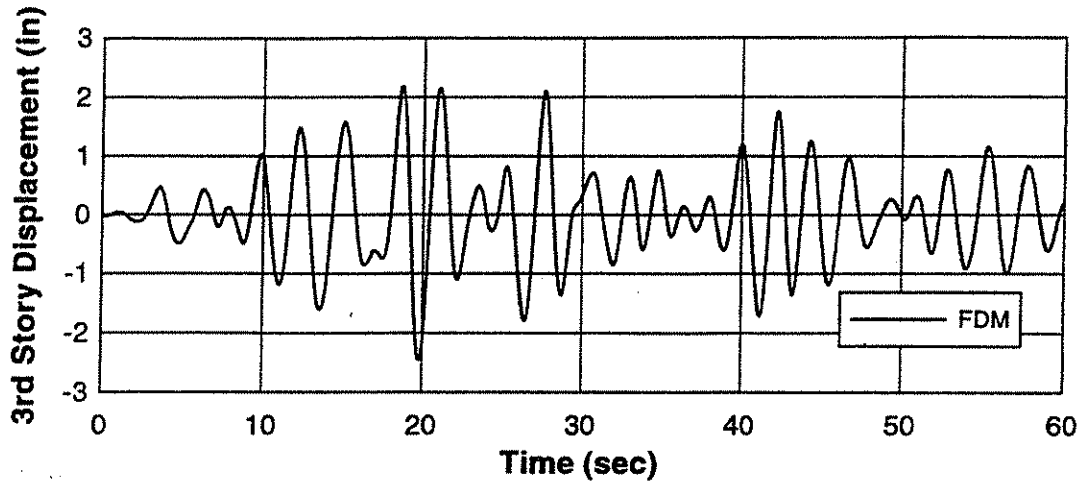

Fig. 6.56a - FDM predicted displacement response at third story for Frigorifico.

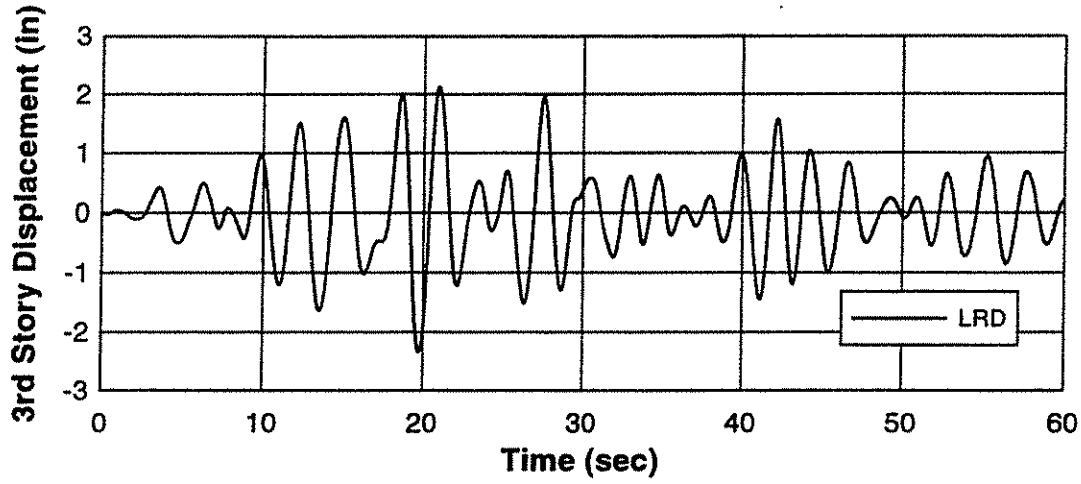

Fig. 6.56b - LRD predicted displacement response at third story for Frigorifico.

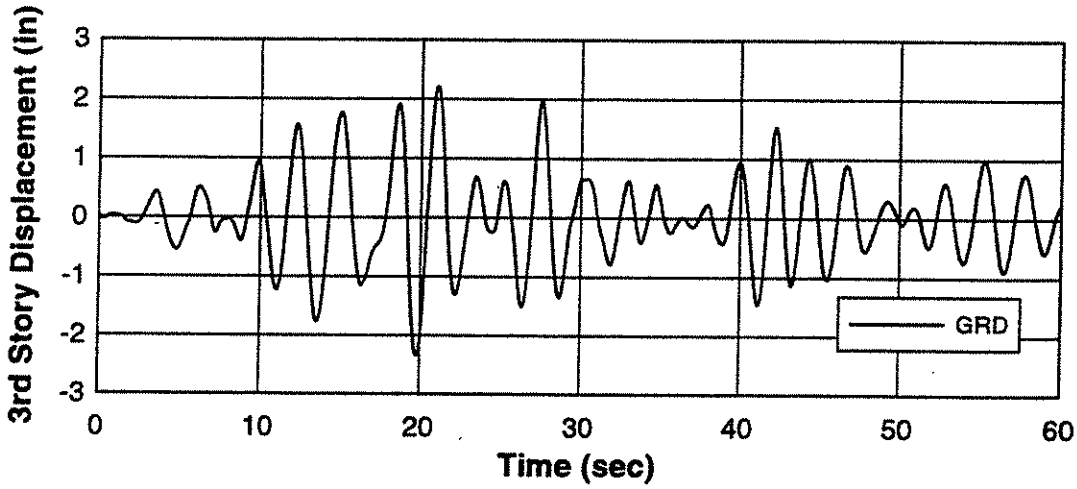

Fig. 6.56c - GRD predicted displacement response at third story for Frigorifico.

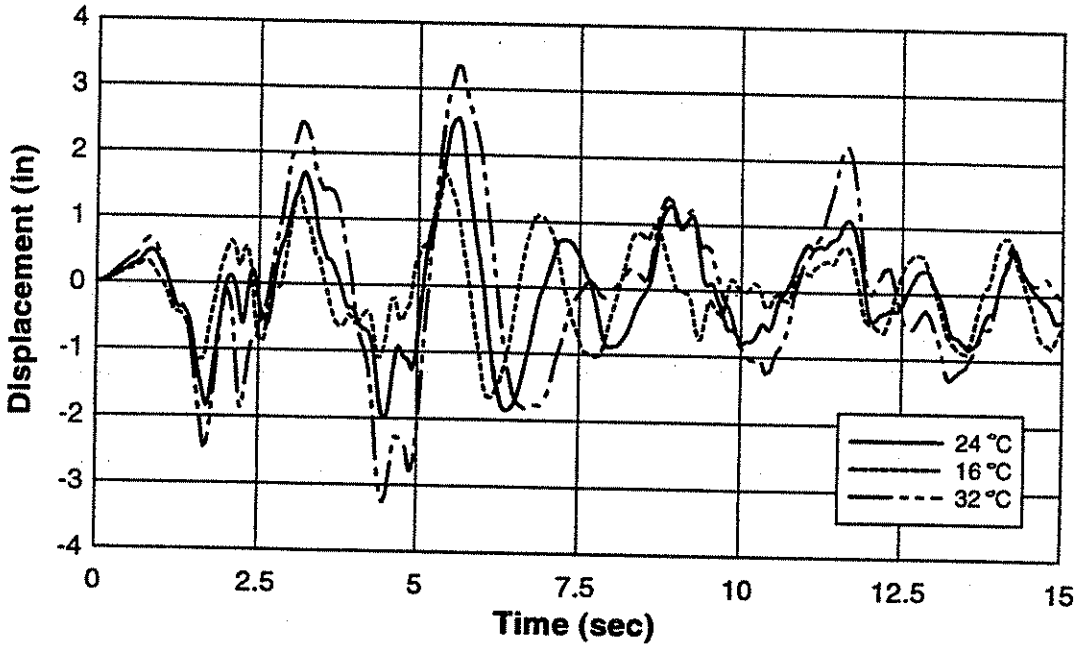

Fig. 6.57 - Predicted displacement response at third story for El Centro with different initial damper temperatures of 16, 24, and 32 °C.

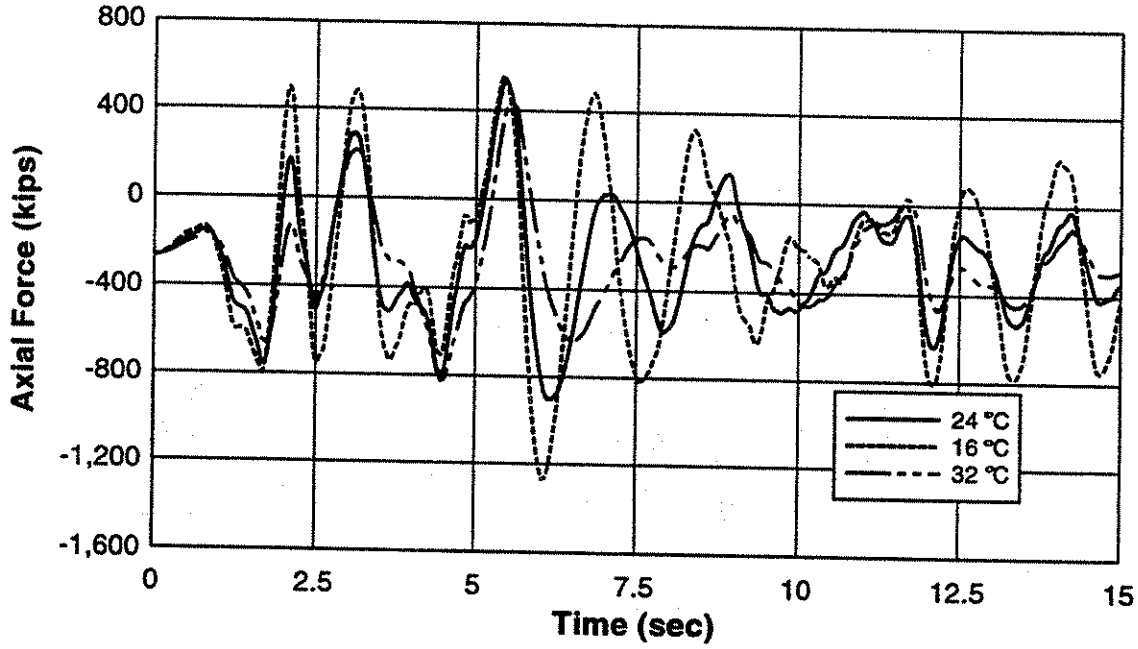

Fig. 6.58 - Predicted axial force response in first story column for El Centro with different initial damper temperatures of 16, 24, and 32 °C.

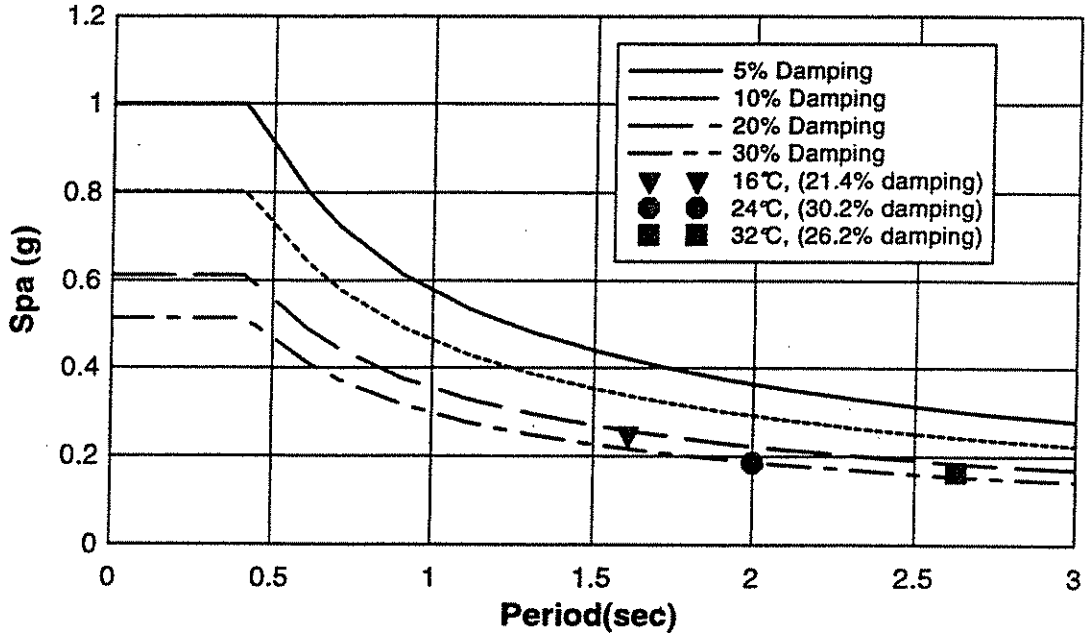

Fig. 6.59 - Comparison of VE-frame spectral acceleration at initial temperatures of 16, 24, and 32 °C with NEHRP pseudo-acceleration spectra (C_v=0.48, C_s=0.40) for various damping ratios.

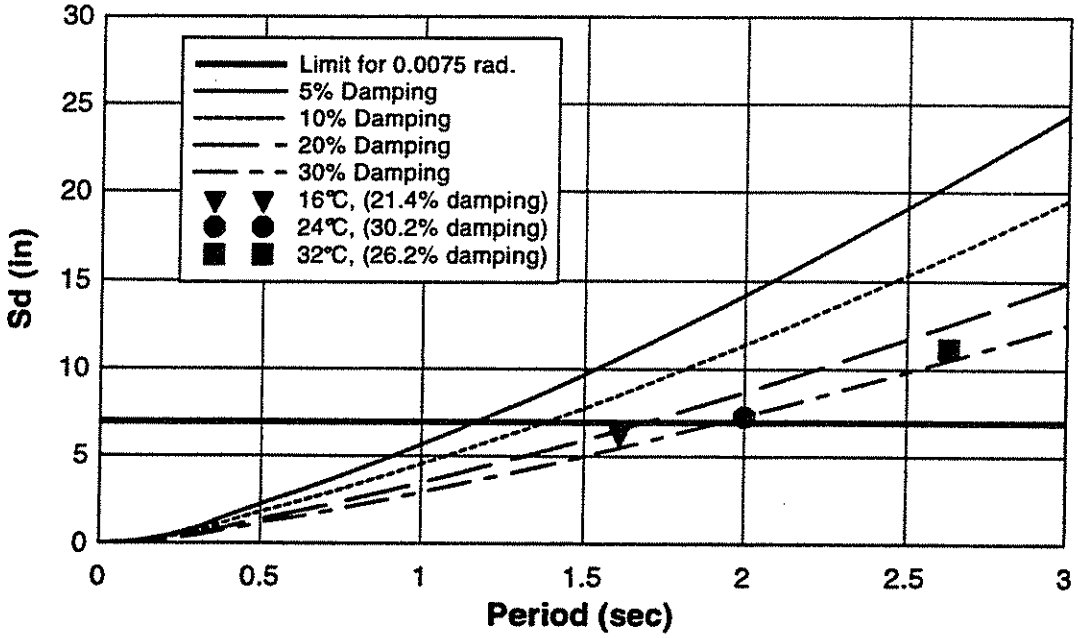

Fig. 6.60 - Comparison of VE-frame spectral displacement at initial temperatures of 16, 24, and 32 °C with NEHRP displacement spectra (C_v=0.48, C_s=0.40) for various damping ratios.

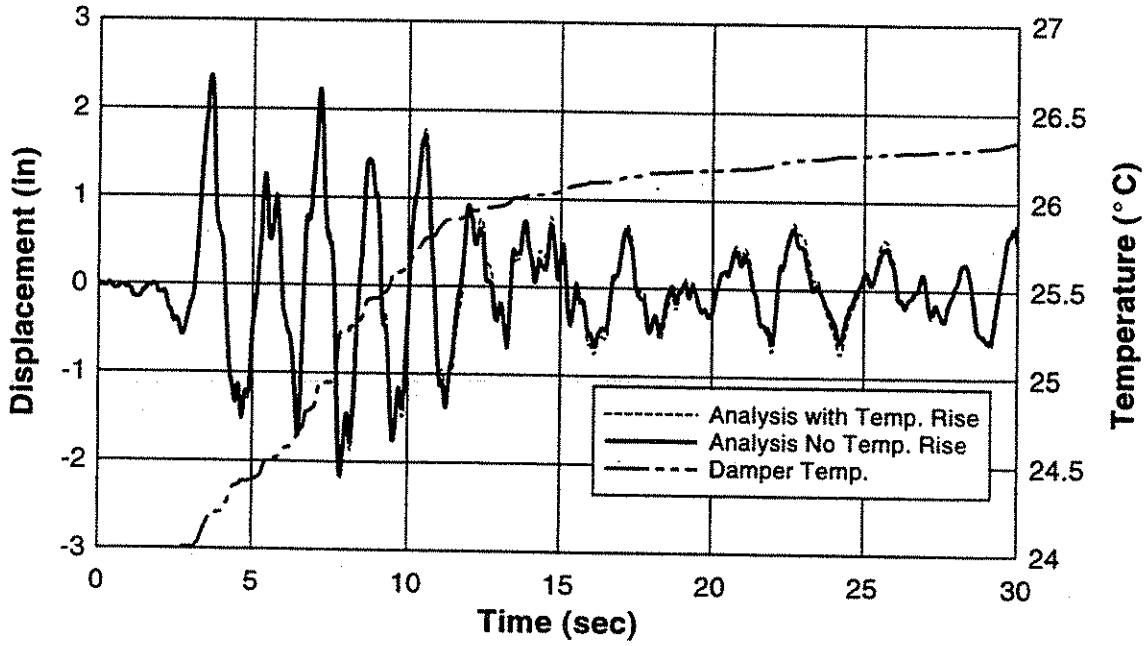

Fig. 6.61 - Third story displacement response for VE-frame with and without including damper temperature rise when subjected to Taft ground motion. Example damper temperature is also shown for case with temperature rise.

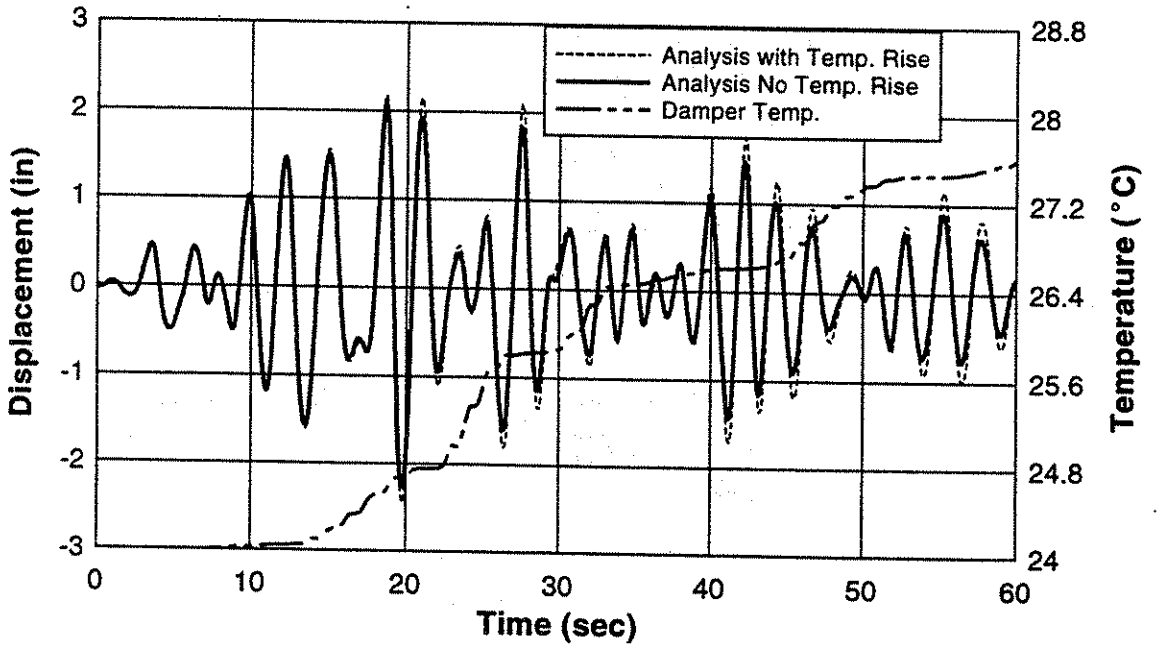

Fig. 6.62 - Third story displacement response for VE-frame with and without including damper temperature rise when subjected to Frigorifico ground motion.

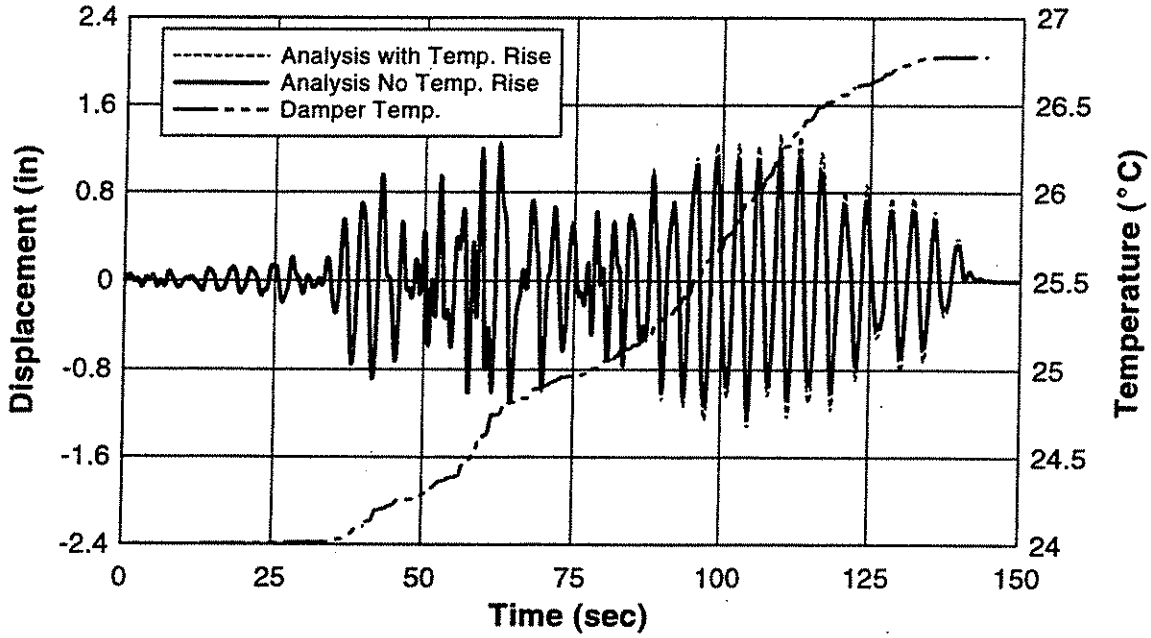

Fig. 6.63 - Third story displacement response for VE-frame with and without including damper temperature rise when subjected to Oficina ground motion. Example damper temperature is also shown for case with temperature rise.

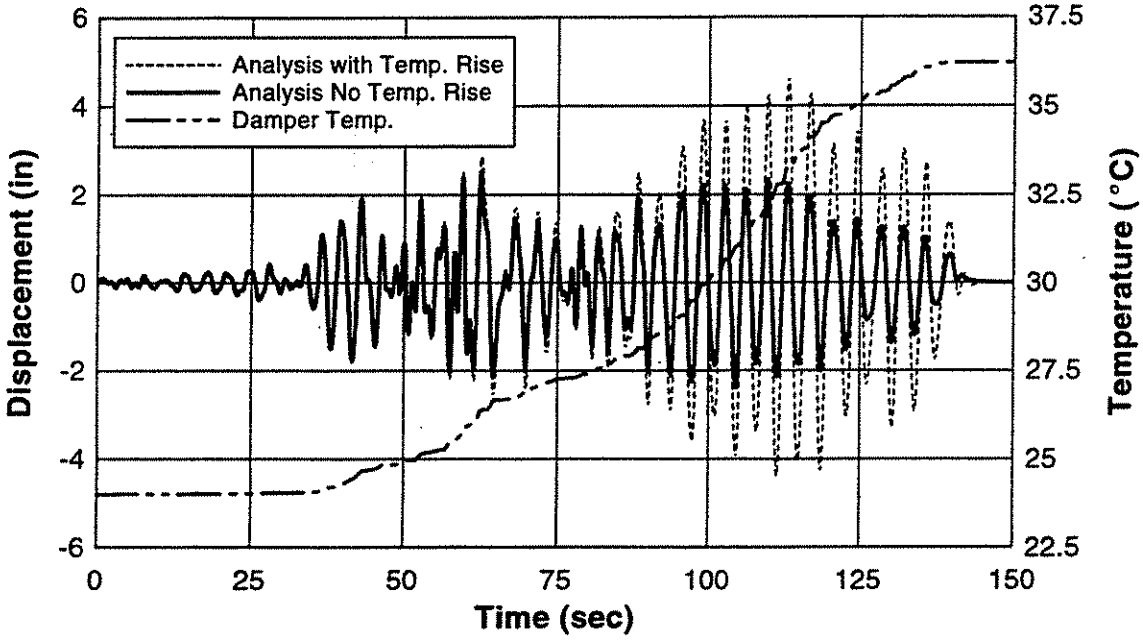

Fig. 6.64 - Third story displacement response for VE-frame with and without including damper temperature rise when subjected to 2 x Oficina ground motion.

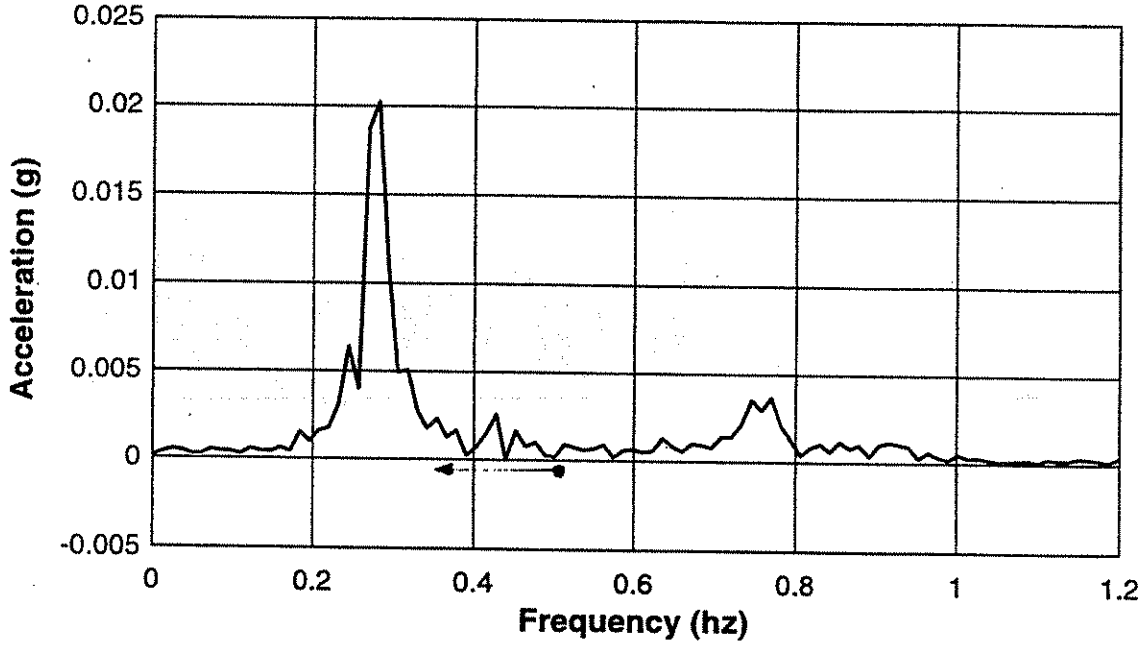

Fig. 6.65 - FFT for second half (75 to 140 seconds)of Oficina acceleration ground motion.

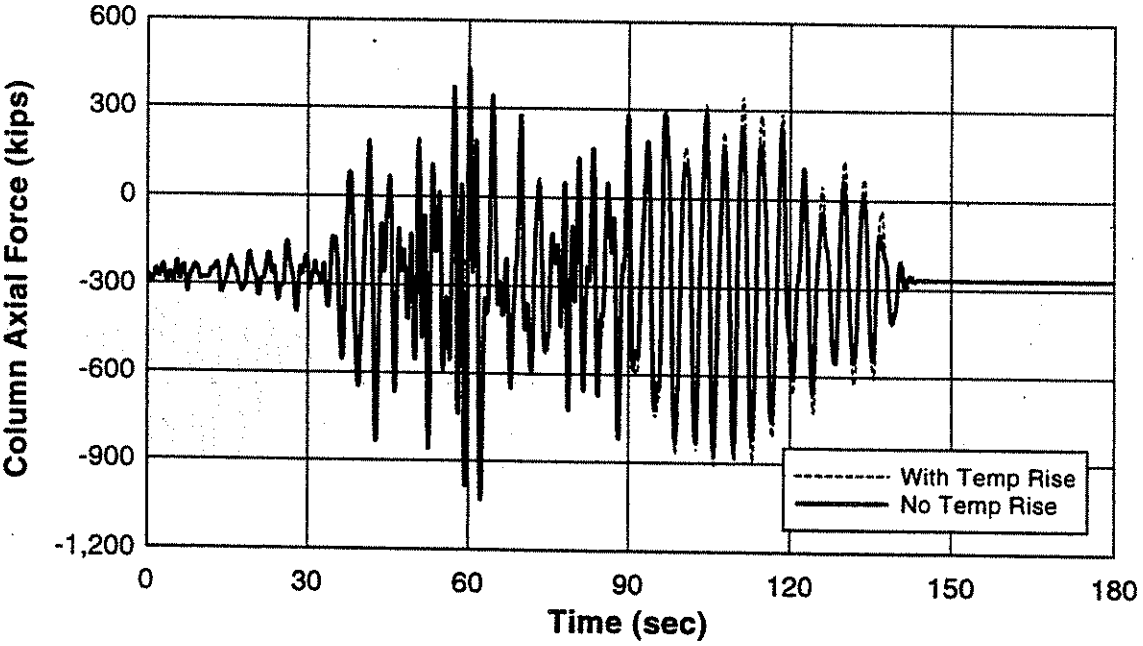

Fig. 6.66 - Column axial force in first story column for VE-frame with and without including damper temperature rise when subjected to 2 x Oficina ground motion.

CHAPTER 7.0 WIND RESPONSE:

SIMULATION, TESTING, AND ANALYSIS

7.1 Introduction

This chapter presents results of the experimental and analytical research program for wind effect simulations on a prototype steel frame building with VE-dampers. A provisional wind design methodology is presented for the prototype VE-damped frame. Along-wind and across-wind response of the structure were independently considered. Artificial wind forces were generated using Monte Carlo techniques and spectral functions for along-wind gusts or across-wind forces. Dynamic wind response of the prototype frame was determined from dynamic time history analysis of the structure subjected to the artificially simulated wind forces. Analytically predicted structural response was imposed on the test frame in real-time and experimental results are presented including overall frame response, member response, damper behavior, and VE-material temperature rise. Analyses were performed to assess the influence of VE-dampers on wind induced structural response, and random vibration analysis techniques are presented to predict frame response. Finally, conclusions are presented.

7.2 Prototype Design for Wind Forces and Test Methodology

A prototype steel frame was designed to permit assessment of wind induced behavior for a full-scale VE-damped steel frame. Due to the size of the specimen and cost of fabrication, only one test structure could be constructed. Therefore, a wind prototype frame was designed which made use of the VE-damped frame developed for seismic applications as described in Chapter 6.

Wind forces and their effects are generally greater on taller buildings, however, due to the above described limitations, the wind prototype frame was limited to only 10 stories. Though this relatively short building may not demonstrate the full significance of VE-dampers on wind induced vibrations, it does permit investigation of the likely behavior of a VE-damped structure subjected to wind forces.

Design of the wind prototype frame was done considering along-wind forces only. Across-wind forces were not part of the design criteria, but were considered when assessing the performance of the VE-frame as discussed later in section 7.4. No detailed guidance is available in the technical literature for wind design of VE-damped buildings and a provisional design procedure was developed. This trial procedure included the following steps:

- Wind forces were computed based on ASCE Minimum Design Loads for Buildings and Other Structures (ASCE 7-95) [ASCE, 1996]. No reduction of code specified forces was taken based on the theorized high damping provided by the VE-dampers. As will be

shown later, the fundamental period of the wind prototype frame was below 1 hz and therefore required use of the procedure provided in the commentary for computing gust factors. For conservative design, a low damping ratio (2% of critical) was used to compute the gust factors.

- Wind energy is concentrated in the low frequency regime, and VE-dampers are known to have reduced stiffness at such frequencies. To ensure sufficient lateral strength and stiffness, the wind frame was designed to resist code wind forces as a moment resisting frame with no stiffness contribution from the dampers.
- The natural frequency of the wind prototype was calculated as described in Chapter 6 and did include the stiffness contribution of the dampers.
- Static analysis of the wind prototype frame was performed to ensure sufficient lateral strength under the code prescribed wind forces.
- Drift checks were performed to ensure deflections were below 1/500 for short term effects [ASCE 7-95]. For these deflection analyses, no contribution was considered from the dampers.
- Stability of the frame without dampers was checked for code specified wind loads and appropriate gravity loads.
- The frame was also checked for compliance with the seismic design provisions of ASCE 7-95. The dampers were considered part of the lateral force resisting system for earthquake forces.

Using these guidelines, a prototype frame was developed which met the prescribed design criteria and the constraint of using the same bay and story dimensions, members sizes, and VE-dampers as the seismic prototype frame.

The wind prototype frame, classified with an occupancy of Category II [ASCE 7-95], was located in an urban environment in Miami, Florida and is shown in Fig. 7.1. Design of the frame was based on analysis of along-wind forces acting in the east-west direction only. Frames and members in the north-south direction were assumed to be appropriately designed and no torsional response was considered. As seen in this figure, there are three lateral force resisting bents in the structure. In each of these bents, there is a single VE-damped frame and several plain moment resisting frames (only 3 VE-frames in the east-west direction). Plain moment resisting frames were chosen to have the same frame stiffness of the VE-damped frame (when there are no dampers in the frame). Based on static analysis, five MRFs were required in each lateral force resisting bent to provide sufficient strength for the code specified wind loads. The final building configuration was determined based on the number of MRFs required. For the given layout and member sizes, a fundamental period of 2.7 seconds (0.37 hz) was calculated for the VE-frame using static analysis and Rayleigh's method. Calculation of the fundamental period for the VE-frame was performed by modeling the VE-dampers as an equivalent elastic truss element with in-phase stiffness only as described in Chapter 6. Using static analysis and Rayleigh's method, the fundamental period of the unbraced wind prototype frame was determined as 3.3 seconds (0.30 hz). Damping was estimated for the VE-frame using the first mode and the MSE approach described in Chapter

6. The frame without dampers was assigned a damping ratio of 2% and a damping ratio of 10% was computed for the VE-frame.

The testing methodology used for the wind prototype frame was similar to that used for the seismic prototype frame. The experimental response was determined from analysis of a beam-column and VE-damper finite element model of the wind prototype frame subjected to simulated dynamic wind forces. Dynamic wind loads applied to the finite element model were generated using mathematical models of natural wind forces as described below. Wind induced vibrations including both along-wind and across-wind response were investigated. Along-wind response is vibration of the structure in the direction of the wind stream as illustrated in Fig. 7.2a. Across-wind response is vibration of the structure transverse to the wind stream as illustrated in Fig. 7.2b. Response of the analytical model at the third story was imposed to the test specimen in real-time. The test specimen, set-up, and procedure were identical to those used for seismic testing as described in Chapter 6. Instrumentation layout was also identical to that used for earthquake tests.

7.3 Simulated Along-Wind Loading

7.3.1 Analytical Prediction of Along-Wind Forces

To assess wind induced dynamic structural response, in the direction of the wind, a 10-story wind prototype VE-damped building was developed as described in section 7.2. To assess the dynamic response of the frame, dynamic wind forces on the wind prototype building were

calculated by modifying the ASCE 7-95 code based approach which prescribes static wind forces. Wind pressures were computed as a function of the stagnation pressure for each story elevation:

$$q(z) = \frac{1}{2}\rho I\left(\overline{V}(z)\right)^2 \qquad [7.1]$$

where q(z) is the velocity pressure (N/m^2) at height z, ρ is the air density (1.225 kg/m^3), I is an importance factor, and $\overline{V}(z)$ is the mean wind velocity (m/s) of the undisturbed wind stream at height z (m). The wind prototype building was classified as category II, resulting in an importance factor of 1.0 [ASCE 7-95]. Gust response factors were not included in the calculated wind pressures as the dynamic nature of the wind is numerically simulated as described below.

Wind velocity was modeled by considering that at an instant of time, the velocity consists of a temporal mean component and a random fluctuating component as shown in Fig. 7.3. No velocity variations horizontally across the wind stream were considered, however, correlation between wind velocities at different vertical separations were included as described later. Several different return periods were considered for selection of the mean wind speed including; mean recurrence intervals of 5, 50, and 500 years [ASCE 7-95]. One hour duration wind events were chosen for assessment of VE-response. The three second gust wind speed of 65m/s (145 mph) prescribed for Miami, Florida was converted to a probable hourly mean wind speed using Fig. 7.4 [ASCE 7-95] for a hurricane prone location. Temporal hourly mean velocities at the reference height of 10 m were 13.1, 25.0, and 33.5 m/s for wind events

of 5, 50, and 500 year return periods respectively. The temporal mean velocity was determined for each story elevation according to the power law [Blevins 1990]:

$$\frac{\overline{V}(z)}{\overline{V}_g} = \left(\frac{z}{z_g}\right)^{\alpha} \qquad [7.2]$$

Where $\overline{V}(z)$ is the mean velocity (m/s) at a specified elevation z (m), $\overline{V}_g$ is the gradient velocity (m/s) at the top of the boundary layer, z_g is the gradient height (m) at which the gradient velocity matches the velocity profile, and α is the exponent for the specified surface conditions.

Random wind velocity components were determined using a multidimensional random process simulation technique [Shinozuka 1971]. The fluctuating wind velocity $\tilde{V}(t,z)$ (m/s), as a function of both time and elevation, was simulated as an ensemble of cosine waves :

$$\tilde{V}(t,z) = \sigma_v \left(\frac{2}{N}\right)^{\frac{1}{2}} \sum_{k=1}^{N} \cos\left(\omega_k t + \Omega_k z + \varphi_k\right) \qquad [7.3]$$

where

$$\sigma_v = \left[\int_{-\infty}^{\infty} S_v(\omega) d\omega\right]^{\frac{1}{2}} \qquad [7.4]$$

The variables ω_k and Ω_k are jointly distributed random variables simulated using Monte Carlo techniques as described by Shinozuka [1971], N is the number of cosine waves which constitute the ensemble, $S_v(\omega)$ is the power spectral density function, t is time, z is elevation, and φ_k is a random phase angle uniformly distributed between 0 and 2π. Davenport's power spectral density was chosen to model the horizontal gustiness of the wind [Davenport 1961]:

$$S_V(f)df = 4.0\kappa\overline{V}_{10}\frac{x}{\left(1+x^2\right)^{4/3}}dx \qquad [7.5]$$

where

$$x = \frac{1200f}{\overline{V}_{10}} \qquad [7.6]$$

$S_V(f)$ is the power spectrum of horizontal wind gusts, independent of elevation, κ is the drag coefficient for the referenced mean velocity at 10 m, $\overline{V}_{10}$ is the mean velocity (m/s) at an elevation of 10 m, and f is frequency (hz). Coherence among wind velocities at differing elevations were incorporated assuming negligible quadrature density [Shinozuka 1971] and using the coherence relationship described by Davenport [1961]:

$$\lambda^2 = \frac{C^2(f,\Delta z)}{S_V^2(f)} = \left(e^{-7.7\frac{\Delta z f}{\overline{V}_{10}}}\right)^2 \qquad [7.7]$$

Where λ^2 is the coherence of wind velocities for stations vertically separated by Δz, and $C(f,\Delta z)$ is the co-spectrum of velocity fluctuations between the vertically separated stations.

The multidimensional random process simulation for wind velocity was implemented using an ensemble of 3000 cosine waves at a time interval of 0.25 seconds, and records were generated for a one hour wind event. The maximum frequency for wind gusts was 2 hz for the specified time interval. The prototype building was located in a large urban center with many buildings over 70 feet, corresponding to ASCE 7-95 exposure type A. Salient wind properties for the site are presented in Table 7.1. Wind velocity time records were generated for the fluctuating wind velocity components and example records are shown in Figs. 7.5 and

7.6. Generated records have a Gaussian distribution with zero mean as illustrated in Figs. 7.7a to 7.7c. Spectral densities of the generated wind records were computed according to the procedure outlined by Blackman and Tukey [1960] and are compared with the target spectrum in Figs. 7.8a to 7.8c. Coherence between records at different separations correspond well with the target coherence as shown in Figs. 7.9a to 7.9c. Records also exhibit time lag effects similar to those described by Shiotani and Iwatani [1971] as shown in Figs. 7.10a to 7.10c. As might be expected, phase lag relationships and coherence were not as well predicted (Figs. 7.9a and 7.10a) for larger spatial separations. In general, the simulation method provides a reasonable representation of natural fluctuating wind velocities including spatial correlations which can be used to compute dynamic wind forces for use in time history analysis. This simulation technique provides an analytical method to assess the wind response of a VE-damped structure which would otherwise not be available through conventional means.

Total wind velocity was determined by combining the temporal mean and the random wind velocity components. Wind velocity pressures were calculated according to Eq. 7.1. Finally, dynamic wind forces were calculated, including both windward and leeward pressure coefficients of .8 and -.5 respectively, by multiplying the total pressure with the tributary area of each story. The computed dynamic wind forces were then applied to the 10-story PC-ANSR finite element model to determine the dynamic structural response as illustrated in Fig. 7.11. VE-damper finite element parameters were identical to those described in the seismic analytical model. Heat convection was recognized as a significant parameter for VE-damper performance during long duration events as shown in Chapter 3. To reduce the temperature rise in the dampers during the wind event due to heat convection, the specific heat and density

of the VE-material were artificially increased for the analyses (Eq. 3.6). Analytically determined displacement time history at the third story are shown in Figs. 7.12a and 7.12b, 7.13a and 7.13b, and 7.14a and 7.14b for the 5, 50 and 500 year return period events.

7.3.2 Experimental Response of VE-Frame to Along-Wind Forces

Analytically computed response at the third story was imposed on the test specimen in real-time. The one hour duration analytical third story displacement response was discretized into 3543 equally spaced displacement-time pairs. This array size was the limit for the hydraulic control system software. Displacement control of the actuators was performed using ramp functions from point to point of the discretized analytical displacement history. This control method (using a small number of widely spaced data) was adequate to simulate the structural response only due to the relatively low frequency loading history. Data were acquired from the hour long tests for the 196 channels of instrumentation at an acquisition rate of 4 hz (separation of 0.25 seconds between samples). This relatively slow acquisition rate was adequate to determine the continuous overall frame behavior, member response, and damper temperature rise. The slow acquisition rate did not permit detailed assessment of the interaction of between the frame member forces and damper forces or time lag responses. To permit investigation of these parameters, data were acquired at 100 hz (separation of 0.01 seconds between samples) for one minute segments of the hour long tests. Only two or three one minute segments were acquired at the high acquisition rates for each hour test.

Measured displacement time histories at the third story from the experiment are shown in Figs. 7.13c and 7.13d and Figs. 7.14c and 7.14d for the 50 and 500 year return period events respectively. The 5 year event was not tested because the response was so small as to be negligible. Measured overall force-deformation response for the frame is shown in Fig. 7.15 for the 50 year and Fig. 7.16 for the 500 year return period events. The beginning of the force-deformation response is shown in Figs. 7.17 for the 50 year event and 7.18 for the 500 year event. As shown in these figures, a slow loading rate of 0.5in/min is used to move the frame to beginning position of the random loading. At this low loading rate, the dampers contribute limited resistance and the equivalent frame stiffness was 30.0 kips/in (unbraced frame stiffness was 17.0 kips/in from Chapter 4). However, at the start of the random response the stiffness suddenly increases, indicating the dampers contribute significantly to the dynamic stiffness of the structure even for the relatively low frequency of loading associated with the wind spectrum. The overall response (Figs. 7.15 and 7.16) indicate the dampers provide significant energy dissipation. The total energy dissipated was determined by integrating the overall force-deformation response.

The significant amount of energy dissipated by the structure would indicate the dampers exhibit temperature increase. Example force-deformation response for the second story East VE-damper during the complete test is shown in Figs. 7.19 and 7.20 for the 50 and 500 year return period events respectively. The beginning of the force-deformation response is shown in Figs. 7.21 and 7.22 for the 50 and 500 year events respectively. As shown in these figures, the damper stiffness is relatively low during the initial displacement ramp to the start of the random response portion. At the beginning of the random response, the damper stiffness

exhibits a significant increase. Two minute segments of the damper response are shown in Figs. 7.23a and 7.24a near the beginning of the response (after 2 minutes) and Figs. 7.23b and 7.24b near the end of the response (after 57 minutes). As shown in these figures, there was no appreciable change in damper stiffness between the start and end of the test, indicating no significant temperature rise.

Measured temperature rise for these dampers are shown in Figs. 7.25 and 7.26 for the 50 and 500 year return period events respectively. Damper temperatures rose at the initiation of loading and then remained relatively stable during the experiment. Final temperature rise was small (0.2 °C) for the 50 year return period event and no significant material property changes occurred due to the small temperature change (Fig. 7.23). Only a moderate temperature rise (1.7 °C) was observed for the 500 year return period event and no significant material property changes occurred due to the temperature change (Fig. 7.24). Damper temperatures were predicted, as shown in Fig. 7.27, by integrating the damper stress-strain response and dividing by the specific heat and density of the VE-material (Eq. 3.6). As shown in Fig. 7.27, if heat transfer between the damper and environment is neglected, predicted damper temperatures would be significantly higher than the measured values. This indicates that for long duration loading events, heat transfer should be considered to accurately predict structural response at later stages of the loading history. An alteration to the VE-damper finite element is currently underway which incorporates heat convection between the damper and environment [Kasai *et al.*, 1997a][Kasai *et al.*, 1997b].

To investigate the frame response in more detail and assess the phase relationships between members and damper forces, data were acquired for one minute segments of the one hour tests at a high acquisition rate (100 hz). Frame displacement at the third story for the one minute segments are shown in Figs. 7.28 and 7.29 for the 50 and 500 year return period events respectively. The overall frame force-displacement responses for these segments are shown in Figs. 7.30 and 7.31. Example force-deformation response for the second story East VE-damper is shown in Fig. 7.32 for the 50 year event and in Fig. 7.33 for the 500 year event. Both the frame and damper responses showed many small cycles and only a few larger cycles. The smaller cycles ride on the large excursions as best illustrated in Fig. 7.32.

Phase relationships between member forces and dampers, were determined by normalizing the measured member force responses. The phase relationships for the along-wind response were similar to those described in Chapter 5. Example phase relationships between the level 2 East VE-damper and East second story column forces are shown in Figs. 7.34 and 7.35 for the 50 and 500 year events respectively. Column moments were in-phase with displacements, as demonstrated by the straight line response in Figs. 7.34 and 7.35. Axial forces were more in-phase with the damper force, as indicated by the hysteretic response similar to that of the VE-damper. As a result, the axial force-moment interaction exhibits hysteresis as shown in Fig. 7.36 and 7.37 for the 50 and 500 year events respectively. The phase lag causes maximum axial force and maximum moment to occur at different instances of time.

7.3.3 Analytical Prediction of Along-Wind VE-Frame Response

7.3.3.1 Effect of VE-Dampers on Along-Wind Response

The provisional wind design procedure described in section 7.2 ignores the influence of VE-dampers on the strength and stiffness of the steel frame. As a result, direct comparisons can be made between the behavior of the frame with and without dampers when subjected to the same input forces. To perform this comparison, two analytical models of the wind prototype frame were developed. One model contained VE-dampers and the other did not. Synthetic wind forces were generated as described in section 7.3.1 and applied to the analytical models. Response of the structures to these wind forces was computed and comparisons were made.

Analytically predicted displacement response at the roof story is shown in Figs. 7.38 and 7.39 for the frame with and without VE-dampers respectively, for a 50 year return period, one hour wind event. A two minute segment is shown in Fig. 7.40 to permit closer examination of the displacement response. As shown in these figures, the frame without VE-dampers exhibited larger peak displacement amplitudes than the VE-frame but both frames exhibited similar mean deflection response. The frame without dampers had a mean displacement at the roof level of 1.67 in. and the frame with VE-dampers had a 1.31 in. mean displacement. Due to the slow loading rate associated with the wind forces, the VE-dampers exhibit a relatively low stiffness. This low damper stiffness results in a small frame stiffness increase compared to the frame without dampers. The small increase in VE-frame stiffness, slightly reduced the mean deflection response as compared to the frame without dampers.

As shown in the displacement response, there is a strong natural frequency component for the frame without dampers. The frame with VE-dampers does not exhibit this type of response. To determine the frequency content of the displacement response, a FFT was performed as shown in Figs. 7.41 and 7.42. The frame without damper exhibits a very strong response component associated with the natural frequency of 0.3 hz in addition to the response associated with the wind spectrum (Fig. 7.41). The VE-frame response is primarily associated with the wind spectrum and exhibits a very small natural frequency contribution near 0.4 hz (Fig. 7.42). The computed natural frequency of the VE-frame was 0.37 hz. With the exception of the natural frequency components, the response of both frames with respect to the wind spectrum was similar. Adding VE-dampers to the frame resulted in almost complete elimination of vibration at the natural frequency, which rides on the low frequency response associated with the wind spectrum. Therefore, the dampers do not significantly reduce frame response associated with the wind spectrum, but do suppress natural frequency vibrations induced by wind gusts. This suppression of the natural frequency vibration does not change the mean value of the response but does significantly reduce the mean square response. Reduction of the mean square response directly results in reduced peak response as described by Eqs. 7.17 and 7.18 in section 7.3.3.2.

Building accelerations are an important serviceability consideration, particularly for tall building design. Accelerations in tall buildings are typically limited by the structural designer to ensure the comfort of occupants. Typical occupant response to different acceleration levels are shown in Table 7.2. Acceleration response at the roof level of the wind prototype frame is shown in Figs. 7.43 and 7.44 for the frame with and without VE-dampers respectively. The

VE-frame exhibited significantly lower accelerations than the frame without dampers. Peak acceleration in the frame without dampers was 0.048g compared to 0.017g for the VE-frame. Reductions in floor accelerations were due mainly to suppression of the natural frequency vibration by the VE-dampers.

VE-dampers also reduced the stress range and number of stress cycles in the frame members and connections. The stress range in frame members and connections can be assumed proportional to the frame displacement. By reducing the mean square value of displacement response, as described above, the VE-dampers effectively reduce the stress range in the frame elements. Peak-to-peak displacement amplitude in Fig. 7.38 for the VE-frame was 4.4 in. and the peak-to-peak displacement amplitude in Fig. 7.39 for the frame without dampers was 10.1 in. The VE-dampers reduced the displacement range by a factor of approximately 2.3, which indicates a reduction in stress-range of the same factor.

VE-dampers also reduced the number of stress cycles in the members. The number of cycles was determined by removing the mean displacement value from the total displacement response and counting the number of times the roof displacement crossed the time axis. The VE-damped frame experienced 839 zero crossings, while the frame without VE-dampers exhibited 1635 zero crossings. The dampers reduced the number of cycles by a factor of approximately 2. It should be noted that the total number of zero crossings included small, moderate, and large amplitudes which contribute differently to the cumulative damage experienced by the structure. However, the combined results of smaller stress range with

smaller total number of cycles, as demonstrated by the VE-damped frame, can improve the high cycle fatigue life of members and connections.

7.3.3.2 Prediction of Along-Wind Response for VE-Frames

A method to predict response of VE-damped building structures subjected to along-wind induced vibrations was developed. The method employs random vibration theory combined with dynamic response properties computed from static analysis. The procedure is summarized below.

A structure is designed to satisfy the static wind loading strength and deflection requirements for the particular building code. This design is performed by neglecting any contribution of the VE-dampers to the strength or stiffness of the building. The structure has a particular mass M_{tot}, stiffness K, and inherent damping ratio ξ_o. An estimate of the undamped frame natural frequency f_n is made, using a modified Rayleigh method and static analysis as described in Chapter 6.

The performance of the structure is determined for a one hour wind event. Hourly mean wind speeds are determined by modifying the 3 second gust wind speed of ASCE 7-95 by a factor which accounts for an hour duration averaging time. The modification factor depends on the proximity of the structure to hurricane-prone regions and averaging time as shown in Fig. 7.4. Specific hourly mean wind velocities required in subsequent analysis include the mean velocity at the reference height $\overline{V}_{10}$, and mean velocity at the roof level $\overline{V}_h$. These two wind velocities must be adjusted for the specific exposure classification and $\overline{V}_h$ can be computed

according to the power law (Eq. 7.2). Other duration events may be considered if desired and the mean wind speed adjusted by using an appropriate factor for the averaging time.

Static wind induced pressures for the hourly mean wind speed are computed according to the ASCE 7-95 code procedure including importance factor, exposure coefficients, and drag coefficients. Gust factors are assumed equal to 1.0 as the dynamic influence of the wind is directly computed as described below. Wind forces along the building elevation are computed using the tributary area and computed wind pressures. Static analysis is performed using these wind forces or an analytical model of the structure without VE-dampers. The computed response is the mean displacement of the structure during the hour-long wind event $\overline{X}$.

To assess the amount of damping and frequency shift contributed by the VE-dampers, an analytical model of the frame with VE-dampers is developed. The fundamental period of the VE-frame is estimated using a Rayleigh procedure and modeling the dampers as elastic truss elements which have in-phase stiffness only as described in Chapter 6. Equivalent viscous damping ratio for the VE-frame is estimated assuming first mode response only and static analysis as described in Chapter 6.

The fluctuating property of wind is described by the power spectral density or spectrum of wind gusts. Several spectra have been proposed to describe wind gusts and are presented by Simiu and Scanlan [1996]. Davenport's spectra as described in section 7.3.1 and Eq. 7.5 was

chosen to represent wind gusts for this study. The relationship between the force spectrum $S_F(f)$ and velocity spectrum $S_V(f)$ can be written as [Houghton and Carruthers, 1976]:

$$\frac{S_F(f)}{\overline{F}^2} = \frac{4|J(f)|^2 S_V(f)}{\overline{V}_h^2} \qquad [7.8]$$

where $\overline{F}$ is mean force (N) and $|J(f)|^2$ is the aerodynamic admittance. Aerodynamic admittance is a measure of the effect of the wind gusts on the drag forces and accounts for both vertical and horizontal correlation of wind pressures over the surface of the building. Aerodynamic admittance can be approximated as [Houghton and Carruthers, 1976]:

$$|J(f)|^2 = (1+\alpha)^2 |J_z(f)|^2 |J_h(f)|^2 \qquad [7.9]$$

$$|J_z(f)|^2 = \frac{1}{(1+\alpha)^2} \frac{1}{1+\psi/3} \qquad [7.10]$$

$$|J_h(f)|^2 = \frac{1}{1+\psi'/2} \qquad [7.11]$$

where $|J_z(f)|^2$ is the vertical acceptance, $|J_h(f)|^2$ is the horizontal acceptance, α is the exponent for the power law, $\psi \approx 8Hf/\overline{V}_{10}$, $\psi' \approx 20Bf/\overline{V}(z)$, H is the height of the building (m), and B is the width of the building subjected to the along wind forces (m). For the current study, horizontal correlations are neglected and $|J_h(f)|^2$ is set equal to unity. The aerodynamic admittance $|J(f)|^2$ can be conservatively neglected by setting it to unity.

From random vibration theory, the structural response spectrum $S_X(f)$ is related to the force spectrum as [Crandall and Mark, 1963]:

$$S_X(f) = \frac{|H(f)|^2 S_F(f)}{(2\pi f_n)^4 M^{*2}} \qquad [7.12]$$

where $|H(f)|^2$ is the mechanical admittance function and M^* is the generalized mass. The mechanical admittance function is defined as [Simiu and Scanlan 1996]:

$$|H(f)|^2 = \frac{1}{\left(1-\left(\frac{f}{f_n}\right)^2\right)^2 + \left(2\xi\frac{f}{f_n}\right)^2} \qquad [7.13]$$

where f_n is the natural frequency (hz), and ξ is the damping ratio which assumed constant for all frequencies ($\xi = \xi_o$ for the frame without dampers and $\xi = \xi_{tot}$ for the frame with VE-dampers). The generalized mass M^* is defined as [Simiu and Scanlan 1996]:

$$M^* = \int_0^H \phi_i^2(z)\overline{m}(z)dz \qquad [7.14]$$

where ϕ_i is the modal displacement, $\overline{m}(z)$ is the uniformly distributed mass along the building height $\overline{m}(z) = M_{tot}/H$. The fundamental mode shape can be approximated by $\phi_1 = (z/H)^\beta$, where β is a coefficient which describes the mode shape (=1.0 for straight line, =1.86 for a bending cantilever). Substituting Eq. 7.8 into Eq. 7.12 and assuming the mean force $\overline{F}$ is the force associated with the stagnation pressure at the roof level $= \frac{1}{2}\rho C_D \overline{V}_h^2 BH$ [Blevins, 1990], the response spectrum becomes:

$$S_X(f) = \left(\frac{1}{2}\rho C_D \overline{V}_h^2 BH\right)^2 \frac{4|J(f)|^2|H(f)|^2 S_V(f)}{(2\pi f_n)^4 \overline{V}_h^2 M^{*2}} \qquad [7.15]$$

where C_D is the drag coefficient as shown in Table 7.3, and ρ is the air density (= 1.225 kg/m^3). As seen from Eq. 7.15 and Eq. 7.13, addition of VE-dampers only affects the

mechanical admittance term in the form of increased damping ratio and increased natural frequency.

The mean square value of the displacement response of the structure is determined by integrating the displacement response spectrum over the frequency range:

$$\sigma_X^2 = \int_0^\infty S_X(f)df = \int_0^\infty \left(\frac{1}{2}\rho C_D \overline{V}_h^2 BH\right)^2 \frac{4|J(f)|^2|H(f)|^2 S_V(f)}{(2\pi f_n)^4 \overline{V}_h^2 M^{*2}} df \qquad [7.16]$$

The likely maximum value of displacement X_{max} for the structure in gusty wind is of primary concern to the structural engineer. The probable maximum value can be estimated from the gust factor G and mean displacement $\overline{X}$ as:

$$X_{max} = G\overline{X} \qquad [7.17]$$

The gust factor can be determined from [Simiu and Scanlan, 1996]:

$$G = 1 + \frac{g\sqrt{\sigma_X^2}}{\overline{X}} \qquad [7.18]$$

where σ_X^2 is the mean square value of the displacement response (Eq. 7.16), g is the peak factor which is defined as the ratio of the maximum value of response to the root mean square value. From Davenport [1961], the peak factor is defined as:

$$g = \sqrt{2\ln(f_{equiv}T)} + \frac{0.577}{\sqrt{2\ln(f_{equiv}T)}} \qquad [7.19]$$

where T is the time interval of the record considered (3600 seconds for the current study), and f_{equiv} is the equivalent frequency. The equivalent frequency is defined as:

$$f_{equiv}^2 = \frac{\int_0^\infty f^2 S_X(f) df}{\int_0^\infty S_X(f) df} \qquad [7.20]$$

For a lightly damped structure, f_{equiv} can be taken as the natural frequency f_n [Houghton and Carruthers, 1970]. Values for the peak factor g are typically in the range of 2.5 to 4.5 [Cevallos-Candau, 1980] and Vickery [1971] proposed use of a peak factor of 3.5 for typical design cases.

Using the above relationships, the along-wind displacement response was predicted for the frame with and without VE-dampers. Parameters used to predict the along-wind response are shown in Table 7.4. The computed normalized response spectra (Eq. 7.15) for the frame with and without VE-dampers is shown in Fig. 7.45. As seen in this figure, there are two main sources which contribute to the displacement response. One component is called the background part which results directly from the wind spectrum and the other is called the resonant part which is vibration of the structure at its natural frequency which is excited by the wind gusts. The relative contribution of these two parts is determined from the mechanical admittance function (Eq. 7.13). As seen in Fig. 7.45, the frame without dampers (2% damping) has a very strong component near the natural frequency. This was also observed from the dynamic time-history analysis described in section 7.3.3.1. The VE-frame (10% damping) exhibits a similar spectrum associated with the background response but exhibits dramatically reduced resonant response.

To assess the relative contribution of the two response parts, the mean square response over the full frequency range was divided by the resonant response near the natural frequency. A band width equal to $f_n \pm 10\% f_n$ was chosen as the resonant response frequency band. The resonant part accounted for 66% of the response spectrum for the frame without VE-dampers, and 17% for the frame with VE-dampers. Similarly, the analytically predicted displacement time-history from dynamic analysis was filtered using a band pass filter to remove the resonant component from the overall response for the frame without dampers and the VE-frame as shown in Fig. 7.46. A band width of $f_n \pm 10\% f_n$ was used in the band pass filter. The maximum resonant response roof displacement for the frame without dampers was ± 3.5 in. which comprised 48.8% of the total response at the maximum displacement. The VE-frame exhibited a much smaller resonant response contribution, with a maximum roof displacement of ± 0.67 in. This comprised only 15.5% of the total response at peak displacement. The magnitude of VE-frame resonant displacement response was approximately 1/5 that of the frame without VE-dampers. The magnitude of reduction in the resonant response R_R between the two frame cases, assuming equal mean displacements, can be determined from the dynamic amplification factor at the resonance frequency as:

$$R_R = \frac{\frac{1}{2\xi_o}}{\frac{1}{2\xi_{tot}}} = \frac{\xi_o}{\xi_{tot}} \qquad [7.21]$$

A resonant response reduction factor of 5 was computed from Eq. 7.21 which corresponded with time-history analysis results.

Peak frame displacements were predicted by integration of Eq. 7.16 and applying Eq. 7.18 to compute the gust factors for the two frames. The predicted gust factor G was 5.0 for the frame without dampers and 2.6 for the VE-frame. The probable maximum displacement X_{max} using these gust factors and Eq. 7.17 was 8.3 in. for the frame without VE-dampers and 4.4 in. for the VE-frame. Time-history analysis results indicated a peak displacement of 7.2 in. for the frame without VE-dampers and 4.3 in. for the VE-frame. The spectrum approach overestimated the peak displacement for the frame without VE-dampers and reasonably predicted peak displacement for the VE-frame.

Along-wind mean square value of acceleration can be predicted from the displacement response by [Simiu and Scanlan, 1996]:

$$\sigma_{\ddot{X}}^2 = 16\pi^4 \int_0^\infty f^4 S_X(f) df \qquad [7.22]$$

The expected peak value for acceleration is computed as :

$$\ddot{X}_{max} = g\sigma_{\ddot{X}} \qquad [7.23]$$

where $\ddot{X}_{max}$ is the probable maximum acceleration occurring during the interval **T**, and g is the peak factor determined from Eq. 7.19. Computing the root mean square value of acceleration at the roof level from Eq. 7.22 and applying Eq. 7.23, results in a probable peak acceleration of 0.061g for the frame without VE-dampers and 0.019g for the VE-frame. Time history analysis peak accelerations were 0.048g for the frame without VE-dampers and 0.017g for the VE-frame. The spectrum approach and time-history analysis produced reasonably similar results.

It should be noted that different theories for predicting along-wind response can differ from each other by as much as 50% [Blevins, 1990]. While the approximate analysis method presented here may also exhibit this wide variability, it does provide a method for assessment of structures subjected to identical input forces which enables direct comparison of the effects of VE-dampers on structural response.

7.4 Simulated Across-Wind Loading

7.4.1 Analytical Prediction of Across-Wind Forces

For many tall buildings, across-wind response can be more significant than along-wind response. While the relatively short structure examined in this study is not particularly susceptible to these conditions, this phenomenon was considered to illustrate across-wind response for a VE-frame. Across-wind vibration is caused by three sources: buffetting due to across-wind turbulence, wake excitation due to vortex shedding, and aeroelastic phenomena [Belandra, 1993]. Aeroelastic phenomena include lock-in, galloping, and flutter. Typical building structures are generally not influenced by galloping or flutter. Lock-in phenomena can occur for structures with low stiffness and low damping when the vortex shedding frequency is very close to the natural frequency of the structure. The critical wind velocity at lock-in can be calculated:

$$\overline{V}_{crit} = \frac{f_n B}{S} \qquad [7.24]$$

Where $\overline{V}_{crit}$ is the critical mean wind velocity (m/s), f_n is the building fundamental frequency (hz) in the across-wind direction, B is the building width (m) in the along-wind direction, and S is the Strouhal number. Typical Strouhal numbers for rectangular buildings are illustrated in Fig. 7.47. Eq. 7.24 can also be rearranged to compute the frequency of vortex shedding, f_e, for a given mean wind velocity $\overline{V}$:

$$f_e = \frac{S\overline{V}}{B} \qquad [7.25]$$

Two models were considered to determine the response of the wind prototype VE-frame to across-wind vibration. The first model is based on the Ontario Highway Bridge Design Code for across-wind vibration of luminaires and sign structures [Ontario Ministry of Construction, 1991]. This procedure provides an excitation force at a single frequency which acts in-phase along the height of the structure:

$$F_s(t,x) = \frac{1}{2}\rho \overline{V}_h^{\,2} C_s B \sin(2\pi f_e t) \qquad [7.26]$$

Where $\overline{V}_h$ is the along-wind velocity (m/s) at the top of the structure, C_s is the vortex shedding coefficient for the cross section (=0.85 for square and multisided prismatic sections [Ontario Ministry of Construction, 1991]), and f_e is the frequency of vortex shedding (hz) as computed in Eq. 7.25. A second method was developed which models the across-wind forcing function as a broader band stationary random process. This simulation, is based on wind tunnel studies of square building geometries and characteristics of the longitudinal wind flow to determine the spectral density of the across-wind force on the structure [Kareem 1984]:

$$S_F(f) = \frac{\alpha^* \beta^* \left(\frac{f}{f_e}\right)^{0.9} \sigma_F^2}{f} \quad \text{for} \quad f < f_e \qquad [7.27]$$

$$S_F(f) = \frac{\alpha^* \beta^* \left(\frac{f}{f_e}\right)^{0.3} \sigma_F^2}{f} \quad \text{for} \quad f \geq f_e \qquad [7.28]$$

where

$$\alpha^* = \frac{I(z)\sqrt{2}}{\left[1 - \left(\frac{f}{f_e}\right)^2\right]^2 + \left[2 \cdot \left(I(z)\sqrt{2}\right)\left(\frac{f}{f_e}\right)\right]^2} \qquad [7.29]$$

$$\beta^* = 1.32\sqrt{\frac{1}{3\alpha}} \qquad [7.30]$$

I(z) is the intensity of the along wind gusts, and α is the power law exponent. The forcing function represents the total lateral force produced on the sides of the structure due to wake excitation, however, forces are distributed uniformly over the height of the structure. Normalized across-wind force spectrum were computed for an intensity of 19%, a 50 year return period mean wind speed of 33.69 m/s at the roof, and urban exposure ($\alpha = 0.33$). Note that α=0.33 for this portion of the study to be consistent with the work done by Kareem in establishing Eqs. 7.27 to 7.30. Values for the across-wind force variance, σ_F^2, were selected to correspond with spectra for a structure with a similar plan aspect ratio presented by Saunders and Melbourne [1977] as shown in Fig. 7.48. A similar numerical technique was used to determine the across-wind forcing function as was previously described for simulation of the along-wind velocity. However, no spatial correlations were considered as the forcing function acts in-phase along the entire height of the building (Ω_k=0 in Eq. 7.3).

Multidimensional random process simulation for the across-wind forcing function was implemented using an ensemble of 2000 cosine waves at a time interval of 0.125 seconds, and records were generated for a 30 minute event. The maximum forcing frequency was 4 hz for the specified time interval. The simulated across-wind force-time record is shown in Fig. 7.49. The generated record has a near Gaussian distribution with a mean value close to zero as illustrated in Fig. 7.50. Spectral densities of the generated force record were computed [Blackman and Tukey, 1960] and are compared with the target spectrum in Figs. 7.51.

Peak value of the lateral across-wind force using the numerical simulation technique (208.2 kips) was very close to the magnitude of sinusoidal across-wind force predicted by the Ontario Highway Bridge Design Code method (205.5 kips). Only the numerical simulation method was used to predict across-wind vibration of the VE-frame. Computed across-wind forces were applied to the analytical model of the wind prototype frame and the dynamic response was computed. Analytical displacement time history at the third story is shown in Fig. 7.52 for the 30 minute event.

7.4.2 Experimental Response of VE-Frame to Across-Wind Forces

Analytically computed response at the third story was imposed on the test specimen in real-time. The 30 minute duration third story displacement response from analysis was discretized into 1803 equally spaced displacement-time pairs. Displacement control of the actuators was performed using ramp functions from point to point of the discretized analytical displacement history. Data were acquired from the hour long tests for the 196 channels of instrumentation

at an acquisition rate of 5.7 hz (separation of 0.175 seconds between samples). This acquisition rate was adequate to determine the continuous overall frame behavior, member response, and damper temperature rise as well as permit assessment of the interaction of between the frame member forces and damper forces or time lag responses.

Measured displacement time history at the third story is shown in Fig. 7.53. Measured overall force-deformation response for the frame is shown in Fig. 7.54. The average equivalent frame stiffness for the whole test was 41.0 kips/in (unbraced frame stiffness was 17.0 kips/in from Chapter 4). The overall response (Fig. 7.54) indicates the dampers provided significant energy dissipation capacity.

Example force-deformation response for the second story East VE-damper during the complete test is shown in Fig. 7.55. As shown in this figure, there was no appreciable change in damper stiffness during the test, indicating no significant temperature rise. Measured temperature rise for the second story East damper is shown in Fig. 7.56. Damper temperatures rose at the initiation of loading and then remained relatively stable during the rest of the experiment. Final temperature rise was only 0.2 °C and no significant material property changes occurred due to this small temperature change (Fig. 7.55). As in the along-wind tests, if heat transfer between the damper and environment is neglected, predicted damper temperatures would be significantly higher than the measured values. This again indicates that for long duration loading events, heat transfer should be considered to accurately predict structural response at later stages of the loading history.

Damper and structural member forces exhibited phase relationships similar to those described previously. Phase relationships between member forces and dampers, were determined from normalized member force responses. Example phase relationships between the level 2 East VE-damper and East second story column forces are shown in Fig. 7.57. Again, column moments were in-phase with displacement while axial forces were more in-phase with the damper force. As a result, the axial force-moment interaction exhibited hysteresis as shown in Fig. 7.58. The phase lag causes maximum axial force and maximum moment to occur at different instances of time.

7.4.3 Analytical Prediction of Across-Wind VE-Frame Response

7.4.3.1 Effect of VE-Dampers on Across-Wind Response

A direct comparison was made between the behavior of the frame with and without dampers when subjected to the same across-wind forces. Two analytical models of the wind prototype frame were developed to perform this comparison. One model contained VE-dampers and the other did not. Across-wind forces were generated as described in section 7.4.1 and applied to the models. The response of the structures to these wind forces was computed and response comparisons were made.

Analytically predicted displacement response at the roof story is shown in Figs. 7.59 and 7.60 for the frame with and without VE-dampers respectively, during the 50 year return period, 30 minute wind event. As shown in these figures, the frame without dampers exhibited larger

deflections than the VE-frame. The frame without dampers had a peak roof displacement of 2.28 in. and the frame with VE-dampers had a peak roof displacement of 1.70 in. The increased stiffness provided VE-dampers reduced the peak deflection response as compared to the frame without dampers.

It is important to note that the complete role of VE-dampers on across-wind response can not be fully realized due to limitations in the simulation method. The method relies on an across-wind force spectrum to generate a forcing function. This spectrum is based on wind tunnel studies of building models with small damping ratios. It is believed that high damping (provided by the dampers) would result in reduced across-wind response of the wind tunnel models and therefore produce a reduced across-wind force spectrum. The analyses of the frame with and without dampers was performed using the same forcing function on both structures. Consequently, the results mainly reflect the stiffness contribution of the dampers in reducing across-wind response because the damping contribution should also be included by a reduction in the forcing function. To include this effect, would require across-wind force spectra for models with high damping ratios.

7.4.3.2 Prediction of Across-Wind Response

Across-wind response can be predicted using random vibration theory. Idealizing the building as a distributed parameter system, the equation of motion can be described as [Balendra]:

$$M_i^* \ddot{r}_i + C_i^* \dot{r}_i + K_i^* r_i = F_i^*(t) \qquad [7.31]$$

where, i is the mode, r is the normal coordinate, and M_i^*, C_i^*, K_i^*, and $F_i^*(t)$ are the generalized mass, damping, stiffness and force in the i-th mode respectively which are defined as:

$$M_i^* = \int_0^H \overline{m}(z)\phi_i^2(z)dz \qquad [7.32]$$

$$K_i^* = (2\pi f_i)^2 M_i^* \qquad [7.33]$$

$$C_i^* = 2\xi_i \sqrt{M_i^* K_i^*} \qquad [7.34]$$

$$F_i^*(t) = \int_0^H f(z,t)\phi_i(z)dz \qquad [7.35]$$

where $\overline{m}(z)$ is the mass per unit height $=M_{tot}/H$, f_i is the i-th mode frequency, ξ_i is the i-th mode damping ratio, f(z,t) is the across-wind force per unit height, and ϕ_i is the modal displacement. The first mode can be approximated by $\phi_1=(z/H)^\beta$, where β is a coefficient which describes the shape (=1.0 for straight line, =1.86 for a bending cantilever). From random vibration theory, spectral density of the normal coordinate $S_{r_i}(f)$ can be expressed as:

$$S_{r_i}(f) = \frac{|H(f)|^2 S_F(f)}{(2\pi f_i)^4 M_i^{*2}} \qquad [7.36]$$

where $|H_n(f)|^2$ is defined by Eq. 7.13, and $S_F(f)$ is defined by Eqs. 7.27 and 7.28. The mean squared response can be determined according to :

$$\sigma_{r_i}^2 = \int_0^\infty S_{r_i}(f)df \qquad [7.37]$$

The variance of the across-wind displacement can be determined by summing the contributions of all modes [Balendra, 1993]:

$$\sigma_X^2 = \sum_{i=1}^{N} \phi_i^2 \sigma_{r_i}^2 \qquad [7.38]$$

Considering only a single mode with a straight line mode shape (β=1), the across-wind force spectrum (Eqs. 7.27 and 7.28) with mean squared force of 289546 N (65.1 kips) determined from the numerically simulated forcing function computed in section 7.4.1, and a peak factor g of 3.5, the likely peak roof displacement was 1.8 in. for the VE-frame and 2.7 in. for the frame without dampers. Based on numerical experiments of Eqs. 7.32 to 7.38, using the across-wind force spectrum described above(Eqs. 7.27 and 7.28), the response reduction for the VE-frame is due primarily to shifting of the fundamental period, and the damping has little effect on the reduction for the given building properties and across-wind spectrum. Damping had little impact on the response because the frequency range of the narrow band forcing function is widely separated from the natural frequency for this particular building and selected wind properties. If the forcing function were close to the natural frequency of the structure, as would be the case at lock-in, the damping effect would be significantly greater.

7.5 Conclusions

Results of the simulated along-wind and across-wind tests and analyses are summarized below:

- A unique methodology was developed which permitted testing of the full-scale lower three story portion of the 10-story prototype VE-damped frame subjected to wind and gravity forces.
- The testing methodology relied on simulated wind forces and time history analysis to determine the imposed displacement history on the test specimen.
- Experimental frame response demonstrated VE-dampers provide significant dynamic stiffness and damping even at the relatively low frequencies associated with the wind spectrum.
- Measured temperature rise in the VE-dampers indicated that significant heat convection takes place between the dampers and environment. Heat convection resulted in no appreciable temperature induced change in damper properties. To accurately predict damper and frame response for long duration events, heat convection should be considered.
- Frame member axial forces were in-phase with damper forces while moments were in-phase with frame displacement. This resulted in peak moments and axial forces occurring at different instances of time.
- Analytical prediction of along-wind response indicated VE-dampers can effectively reduce the mean square displacement response of the frame. Displacement response

reduction mainly results from suppression of the resonant frame response which would otherwise be excited by the wind gusts.

- Suppression of the resonant response occurs due to the increased damping provided by the VE-dampers and shifting of the natural frequency away from the energy of the wind spectrum by the additional stiffness provided by the VE-dampers.
- The VE-frame exhibited significantly lower building accelerations, lower stress ranges, and fewer stress cycles than an equivalent frame without dampers. Reduction of these parameters were directly related to reduction in resonant response.
- An analytical method was used to predict the along-wind response. Results indicate the method can reasonably predict frame response and can be used to determine the amount of reduction associated with the resonant part of the response.
- Analytical prediction of across-wind response indicated VE-dampers reduced the peak displacement response of the frame. Displacement response reduction primarily resulted from the natural frequency shift caused by the additional stiffness provided by the VE-dampers.
- The full role of VE-dampers on across-wind response could not be fully realized due to limitations in the simulation method. The method relies on across-wind force spectra to generate a forcing function which is based on wind tunnel studies of building models with small damping ratios. High damping may have the additional benefit of reducing the across-wind force spectra. There is a lack of information to determine this reduction.
- An analytical method was used to predict the across-wind response. Results indicate the method can reasonably predict frame response for the assumed across-wind force spectrum.

Wind Parameter	One Hour Duration		
	5 Year Return Period	50 Year Return Period	500 Year Return Period
V_{10} (m/s)	13.1	25.0	33.4
V_g (m/s)	28.8	55.1	73.6
z_g (m)	520	520	520
α	1/5	1/5	1/5
κ	0.025	0.025	0.025
Coherence	0.2948	0.1539	0.1153

Table 7.1 - Wind Parameters for different return period wind events considered.

Peak Acceleration	<0.005g	0.005g to 0.015g	0.015g to 0.05g	0.05g to 0.15g	> 0.15g
Human Perception	Imperceptible	Perceptible	Annoying	Very Annoying	Intolerable

Table 7.2 - Human discomfort to building accelerations [Simiu and Scanlan, 1996].

D/B	0.20	0.40	0.50	0.65	0.80	1.00	1.20	1.50	2.00	3.00
C_D	2.1	2.35	2.5	2.9	2.3	2.2	2.1	1.8	1.6	1.3

D Length of structure parallel to wind direction.
B Width of structure perpendicular to wind direction.
C_D Drag Coefficient.

Table 7.3 - Drag coefficients for rectangular building [Blevins, 1990].

Parameter	Frame without VE-dampers	VE-Frame	Units
ξ	2%	10%	(%)
f_n	0.3	0.37	(hz)
V_{10}	25.0	25.0	(m/s)
V_h	33.1	33.1	(m/s)
β	1.86	1.86	
C_D	1.6	1.6	
ρ_{air}	1.225	1.225	(kg/m^3)
H	35.51	35.51	(m)
B	26.82	26.82	(m)
M_i	1350869	1350869	(kg)
f_{equiv}	0.261	0.211	(hz)
g	3.86	3.80	
G	5.0	2.6	
X_{max}	8.35	4.36	(in)

Table 7.4 - Parameters used for along-wind response prediction.

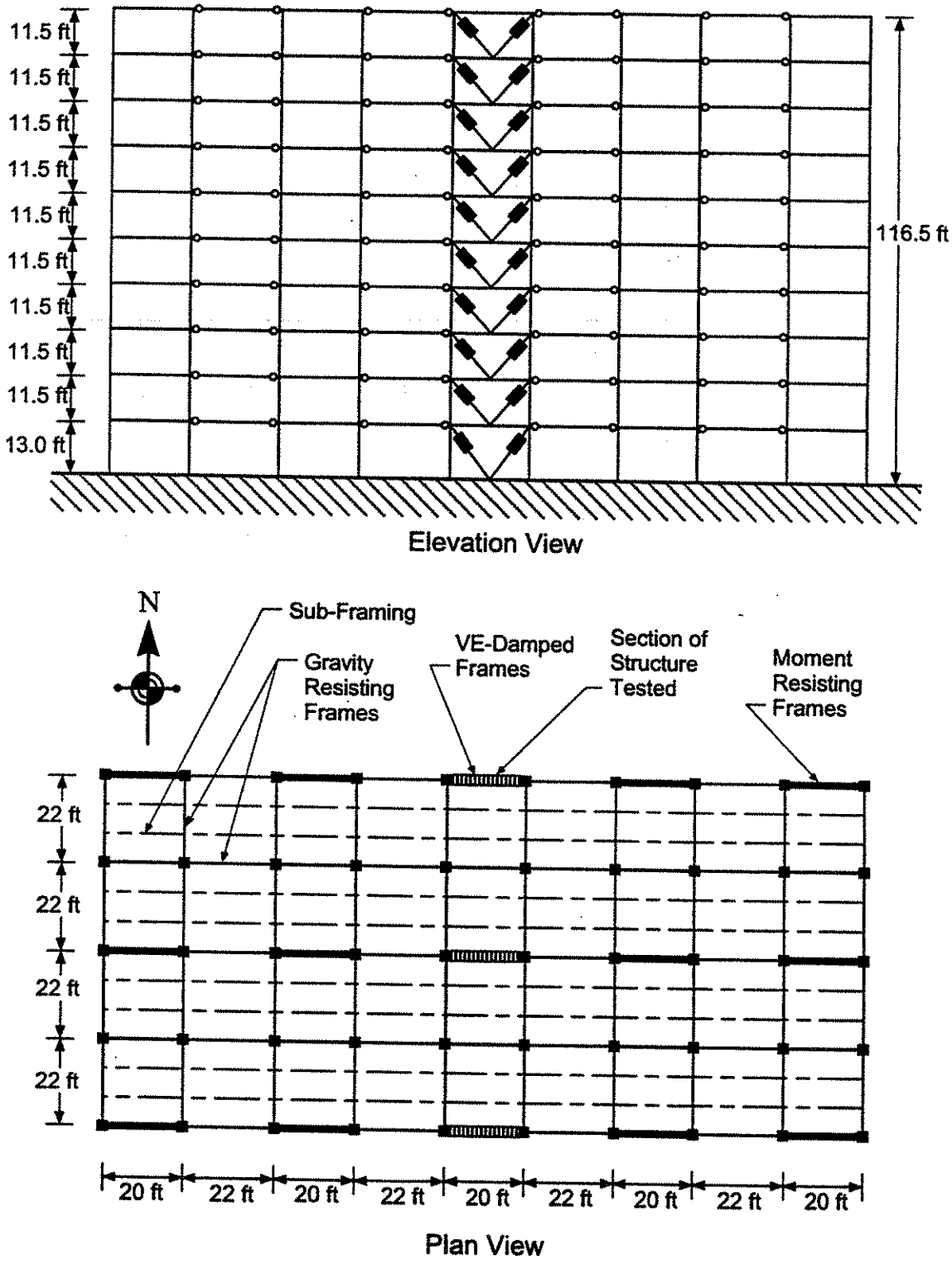

Fig. 7.1 - Wind prototype frame VE-frame.

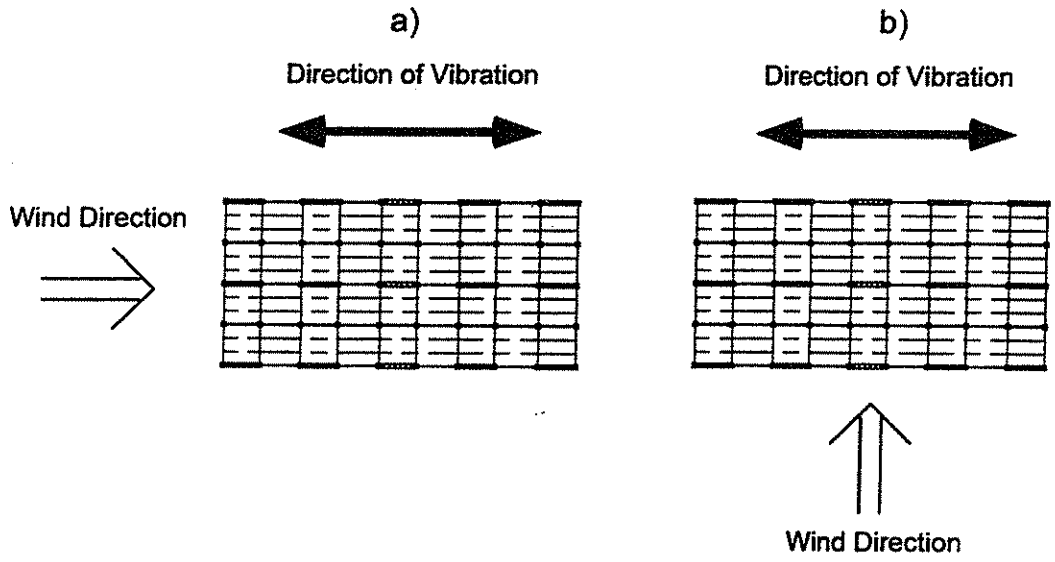

Fig. 7.2 - a) Along-wind vibration of building and b) Across-wind vibration of building.

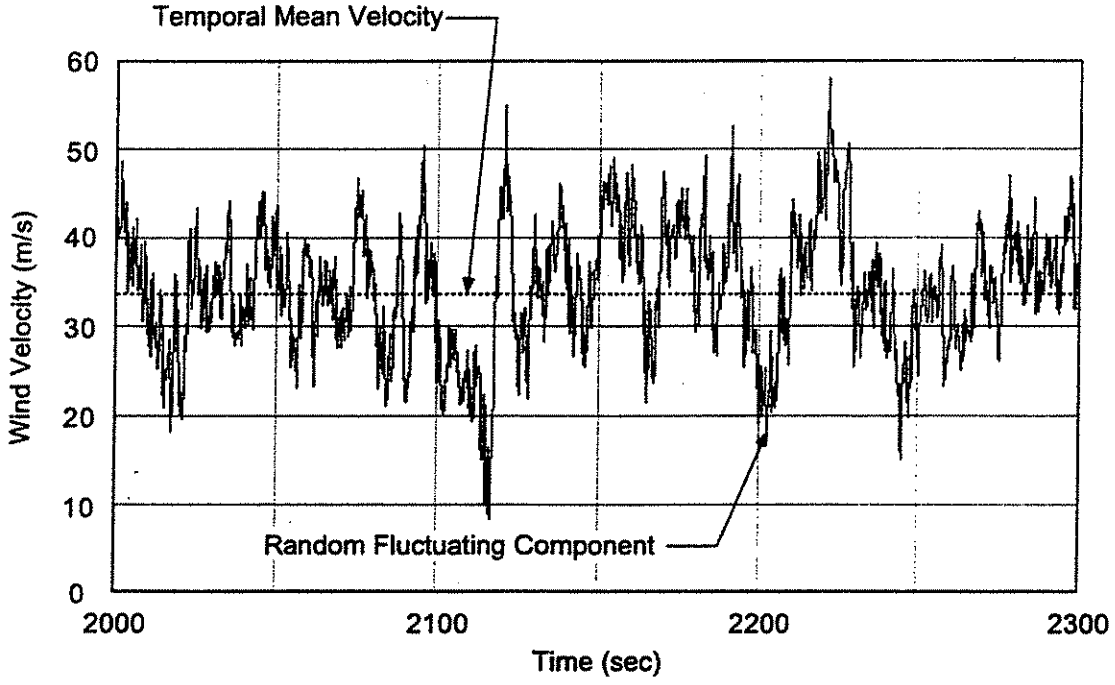

Fig. 7.3a - Components of wind velocity.

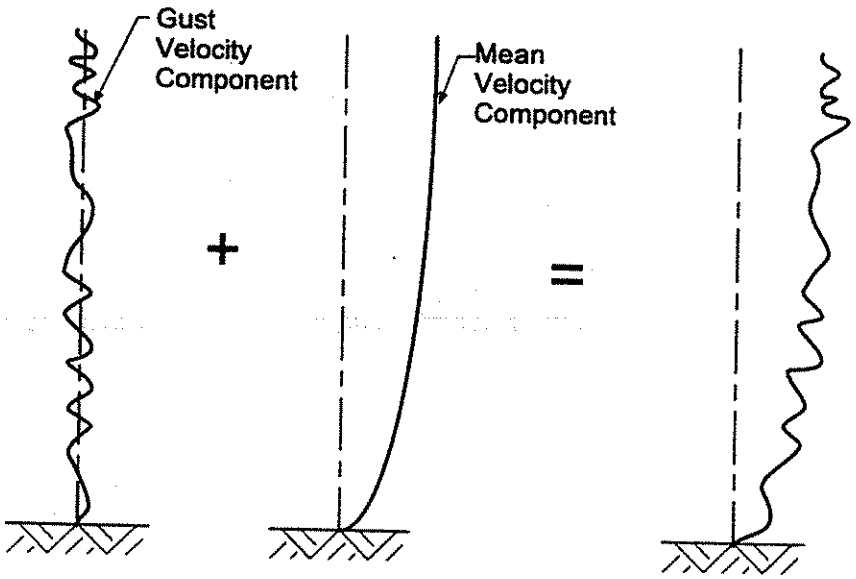

Fig. 7.3b - Schematic representation of wind components.

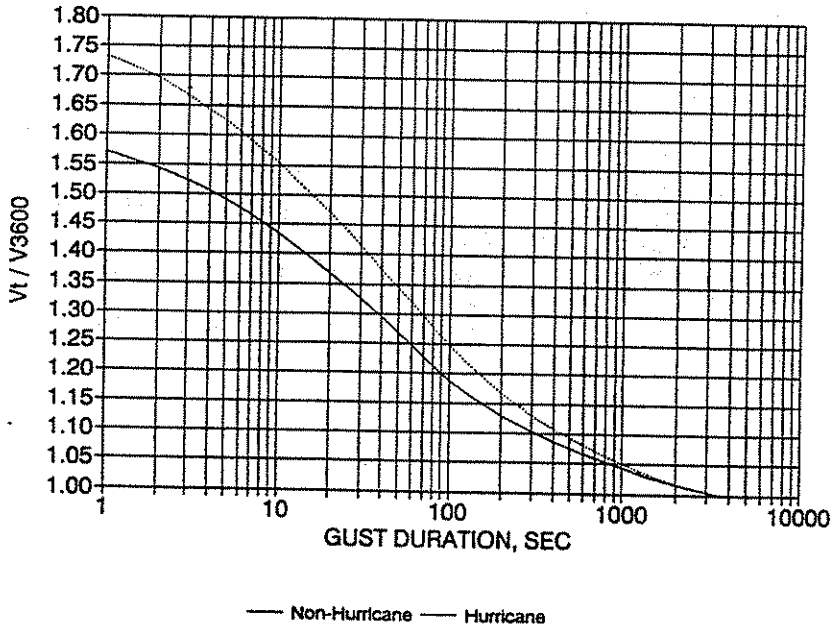

Fig. 7.4 - Ratio of probable maximum wind speed averaged over a period of t seconds to that averaged over an hour [ASCE, 1995].

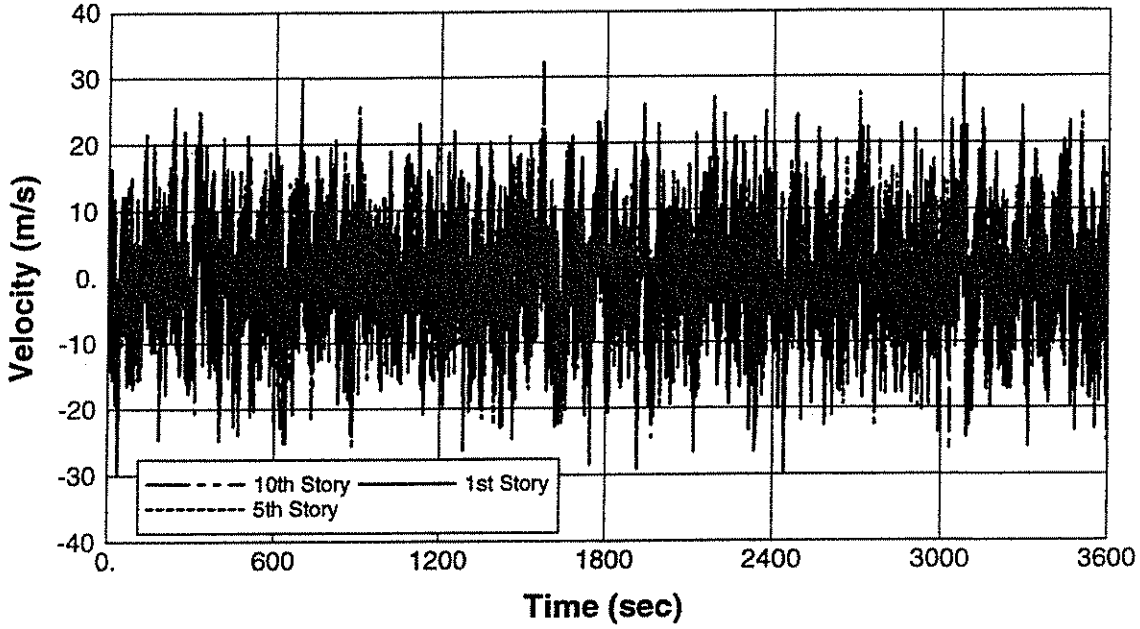

Fig. 7.5 - Example of simulated fluctuating component wind velocities.

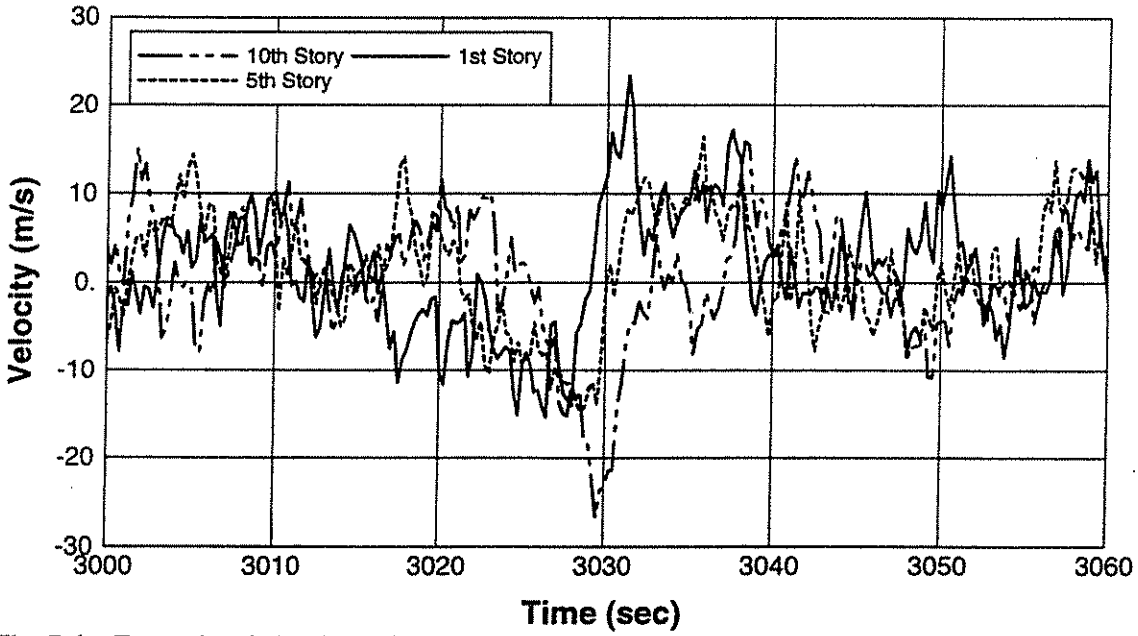

Fig. 7.6 - Example of simulated fluctuating component wind velocities illustrating phase lag between records due to spatial separations.

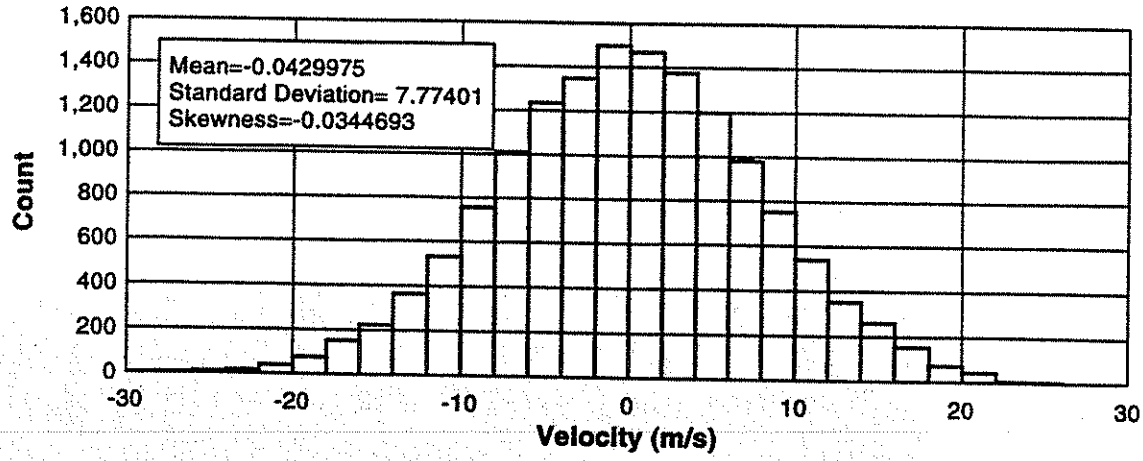

Fig. 7.7a - Example of Gaussian distribution of simulated fluctuating component wind velocities at the first story level.

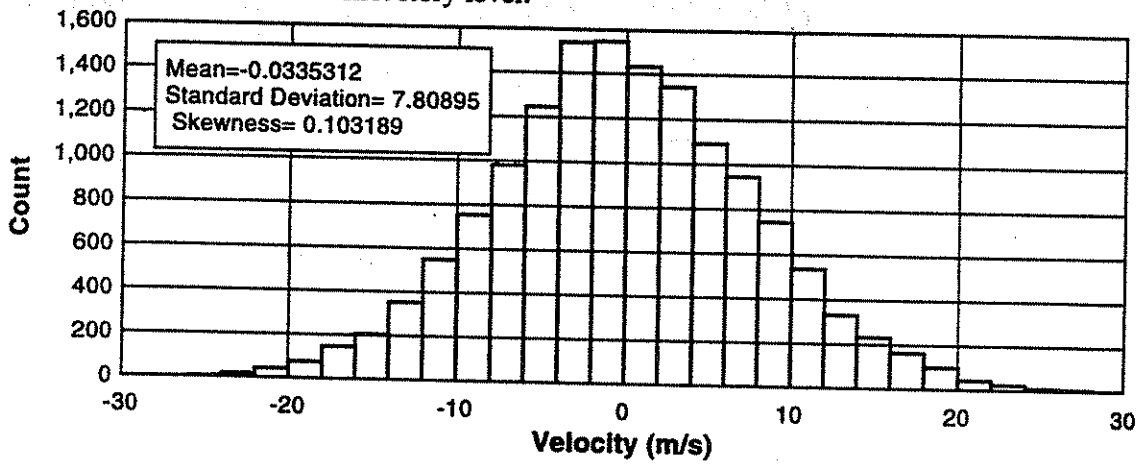

Fig. 7.7b - Example of Gaussian distribution of simulated fluctuating component wind velocities at the fifth story level.

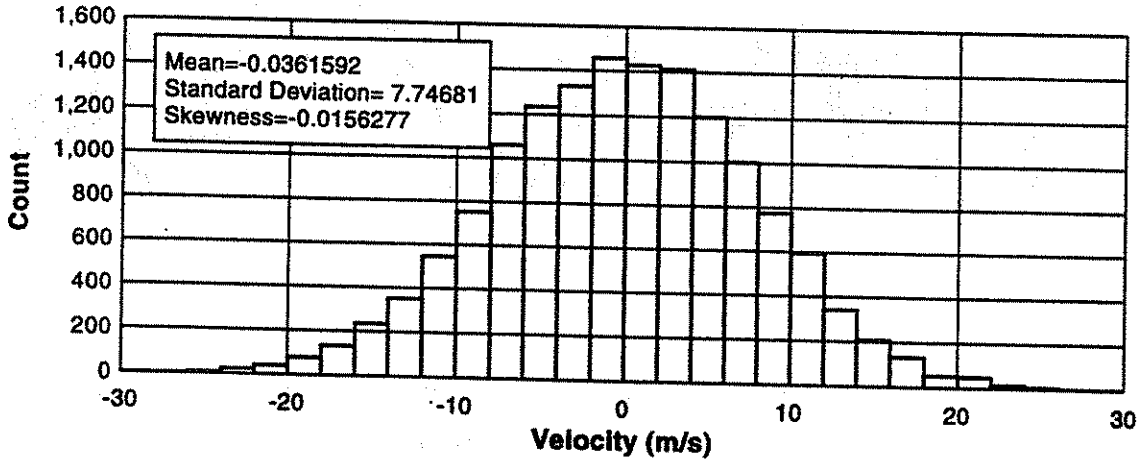

Fig. 7.7c - Example of Gaussian distribution of simulated fluctuating component wind velocities at the tenth story level.

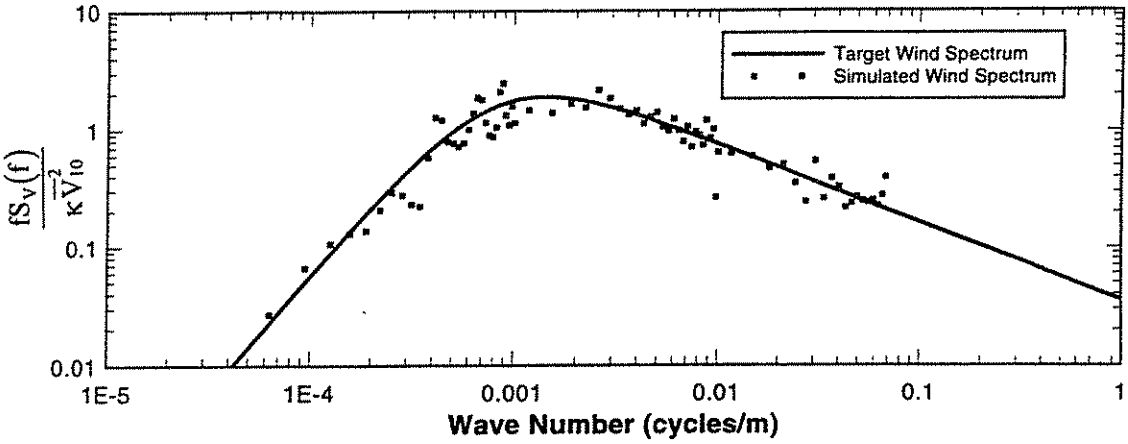

Fig. 7.8a - Example of target and simulated fluctuating component wind velocity spectra at the first story level.

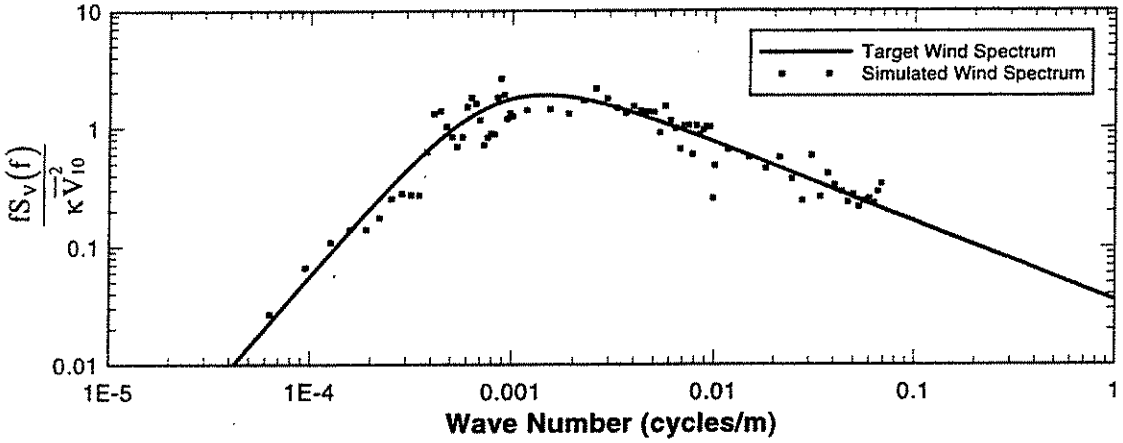

Fig. 7.8b - Example of target and simulated fluctuating component wind velocity spectra at the fifth story level.

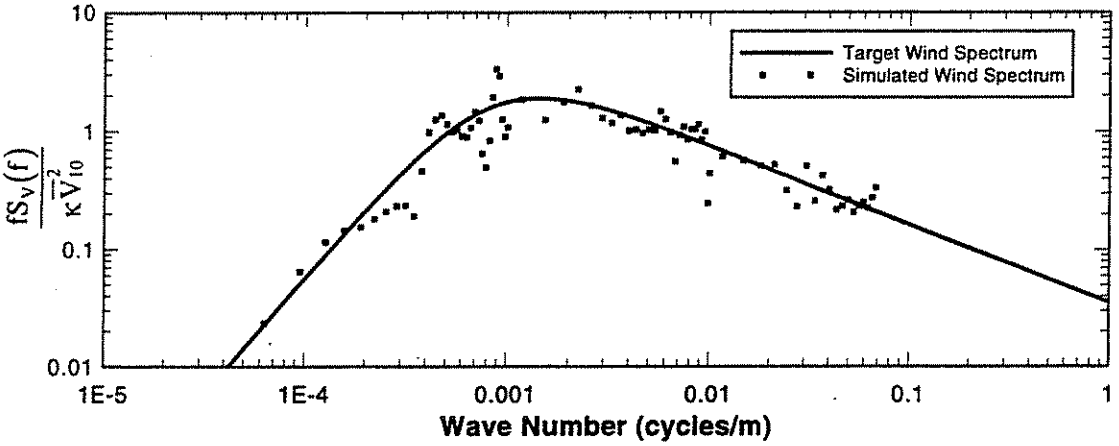

Fig. 7.8c - Example of target and simulated fluctuating component wind velocity spectra at the tenth story level.

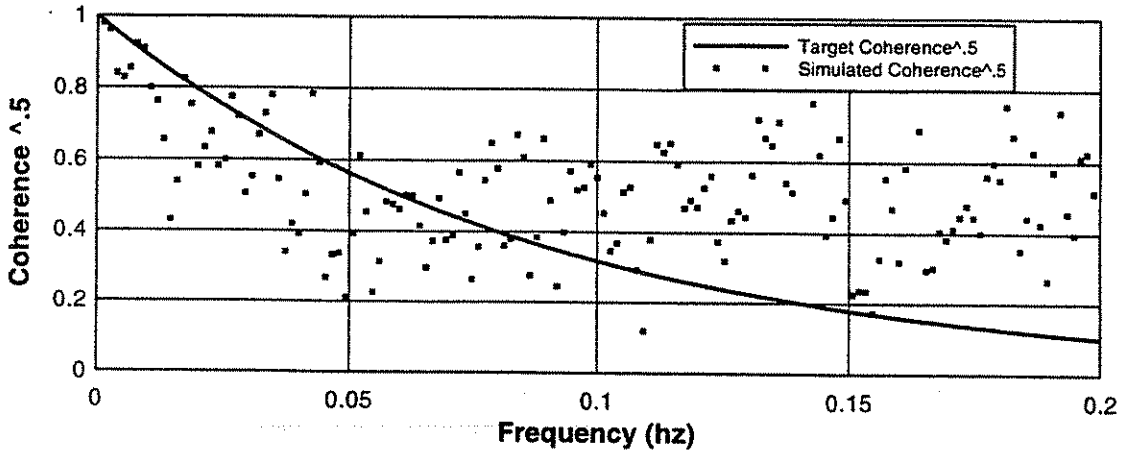

Fig. 7.9a - Example of target and simulated coherence between first and tenth story levels.

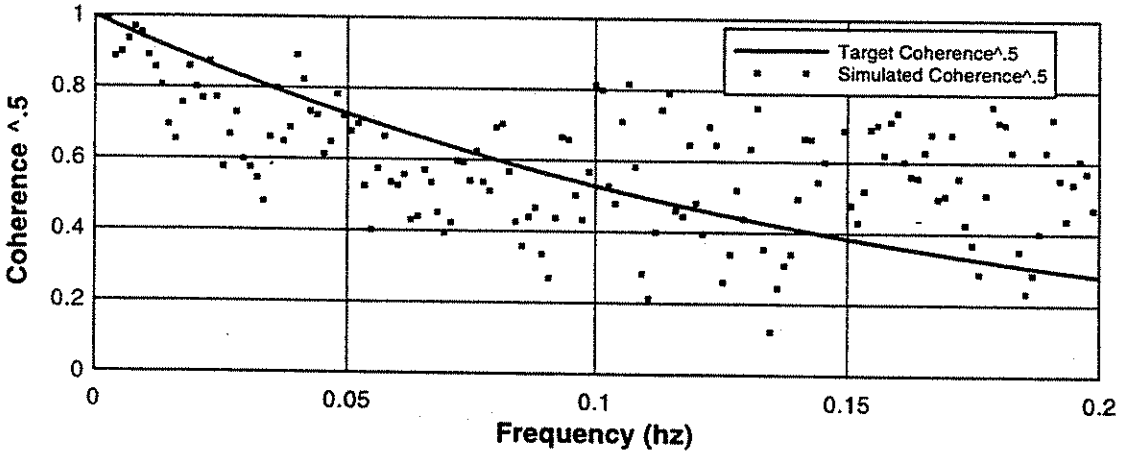

Fig. 7.9b - Example of target and simulated coherence between fifth and tenth story levels.

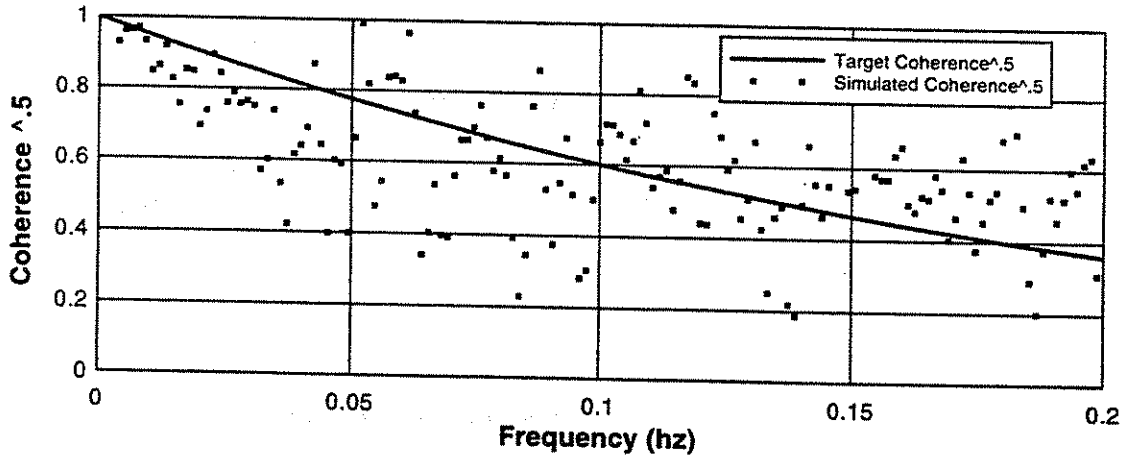

Fig. 7.9c - Example of target and simulated coherence between the first and fifth story levels.

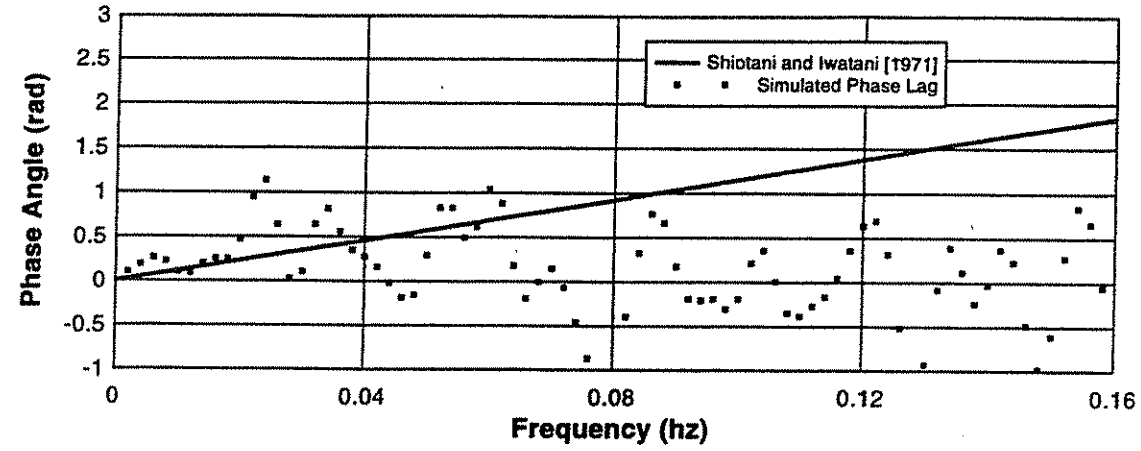

Fig. 7.10a - Example of target and simulated phase lag between first and tenth story levels.

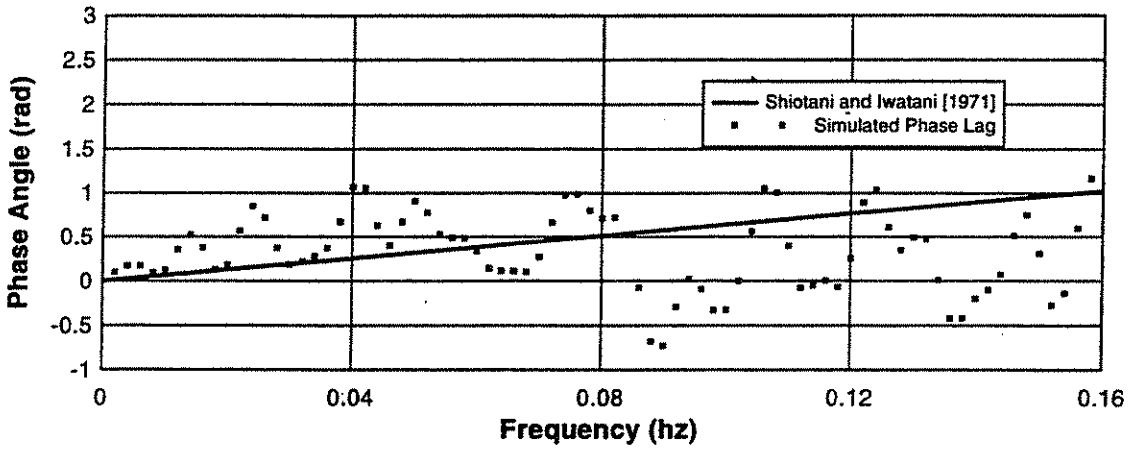

Fig. 7.10b - Example of target and simulated phase lag between fifth and tenth story levels.

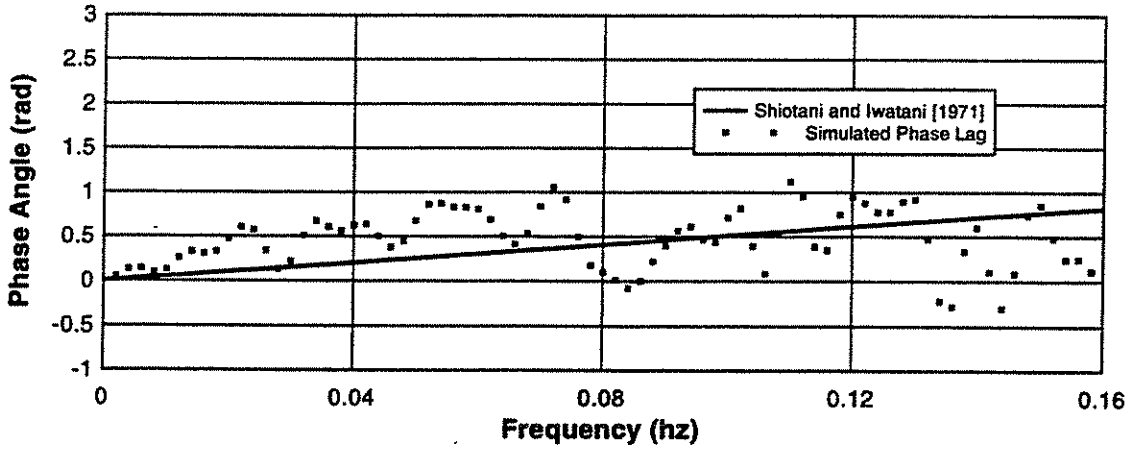

Fig. 7.10c - Example of target and simulated phase lag between the first and fifth story levels.

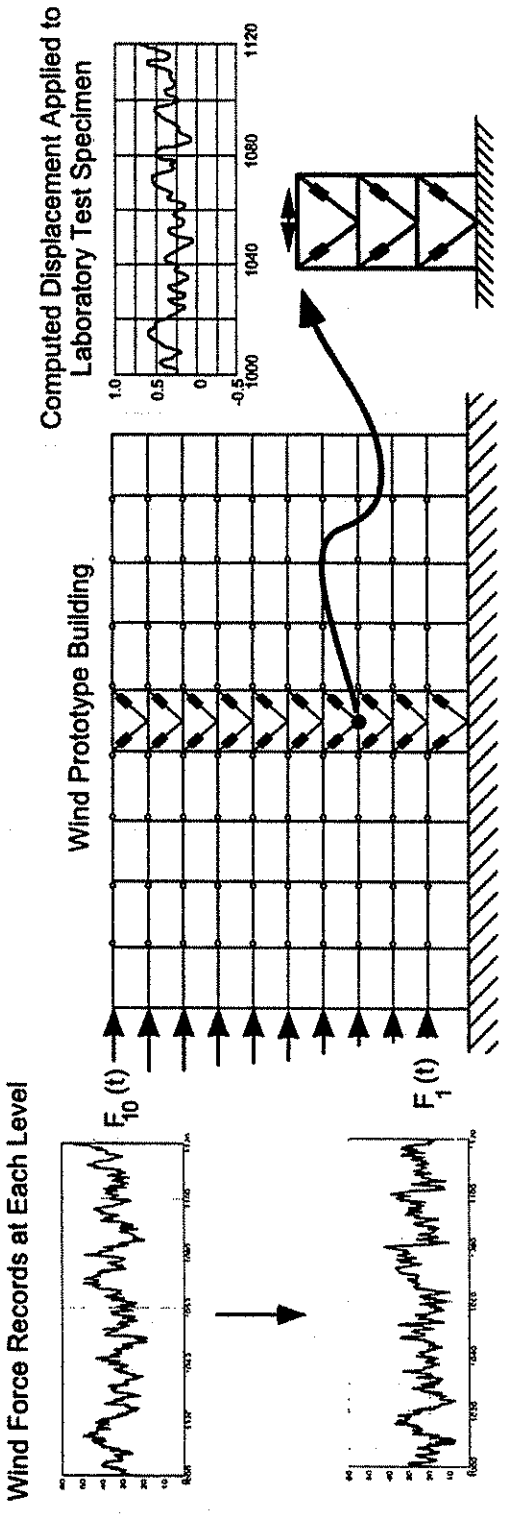

Fig. 7.11 - Schematic representation of methodology used to test wind response of VE-frame.

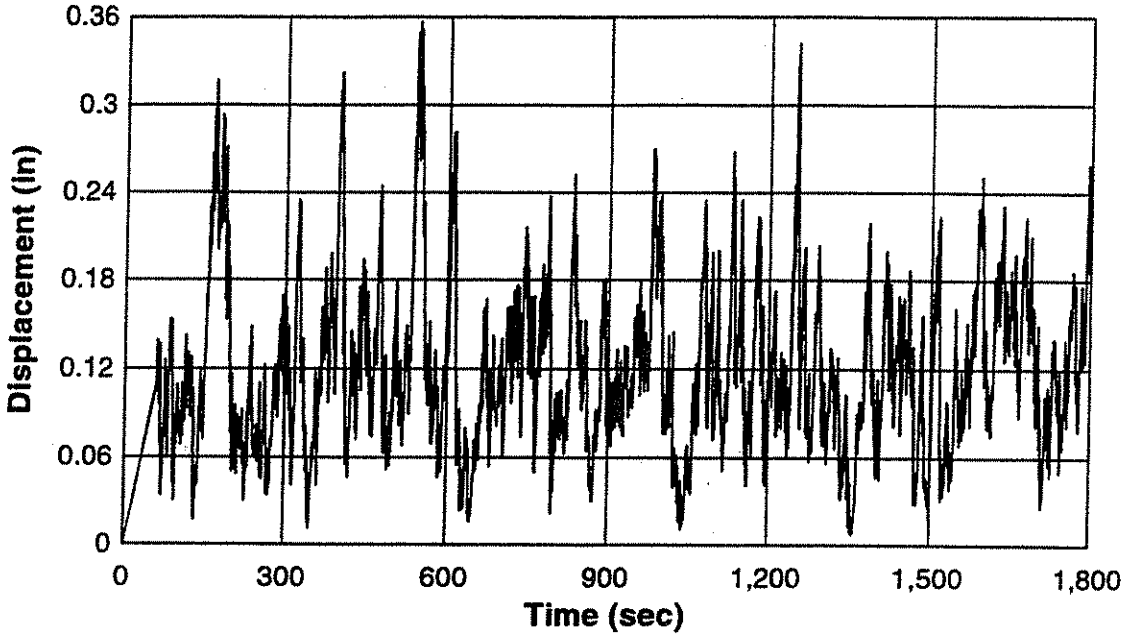

Fig. 7.12a - First half of predicted third story level displacement response for a wind event of one hour duration and 5 year return period.

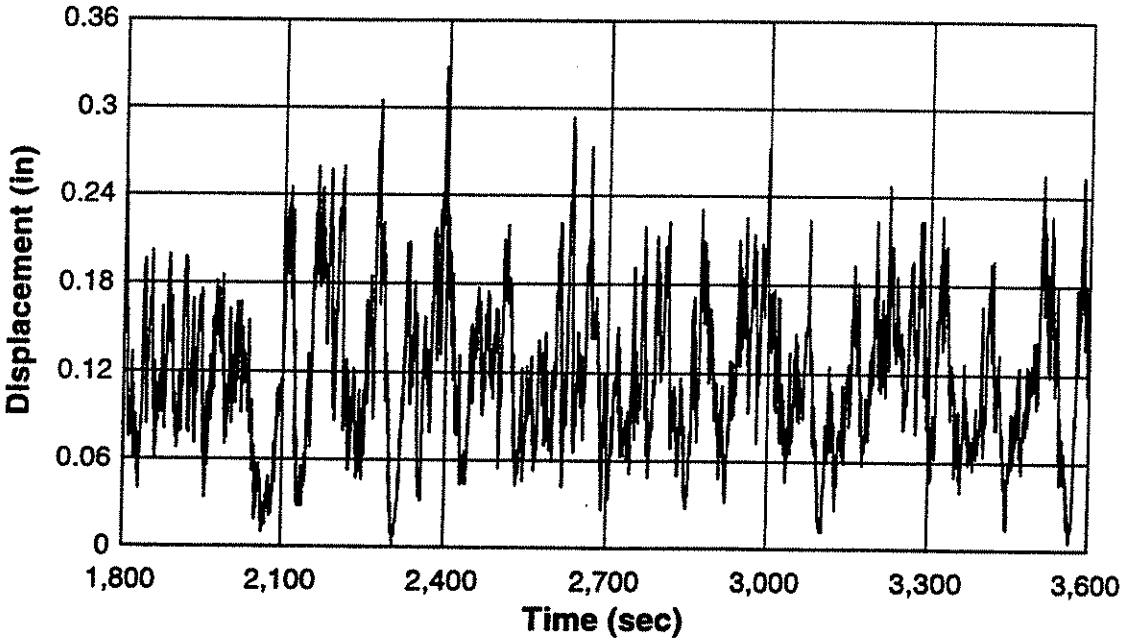

Fig. 7.12b - Second half of predicted third story level displacement response for a wind event of one hour duration and 5 year return period.

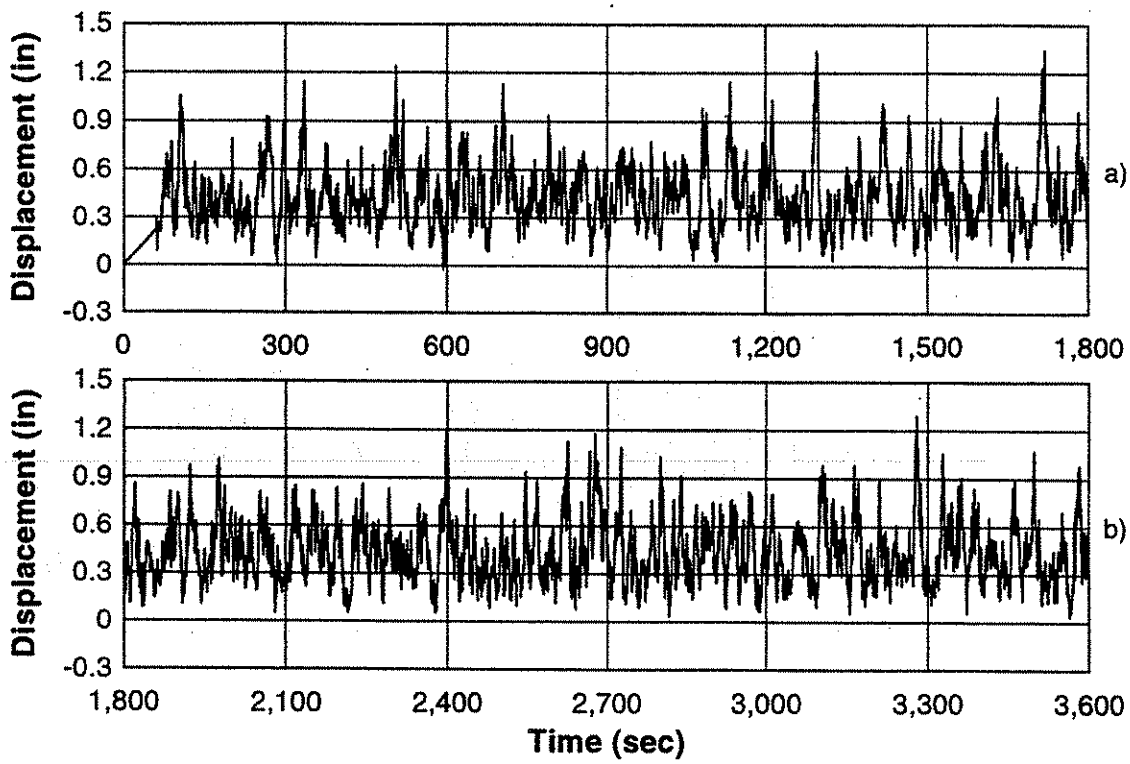

Fig. 7.13a,b - a) First half and b) Second half of predicted third story level displacement response for a wind event of one hour duration and 50 year return period.

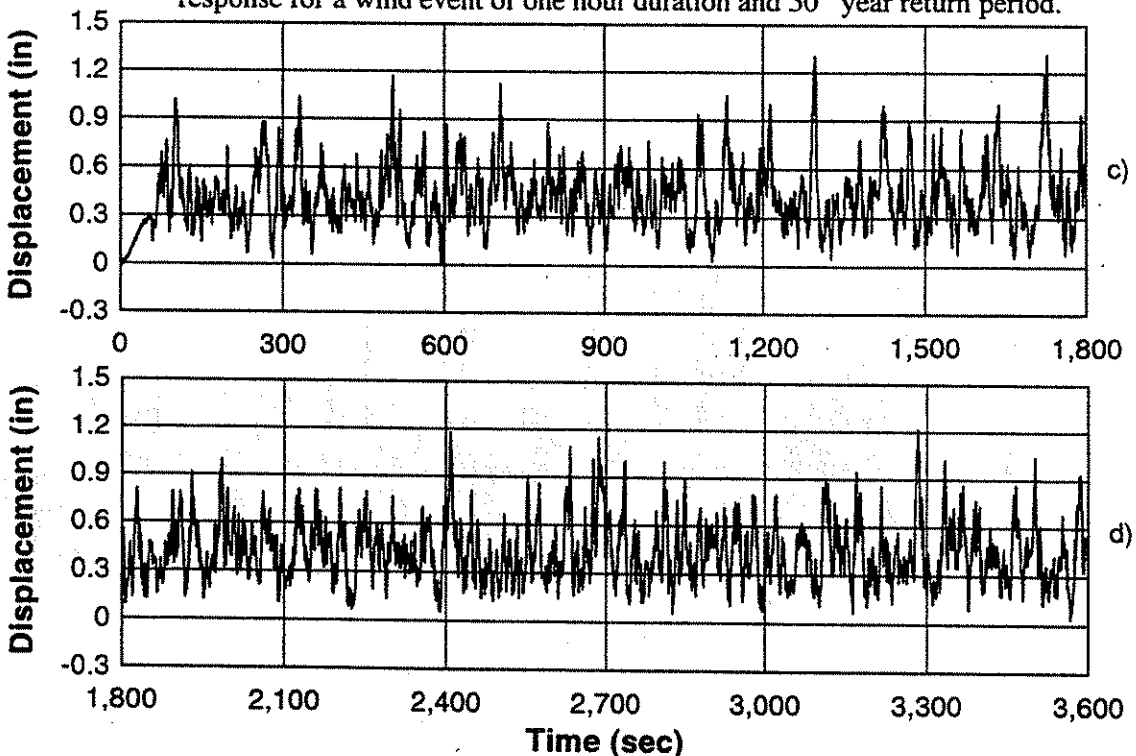

Fig. 7.13c,d - c) First half and d) Second half of measured third story level displacement response for a wind event of one hour duration and 50 year return period.

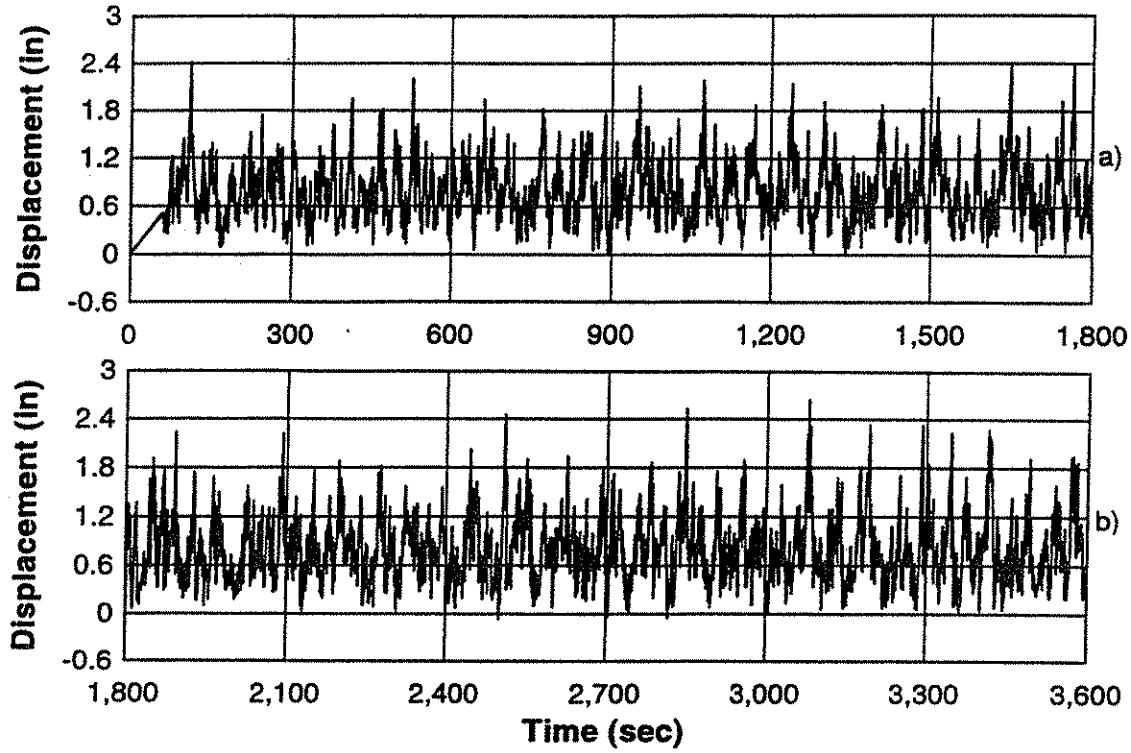

Fig. 7.14a,b - a) First half and b) Second half of predicted third story level displacement response for a wind event of one hour duration and 500 year return period.

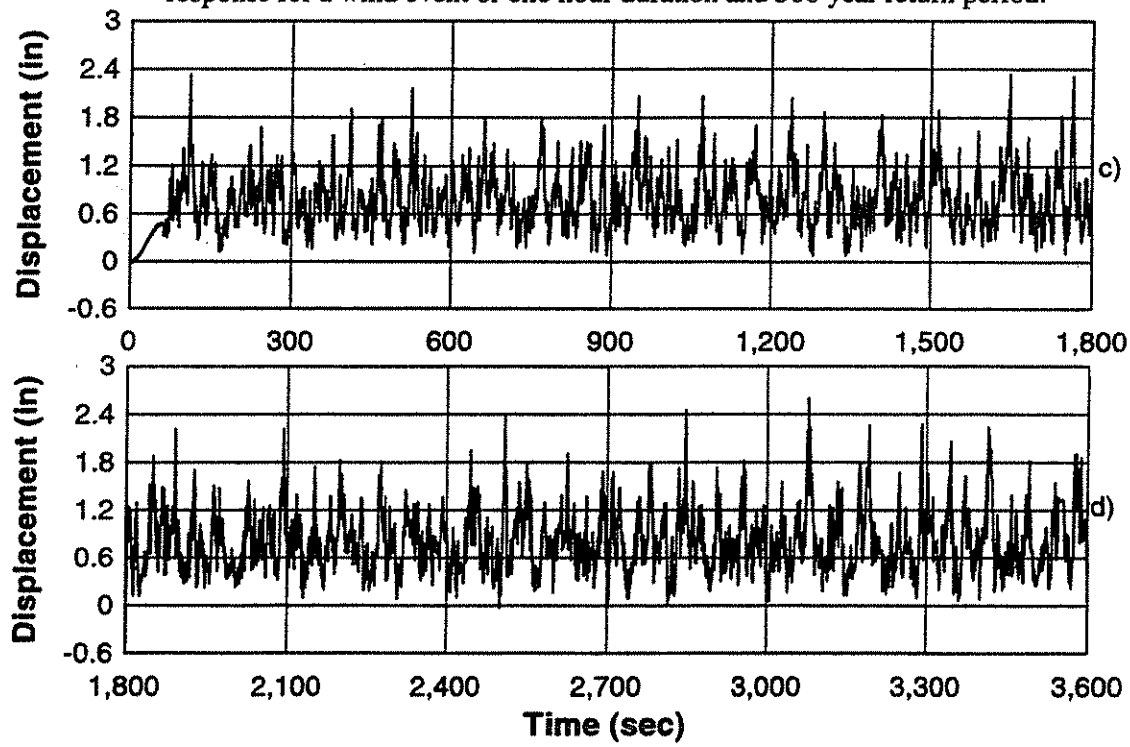

Fig. 7.14c,d - c) First half and d) Second half of measured third story level displacement response for a wind event of one hour duration and 500 year return period.

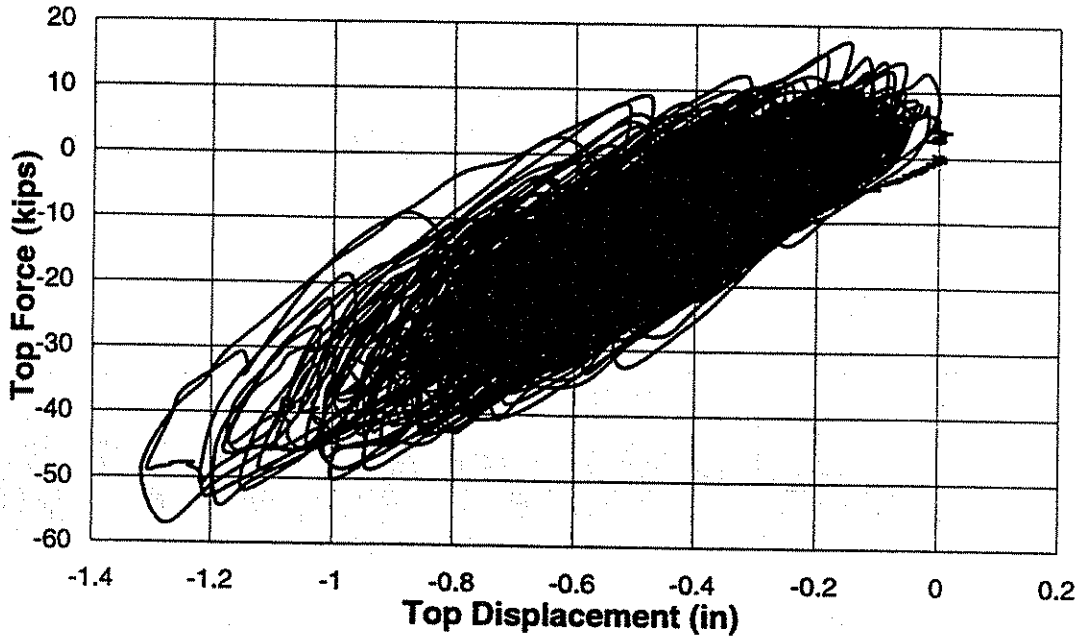

Fig. 7.15 - Measured overall force-displacement response for one hour duration 50 year return period wind event.

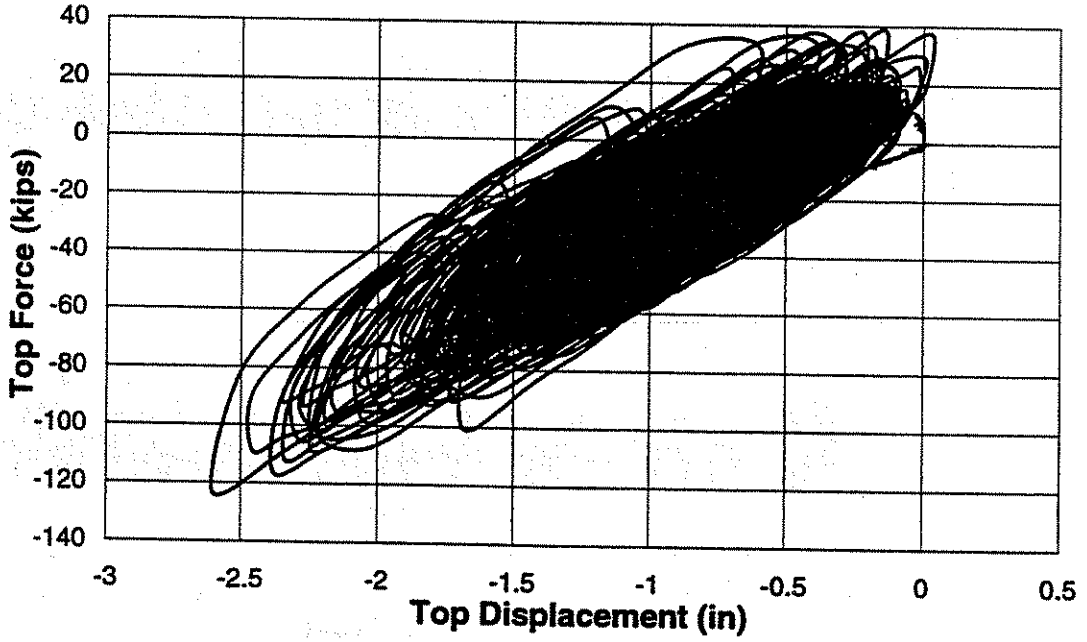

Fig. 7.16 - Measured overall force-displacement response for one hour duration 500 year return period wind event.

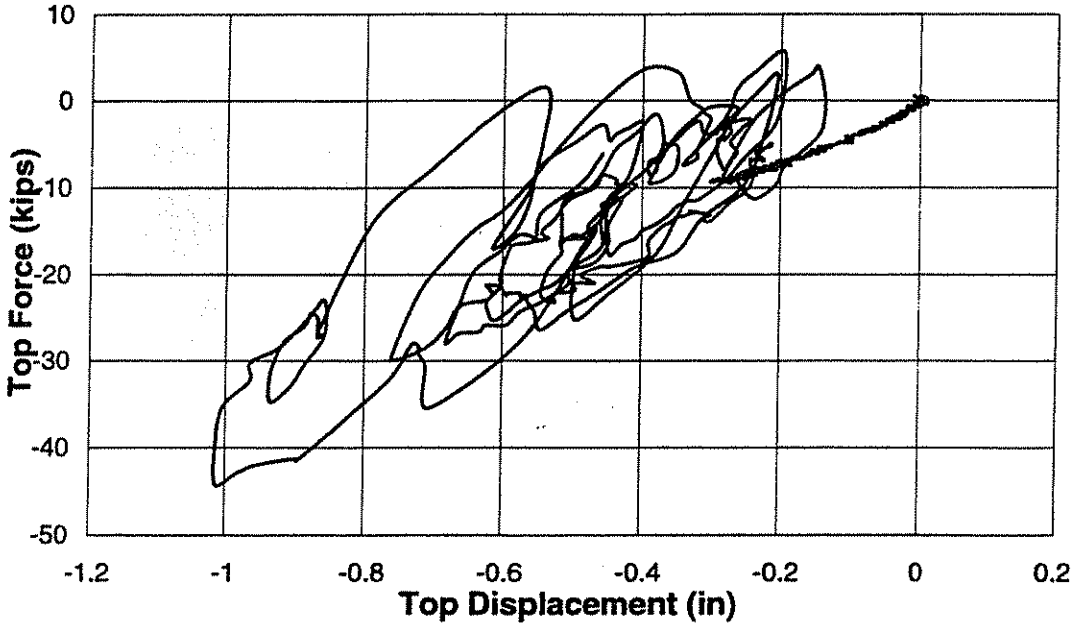

Fig. 7.17 - Measured overall force-displacement response at beginning of one hour duration 50 year return period wind event.

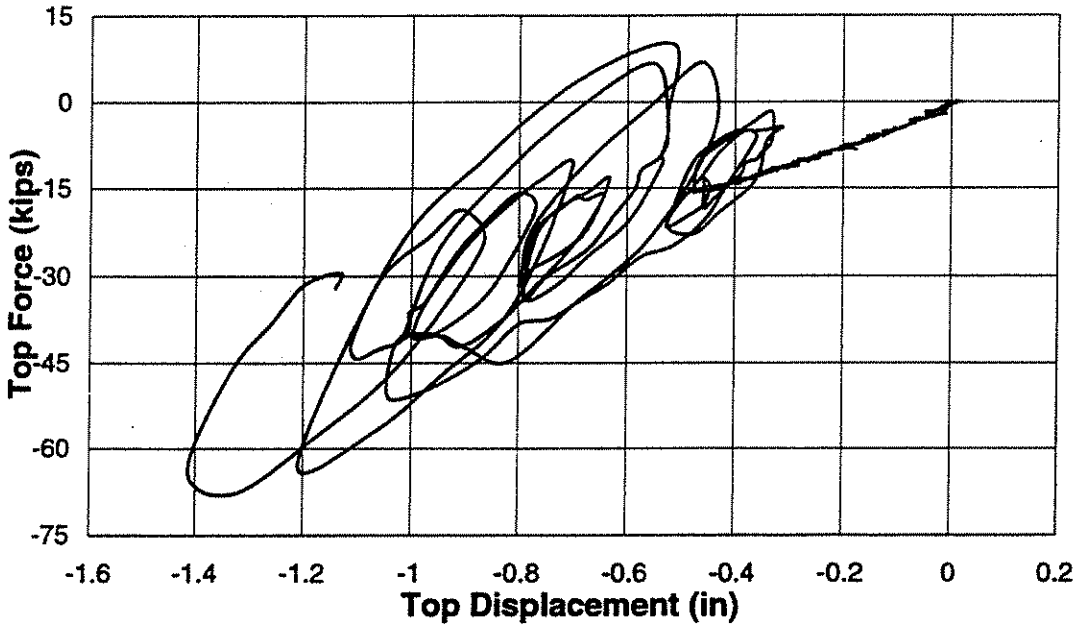

Fig. 7.18 - Measured overall force-displacement response at beginning of one hour duration 500 year return period wind event.

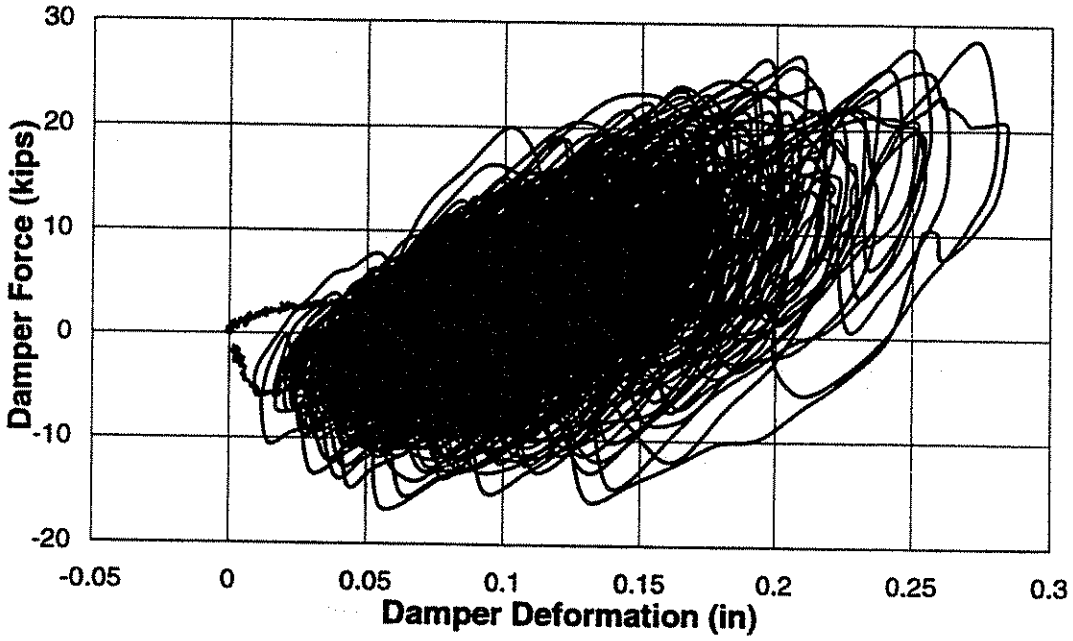

Fig. 7.19 - Example measured force-deformation response for East second story level damper during one hour duration 50 year return period wind event.

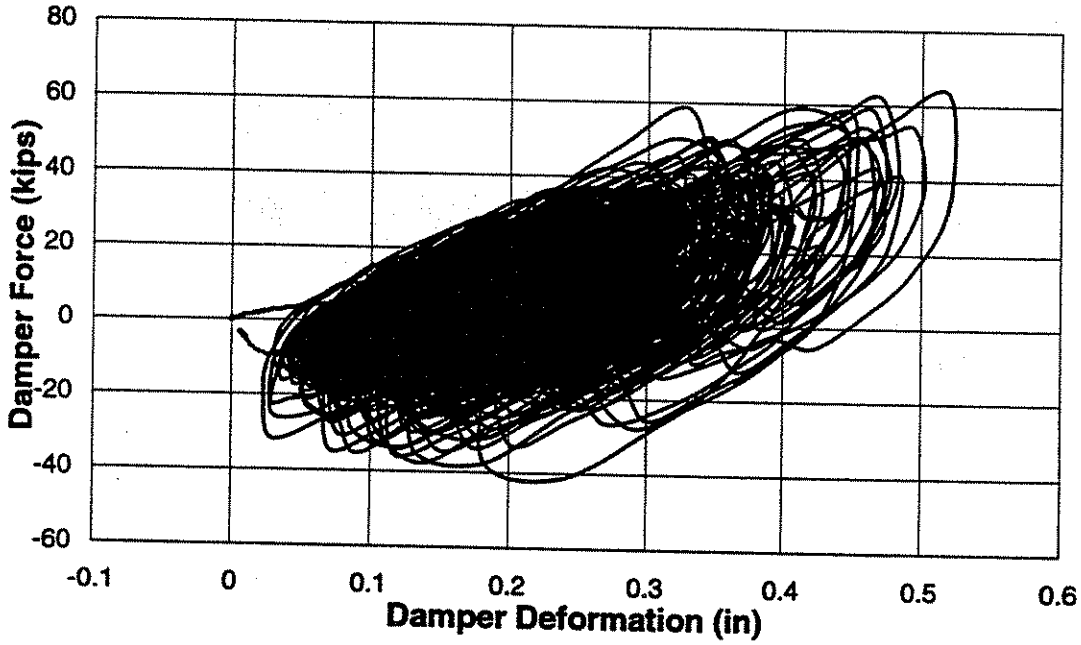

Fig. 7.20 - Example measured force-deformation response for East second story level damper during one hour duration 500 year return period wind event.

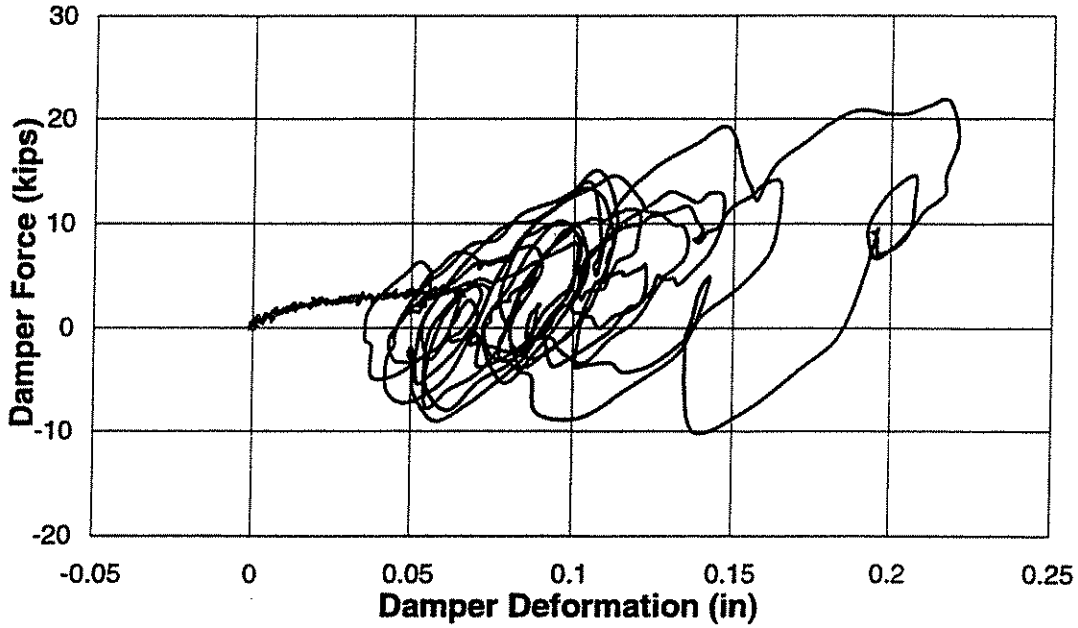

Fig. 7.21 - Example measured force-deformation response for East second story level damper at start of one hour duration 50 year return period wind event.

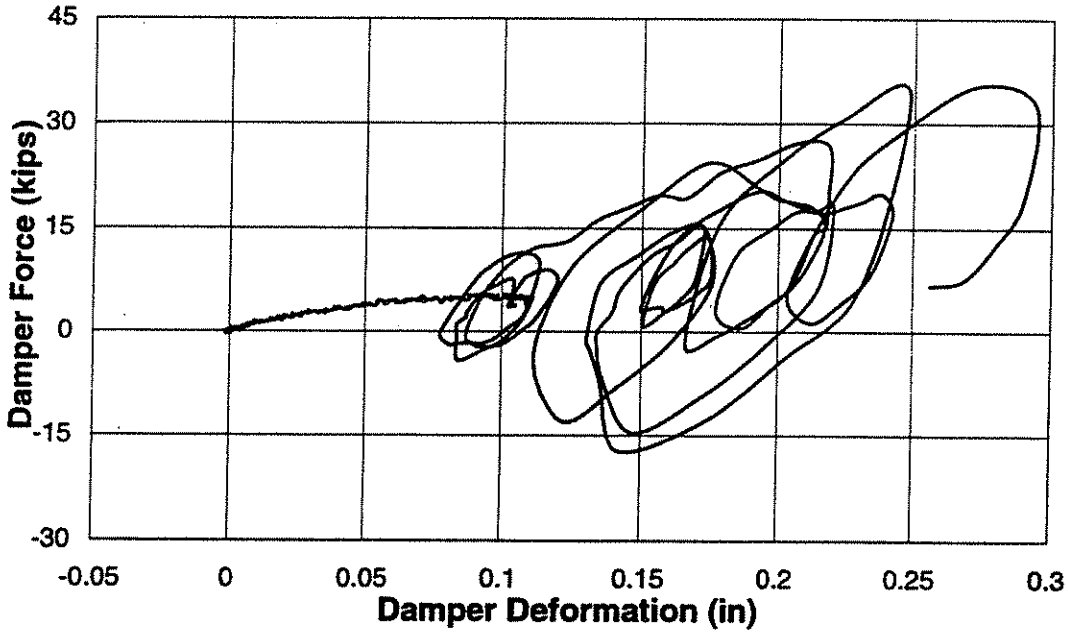

Fig. 7.22 - Example measured force-deformation response for East second story level damper at start of one hour duration 500 year return period wind event.

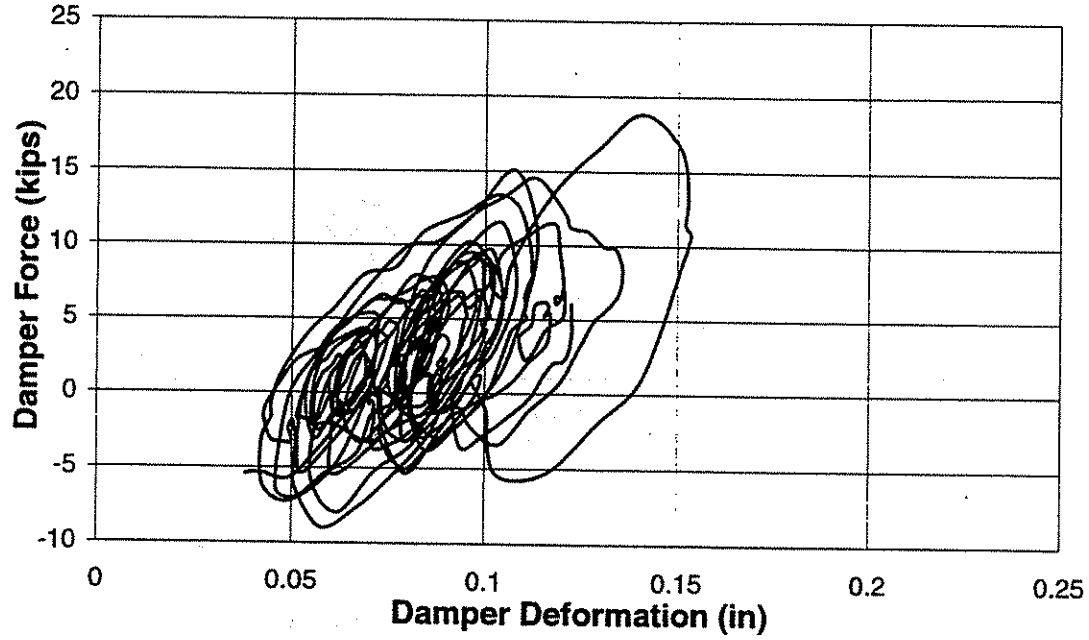

Fig. 7.23a - Example measured force-deformation response for East second story level damper near beginning of one hour duration 50 year return period wind event.

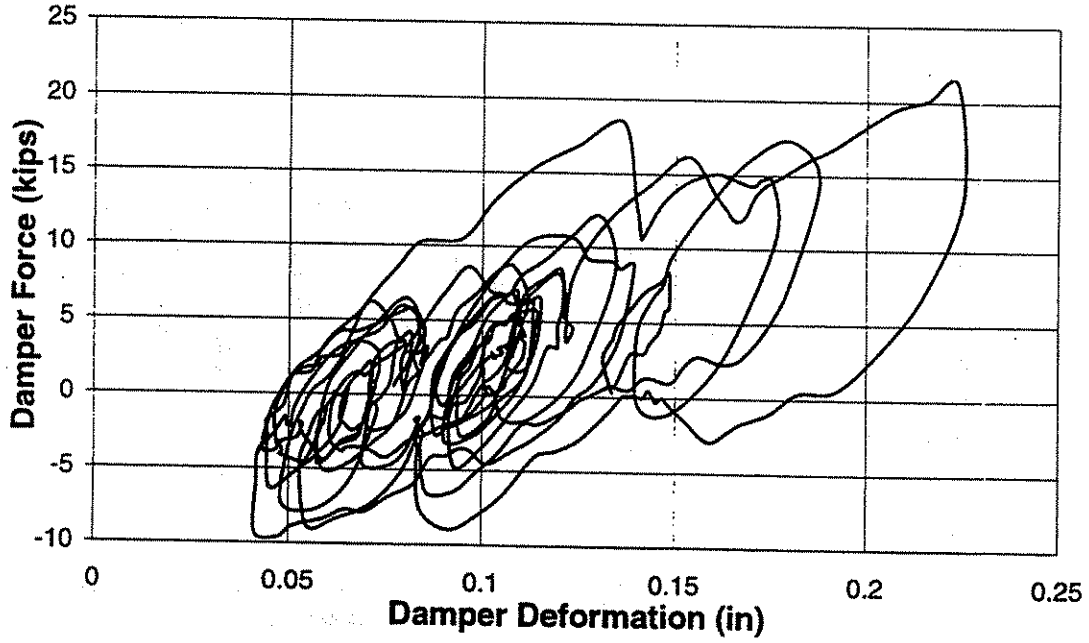

Fig. 7.23b - Example measured force-deformation response for East second story level damper near end of one hour duration 50 year return period wind event.

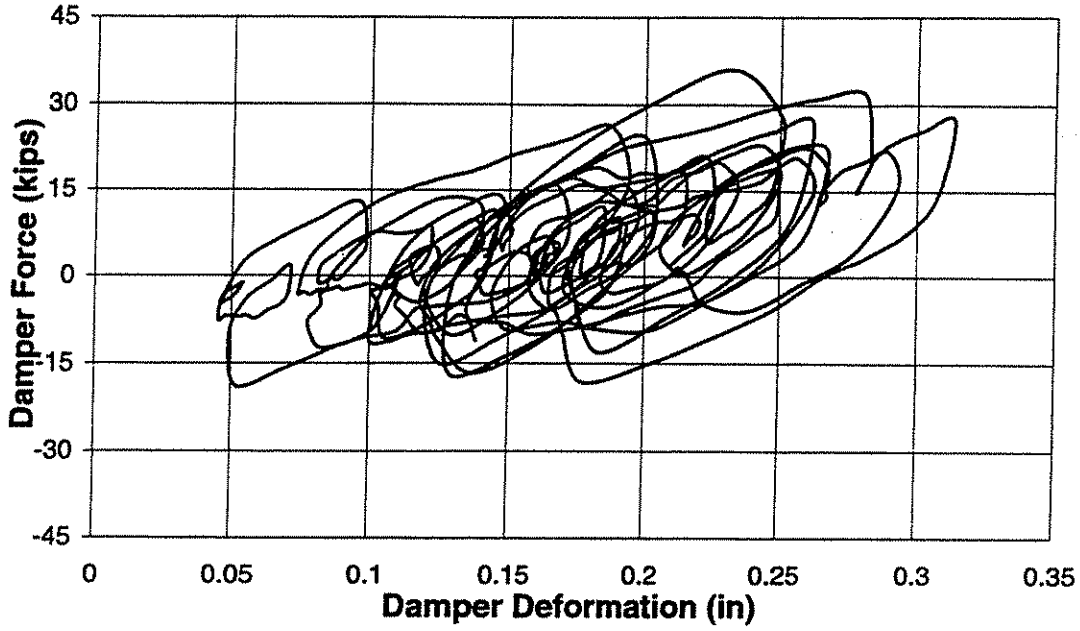

Fig. 7.24a - Example measured force-deformation response for East second story level damper near beginning of one hour duration 500 year return period wind event.

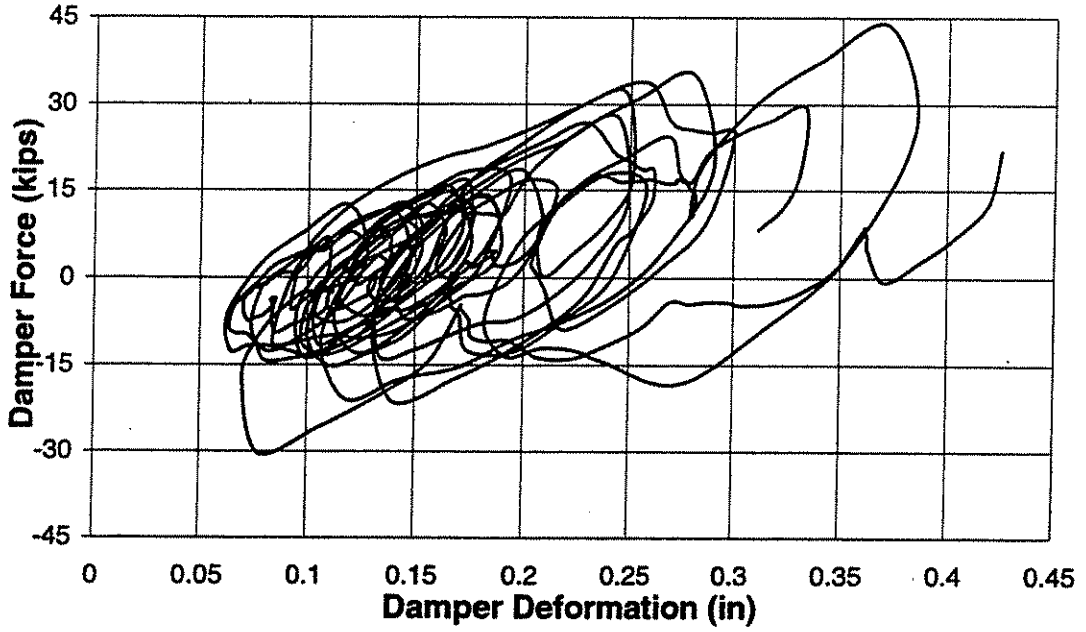

Fig. 7.24b - Example measured force-deformation response for East second story level damper near end of one hour duration 500 year return period wind event.

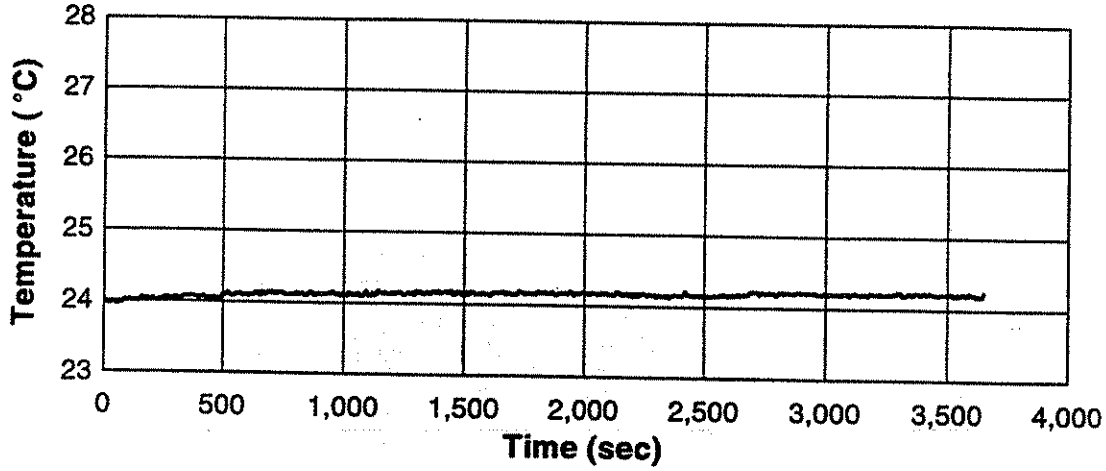

Fig. 7.25 - Example measured temperature rise for East second story level damper for one hour duration 50 year return period wind event.

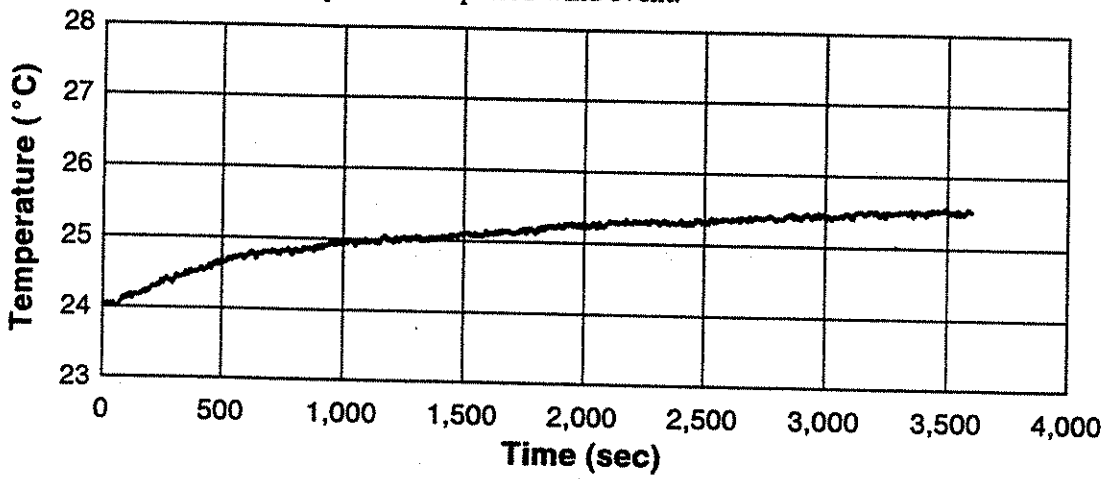

Fig. 7.26 - Example measured temperature rise for East second story level damper for one hour duration 500 year return period wind event.

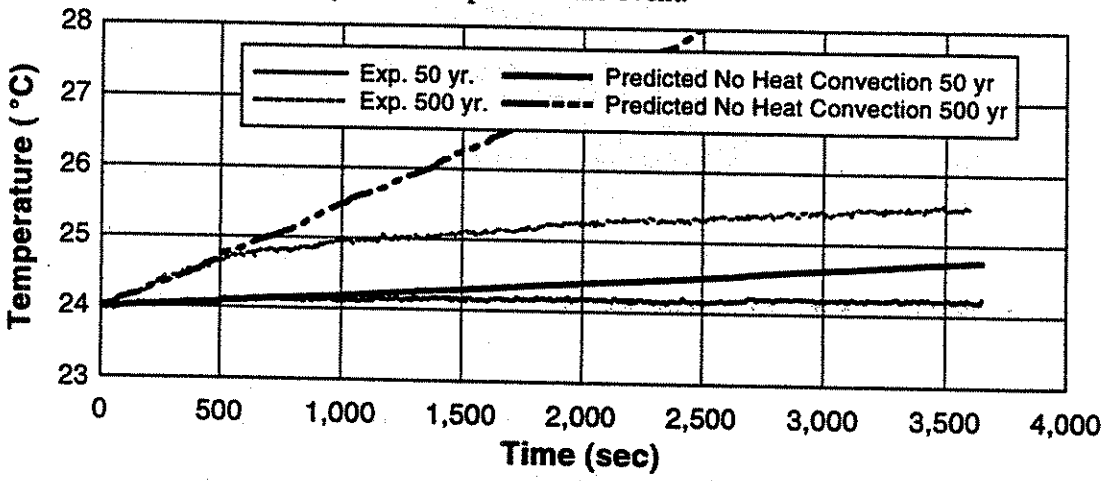

Fig. 7.27 - Comparison of measured damper temperature and predicted damper temperature if heat convection is neglected.

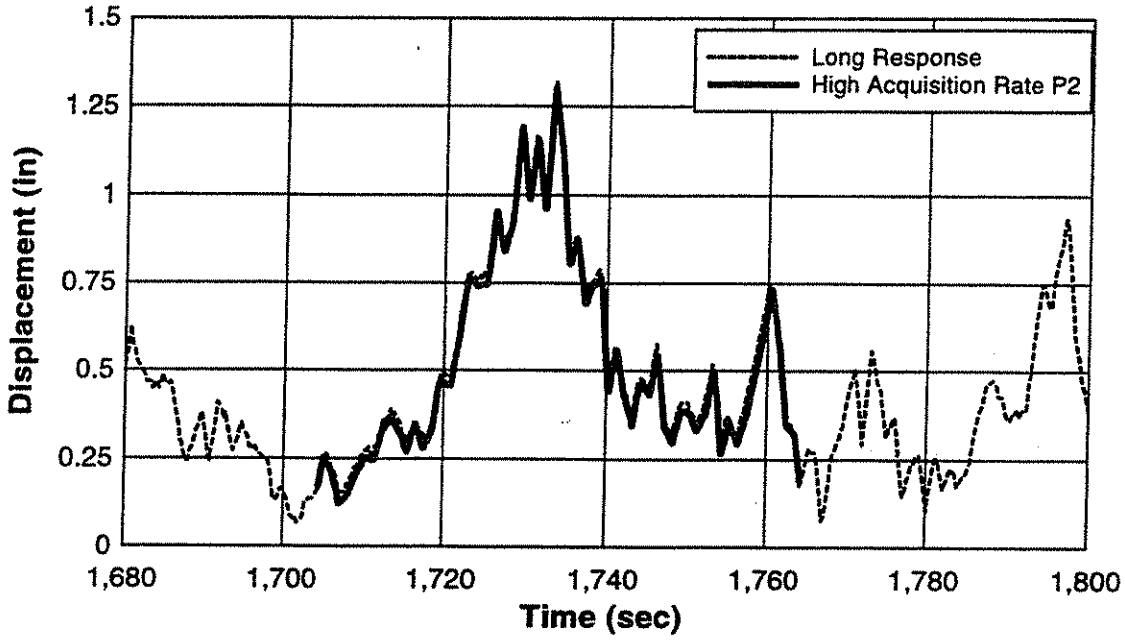

Fig. 7.28 - One minute segment of hour duration test with 100 hz data sampling rate for 50 year return period wind event.

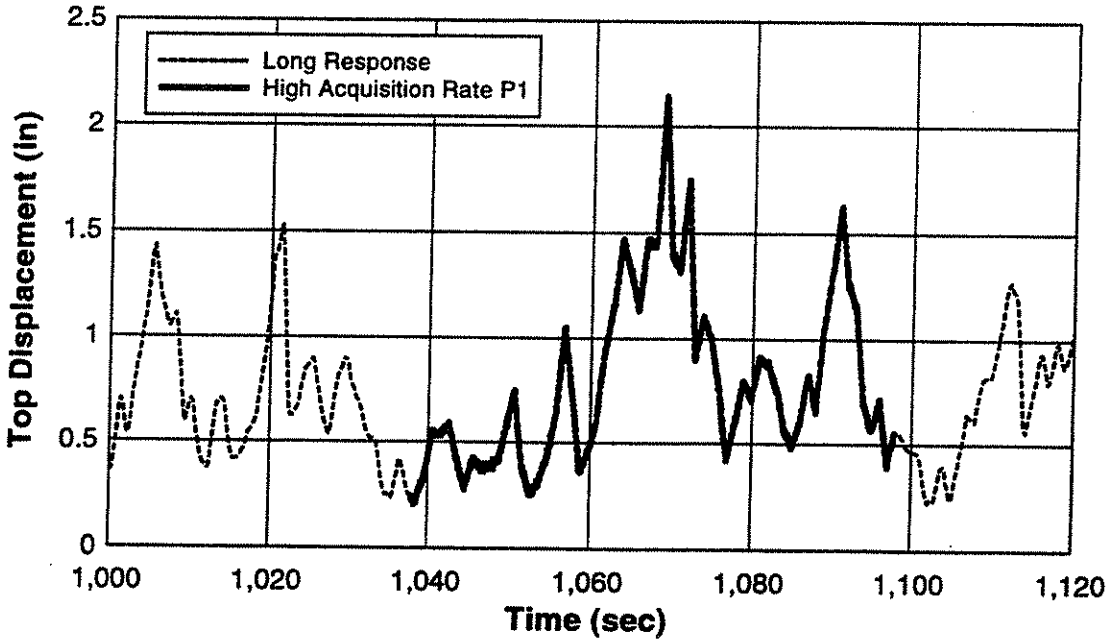

Fig. 7.29 - One minute segment of hour duration test with 100 hz data sampling rate for 500 year return period wind event.

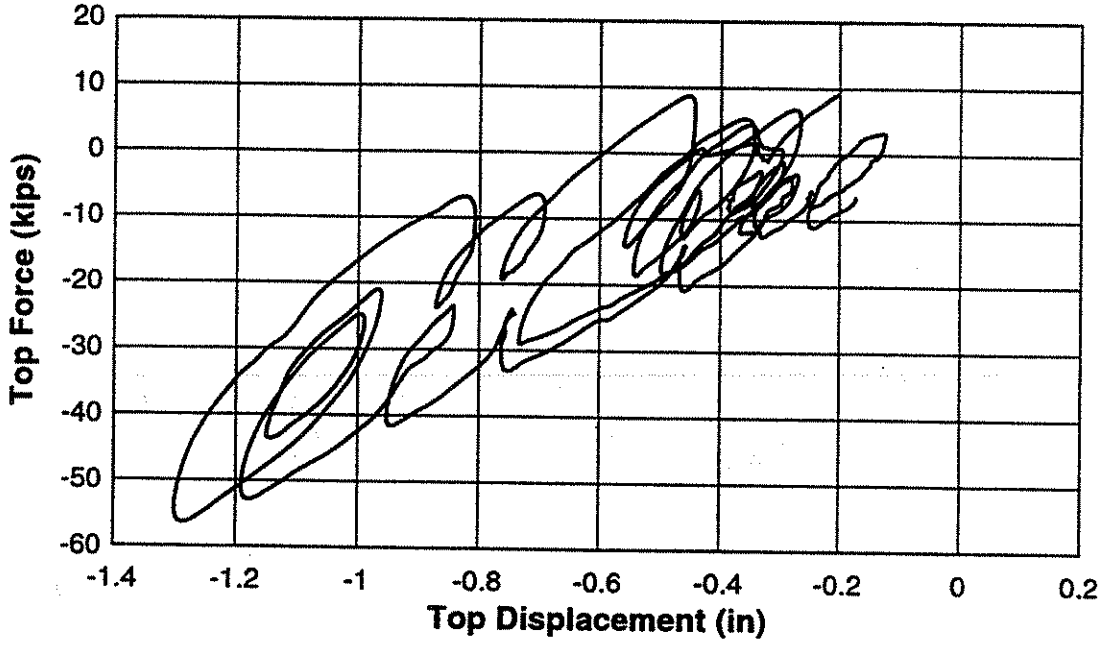

Fig. 7.30 - Measured overall force-displacement response for one minute segment of 50 year return period wind event.

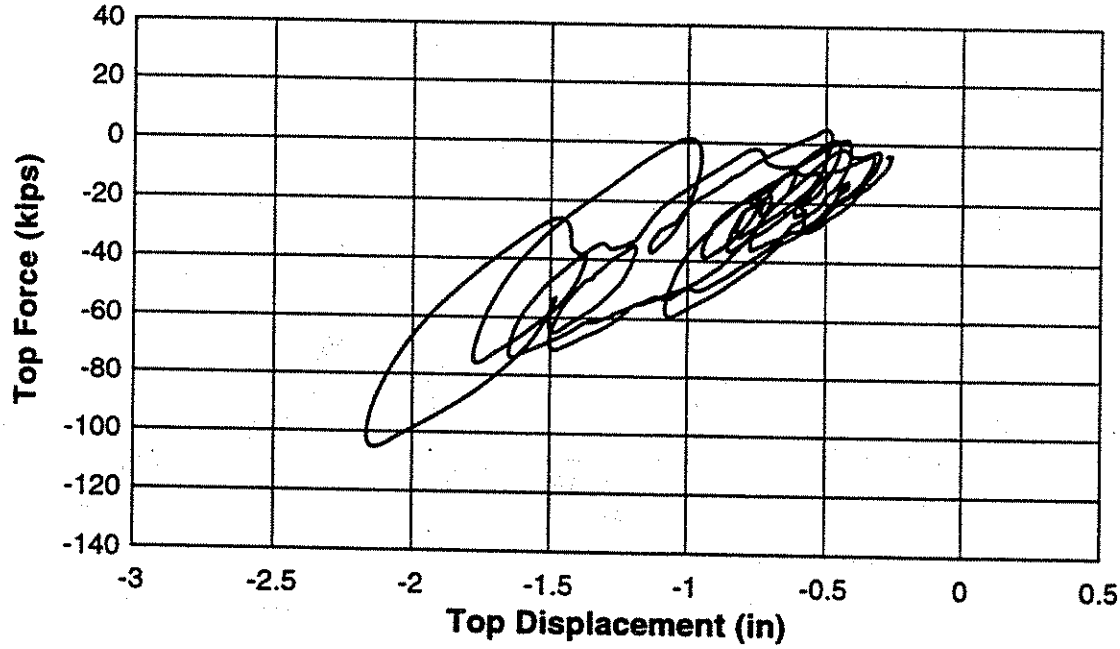

Fig. 7.31 - Measured overall force-displacement response for one minute segment of 500 year return period wind event.

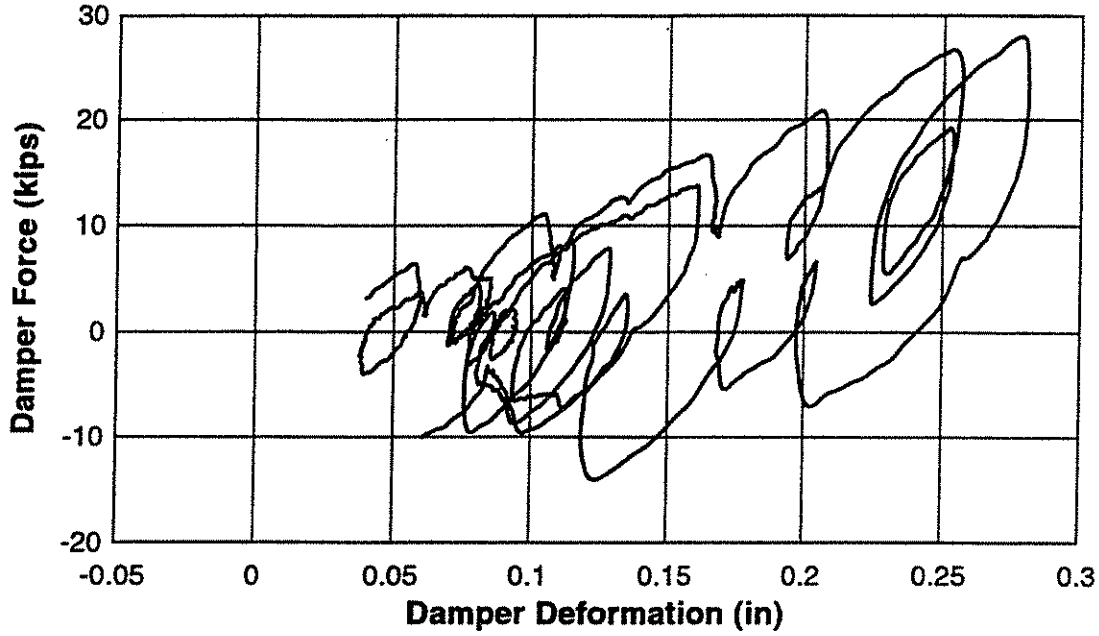

Fig. 7.32 - Example measured force-deformation response for East second story damper during one minute segment of 50 year return period wind event.

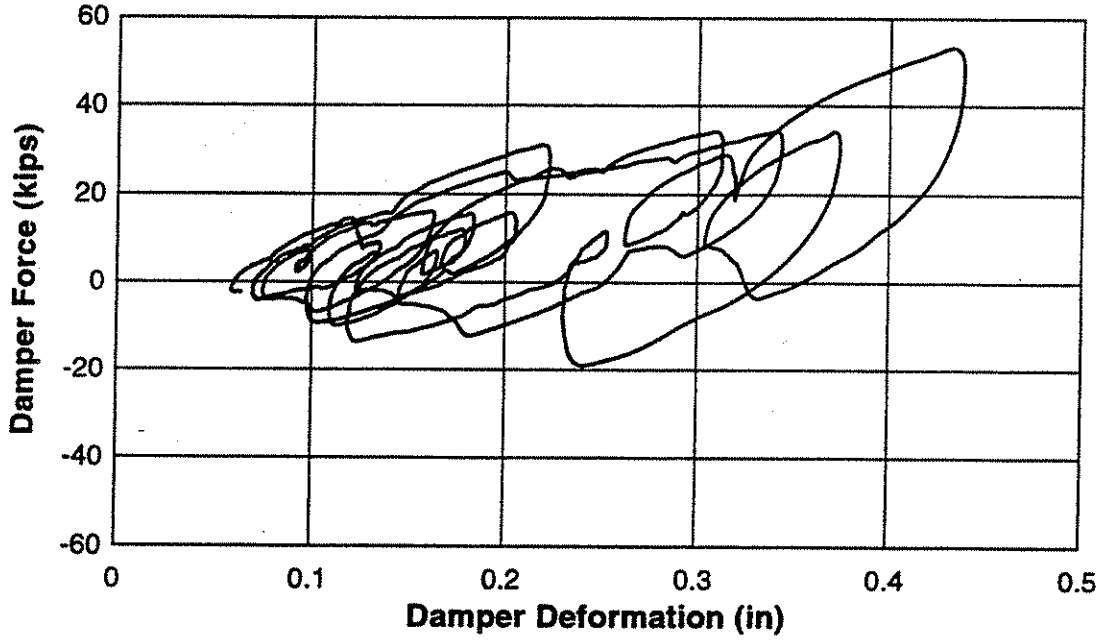

Fig. 7.33 - Example measured force-deformation response for East second story damper during one minute segment of 500 year return period wind event.

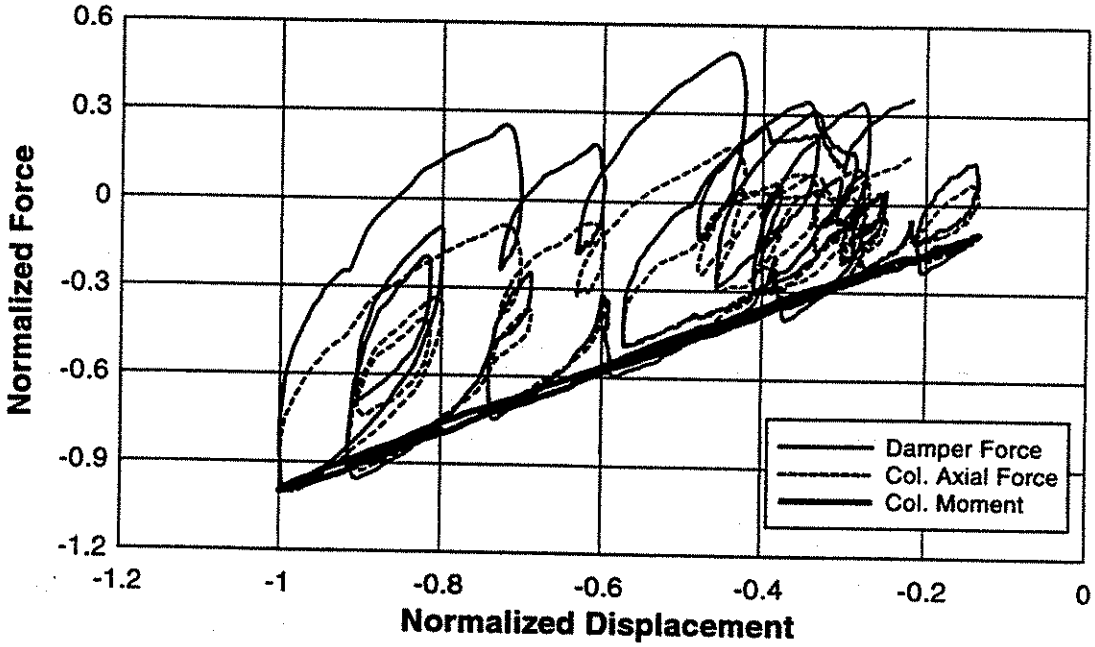

Fig. 7.34 - Example normalized force-deformation responses for East second story column and East second story damper during one minute segment of 50 year return period wind event.

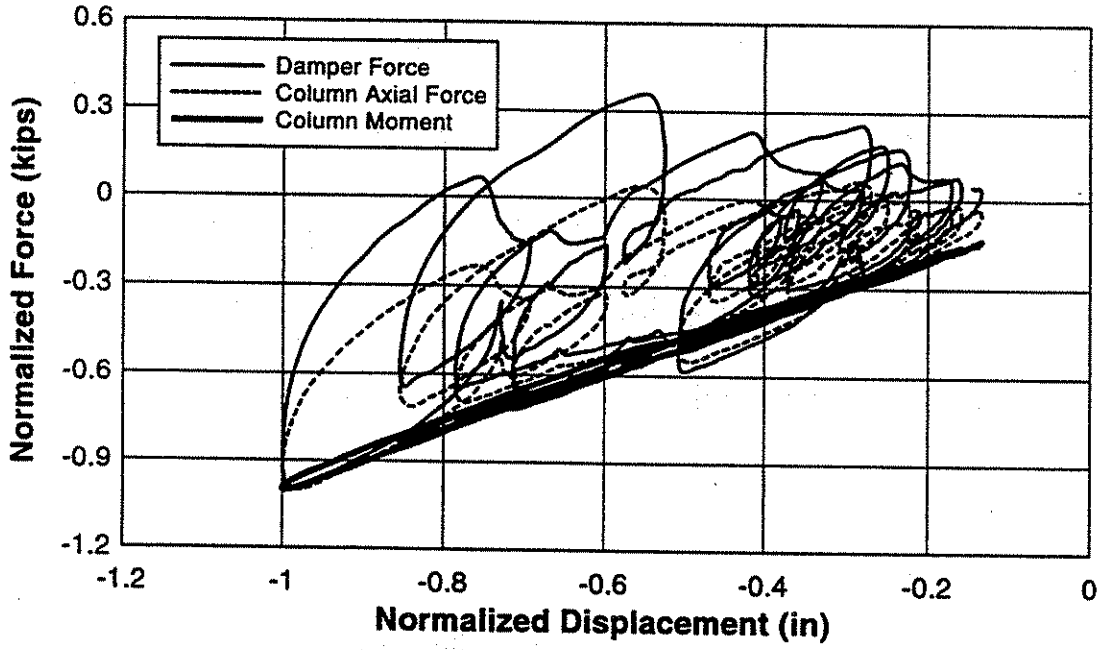

Fig. 7.35 - Example normalized force-deformation responses for East second story column and East second story damper during one minute segment of 500 year return period wind event.

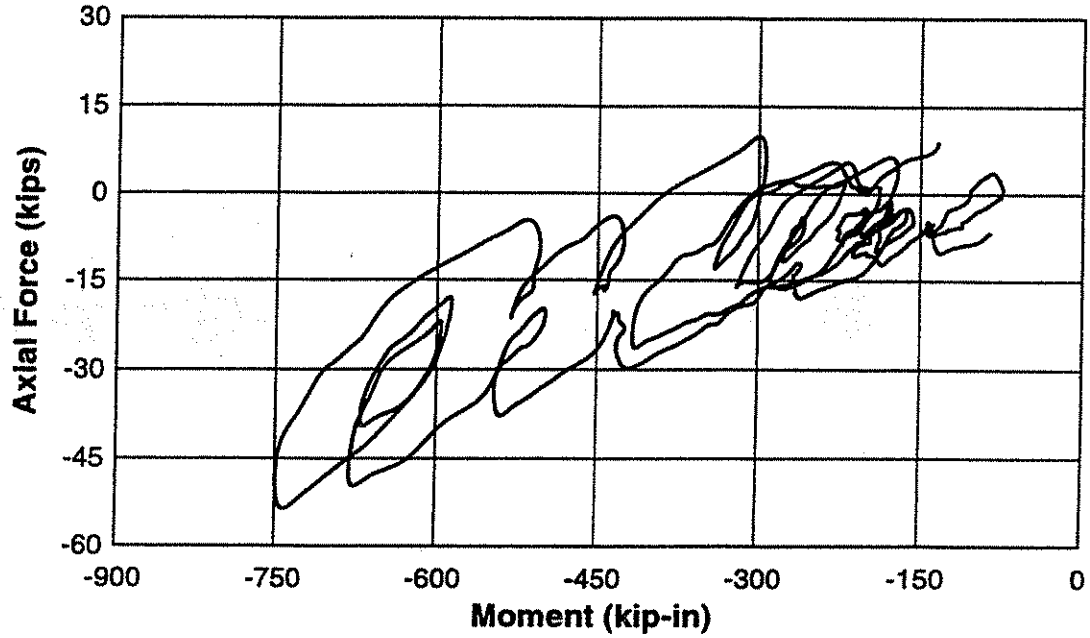

Fig. 7.36 - Example axial force-moment interaction for East second story column during one minute segment of 50 year return period wind event.

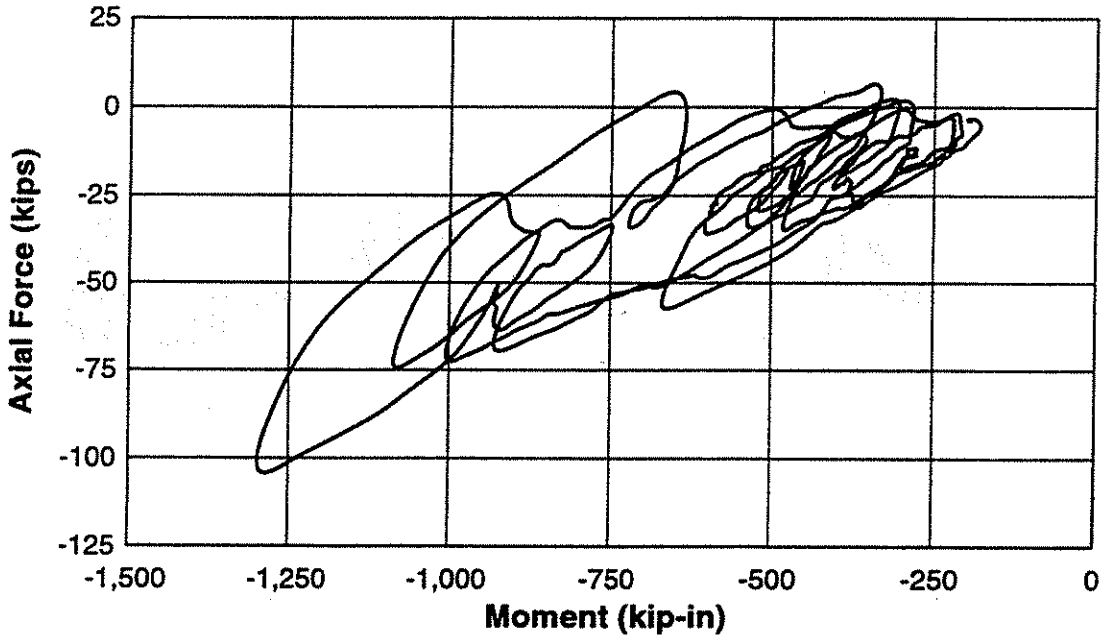

Fig. 7.37 - Example axial force-moment interaction for East second story column during one minute segment of 500 year return period wind event.

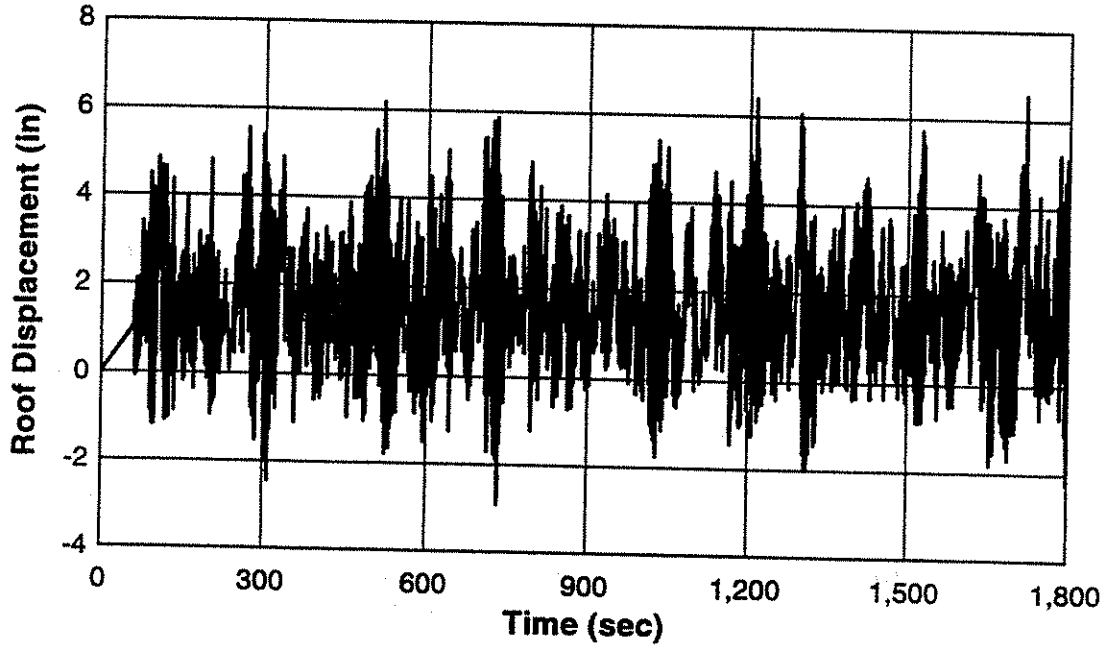

Fig. 7.38a - Predicted roof displacement during first half of 50 year return period wind event for wind prototype frame without dampers.

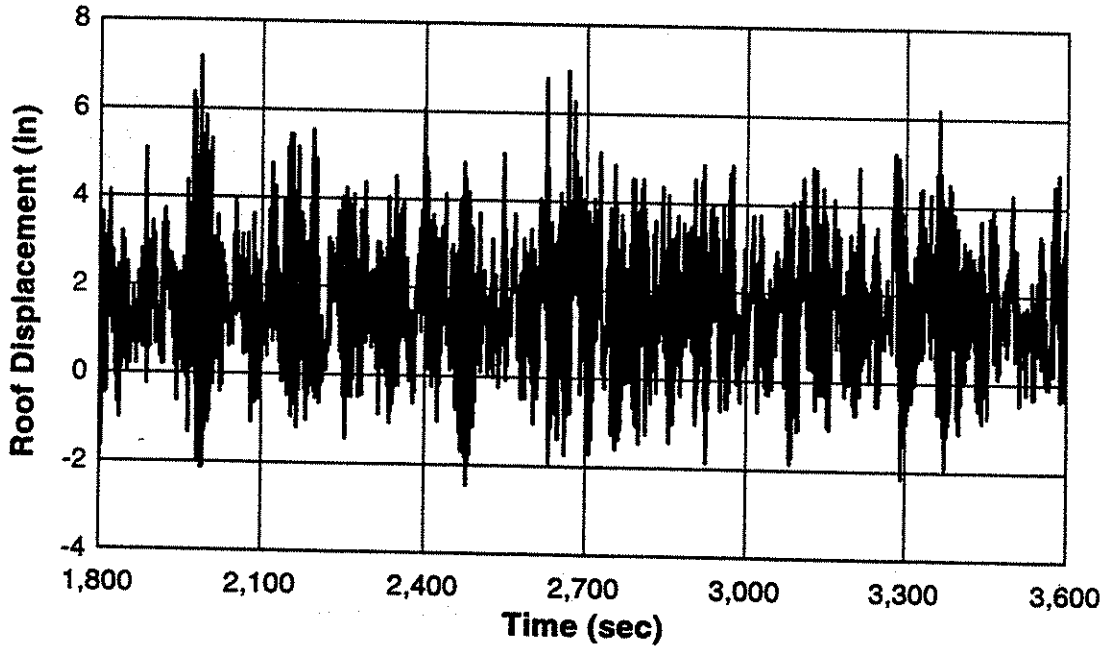

Fig. 7.38b - Predicted roof displacement during second half of 50 year return period wind event for wind prototype frame without dampers.

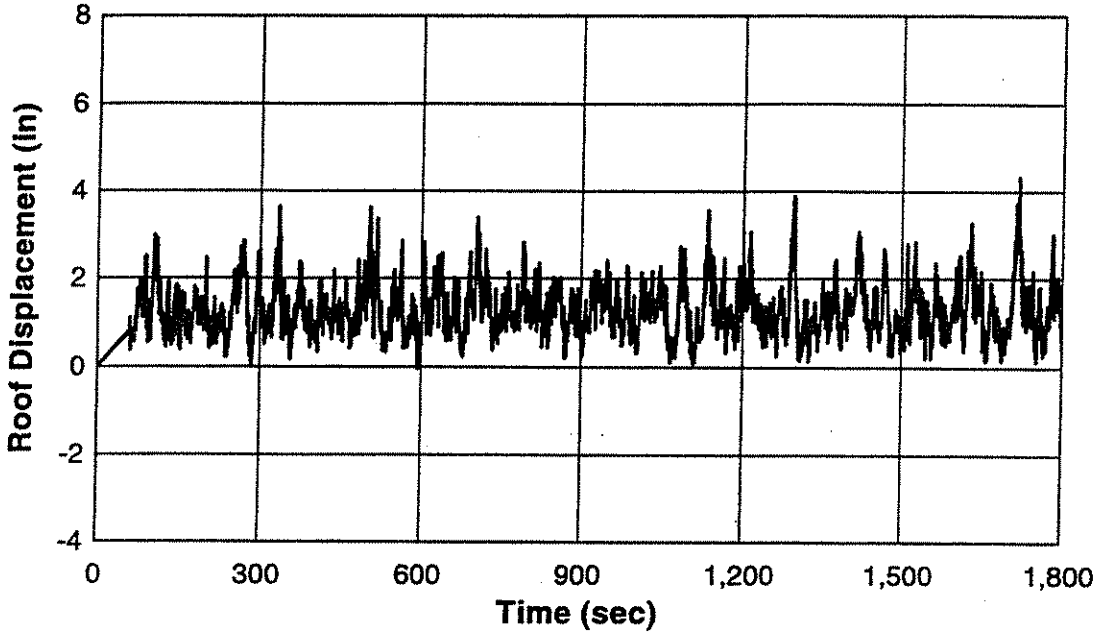

Fig. 7.39a - Predicted roof displacement during first half of 50 year return period wind event for wind prototype frame with VE-dampers.

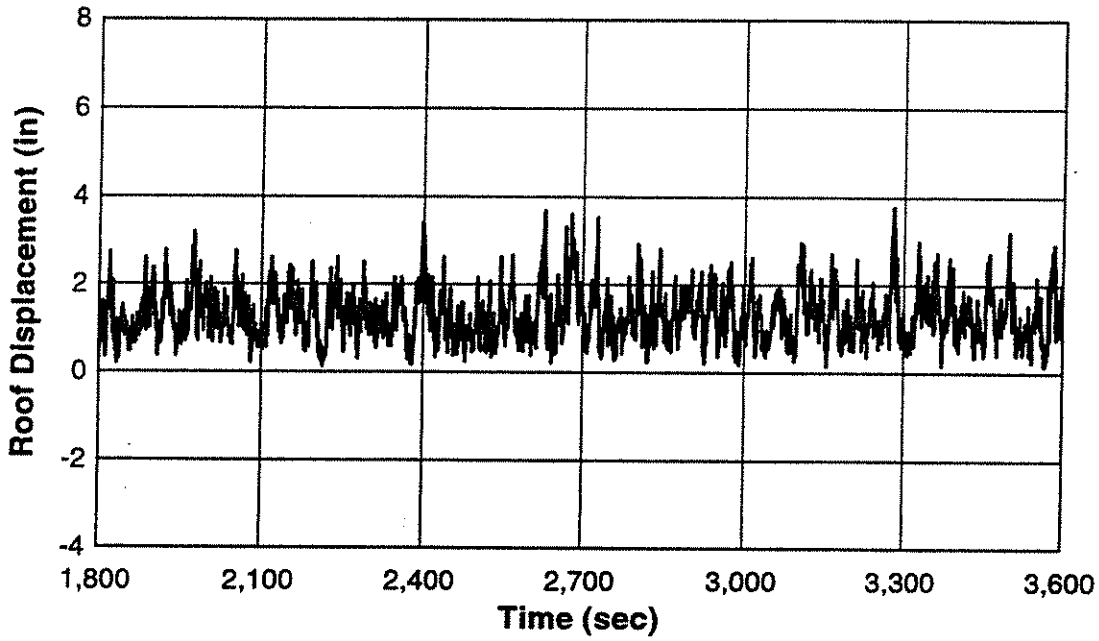

Fig. 7.39b - Predicted roof displacement during second half of 50 year return period wind event for wind prototype frame with VE-dampers.

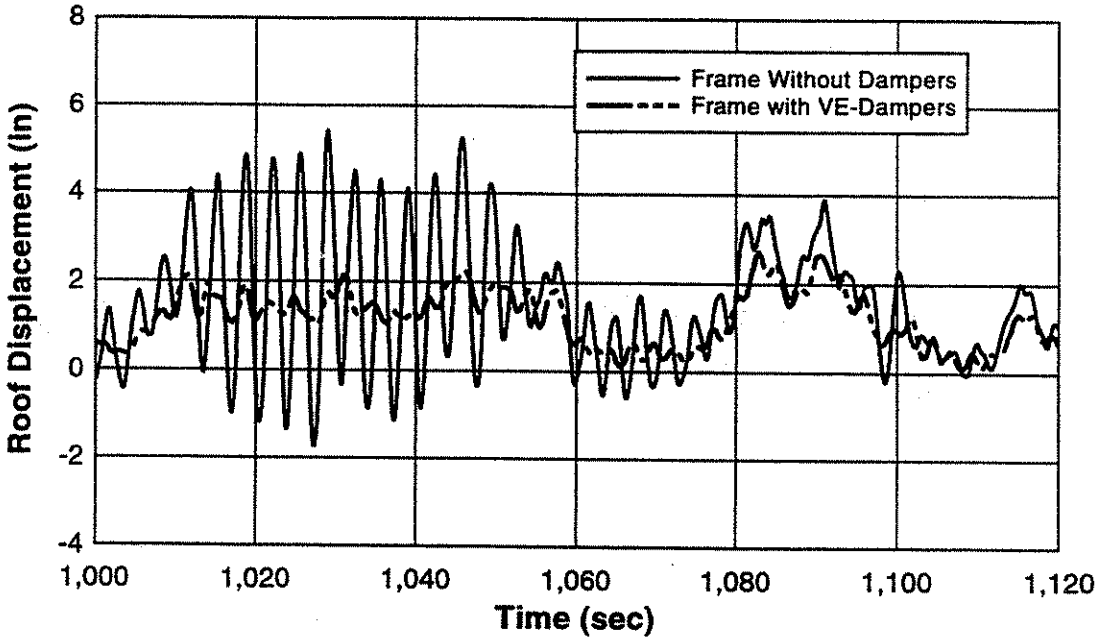

Fig. 7.40 - Two minute portion of roof displacement response for wind prototype frame with and without VE-dampers.

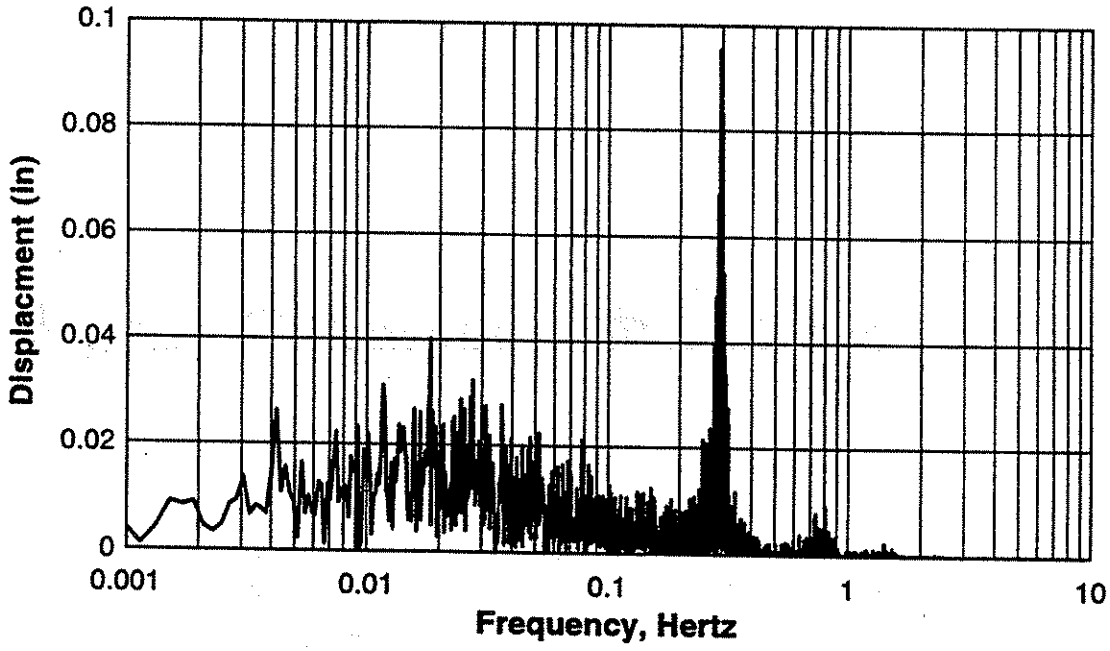

Fig. 7.41 - FFT of roof displacement response for wind prototype frame without VE-dampers.

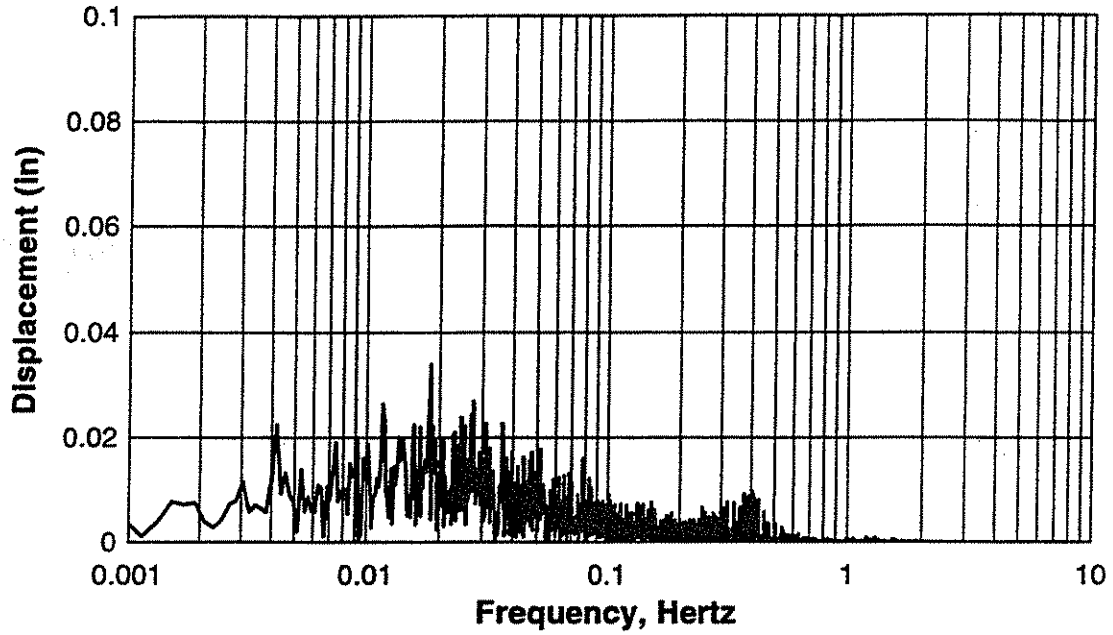

Fig. 7.42 - FFT of roof displacement response for wind prototype frame with VE-dampers.

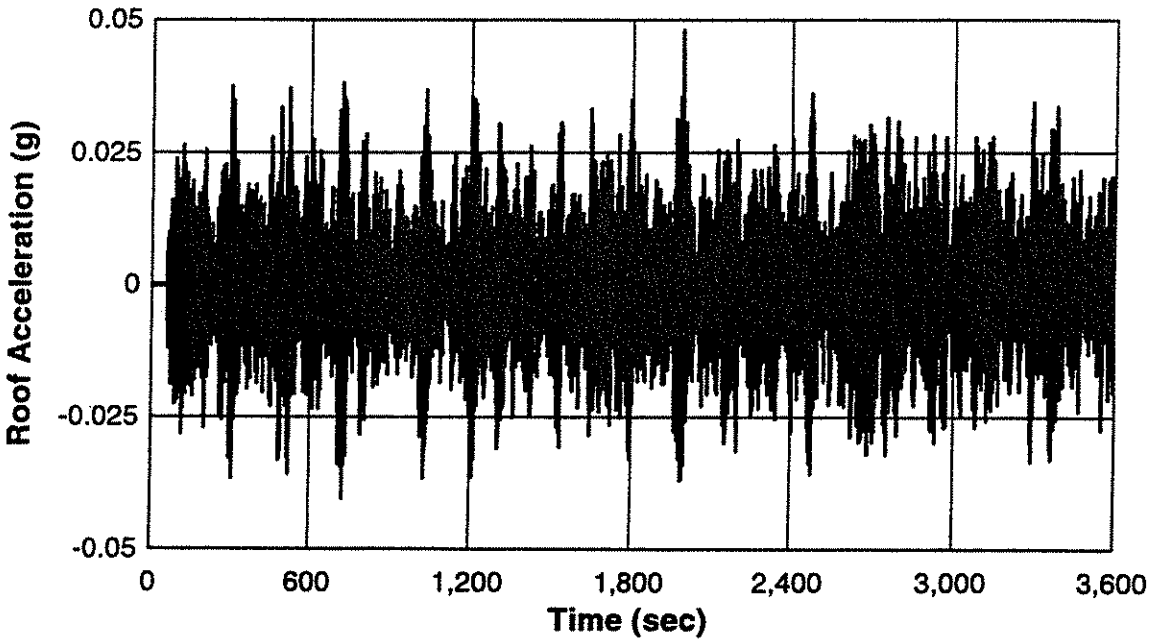

Fig. 7.43 - Roof acceleration for wind prototype frame without VE-dampers.

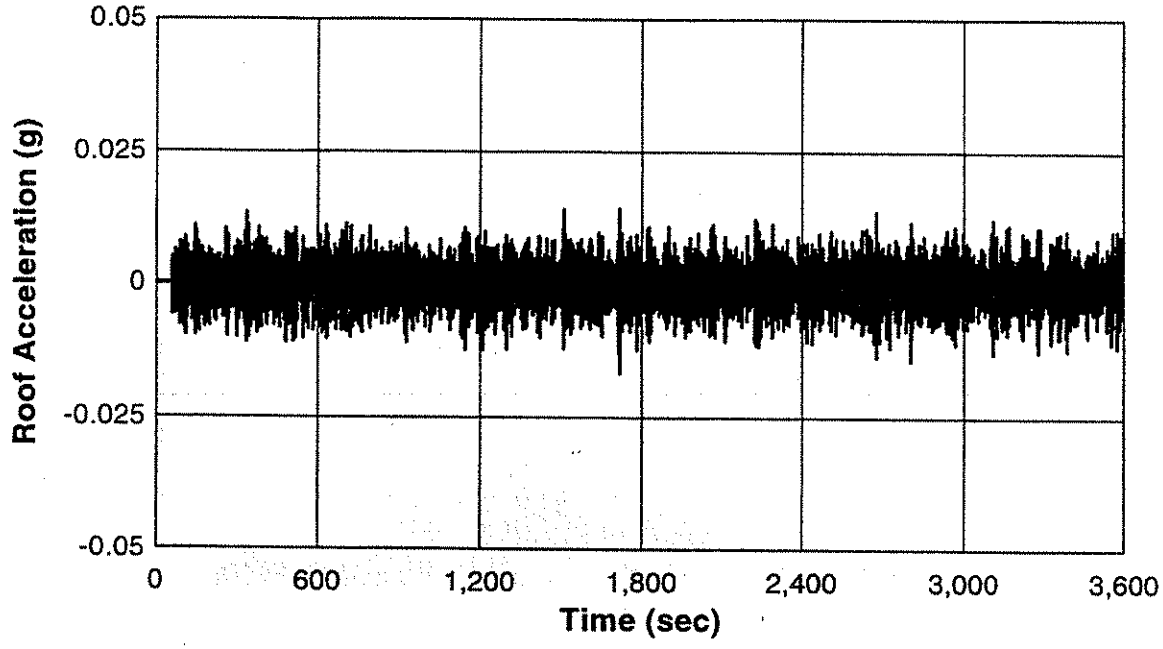

Fig. 7.44 - Roof acceleration for wind prototype frame with VE-dampers.

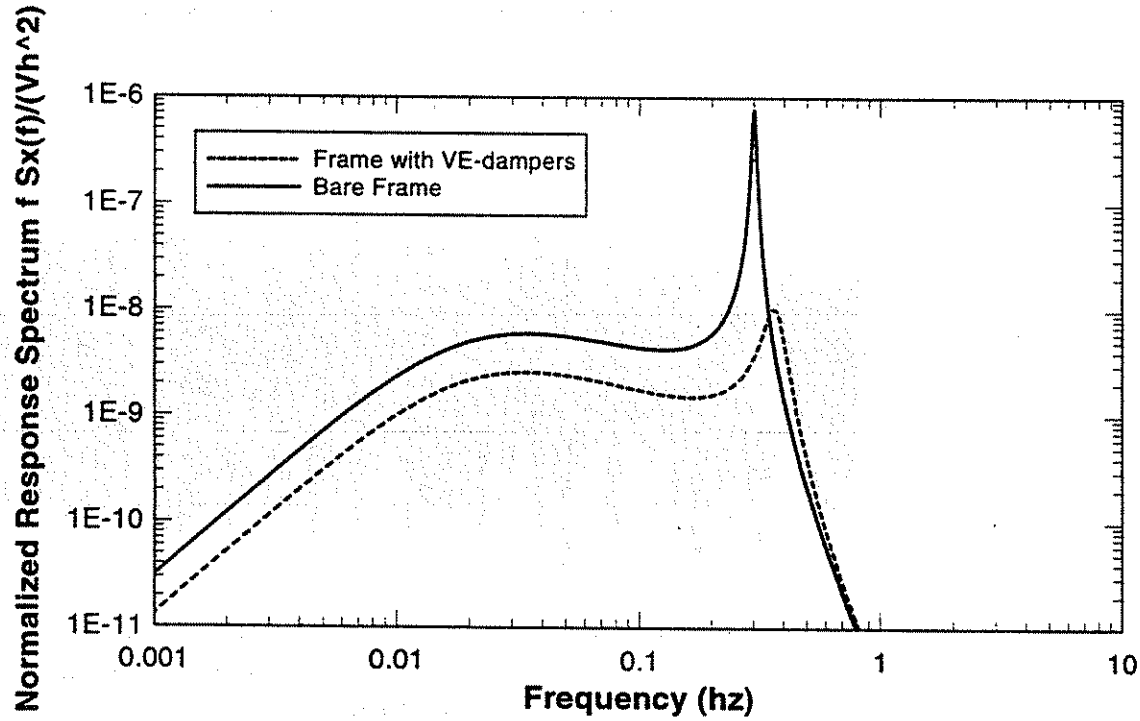

Fig. 7.45 - Along-wind displacement response spectrum for wind prototype frame with and without VE-dampers.

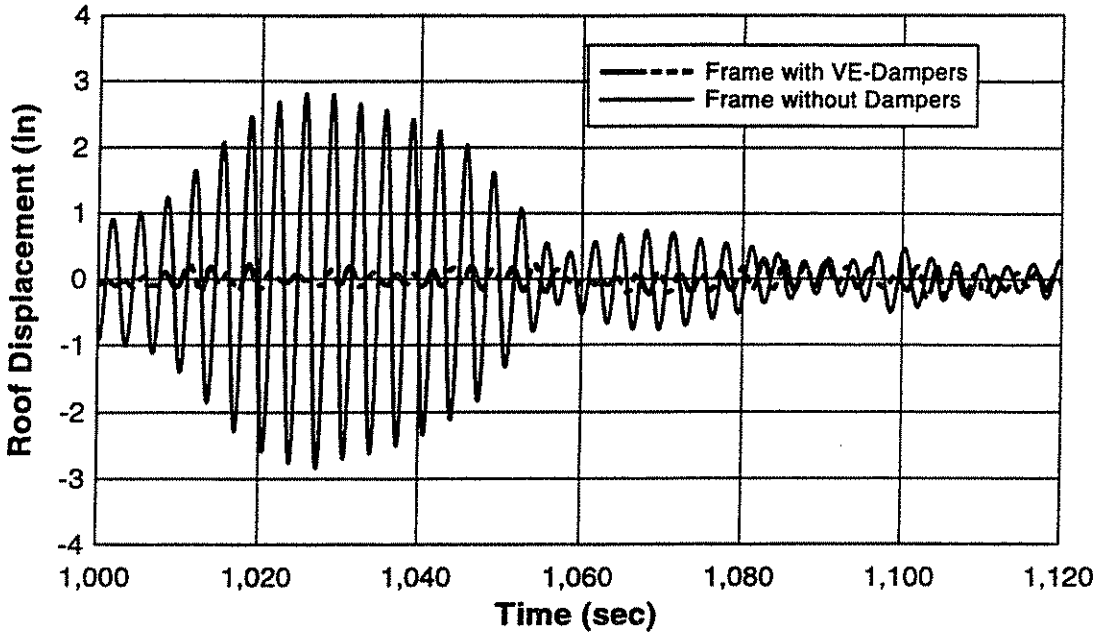

Fig. 7.46 - Natural frequency vibration component of roof displacement for wind prototype frame with and without VE-dampers.

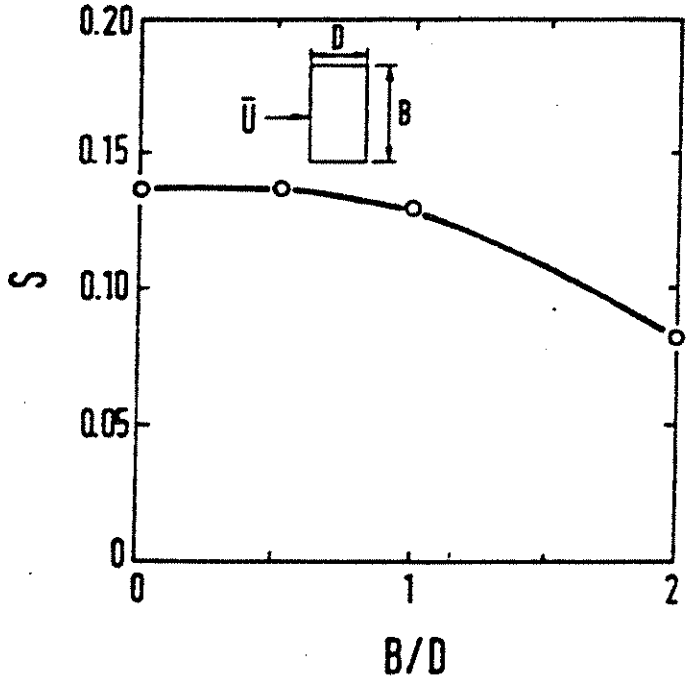

Fig. 7.47 - Strouhal numbers for rectangular cross section [Balandra, 1993].

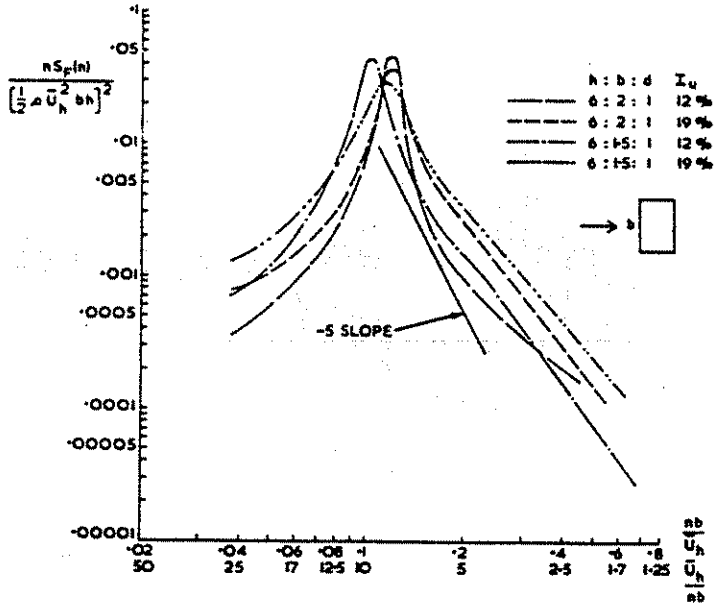

Fig. 7.48 - Across-wind force spectra for rectangular section [Saunders and Melbourne, 1975].

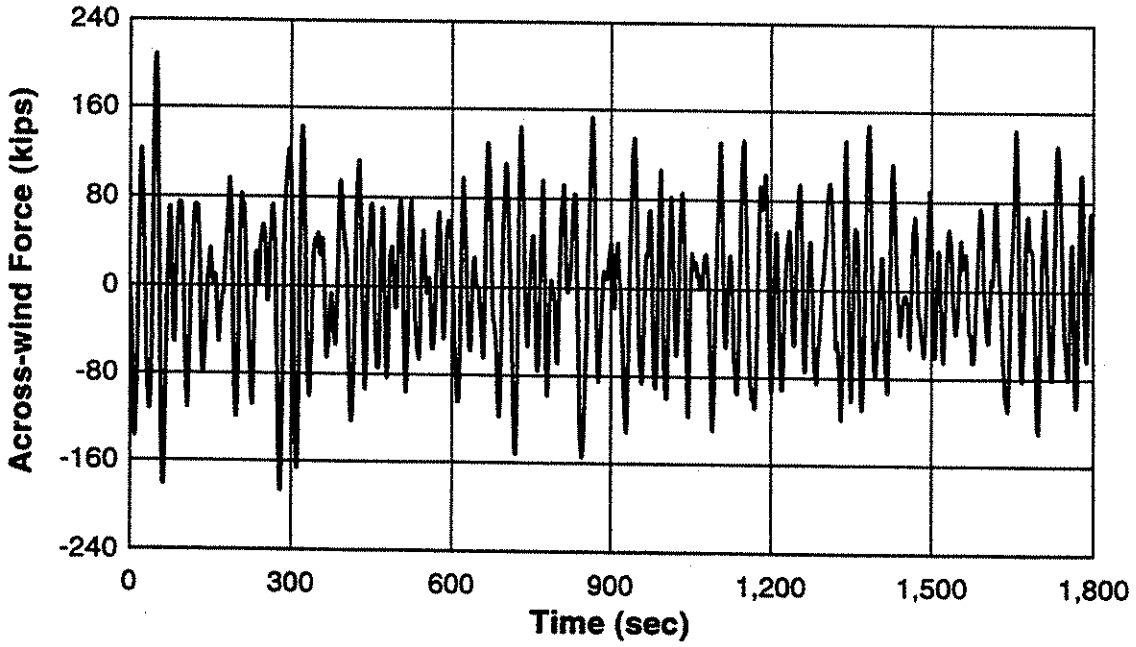

Fig. 7.49 - Simulated across-wind force for 50 year return period wind event.

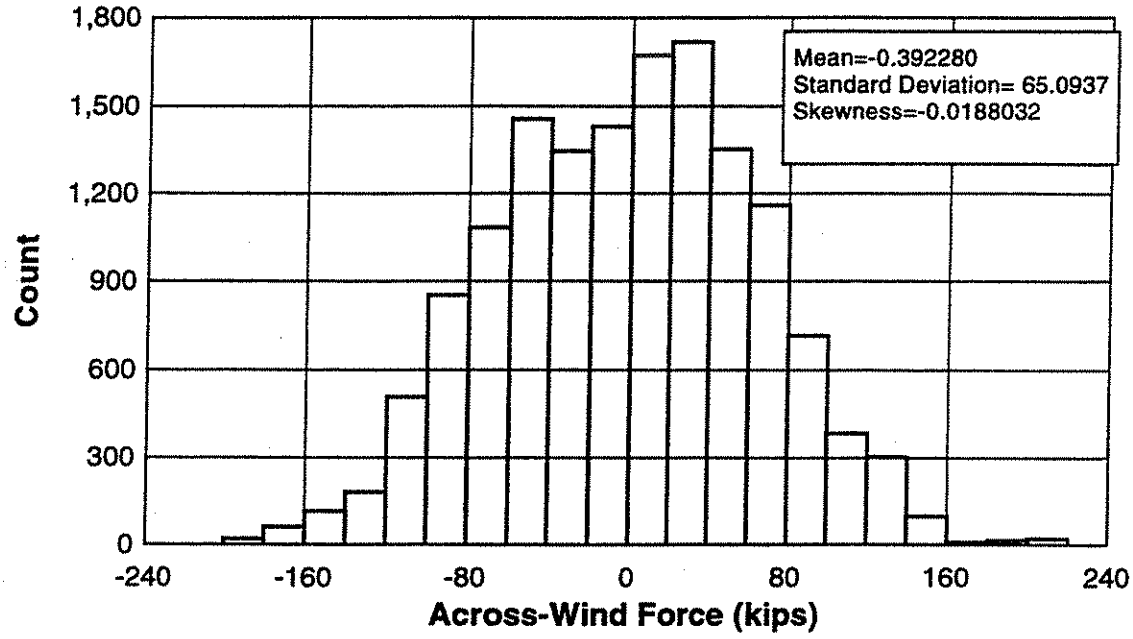

Fig. 7.50 - Distribution of simulated across-wind force for 50 year return period wind event.

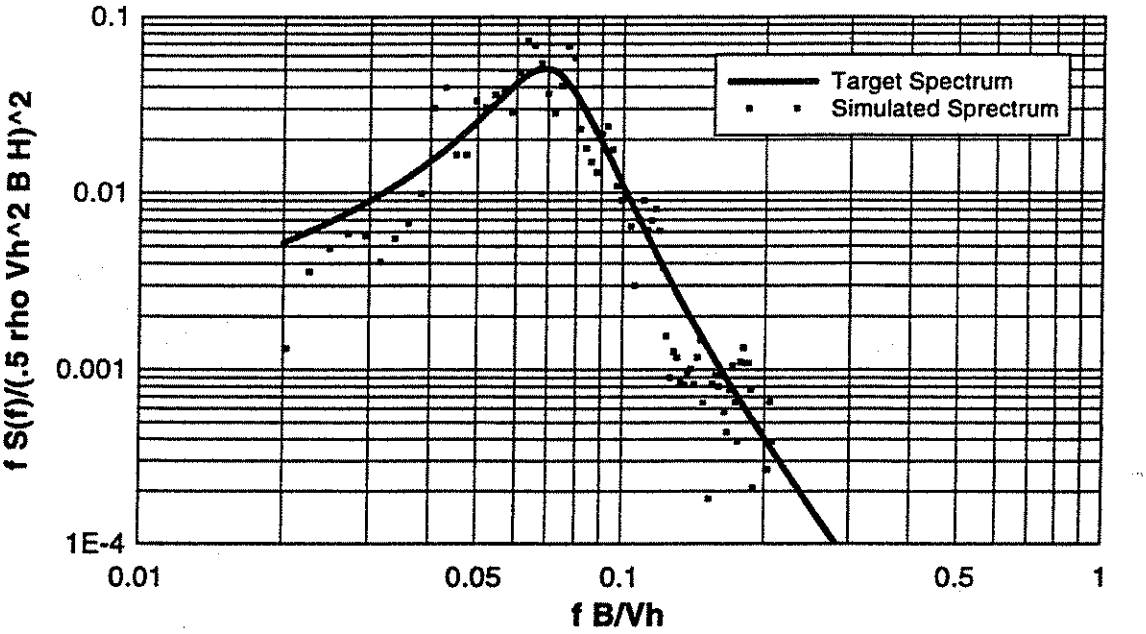

Fig. 7.51 - Comparison of target and simulated across-wind force spectra.

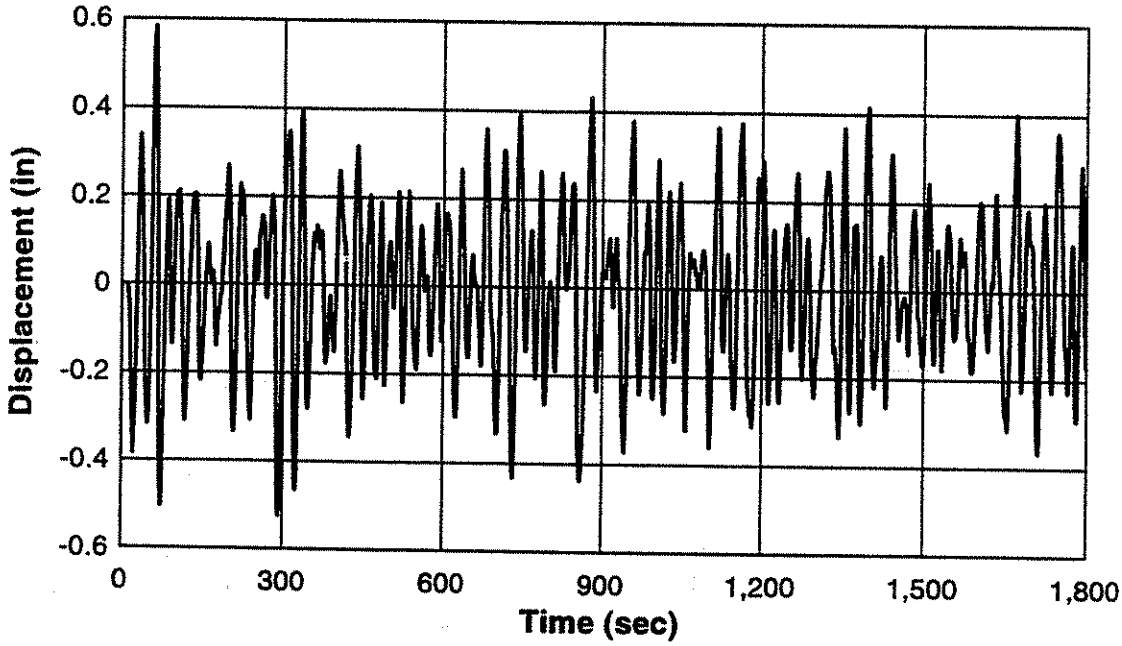

Fig. 7.52 - Predicted across-wind displacement response at third story.

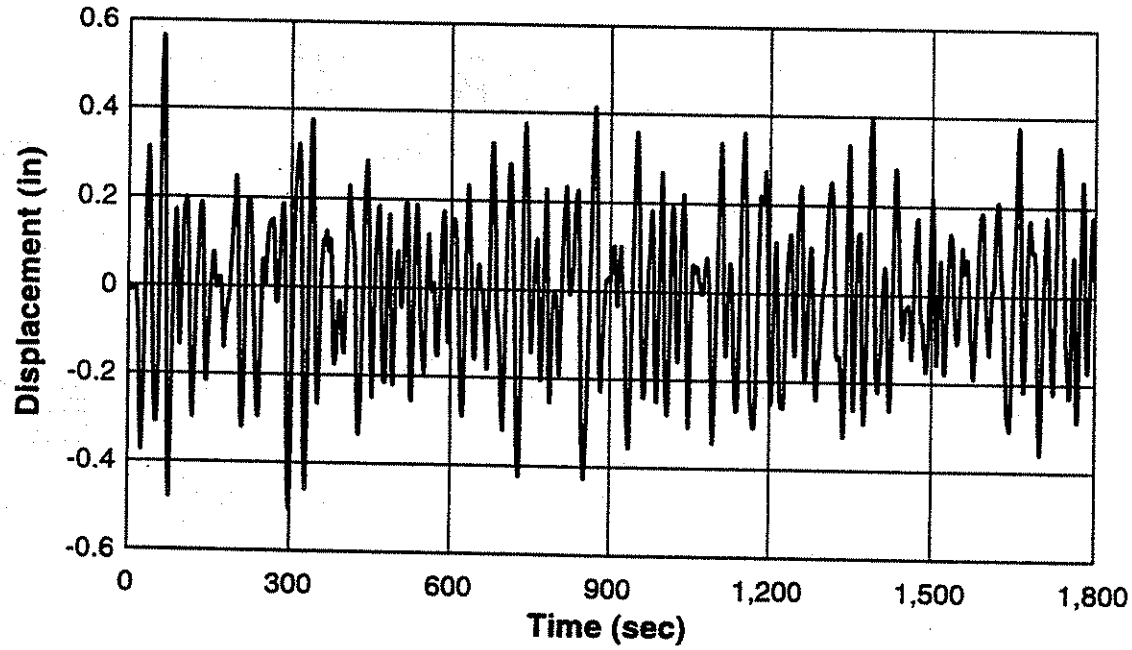

Fig. 7.53 - Measured across-wind displacement response at third story.

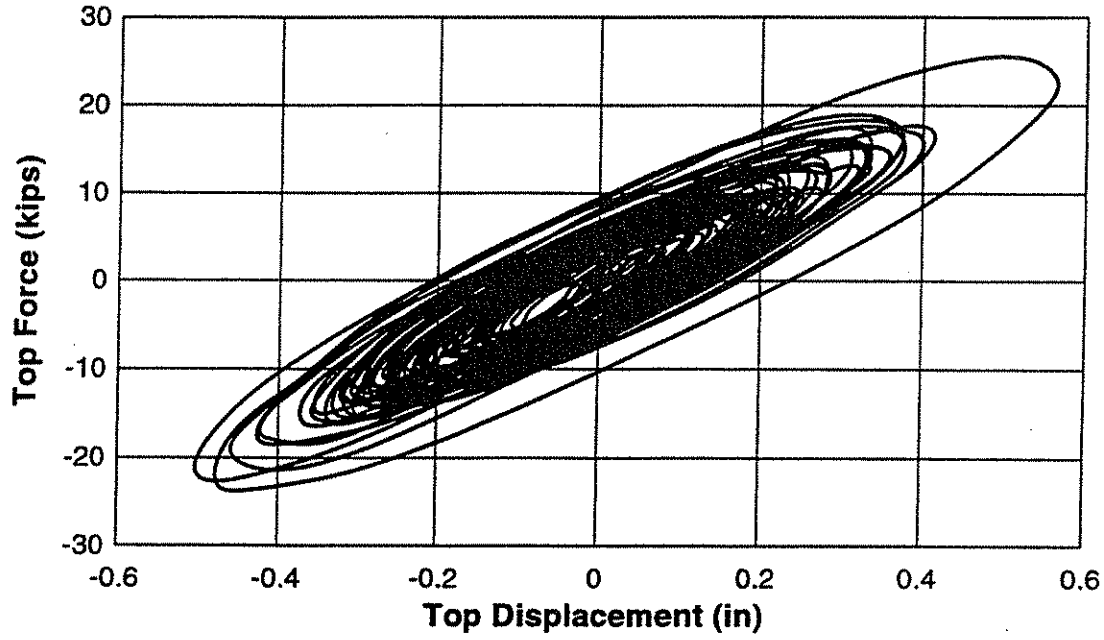

Fig. 7.54 - Measured overall force-displacement response for across-wind test.

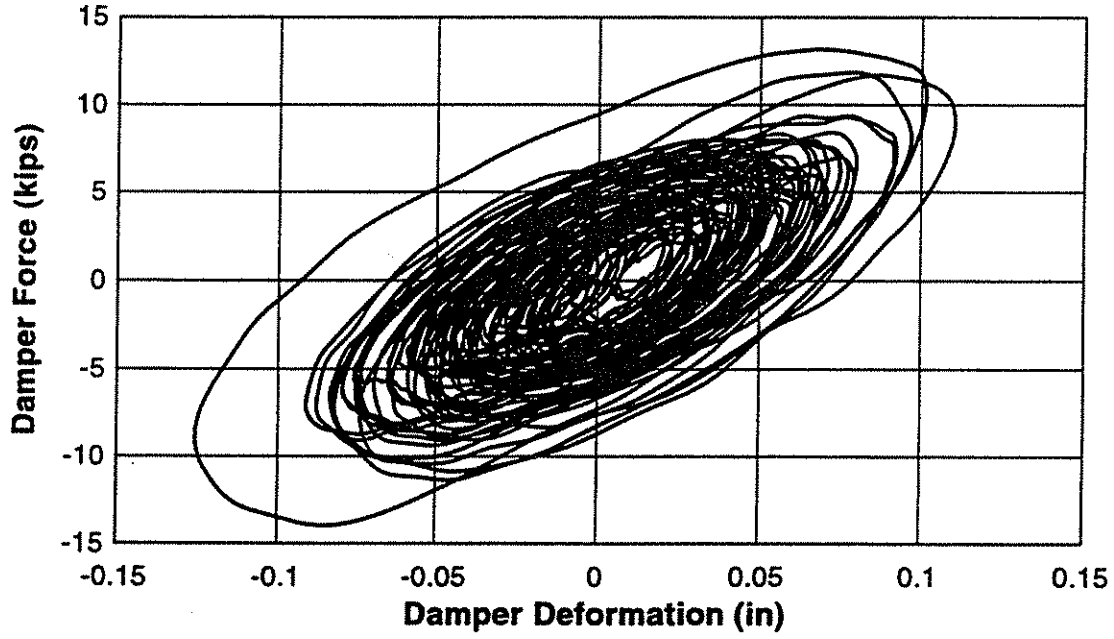

Fig. 7.55 - Example measured force-deformation response for East second story level damper during across-wind test.

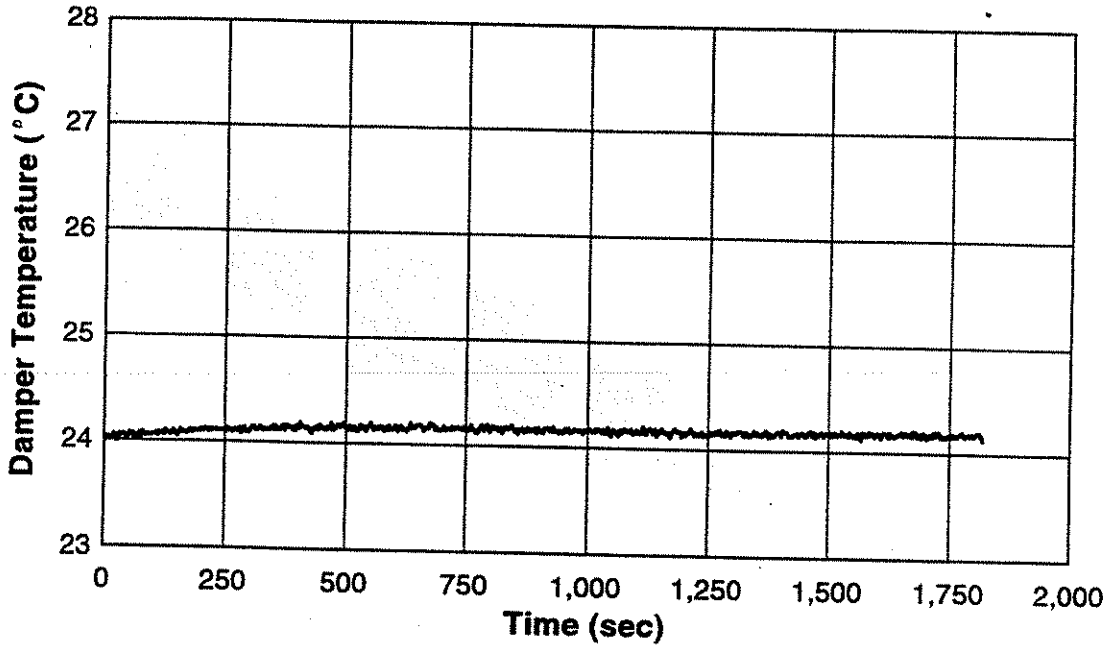

Fig. 7.56 - Measured temperature in East second story level damper during across-wind test.

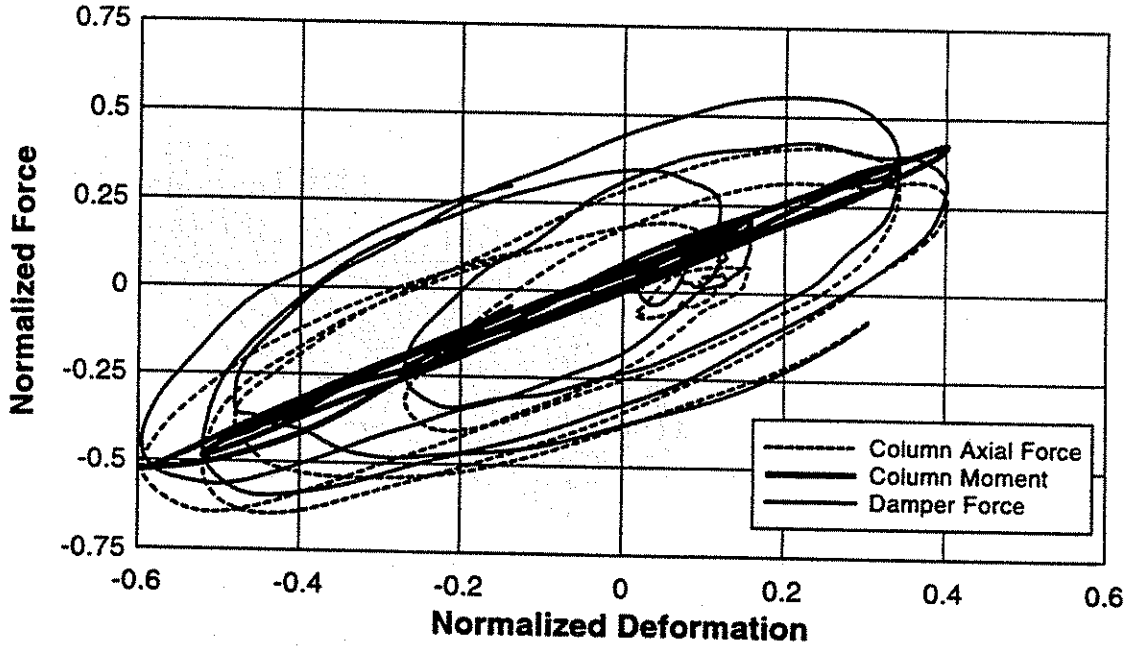

Fig. 7.57 - Example normalized force-deformation responses for East second story column and East second story damper during one minute segment of across-wind test.

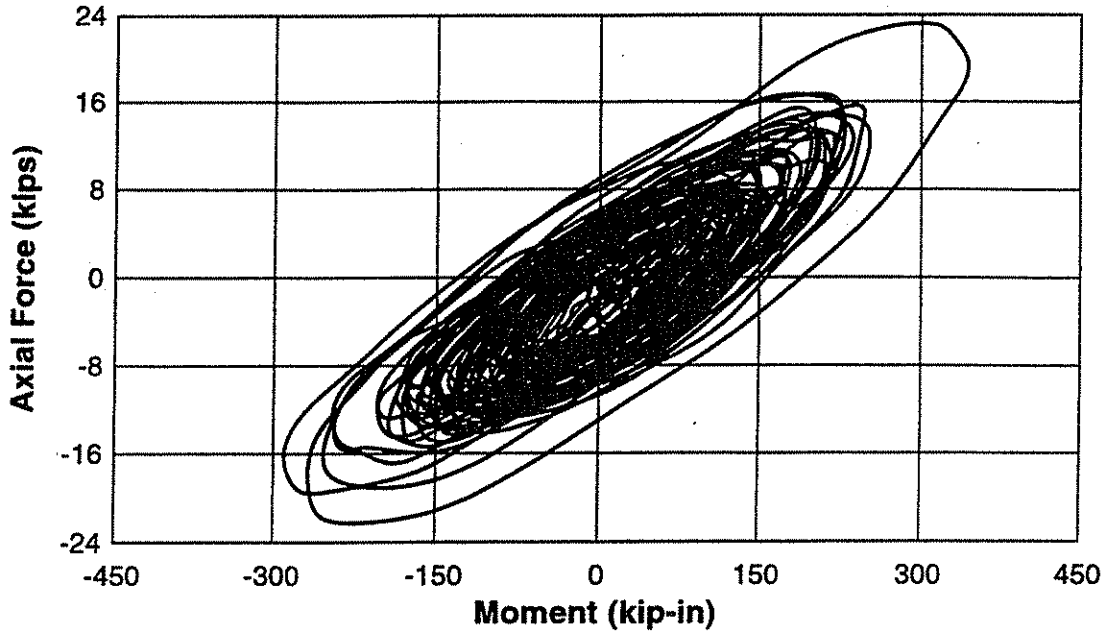

Fig. 7.58 - Example axial force-moment interaction for East second story column during one minute segment of across-wind test.

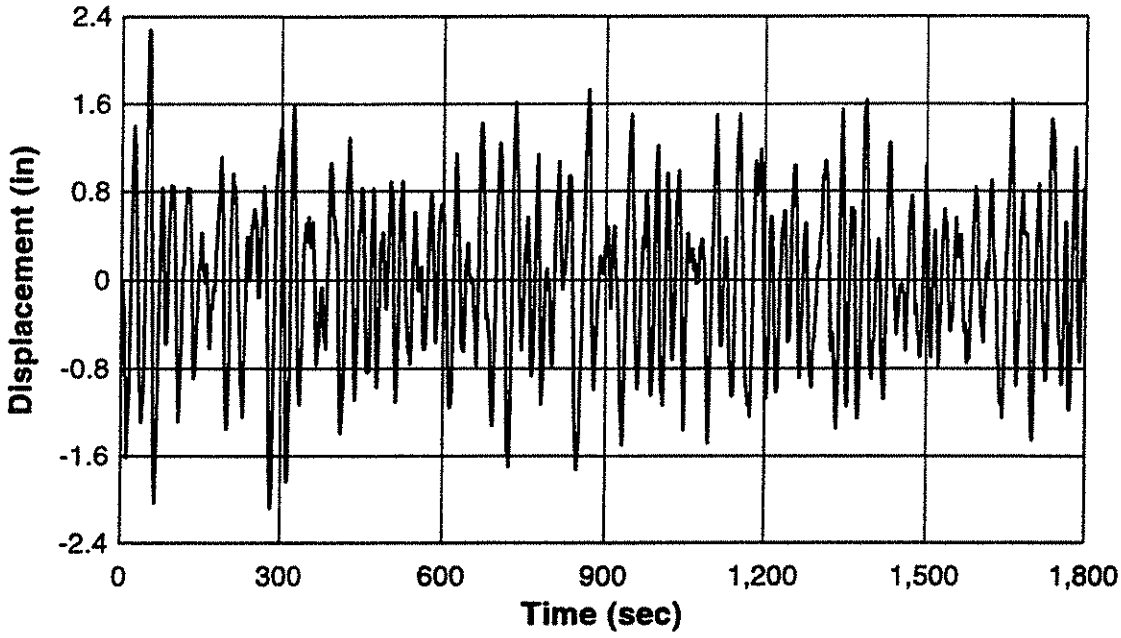

Fig. 7.59 - Predicted roof displacement for across-wind loading of wind prototype frame without VE-dampers.

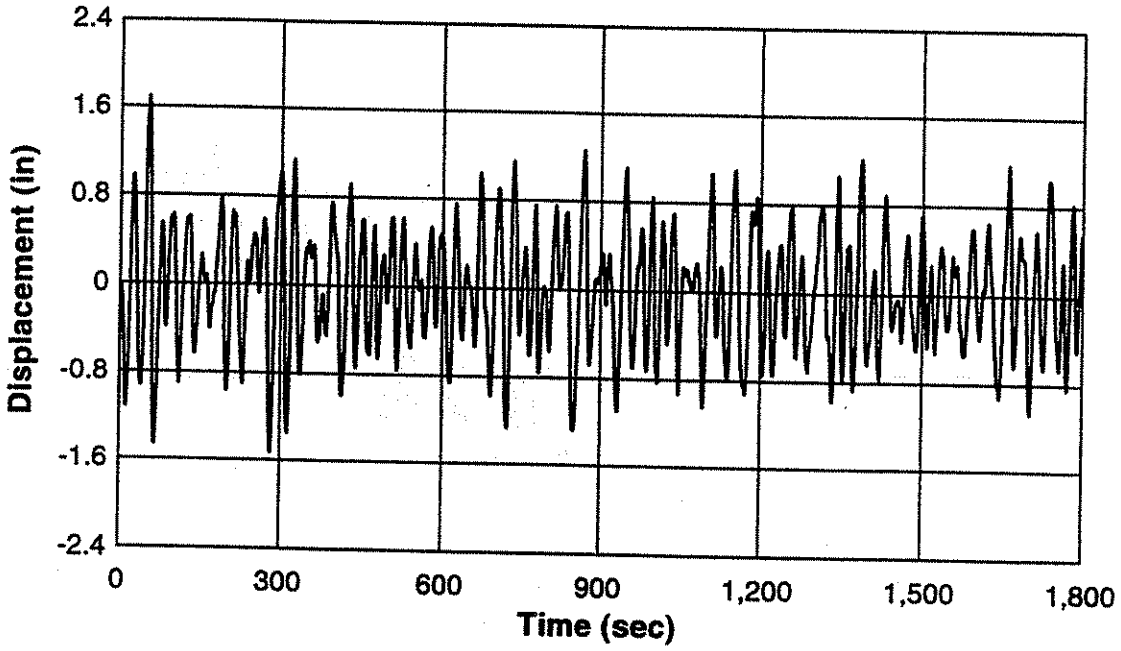

Fig. 7.60 - Predicted roof displacement for across-wind loading of wind prototype frame with VE-dampers.

CHAPTER 8.0 SUMMARY, SIGNIFICANT FINDINGS, AND FUTURE RESEARCH

8.1 Introduction

This chapter presents a summary of the experimental and analytical investigation of the dynamic response of a VE-damped steel frame subjected to harmonic, relaxation, seismic, and wind loading cases. Significant findings from each chapter are presented and recommendations for future research are made.

8.2 Summary and Significant Findings

The application of viscoelastic dampers to steel framed buildings to reduce both seismic and wind induced response has been investigated through full-scale real-time experiments and correlative analyses. An individual damper was tested to determine damper material properties at different initial damper temperatures, loading frequencies, and strain amplitudes. Analytical properties for an available VE-damper finite element model were developed from test results. Correlative analyses of individual damper test results were performed using a

fractional derivative model for the VE-damper behavior. Significant findings of the individual damper investigation were:

- The VE-damper demonstrated the well known frequency, temperature and amplitude sensitivities for VE-materials and VE-material properties (G' and η_d) corresponded well with values provided by the manufacturer.
- Temperature rise within the damper can be reasonably predicted using Eq. 3.6 for short duration loading where heat transfer between the damper and environment are not significant.
- Brace elastic stiffness K_b, which plays an important role in determining damper performance, can be estimated using a simplified analytical procedure as illustrated in Fig. 3.35.
- Damper performance, over a sufficiently wide frequency, temperature, and strain amplitude range, can be predicted using the fractional derivative based VE-finite element for short duration loading cases when no significant heat transfer occurs between the damper and environment. Heat transfer between the VE-damper and environment should be considered to accurately predict damper behavior for long duration loading when significant heat transfer occurs between the damper and environment.

Before installation of the VE-dampers, the bare frame was tested. Experimental results provided the unbraced frame stiffness, damping ratio, and local connection responses. An analytical model of the unbraced frame was developed for use in subsequent time history analyses. Significant findings of the unbraced frame tests were:

- Column base connection stiffness was dependent on the column axial force. The connection base stiffness was modeled using an average stiffness to account for varying axial force level in the column during frame tests. Bolt forces were influenced by column axial forces with less demand on the bolts for higher initial column axial compression.
- The bolted beam-column connections provided stiffness comparable to rigid all welded connections due to the rigid end-zones created by the gusset plates used to attach the VE-dampers to the frame.
- Damping ratio was dependent on frame displacement amplitude. A damping ratio of 2% was selected for analytical frame models which is typical of the measured damping at larger displacement amplitudes and corresponds to the traditionally assumed value for steel frame buildings.
- Cracking was observed along the fillet weld which attached the gusset plates to the beam flanges. The cracking was caused by significant secondary stresses, a large number of cycles, and a poor weld detail.
- An analytical model of the unbraced frame was developed which included the effects of the column base connection stiffness and beam-column connection stiffness. Analyses were conducted which reasonably predicted the experimentally observed overall frame response and local member forces.

After unbraced frame tests, VE-dampers were installed in the frame and sinusoidal and relaxation tests were conducted. Global frame stiffness, damping, local member, and damper responses were determined. Correlative analyses of the sinusoidal test results were performed

using fractional derivative (FDM), global Rayleigh damping (GRD), and local Rayleigh damping (LRD) methods in addition to modified static and portal analysis methods. Significant findings of the basic loading VE-frame investigation were:

- Sinusoidal and relaxation tests provided detailed comprehensive data for global frame response as well as local member force and connection response.
- The overall VE-frame response exhibited frequency and temperature dependent behavior typical of VE-materials. Higher temperatures and lower frequencies resulted in lower VE-frame stiffness. Equivalent viscous damping was more complex and would increase or decrease depending on initial damper temperature and frequency.
- The VE-frame exhibited fairly stable damping ratio through the range of initial temperatures investigated (16 to 32 °C) for the 0.5 hz loading frequency. This frequency is the natural frequency of the seismic prototype frame used as the basis for design of the test specimen as presented in Chapter 6. The VE-frame also exhibited fairly stable damping ratio through the range of loading frequencies investigated for the initial damper temperature of 24 °C.
- Bending moments and shear forces for frame members were typically in-phase with structural displacements. Axial forces in the beams and columns has significant out-of-phase components. The phase lag between moment and axial force in the beams and columns results in peak forces occurring at different instances of time. As a result, determining the critical design load can be difficult. A proposed simplification would conservatively design members assuming the peaks occur simultaneously.
- Elastic brace stiffness was measured and could be reasonably predicted using the method presented in Chapter 3. Accuracy of Eqs. 5.3 and 5.4 for computing the stiffness and loss

factor of the added components was verified by experimental measurements. Added component stiffness was not sensitive to brace stiffness but the added component loss factor was sensitive to the brace stiffness.

- In-plane bending of the added components was measured. Bending was induced by frame drift and connection rotation and is out-of-phase with damper force. Guide bolts provided in the damper design limited through-thickness direction stresses in the VE-material and no apparent adverse effects on damper performance were observed. Brace bending should be considered in design of VE-dampers to limit through-thickness direction stresses on the VE-material. Negligible out-of-plane bending of the added components was observed. Accidental out-of-plane brace bending due to misalignment should be considered in design of VE-dampers to limit through-thickness direction stresses on the VE-material by providing guide bolts.
- The VE-dampers contributed to frame stiffness even after very long relaxation times. This indicates the dampers can provide some level of stiffness for slowly applied loads such as wind and gravity forces.
- Results of the analytical correlations indicated all methods (some only after correction) were reasonably able to predict the frame response and member forces. The GRD method tended to slightly over-predict the equivalent viscous damping of the VE-frame. The GRD, static, and portal methods assume all member forces are in-phase with displacement and required corrections to predict peak member forces. The LRD and FDM were able to model out-of-phase damper forces directly. The FDM had the added advantage of being able to capture the temperature rise effect in the dampers.

- The portal method with correction for peak member force provides an excellent means for preliminary design and analysis of VE-frames considering the simplicity and reasonable results.

A 10-story seismic prototype VE-frame was developed to investigate the earthquake response of a VE-damped steel frame. The design methodology for the prototype frame was described and the unique testing methodology for full-scale real-time testing of the lower three story portion of the prototype VE-frame was presented. Nine different earthquake motions were investigated and measured global frame response, local member forces, VE-damper response, and temperature rise were presented. Analytical correlation of earthquake induced structural response was conducted using fractional derivative, global Rayleigh damping, and local Rayleigh damping methods. Influence of initial damper temperature and damper temperature rise on structural response were addressed. Significant findings of the seismic VE-frame investigation were:

- A prototype 10-story VE-frame was designed using an equivalent lateral force procedure. Design criteria included elastic performance and small drift (<0.0075 rad.) at the reference temperature. Subsequent analysis and testing indicated these goals were achieved and the design methodology provides a practical means of designing VE-damped steel frames.
- A unique methodology was developed which permitted testing of the full-scale lower three story portion of the 10-story prototype VE-damped frame subjected to significant seismic and gravity forces. The testing methodology relies on analysis to predict

structural response to earthquake ground motions. Correlative analyses of small-scale shaking table studies indicate the analysis method reasonably predicts the frame response.

- Measured overall frame response indicated significant energy dissipation by the VE-dampers and elastic response of the steel members. Local member forces and damper behavior were in general reasonably captured by the test method. Column axial forces were significantly lower in the test specimen than the 10-story prototype frame due to overturning moment contributions from lateral forces at the upper stories which could not be implemented by the testing method. Measured temperature rise in the dampers corresponded reasonably well with predicted values.
- Analytical prediction of seismic response for the VE-frame can be adequately performed for short duration earthquake motions using both the LRD and GRD methods. Temperature rise, which may occur during long or intense motions, is not considered by either the LRD or GRD method. As a result, these procedures can seriously under-predict frame response when significant temperature rise occurs.
- Temperature rise during an earthquake does not appear to be a significant factor in determining the VE-frame response for the short duration ground motions investigated as part of this study.
- The VE-frame exhibited some degree of temperature sensitivity, particularly related to frame stiffness. Damping ratio was less sensitive to initial damper temperatures. Adequate structural performance of the VE-frame was achieved by selection of a stiff damper and brace relative to the unbraced frame stiffness which minimized the temperature sensitivity. More stable VE-frame performance could be achieved with a less temperature sensitive material, which is currently under development. The experimental

technique and measured behavior trends as well as analysis tools which have been developed and applied to the temperature sensitive VE-material will be applicable to these new materials.

- Seismic forces and frame drift vary due to shifting of the fundamental period and damping ratio caused by damper temperature changes. An ideal damper design should optimize the VE-frame performance by minimizing the influence of these two factors.

A 10-story wind prototype VE-frame was developed to investigate the wind response of a VE-damped steel frame. A provisional design methodology for the prototype frame was described and the testing methodology for full-scale real-time testing of the lower three story portion of the prototype VE-frame was presented. Along-wind and across-wind responses were investigated and measured overall frame response, local member forces, VE-damper response, and temperature rise were presented. Frame response was predicted using random vibration techniques. Significant findings of the wind VE-frame investigation were:

- A method was developed to test a full-scale VE-damped frame subjected to wind forces which conservatively neglects the contribution of the VE-dampers to frame strength and stiffness.
- Experimental frame response demonstrated VE-dampers provide significant dynamic stiffness and damping even at the relatively low frequencies associated with the wind spectrum.
- Measured temperature rise in the VE-dampers indicated that significant heat convection takes place between the dampers and environment. Heat convection resulted in no

appreciable temperature induced change in damper properties. To accurately predict damper and frame response for long duration events, heat convection should be considered.

- Analytical prediction of along-wind response indicated VE-dampers can effectively reduce the mean square displacement response of the frame. Displacement response reduction mainly results from suppression of the resonant frame response which would otherwise be excited by the wind gusts. Suppression of the resonant response occurs due to the increased damping and moving the natural frequency away from the energy of the wind spectrum by the additional stiffness provided by the VE-dampers. The VE-frame also exhibited significantly lower building accelerations, lower stress ranges, and fewer stress cycles than an equivalent frame without dampers due to suppression of the resonant response component.
- An analytical method was used to predict the along-wind response using random vibration techniques. Results indicate the method can reasonably predict frame response and can be used to determine the amount of reduction associated with the resonant part of the response.
- Analytical prediction of across-wind response indicated VE-dampers reduced the peak displacement response of the frame. Displacement response reduction primarily resulted from the natural frequency shift caused by the additional stiffness provided by the VE-dampers.
- The full role of VE-dampers on across-wind response could not be fully realized due to limitations in the simulation method which relies on an across-wind force spectrum to generate a forcing function, based on wind tunnel studies of building models with small

damping ratios. High damping may have the additional benefit of reducing the across-wind force spectra.

- An analytical method was used to predict the across-wind response using random vibration techniques. Results indicate the method can reasonably predict frame response for the assumed across-wind force spectrum.

8.3 Recommendations for Future Research

The following topics are recommended for future research:

- New VE-materials should be investigated which exhibit reduced temperature sensitivity. The experimental techniques, design methodology, and analysis tools should be applied to these materials to ensure the structural response can be predicted.
- Existing structures with VE-dampers in seismic areas should be instrumented and monitored to permit collection of response data for actual earthquake performance of VE-frames.
- The seismic application of VE-dampers appears to be reaching maturity and implementation of VE-dampers in additional steel frame buildings should be actively pursued. This implementation should include both new construction and retrofit of existing buildings to provide a larger database for assessment of VE-performance during future earthquakes. A less temperature sensitive VE-material may facilitate this implementation.

- The interaction of seismic forces and building drift related to fundamental period and damping ratio shift due to damper temperature changes should be further investigated to optimize structural performance from both strength and stiffness criteria.
- Additional research should be conducted for VE-damper applications to control wind response. Designs should be investigated to determine VE-damper proportions with consideration of heat convection, strain amplitudes, and stiffness to achieve optimum structural performance.
- The effect of dampers on the performance of tall buildings should be further investigated including assessment of existing wind response data for buildings with VE-dampers. The importance of chord and shear deformations on VE-damper effectiveness should be investigated. Wind tunnel studies should be performed for VE-buildings with higher damping ratios and results compared with time history analyses using simulated wind forces to correlate overall frame response. The influence of higher modes should be considered for VE-damped buildings with small damping ratios. Wind tunnel studies should also be conducted to determine the effect of higher damping ratios on across-wind force spectra. Additional research should be performed to determine the properties of VE-dampers in the low frequency range, including both damping and stiffness.

REFERENCES

3M. (1995). "Viscoelastic Dampers for Seismic and Wind Applications," Product Literature, 3M, St. Paul, MN.

Abbas, H. and Kelly, J.M. (1993). "A Methodology for Design of Viscoelastic Dampers in Earthquake Resistant Structures," *Technical Report UCB-EERC-93/09*, University of California at Berkeley, CA.

AIJ. (1990). "Ultimate Strength and Deformation Capacity of Buildings in Seismic Design," Architectural Institute of Japan (AIJ), Tokyo (in Japanese).

Aiken, I. and Kelly, J.M. (1991). "Earthquake Simulator Testing of Two Damping Systems for Multistory Structures," *Proceedings of Damping 1991 Vol. II*, San Diego, CA, FCA-1-FCA-13.

Aiken, I., Kelly, J. M., and Mahmoodi, P. (1990). "The Application of Viscoelastic Dampers to Seismically Resistant Structures," *4th US National Conference on Earthquake Engineering Vol.3*, Palm Springs, CA, 499-506.

Aiken, I. D., Nims, D. K, Wittaker, A. S., and Kelly, J.M. (1993). "Testing of Passive Energy Dissipation Systems," *Earthquake Spectra*, EERI, 9(3), 335-370.

American Institute of Steel Construction (AISC). (1993). "Manual of Steel Construction-Load and Resistance Factor Design," Second Edition, AISC, Chicago, IL.

American Society of Civil Engineers (ASCE). (1996). "ASCE 7-95 Minimum Design Loads for Buildings and Other Structures," ASCE, New York, NY.

Balandra, T. (1993). Vibration of Buildings to Wind and Earthquake Loads, Springer-Verlag, London, England.

Bergman, D. M. and Hanson, R. D. (1993). "Viscoelastic Damping Devices Tested at Real Earthquake Displacements," *Earthquake Spectra*, 9(3), 389-418.

Blackman, R. B., and Tukey, J. W. (1958). The Measurement of Power Spectra, Dover Publications, Inc., New York, NY.

Blevins, R. D. (1990). Flow Induced Vibration, Van Nostrand Reinhold, New York, NY.

Blondet, M. (1993). "Dynamic Response of Two Viscoelastic Dampers," *Report to County of Santa Clara Construction Services Division Project No.ES-2046*, University of California at Berkeley, CA.

Cermak, J. E., Woo, H. G. C., Lai, M. L., Chan, J., and Danielson, S. L. (1993). "Aerodynamic Instability and Damping of a Suspension Roof," Proceedings of the 3rd Asia-Pacific Symposium on Wind Engineering, Hong Kong, 699-704.

Cevallos-Candau, P. J., and Hall, W. J. (1980). "The Commonality of Earthquake and Wind Analysis," Department of Civil Engineering, University of Illinois at Urbana-Champaign, Report No. UILU-ENG-80-2002.

Chang, K.C., Hsu, C. J., Chen, S.G., Chou, F. P., and Lai, M. L. (1994). "Inelastic Seismic Behavior of a 2/5 Scale Steel Frame with Added Viscoelastic Dampers," *First World Conference on Structural Control*, Los Angeles, CA.

Chang, K. C., Lai, M. L., Soong, T. T., Oh, S. T., Hao D. S., and Yeh, Y. C. (1993a). "Seismic Behavior and Design Guidelines for Steel Frame Structures with Added Viscoelastic Dampers," *Technical Report NCEER-93-0009*, State University of New York at Buffalo, NY.

Chang, K. C., Soong, T. T., Lai, M. L., and Nielsen, E. J. (1993b). "Development of a Design Procedure for Structures with Added Viscoelastic Dampers," *ATC-17-1 Seminar*, San Francisco, CA, 473-484.

Chang, K. C., Soong, T. T., Oh, S. T., and Lai, M. L., (1995). "Seismic Behavior of Steel Frame with Added Viscoelastic Dampers," *Journal of Structural Engineering*, ASCE, 121(10), 1418-1426.

Chang, K. C., Soong, T. T., Oh, S. T., and Lai, M. L. (1992). "Seismic Response of Steel Frame Structures with Viscoelastic Dampers," *10th World Conference on Earthquake Engineering*, Madrid, Spain, Vol. 9, 5169-5173.

Chang, K. C., Soong, T. T., Oh, S. T., and Lai, M. L., (1991). "Seismic Response of a 2/5 Scale Steel Structure with Added Viscoelastic Dampers," *Technical Report NCEER-91-0012*, State University of New York at Buffalo, NY.

Chou, F. P. (1994). "Seismic Behavior of Steel Frames with Added VE-Dampers," Masters Thesis, Department of Construction Engineering, National Taiwan Institute of Technology (in Chinese).

Clough, R. W. and Penzien, J. (1993). Dynamics of Structures, McGraw Hill, Inc., New York, NY.

Davenport, A.G. (1961a). "The Spectrum of Horizontal Gustiness Near the Ground in High Winds," *Quarterly Journal of the Royal Meteorological Society*, 87, 194-211.

Davenport, A.G. (1961b). "The Application of Statistical Concepts to the Wind Loading of Structures," *Proceedings, Institution of Civil Engineers*, 19, 449-472.

Ferry, J. D. (1980). Viscoelastic Properties of Polymers, John Wiley and Sons, New York, NY.

Gemant, A. (1936). "A Method of Analyzing Experimental Results Obtained from Elasto-Viscous Bodies," *Physics*, 7, 311-317.

Higgins, C., Chen, S. J., and Chou, F. P. (1995). "Testing and Analysis of a Steel Frame with Viscoelastic Dampers," *Eleventh World Conference on Earthquake Engineering*, Acapulco, Mexico.

Hirsch, G. H. (1994). "Damping Measures to Control Wind-Induced Vibrations," in *Wind-Excited Vibrations of Structures*, H. Sockel (ed.), Springer-Verlag, New York.

Houghton, E. L. and Carruthers, N. B. (1976). Wind Forces on Buildings and Structures, J. Wiley and Sons, New York, NY.

Inaudi, J. A., Zambrano, A. and Kelly, J. M. (1993). "On the Analysis of Structures with Viscoelastic Dampers," *Technical Report UCB-EERC-93/06*, University of California at Berkeley, CA.

Jeary, A. P., and Ellis, B. R. (1984). "On Predicting the Response of Tall Buildings to Wind Excitation," *Wind Engineering 1983, Proceedings of the Sixth International Conference on Wind Engineering*, J. D. Holmes, P. S. Jackson, and W. H. Melbourne (ed.), Elsevier, New York, 173-182.

Kareem, A. (1984). "Model for Predicting the Across-Wind Response of Buildings," *Journal of Engineering Structures*, 6, 136-141.

Kasai, K., Huang, Y., and Wada, A. (1997a). "Hysteretic Model of Visco-Elastic Damper for Long Duration Loading," *AIJ Conference*, Kanto-Branch, Japan (in English).

Kasai, K., Huang, Y., and Wada, A. (1997b). "Two Viscoelastic Damper Nonlinear Models: Seismic Load Model and Wind Model," *ASME/ASCE Mechanics Conference (McNU '97)*, Evanston, Illinois.

Kasai, K., Fu, Y. M., and Watanabe, A. (1997c). "Two Types of Passive Control Systems for Seismic Damage Mitigation," *Journal of Structural Engineering*, ASCE, (to be published).

Kasai, K., and Fu, Y. M. (1995). "Seismic Analysis and Design Using Viscoelastic Dampers," *A New Direction in Seismic Design*, Tokyo, 113-140.

Kasai, K., and Munshi, J. A. (1994). "Seismic Response of Viscoelastic Frame with Yielding Members," *5NCEE* , Chicago, IL, 253-262.

Kasai, K., Munshi, J. A., Lai, M. L., and Maison, B. F. (1993). "Viscoelastic Damper Hysteretic Model: Theory, Experiment, and Application," *Proceedings, ATC 17-1 Seminar on Seismic Isolation, Passive Energy Dissipation, and Active Control*, Applied Technology Council, Vol. 2, San Francisco, CA.

Kasai, K. and Munshi, J. A. (1994). "Seismic Response of Viscoelastic Frame with Yielding Members," *5NCEE* , Chicago, IL, 253-262.

Kasai, K., and Popov, E. P. (1986). "A Study of Seismically Resistant Eccentrically Braced Frames," *EERC Report 86-01*, University of California, Berkeley, CA.

Keel, C. and Mahmoodi, P. (1986). "Design of Viscoelastic Dampers for the Columbia Center Building," *Proceedings ASCE Structures Congress* , Seattle, WA, 66-82.

Kirekawa, A., Ito, Y., and Asano, K. (1992). "A Study of Structural Control Using Viscoelastic Material," *Proceedings, 10th World Conference on Earthquake Engineering*, Madrid, Spain, 2047-2054.

Koh, C. G., and Kelly, J. M. (1990). "Application of Fractional Derivatives to Seismic Analysis of Base-Isolated Models," *Earthquake Engineering and Structural Dynamics*, 19(2), 229-241.

Lai, M. L., Chang, K. C., Soong, T. T., Hao, D. S., and Yeh, Y. C. (1995). "Full Scale Viscoelastically Damped Steel Frame," *Journal of Structural Engineering*, ASCE, 121(10), 1443-1447.

Lai, M. L., Lu, P., Lunsford, D. A., Kasai, K., and Chang, K. C. (1996). "Viscoelastic Damper: A Damper with Linear or Nonlinear Material?," *Eleventh World Conference on Earthquake Engineering*, Acapulco, Mexico.

Lin, R. C., Liang, T. T., Soong, T. T., Zhang, R. H., and Mahmoodi, P. (1991). "An Experimental Study on Seismic Behavior of Viscoelastically Damped Structures," *Engineering Structures*, 13, 75-84.

Mahmoodi, P. (1969). "Structural Dampers," *ASCE Journal of Structural Division*, ASCE, 95(8), 1661-1672.

Mahmoodi, P., and Keel, C. (1986). "Performance of Viscoelastic Structural Dampers for the Columbia Center Building," *Proceedings ASCE Structures Congress* , Seattle, WA, 83-106.

Mahmoodi, P., Robertson, L., Yontar, M., Moy, C., and Feld, L. (1987). "Performance of Viscoelastic Dampers in the World Trade Center Towers," *Proceedings ASCE Structures Congress* , Orlando, FL.

Maison, B. F. (1992). "PC-ANSR: A Computer Program for Nonlinear Structural Analysis," National Information Service for Earthquake Engineering, Berkeley, CA.

Mander, J. B., Chen, S. S., Shah, K. M., and Madan, A. (1992). "Investigation of Light Pole Base Integrity," Department of Civil Engineering, State University of New York at Buffalo.

Miranda, E. (1993). "Evaluation of Site Dependent Inelastic Seismic Design Spectra," *Journal of Structural Engineering*, ASCE, 119(5), 1319-1338.

Munshi, J. A., and Kasai, K. (1994). "Modal Analysis Procedures for Viscoelastic Frames," *5NCEE* , Chicago, IL, 1055-1064.

Nashif, A. D., Jones, D. I., and Henderson, J. P. (1985). Vibration Damping, John Wiley and Sons, New York, NY.

National Earthquake Hazards Reduction Program (NEHRP). (1994). "NEHRP Recommended Provisions for Seismic Regulations for New Buildings," Building Seismic Safety Council, Washington, D.C.

Ontario Ministry of Transportation. (1991). "Ontario Highway Bridge Design Code (Bridge Code)," Ontario Ministry of Transportation, Toronto, Canada.

Robertson, L. E. (1975). "The Relevance of Static and Dynamic Loading to Building Systems," *Proceedings of the Fourth International Conference on Wind Effects on Buildings and Structures*, Cambridge University Press, 777-783.

Saunders, J. W., and Melbourne, W. H. (1975). "Tall Rectangular Building Response to Cross-Wind Excitation," *Proceedings of the Fourth International Conference on Wind Effects on Buildings and Structures*, Cambridge University Press, 369-379.

Sause, R., Hemmingway, G., and Kasai, K. (1994). "Simplified Seismic Response Analysis of Viscoelastic-Damped Frame Structures," *5NCEE* , Chicago, IL, 834-848.

Seed, H. B., Ugas, C., and Lysmer, J. (1976). "Site-Dependent Spectra for Earthquake-Resistant Design," *Bulletin of the Seismological Society of America*, 66(1), 221-241.

Shinozuka, M. (1971). "Simulation of Multivariate and Multidimensional Random Processes," *The Journal of the Acoustical Society of America*, 49(1), 357-367.

Shiotani, M., and Iwatani, Y. (1971). "Correlations of Wind Velocities in Relation to the Gust Loadings," *Proceedings, Wind Effects on Buildings and Structures*, Saikon, Co. Tokyo, 57-67.

Simiu,E., and Scanlan, R. H. (1996). Wind Effects on Structures, John Wiley and Sons, New York, NY.

Skilling, J. B., Tschanz, T., Isyumov, N., Loh, P., and Davenport, A. G. (1986). "Experimental Studies, Structural Design, and Full-Scale Measurements for the Columbia Seafirst Center, " in *Building Motion in Wind*, N. Isyumov and T. Tschanz, (ed.), ASCE, NY.

Soong, T. T. (1994). "Seismic Retrofit Using Viscoelastic Dampers," *NCEER Bulletin*, 8(1), 2-3.

Soong, T. T., and Lai, M. L. (1991). "Correlation of Experimental Results with Predictions of Viscoelastic Damping for a Model Structure," *Proceedings of Damping '91*, San Diego, CA, Vol. II, FCB1-FCB9.

Tsai, C. S., and Lee, H. H. (1993). "Application of Viscoelastic Dampers to High-Rise Buildings," *Journal of Structural Engineering*, ASCE, 119 (4), 1222-1233.

"Uniform Building Code." (1994). International Conference of Building Officials, Whittier, CA.

Vickery, B. J. (1971) "On the Reliability of Gust Loading Factors," *Civil Engineering Transactions*, April, 1-9.

Wolfram, S. (1996). The Mathematica Book, 3rd ed., Wolfram Media/Cambridge University Press, Illinois.

Zhang, R. H., and Soong, T. T. (1992). "Seismic Design of Viscoelastic Dampers for Structural Applications," *Journal of Structural Engineering*, ASCE, 118(5), 1375-1392.

APPENDIX A

The fractional derivative constitutive rule [Kasai *et al.*, 1993] was defined in Chapter 2 as:

$$\tau(t)+aD^{\alpha}\tau(t)=G\left[\gamma(t)+bD^{\alpha}\gamma(t)\right] \qquad [A.1]$$

where a and b are constants, G = an elastic parameter, and α is the fractional derivative order ($0 < \alpha < 1.0$), D^{α} is the fractional derivative operator, $D^{\alpha}\tau(t)$ and $D^{\alpha}\gamma(t)$ are defined according to the Riemann-Liouville integral. Using the fractional derivative rule, it has been shown [Kasai *et al.*, 1993] that the storage modulus G' and loss modulus G'' can be expressed as:

$$G' = G\frac{\left[1+b\omega^{\alpha}\cos(\alpha\pi/2)\right]\left[1+a\omega^{\alpha}\cos(\alpha\pi/2)\right]+\left[ab\omega^{2\alpha}\sin^{2}(\alpha\pi/2)\right]}{\left[1+a\omega^{\alpha}\cos(\alpha\pi/2)\right]^{2}+\left[a\omega^{\alpha}\sin(\alpha\pi/2)\right]^{2}} \qquad [A.2]$$

$$G'' = G\frac{\left[b\omega^{\alpha}\sin(\alpha\pi/2)\right]\left[1+a\omega^{\alpha}\cos(\alpha\pi/2)\right]-\left[a\omega^{\alpha}\sin(\alpha\pi/2)\right]\left[1+b\omega^{\alpha}\cos(\alpha\pi/2)\right]}{\left[1+a\omega^{\alpha}\cos(\alpha\pi/2)\right]^{2}+\left[a\omega^{\alpha}\sin(\alpha\pi/2)\right]^{2}} \qquad [A.3]$$

and the loss factor η as:

$$\eta=\frac{G''}{G'}=\frac{[b-a]\omega^{\alpha}\sin(\alpha\pi/2)}{1+[a+b]\omega^{\alpha}\cos(\alpha\pi/2)+ab\omega^{2\alpha}} \qquad [A.4]$$

Implementation of the fractional derivative model (FDM) for the stress-strain behavior of a VE-material requires determination of the model parameters. This is performed using harmonic test data of a VE-material at a selected reference temperature, with small strain

amplitudes, and a range of frequencies. Small strains, equal to 5%, are used to determine the model parameters independent of temperature rise. The reference temperature of 24 °C was selected based on convention. From Eq. A.4, values of η must be known from sinusoidal tests at 5% strain and reference temperature of 24 °C for at least three different frequencies ($\eta(\omega_1)$, $\eta(\omega_2)$, and $\eta(\omega_3)$) to determine the parameters a_{ref}, b_{ref}, and α_{ref}. Equations are written for each frequency as:

$$\frac{[b-a]\omega_1^{\alpha}\sin(\alpha\pi/2)}{1+[a+b]\omega_1^{\alpha}\cos(\alpha\pi/2)+ab\omega_1^{2\alpha}}-\eta(\omega_1)=0 \qquad \text{[A.5a]}$$

$$\frac{[b-a]\omega_2^{\alpha}\sin(\alpha\pi/2)}{1+[a+b]\omega_2^{\alpha}\cos(\alpha\pi/2)+ab\omega_2^{2\alpha}}-\eta(\omega_2)=0 \qquad \text{[A.5b]}$$

$$\frac{[b-a]\omega_3^{\alpha}\sin(\alpha\pi/2)}{1+[a+b]\omega_3^{\alpha}\cos(\alpha\pi/2)+ab\omega_3^{2\alpha}}-\eta(\omega_3)=0 \qquad \text{[A.5c]}$$

These three equations are solved simultaneously to calculate a, b, and α. For the present study, a software program Mathematica 3.0 [Wolfram, 1996] was used to solve the set of equations. Using $\eta(\pi/5)$=1.12, $\eta(\pi)$=1.31, and $\eta(2\pi)$=1.35, solving Eqs. A.5a, A.5b, and A.5c simultaneously produces a_{ref}=0.003698, b_{ref}=7.537, α_{ref}=0.622. The parameter G is now determined from Eq. A.2 using the values of a_{ref}, b_{ref}, and α_{ref} determined above. G is computed at several different frequencies to compute an average value. Using G′ at the four test frequencies of $\pi/5$, π, 2π, and 4π (corresponding to the loading frequencies of 0.1, 0.5, 1.0, and 2.0 hz), four G values are computed and the average taken. Following determination of the FDM parameters, several analyses are performed for different loading frequencies at the reference temperature and 5% strain to ensure the parameters are reasonable. Recognizing there is some variability associated with η and G′ values determined from

experimental measurements, slight adjustments to the FDM parameters can be made to ensure analyses reflect experimental responses. For the test data in Chapter 2, G=14.0 psi.

To account for material property changes of the VE-material at different temperatures, the temperature shifting factor $c(\theta)$ must be determined. The shifting factor is computed according to Ferry [1980]:

$$c = e^{-p_1(\theta-\theta_{ref})/(p_2+\theta-\theta_{ref})} \qquad [A.6]$$

where p_1 and p_2 are constants depending on the specific VE-material. This is included by relating the constants a and b for the fractional derivative model to the values at the reference temperature [Kasai *et al.*, 1993] as:

$$a = a_{ref} c^{\alpha} \qquad [A.7]$$

$$b = b_{ref} c^{\alpha} \qquad [A.8]$$

Substituting Eq. A.7 and A.8 into Eq. A.2 results in:

$$G\frac{\left[1+b_{ref}c^{\alpha}\omega^{\alpha}\cos(\alpha\pi/2)\right]\left[1+a_{ref}c^{\alpha}\omega^{\alpha}\cos(\alpha\pi/2)\right]+\left[a_{ref}c^{\alpha}b_{ref}c^{\alpha}\omega^{2\alpha}\sin^2(\alpha\pi/2)\right]}{\left[1+a_{ref}c^{\alpha}\omega^{\alpha}\cos(\alpha\pi/2)\right]^2+\left[a_{ref}c^{\alpha}\omega^{\alpha}\sin(\alpha\pi/2)\right]^2}-G'=0 \qquad [A.9]$$

Using the computed parameters a_{ref}=0.003698, b_{ref}=7.537, α_{ref}=0.622, and G=14.0 psi, with test data at 5% strain for G' at different initial temperatures, c values are computed by determining the root of Eq. A.9 for each loading frequency ($\pi/5$, π, 2π, and 4π). Example computed c values are plotted in Fig. 3.44 for the 0.1 hz loading frequency. Parameters p_1 and p_2 are determined by performing a nonlinear regression of the c data at each loading frequency to produce a best fit curve of the form of Eq. A.6. Nonlinear curve-fitting was performed using Mathematica 3.0. Final values for p_1 and p_2 were determined by averaging

values computed for each frequency. Following determination of the temperature shifting parameters, several analyses are performed for different temperatures to ensure the coefficients are reasonable. Again, considering the variability associated with test data, slight adjustments to the parameters can be made to ensure analyses reflect experimental responses. For the test data in Chapter 3, the final values p_1=17.8755 and p_2=88.5054 were determined.